MATERIALS SCIENCE & ENGINEERING

A

Structural Materials: Properties, Microstructure and Processing

Editor-in-Chief:
H. Herman

19970609 117

DTIC QUALITY INSPECTED 3

ELSEVIER

MATERIALS SCIENCE & ENGINEERING

A

Structural Materials: Properties, Microstructure and Processing

ELSEVIER

DTIC QUALITY INSPECTED 3

Contents

Contents

The manuscript for thses Proceedings were received by the Publishers: June 1995.

Preface

In the past few years, nanostructured materials have received a great deal of attention for their unusual solid state properties for structural, magnetic, catalytic, electronic and optical applications. The contents of this special volume comprise the proceedings of a symposium on "Engineering of Nanostructured Materials" held in Boston, MA, USA during November 28–30, 1994. The papers in this volume present recent advances in the processing of nanocrystals as bulk solid systems, and the tailoring of nanostructured materials for engineering of properties on the nanometer-scale. Various issues on grain boundary structure, compositional flexibility, grain and pore size control, as well as surface reactivity of these unique materials are discussed for design of materials characteristics.

The symposium organizers have served as guest editors for this special volume. We wish to express our gratitude to the reviews of the manuscripts, and to the participants of the symposium, especially the invited speakers and the session chairs. We are grateful to Office of Naval Research and Nanophase Technologies Corporation for sponsoring this symposium. The help of Kenneth J. Bryden, Lei Zhang, Linda L. Mousseau and Ellen L. Weene of MIT in preparation of this volume is also appreciated.

Jackie Y. Ying, Massachusetts Institute of Technology
Merrilea J. Mayo, Pennsylvania State University
Yet-Ming Chiang, Massachusetts Institute of Technology
Lawrence T. Kabacoff, Office of Naval Research
Guest Editors

Young's modulus of nanocrystalline Fe measured by nanoindentation

G.E. Fougere[a,1], L. Riester[b], M. Ferber[b], J.R. Weertman[a] R.W. Siegel[c]

[a]*Department of Materials Science and Engineering, Northwestern University, Evanston, IL 60208, USA*
[b]*High Temperature Materials Laboratory, Oak Ridge National Laboratory, Oak Ridge, TN 37831, USA*
[c]*Materials Science Division, Argonne National Laboratory, Argonne, IL 60439, USA*

Abstract

Nanoindentation techniques were used to measure Young's modulus for nanocrystalline Fe samples produced by inert-gas condensation and warm consolidation. The samples had grain sizes of 4–20 nm and residual porosity of 2–30% calculated relative to conventional Fe. Values of Young's modulus for the nanocrystalline Fe are reduced relative to that of conventional, fully dense Fe. A review of Young's modulus for other nanocrystalline materials showed similar trends. Published results for porous conventional Fe showed similar reductions in Young's modulus for samples with comparable porosity levels. The observed reductions in Young's modulus for both the nanocrystalline and the conventional porous Fe can be described adequately by several theories utilizing spheroidal porosity.

Keywords: Young's modulus; Nanoindentation; Iron

1. Introduction

The elastic modulus of a material is an indication of the atomic binding forces and therefore the elastic properties of a material under loading. For a full dense material in the elastic regime, Hooke's law relates the applied stress σ to the resultant strain ε by Young's modulus E_0:

$$\sigma = E_0 \varepsilon \tag{1}$$

Materials with residual porosity may not exhibit the expected Young's modulus E_0 for bulk materials that are fully dense. Pores and flaws from processing reduce the effective load-bearing area in a material, which in turn increases the effective stress and changes the elastic response of the material. Pores with crack-like features also concentrate the stress because of their shape and their orientation relative to the stress axis. A theory [1] developed to explain the empirical results of reduced moduli of porous materials relates the apparent reduced Young's modulus E, to the value E_0 for a fully dense material by an exponential function:

$$E = E_0 \exp(-\beta p) \tag{2}$$

where p is the volume fraction of pores and β is a factor between 2 and 4. The value of β appears to be dependent upon the material and the processing and to result from a specific number of open and closed pores. The limitations of this exponential relationship are the narrow range of porosities [2,3] over which it is valid and its applicability only at small values of p. To address these limitations, other power law and double-exponential relationships [3–6] have been developed, and these relations agree with both boundary conditions for the limits of p, operate over wider ranges of porosity and often provide a better fit to the experimental data.

Recently, Boccaccini et al. [7] have developed a universal model for porous metals, ceramic and glasses to correlate the apparent modulus with porosity and the model appears to agree well with experimental data for these various materials. The model is based on earlier theoretical work on two-phase composite materials [8]. The apparent Young's modulus E is related to the value E_0 for a fully dense material and the volume fraction of pores p through the following:

$$E = E_0(1 - p^{2/3})^{1.21s} \tag{3}$$

where the power factor s is

$$s = \left(\frac{z}{x}\right)^{1/3}\left\{1 + \left[\left(\frac{z}{x}\right)^{-2} - 1\right]\cos^2 \alpha_d\right\}^{1/2} \tag{4}$$

---

[1] Present address: Motorola, Inc., Automotive, Energy and Controls Group Northbrook, IL 60062, USA

Table 1
Young's modulus results for nanocrystalline materials

Material	Grain size (nm)	Synthesis	p (%)	E (GPa)	E_0 (GPa)	E/E_0 (%)	E test[a]	Reference
CaF$_2$	7	IGC	Not specified	38	111	34	S, T	[9]
Pd	8	IGC	Not specified	88	123	72	S, T	[9]
Mg	12	IGC	Not specified	39	41	95	S, T	[9]
ZnO	24–140	IGC	10–15	35–100	123.5	28–81	N	[10]
TiO$_2$	12–243	IGC	10–25	40–240	284	14–85	N	[11]
Cu	25 and 50	IGC	Not measured	36–45	130	28–35	T	[12]
Pd	5–15	IGC	4–17	21–66	120	18–55	T	[12]
Ag	60	IGC	3	64	80	80	S	[13]
Ni–1.2 wt.% P	7	Electroplating	0	225	221	102	T	[14]

[a] Young's modulus measured by sound velocity measurements (S), by tensile testing (T) and by nanoindentation experiments (N).

The model assumes closed porosity and uses "spheroidal" pores with a known aspect ratio z/x. The pores impart different effects based on their relative orientation to the stress axis, described by the angle α_d. The orientation factor $\cos^2 \alpha_d$ is equivalent to 0.31 for material with a random orientation of pores, which correspond to an α_d of 56°. This theory was shown to be valid over a wide range of porosities and materials, although the experimental data deviate from the theory when the pores are interconnected at high values of p.

A possible density decrement associated with the numerous interfaces in nanocrystalline (n-) materials could also affect their Young's moduli. The intrinsic structure of nanocrystalline materials consists of small dense grains and a comparable volume fraction of interfaces (e.g. grain or phase boundries and triple junctions). Nanocrystalline materials may also contain extrinsic defects from processing (e.g. flaws and pores). Table 1 contains Young's modulus data for a variety of nanocrystalline metals and ceramics produced by inert gas condensation (IGC) or electroplating.

The majority of the nanocrystalline materials showed significant reductions in their Young's moduli, and a variety of reasons were proposed. The results for CaF$_2$, Mg and Pd [9] were ascribed to the increased average interatomic distances in the grain boundary regions; however, the level of porosity in the samples in [9] was not specified. The E results for n-ZnO [10] and n-TiO$_2$ [11] were attributed to the porosity in their samples, and porosity was considered as a possible cause of the decrement in E for n-Pd and n-Cu in [12], although the accuracy of the measurement of E for the metals was questioned by the authors. The reduced Young's modulus for n-Ag [13] was hypothesized to result either from a combination of internal stresses enhancing intergrain sliding or from anelastic effects from a reversible stress-induced transformation.

The significant porosity commonly present in nanocrystalline materials is expected to have a strong effect on their Young's moduli. In contrast with the majority of the data in Table 1, n-NiP, produced by electroplating with negligible porosity levels, showed an E value which was almost identical to that of fully dense conventional Ni [14]. This result for n-NiP led Krstic et al. [15] to develop a model for the elastic response of nanocrystalline materials compacted from powders that is based on the presence of extrinsic defects (e.g. pores and cracks) in these materials. Krstic et al. extended the theory of porous solids (cf. Eq. (2)) to include a pore radius, R and a crack of length S extending from the pore surface in the following relation:

$$E = E_0 \left[1 + \left(\frac{4p(1-v^2)}{\pi} \right) \phi \right]^{-1} \tag{5}$$

where v is Poisson's ratio and the factor ϕ is calculated from the following:

$$\phi = \left(1 + \frac{S}{R} \right)^3 + \frac{9}{2(7-5v)(1+S/R)^2} + \frac{4-5v}{2(7-5v)} \tag{6}$$

Krstic et al. reported good agreement for their theory with the results for n-Pd tested in tension [12]. The stress concentration associated with the pore and the crack tip stress field during crack opening under load resulted in a drastic reduction in the apparent Young's modulus.

The objective of the present study was to examine the effects of porosity on Young's modulus for n-Fe with average grain sizes of about 4–20 nm. The porosity level in these samples ranges from 2 to 30%. Therefore the grain size varies by a factor of 5, and the porosity level changes by a factor of 15. The results for n-Fe with varying grain sizes and porosity levels are contrasted to those for fully dense and for porous Fe with conventional grain sizes. The respective elastic behaviors of the Fe samples are modeled in terms of p.

2. Experimental procedures

The n-Fe samples were made by IGC and warm compaction at temperatures ranging from 25 to 294 °C [16]. The samples were characterized to determine their grain size, density, and composition, as described in [16]. The aspect ratio of the pores in these samples was determined by analyzing micrographs taken with the Hitachi S4500 field-emission scanning electron microscope at Oak Ridge National Laboratory and using an image analysis program. The calculated pore aspect ratio x/z was about 3.

The elastic response of the Fe samples was studied using nanoindentation [17,18]. The nanoindentater has a displacement resolution of 0.16 nm and a load resolution of 0.3 μN, allowing precise measurements of the depth h and load w. A nanoindenter constantly records the displacement of the indenter and the load during the loading and unloading to form an indent at a specified depth. The slope dw/dh of the unloading curve from a nanoindentation indent can be used to measure E. This method of analysis assumes that, during the initial unloading, only elastic recovery of the indent occurs, and the area of the indent remains in perfect contact with the indenter [17]. (Beyond this point, the unloading curve becomes curved as the material laterally surrounding the indent elastically recovers as well). The slope dw/dh is then calculated from a linear fit to the first portion of the unloading curve and extrapolated to the depth at zero load [17]. The slope is related to the reduced modulus E_r and the plastic area A of the indent, calculated from the extrapolated indent depth at zero load, through the following:

$$\frac{dw}{dh} = 2 \left(\frac{A}{\pi} \right)^{1/2} E_r \qquad (7)$$

The reduced modulus E_r represents a composite measure of the compliance of the sample and of the indenter:

$$\frac{1}{E_r} = \frac{1 - v_i^2}{E_i} + \frac{1 - v_s^2}{E_s} \qquad (8)$$

The properties of the diamond indenter used were as follows: Poisson's ratio $v_i = 0.07$; Young's modulus $E_i = 800$ GPa [18]. The value of the Poisson's ratio v_s used for the Fe samples was 0.293. This method has been used to measure E for most materials to within 3% of the literature values [17–19].

Ten nanocrystalline samples and one coarse-grained Fe sample were mounted and vibratory polished to a 0.05 μm finish. The polishing was done with caution to minimize the impact and the loading to reduce the amount of deformation during polishing. A Nano Instruments, Inc. nanoindenter at the Oak Ridge National Laboratory was used for these experiments. The depth and rates of loading and unloading were pro-grammed and a pattern for a set of indents was established. Each sample was tested in an area of nine indents spaced at least 20 μm apart. Each indent was loaded to four different target depths (i.e. 100, 300, 500 and 700 nm) and then unloaded, providing 36 unloading slopes per sample for the determination of E. The data were corrected for the imperfect geometry associated with blunting of the indenter tip by knowledge of the cross-sectional area of the indenter as a function of the distance from its tip [19], and the data were also corrected for the compliance of the machine [17].

3. Results

The coarse-grained, fully dense Fe standard was first tested twice to determine the accuracy of the nanoindenter and the associated analysis in calculating Young's modulus. The results for the coarse-grained Fe sample are shown in Fig. 1 as the data at $p = 0$. The mean value, 217 GPa, agreed to within about 3% of the literature value of 211 GPa for conventional Fe, and the standard deviation of these measurements was about 10%. (Single-crystal Fe is highly anisotropic with an E value equal to 275 GPa in the [111] direction and 125 GPa in the [100] direction.) The E data for the n-Fe samples range from about 90 to 233 GPa with a standard deviation of 10–15%. The porosity of the samples appears to be the dominant feature controlling Young's modulus in the grain size regime studied.

Fig. 1 represents the data for the n-Fe samples (filled squares and $p > 0$) plotted with the theoretical predictions from Eqs. (3)–(6) [8,15]. The measured Young's modulus values for the n-Fe samples are plotted against the volume fraction of pores p which was calculated from the measured density relative to the theoretical density of Fe. The p values of the n-Fe samples range from 0.02 to 0.30 while the average grain size ranges from 4 to 20 nm. Also included in Fig. 1 are the theoretical predictions of Boccaccini et al. [7] and Mazilu and Ondracek [8] for the reduced moduli of porous sintered materials using Eqs. (3) and (4). Boccaccini et al. [7] assumed spheroidal pores with an aspect ratio of about 3 and this x/z was also found to be valid for the n-Fe in the present study. Boccaccini et al. [7] assumed a random orientation of the pores with $\cos^2 \alpha_d = 0.31$ for the porous conventional Fe, and this treatment was taken to be valid for the porous n-Fe samples as well. Fig. 1 also contains the data that Boccaccini et al. used to demonstrate the validity of their theory. The data (open squares) are for porous sintered Fe with p values that range between 0.05 and 0.25 [8]. The deviation of their theory from these data at the high p values was attributed to interconnected porosity.

Fig. 1 also includes the theoretical predictions of Krstic et al. [15] as well as the experimental data for
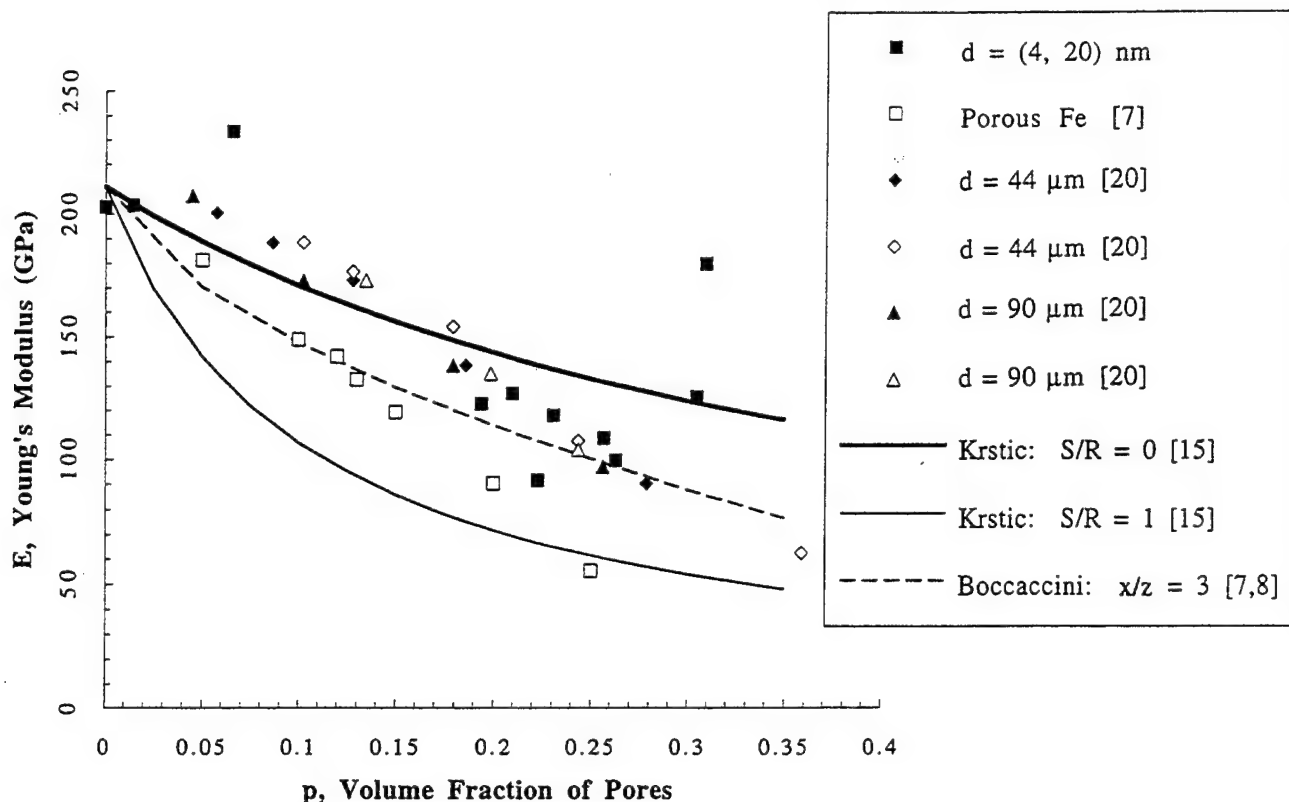
Fig. 1. Young's modulus of porous n-Fe and conventional Fe samples [7,20] plotted against the volume fraction of pores. Also shown are predictions of theories from Krstic et al. [15], Boccaccini et al. and Mazilu and Ondracek [8].

other porous sintered Fe samples with conventional grain sizes (diamonds and triangles) [20]. The theoretical predictions of Krstic et al. [15] using Eqs. (5) and (6) are shown with $S/R = 0$ and $S/R = 1$. The E data for porous sintered Fe samples were obtained from material processed by the pressing and sintering of powder produced either by electrolytic methods or hydrogen reduction [20]. One set had grain sizes of 44 μm and p values of 0.05–0.35 (diamonds); the other set of data had 90 μm grain sizes and p values ranging from 0.04 to 0.25 (triangles).

The volume fraction of pores p of all the Fe samples shown in Fig. 1 varies from about 0.02 to 0.35 and represents a wide range of grain sizes (4 nm–90 μm). The data for all these can be adequately described by the two theories [7,15]. In general, the theories using spheroidal pores without cracks appear to describe adequately the data for the porous Fe samples of all grain sizes shown, except at low p values, where the theories overestimate the effects of pores in reducing Young's modulus.

4. Discussion

The decrement in modulus shown by most of the n-Fe samples agrees qualitatively with the published results for other nanocrystalline materials shown in Table 1 [9–13]. The modulus values measured for the n-Fe are also in agreement with those in the literature for porous sintered Fe with conventional grain sizes [7,20]. For similar levels of p, the elastic behavior of n-Fe is similar to that of coarse-grained Fe. The results suggest that the effect of porosity in decreasing the Young's modulus for Fe dominates the influence of grain size and the synthesis method used to produce the powder.

Young's modulus results for porous sintered Fe samples of various grain sizes and produced by different synthesis methods are best described by two theories which involve porosity [7,8] and neglect the effect of cracks [14,15] in reducing the modulus. The stress state in the vicinity of an indenter is complex but is expected to be largely compressive directly under the tip. Cracks emanating from pores would remain closed in pure compression and thus would not greatly affect the value of E measured by nanoindentation. It is not surprising that the curve of E vs. p for $S/R = 1$ predicts too large a decrement in E. However, at other areas underneath the indenter, the stress state is more complicated and different crack orientations are possible. The presence of cracks could affect the compliance of the material and therefore alter Young's modulus under these circumstances.

For two of the ten n-Fe samples, the measured E values in excess of that predicted by the theories consid-
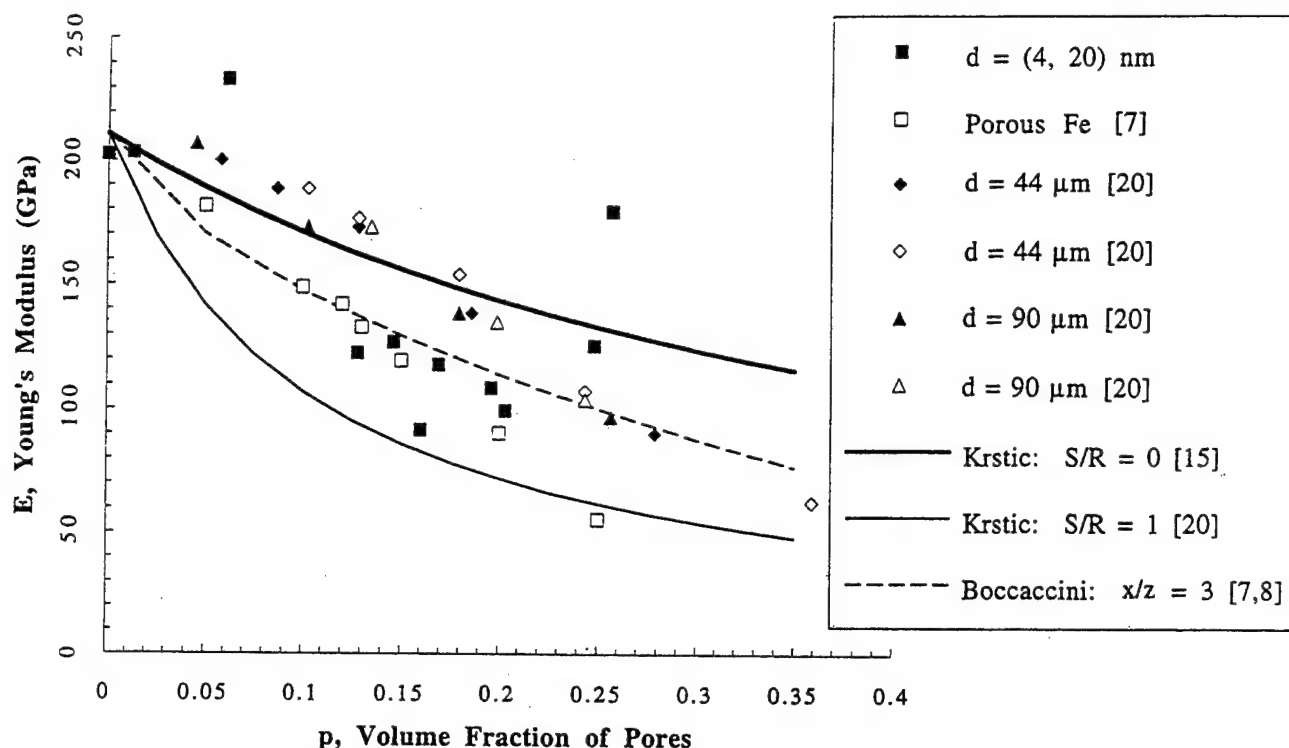
Fig. 2. Young's modulus of porous n-Fe and conventional Fe samples [7,20] plotted against the volume fraction of pores. The volume fraction of pores was calculated by treating the n-Fe as a composite of Fe and Fe oxide and comparing the n-Fe density with that of the composite. Also shown are the theoretical predictions of Krstic et al. [15], Boccaccini and Mazilu and Ondracek [8].

ering their porosity levels. These two samples (shown in Fig. 1 at $p = 0.06$ and $p = 0.31$) had very high hardness values of 8–9 GPa, compared with the average value of about 4.5 GPa for the majority of the samples [16]. (One other n-Fe sample, shown in Fig. 1 at $p = 0.02$, also had a very high hardness of 9 GPa). Doerner and Nix [17] found a few of their samples with higher hardness-to-modulus ratios had non-linear unloading curves and subsequently overly high E values. During unloading, large compressive strains which develop change the contact area in a non-linear fashion and result in curvature of the unloading curve. Indentation of higher hardness samples involves higher strain rates and, in materials which are strain rate sensitive, the unloading curve can become curved. The unloading curves of these n-Fe samples did not indicate substantial curvature. The measurements of the strain rate sensitivity m of the n-Fe samples resulted in values which were quite low (i.e. $m = 0.02$) [21]; so a small effect from strain rate sensitivity is expected.

The data for those samples of n-Fe with E values falling well above the theoretical predictions for their porosity may be affected by oxygen contamination. Measurements of oxygen content by fast neutron activation analysis indicated that the samples contained on average 15 at.% O, although the amount varied considerably from sample to sample. The elastic modulus of a n-Fe oxide should be similar to that of pure n-Fe as is

the case for conventional Fe_2O_3 (210 GPa) and Fe_3O_4 (220 GPa) relative to coarse-grained Fe (211 GPa). The values of p for the n-Fe data points in Fig. 1 were calculated on the assumption that the samples consist of pure Fe. It is possible that the decreased density of the compacts results from a significant contribution from a lighter oxide rather than solely from pores in the material. As a limiting case, it is assumed that all of the oxygen is in the form of iron oxide. The densities of the Fe oxide composite (a mixture of Fe and Fe_2O_3 and Fe_3O_4) were calculated using the measured oxygen contents. For the calculation, the density of Fe_2O_3 and Fe_3O_4 was taken to be 5.2 g cm^{-3} and the density of Fe was 7.87 g cm^{-3}. Fig. 2 shows the relationship between modulus and porosity based on this assumed limiting case. Although some of the points are moved horizontally by substantial amounts, the data are still reasonably well described by the models using spheroidal or spherical porosity.

The impact of sample inhomogeneities on Young's modulus was examined by retesting one of the samples with high values of E. The sample was repolished and measured in four additional areas with six indents and four target depths, providing 96 values of E. The E results were quite repeatable in all the areas measured and agreed with the first set of measurements to within a standard deviation, indicating that the sample data were representative. Therefore it is probable that this is

a real effect. For the two anomalous samples, the hardness measured by nanoindentation was much higher than that measured with the higher load Vickers microhardness testing. Because nanoindentation samples a smaller volume of the sample, the near-surface area impacted could be more dense, possibly resulting from polishing. The result would be that the material would appear harder and also stiffer, with a higher E value than that expected on the basis of bulk porosity measured on the whole sample. Sample inhomogeneities therefore could contribute to the existence of these apparent errors and the nanoindentation measurement could be more representative of the intrinsic (i.e. pore-free) structure of n-Fe.

The possibility that the apparently high values of E for the two samples originated from errors in the analytical methods was also investigated. Oliver and coworkers [18,19] have found that the unloading curve is better described by a power law relation between the loading and the depth. The data from one of the anomalous n-Fe samples were analyzed according to Oliver and coworkers, and the results agreed with the first set of measurements by the Doerner and Nix [17] method to within a standard deviation. This result lent credence to the efficacy of the Doerner and Nix method.

5. Conclusions

Young's modulus for a series of n-Fe samples made by IGC and compaction was measured by nanoindentation. The porosity of the samples varied from 2 to 30%, a factor of 15, while the grain size ranged from 4 to 20 nm, a factor of 5. As has been observed in other nanocrystalline materials, the modulus is considerably reduced below the fully dense value. Results of the measurements indicate that porosity is the dominant microstructural feature in determining the extent of this decrement in E.

The modulus results for n-Fe are reasonably well described by theories based on the presence of spherical or spheroidal pores. A survey of modulus values for porous Fe with grain sizes in the conventional range shows that porosity is the dominant feature in the decrease in Young's modulus for Fe.

Acknowledgments

References

[1] R.M. Spriggs, *J. Am. Ceram. Soc.*, *44* (1961) 628; R.M. Spriggs, L.A. Brissette and T. Vassals, *J. Am. Ceram. Soc.*, *45* (1962) 400; F.P. Knudsen, *J. Am. Ceram. Soc.*, *45* (1962) 94; R.M Spriggs, *J. Am. Ceram. Soc.*, *45* (1962) 454.

[2] K.K. Phani, S.K. Niyogi, A.K. Maitra and M. Rochaudhury, *J. Mater. Sci.*, *21* (1986) 4335; I. Soroka and P.J. Sereda, *J. Am. Ceram. Soc.*, *51* (1968) 337.

[3] J.C. Wang, *J. Mater. Sci.*, *19* (1984) 809.

[4] *D.P.H. Hasselman, J. Am. Ceram. Soc.*, *45* (1962) 452.

[5] S. Spinner, F.P. Knudsen and L. Stone, *J Res. Natl. Bur. Std. C*, *67* (1963) 39.

[6] K.K. Phani and S.K. Nioygi, *J. Mater. Sci. Lett.*, *6* (1987) 511.

[7] A.R. Boccaccini, G. Ondracek, P. Mazilu and D. Windelberg, *J. Mech. Behav. Mater.*, *4* (1993) 119.

[8] P. Mazilu and G. Ondracek, in K.P. Herman and Z.S. Olesiak (eds.), *Thermal Effects in Fracture of Multiphase Materials*, Springer, Berlin, 1989, p. 255.

[9] D. Korn, A. Morsch, R. Birringer, W. Arnold and H. Gleiter, *J. Phys. (Paris), Colloq. C5, Suppl. 10, 49* (1988) 769.

[10] M.J. Mayo, R.W. Siegel, Y.X. Liao and W.D. Nix, *J. Mater. Res.*, *7* (1992) 973.

[11] M.J. Mayo, R.W. Siegel, A. Narayanasamy and W.D. Nix, *J. Mater. Res.*, *5* (1990) 1073.

[12] G.W. Nieman, J.R. Weertman and R.W. Siegel, *J. Mater. Res.*, *6* (1991) 1012.

[13] N.P. Kobelev, Ya.M. Soifer, R.A. Andrievski and B. Gunther, *Nanostruct. Mater.*, *2* (1993) 537.

[14] L. Wong, D. Ostrander, U. Erb, G. Palumbo and K.T. Aust, in R.D Shull and J.M. Sanchez (eds.), Metallurgical Society of AIME, *Proc. Symp. on Nanophases and Nanocrystalline Structures*, Warrendale, PA, 1994, p. 85.

[15] V. Krstic, U. Erb and G. Palumbo, *Scr. Metall. Mater.*, *29* (1993) 1501; V.D. Krstic and W.H. Erickson, *J. Mater. Sci.*, *22* (1987) 2881; V.D. Krstic and W.H. Erickson, *J. Mater. Sci.*, *23* (1988) 4097.

[16] G.E. Fougere, J.R. Weertman and R.W. Siegel, *Nanostruct. Mater.*, *5* (1995) 127.

[17] M.F. Doerner and W.D. Nix, *J. Mater. Res.*, *1* (1986) 601.

[18] W.C. Oliver and G.M. Pharr, *J. Mater. Res.*, *7* (1992) 1564.

[19] W.C. Oliver, B.N. Lucas and G.M. Pharr, in M. Nastasi, D.M. Parkin and H. Gleiter (eds.), *Mechanical Properties and Deformation Behavior of Materials with Ultrafine Microstructures*, Kluwer, Dordrecht, 1993, p. 417.

[20] A. Squire, *Trans. AIME*, *171* (1947) 485.

[21] G.E. Fougere, *Ph.D. Dissertation*, Northwestern University, 1995.

Residual stress, strain and faults in nanocrystalline palladium and copper

P.G. Sanders[a], A.B. Witney[a], J.R. Weertman[a], R.Z. Valiev[b], R.W. Siegel[c,1]

[a]*Materials Science and Engineering Department, Northwestern University, Evanston, IL 60208-3108, USA*
[b]*Institute of Metals Superplasticity, Russian Academy of Sciences, Ufa 450001, Russian Federation*
[c]*Materials Science Division, Argonne National Laboratory, Argonne, IL 60439, USA*

Abstract

Nanocrystalline Pd and Cu, prepared by inert-gas condensation and warm compaction, were studied using X-ray diffraction techniques. A sample of Cu with submicrometer grain size produced by severe plastic deformation was also examined. The Warren–Averbach technique was used to separate the line broadening due to grain size, t.m.s. strain and faults. Peak shifts and asymmetry were used to determine the long-range surface stresses, stacking-fault probability and twin probability. Young's modulus for a Pd sample was determined by an ultrasonic technique and compared with the coarse-grained, fully dense value.

Keywords: Nanocrystalline; Faults; Strain; Palladium; Copper

1. Introduction

The ultimate goal of this investigation is the determination of the intrinsic mechanical behavior of nanocrystalline (n-) Pd and Cu. Toward this end, it is important to understand the structure of these materials. For this reason, the grain size, residual stress, stacking faults and twins are significant structural features to understand so that their impact on mechanical properties may be evaluated. Twins and r.m.s. strains are commonly observed in fine-grained materials, but their variation as a function of grain size and preparation conditions is not fully understood. In addition, it is important to compare materials made by different processes, because techniques and methods of structural determination may vary between laboratories. In this study, the structure of Cu with submicrometer grain size, denoted as ultrafine-grained (UFG-), was compared with that of n-Cu.

2. Experimental procedure

The n-Pd and n-Cu samples were prepared by inert

gas condensation (IGC) and warm compaction at Argonne National Laboratory [1]. High purity (99.997%) Pd wire and high purity (99.999%) Cu shot were evaporated from alumina-lined boats into an atmosphere of ultrahigh-purity (99.9999%) He at 650 Pa. The resulting powder, after being warmed following collection on a liquid-nitrogen-cooled surface, was compacted with 1.4 GPa of pressure for 10 min at temperatures ranging from 100 to 300 °C. Typical samples were 9 mm in diameter and 0.1–0.5 mm thick. The UFG-Cu sample was prepared by severe plastic deformation by torsion under high pressure at room temperature to a true logarithmic strain $\varepsilon \approx 7$ [2]. (In the following graphs for Cu, this sample is denoted as sample 8 or the sample with the largest grain size.) Density measurements were made on each sample using Archimedes' principle, with particular care used to ensure minimal thermal effects in the liquid measurement. X-ray diffraction (discussed below) was used to determine the grain size, r.m.s. strain $\langle \varepsilon^2 \rangle^{1/2}$, stacking fault probability α, twin probability β and residual surface stress. The residual stress was remeasured after the samples were polished to 0.05 μm surface finish. A measurement of Young's modulus by an ultrasonic technique was used to estimate the error resulting from assuming the coarse-grained, fully dense values of the elastic constants.

---

[1] Present address: Materials Science and Engineering Department, Rensselaer Polytechnic Institute, Troy, NY 12180-3590, USA.

Transmission electron microscopy (TEM) was performed on a Hitachi H-700 microscope operating at 200 kV.

For the Warren-Averbach (W–A) analysis [3] in n-Pd and n-Cu, the 111, 200, 311, 222 and 400 X-ray peaks were scanned over a range of ±5 times the full width at half-maximum (FWHM). A pseudo-Voight or Lorentzian function was fitted to the data only to remove the background and to deconvolute overlapped tails. The data were then corrected for functions which vary with 2θ, including the Lorentz–polarization factor, the variation in the structure factor, the Debye–Waller factor and the dispersion-corrected scattering factor. The range of the data was selected to correspond to a 1 nm interval in real space, and then the Fourier transform was numerically integrated. The instrumental function was deconvoluted using the Stokes [4] correction with a standard sample made from annealed compacted filings of high purity Pd or Cu. The data were then normalized using the method of Rothman and Cohen [5], and only a cosine expansion was used to separate the broadening due to size and strain. Two orders of a reflection (e.g. 111–222) were used to separate size and strain, while two different sets of peaks (e.g. 111–222 and 200–400) were used to separate the grain size broadening from that due to intrinsic stacking faults and twins (deformation and growth faults respectively in Warren's terminology). Independent confirmation of these results was obtained by determining α using peak shifts between a standard and the sample [3], and β using the difference between the peak maximum and the centroid [6].

Residual surface stress measurements were made with Cr Kα radiation on n-Pd samples using the 311 peak ($2\theta \approx 155°$), where the $1/e$ penetration depth is 0.3 μm. All five samples received identical processing treatments, including a 200 °C compaction. The samples ranged between 0.15 and 0.48 mm thick, and all were 94% or more dense. The biaxial residual stress was determined using the $\sin^2 \psi$ technique [7], where scans were performed for six different values of $\sin^2 \psi$. After background subtraction and employing all the angular corrections listed above, plus the absorption factor (which varies with ψ), the top approximately 15% of the peak was fitted with a parabola [7]. For biaxial stress, a plot of $\sin^2 \psi$ vs. d is linear with a slope proportional to the residual surface stress, where Young's modulus and Poisson's ratio used in the calculation were an average of the single-crystal elastic constants [8]. As a test of the method's accuracy, the annealed Pd standard used in the W–A analysis was tested, and the residual stress was found to be -3.8 ± 0.1 MPa, or almost zero compared with all the other measurements, which were usually about an order of magnitude higher.

All X-ray data uncertainties in this paper are standard deviations propagated from counting statistics using standard methods (e.g. that of Beers [9]); other sources of error have not been quantified. Propagation of errors through the W–A analysis follows the treatment of Wilson [10] and Schlosberg and Cohen [11].

3. Results

3.1. Warren–Averbach analysis

Grain size data from the W–A analysis of n-Pd and n-Cu are shown in Fig. 1. The first feature noticed is the measurable difference between the 111–222 W–A value, which is typically reported, and the grain size after removal of the stacking fault and twin contributions (data labelled W–A (no α & β)). The TEM grain size was found to be in the same range as the X-ray data, but more work is necessary to obtain quantitative data. The X-ray grain size of the UFG-Cu was found to be 52.8 ± 0.5 nm, which is smaller than the approximately 170 nm size observed by TEM [2]. However, this difference may be due to the high dislocation density ρ. Using a relation from Mikkola and Cohen [12], where ρ can be calculated from the 111–222 and 200–400 W–A sizes and r.m.s. strains, ρ was found to be $(6–12) \times 10^{14}$ m^{-2}, which agrees well with the TEM value of $(5–10) \times 10^{14}$ m^{-2} [2]. Also plotted in Fig. 1 is the grain size calculated from the Scherrer formula, where an attempt has been made to remove the instrumental function by subtracting the square of the standard's FWHM from that of the nanocrystal. Without going into too much depth, it must be noted that the Scherrer method assumes that the only source of broadening is the small size of the crystallites. In addition, the Scherrer method volume averages, while the W–A method area averages grain size.

The grain size and faulting probabilities (only the sum $1.5\alpha + \beta$ can be obtained from the W–A analysis) were separated using the 111–222 and 200–400 W–A sizes. In n-Pd and n-Cu, α is almost zero, considering the standard deviation of the measurement (Fig. 2). This is not surprising because stacking faults are typically remnants of plastic deformation and dislocation motion in f.c.c. crystals, and little of this has occurred in these nanocrystalline samples. However, α was about an order of magnitude higher (0.002 with a small uncertainty compared with about 0.0002 for the n-Cu) in the UFG-Cu, which makes sense considering it was made by severe plastic deformation. Since α is small, values of β should agree with those of $1.5\alpha + \beta$ from W–A. As seen in Fig. 2, the agreement is excellent. Both the magnitude of β and the trend of decreasing β with increasing grain size are similar in n-Cu and n-Pd, even though the twin energy is higher in Pd. Large

numbers of twins in n-Cu made by IGC have been observed with high resolution electron microscopy [13].

TEM studies have shown that twins are very common in small clusters (e.g. [14]) perhaps owing to growth faults and/or to reduce surface energy. In accordance with these observations, it was postulated that the twins form during cluster condensation, and not during compaction. To test this hypothesis, loose powder and a compacted sample from Pd evaporation were
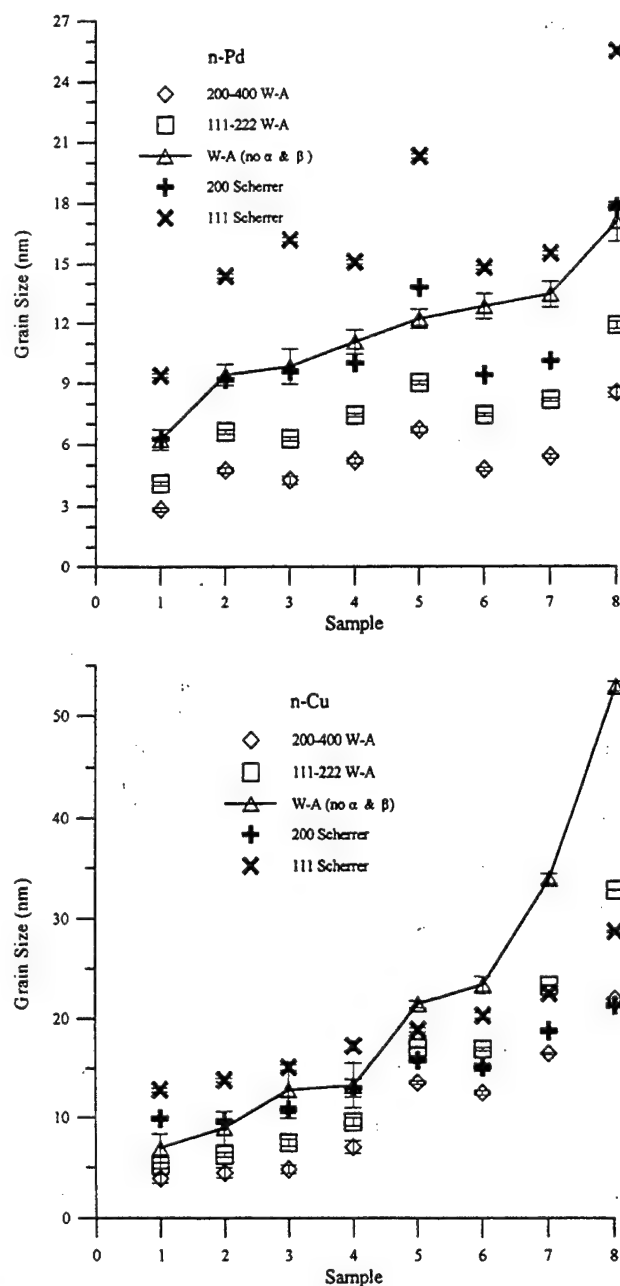
Fig. 1. Comparison of grain sizes determined from X-ray analysis of line broadening for (a) n-Pd and (b) n-Cu. Sample 8 in (b) is UFG-Cu.
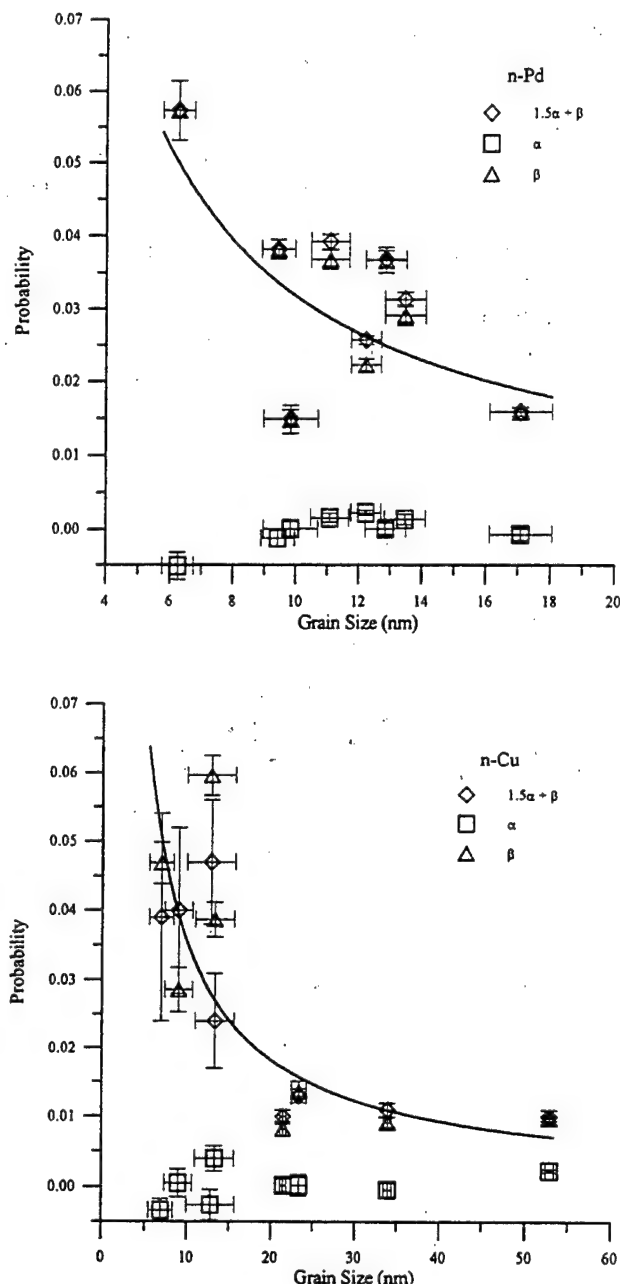
Fig. 2. Stacking fault probability α and twin probability β as functions of grain size for (a) n-Pd and (b) n-Cu. Also note the agreement for the two methods used to determine α and β. The sample with the largest grain size in (b) is UFG-Cu.

X-rayed and their respective β calculated. The β for both the powder and the compacted sample were in the same range considering experimental error (which was larger for the powder sample); so it can be concluded that most of the twins are present in the original powder.

The r.m.s. strain was measured for the 111–222 and 200–400 peaks at a coherence length of 5 nm. As shown in Fig. 3, the 200–400 strain is always higher than the 111–222 strain for a given sample. It was

noticed that the strains also seemed to decrease with increasing grain size in n-Pd and n-Cu. This trend is weaker in n-Cu, owing in part to the poor counting statistics. The n-Pd powder and a consolidated sample from the same evaporation analyzed by the W–A method showed nearly identical r.m.s. strains, which implies that the high strains are inherent in the free clusters. The r.m.s. strain in UFG-Cu is slightly higher than that predicted by the r.m.s. strain curve for the IGC samples. The local strain near the grain boundaries in this severely deformed material may be even higher, but the large fraction of grain interior that

is less strained would cause the average r.m.s. strain to be closer to that for n-Cu. Other measurements of the r.m.s. strain in UFG-Cu have given values in exactly the same range [2].

3.2. Residual stress

All measurements made, without exception, showed a negative biaxial strain, which implies that the surface layer is under compression. The $\sin^2 \psi$ vs. d plots were linear, signaling that the stress state can be accurately described as biaxial. After polishing off 0.02–0.04 mm of the surface, the biaxial stress increased by a statistically significant margin about half the time. Before polishing, the surface stresses ranged between -20 and -40 MPa while, after polishing, the stresses were between -40 and -105 MPa. No strong correlations were observed between the residual stress and density, thickness or amount of material removed during polishing. One sample was accidentally broken after testing in the unpolished state. While not showing the general trend of increasing residual stress with polishing, the measured stress in this broken sample did not decrease either, meaning that the stress state is not completely dependent on having a fully formed disc.

As mentioned previously, Young's modulus and Poisson's ratio used to calculate the residual stress were the coarse grained, fully dense values. Many investigators have seen changes in the elastic properties of nanocrystalline metals (e.g. [15]). Ultrasonic techniques provide one method of measuring Young's modulus. Using the density and the longitudinal wave speed (and assuming that Poisson's ratio is 0.33), Young's modulus for a $97.17 \pm 0.05\%$ dense n-Pd sample ($d = 12.2 \pm 0.5$ nm) was found to be $(82 \pm 4)\%$ of the standard's modulus [16]. The lower modulus may result from the 3% density decrement and/or the slight increase in the overall atomic spacing in these grain boundary dense materials. In any case, the residual stresses calculated from the handbook value of the elastic modulus may be high by about 18%.

4. Conclusions

The W–A grain size corrected for the effect of $1.5\alpha + \beta$ agrees with the TEM grain size, at least in the small-grain-size regime. In n-Pd and n-Cu, the stacking fault probability α is virtually zero, while the twin probability β is significant. Both β and the r.m.s. strains decrease with increasing grain size. Similar trends for β were seen in the UFG-Cu, although the r.m.s. strain and α seemed to be slightly higher. Uncompacted n-Pd powder showed similar values of β and r.m.s. strain to those in n-metals, signaling that these structural features may result from the fine particle size,
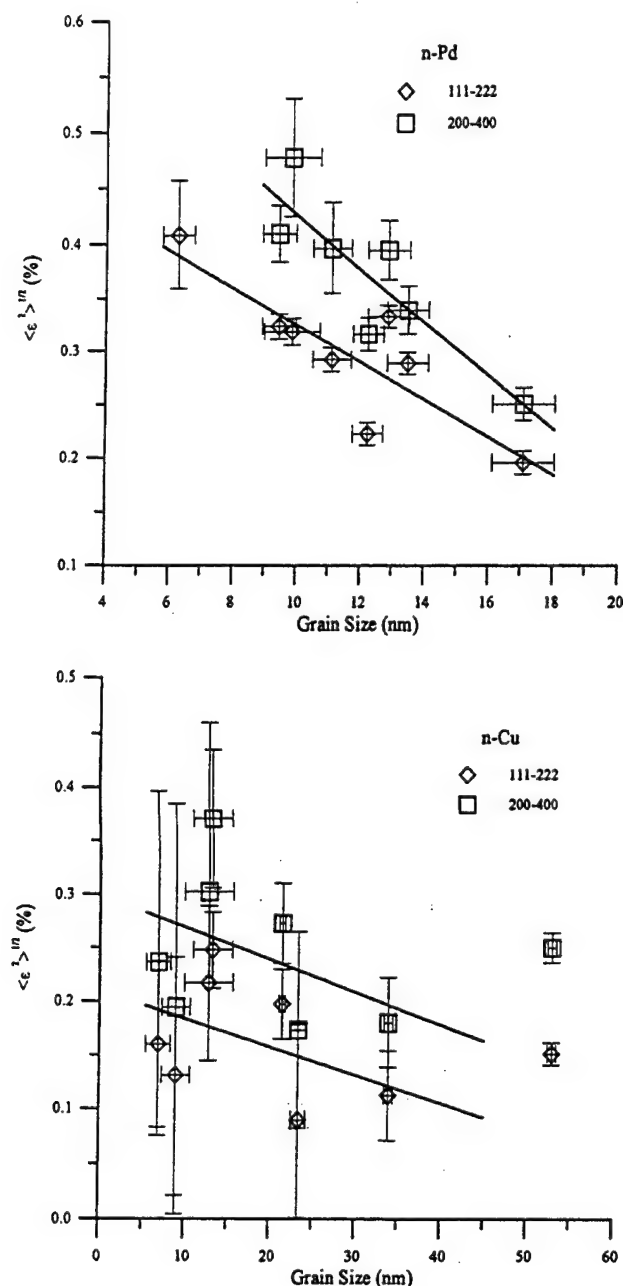
Fig. 3. R.m.s. strain as a function of grain size for (a) n-Pd and (b) n-Cu. The sample with the largest grain size in (b) is UFG-Cu.

and not compaction. The residual surface stresses in n-Pd are compressive and relatively low in magnitude. Young's modulus for n-Pd was found to be smaller than the coarse-grained, fully dense value by a significant amount.

Acknowledgements

References

[1] R.W. Siegel, S. Ramasamy, H. Hahn, Z. Li, T. Lu and R. Gronsky, *J. Mater. Res.*, 2 (1988) 1367.

[2] V.Y. Gertsman, R. Birringer, R.Z. Valiev and H. Gleiter, *Scripta Metall. Mater.*, 30 (1994) 229.

[3] B.E. Warren, *X-ray Diffraction*, Dover, New York, 1990, pp. 251–298.

[4] A.R. Stokes, *Proc. Phys. Soc. London*, 61 (1948) 382.

[5] R.L. Rothman and J.B. Cohen, *Adv. X-ray Anal.*, 12 (1969) 304.

[6] J.B. Cohen and C.N.J. Wagner, *J. Appl. Phys.*, 33 (1962) 2073.

[7] I.C. Noyan and J.B. Cohen, *Residual Stress*, Springer, New York, 1987, pp. 117–209.

[8] G. Simmons and H. Wang (eds.), *Single Crystal Elastic Constants and Calculated Aggregate Properties: A Handbook*, MIT Press, Cambridge, MA, 1971, p. 233.

[9] Y. Beers, *Introduction to the Theory of Error*, Addison-Wesley, Reading, MA, 1957, pp. 26–36.

[10] A.J.C. Wilson, *Acta Crystallogr.*, 23 (1967) 888.

[11] W.H. Schlosberg and J.B. Cohen, *J. Appl. Crystallogr.*, 16 (1983) 304.

[12] D.E. Mikkola and J.B. Cohen, in J.B. Cohen and J.E. Hilliard (eds.), *Local Atomic Arrangements Studied by X-ray Diffraction*, Gordon and Breach, New York, 1966, pp. 289–340.

[13] G.W. Nieman, J.R. Weertman and R.W. Siegel, *Materials Research Society Symp. Proc.*, Vol. 206, Matrials Research Society, Pittsburgh, PA, 1991, p. 493.

[14] T. Hayashi, T. Ohno, S. Yaisuya and R. Uyeda, *Jpn. J. Appl. Phys.*, 16 (1977) 705.

[15] G.E. Fougere, L. Riester, M. Ferber, J.R. Weertman and R.W. Siegel, *Mater. Sci. Eng.*, A204 (1995) 106.

[16] M.L. Peterson, personal communication, 1994.

Influence of strain rate on the mechanical properties in fine-grained aluminum alloys

Toshiji Mukai[a,1], Koichi Ishikawa[b], Kenji Higashi[a]

[a]Department of Mechanical Systems Engineering, University of Osaka Prefecture, Sakai, Osaka 593, Japan
[b]Mechanical Engineering Department, Osaka Municipal Technical Research Institute, Joto-Ku, Osaka 536, Japan

Abstract

Fine-grained IN905XL aluminum alloys with five grain sizes between 0.8 and 8.1 μm have been developed by a combination of mechanical alloying and conventional extrusion in order to investigate the influence of the strain rate on the mechanical properties. Negative strain rate sensitivity of flow stress is observed up to $10 \, s^{-1}$ for all samples. Above the strain rate of $1 \times 10^3 \, s^{-1}$, however, all samples show the positive strain rate sensitivity of strength. Total elongation at high strain rates is generally larger than that at low strain rates. Flow stresses increase with decreasing grain size for all strain rates. The measured values of strength of the coarse grained IN905XL with sizes above 4.3 μm agree with the values estimated from a cooperation of the strengthening by the grain size refinement, magnesium solute atoms and oxides and carbides dispersion. In the Hall–Petch relations at high strain rates, the gradient of the curve increases with increasing reciprocal square root of the grain size. For fine-grained samples, therefore, an additional strengthening mechanism should be considered such as the difference in the characteristics of the boundary.

Keywords: Strain rate; Mechanical properties; Aluminium alloys; Mechanical alloying

1. Introduction

Recently, it has been reported that in the nanocrystalline regime an apparent softening with grain refinement occurs and the yield stress does not obey the Hall–Petch relationship [1,2]. It is very interesting how the mechanical properties are changed with grain refinement for the materials which consist of near-nanometric and/or nanometric scale grains. However, the influence of grain size on the ductility for a nanocrystalline materials has not been reported yet, owing to the difficulty in making a bulk sample with sufficient volume and/or the sensitivity to flaws on the surface at tensile testing. It has been reported for Al–Mg system alloys that total elongation decreases with decreasing grain size from 200 to 1 μm for both high and low strain rates, and the difference between the elongations of the two strain rates decreases with decreasing grain size [3]. It is clearly noted that influence of strain rate changes with decreasing grain size even in a near-nano-

metric-scale grained regime. Very few reports, however, have been available on the influence of strain rate on the mechanical properties in fine-grained materials even in the near-nanometric scale or submicron scale.

The purpose of this work is to investigate the influence of strain rate on the mechanical properties for fine-grained materials with near-nanometric scale in the wide strain rate range from 1×10^{-3} to $2 \times 10^3 \, s^{-1}$. In order to investigate the influence of grain size the mechanical properties of the mechanically alloyed IN905XL aluminum alloy with five different grain sizes are characterized.

2. Experimental procedure

2.1. Material

The mechanically alloyed IN905XL (Al–4Mg–1.5Li–1.2C–0.4O where the composition is given in weight per cent) has a density of $2.58 \, Mg \, m^{-3}$ (8.2% lower than Al alloy 7075). The material has a fine grain size (about 0.8 μm) with fine aluminum carbide and aluminum

oxide (5–30 nm in diameter) dispersions [4]. In this work, IN905XL with five different grain sizes was prepared as-received (extrusion condition), and as-received plus further extrusion at 673, 723, 773 and 823 K (extrusion ratio of 7.1:1). The extrusion produces samples (15 mm diameter) with coarse grain sizes. Prior to tensile testing all specimens were heat treated at 755 K for 2 h and water quenched. The mean grain sizes of these heat-treated samples are about 0.8, 1.4, 1.9, 4.3 and 8.1 μm respectively (herein referred to as fine-grained type (FG), intermediate-grained type 1 (IG1), intermediate-grained type 2 (IG2), coarse-grained type 1 (CG1) and coarse-grained type 2 (CG2)). Typical microstructures for the FG, IG2 and CG2 samples are shown in Figs. 1(a), (b) and (c) respectively. Dispersoids along grain boundaries and dislocation loops within grains can be seen readily.

2.2. Experimental apparatus

To investigate the influence of strain rate on the
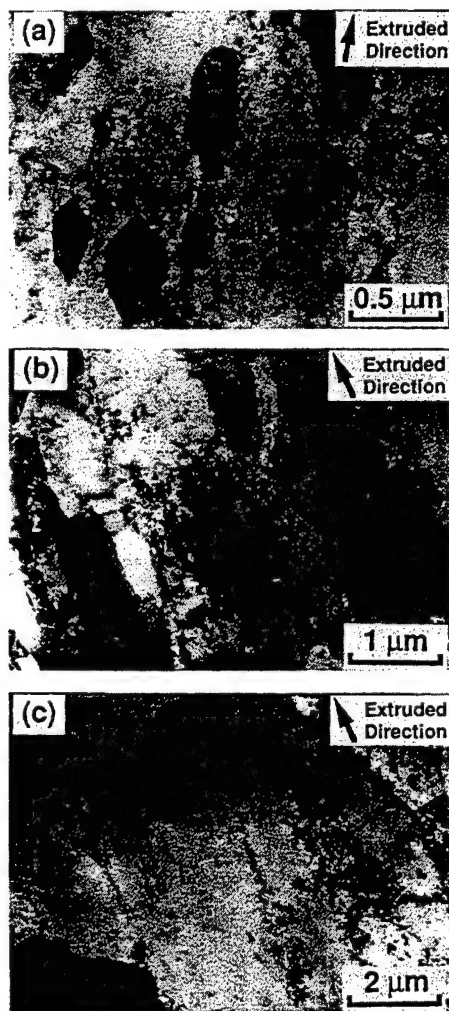
Fig. 1. Typical microstructures: (a) FG sample; (b) IG2 sample; (c) CG2 sample.

mechanical properties in a wide range of strain rates, three different testing machines were used. The low strain rate tensile tests (1×10^{-3} and 5×10^{-2} s^{-1}) were performed with an Instron testing machine, and the intermediate strain rate tests (1 and 10 s^{-1}) were done with a hydraulic tensile testing machine. For the dynamic tensile tests (1×10^3 and 2×10^3 s^{-1}) a modified Hopkinson bar method was used. All tests were carried out at room temperature.

Tensile specimens, machined from extruded bars, had their tensile axes parallel to the extruded direction. The gauge length of the specimen is 5.0 mm, and the diameter is 2.5 mm.

3. Results

3.1. Stress–strain relation

Typical stress-strain curves for all samples with five different grain sizes are shown in Fig. 2. Bold curves are the results for the high strain rates of 2×10^3 s^{-1}, and the thin curves for a low strain rate of 1×10^{-3} s^{-1}. It is clearly noted that flow stress increases with decreasing grain size for both the strain rates.

For the FG samples, an almost steady state in flow stress is found in an early stage of the plastic strains ($\varepsilon < 0.03$) at both the strain rates. For the IG and CG samples, the flow stress at high strain rate is higher than that at the low strain rate in an early stage of deformation ($\varepsilon < 0.01$); however, the flow stress beyond this strain at the high strain rate is lower than that measured at the low strain rate. One of the interesting results worth noting is this negative strain rate sensitivity of flow stress.

The slope of the curves relating to the strain-hardening exponent appears to decrease with increasing grain size. The fine-grained samples, which exhibit a higher strength, have a lower mobile dislocation density. Therefore its strain-hardening exponent is expected to be low.

A pronounced yield drop and Luders band propagation are also observed for the finer-grained samples of FG, IG1 and IG2. As the grain size increases, the yield stress decreases, and the extent of inhomogeneous yielding decreases. This trend is essentially same as that reported by Lloyd [5] for an Al–Ni alloy.

3.2. Influence of strain rate on the strength

The variation in yield stress is shown in Fig. 3 as a function of strain rate for the five samples of IN905XL. No significant change is observed in the shape of the stress–strain rate curves; in the strain rate range from 1×10^{-3} to 10 s^{-1}, the yield stress does not appear to depend on the strain rate while the yield stress increases
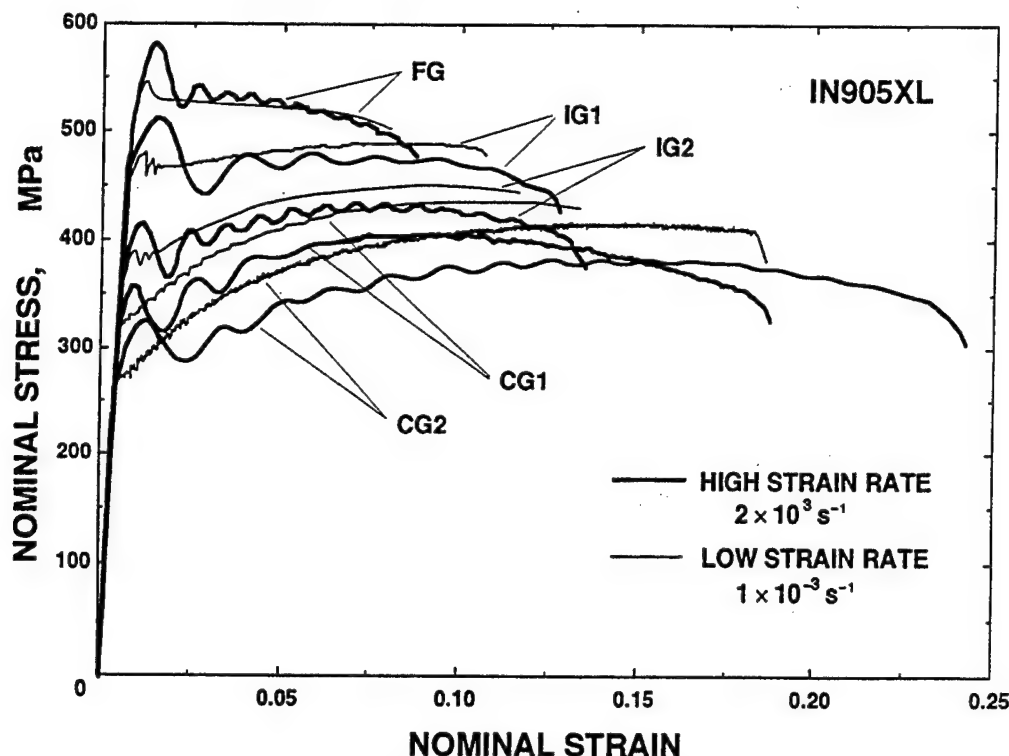
Fig. 2. Typical stress–strain curves for all samples with five different grain sizes.

markedly with increasing strain rate at strain rates in excess of $1 \times 10^3 \, s^{-1}$. The yield stress also increases with decreasing grain size.

The variation in true stress at the fixed strain of 0.06 is also shown in Fig. 4 as a function of strain rate. The greater the grain size, the higher is the true stress. The true stress at $\varepsilon = 0.06$ decreases with increasing strain rate in the range from 1×10^{-3} to $10 \, s^{-1}$. Beyond this strain rate range, the true stress increases with increasing strain rate. A possible negative strain rate sensitivity of flow stress is observed.

Negative strain rate sensitivity of flow stress has been reported in some kinds of solution-strengthening material, such as Al–Mg system alloys [6–11]. Lindholm et al. [8], Dotson [9] and Lloyd [10] consider the Portevin–Le Chatelier (P–L) effect in solid solution alloys as explaining this fact. The present alloy IN905XL, which is an Al–Mg system alloy, also shows a possible negative strain rate sensitivity. This result is explained as follows.

The dislocation–solute interaction cannot be observed at very small strains near yield point. The increment in strength at low strain rates seems to result from dynamic strain aging. It is reported, on the contrary, that the strength at high strain rates increases owing to the damping mechanisms [12]. At intermediate strain rates an apparent minimum in strength appears caused by the lower dislocation–solute interaction and the softening by the adiabatic temperature rise.

3.3. Influence of strain rate on ductility

The variation in total elongation is shown in Fig. 5 as a function of strain rate for the five samples of IN905XL. No significant change is observed in a shape of the elongation–strain rate curves. In the strain rate range from 1×10^{-3} to $10 \, s^{-1}$, the total elongation does not appear to depend on the strain rate while the total elongation increases markedly with increasing strain rate over a strain rate of $1 \times 10^3 \, s^{-1}$. With increasing grain size, the total elongation increases as does the difference in the elongation at the lowest vs. the highest strain rates.

4. Discussion

4.1. Influence of grain size on yield strength

Fine grained structures can lead to a high strength in an alloy, as described by the Hall [13]–Petch [14] relation and shown by the following equation:

$$\sigma_f = \sigma_0 + kd^{-1/2} \tag{1}$$

Here, σ_0 is the flow stress of a single grain owing to all the strengthening mechanisms [15], k is the constant relating to how effective the grain boundaries are for increasing flow stress [15], and d is the grain size. The yield stresses in differently grained IN905XL at the lowest strain rate of $1 \times 10^{-3} \, s^{-1}$ and the highest strain
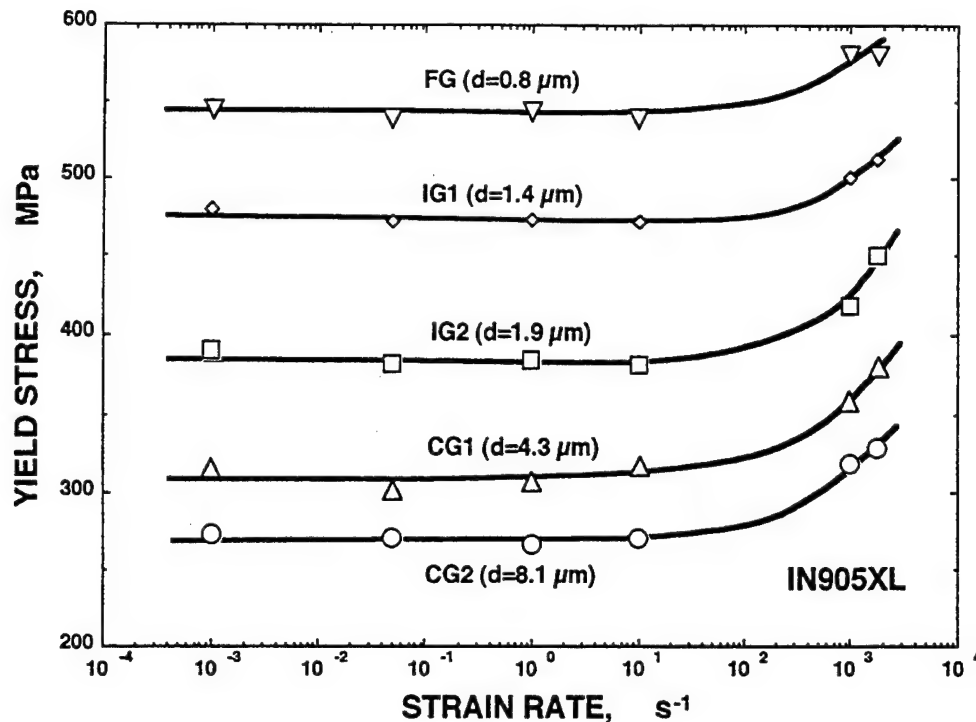
Fig. 3. The variation in yield stress as a function of strain rate for IN905XL with five different grain sizes.

rate of 2×10^3 s^{-1} as a function of the reciprocal square root of the grain size are plotted in Fig. 6. Also included are the data obtained for the yield stresses at low strain rates for pure aluminum by Fujita and Tabata [16], and Wyrzykowski and Grabski [17], for Al–6Mg–0.6Mn and Al–2Cu–2Mg–1Ni–1Fe alloys by Rabinovich and Markushev [18], and for Al–6Ni alloy by Lloyd [5].

All the alloys exhibited an increase in yield strength with the refinement of grain size, i.e. the Hall–Petch relation. The slope of the lines fit to the data of pure aluminum, Al–6Mg–0.6Mn and Al–2Cu–2Mg–1Ni–1Fe alloys is about 2. On the contrary, a large value of about 10 is obtained for IN905XL at both the lowest and the highest strain rates. This trend in the grain size dependence on the yield stress was also observed for Al–6Ni alloy by Lloyd [5]. In the coarse-grain-size regime the slope of the curve for Al–6Ni alloy is smaller than that in the fine-grain-size regime and is comparable with that of pure aluminum. In general, it can be expected in the coarse-grain regime below 10 μm, that the yield stress follows the Hall–Petch relation for the aluminum alloys examined.

The strengthening effect of the grain size refinement $\Delta\sigma_{rg}$ can be estimated from the experimental data on pure aluminum and the following equation: $\Delta\sigma_{rg} = 10 + 2d^{-1/2}$. On the contrary, it has been reported that the strength of a binary Al–Mg alloy can be evaluated by the experimental equation $\sigma = \sigma_0 + kc^n$ where c is the magnesium content (weight per cent), $\sigma_0 = 11.8$ MPa, $k = 13.8$ and $n = 1$ [19]. On the assump-

tion that the lines of a Hall–Petch relation for Al–Mg alloys with various magnesium contents are parallel to each other, the strengthening effect of solute magnesium can be estimated as 13.8c. For IN905XL, $c = 4$ wt.%; therefore the strengthening effect $\Delta\sigma_s$ of solute magnesium can be estimated as about 60 MPa. An additional strengthening by the dispersion content in IN905XL can also be calculated from the following Orowan Eq. [20]:

$$\Delta\sigma_d = \frac{0.81 Gb}{2\pi(1-v)^{1/2}} \frac{\ln(2r_s/r_0)}{\lambda_s - 2r_s} \qquad (2)$$

In Eq. (2), G is the shear modulus, b is Burgers vector and v is Poisson's ratio. Also, r_0 is the dislocation core radius ($b \sim 2b$), r_s is the average particle radius and λ_s is the average center-to-center spacing of particles [3]. Using $G = 25.9$ GPa, $b = 0.286$ nm, $v = 0.33$, $r_0 = 2b \sim b$, $r_s = 8.75$ nm and $\lambda_s = 38.3$ nm, for aluminum, $\Delta\sigma_s$ is estimated from Eq. (2) as about 190–230 MPa.

The relation estimated from a combination of the strengthening effect of the grain refinement $\Delta\sigma_{rg}$, solution strengthening $\Delta\sigma_s$ of magnesium atoms and dispersion strengthening $\Delta\sigma_d$ of oxides and carbides in IN905XL can be described by the gray-colored zone in Fig. 6. The points for CG1 and CG2 are close to the gray-colored zone. However, the points IG1, IG2 and FG do not fall in this zone and show a higher value than expected from the analysis. This is caused by the difference in characteristics of boundary such as misorientation angle, energy of boundary and texture. This trend also can be seen in Al–6Ni alloy [5]. It has been
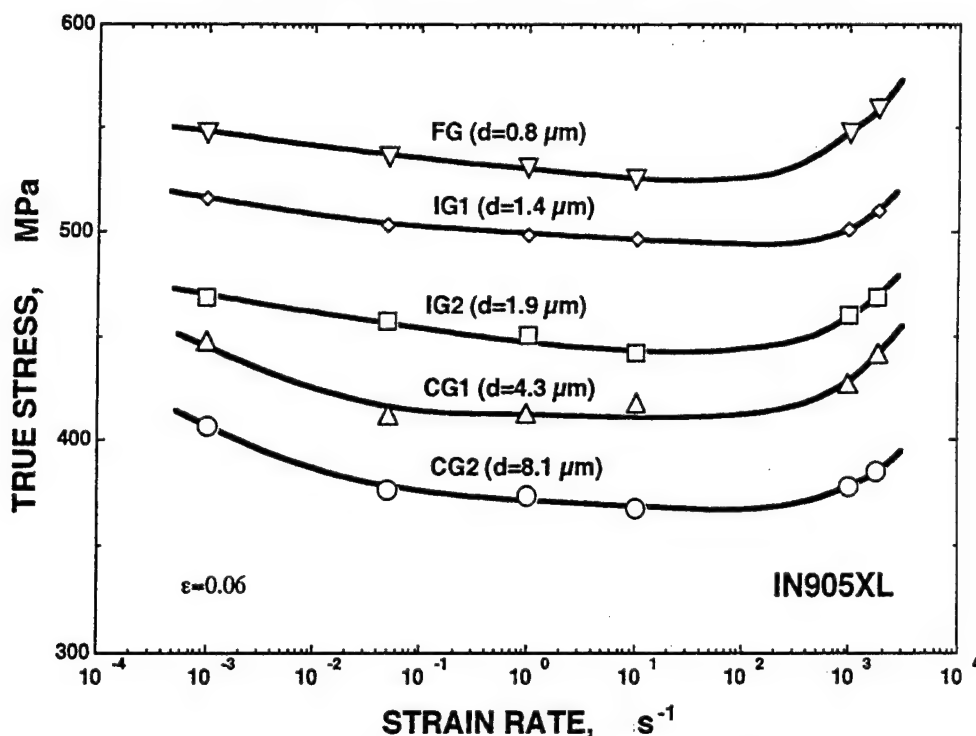
Fig. 4. The variation in true stress at the fixed strain of 0.06 as a function of strain rate.

explained that the deviation from the Hall–Petch relation may be due to the inhomogeneous yielding associated with the very fine grain size.

The yield stress in IN905XL at the highest strain rate is also shown in Fig. 6. The effect of the grain refinement on yield stress at the highest strain rate is almost similar to that at the lowest strain rate. The differences between yield stresses at the two strain rates, however, decreases with grain size.

4.2. Texture

In order to investigate the deviation from the Hall–Petch relation in IN905XL, the initial textures before testing were observed. Figs. 7(a), 7(b) and 7(c) show the initial texture of FG, IG2, CG2, respectively. It is clearly seen in Fig. 7(a) that a combination of a typical extrusion fiber texture oriented to $\langle 111 \rangle$ and $\langle 100 \rangle$ exists in the FG sample. The tensile strength of a single crystal oriented near the $\langle 111 \rangle$ direction is expected to be higher because of the multiple slip with deformation. Therefore an f.c.c. polycrystalline alloy consisting of the texture oriented to $\langle 111 \rangle$ exhibits a higher strength than an alloy consisting of the texture oriented to another direction. In the present study, the textures of IN905XL change from $\langle 111 \rangle$ to $\langle 110 \rangle$ with increasing grain size. As a result, the strength of the FG sample is higher than that of the CG2 sample. Therefore one of the possible reasons for the deviation from the linear Hall–Petch relation at the finer grain sizes may be expected to be the difference in the textures.

It is concluded that the yield stress in the coarse-grained IN905XL agrees with the value estimated from a combination of the strengthening by the grain size refinement, magnesium solute atoms and oxides and carbide disperison. With decreasing grain size due to the inhomogeneous yielding and/or the change in the texture, however, the yield stress shows a higher yield stress than expected from the Hall–Petch relation.

Furthermore, this influence of texture and the difference in characteristics of boundary such as misorientation angle and the energy of boundary should be taken into consideration to investigate the characteristics of near-nanocrystalline and/or nanocrystalline materials in the near future.

5. Conclusions

(1) The yield strength for IN905XL is a weak function of strain rate below the strain rate of 10 s^{-1} and is a strong function of strain rate up to $1 \times 10^3 \text{ s}^{-1}$.

(2) IN905XL exhibits a possible negative strain rate sensitivity of the flow stress which may be attributed to adiabatic heating and the absence of the P–L effect occurring during high strain rate testing.

(3) Total elongation increases markedly with increasing strain rate over the strain rate of $1 \times 10^3 \text{ s}^{-1}$. It is also clearly noted that total elongation increases with increasing grain size, and the increment in total elongation over the strain rate range increases with increasing grain size.
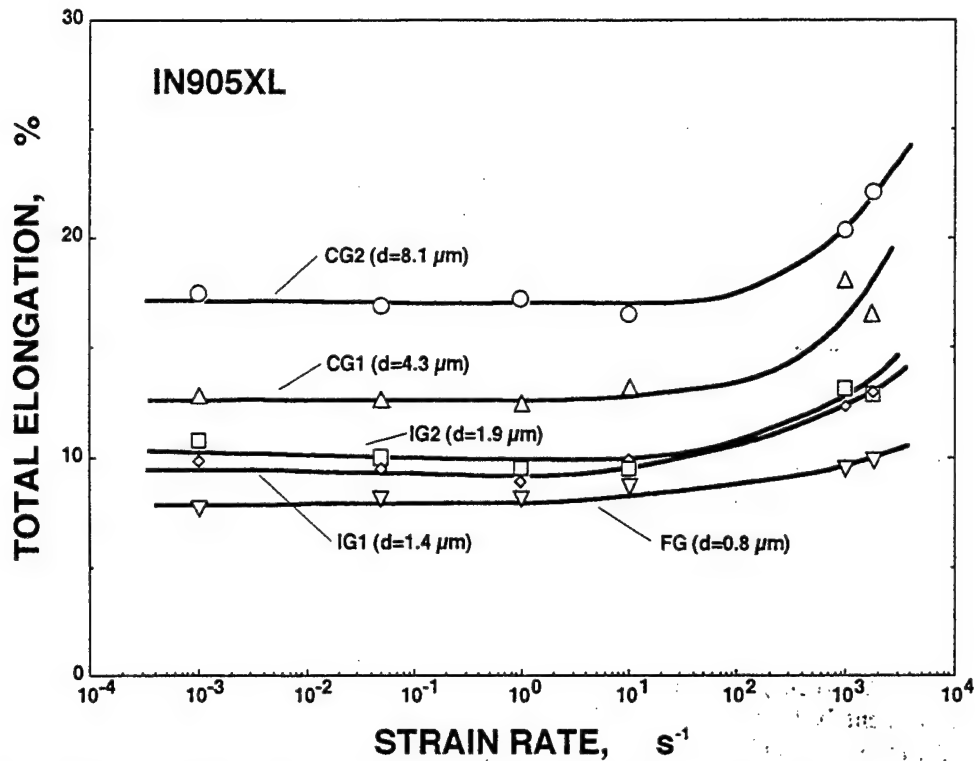
Fig. 5. The variation in total elongation as a function of strain rate for IN905XL with five different grain sizes.
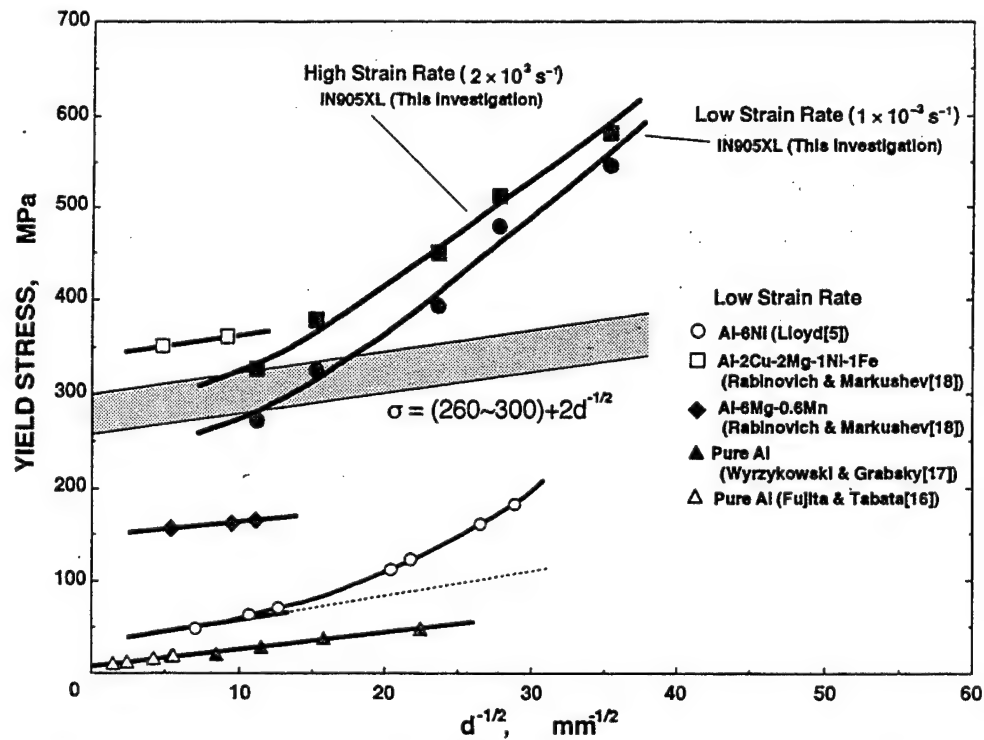
Fig. 6. The yield stresses in IN905XL with different grain sizes at the lower strain rate of 1×10^{-3} s^{-1} and the highest strain rate of 2×10^3 s^{-1} as a function of the reciprocal square root of the grain size. Also included are the data for pure Al [16,17] etc.

(4) The grain size dependence of the yield strength at high strain rates is similar to that at low strain rates. The yield strength of IN905XL can be basically presented by three strengthening mechanisms: grain size refinement; magnesium solute; carbide and oxide dispersion. Another possible strengthening mechanism can
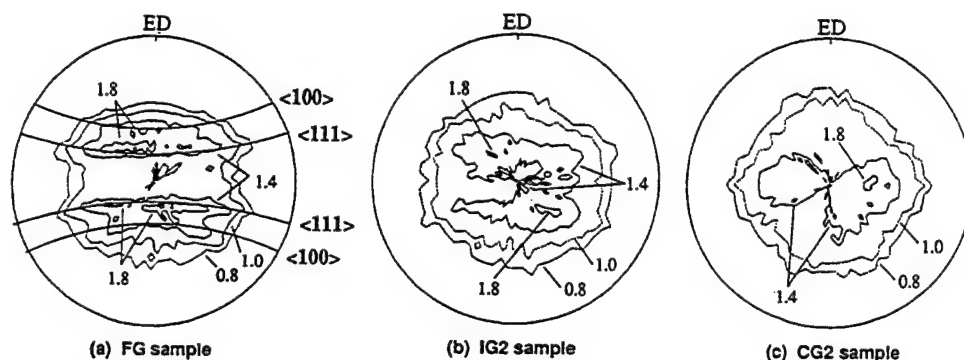
Fig. 7. {111} pole figure of initial samples: ED, extrusion direction.

be expected to be due to the difference in fiber texture produced by extrusion, especially for the finer grain sizes studied.

Acknowledgments

The authors like to express their gratitude to Mr. M. Mabuchi of the Government Industrial Research Institute of Nagoya, and Mr. S. Matsuda of the Smitomo Light Metal Industries, Ltd., who performed the extrusion.

References

[1] A.H. Chokshi, A. Rosen, J. Karch and H. Gleiter, *Scr. Metall.*, *23* (1989) 1679–1684.

[2] G.W. Nieman, J.R. Weertman and R.W. Siegel, *J. Mater. Res. 6* (1991) 1012–1027.

[3] T. Mukai, K. Ishikawa and K. Higashi, *Metall. Trans. A*, submitted.

[4] P.S. Gilman, J.W. Brooks and P.J. Bridges, Al–Li Alloys III, *Proc. 3rd Int Conf. on Aluminium–Lithium Alloys, Oxford, 1985*, Institute of Metals, London, 1986, pp. 112–120.

[5] D.J. Lloyd, *Met. Sci.*, *(1980)* 193–198.

[6] B.A. Wilcox and A.R. Rosenfield, *Mater. Sci. Eng.*, *1* (1966) 201–205.

[7] A. Korbel and H. Dybiec, *Acta Metall.*, *29* (1981) 89–93.

[8] U.S. Lindholm, R.L. Bessey and G.V. Smith, *J. Mater.*, *6*(1) (1971) 119–133.

[9] C.L. Dotson, *J. Eng. Mater. Technol.*, (1974) 115–122.

[10] D.J. Lloyd, *Metall. Trans. A*, *11* (1980) 1287–1294.

[11] K. Higashi, T. Mukai, K. Kaizu, S. Tsuchida and S. Tanimura, *J. Phys. (Paris) IV Colloq. C3*, (1991) 341.

[12] P. Perzyna, *Mechanical Properties at High Rate of Strain in Inst. Phys. Conf. Ser.*, *21* (1974) 138.

[13] E.O. Hall, *Proc. Phys. Soc. B*, *64* (1951) 747.

[14] N.J. Petch, *J. Iron Steel Inst., London*, *174* (1953), 25.

[15] V.R. Bennett, W.D. Nix and A.S. Tettleman, *The Principles of Engineering Materials*, Prentice-Hall, Englewood Cliffs, NJ, 1973, p. 226.

[16] H. Fujita and T. Tabata, *Acta Metall.*, *21* (1973) 355.

[17] J.W. Wyrzykowski and M.W. Grabski, *Philos. Mag.*, *53* (1986) 505.

[18] M.K. Rabinovich and M.V. Markushev, personal communication, in Oikawa et al. (eds.) *Strength of Materials*, Japan Institute of Metals, Tokyo, 1994, pp. 661–664.

[19] T. Mukai, K. Higashi and S. Tanimura, *Mater. Sci. Eng.*, *A176* (1994) 181–189.

[20] Y.W. Kim, in Y.W. Kim and W.M. Griffith (eds.), *Dispersion Strengthened Aluminum Alloys*, Metals and Materials Society, 1988, p. 157.

Synthesis, structure, properties and magnetic applications of carbon-coated nanocrystals produced by a carbon arc

M.E. McHenry[a,*], S.A. Majetich[b], E.M. Kirkpatrick[b]

[a]Department of Materials Science and Engineering, Carnegie–Mellon University, Pittsburgh, PA 15213-3890, USA
[b]Department of Physics, Carnegie–Mellon University, Pittsburgh, PA 15213-3890, USA

Abstract

Out of the fullerene field has grown the exciting potential for synthesis of magnetic nanoparticles of both scientific and technical interest. We employ a Kratschmer–Huffman carbon arc method to synthesize carbon-coated elemental transition metal and alloy particles with nanocrystalline dimensions. These have included FeC_x, Co[C] and Ni[C] ferromagnetic particles. Recently, $SmCo_x$[C] particles with nanocrystalline dimensions have been produced by this method starting with a Sm_2Co_7 metallic precursor. Structural characterization by X-ray diffraction and high resolution transmission electron microscopy illustrate the phases present and the particle size distribution. Magnetic properties, as determined by superconducting quantum interference device magnetometry are also reported. These include hysteretic, temperature and time-dependent magnetic responses and an inferred superparamagnetic response. A unifying theme in this research is the carbon arc synthesis of materials with interesting magnetic properties and assessment of their use in xerography, magnetic resonance imaging, ferrofluids, data storage and magnetic inks.

Keywords: Magnetic applications; Carbon-coated nanocrystals; Carbon-arc

1. Introduction

The field of fullerene [1] synthesis and chemistry has continued to progress in large part owing to the discovery of the Krätschmer et al. [2] carbon arc process [2] for producing C_{60}, C_{70} and higher fullerene cage molecules. This discovery was followed by the discovery of "buckytubes" [3] and "buckyonions" [4] as byproducts of the carbon arc process. Yet another important development has been the discovery of techniques for the endohedral doping of fullerence [5] produced by the carbon arc. An exciting adjunct of fullerene production is in the formation of carbon-coated metal or metal carbide nanocrystals [6,7]. An adherent onion-skin-like graphitic carbon coating on these particles has led to them being classified as "giant fullerences". Our group has recently described the preparation of rare earth carbide nanocrystals [8,9], as well as a novel method for their separation which takes advantage of the large paramagnetic moments of the rare earth species. Carbon-coated ferromagnetic nanocrystals [10,11] have also been produced and are suggested for a variety of applications where fine particle magnetism is important and where adherent protective C-coating have implications for tribology, dissolution and most importantly oxidation resistance.

Here we review the synthesis C-coated Co[C] and Sm–Co–C nanocrystals of interest for potential applications. The magnetic particles produced by this process are predominantly of a single-domain nature. The carbon coating provides an effective oxidation barrier. Our data provide the first link betweeen fullerene-related nanocrystals and the studies of fine particle magnetism. We discuss efforts to produce carbon-coated $Sm_{1-x-y}Co_xC_y$ with the aim of engendering larger magnetocrystalline anisotropy. These carbon-coated magnetic metal nanocrystals are of interest for potential applications in which $\gamma\text{-}Fe_2O_3$ particles are currently used: i.e. in magnetic data storage, for magnetic toner in xerography, in magnetic inks, in ferrofluids and as contrast agents in magnetic resonance imaging.

* Corresponding author.

2. Theory of fine-particle magnetism

Technical magnetic properties of a ferromagnetic material are described by the metastable magnetic hysteresis curve. Two important technical magnetic properties are the remnant magnetization M_r and the coercive field H_c. For large H, all the atomic magnetic dipole moments are aligned and the ferromagnet is said to be saturated, having a saturation magnetization $M_s = N_m\mu$, where N_m is the number of magnetic dipoles per unit volume and μ is the atomic dipole moment. Upon reduction of the applied field to zero the magnetization is reduced owing to rotational processes. The remaining or remnant magnetic moment at zero field results from energy barriers to the reversal of the magnetization. It is not until a reverse field equal to the coercivity H_c is applied that the magnetization is returned to zero. For applications in which the remnant magnetization is to be exploited, it is important for H_c to be large enough to prevent switching to the magnetizaiton due to fluctuations in the field. For applications in magnetic recording, for example, a moderate coercivity is desirable to prevent induced switching; however, too large an H_c is undesirable for writing information (i.e. reversal in an applied field).

An upper bound for the coercivity H_c is the so-called anisotropy field $H_K = 2K_u/M_s$, where K_u is a (uniaxial) energy density of the magnet having its magnetization aligned parallel or antiparallel to a (uniaxial) easy axis of magnetization. The common origins of magnetic anisotropy include magnetocrystalline anisotropy, shape anisotropy and stress (magnetostrictive) anisotropy [12,13]. Typically the coercivity takes on values much less than the anisotropy field which considers coherent reversal over the anisotropy energy barrier as the mechanism of reversal (Fig. 1). In large volumes the reversal field is reduced owing to the nucleation and growth, via domain wall motion, of reverse domains. For collections of single-domain particles, only rotational processes are important and the switching of individual particles can be described by a switching field distribution (SFD) equal to $\Delta H/H_c$, where ΔH is the full width at half-maximum of dM/dH.

Interest in fine-particles magnets stems from the strong variation of their technical magnetic properties, notably H_c, with respect to particle size [14]. The coercivities for a variety of elemental, alloy and oxide ferromagnets have been observed to have maxima H_c^{max} as a function of particle size (several 100 nm) corresponding to the limiting size for single-domain ferromagnets [14]. Above this size, multiple-domain configurations are possible and domain wall nucleation and mobility must be considered to understand the reversal process. Below this size, particles are typically of a single-domain nature and the reversal of the magnetization can be ascribed to coherent rotation (rotation in unison) of the particle moments, if the particles do not interact (i.e. fanning or curling modes are inoperative) [12,13].

To ascertain whether a particle will be single or multiple-domain, one needs to compare the energy of a particle with and without a domain wall. In the latter, the magnetostatic self-energy (demagnetization) results from free poles on the particle surface. In the former, the self-energy is reduced through domain formation but at the expense of domain wall energy. If the reduction in self-energy exceeds the domain wall energy, then a multiple-domain configuration will be stable. The self-energy is of the form $N_d(4\pi M_s^2)$ where N_d is the demagnetization factor $(0 < N_d < 1)$ and the domain wall energy is calculated by minimizing the sum of the exchange energy JV and anisotropy energy KV in the volume V over which the magnetization rotates from one direction to another (the domain wall). For a 180° Bloch wall in a crystal with a lattice constant a the domain wall thickness δ which minimizes this total energy is given by [15] $\delta = Na = \pi S(J/Ka)^{1/2}$, where S is the spin moment per atom and N is the number of atoms over which the magnetization rotates in the wall. This yields a wall energy (per unit area) of $\gamma = 2\pi S(JK/a)^{1/2}$. For b.c.c. iron, e.g. $\gamma \approx 1.1$ erg cm^{-2} and $\delta \approx 45$ nm. A comparison of the magnetostatic self-energy and the domain wall energy predicts that spherical particles with radius less than about 10–100 nm will be stable as single-domain ferromagnets. All nanoparticles discussed here are of sizes well below that necessary to stabilize multiple-domain configurations.

For fine-particle magnets the possibility of thermally activated switching and consequent reduction in $H_c(T)$ must be a consequence of a superparamagnetic response. Superparamagnetic response refers to the probability of thermally activated switching of a magnetic
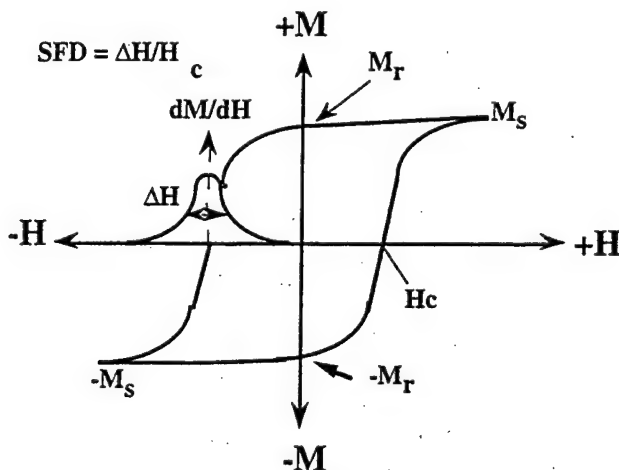

Fig. 1. Prototypical magnetic hysteresis curve $M(H)$ for a collection of single-domain particles with an operative Stoner–Wohlfarth rotational switching mechanism.

fine particle moments. This thermally activated switching can be described by an Arrhenius law for which the zero-field activation energy barrier is $K_u \langle V \rangle$, where $\langle V \rangle$ is the particle volume. The switching frequency becomes larger for smaller particle size, smaller anisotropy energy density and at higher T. Above a blocking temperature T_B, the switching time is less than the experimental time and the hysteresis loops is observed to collapse, i.e. the coercive force becomes zero. Above T_B, the magnetization scales with field and temperature in the same way as does a classical paramagnetic material, with the exception that the inferred dipole moment is a particle moment and not an atomic moment. $M(H,T)$ can be fit to a Langevin function L using the relation $M/M_0 = L(a) = \coth a - 1/a$, where M_0 is the 0 K saturation magnetization and $a = \mu H/k_B T$. The particle moment μ is given by the product $M_s \langle V \rangle$ where M_s is the saturation magnetization and $\langle V \rangle$ is the average particle volume.

Below the blocking temperature, hysteretic magnetic response is observed for which the coercivity has the temperaure dependence $H_c = H_{c0}[1 - (T/T_B)^{1/2}]$. In the theory of superparamagnetism [16,17], the blocking temperature represents the temperature at which the metastable hysteretic response is lost for a particular experimental time frame. In other words, below the blocking temperature a hysteretic response is observed since thermal activation is not sufficient to allow the immediate alignment of particle moments with the applied field. For spherical particles with a uniaxial anisotropy axis, the rotational energy barrier to alignment is $K_u \langle V \rangle$. For hysteresis loops taken over about 1 h, the blocking temperature should roughly satisfy the relationship $T_B = K_u \langle V \rangle / 30 k_B$. The factor of 30 represents $\ln(\omega_0/\omega)$, where ω is the inverse of the experimental time constant (about 10^{-4} Hz) and ω_0 an switching attempt frequency (about 1 GHz).

The phenomenon of thermally activated switching also gives rise to the phenomenon of magnetic relaxation. For thermally activated switching of identical particles with identical rotational activation energy barriers, magnetic relaxation follow an exponential law $M(t) = M(0) \exp(-t/\tau)$. On the contrary, for particles with distributed anisotropy energy densities or volumes the energy barriers for rotation will be distributed and, under certain conditions, magnetic relaxation with a logarithmic time dependence is to be expected: $M(t) = M(0) + S \ln t$, where the parameter $S = dM/d \ln t$ is called the magnetic viscosity [18–20]. Using simple models [20] for the distribution of rotational energy states it is possible to relate the magnetic viscosity to the range of rotational energies sampled during relaxation.

3. Experimental procedure

Nanocrystals (typical 1–50 nm) have been produced by the Krätschmer et al. carbon arc process. In this process, graphite rods have been drilled and packed with a mixture of oxide powder (Co_3O_4) or metallic species (Co or Sm_2Co_7) and a combination of graphite powder and graphite cement or dextrin powder as a binder. Rods were baked to drive off H_2O and to sinter the powders. For Co[C] we have sucessfully consumed rods with up to 50 wt.% Co. Rods made with oxides had smaller fractions to avoid exceeding the percolation limit and inhibiting arc stability. Rods were placed in the upper electrode position in a d.c. carbon arc with a C counterelectrode employed. The rods were consumed under arc conditions of 100 A and a 125 Torr He gas pressure. A fixed voltage of about 20 V was maintained. Soots contain a mixture of graphitic particles, C-coated and uncoated nanocrystals; fullerenes were removed from the reactor wall and from a cathode deposit (pancake). It is of course also possible to synthesize a metal carbide phase as observed for Gd- and Ho-containing materials [8,9]. Whether or not a carbide is formed depends on the metal–carbon phase diagram (e.g. Co is a poor carbide former, but Gd_x readily forms carbides). Nanoparticles were characterized by X-ray diffraction (XRD), transmission electron microscopy (TEM) and high resolution TEM analysis. Magnetic properties are determined by superconducting quantum interference device magnetometry.

4. Results and discussion

Results of magnetic studies of Co[C] and other elemental transition metal nanocrystals have been described in [10,11]. Among the more significant results has been the observation of approximately 20 (± 8–10) nanoparticles with adherent graphitic C coatings as illustrated in Fig. 2(a). In this size range the metastable f.c.c. configuration of Co is observed as shown in the XRD pattern for a sample containing nominally 50 wt.% Co. The observation of f.c.c. Co has been confirmed by electron diffraction on individual particles, by XRD on dilute samples and most recently by XRD on concentrated samples. The XRD on concentrated samples offers the most convincing data to date on the predominance of f.c.c. Co nanocrystals. Using the full width at half-maximum of the XRD peaks in Fig. 2(b) in the Debye–Scherrer formula predicts a particle size of 20–28 nm, which is in excellent agreement with the TEM observations. The experimental details as to the synthesis of soots containing large concentrations of Co nanocrystals have been described in [21]. Co-nanoparticle-containing soots have been produced with saturation magnetization (per gram of soot)
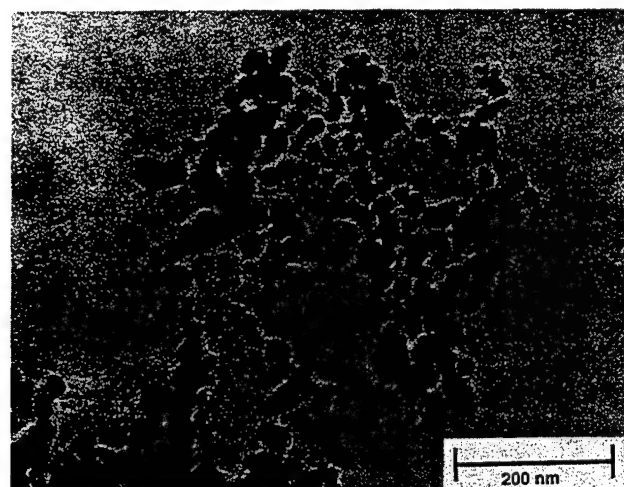
(a)
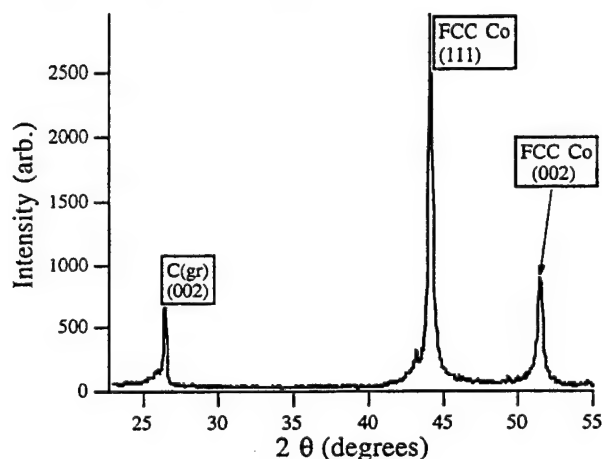
(b)

Fig. 2. (a) TEM image of C-coated Co nanoparticles produced by the Krätschmer et al. carbon arc process starting with Co-packed anodes of nominal Co content 50 wt.%. (b) XRD intensity vs. 2θ for the same with f.c.c. Co peaks labeled.

in excess of 100 emu g^{-1}. These materials typically have approximately 500 Oe coercivities extrapolated to 0 K in excellent agreement with previous observations of Co nanoparticles [14], with some slight variation (less than $\pm$ 100 Oe) in concentration. Values of $M_r/M_s \approx 0.5$ for randomly aligned particles are observed in agreement with the Stoner–Wohlfarth [22] coherent rotation model. SFDs of about 4–6 are observed for randomly oriented particles at 5 K. For collections of particles which have been magnetically aligned prior to being immobilized in epoxy the SFD can be reduced to less than 0.5 which is a benchmark for recording media [23].

A superparamagnetic response is observed for these particles above a blocking temperature $T_B \approx 160$ K, and therefore these materials are not particularly exciting for room-temperature applications in which a thermally stable hysteretic response is desired (e.g. magnetic recording). On the contrary, ferrofluidic applications,

and applications in magnetic resonance imaging enhancement agents may both be viable. These results suggest that, to achieve the goal of stable hysteresis at room temperature, either the particle volumes and/or the magnetic anisotropy must be increased so as to increase rotational energy barriers. The former is undersirable owing to both the desire to retain single-domain particles and to record information densely. The latter may be achieved through alloying which influences the magnetocrystalline anisotropy energy density or by techniques which engender shape or stress anisotropies. We suspect that magnetocrystalline anisotropy is the primary determinant of the rotational energy barriers in our particles. However, further work is necessary to assess definitively the contribution due to magnetostatic energy in elongated or acicular particles and magnetostriction in stressed materials. TEM analysis has thus far indicated monodisperse and spherical particles for f.c.c. Co[C] but with a significant fraction of stacking faults. The similarity between our coercivity values and those observed earlier and attributed to magnetocrystalline anisotropy suggests that the same anisotropy mechanism may be also be operative in our particles. Spherically shaped particles would seem to preclude a large contribution from shape anisotropy.

Out most recent efforts seek to produce compounds with large magnetocrystalline anisotropy (MnAl [24–26], MnBi [27], and SmCo$_5$ [28]) and methods for engendering shape anisotropy (taking advantage of anisotropic growth rates). These alloy systems include those known to have large magnetocrystalline anisotropies as previously investigated in bulk but which have not been investigated as fine-particle magnets. We seek to understand the influence of increased magnetocrystalline anisotropy on barriers to rotational magnetic hysteresis. Here we describe magnetic properties of similarly produced $Sm_{1-x-y}Co_xC_y$ nanocrystals chosen so as to explore the possibility of producing nanoparticles with increased magnetocrystalline anisotropy. The Sm–Co system has several notable permanent magnet phases including SmCo$_5$, Sm$_2$Co$_7$ and Sm$_2$Co$_{17}$. These phases are interesting because of their large moments and large anisotropy constants which give rise to large coercivities in bulk magnets. Our experiments with carbon-coated SmCo$_x$ nanocrystals seek to exploit these large anisotropies to produce fine-particle magnets stable to much higher temperatures than the previously studied elements.

Fig. 3(a) illustrates a typical 5 K magnetic hysteresis curve for $Sm_{1-x-y}Co_xC_y$ nanocrystals. Preliminary TEM results show these to be about 20 nm particles of nearly spherical shape. XRD reveals f.c.c. Co and SmCo$_5$ as predominant among the several phases observed; a detailed discussion of the phases present will be presented elsewhere. This represents our first at-

tempts at synthesizing the hard SmCo phases. Work is in progress to vary the chemistry and to investigate post-synthesis annealing protocols and their influence on magnetic properties. Fig. 3(b) shows the SFD for the same material. A bimodal distribution is observed and attributed to both Co and $SmCo_x$ nanocrystals as observed in XRD. A rounded hysteretic response is consistent with a collection of particles with randomly aligned easy axes, as is the ratio $M_r/M_s \approx 0.5$. For these particles, SFDs range from about 2.5 to 4. Magnetic alignment of these particles has not yet been attempted. If successful, the SFD may be further reduced as was the case for f.c.c. Co nanoparticles. Significant in the temperature-dependent magnetic response of these particles is the fact that significant hysteresis is still observed at 300 K for these particles. Observations of $H_c < 100$ Oe for the wall soot and $H_c < 450$ Oe for the pancake material suggest that these materials may be potentially interesting room-temperature magnets. The
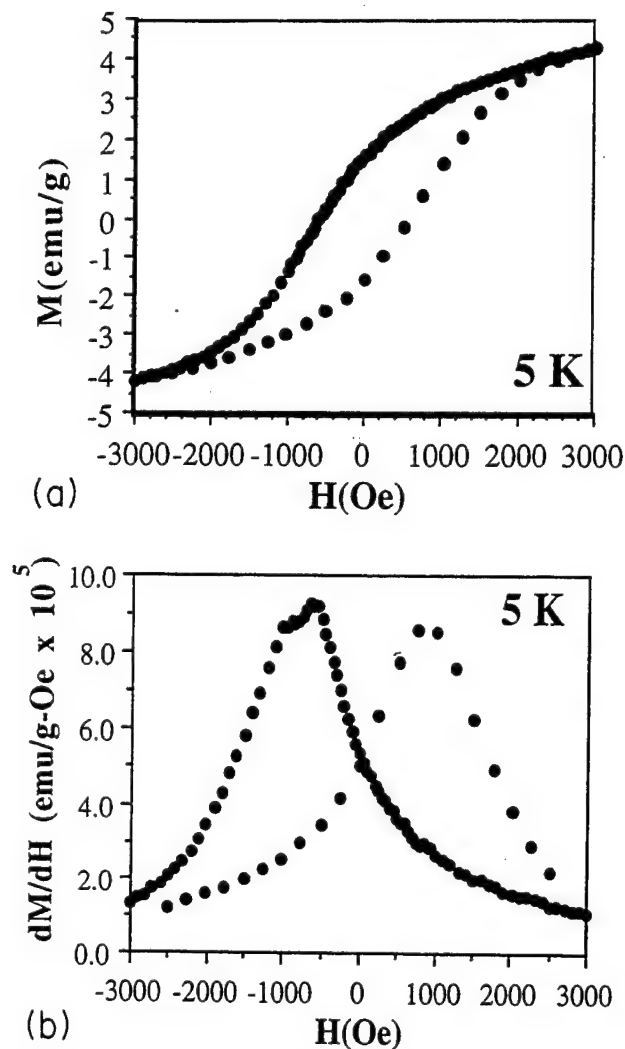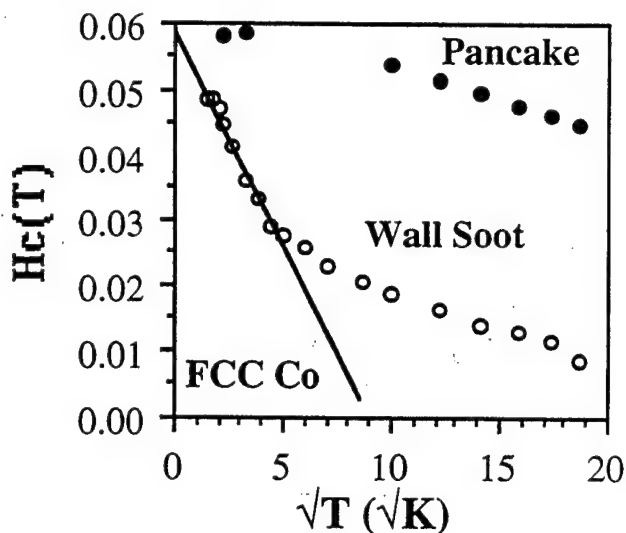
Fig. 4. Coercivity as a function of $T^{1/2}$ for $SmCo_x$[C] nanocrystals. Deviations at low T are believed to be due to a minority f.c.c. Co phase. The majority phase is $SmCo_5$. For this sample the wall soot $T_B > 700$ K. For particles collected in the pancake region, T_B is much larger.

difference between these two observed values is not yet well understood.

Fig. 4 shows a typical temperature dependence of the coercivity H_c, showing that a blocking temperature must greatly exceed room temperautre. A contribution at low temperatures is similar to that observed previously for Co[C] nanocrystals. A $T^{1/2}$ dependence of H_c is again seen to be approximately obeyed. Further experiments, at higher temperatures, will be necessary to determine whether this temperature dependence is simply reflective of thermally activated switching or whether the intrinsic temperature dependence of the magnetic order parameter also plays a role (i.e. if 300 K is a significant fraction of the Curie temperature T_C).

Fig. 5 shows the field dependence of the magnetic relaxation rate $S = dM/d\ln t$, at various temperatures. The response is thermally activated, roughly proportional to the SFD at the given temperature and peaked at a field equal to the coercive field $H_c(T)$. These results are consistent with a model for thermally activated switching over a rotational energy barrier. In future work a full analysis of the distribution of rotaional energy barriers will be presented.

5. Conclusions

The Krätschmer et al. carbon arc method has been used to produce carbon-coated transition metal and rare earth–transition metal (carbide) nanocrystals. Particles have a nominally spherical morphology with about 20 nm radii (for Co) as determined from TEM. Small single-domain particles of elemental (carbide) magnets exhibit a superparamagnetic response with

Fig. 3. (a) $M(H)$ at 5 K and (b) SFD at 5 K for $Sm_{1-x-y}Co_xC_y$ nanocrystals (collected from carbon arc pancake region).
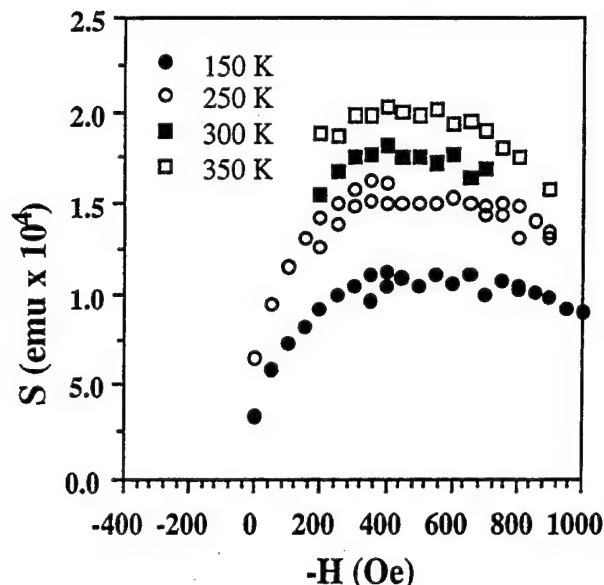
Fig. 5. Magnetic viscosity $S(T,H)$ for $Sm_{1-x-y}Co_xC_y$ nanocrystals.

hysteresis only below T_B. Protective carbon coatings and novel magnetic properties make these potentially interesting for applications. To be viable for recording or other applications requiring stable moments at room temperature, larger particles and/or magnetic anisotropy will need to be developed. Alloy magnets with large magnetocrys-talline anisotropies offer promise as potentially thermally stable fine-particle magnets. $SmCo_x$ fine-particle magnets produced by a carbon arc process have large blocking temperatures, making them attractive as thermally stable magnets at room temperature.

Acknowledgements

References

[1] H.W. Kroto, J.R. Heath, S.C. O'Brien, R.F. Curl and R.E. Smalley, *Nature, 318* (1985) 162.
[2] W. Krätschmer, L.D. Lamb, K. Fostiropoulos, and D.R. Huffman, *Nature, 347* (1990) 354.
[3] S. Ijima, *Nature, 354* (1991) 57.
[4] D. Ugarte, *Nature, 359* (1992) 707. H.W. Kroto, *Nature, 359* (1992) 6701.
[5] Y. Chai, T. Guo, C. Jin, R.E. Haufler, L.P.F. Chibante, J. Fure, L. Wang, J.M. Alford and R.E. Smalley, *J. Phys. Chem., 95* (1991) 7564.
[6] R.S. Ruoff, D.C. Lorents, B. Chan, R. Malhotra and S. Subramoney, *Science, 259* (1993) 346.
[7] M. Tomita, Y. Saito and T. Hayashi, *Jpn. J. Appl. Phys., 32* (1993) L280.
[8] S.A. Majetich, J.O. Artman, M.E. McHenry, N.T. Nuhfer and S.W. Staley, *Phys. Rev. B, 48* (1993) 16 845.
[9] E.M. Brunsman, M.E. McHenry, S.A. Majetich, J.O. Artman, M. De Graef, S.W. Staley, R. Sutton, E. Bortz, S. Kirkpatrick, K. Midelfort, J. Williams and B. Brunett, *J. Appl. Phys., 75* (1994) 5879.
[10] M.E. McHenry, S.A. Majetich, J.O. Artman, M. De Graef and S.W. Staley, *Phys. Rev. B, 49* (1994) 11 358.
[11] E.M. Brunsman, R. Sutton, E. Bortz, S. Kirkpatrick, K. Midelfort, J.M. Williams, P. Smith, M.E. McHenry, S.A. Majetich, J.O. Artman and S.W. Staley, *J. Appl. Phys., 75* (1994) 5882.
[12] B.D. Cullity, *Introduction to Magnetic Materials*, Addison-Wesley, Reeding, MA, 1972.
[13] S. Chikazumi, *Physics of Magnetism*, Kreiger, Malabar, FL, 1978.
[14] F.E. Luborsky, *J. Appl. Phys. 32* (1961) 171S–183S.
[15] C. Kittel, *Introduction to Solid State Physics*, Wiley, New York, 5th edn., 1976.
[16] C.P. Bean and J.D. Livingston, *J. Appl. Phys., 30* (1959) 120S–129S.
[17] I.S. Jacobs and C.P. Bean, in G.T. Rado and H. Suhl (eds.), *Magnetism*, Vol. 3, Academic Press, New York, 1963.
[18] R. Street and J.C. Wooley, *Proc. Phys. Soc. (London) A, 62* (1949) 562.
[19] P. Gaunt, *J. Appl. Phys., 48* (1977) 3470.
[20] J.F. Herbst, *Rev. Mod. Phys., 63* (1991) 819.
[21] E. Brunsman, S. Anna, S.A. Majetich and M.E. McHenry, *Mater. Res. Soc. Symp. Proc., 359* (1995).
[22] E.C. Stoner and E.P. Wohlfarth, *Philos. Trans. Roy. Soc. London A, 240* (1948) 599.
[23] G. Bate, *Proc. IEEE, 74* (1986) 1513.
[24] A.J.J. Koch, P. Hokkeling, M.G.V.D. Steeg and K.J. De Vos, *J. Appl. Phys., 31* (1960) 75S.
[25] Y.J. Kim and J.H. Perepezko, *J. Appl. Phys., 71* (1992) 676.
[26] Kh. Y. Mulyukov and S.B. Khaphizov, *J. Alloys Comp., 182* (1992) 69.
[27] H. Gobel, E. Wolfgang and H. Harms, *Phys. Status Solidis 34* (1976) 553 and references cited therein.
[28] J. Becker, *IEEE Trans. Magn. 5* (1969) 211, and references cited therein.

Magnetotransport properties of annealed (Fe–Co)/Ag multilayers

D.V. Dimitrov, A.S. Murthy, G.C. Hadjipanayis

Department of Physics and Astronomy, University of Delaware, Newark, DE 19716, USA

Abstract

The dependence of the giant magnetoresistance (GMR) on the sputtering pressure, the presence of a Ta underlayer and overlayer, the annealing temperature and the bilayer thickness has been studied in sputtered (Fe–Co)/Ag multilayers. The optimum sputtering pressure was found to be 5 mTorr. The Ta underlayer and overlayer influence greatly the microstructural changes during heat treatment and consequently the magnitude of magnetoresistance. The magnetoresistance increases initially with increasing annealing temperature, reaches a maximum in the region between 250 and 325 °C and after that decreases. The maximum GMR was 8.43% at 46 K and 5.29% at room temperature for films with Ta layers annealed at 275 °C. The magnetic properties are also affected by the annealing. The as-sputtered samples show coercivity in the range 60–220 Oe. After heat treatment in vacuum for 10 min the coercivity drops dramatically in all samples. The films with the highest GMR are believed to be superparamagnetic.

Keywords: Magnetotransport properties; Annealing; Sputtering

1. Introduction

Since the discovery of giant magnetoresistance [1] an immense number of studies covering different aspects of the phenomenon have been published. Giant magnetoresistance (GMR) has been observed in multilayers [1], granular filme [2,3] and recently in broken (Fe–Ni)/Ag multilayers [4]. The latter of these do not exhibit a very high GMR, about 25% [5] at room temperature, but they are interesting because of their sharp magnetoresistive curves and consequently their high sensitivity. This work is a continuation of our previous study on (Fe–Co)/Ag granular films [6] and annealed multilayers [7]. In the first system the main focus was on the dependence of GMR on composition. It was found that the maximum GMR occurs for 65–70 at.% for which there is a substantial fraction of magnetic material but still the samples are far from percolation. The optimum composition for the magnetic component was found to be 33 at.% Fe and 67 at.% Co and the corresponding GMR was 29% at 30 K and 11% at 300 K. For this particular composition it was observed that the magnetorsisance curve is much sharper than that of Co/Ag granular films. In the second system we studied the influence of annealing conditions on the magnitude of GMR. The optimum annealing temperature was found

to be around 300 °C. In both systems the samples with the highest GMR were superparamagnetic as indicated by their negligible coercivity and overlapping M vs. H/T curves. The main objectives of this work are to study the influence of the sputtering pressure, the annealing temperature, the bilayer thickness and the presence of Ta underlayer and overlayer on the magnetic and saturating fields of GMR as well as on microstructure and magnetic properties.

2. Experimental

$(Fe_{33}Co_{67}/Ag)_{10}$ multilayers were deposited on water-cooled substrates using d.c. magnetron sputtering from composite targets. The presputtering pressure was 8×10^{-8} Torr. Sputtering was performed at 5 mTorr Ar pressure for the Ag and Ta layers and at 3, 5 and 10 mTorr for the Fe–Co layers. Two types of film were prepared: one deposited directly and the other sandwiched between 2.7 nm Ta layers. The thickness of the Fe–Co layers was kept constant about 0.7 nm but the thickness of the Ag layers was varied between 2 and 3 nm. The number of bilyers for all films was 10. A summary of the samples prepared is given in Table 1. Pre-cleaned glass strips were used as substrates for

Table 1
Description of the prepared films

Deposited on glass		Ta layers on top and bottom	
Layer thicknesses (nm)	Pressure P (mTorr)	Layer thicknesses (nm)	Pressure P (mTorr)
Fe–Co, 0.7; Ag, 2.0	3	Fe–Co, 0.7; Ag, 2.0	3
	5		5
	10		10
Fe–Co, 0.7; Ag, 3.0	3	Fe–Co, 0.7; Ag, 3.0	3
	5		5
	10		10

GMR and X-ray diffraction (XRD) measurements, carbon-coated copper grids for transmisison electron microscopy (TEM) and aluminum foils for magnetic measurements. Films were annealed in vacuum of 10^{-6} Torr in the temperature interval 200–350 °C for 10 min. Small-angle XRD (Phillips APD 3520) was used to determine the bilayer thickness and a JEOL JEM-200FX transmission electron microscope to study the structure and microstructure. A superconducting quantum magnetometer with fields as high as 50 kOe was used to study the magnetic properties and GMR using the four-point technique at 46 and 300 K.

3. Results and discussion

Transmission electron micrographs show that all the as-sputtered films are uniform and consist of small grains. Fig. 1 shows a typical dark-field image from as-sputtered sample showing that the average grain size is about 5 nm. Selected-area diffraction (SAD) and XRD spectra show the presence of only f.c.c. Ag (Fig. 2). The absence of Fe or Co reflections is similar to the case observed in Co/Ag and Fe/Ag granular films. In Co/Ag [8], previous high resolution TEM studies showed that the size of the Co particles is only 1–2 nm. As a result the reflections from Co are too weak to be observed. For Fe/Ag films [9] it was also found, using thermomagnetic data, that the size of the Fe particles is only a few nanometers as well.

Heat treatment causes changes in microstructure. The films without Ta layers crack. A large number of very large particles, of size about 100 nm, can be seen (Fig. 3). In contrast the films deposited on Ta show a relatively uniform microstructure after annealing with a grain size about 6 nm (Fig. 4). Microdiffraction patterns from the large particles (shown in the inset of Fig. 3) revealed that they are all f.c.c. Ag.

The magnetoresistive data, taken at 46 K, are summarized in Table 2. The upper numbers represent the GMR of the as-sputtered films, and the lower numbers the maximum GMR after annealing. It can be seen that

both the sputtering pressure and the presence of Ta layers have an influence on the magnetoresistance. The presence of Ta layers increases the magnitude of GMR for all samples. This can be attributed to the fact that Ta layers prevent cracking of multilayers and formation of large particles. The sputtering pressure is also observed to play a role. 5 mTorr appears to be the optimum pressure. Small-angle XRD data on samples
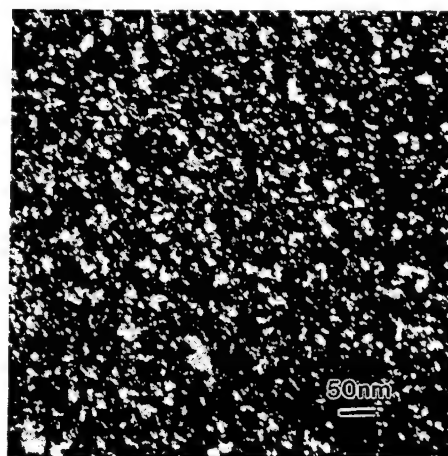
Fig. 1. Dark-field micrograph of as-made sample.
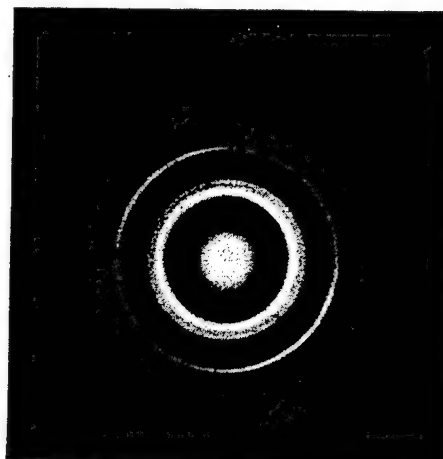
Fig. 2. SAD of as-made sample.
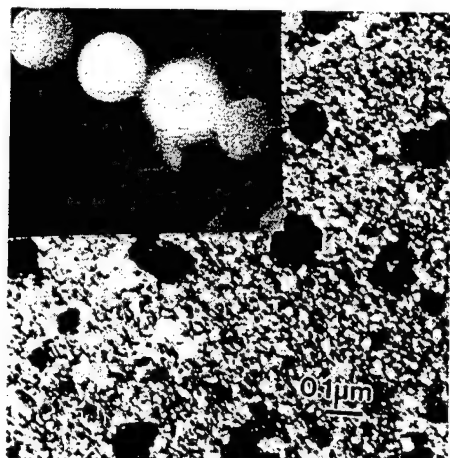
Fig. 3. Dark field micrograph of annealed sample without Ta layers.
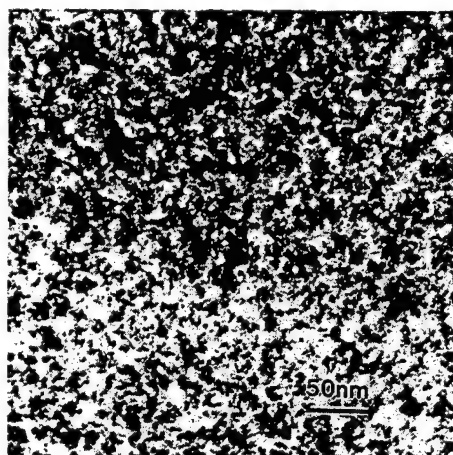
Fig. 4. Dark-field micrograph of annealed sample with Ta layers.

prepared under these conditions are much sharper and clearer compared with those for other pressures. This indicates that the interface roughness is the smallest for this particular pressure.

The dependence of magnetoresistance on annealing temperature is shown in Fig. 5 for films with 3 nm Ag layers deposited directly on glass and in Fig. 6 for the identical films with Ta layers. The GMR initially increases, reaches a maximum in the temperature range 250–325 °C and above 325 °C decreases. It is seen that for high annealing temperatures the behaviors for the two different types of sample are different. The GMR in films without Ta falls off vary rapidly in contrast with films with Ta. This behavior is consistent with the fact that Ta prevents cracking of the magnetic layers and preserves the film uniformity during annealing.

Heat treatment was found to have a substantial influence on the sharpness of the magnetoresistive curves (Fig. 7). The sharpness increases with increasing annealing temperature. Ta layers do not affect this behavior much.

The as-sputtered samples show small but non-zero coercivity in the range 60–220 Oe. Annealing decreases the coercivity substantially. This can be attributed to two factors. The first is that heat treatment decreases the number of defects in the films and this is supported by the observed large decrease (a factor of 2) of resistivity. The second reason is the Ag penetration into Fe–Co layers, which promotes the formation of separated superparamagnetic particles. This was further verified by M vs. H/T plots (Fig. 8) for the sample with 3 nm Ag and Ta layers. The overlapping is clear and this indicates the superparamagnetic behavior of the sample [10]. The size of the superparamagnetic granules in our films was determined to be about 4 nm using the temperature dependence of susceptibility above the blocking temperature. For this purpose we used the fact that an ensemble of superparamagnetic particles obeys the Langevin law. From the slope of the inverse of susceptibility vs. the temperature curve we find the average magnetic moment of the particles which allows

Table 2
Summary of grant magnetoresistance data

Deposited on glass				Ta layers on top and bottom			
Layer thicknesses (nm)	P (mTorr)	Film	GMR (%)	Layer thicknesses (nm)	P (mTorr)	Film	GMR (%)
Fe–Co, 0.7; Ag, 2.0	3	As made	1.4	Fe–Co, 0.7; Ag, 2.0	3	As made	0.98
		Annealed	0.9			Annealed	2.43
	5	As made	1.4		5	As made	6.1
		Annealed	0.9			Annealed	1.91
	10	As made	1.2		10	As made	5.93
		Annealed	1.0			Annealed	5.93
Fe–Co, 0.7; Ag, 3.0	3	As made	1.4	Fe–Co, 0.7; Ag, 3.0	3	As made	2.55
		Annealed	3.5			Annealed	2.83
	5	As made	5.8		5	As made	7.1
		Annealed	6.6			Annealed	8.43
	10	As made	1.6		10	As made	1.34
		Annealed	1.8			Annealed	4.73

D.V. Dimitrov et al. / Materials Science and Engineering A204 (1995) 25–29
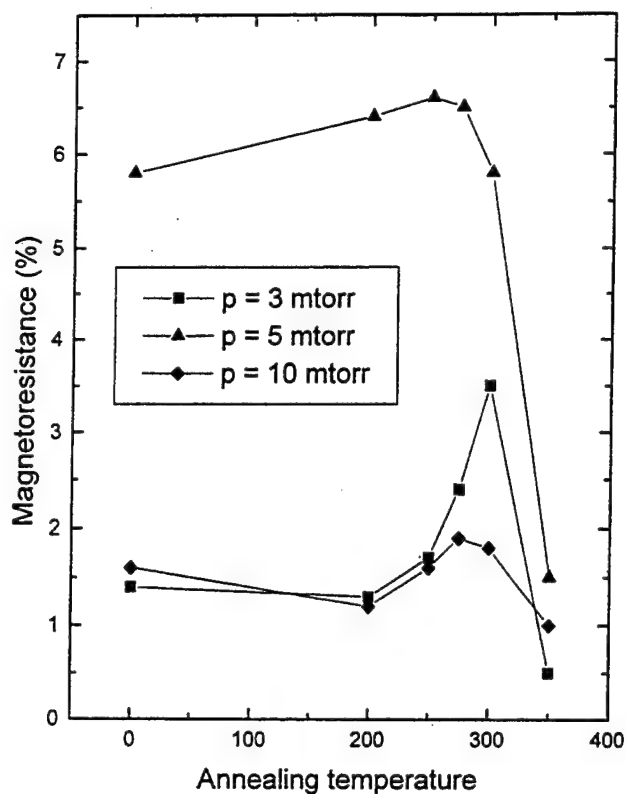
Fig. 5. Dependence of GMR on annealing temperature for film without Ta and 3 nm Ag thickness.
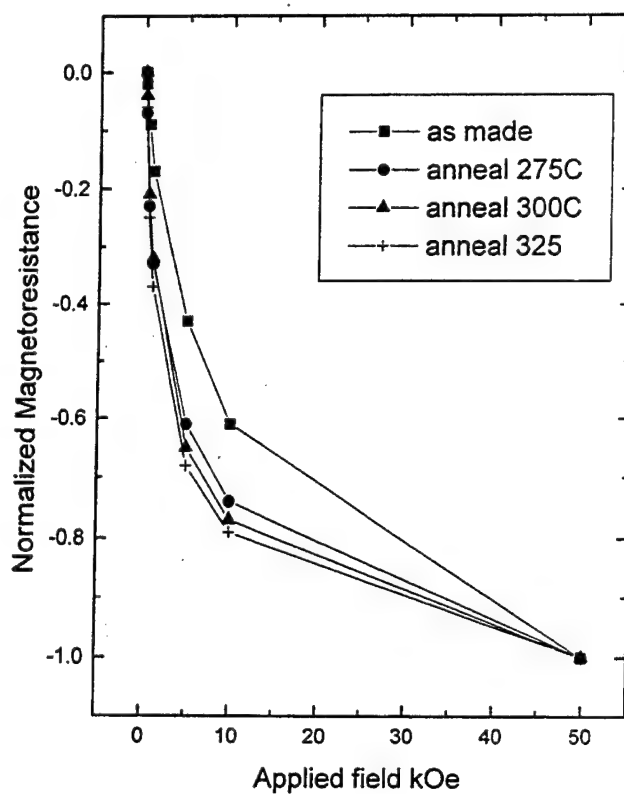
Fig. 7. Normalized GMR curves for as-made and annealed samples.
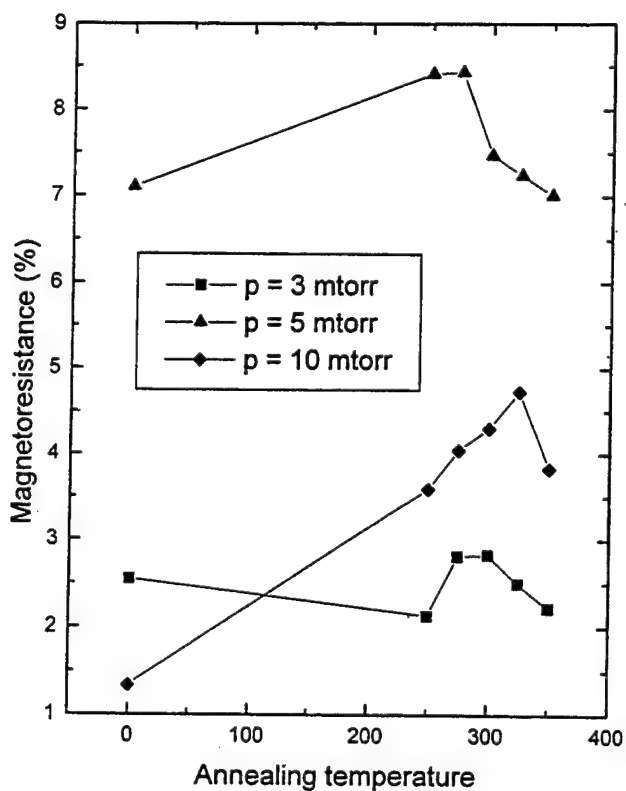
Fig. 6. Dependence of GMR on annealing temperature for films with Ta layers and 3 nm Ag thickness.
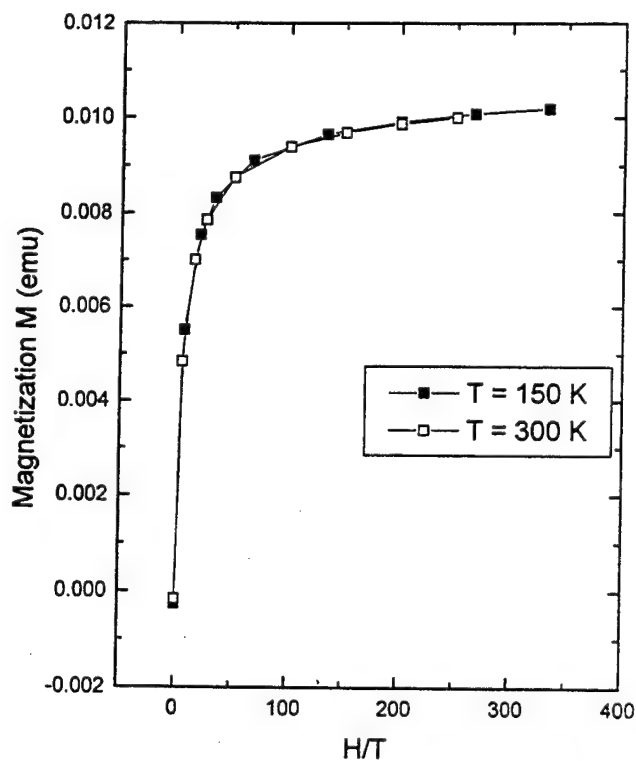
Fig. 8. Superposition of magnetization M vs. applied magnetic field over temperature H/T for 150 and 300 K.

us to estimate the size by dividing it by the saturation magnetization of $Fe_{33}Co_{67}$ [10]. The same superparamagnetic behavior and particle size are also observed for the corresponding samples without Ta layers. For the samples with 2 nm Ag annealed in the same conditions the coercivity also decreases and the M vs. H/T curves are very close to overlapping, but still not exactly. It may be possible that the amount of Ag is not sufficient to break the Fe–Co layers completely and to form isolated superparamagnetic particles.

In summary our data indicate that, during heat treatment, Ag penetrates into Fe–Co and promotes breakup of layers and the formation of isolated magnetic particles. The magnetoresistance occurs because of spin-dependent scattering at the surfaces of these magnetic granules. This is further supported by the fact that the maximum GMR is observed in samples showing superparamagnetic behavior.

Acknowledgment

References

[1] M.N. Baibich, J.M. Broto, A. Fert, F. Nguyen van Dan, F. Petroff, P. Etienne, G. Grenzet, A. Frederich and J. Chazeles, *Phys. Rev. Lett.*, *68* (1988) 2422.

[2] J.Q. Xiao, J.S. Jiang and C.L. Chien, *Phys. Rev. Lett.*, *61* (1992) 3749.

[3] A. Berkowitz, J.M. Carey, J.R. Mitchell, A.P. Young, S. Zhang, F.E. Spada, F.P. Parker, A. Hutten and G.R. Thomas, *Phys. Rev. Lett.*, *68* (1992) 3745.

[4] T.L. Hylton, K.R. Coffey, M.A. Parker and J.K. Howard, *Science 261* (1993) 1021.

[5] S.S.P. Parkin, Invited Talk, *American Physical Society March Meet.*, *Pittsburgh, PA, 1994*.

[6] A. Tsoukatos, D.V. Dimitrov and G.C. Hadjipanayis, *6th Joint MMM–INTERMAG Conf.*, *Albuquerque, NM, 1994*.

[7] D.V. Dimitrov, A. Tsoukatos, A.S. Murthy and G.C. Hadjipanayis, *American Physical Society March Meet. Pittsburgh, PA, 1994*.

[8] H. Wan, A. Tsoukatos, C.G. Hadjipanayis and Z.G. Li, *Phys. Rev. B*, *49* (1994) 1524.

[9] J.-Q. Wang and G. Xiao, *Phys. Rev. B.*, *49*(6) (1994) 3982.

[10] B.D. Cullity, *Introduction to Magnetic Materials*, Addison-Wesley, Reading, MA, 1972.

Structural and magnetic properties of granular $Cr_{100-x}Fe_x$

J.A. Christodoulides, A.S. Murthy, G.C. Hadjipanayis

Department of Physics and Astronomy, University of Delaware, Newark, DE 19716, USA

Abstract

Granular films of Cr–Fe have been prepared by d.c. magnetron sputtering over the Cr content range 10–90 at.%, on both heated and water-cooled substrates. Transmission electron microscopy studies, used for the microstructural characterization of the samples, show a composition-dependent grain size, in the range 10–150 Å. X-ray studies showed that the CR-rich and Fe-rich samples are b.c.c. Those with intermediate composition showed extra diffraction lines which may be indexed with the Cr s.c. structure. Magnetic properties, such as coercivity H_C and giant magnetoresistance, were also found to be strongly composition dependent, with maximum values of 320 Oe and 7.5% respectively, measured at 35 K.

Keywords: Magnetic properties; Chromium; Iron; D.C. magnetron sputtering

1. Introduction

Metallic granular films, consisting of magnetic granules in a non-magnetic matrix, have attracted much interest in the last few years because of their magnetic hysteresis and giant magnetoresistance behavior. Examples of such metallic systems, include Co–Ag [1], Fe–Ag [2,3] and Co–Cu [4] films. The grant magnetoresistance (GMR) effect was first discovered in magnetic multilayers such as Co–Cu [5] and Cr–Fe [6,7], and then in granular (Fe,Co)–(Ag,Cu) films [8,9]. Recently, GMR has also been reported in Cr–Fe heterogeneous alloy films [10]. Cr–Fe has an isostructure two-phase region below 475 °C. A σ phase is present in the temperature range from 475 to 820 °C and this makes high temperature annealing for inducing phase separation difficult. Above 820 °C, Cr and Fe are entirely miscible [11]. We have initiated a study to understand the origin of GMR in Cr–Fe films by correlating their magnetic and GMR properties with their structure and microstructure. Preliminary results of this study are reported in this article.

2. Experimental procedure

Cr–Fe films were prepared by d.c. magnetron sputtering using the tandem deposition method [12] on both water-cooled (about 10 °C) and heated (200 °C) Al substrates. The particular deposition method was chosen in order to ensure that the resulting specimens were stable phase-separated granular films. The chamber base pressure was of the order of 10^{-8} Torr, while during sputtering an argon gas presure of 5 mTorr was maintained. The deposition rate was in the range 0.7–2.9 Å s^{-1}. Inductively coupled plasma emission, provided the composition data for the films. The Cr volume percentage was varied between $x_v = 10.0$ and $x_v = 90.0$, whereas the thickness of the films was kept constant at about 2000 Å.

The magnetic properties were measured using a superconducting quantum interference device magnetometer in the temperature range 10–300 K. Magnetoresistance (MR) was measured at 35 K by the conventional four-probe technique. Coercivity H_C was also measured at 35 K for all samples. Transmission electron microscopy (JEOL 2000FX) and X-ray diffraction (XRD) (Philips APD3520) studies were used to determine the crystal structure and microstructure of the samples. Heat treatment of films was performed in order to promote phase separation and particle growth. In preparation for annealing, the samples were encapsulated in glass tubes under a vacuum of 10^{-6} Torr. The annealing time was 30 min at a temperature of 450 °C.

3. Results and discussion

Fig. 1 shows the dark-field images and the corresponding selected-area diffraction (SAD) patterns of as-made $Cr_{100-x}Fe_x$ with $x = 15.9$, 50.2 and 80.4 at.% respectively, deposited at a low temperature (about 10 °C). The SAD patterns indicate that the Fe-rich and Cr-rich samples have a b.c.c. structure as expected (both Fe and Cr are b.c.c. with lattice parameters $a = 2.8664$ and 2.8839 Å respectively). However, the SAD patterns of samples with Cr content in the range $x = 19.4$–66.0 at% appear to be different. Indexing of these patterns indicates that Cr may have an s.c. structure. Previous studies [13] have also reported an s.c. structure for pure Cr films evaporated at a low pressure

Fig. 2. XRD patterns of as-made $Cr_{100-x}Fe_x$, with $x = 15.9$, 50.2 and 80.4 at.%.

in the presence of pure argon. The same studies claimed that this structure transforms to b.c.c. upon annealing at 450 °C. This behavior was also verified by XRD (Fig. 2). The grain size of Fe particles is found to vary almost linearly with the Fe content, from 15 to 190 Å (Fig. 3). Upon annealing at 450 °C, the films transform to b.c.c. for the entire composition range. In both the as-made and the annealed samples, with low Fe content ($x < 24$ at.%) there is a tendency for cluster formation with a size about 1000 Å. These clusters are probably due to the presence of Fe-rich ferromagnetic isostructural particles.

M. vs. H loops, show that as-made films with a high Fe content (34 at.% or less) saturate at low applied fields while the Cr-rich films appear to be paramagnetic (Fig. 4). Thermomagnetic data for the former films show a peak at around $T = 50$ K for most samples which can be related to the blocking temperature of the magnetic granules (Fig. 5).

$Cr_{84.1}Fe_{15.9}$

$Cr_{49.8}Fe_{50.2}$

$Cr_{19.6}Fe_{80.4}$

Fig. 1. SAD and corresponding dark-field images of as-made $Cr_{100-x}Fe_x$, with $x = 15.9$, 50.2 and 80.4 at.%.
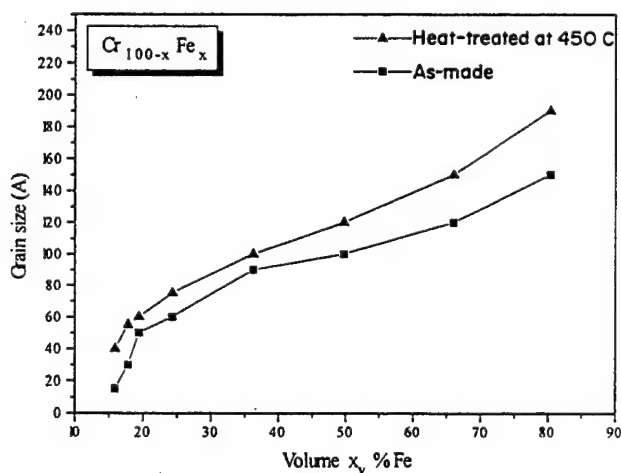
Fig. 3. Fe content dependence of grain size for as-made and heat-treated samples.
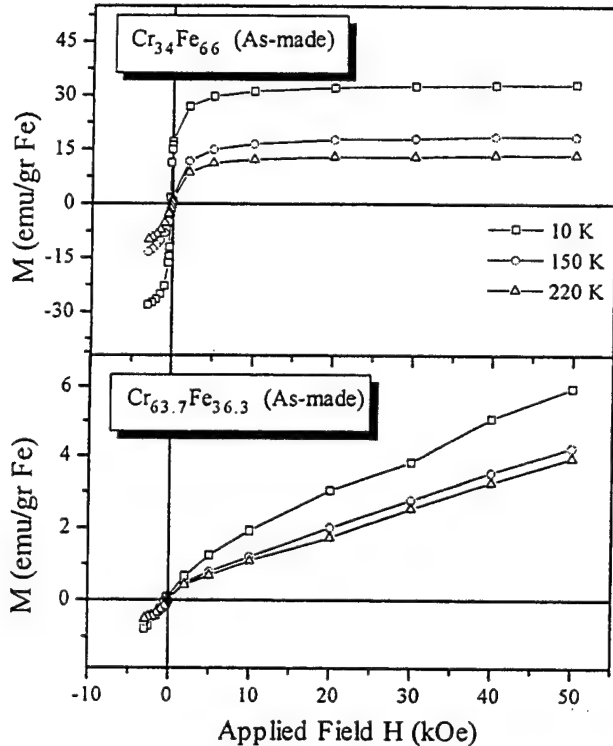
Fig. 4. $M_T(H)$ curves of $Cr_{34}Fe_{66}$ and $Cr_{63.7}Fe_{36.3}$ as-made films.

The coercivity as a function of Fe contant can be seen in Fig. 6, for both the as-made and the annealed samples. Since the Fe content depends almost linearly on the grain size, we can expect a similar trend for the
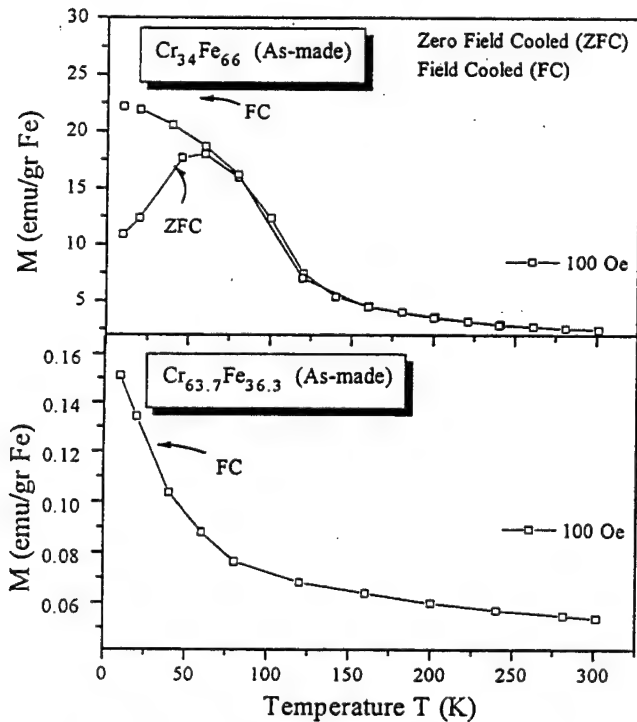
Fig. 5. Thermodynamic data of $Cr_{34}Fe_{66}$ and $Cr_{63.7}Fe_{36.3}$ as-made films.
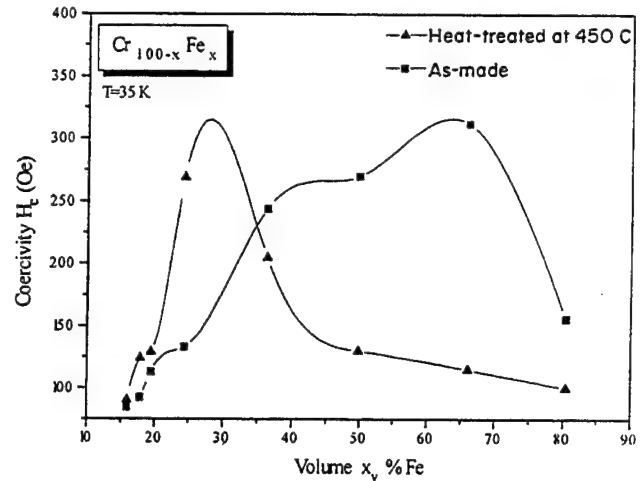
Fig. 6. Fe content dependence of coercivity H_C at $T = 35$ K, for as-made and heat-treated samples.

coercivity (Fig. 7). When the particle size is increased, H_C is increased because of thermal effects. The decrease on higher Fe content is due to the onset of percolation. Upon annealing, H_C increases for films with Fe content below 30 at.%. The reason for this behavior is believed to be the increase in grain size. The maximum coercivity for the as-made samples is 312 Oe and it is observed for $Cr_{34}Fe_{66}$. For the heat-treated films a maximum H_C of 269 Oe is observed for $Cr_{75.7}Fe_{24.3}$.

The magnetic studies indicate that the films with high Fe contant have a ferromagnetic behavior. As we decrease the Fe content, the films exhibit paramagnetic behavior. Finally, at low Fe content (less than 17 at.%), there is an indication of superparamagnetic behavior, which is also verified from the overlapping of the corresponding M vs. H/T curves. This behavior is probably due to the small Fe particle size (of the order of 10 Å).
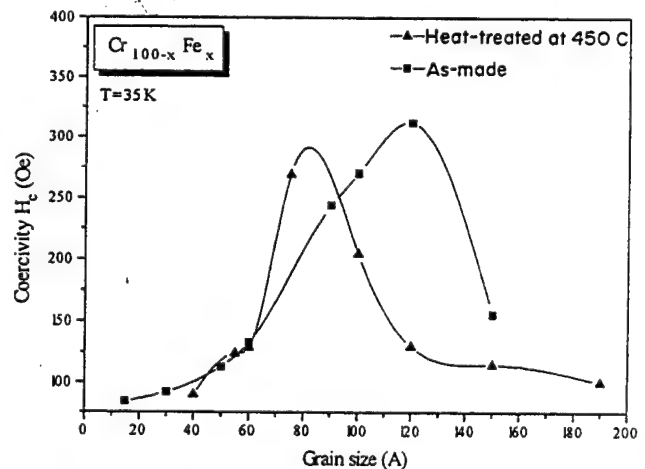
Fig. 7. Grain size dependence of coercivity H_C at $T = 35$ K, for as-made and heat-treated samples.
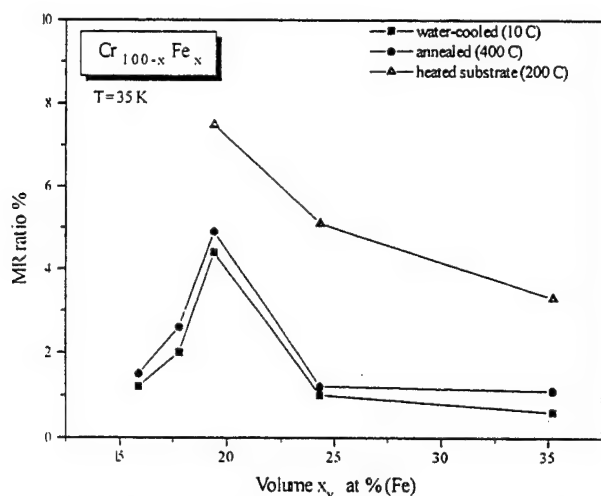
Fig. 8. Fe content dependence of MR ratio, at $T = 35$ K.

GMR was observed in all three sets of samples, with the highest value obtained in samples grown on heated substrates. The GMR was found to be composition dependent. Fig. 8 shows values of the MR ratio $(\rho_{(H=0)} - \rho_{(H=50\,\mathrm{kOe})})/\rho_{(H=50)}$ vs. Fe content. The MR ratio has a maximum value of 7.5% at around $x = 19$ at.% Fe, for all samples. Similar behavior has been observed in other systems such as Ag–Fe [2]. However, the MR ratio is higher for the heated substrate than for the water-cooled substrate.

4. Conclusions

Our structural studies of sputtered granular $Cr_{100-x}Fe_x$ indicate an s.c. structure for as-made films deposited onto water-cooled substrates, in the range $x = 20$–66 at.%. After heat treatment at 450 °C, this structure transforms to b.c.c. The grain size appears to increase with the increasing Fe content of the films and upon annealing grows by about 25%. Coercivity was found to be strongly composition dependent with a

maximum value of 312 Oe for as-made $Cr_{34}Fe_{66}$. The MR ratio showed a maximum value at around $x = 19$ at.% Fe for all sets of samples. The largest MR value of 7.5% was measured on samples deposited on heated substrates.

References

[1] J.Q. Xiao, J.S. Jiang and C.L. Chien, *Phys. Rev. B*, *46* (1992) 9266.
[2] G. Xiao, J.Q. Wang and P. Xiong, *Appl. Phys. Lett.*, *62* (1993) 420.
[3] S.A. Makhlouf, K. Sumiyama, K. Wakoh, K. Suzuki, K. Takanashi and H. Fujimori, *J. Magn. Magn. Mater.*, *126* (1993) 485.
[4] A.E. Berkowitz, J.R. Mitchell, M.J. Carey, A.P. Young, S. Zhang, F.E. Spada, F.T. Parker, A. Hutten and G. Thomas, *Phys. Rev. Lett.*, *68* (1992) 3745.
[5] S.S. Parkin, Z.G. Li and D.J. Smith, *Appl. Phys. Lett.*, *58* (1991) 2710.
[6] M.N. Baibich, J. Broto, A. Nguyen van Dau, F. Petroff, P. Etienne, G. Creuzet, A. Friedrich and J. Chazelas, *Phys. Rev. Lett.*, *61* (1988) 2472.
[7] L.H. Chen, T.H. Tiefel, S. Jin, R.B. Van Dover, E.M. Gyorgy and R.M. Fleming, *Appl. Phys. Lett.*, *63* (1993) 1279.
[8] A. Tsuokatos, H. Wan, G.C. Hadjipanayis and Z.G. Li, *Appl. Phys. Lett.*, *61*(25) (1992) 3059.
[9] A.E. Berkowitz, J.R. Mitchell, M.J. Carey, A.P. Young, S. Zhang, F.E., Spada, F.T. Parker, A. Hutten and G. Thomas, *J. Appl. Phys.*, *73*(10) (1993) 5320.
[10] K. Tanakashi, T. Sugawara, K. Hono and H. Fujimori, to be published.
[11] T.B. Massalski, J.L. Murray, L.H. Bennett and H. Baker (eds.), *Binary Alloy Phase Diagrams*, American Society for Metals, Metals Park, OH, 1986, p. 822.
[12] A. Tsoukatos, H. Wan, G.C. Hadjipanayis and K.M. Unruh, *J. Appl. Phys.*, *73* (1993) 5509.
[13] Kimoto and Nishida, *J. Phys. Soc. Jpn.*, *22* (1967) 744.

Thermal expansion and heat capacity of porosity-free nanocrystalline materials

Tibor Turi, Uwe Erb

Department of Materials and Metallurgical Engineering, Queen's University, Kingston, Ont. K7L 3N6, Canada

Abstract

The large fraction of atoms associated with the interfacial regions of nanocrystalline materials has been recognized to influence many properties. In the present work, the temperature dependent linear coefficient of thermal expansion and isobaric heat capacity of porosity-free nanocrystalline materials produced by electrodeposition were measured and compared with results obtained for conventional polycrystalline material and other nanocrystalline materials. The results show that neither of these properties is strongly affected by grain size in porosity-free materials, suggesting that the relatively large changes previously reported for gas condensed materials may be due to porosity rather than the small grain size per se.

Keywords: Thermal expansion; Heat capacity; Nanocrystalline materials

1. Introduction

One of the main areas of scientific interest of nanocrystalline materials is their thermodynamic properties. Since the atomic structure of materials, their stability, and their atomic interactions are related in complex ways to their thermodynamic properties, it is of great fundamental interest to explore the thermodynamic consequences of a material system with a high volume fraction of atoms associated with interfacial regions. The coefficient of linear thermal expansion α_L and the isobaric heat capacity C_p are considered here.

Rupp and Birringer [1] found α_L for nanocrystalline copper of 8 nm grain size to be nearly twice that of regular polycrystalline copper. However, the nanocrystalline copper was only 90% dense. Heat capacities of nanocrystalline copper and palladium were also found to be increased by 10% and 40% respectively [1]. Thermodynamic models based on quasiharmonic approximations used to predict theoretically the thermodynamic properties as a function of grain boundary free volume have produced similar increases in α_L (70%–85%) and C_p (10%–25%) for nanocrystalline palladium with respect to conventional polycrystalline palladium [2]. Fecht's calculations [3] also predict increases by a factor of 2 in both volumetric thermal expansion and heat capacity.

More recent results by Gleiter [4] show that the differences for α_L between nanocrystalline and conventional microcrystalline copper depend strongly on the applied pressure during consolidation of gas condensed powder. The general trend was that this difference decreased with increasing compaction pressure. Some compacted nanocrystals even showed a slight reduction of α_L from the value of polycrystalline material. Lu et al. [5] observed an increase in α_L of about 60% and 12% in C_p for Ni–P alloys crystallized from amorphous precursors. However, these materials consisted of two phases (f.c.c. Ni and b.c.t. Ni_3P) and cannot be compared directly with single-phase materials.

Many of the previously measured properties of nanocrystalline solids were obtained on consolidated gas condensed materials which have a considerable amount of entrained porosity. This porosity effectively lowers the density of the material and may drastically alter the experimental results and, therefore, impair the reliability and accuracy in the measurement of the intrinsic properties of nanostructured materials [6]. In fact, recent results have shown several inconsistencies in measured properties between these consolidated materials and porosity-free electrodeposited nanocrystalline materials [7]. It is the objective of this work to examine to what extent changes in thermal expansion
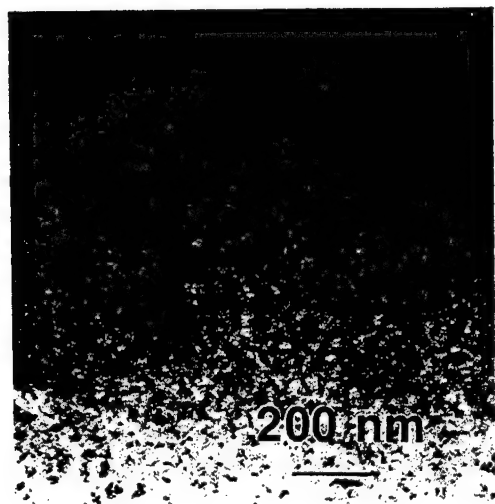
(a)

(b)
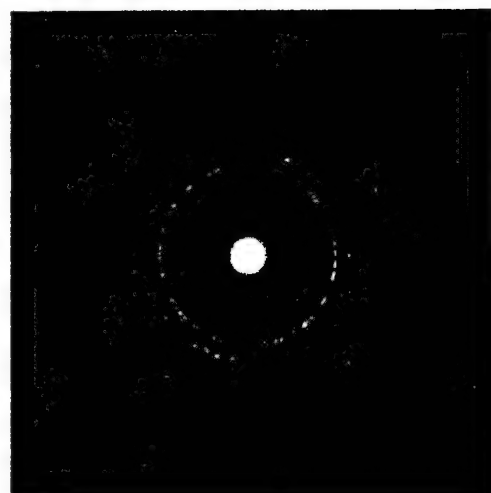
(c)

Fig. 1. Transmission electron micrographs of as-electrodeposited nickel with 20 nm average grain size: (a) bright field micrograph, (b) dark field micrograph, (c) electron diffraction pattern.
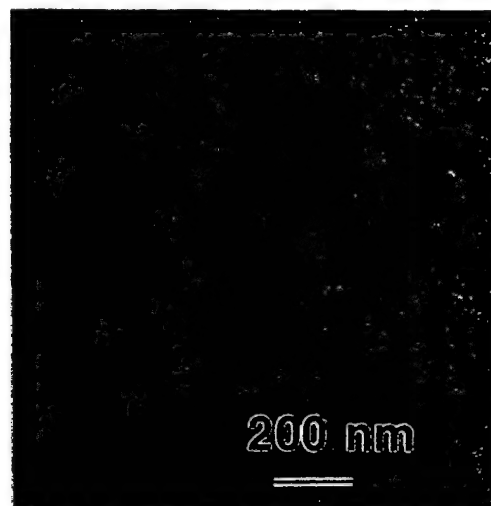
(a)
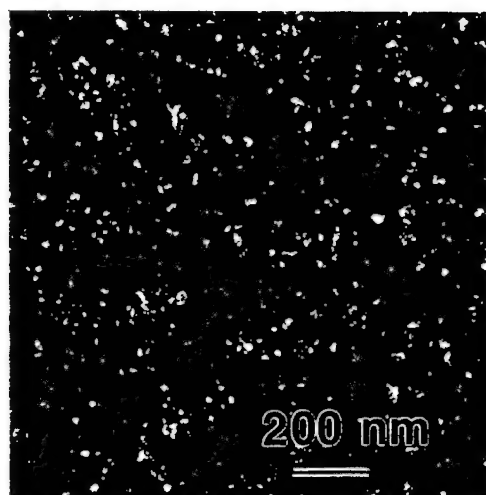
(b)

(c)

Fig. 2. Transmission electron micrographs of as-electrodeposited 80Ni–20Fe with 15 nm average grain size: (a) bright field micrograph, (b) dark field micrograph, (c) electron diffraction pattern.

and heat capacity may be correlated to grain size reduction in the absence of any entrained porosity.

2. Experimental

The nanocrystalline samples used in this study were electrodeposited onto a titanium electrode using recently developed synthesis techniques [8,9]. Nanocrystalline materials produced by these techniques are essentially fully dense [10]. Bulk nanocrystalline samples of two different compositions were plated to a thickness of about 200 μm and then mechanically stripped from the substrate for property measurements: (1) nanocrystalline nickel with 20 nm grain size and 99.9% purity [8], and (2) an 80 at.% nickel and 20 at.% iron nanocrystalline nickel–iron alloy of composition close to that of conventional Permalloy [9]. The composition of the nickel-iron alloy electrodeposit was determined by energy dispersive X-ray spectroscopy. A conventional polycrystalline nickel sheet of 100 μm grain size, 500 μm thickness, and 99.98% purity was used as a fully annealed reference material.

Thin foils for transmission electron microscopy (TEM) were obtained by jet-polishing in an electrolyte consisting of 10% perchloric acid, 15% acetic acid, and 75% methanol at about 25 V d.c. and a temperature of −10 °C. TEM dark field micrographs were used to determine directly the average grain size based on 200 grain diameter measurements.

The 20 nm nickel and 15 nm nickel–iron samples were cut by electric discharge machining into 25 mm long by 6 mm wide specimens required for measurement of thermal expansion. A Theta differential quartz pushrod dilatometer using a linear variable differential transducer equipped with a cryogenic temperature attachment was used for this experiment and was calibrated in situ against a tungsten reference. For all experiments, helium was used as a purge gas and a linear temperature ramp rate of 5 K min^{-1} was applied.

A TA Instruments 2910 modulating differential scanning calorimeter (MDSC) [11] with a cryogenic temperature apparatus was employed to determine continuously the constant pressure heat capacity C_p as a function of temperature. The MDSC was calibrated using a sapphire reference and the sample chamber was continuously purged with nitrogen. A linear heating rate of 5 K min^{-1}, a temperature modulation wavelength of 100 s, and an amplitude modulation of ±1.0 K were applied for all experiments.

3. Results and discussion

Figs. 1 and 2 show bright field (a) and dark field (b) electron micrographs as well as electron diffraction

patterns (c) of the as-plated nickel with an average grain size of 20 nm and nickel–iron with 15 nm grain size respectively. The well defined continuous rings in Figs. 1(c) and 2(c) are characteristic of an equiaxed nanocrystalline material with more or less random grain orientation distribution. It should be noted that over the temperature range used in the present work (140–500 K), the crystallographic texture of the nanocrystalline nickel has been shown not to be significantly altered from its as-deposited state [12]. Also, no significant grain growth occurs in this temperature range.

Fig. 3 shows the temperature dependence of the linear thermal expansion coefficient α_L for both the as-plated nanocrystalline nickel and conventional nickel between 140 and 500 K. Between 140 and 205 K, α_L is slightly higher for the nanocrystalline nickel. However, between 205 and 500 K, α_L of nanocrystalline nickel is reduced from the value observed for polycrystalline nickel, the maximum reduction being 2.6% at 500 K. Overall, the effect of grain size on α_L for pure nickel is rather small in contrast to previous observations on gas condensed materials [1].

Fig. 4 shows α_L for the 15 nm nickel–iron permalloy alloy as a function of temperature in comparison with normal polycrystalline nickel. For temperatures below 350 K the nanocrystalline nickel–iron alloy shows essentially the same behaviour as pure nanocrystalline nickel. However, beginning at 350 K a marked negative deviation in α_L with increasing temperature is observed. This phenomenon can be attributed to alloying effects and will be discussed elsewhere in more detail [13].
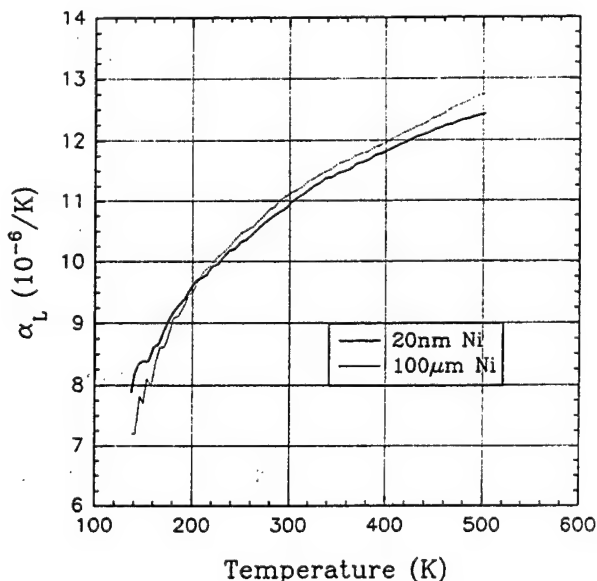
Fig. 3. Temperture dependent coefficient of linear thermal expansion of 20 nm nickel and conventional polycrystalline nickel.
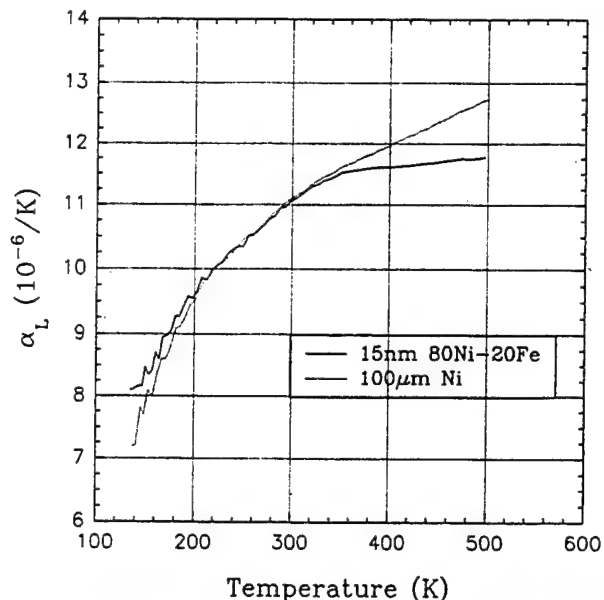
Fig. 4. Temperature dependent coefficient of linear thermal expansion of 15 nm grain size nickel–iron and conventional polycrystalline nickel.

Fig. 5 shows the heat capacity C_p as a function of temperature for nanocrystalline and normal polycrystalline nickel. Over the entire temperature range the heat capacity of nanocrystalline nickel is marginally increased above C_p for polycrystalline nickel by 2.5%–5%. As in the case of the thermal expansion coefficient, this result conflicts with observations made on gas condensed materials [1].

The structural variability of nanocrystalline materials produced by different synthesis methods may be the cause of the conflicting thermodynamic properties, in a way similar to that previously reported for mechanical and magnetic properties [7]. Before a complete understanding of the true nature of the nanocrystalline state can be obtained, it will be essential to characterize more rigorously this class of materials in terms of numerous microstructure parameters [14] including crystallographic texture, grain boundary and triple junction character distributions, impurity content, etc. as well as residual porosity, before specific properties can be unequivocally attributed to nanocrystalline grain size alone.

4. Summary

The linear thermal expansion coefficient of porosity-free electroplated nanocrystalline nickel was meaured to be approximately the same as for conventional polycrystalline material in the temperature range between 140 and 500 K. The isobaric heat capacity of nickel was found to be 2.5%–5% larger for the nanocrystalline nickel than for the conventional nickel. For nanocrystalline nickel–iron a reduction in the thermal expansion was observed for temperatures above 350 K which can be attributed to alloying effects.

Fig. 5. Temperature dependent isobaric heat capacity of 20 nm grain size nickel and conventional polycrystalline nickel.

References

[1] J. Rupp and R. Birringer, *Phys. Rev. B*, *36* (1987) 7888.
[2] M. Wagner, *Phys. Rev. B*, *45* (1992) 376.
[3] H.J. Fecht, *Phys. Rev. Lett.*, *65* (1990) 610.
[4] H. Gleiter, presented at *2nd Int. Conf. on Nanostructured Materials, Stuttgart, October 1994*.
[5] K. Lu, J.T. Wang and W.D. Wei, *J. Phys. D*, *25* (1992) 808.
[6] A.M. El-Sherik, U. Erb, V. Krstic, B. Szpunar, M.J. Aus, G. Palumbo and K.T. Aust, *Mater Res. Soc. Symp. Proc.*, *286* (1993) 173.
[7] U. Erb, *Nanostruct. Mater.*, *6* (1995) 533.
[8] A.M. El-Sherik and U. Erb, *J. Mater Sci.*, in press.

[9] C. Cheung, G. Palumbo and U. Erb, *Mater. Sci. Eng., A185* (1994) 39.

[10] T.R. Haasz, K.T. Aust, G. Palumbo, A.M. El-Sherik and U. Erb, *Scr. Metall. Mater., 32* (1995) 423.

[11] P.S. Gill, S.R. Sauerbrunn and M. Reading, *J. Thermal Anal., 40* (1993) 931.

[12] M.J. Aus, B. Szpunar, A.M. El-Sherik, U. Erb, G. Palumbo and K.T. Aust, *Scr. Metall. Mater., 27* (1992) 1639.

[13] T. Turi et al., to be published.

[14] A.M. El-Sherik, U. Erb, G. Palumbo and K.T. Aust, *Scr. Metall. Mater., 27* (1992) 1185.

Microstructural and magnetic studies of granular Gd–W films

N.B. Shevchenko*, A.S. Murthy, G.C. Hadjipanayis

Department of Physics and Astronomy, University of Delaware, Newark, DE 19716, USA

Abstract

We have studied the microstructural and magnetic properties of sputtered nanocrystalline granular Gd–W thin films as a function of annealing temperature. Granular Gd–W films were formed by annealing the as-deposited amorphous films in the temperature range 700–950 °C for 15 min. The TEM studies on the annealed samples indicate that the Gd and W phases crystallize as separate phases around 825 °C. The grain sizes of these granular phases were estimated to be about 10–30 nm. Magnetic measurements of samples annealed at 875 °C indicate the coexistence of superparamagnetic Gd with a blocking temperature near 50 K and ferromagnetic Gd with a Curie temperature near 293 K. Higher temperature annealings led to bulk-like ferromagnetic Gd behavior.

Keywords: Magnetic properties; Granular; Gadolinium; Tungsten

1. Introduction

Phase separated materials continue to be a subject of interest and investigation [1,2]. Among such materials are granular solids. The fine grain structure in granular solids gives rise to a variety of physical phenomena such as the size dependence of the Curie temperature, the ferromagnetic single domain particles, and superparamagnetism [3,4]. Most studies to date have been done on systems involving a ferromagnetic transition metal (Fe, Co, Ni) in a non-magnetic matrix material (SiO_2, Al_2O_3, BN, Cu, Ag) [5,6]. The main criteria for material selection are that they do not alloy with each other and that they do not react to form compounds. Very little work has been done outside of these said systems, especially for granular solids in which the magnetic constituent is a rare earth metal. Thus, in this study we have investigated the possibility of forming a granular solid with a rare earth metal.

The Gd–W system has been chosen for this study. It is known that Gd and W form no chemical compounds, and have very low mutual solubility. Furthermore, Gd orders ferromagnetically below its Curie temperature of 293 K while W remains paramagnetic down to very low temperatures. Thus it seems that Gd and W are ideal

ingredients for a granular solid. In this study, we have investigated the synthesis of sputtered thin film granular solids of the Gd–W system, and correlated the microstructure and magnetic properties of the films in the as-deposited state and at several stages of crystallization.

2. Preparation and measurement

Gd–W thin films were deposited on Ta foil and carbon supported Ni grids by d.c. magnetron sputtering. The tandem method of deposition was used and sputtering occurred from high purity solid metal targets. The system base pressure was 10^{-8} Torr, and sputtering was done with 5 mTorr of Ar gas pressure. A high deposition rate was used (~ 5 Å s^{-1}) to ensure an amorphous as-deposited film. A 20 Å protective overlayer of W was applied to prevent oxidation of Gd near the film surface while handling samples in air. A total film thickness of 300 Å resulted. The as-deposited films were then annealed in vacuum for 15 min at temperatures between 700 °C and 950 °C to separate the two metals. Bright field, dark field, and selected area diffraction patterns were obtained using a Jeol JEM 2000 FX transmission electron microscope. The magnetization of the films was measured as a function of temperature and magnetic field via SQUID magnetometry in the temperature range 5–300 K, with ap-

---

* Corresponding author.

plied fields of up to 50 kOe. The data were corrected for the paramagnetic contributions by Ta and W to the magnetization. This was done by preparing a W only film on Ta foil, and then subtracting proportionate amounts of its magnetic signal from the signals of the Gd-containing films. Thus the magnetization value reported for the films are due only to the Gd component. The film composition was determined by the inductively coupled plasma emission technique (ICP), and found to be $Gd_{25}W_{75}$.

3. Results and discussion

Transmission electron microscopy studies on the as-sputtered and heat-treated samples indicated that the Gd-W films remained amorphous up to 800 °C. Selected area diffraction (SAD) patterns show the characteristic halo indicative of amorphous structure (Fig. 1). Magnetic measurements show an ordering temperature near 40 K (Fig. 2(a)), and a magnetically soft behavior at cryogenic temperatures as expected for Gd alloys (Fig. 2(b)). The crystallization of both Gd and W was observed to occur around 825–850 °C. SAD patterns for the crystallized samples show two sets of diffractions, one corresponding to Gd and the other to W. Particles of Gd and W could be clearly observed in samples annealed at 850, 875, and 900 °C. The sample annealed at 850 °C showed homogeneously distributed particles of 10–20 nm size (Fig. 3(a)). Annealing at higher temperature had the effect of increasing particle size, 20–30 nm particles were observed in the 900 °C sample (Fig. 3(b)). An occasional coalescence of particles could be observed in the sample annealed at 900 °C. A percolated structure of Gd and W particles is evident in the images obtained from the samples annealed at 925 and 950 °C (Fig. 4). This is an indication
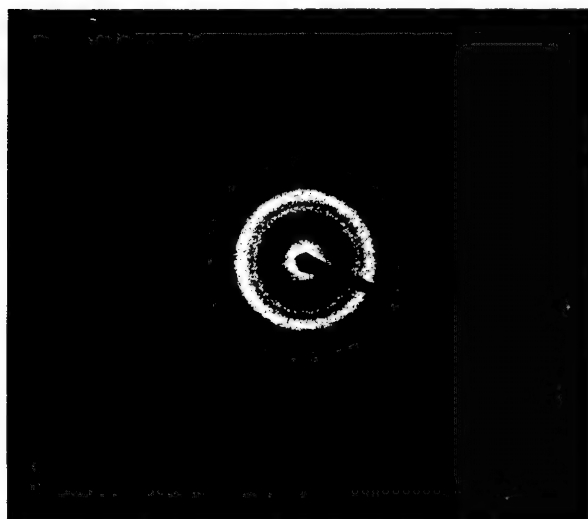
Fig. 1. Selected area diffraction image of as-deposited $Gd_{25}W_{75}$.

(a)

(b)
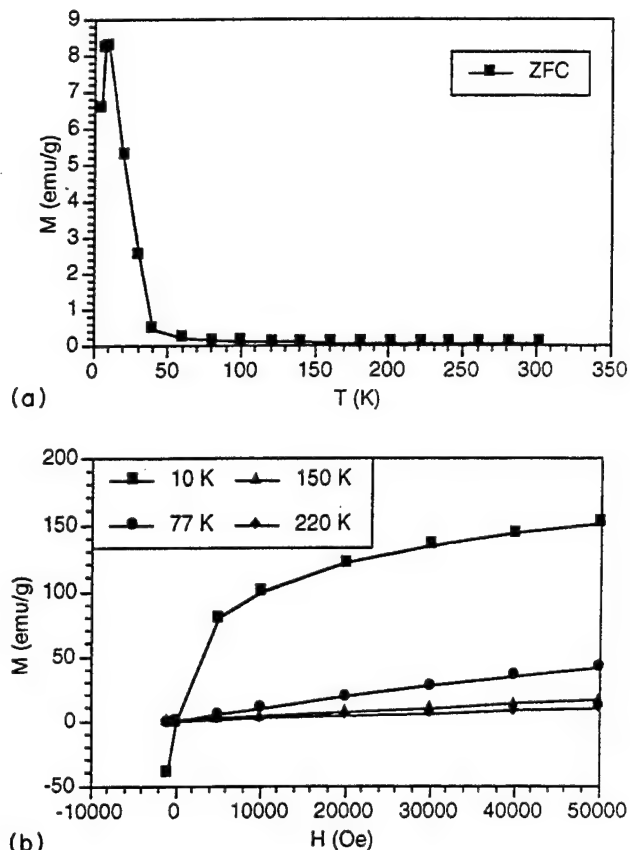
Fig. 2. (a) Temperature dependence of magnetization for as-deposited $Gd_{25}W_{75}$. (b) Magnetization curves at different temperatures.

that an atomic concentration of 25% Gd is greater than the percolation threshold for thin films of the Gd-W system. Thus, the particulate state of these films is merely a transition to the state in which continuous Gd paths form.

Magnetic measurements taken for the 875 °C sample show a Curie temperature of about 250 K, and a blocking temperature of about 50 K (Fig. 5). Magnetic measurements taken for the samples annealed at 925 °C show a Curie temperature of about 293 K and a ferromagnetic response to applied fields.

A description and explanation of the evolution of these effects is as follows. Upon the initial crystallization of the system from the amorphous state, very fine particles of Gd form. These particles exhibit superparamagnetism. A range of particle sizes are present in the 850–900 °C samples, 10 –30 nm. While some of these particles are small enough to be superparamagnetic, the larger particles behave ferromagnetically. These larger particles possibly show the size effect of depressing the Curie temperature from the bulk value of 293 K to 250 K. For samples annealed at 900 °C, the average grain size has increased above that which exhibits superparamagnetic behavior, and the magnetic response is that of bulk Gd. At 900 °C the onset of particle coalescence is evident. This behavior continues to form the percolated

structures seen for the 925 °C and 950 °C samples, which also displayed magnetic properties of bulk Gd.

The measured blocking temperature (T_B) of 50 K is in agreement with the value predicted for uniaxial Gd particles. Using the expression $T_B = KV/25k$, where K is the anisotropy value for Gd (1.3×10^5 erg cm^{-3}) and k is the Boltzmann constant, with an observed particle volume V of 10^{-18} cm^3, a temperature of 37 K is obtained.

Using the information in Fig. 5(b), and applying the Curie law $C = C/T$, where $C = N\mu^2/3km$, μ is the particle moment and m is the mass of Gd, the number N of superparamagnetic particles can be predicted. A value of 3.7×10^9 particles has been obtained for the sample annealed at 875 °C. This number falls short of that predicted if all the Gd was in the form of superparamagnetic particles (2.7×10^{13}). This result in combination with the observed Curie temperature, near that of

Fig. 4. Dark field image of Gd$_{25}$W$_{75}$ annealed at 925 °C for 15 min.

bulk Gd, supports the assertion that both bulk Gd and superparamagnetic Gd particles coexist in the 875 °C sample.

4. Conclusions

In conclusion it has been seen that it is possible to form a granular solid with the Gd$_{25}$W$_{75}$ system. The
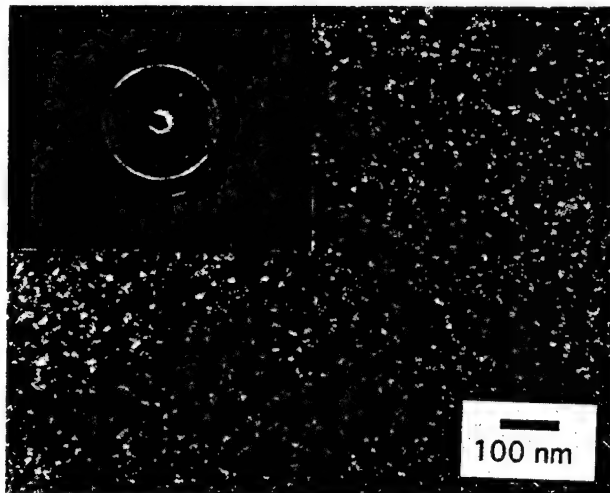
(a)
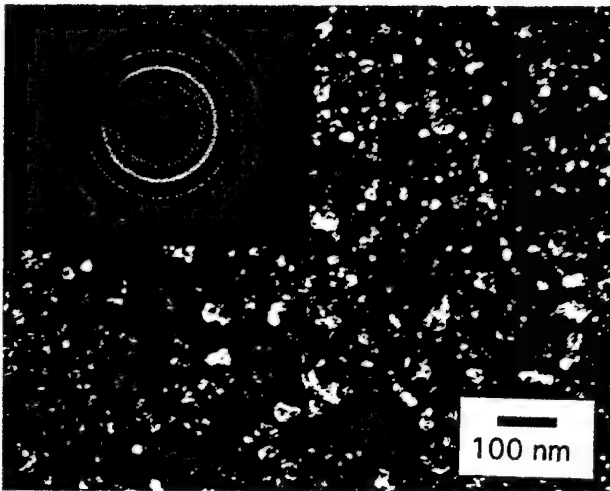
(b)

Fig. 3. (a) Bright field image with SAD inset of Gd$_{25}$W$_{75}$ annealed at 850 °C for 15 min. (b) Dark field image with SAD inset of Gd$_{25}$W$_{75}$ annealed at 900 °C for 15 min.
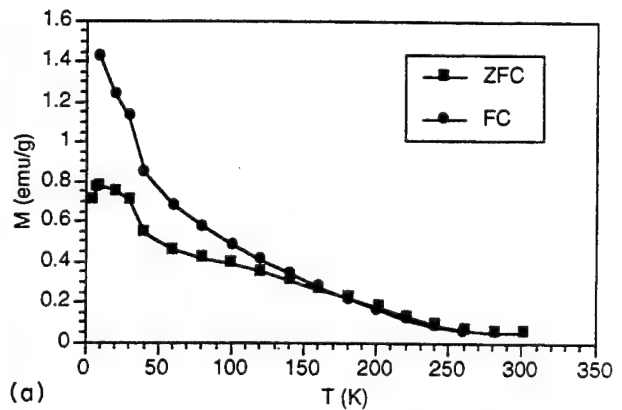
(a)
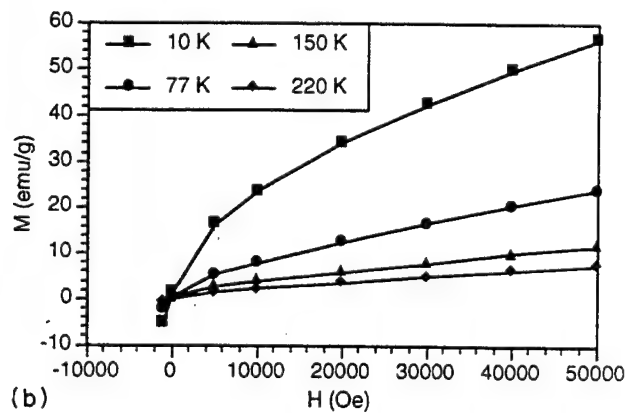
(b)

Fig. 5. (a) Thermomagnetic data and (b) $M_T(H)$ curves for Gd$_{25}$W$_{75}$ annealed at 875 °C for 15 min.

amorphous as-deposited film segregates into a fine-grained mixture of pure Gd and W upon annealing. The small Gd particles (10–20 nm) exhibit superparamagnetic behavior. As particle sizes increase, the Gd component takes on properties similar to bulk Gd but with size effects (depressed T_C). Larger particles behave like bulk with $T_C \sim 295°C$.

Acknowledgement

References

[1] A. Tsoukatos, H. Wan, G.C. Hadjipanayis and Z.G. Li, *App Phys. Lett.*, *61* (1992) 3059.

[2] A.K. Petford-Long, R.C. Doole and P.E. Donovan, *J. Magi Magn. Mater.*, *126* (1993) 41.

[3] D.P. Landau and K. Binder, *J. Appl. Phys.*, *63*(8) (1988) 307.

[4] G.G. Kenning, J.M. Slaughter and J.A. Cowen, *Phys. Rei Lett.*, *59* (1987) 2596.

[5] A.S. Edelstein, B.N. Das, R.L. Holtz, N.C. Koon, M. Ru binstein, S.A. Wolf and K.E. Kihlstrom, *J. Appl. Phys.*, *61*(8 (1987) 3320.

[6] J.Q. Xiao, J.S. Jiang and C.L. Chien, *Phys. Rev. B46* (1992 9266.

Microscopic investigations of the nanocomposite WGa

H. Wolf[a],*, H.G. Zimmer[a], T. Filz[a], St. Lauer[a], Th. Wichert[a], W. Krauß[b]

[a]*Technische Physik, Universität des Saarlandes, D-66041 Saarbrücken, Germany*
[b]*Institut für Werkstoffwissenschaften, Universität des Saarlandes, D-66041 Saarbrücken, Germany*

Abstract

The nanocomposite WGa was investigated by perturbed $\gamma\gamma$-angular correlation spectroscopy (PAC) using the probe atom [111]In. The WGa samples were prepared by inert gas condensation; the Ga content ranged between 10 at.% and 50 at.%. The radioactive ^{111}In atoms were diffused into the WGa samples at temperatures between 600 K and 740 K. Two distinct locations of the ^{111}In probe atoms were observed. One was identified as a substitutional site within precipitated α-Ga, for which a depression of the melting temperature was observed. The other was due to specific properties of the composite WGa and is stable up to temperatures of at least 500 K.

Keywords: Gallium; Tungsten; Nanocomposites

1. Introduction

The properties of nanostructured materials are mainly determined by the size of the crystallites and the interconnecting grain boundaries, as well as by their defect structures and, therefore, are evidently different from those of polycrystals of the same chemical composition. For example, the composite WGa cannot be formed by melting, because W and Ga do not form an alloy. Using the inert gas condensation technique [1], a nanocrystalline composite consisting of W and Ga can be formed, which has completely new properties, different from those of the constituents. While the technology for manufacturing nanocrystalline materials has been developed to some extent, a fundamental understanding of the special properties of nanocrystalline materials is still lacking [2]. Here, locally sensitive experimental techniques, like Mössbauer spectroscopy, EXAFS or perturbed $\gamma\gamma$-angular correlation (PAC), might be helpful in obtaining more information about grain boundaries, interfaces and defects within the formed crystallites.

This work presents PAC results obtained on nanocrystalline WGa composites that were produced by inert gas condensation and subsequently diffused with the radioactive PAC probe atoms [111]In. In this

way, new results were obtained which reflect specific properties of the composite WGa. The results observed in the produced WGa samples also include effects of the thermal diffusion treatment, such as a growth of the W particles, which were originally about 10 nm in diameter, and the precipitation of Ga. In principle, in-situ doping of the nanocomposite WGa with ^{111}In should be possible in order to avoid the additional thermal treatment for radioactive doping. For technical reasons, PAC experiments on in-situ doped WGa samples will be the subject of future projects.

2. Experimental details

PAC spectroscopy commonly uses the radioactive probe atom ^{111}In which decays to the excited level of its daughter isotope [111]Cd (see Fig. 1). From this level two γ-quanta are emitted, thereby populating a spin $I = 5/2$ level with a half-life of 85 ns. The emission probability of the second γ-quantum with respect to the first one has a spatial anisotropy due to the conservation of the angular momentum during the decay process. This anisotropy is governed by the nuclear spins taking part in the decay process as well as by the multipolarities of the emitted γ-quanta. For the $\gamma\gamma$-cascade of the [111]Cd nucleus the anisotropy is $A_2 = -0.14$. The $I = 5/2$ level has a nuclear quadrupole moment of $Q = 0.8$ b and is

* Corresponding author.

used for detecting the parameter of interest, namely the electric field gradient (EFG). The EFG is the second derivative of the electrostatic potential and, therefore, can be described by a second rank, traceless tensor. In its principal axis system this tensor is completely described by two quantities, namely its largest component V_{zz} and the asymmetry parameter $\eta = (V_{xx} - V_{yy})/V_{zz}$, for which the relation $0 \leqslant \eta \leqslant 1$ holds if $|V_{xx}| \leqslant |V_{yy}| \leqslant |V_{zz}|$ is chosen. The hyperfine interaction of the quadrupole moment with the EFG at the site of the probe nucleus causes a threefold splitting of the $I = 5/2$ level, or in a classical framework, a periodic motion of the nuclear spin which leads to a modulation of the emission probability of the second γ-quantum. This modulation is governed by the three frequencies ω_1, ω_2, and $\omega_3 = \omega_1 + \omega_2$, resulting from the three possible energy differences of the split nuclear $I = 5/2$ state (see Fig. 1). The frequencies are proportional to the product QV_{zz} and, therefore, are a measure of the strength of the EFG. The asymmetry parameter η is determined by the ratio ω_2/ω_1 and the strength of the EFG is usually expressed by the quadrupole coupling constant $\nu_Q = eQV_{zz}/h$, which is proportional to ω_1. In a PAC experiment, the second γ-quantum is recorded coincidentally with the first one, using two γ-detectors which are arranged under a fixed angle θ. In general, four γ-detectors arranged along two orthogonal axes are used. This setup enables the simultaneous recording of 12 coincidence spectra, eight with a relative angle of 90° and four with a relative angle of 180°. By proper combination of the measured coincidence spectra the exponential decay function is eliminated [3] and the resulting modulation function can be written in the following way:

$$W(\theta,t) = 1 + P(\theta) \cdot R(t),$$

with

$$R(t) = A_2 \cdot \{f \cdot (s_0 + \sum_{n=1}^{3} s_n \cos\omega_n t) + (1 - f)\}$$

Here, f denotes the fraction of probe atoms within an environment, producing a particular non-zero EFG, and $(1 - f)$ is the fraction of the remaining probe atoms without an EFG. The angular dependent function $P(\theta)$ corresponds to the second-order Legendre polynominal $P_2(\cos\theta)$ in the case of a polycrystalline sample. If there are different environments surrounding the probe atoms and producing different EFGs, f will be split into different fractions $f(i)$, whereby each one is represented by its own characteristic frequency triplet $\omega_n(i)$. The total amount of ^{111}In necessary for a PAC experiment is of the order of 10^{11} atoms, therefore the resulting volume concentration of probe atoms within the investigated sample is very low, in general. Typically, one gets concentrations of 10^{14}–10^{17} cm^{-3}, depending on the distribution of the probe atoms within the sample. More details on the PAC technique can be found for example in Ref. [3].

The origin of an EFG, existing at the site of the probe atom, can be either a non-cubic structure of the host lattice, or the formation of defect complexes including the probe atom. Strength, asymmetry, and orientation of the EFG tensor with respect to the host lattice are determined by the ratio of the lattice constants, in the case of non-cubic crystals. For example, the orthorhombic Ga lattice produces a non-axially symmetric EFG ($\nu_Q = 142$ MHz, $\eta = 0.2$) at the substitutional lattice site [4], whereas the EFG of the bcc W lattice is zero at substitutional lattice sites. The second case is the agglomeration of one or more defects (impurities or intrinsic defects) about the probe atom. The strenght of an EFG as produced by defect complexes decreases rapidly with the distance of the defects to the probe atom; the maximum distance of a detectable defect corresponds to about 1–2 lattice constants. Asymmetry and orientation of the EFG tensor are determined by the geometrical structure of the formed defect complex. In W, the EFG belonging to different defect complexes, which include trapped vacancies or impurity atoms, are well known [5,6].

3. Results and discussion

The WGa samples investigated by PAC were prepared by inert gas condensation and subsequently compacted into pellets of 8 mm diameter with a thickness of about 0.5 mm. The Ga content of the used samples ranged between 10 at.% and 50 at.%. The size of the W particles was about 10 nm as determined by X-ray diffraction measurements. By measuring the specific heat as a function of temperature (DSC) no precipitated Ga was detected. Subsequently, pieces of about 3
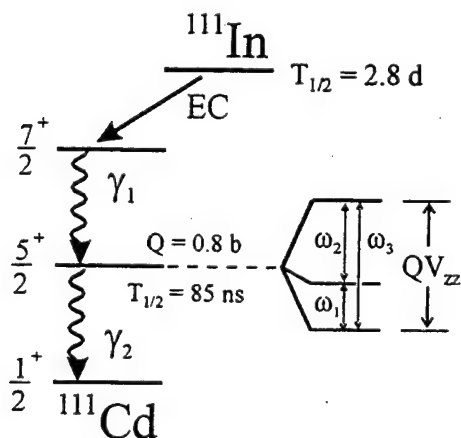

Fig. 1. Decay scheme of the PAC probe ^{111}In/^{111}Cd. The incorporation of the probe atom in the sample is determined by the chemical properties of In, whereas the EFG is measured at the $I = 5/2$ level of ^{111}Cd via the hyperfine interaction of the nuclear quadrupole moment Q with the external EFG.

Table 1
WGa samples investigated by PAC spectroscopy in this work. The Ga content, the diffusion conditions for the respective sample, the transition rate of ^{111}In after diffusion and the population of the resulting local environments by the probe atoms are given. In general, the data for f_{Ga}, f_{WGa}, f_0 and f_r were evaluated at 77 K; for samples 3, 5 and 10, the temperature was 295 K

Sample	at.% Ga	T_{diff} (K)/t_{diff} (h)	^{111}In rate (%)	f_{Ga} (%)	f_{WGa} (%)	f_0 (%)	f_r (%)
1	10–15	600/1,5	60	0	0	12	88
2	10–15	600/2	55	0	0	10	90
3	40–50	593/1,5	11	0	0	7	93
4	40–50	708/16	55	21	14	8	57
5	40–50	700/25	1	0	0	0	100
6	40–50	697/16,3	53	3	14	0	86
7	40–50	740/16,6	66	36	0	0	63
8	33	740/16,5	63	5	0	0	95
9	33	739/4	70	9	0	4	87
10	33	739/4	70	0	0	14	86

mm^3 were cut from those pellets and diffused with the radioactive ^{111}In atoms. The Ga content of the investigated samples and the conditions used for diffusion are listed in Table 1. Additionally, this table contains the transition rates of ^{111}In atoms, which were achieved during the diffusion process, and information about the observed EFG. Note that the variations in the observed fractions, obtained for equivalently treated samples, are not systematic, although the conditions for diffusion with the ^{111}In probe atoms were comparable. Obviously, the ex-situ doping by diffusion is not easily reproducible, so that in-situ doping during inert gas condensation should be envisioned for future experiments. The size of the W paricles was enlargered to about 30 nm due to thermal treatment and, at the same time, precipitated Ga was observed by DSC measurements. For some of the samples, the probe atoms are observed to be incorporated within crystalline Ga as is recognized by the non-axially symmetric EFG ($v_Q = 142$ MHz, $\eta = 0.2$ at $T = 77$ K), which is well known for ^{111}In/^{111}Cd in Ga metal [4]. This fraction rises to $f_{Ga} = 36\%$ for sample 7. A second EFG ($v_Q = 295$ MHz, $\eta = 0$), observed for example in sample 4 was not known until now, neither in Ga nor in W, and reaches a population of $f_{WGa} = 30\%$. In Fig. 2(a), the PAC spectrum recorded for sample 4 at a temperature of $T = 14$ K is plotted, showing both the EFG due to Ga precipitates (f_{Ga}) and the new, axially symmetric EFG (f_{WGa}), which is interpreted as being connected to specific properties of the composite WGa. The small EFG distribution, indicated by the small damping of the $R(t)$ spectrum, requires a highly ordered structure around these probe atoms, and the axial symmetry of the EFG indicates a local hexagonal or tetragonal structure. For the same sample, the PAC spectra in Figs. 2(b) and (c) show that only the axially symmetric EFG, belonging to f_{WGa}, is present at higher sample temperatures.

In order to obtain more information about the composite WGa, the temperature dependences of the EFG and of the associated populations of the different locations in the range 14 K $< T <$ 500 K were investigated. Four different locations of probe atoms could be distinguished during the PAC experiments in the composite WGa; the temperature dependences of their populations are plotted in Fig. 3. Besides the fractions f_{Ga} and f_{WGa}, some of the probe atoms are f_0 located in an environment without an EFG, corresponding to the time-independent part of the $R(t)$ spectrum, e.g. in Fig. 2(c). Finally, some of the probe atoms reside in an undefined environment (f_r), in which the associated EFG produces frequencies that are too high to be resolved by the γ-detectors. Therefore, the value of f_r was determined by the condition that all fractions have to sum to 100%. Below 250 K, the fraction f_{Ga} remains almost constant and vanishes above $T = 288$ K (compare Fig. 2(b)). At the same time, the fraction f_0 increases from 0% to 50% and, in addition, the fraction
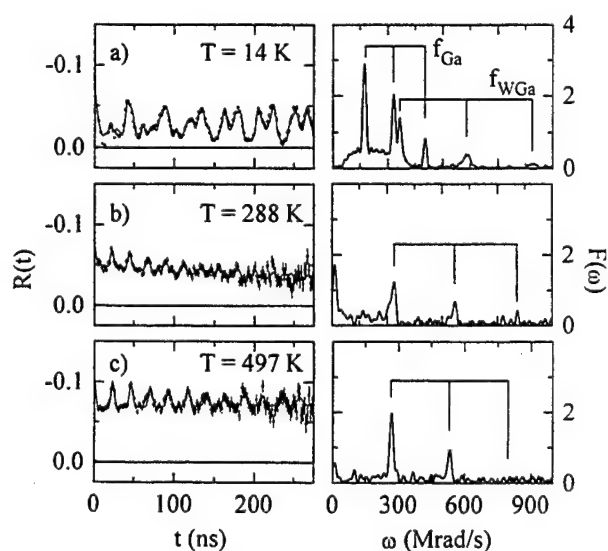
Fig. 2. PAC time spectra and their Fourier transforms for sample 4, recorded for different sample temperatures. They show the typical EFG for Ga precipitates (a) and the composite WGa (a)–(c).
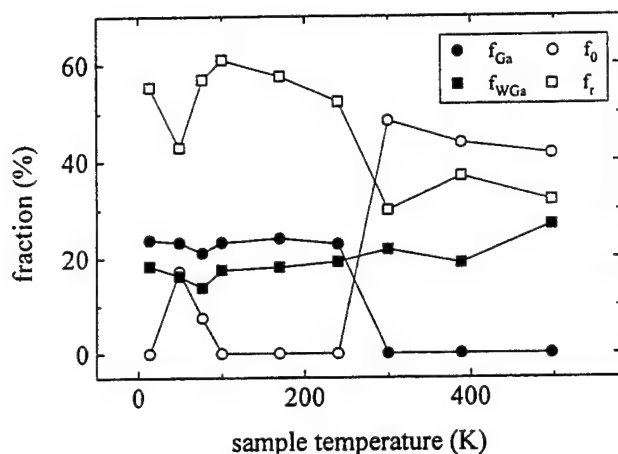
Fig. 3. The temperature dependence of the population of the four detected locations of the probe atom In for sample 4. The disappearance of f_{Ga} between 240 K and 288 K is caused by the melting of the precipitated Ga matrix.

f_r decreases from 50% to 30%. (The exchange between f_0 and f_r at $T = 50$ K is not understood, but is possibly due to an experimental artifact.) The disappearance of f_{Ga} and the decrease in f_r are attributed to the melting of the precipitated crystalline Ga matrix. At the same time, the decrease in f_{Ga} and f_r shows that about one-half of the ^{111}In atoms within the Ga precipitates are located on substitutional sites of crystalline α-Ga. The second result is the reduction in the melting temperature from 302 K for pure Ga down to a temperature between 240 K and 288 K for the observed Ga precipitates. A similar observation was made on a thermally treated WGa sample by DSC measurements. The depression of the melting temperature within nanocrystalline compounds has been observed for different materials and is explained by the size dependence of the thermal vibrations of the matrix atoms [7]. A better quantitative determination of the depression of the melting temperature of precipitated Ga is the subject of current experiments. For sample 9 this temperature range was narrowed down to an interval between 240 K and 260 K.

The fraction f_{WGa} remains almost constant up to a temperature of 400 K and increases irreversibly at higher temperatures. Such an increase, being caused by the sample treatment at higher temperatures, is shown for sample 6 in Fig. 4. After diffusion of the probe atoms ^{111}In, f_{WGa} reaches 10% but increases to 38% after annealing at $T_a = 690$ K for 5 h. At present, the maximum population of f_{WGa} that can be reached under favourable conditions is not known. The fact that the crystalline environment causing f_{WGa} has been thermally stable during PAC experiments up to temperatures far above the melting point of α-Ga, clearly shows that this environment does not correspond to precipitated Ga. The measured value of the EFG is

difficult to use to obtain direct information about the local environment of the probe atom, for theoretical reasons. For the origin of the EFG, three possibilities can be considered. First, the In atoms might be located at interfacial sites within a well-defined surrounding that is not affected by the melting of the precipitated Ga. Second, an intermetallic compound of W and Ga with a hexagonal or tetragonal lattice structure might have been formed in which the In atoms are located at well-defined lattice sites. This compound must be stable up to temperatures of at least 500 K. Third, the In atoms might have diffused into W particles and the observed EFG could be due to a defect complex in the W lattice involving the probe atom ^{111}In. The latter possibility would be very surprising because the diffusion of ^{111}In into polycrystalline W samples should not occur at such low temperatures used for the present sample treatment (see Table 1). A conclusive interpretation of the local structure corresponding to f_{WGa} is still lacking and will require more experimental data from complementary experimental techniques.

In general, the temperature dependence of the EFG also yields information about possible environments for the probe atoms. In Fig. 5, the temperature dependences of the EFG belonging to f_{WGa} and f_{Ga} show a continuous decrease when plotted versus $T^{3/2}$. The temperature dependence of the EFG in non-cubic metals has been extensively studied in the past and in many cases a $T^{3/2}$ dependence was found, which is explained by the thermal excitation of phonons [8]. The temperature dependence of the EFG measured in the crystalline Ga precipitates follows the $T^{3/2}$ behaviour known for α-Ga metal. For the EFG on metal surfaces, a rather linear temperature dependence can be expected, taking into account the properties of the phonon spectrum of a two-dimensional solid [9]. The decrease in the EFG corresponding to f_{WGa} in the range between $T = 14$ K and $T = 500$ K seems to follow neither a $T^{3/2}$ dependence (Fig. 5) nor a linear T dependence. A detailed interpretation of the observed temperature dependence of f_{WGa} has to await further theoretical work.
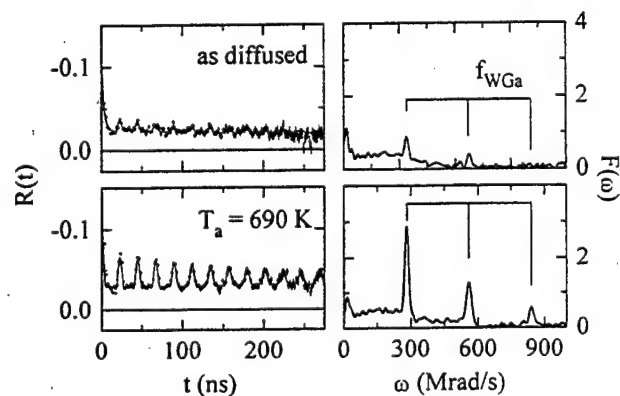
Fig. 4. The influence of heat treatment on the population of the site f_{WGa}.
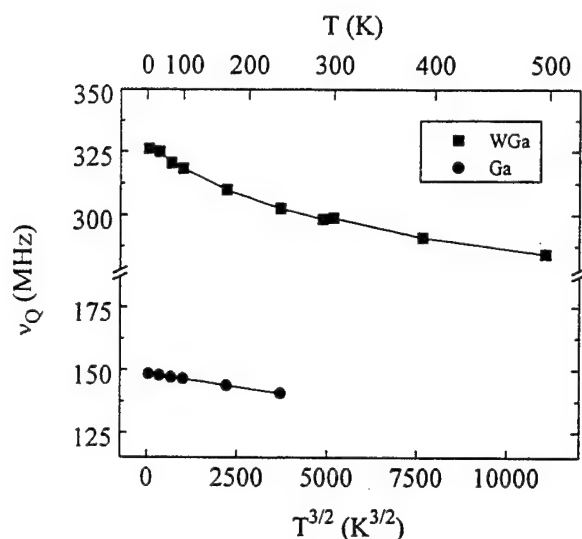
Fig. 5. Temperature dependences of the EFG corresponding to f_{Ga} and f_{WGa}. In contrast to f_{Ga}, f_{WGa} does not follow a $T^{3/2}$ law.

4. Conclusion

From PAC experiments on the nanocomposite WGa two results were obtained. First, the precipitation of Ga as a consequence of the growth of the W particles was deduced from the observation of the EFG of the orthorhombic lattice structure of α-Ga. The melting temperature of the precipitated Ga is evidently reduced and was determined to be in the temperature range between 240 K and 260 K for a WGa sample containing 33 at.% Ga. Second, a new EFG was detected which is typical of the composite WGa, and during the PAC investigations this structure was stable up to temperatures of at least 500 K. The exact local structure corresponding to this EFG is still unknown but some possible interpretations were proposed. The question of the extent to which the local structures observed were affected by ex-situ doping of the samples with ^{111}In probes at temperatures above 600 K, will be subject of future experiments. There, in-situ doping of the WGa samples with ^{111}In atoms during inert gas condensation is envisaged.

Acknowledgements

References

[1] H. Gleiter, *J. Appl. Cryst.*, *24* (1991) 79.
[2] R.D. Shull, *Nanostructured Mater.*, *2* (1993) 213.
[3] Th. Wichert, M. Deicher, G. Grübel, R. Keller, N. Schulz and H. Skudlik, *Appl. Phys.*, *A 48* (1989) 59.
[4] W. Keppner, W. Körner, P. Heubes and G. Schatz, *Hyp. Int.*, *9* (1981) 293.
[5] J.R. Fransen, M.S. Abd El Keriem and F. Pleiter, *J. Phys. Condens. Matter*, *3* (1991) 9871.
[6] M.S. Abd El Keriem, D.P. van der Werf and F. Pleiter, *Phys. Rev.*, *B 47* (1993) 14771.
[7] F.G. Shi, *J. Mater. Res.*, *9* (1994) 1307.
[8] K. Nishijama, F. Dimmling, T. Kornrumpf and D. Riegel, *Phys. Rev. Lett.*, *37* (1976) 956.
[9] T. Klas, R. Fink, G. Krausch, R. Platzer, J. Voigt, R. Wesche and G. Schatz, *Surf. Sci.*, *216* (1989) 270.

In situ TEM sintering of nano-sized ZrO_2 particles

J. Rankin*, B.W. Sheldon

Division of Engineering, Brown University, Providence, RI 02912, USA

Abstract

The sintering behavior of faceted, nano-sized single-crystal particles of ZrO_2 has been investigated using in situ transmission electron microscope heating techniques. These direct observations have provided new information on the morphological and structural evolution of particles, necks and pores during the sintering process. The results indicate that ZrO_2 particle-pairs, which are not attached to other particles and not highly constrained by the TEM grid, reorient themselves with respect to each other during sintering at 890°C. This reorientation can be explained in terms of a minimization of the grain-boundary energy between the two coalescing particles. In addition to changes in particle orientation, these experiments show that the topologies of ZrO_2 particles and their associated necks evolve during heating. During the in situ TEM heating of these particles, the dynamic motion of atom clusters (10–100 atoms) on and off of surfaces is observed, as is the formation and dissolution of ledges and steps on previously smooth facets. The phenomenon of cluster migration is discussed and the ramifications of the results of this study for more highly constrained systems of particles (e.g. ceramic green-bodies) are also considered.

Keywords: In situ TEM; Nanoscale; Sintering; ZrO_2

1. Introduction and background

The sintering process is of tremendous technological importance due to its widespread use in the manufacture of ceramic materials and in powder metallurgy. Most previous investigations of early stage sintering in ceramic powders have employed ex situ heating in idealized systems consisting of polycrystalline micron-sized particles with circular cross-sections [1,2]. Numerous researchers have examined particle, neck, and pore morphology changes in ex situ sintered, micron-sized polycrystalline powders [3]. In recent years, several ex-situ studies of sintering single crystal particles of micron-sized ZrO_2 [4] and nano-sized Al_2O_3 [5,6] have been reported. Although these studies represent significant contributions to the field of sintering, their ex situ nature limits measurements of the neck and particle size and morphology to average values over the total time of the heating cycle. In contrast, in situ heating allows morphology and size to be measured continuously throughout the experiment, and provides the most ac-

curate means of monitoring and understanding the evolution of the nano-scale microstructure. With a few notable exceptions [7–9,11,12] ex situ studies have essentially dominated previous experimental studies of the evolution of neck and pore morphologies that occur during heating.

Recent studies of the in situ TEM sintering of sub-micron, single-crystal, faceted MgO particles show that the contact geometry is critical in determining the sintering behavior of two adjacent particles [9]. In fact, it has been shown that particles that are in contact over small areas can actually desinter during the heating process. Ultimately, two individual particles are created, with no neck between them. Theoretical investigations that consider the precise role of the facets on this process have also been undertaken [10].

Fujita [11] has studied the in situ heating behavior of coarse-grained ($\sim 1~\mu m$), Al_2O_3, $Al_2O_3 + MgO$ and $ZrO_2 + Al_2O_3$ ceramics using high-voltage electron microscopy. In these studies a circular area approximately 8 μm in diameter was viewed.

In light of the successes and shortcomings of the studies discussed above, the primary objectives of the present in situ TEM heating investigation were:

---

* Corresponding author.

(1) to observe particle reorientation and neck growth, and

(2) to further invesigate the origins and ramifications of the observed surface fluctuations.

2. Experimental procedure

Nano-sized powders are ideally suited for TEM studies, because their small size permits high-resolution imaging without significant sample preparation (no thinning of any kind is required). As a consequence, no artifacts associated with the thinning process (e.g. dislocations) are introduced into the samples. By utilizing a novel reactor design, nano-sized, single-crystal particles of ZrO_2 (with a mixture of tetragonal and monoclinic phases) were produced by the turbulent combustion of aerosols of organo-metallic precursors [13]. The particles were subsequently suspended in acetone and deposited on a thin amorphous carbon layer on a molybdenum grid. Molybdenum was chosen because it neither melts nor alloys with the tantalum heating-holder at temperatures between room temperature and 1300°C.

Using a Gatan single-tilt heating holder in a JEOL 2010 transmission electron microscope, the particles were heated to one of two temperatures (890°C and 1100 °C). As a result of thermal gradients across the TEM grid, it is estimated that the actual sample temperature is within ~ 50°C of the thermocouple temperature. Since all of the samples investigated during this part of the study were mounted on the same type of grid, it is reasonable to expect that the thermal contact was essentially the same in all samples. Furthermore, the carbon substrate exhibited significant fluctuations when the thermocouple reading was (900 ± 10)°C, indicating reproducible temperatures. These fluctuations subsided after approximately 15 min, at which point it was possible to obtain good quality TEM images. The data were collected on videotape, which was subsequently analyzed to determine crystallographic relations and growth rates.

Some important characteristics of the ZrO_2 particles studied here are enumerated below:

(1) The particles are 20–200 nm diameter, single-crystals.

(2) There are no internal grain boundaries within the coalescing grains (only at the junction between the two particles).

(3) The heating experiments were performed within the vacuum of a transmission electron microscope ($\sim 10^{-7}$ atm).

(4) The heating experiments were monitored and continuously recorded using a video recorder. This allowed individual particle pairs to be observed throughout their evolution.

3. Results and discussion

Preliminary results on the in situ sintering of ZrO_2 faceted particles can be divided into two distinct categories: those related to particle reorientation during the sintering of two adjacent particles, and those associated with changes in the atomic arrangement of particle surfaces during heating.

Observations of the behavior of pairs of ZrO_2 particles at ~ 890°C reveal particle reorientation during sintering. Although a similar behavior has been observed elsewhere [7,9,12,14] the high-resolution techniques utilized in the present study can provide detailed, dynamic orientational information. At the start of the experiment, as seen in Fig. 1(a), the particle marked '1' is oriented such that cross-fringes are visible, and the second particle, marked '2', is not oriented with any particular zone axis parallel to the electron beam (no fringes are visible). In general it can be assumed that as long as a zone axis is within ~ 8° of the electron beam, the cross-fringes associated with that particular zone will be resolvable. As heating continues, one of the particles moves (presumably to minimize the energy associated with the boundary between the two particles), and one set of fringes becomes visible in the second particle (see Fig. 1(b)). Finally, after approximately 1 h, lattice fringes can be seen in the second (previously unaligned) particle, while the initial cross-fringes are still visible in the first particle. One set of fringes is clearly parallel in the two particles indicating a larger degree of alignment than originally existed. It should be noted that the first particle has not moved more than approximately 8° (the original cross-fringes are still visible), while the second particle has moved appreciably. It is likely that the first particle was more strongly attached to the carbon film (on which the powders were dispersed), and thus its motion was prevented.

For the case of unconstrained particles in contact (as is the case in the previous example), the lowest energy configuration obviously exists when the two particles form an uninterrupted single crystal across their surfaces of contact (i.e. when there is no crystallographic mismatch and therefore no grain boundary). The situation becomes more complicated when the particles are constrained by attachments to other particles. In the case of multiple particles, a reduction of all of the grain boundary energies to form a continuous crystal across contact surfaces is highly unlikely, and the lowest energy state for this configuration would most likely be accomplished through a variety of permutations of orientations of the consituent particles.

In addition to orientational information, the images of Figs. 1(a)–(c) can be used to determine neck radius as a function of time; similar measurements have been made in the MgO system [9]. On the basis of these

measurements, the radius of the neck increases about 18% during this experiment. For all particle pairs observed, the neck radius reached a maximum and did not
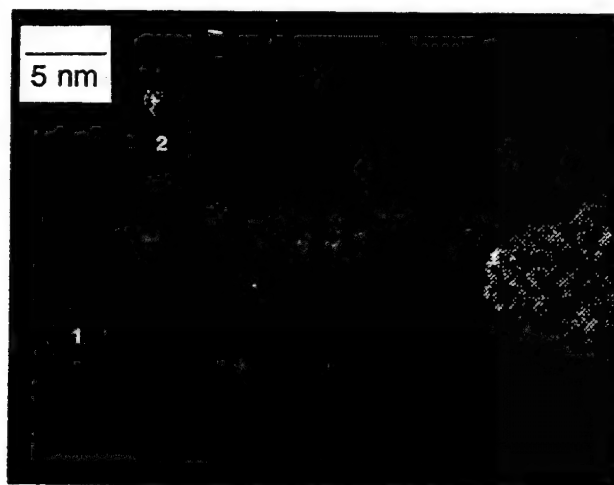
(a)
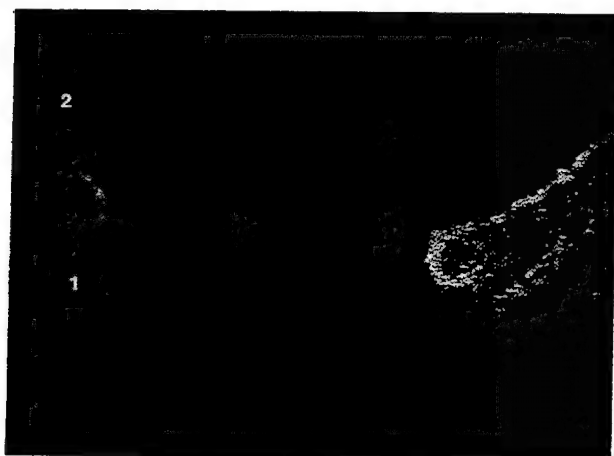
(b)

(c)

Fig. 1. High-resolution still images taken from real-time videotape monitoring of the neck region between two ZrO_2 particles after: (a) 30 min, (b) 60 min, and (c) 90 min at $(890 \pm 30)°C$.

appear to change in size past that point. This is consistent with the findings of other investigators. In previous studies it has been found that necks between micronsized, spherical, single crystal ZrO_2 particles reach a static size, corresponding to a balance between the energy required to create a new grain boundary area and the energy supplied as the overall surface area of the two-particle system decreases [4]. These findings are obviously applicable here, but must be reinterpreted to account for the rearrangement of the particles in order to minimize the contribution of grain boundary energy to the energy of the entire system.

Since no approach of particle centers is measured, surface diffusion and evaporation–condensation are the most probable mechanisms for mass transport, since they do not lead to densification. In general, a maximum evaporation rate can be estimated with a Langmuir evaporation flux equation:

$$J_{evap} = \frac{P}{(2\pi MRT)^{1/2}},\qquad(1)$$

where P and M are the equilibrium vapor pressure and molecular weight of the rate-limiting species, respectively, T is the absolute temperature, and R is the gas constant. For ZrO_2 in a vacuum of 10^{-7} atm at $\sim 1000°C$ the maximum evaporation rate is found to be ~ 0.2 nm h^{-1} (P was estimated using SOLGASMIX-PV [15]). Experimentally, the size of the particles does not decrease significantly, confirming that evaporation effects are not significant in this system. It should be noted that volume diffusion may play a role in the redistribution of material without a resultant particle center approach, if the particles themselves are constrained through attachment to adjacent particles. Order-of-magnitude estimates which assume that volume diffusion is the only operative transport mechanism indicate that it would take $\sim 10^5$ s to move an atom ~ 100 nm from the center of a particle to the neck region; this is much slower than the timescales that were studied.

Since surface diffusion is the dominant transport mechanism, the positive radius of curvature can be related to the time that the neck has been growing through a standard power law dependence (derived by assuming spherical particles and isotropic surface energies):

$$x = [Kt]^{1/7}.\qquad(2)$$

The value of the constant K is obtained from a regression of the data, and can be related to several system parameters as given below [16]:

$$K = \frac{56\Omega R^3 \gamma D_s \delta_s}{k_b T},\qquad(3)$$

where Ω is the molar volume, R is the radius of the sintering particles (assumed to be spherical), γ is the

surface energy (assumed to be isotropic), δ_s is the surface layer thickness, k_b is Boltzman's constant, and T is the absolute temperature. By substituting appropriate values of γ, Ω, R, δ_s, k_b, and T in the equation above, the surface diffusion coefficient, D_s, can be estimated; at 890°C it is found to be between 10^{-12} and 10^{-13} cm^2 s^{-1}.

The second noteworthy phenomenon in the ZrO_2 system is the fluctuations on the surfaces of these particles at ~ 1100°C. This phenomenon has been observed in ZrO_2 [13] and in small gold particles [17]. Because of the nature of high-resolution TEM imaging, single atoms are not detectable, that is, the electron beam must pass through a minimum thickness of material (approximately 3 to 7 unit cells before imaging is possible). When cross-fringes are visible, the sample is oriented with the zone-axis parallel to the electron beam, in which case the TEM image is formed by the passage of the electron beam through columns of atoms which are parallel to the zone-axis. When part of a TEM image 'disappears' it indicates that less than a critical number of atoms remain in a particular column. Therefore, it is logical to conclude that the observed fluctuations arise from the motion or 'hopping' of clusters of atoms on and off of the surfaces of the particles. An example of this cluster motion can be seen in Figs. 2(a)–(c). Each number in Fig. 2 indicates the location of a different column of atoms. The column marked with a '1' is visible in Fig 2(a), but not visible in Fig 2(b), and is visible again in Fig 2(c). Similarly, the site marked with a '2' appears to be filled in Figs. 2(a) and (b), but is not visible in Fig. 2(c). A '3' marks the site where a column is not visible in Fig. 2(a), whereas this site appears to be filled in Fig. 2(b), and is not visible (along with the atoms in site '2') in Fig. 2(c). The images shown here are taken from a videotape of the in situ heating process, and span a time of approximately 5 s.

Measurements from the videotape of the frequency of the motion of clusters on and off of the surface, together with a simplified random-walk calculation, Eq. (4) below, can be used to estimate a diffusion coefficient for this phenomenon. It should be noted that the oscillations observed here reflect the motion of columns of atoms, not the motion of individual atoms normally associated with a random-walk description of surface diffusion [18]:

$$D = \frac{\Gamma}{2} n r^2. \tag{4}$$

The quantity Γ is the jump rate of the column of atoms, and is estimated to be ~ 2 s^{-1}. The jump distance r is of the order of one lattice spacing (~ 0.4 nm), and the number of atoms per column n is probably between 10 and 100. Using these values, the diffusion coefficient is calculated as $2(10)^{-14}$ to $2(10)^{-13}$ cm^2 s^{-1}.
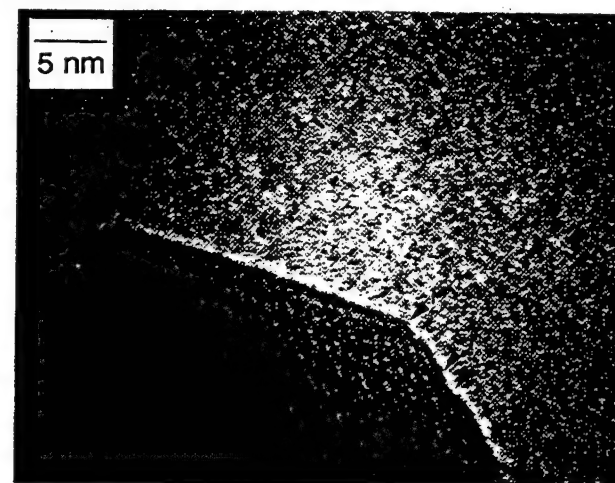
(a)
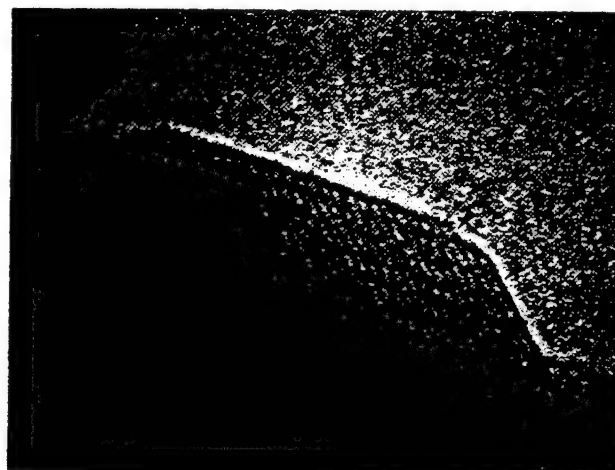
(b)
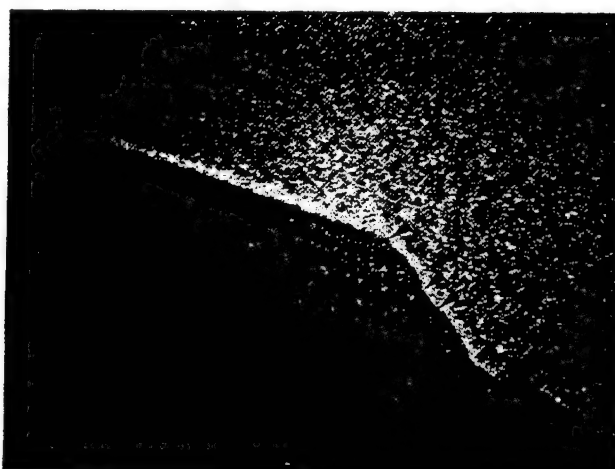
(c)

Fig. 2. High-resolution still images taken from real-time videotape monitoring of the edge of a ZrO_2 particle. The total elapsed time between images (a) and (c) is ~ 5 seconds. The numbers in these images denote the location of columns of atoms which appear and disappear over the course of the experiment.

Recently Kusunoki et al. [12] have made in situ observations of nano-sized ZrO_2 at 1100°C and have reported the occurrence of surface fluctuations (similar to those observed here). They have suggested that these fluctuations correspond to surface diffusion. However, D_s values obtained from the rate of neck growth (i.e. with Eq. (3)) are considerably larger than values obtained from the observed fluctuations (i.e. with Eq. (4)). It is important to note that the estimates made with Eqs. (3) and (4) are approximate, and are probably only accurate to within one or two orders of magnitude. However, the calculations made with Eq. (3) are based on neck growth rates that were measured at a lower temperature (890°C) than the surface fluctuation measurements (1100°C), therefore the flux associated with neck growth is almost certainly much larger than the flux associated with surface fluctuations. Even though the observed rate of surface fluctuations is apparently too low to directly account for neck growth, the surface fluctuations are still probably related to surface mobilities. Instead of the traditional picture of individual atoms moving randomly along a relatively static surface, it appears that surface atoms can form clusters that essentially move as a unit. Additional studies are currently underway to elucidate this phenomenon.

It should be noted that surface oscillations and reconstruction have been observed at both room temperature and elevated temperatures in other systems such as CdTe and CdS, where they have been attributed to electron beam–solid interactions at room temperature and thermal effects at higher temperatures [19,20]. Related studies [21] suggest that electron beam irradiation is responsible for enhanced atomic mobility and dislocation motion at lower temperatures, whereas at higher temperatures the dislocation velocities are thermally activated and exhibit standard Arrhenius-type behavior. In other studies, the electron beam has been shown to induce a room temperature reduction of irradiated surfaces of transition metal oxides to yield either the metal [22], or a lower oxide [23]. In those studies, the frequency of surface oscillation or phase transformation was found to be strongly dependent on the electron beam current and the time of exposure. For the results reported here the incident beam current was varied with no effect on the nature of the oscillations. Additionally, it should be noted that no oscillations are observed at temperatures less than ~ 1000°C even though, as previously discussed, neck growth via surface occurs at 890°C. These observations confirm that the oscillations are thermally induced.

4. Summary

In situ TEM heating studies of ZrO_2 have provided new insights into the sintering process. Specifically, it has been shown that:

(1) Unconstrained, single-crystal particles of ZrO_2 in contact with only one other particle reorient during heating at 890°C.

(2) Neck growth during the early stages of sintering occurs at 890°C. However, at longer times, the necks reach a static size. This observation is in good agreement with the results of other researchers [4]. Measurements of the neck radius as a function of time are used to provide an estimate of the surface diffusion coefficient at this temperature.

(3) Surface fluctuations are observed when ZrO_2 particles are heated to temperatures greater than ~ 1000°C. These fluctuations are associated with the motion of clusters of atoms, and do not appear to be direct evidence of 'traditional' surface diffusion. Additional experiments are essential if the origins and ramifications of cluster migration in this system are to be thoroughly understood.

Acknowledgments

References

[1] G.C. Kuczynski, *J. Trans. AIME*, 185 (1949) 796.
[2] W.D. Kingery and M. Berg, *J. Appl. Phys.*, 26(10) (1955) 1205.
[3] S. Somiya and Y. Moriyoshi (eds.), *Sintering—Key Papers*, Elsevier Science Publishing Co., Inc., New York, NY, 1990.
[4] E.B Slamovich and F. Lange, *J. Am. Ceram. Soc.*, 73(11) (1990) 3368.
[5] J.E. Bonevich and L.D. Marks, *J. Mater. Res.*, 7(6) (1992) 1489.
[6] S. Ijima, *J. Electron Microsc.*, 34 (1985) 249.
[7] K.E. Easterling and A.R. Tholen, *Met. Sci. J.*, 4 (1970) 130.
[8] I. Hansson and A. Tholen, *Phil. Mag. A.*, 37 (1978) 535.
[9] J. Rankin and L.A. Boatner, *J. Am. Ceram. Soc.*, 77(8) (1994) 1987.
[10] W.C. Carter, A.R. Roosen and J.W. Cahn, Oral Presentation at the 96th Annual Meeting of the American Ceramic Society, Indianapolis, IN, 24–27 April 1994 (talk no. SV-11-94).
[11] H. Fujita, *J. Electron Microsc. Technol.*, 12 (1989) 201.
[12] M. Kusunoki, K.Yonemitsu, Y. Sasaki and Y. Kubo, *J. Am. Ceram. Soc.*, 76 (1993) 763.
[13] A. Kilian, *Ph.D. Thesis*, Brown University, Division of Engineering, May 1994.
[14] G. Petzow and H.E. Exner, *Z. Metall.*, 67 (1976) 611.
[15] T. Besmann, *SOLGASMIX-PV, ORNL/TM-5775*, Oak Ridge National Laboratory, Oak Ridge, TN, 1977.
[16] D. Uskokovic and H.E. Exner, *Sci. Sintering*, 9(3) (1977) 265.
[17] O. Bovin, R. Wallenberg and D.J. Smith, *Nature*, 317 (1985) 47.
[18] P. Shewmon, *Diffusion in Solids*, J. Williams Book Co., Jenks, OK, 1983, p. 47.

[19] P. Lu and D.J Smith, *Phys. Rev. Lett.*, *59* (1987) 2177.

[20] D.J. Ehrlich and D.J. Smith, *Appl. Phys. Lett.*, *48* (1986) 1751.

[21] K. Maeda and S. Takeuchi, *Appl. Phys. Lett.*, *42* (1983) 664.

[22] A.K. Petford, L.D. Marks and M. O'Keeffe, *Surf. Sci.*, *172* (1986) 496.

[23] D.J. Smith, M.R. McCartney and L.A. Bursill, *Ultramicroscopy*, *23* (1987) 299.

In situ ultra-high vacuum transmission electron microscopy studies of nanocrystalline copper

Deirdre L. Olynick,* J. Murray Gibson, Robert S. Averback

Materials Research Laboratory, University of Illinois at Urbana-Champaign, 104 S. Goodwin Avenue, Urbana, IL 61801, USA

Abstract

We have built a particle production and transport system that allows the characterization of nanocrystals without exposure to contaminating atmospheres such as air. Nanocrystals (formed by inert gas condensation of a sputtered atom population) are transported in situ via the gas phase to an ultra-high vacuum transmission electron microscope (UHVTEM) equipped with a heating stage and gas exposure system. With this system, we can study various nanoparticle phenomena in real time and under clean conditions. In this paper we discuss the experimental design and preliminary studies using imaging and diffraction techniques. These include, the time-evolution of copper nanoparticle morphology and sintering behavior as a function of particle size, temperature, oxygen/atmosphere exposure and supporting substrate. In particular, we have observed immediate room temperature sintering of clean copper nanocrystals which does not occur with nanoparticles that have been exposed to oxygen. Furthermore, we have seen an interaction between copper nanocrystals and amorphous carbon which produces graphite shells. This shell formation process suggests a solid state analog to that seen when nanoparticles catalyze the growth of carbon fibers through a hydrocarbon atmosphere decomposition.

Keywords: Nanocrystalline copper; Diffraction techniques

1. Introduction

Nanophase materials, with grain sizes of the order of 1–100 nm, are of technological value because of their desirable grain-size dependent properties. These small grain sizes lead to as many as 40% of the atoms situated in grain boundaries and changes to kinetic processes such as lowered sintering temperatures and enhanced diffusivities. Unfortunately, the mechanisms by which these phenomena manifest themselves in the macroscopic, consolidated state, are not well understood. For instance, studies of diffusion properties in nanocrystalline copper have revealed activation energies as much as 40% lower than in polycrystalline copper [1]. Some speculate that the lower activation energy is due to the special nature of the interfaces [2] while others attribute it to a surface-like diffusion along the surfaces of voids [1]. Certainly, knowing the microscopic structure of the nanocrystals prior to consolidation and how they can

be manipulated throughout processing would give insight into this issue. These microscopic characteristics (for instance, initial crystal structure, relative orientation, crystallite surface-to-volume ratio, and initial adhesion and sintering properties) are difficult to decipher once consolidated in techniques such as inert gas condensation (IGC) [3].

Other groups have attempted to study unconsolidated nanocrystals produced by IGC or in smoke by placing a collection grid inside the chamber and studying the particles in a transmission electron microscope (TEM). Although this method gives some information, it introduces ambiguities when the specimens are taken out into atmospheres; nanocrystals are highly reactive and thus very sensitive to contamination. Thus, an in situ, ultra-high vacuum system such as the one we have built and will describe in this paper is ideal for studying nanocrystals.

Using in situ systems similar to ours (a particle production chamber attached to a TEM), Iijima [4] and Bonevich and Marks [5] studied nanocrytals, particu-

* Corresponding author.
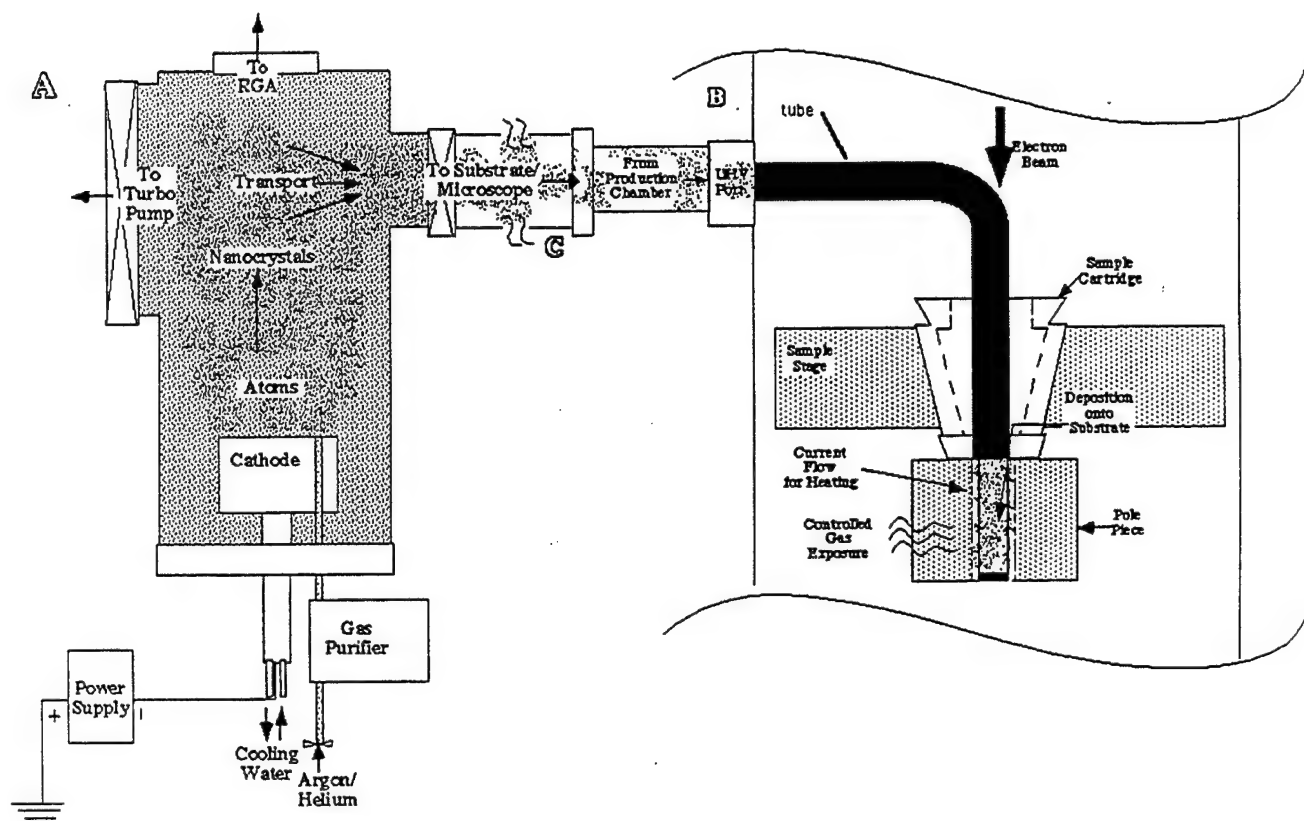
Fig. 1. UHVTEM nanocrystal production and transport system. (A) UHV production chamber. (B) Transport assembly. (C) UHVTEM deposition area.

larly nanocrystal sintering behavior. Iijima had an in situ system that injected a fine particle stream into an electron microscope. Bonevich's UHV system allowed sintering to be done in an adjacent furnace and then transferred in situ to a high resolution transmission electron microscope. Our studies of various nanocrystal phenomena (such as sintering) have the advantages that they could be done in real time, in the presence of different gases, and under ultra-clean conditions.

In this paper we present initial studies done on copper nanocrystals (the morphologies, sintering behavior, substrate/particle catalytic action, and oxidation effects) and the design of the UHV system in which the particles were synthesized and observed.

2. Experimental and design

The schematic arrangement of the experimental system is shown in Fig. 1. The ultra-high vacuum nanoparticle production system consists of a production chamber with a sputtering source, a transport assembly, and a modified JEOL 200CX TEM [6]. Sputtering sources have the advantage that a variety of nanocrystalline materials can be produced, including refractory metals. Our sputtering target was a commercially obtained copper target of 99.999% purity. The

base pressure of the chamber was less than 5×10^{-9} Torr. The base pressure of the microscope was 3×10^{-8} Torr and was sometimes lowered into the 10^{-9} Torr regime through the use of a helium cryoshield. We have found that with copper, it is critical that the vacuum in the growth chamber be UHV. However, the pressure in the microscope without the cryoshield was satisfactory for most studies. Thus we were often able to avoid the experimental difficulties encountered when we introduced high gas loads into the microscope with the cryoshield operating.

To initiate particle deposition, the production system was valved off from both the turbo pump and transport assembly, back filled with clean argon (less than 1 part per billion impurities), evacuated, and filled again to the desired sputtering pressure (between 100 and 1000 mTorr). DC sputtering was executed at approximately 600 W and allowed to proceed for 60–90 s. The particles were introduced into the TEM (while sputtering continued), and traveled to the substrate one of two ways: (i) via a pressure differential or (ii) using forced flow. If a pressure differential was used, the valve between the production chamber and transport assembly was opened and the gas from the chamber would carry the particles into the microscope. If forced flow was used, the 'plumbing' following the gas purifier was used as a ballast tank, filled with clean argon during the

sputtering, and opened at the same time as the valve between the chamber and transport assembly to produce a pressure burst in the chamber between 1 and 3 Torr. The flow conditions and the time duration of the sputtering while collecting particles were critical in producing the desired densities on the substrate. This was modeled and will also be described in a future paper. Three substrates have been used thus far: amorphous carbon and graphite on refractory metal supports and an amorphous Si_xN window in a silicon support. The substrates were cleaned in situ by heating them resistively at 900°C for 2 h. Nanoparticle sintering studies were carried out before and after oxidation in the microscope and data recorded in real time on video or on conventional film. Sintering was observed between room temperature and 800°C. For some of the studies oxygen was introduced at known leak rates into different areas of the production chamber.

3. Results and discussion

3.1. Nanocrystal morphology

A sample deposition is shown in Fig. 2. These particles were deposited under the cleanest possible conditions. The individual crystals all have the multiply twinned icosahedral dodecahedron structure (Fig. 3) and are faceted. Immediately after deposition at room temperature, the particles have already begun to sinter. Several low density depositions done in series showed that particles rarely meet in the gas phase, but meet upon random deposition on the substrate and then sinter. This visual impression was confirmed with image analysis and statistical correlation.
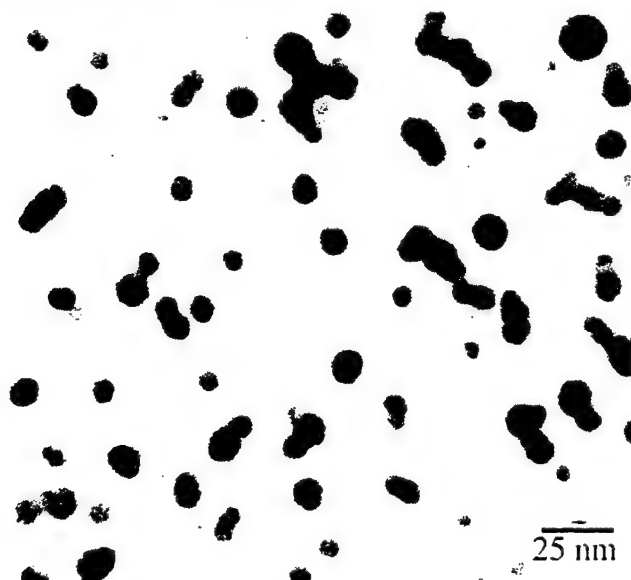
Fig. 2. Copper nanocrystals on a silicon nitride substrate. Average particle size is 10 nm.
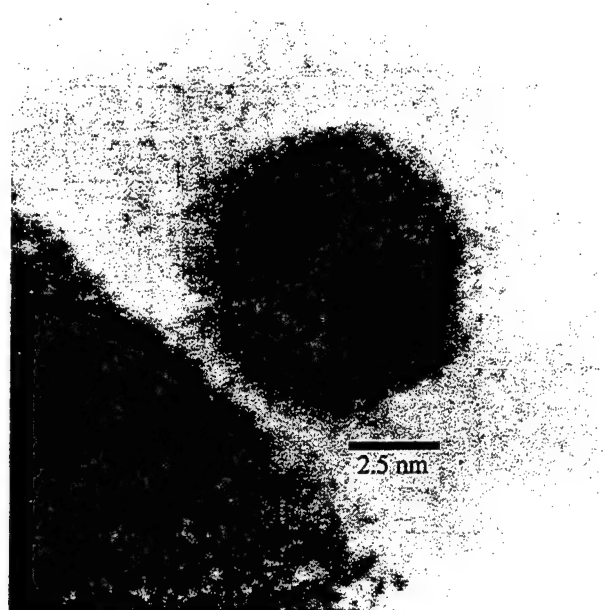
Fig. 3. Copper icosahedral dodecahedron multiply twinned particle on graphite.

Sintered agglomerates do not occur when particles are produced at higher base pressures, i.e. a dirtier system. In dirtier systems the particles maintain their distinct nature. By controllably introducing oxygen into the production chamber, we have found this to be a surface oxygen effect. This will be detailed in a later paper; but briefly, oxygen appears to be a diffusion barrier when introduced after the particles have formed. When introduced during growth, the oxygen actually changes the particle morphologies; the number of multiply twinned icosahedrals are found to decrease as the amount of oxygen exposure increases.

3.2. In situ sintering experiments

After deposition, the support can be resistively heated so that sintering of the nanocrystals can be observed in real time at a large range of temperatures. Fig. 4 shows a video-recorded sintering experiment. The necks between the particles fill in first, and soon after, the grain boundary from the top right crystal sweeps through the other two particles. This coalescence process deemed 'liquid-like coalescence' was observed by Pashley during studies of gold islands on molybdenum disulfide and appears to be due to surface self-diffusion [7]. We hope to use experiments like these to further characterize the diffusion mechanism and measure the diffusion coefficients.

Experiments done at room temperature show the early stages of neck formation between particles initially separated as well as necks already in existence breaking apart (Fig. 5). These phenomena have also
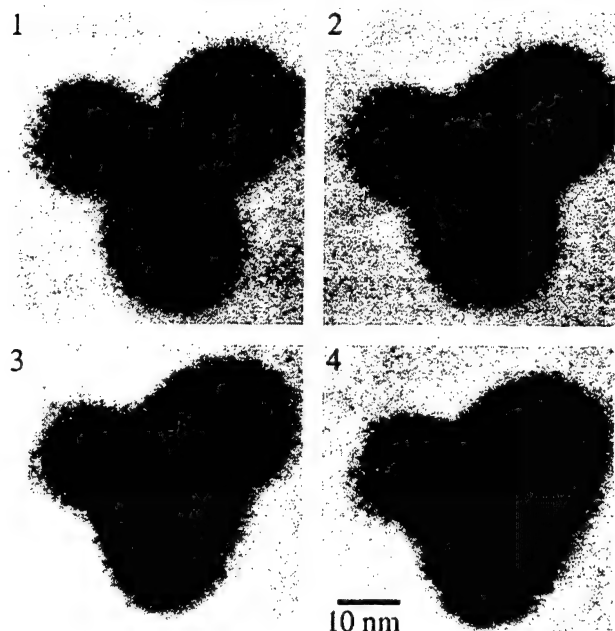
Fig. 4. In situ sintering of three copper nanocrystals on an amorphous carbon substrate. 1–4 are video frames taken at 1/8 s intervals.

been observed by Rankin and Boatner [8] and appear to be due to stresses induced by neighboring crystals.

3.3. Substrate interactions

Copper nanocrystals have catalyzed the etching of graphite and the formation of conformal graphite around the nanocrystals when deposited on either graphite or amorphous carbon. In the presence of the
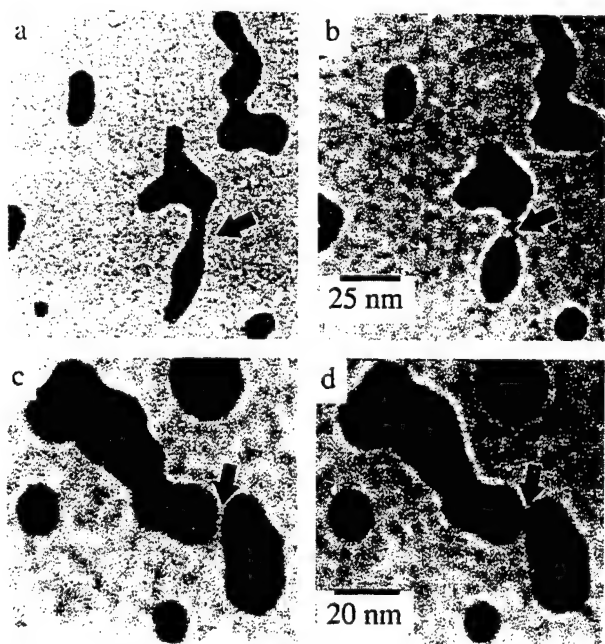
Fig. 5. (a) and (b) Room temperature neck instability. (c) and (d) Room temperature neck formation.
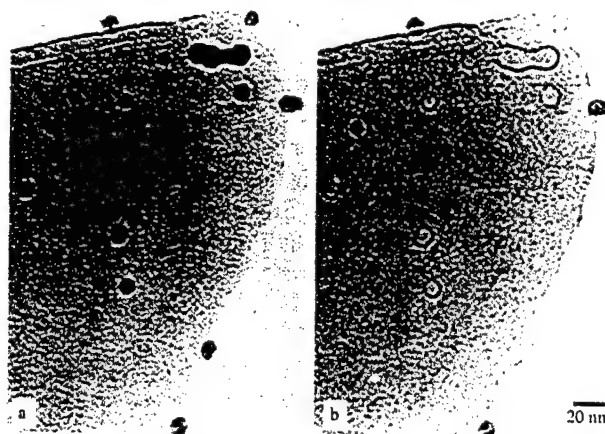
Fig. 6. (a) Graphite shells form on copper nanocrystals on a graphite substrate. (b) After annealing, the graphite shells remain empty.

electron beam and copper nanocrystals, graphite substrates etch, most prominently at steps, and then carbon is redeposited in the vicinity of the copper particles. Furthermore, the particles interact with unetched graphite and amorphous carbon and allow the formation of graphite shells around the nanocrystals when deposited on either graphite or amorphous carbon. Dark field analysis demonstrated continuous diffraction along the shells as the g-vector was rotated, indicating the shells were conformal planes of graphite. This process occurs at room temperature when the particles are formed under very clean conditions, but is more prominent during mild anneals (100–200°C). At higher temperatures, particles diffuse away by what appears to be an atom-by-atom mechansim leaving the empty graphite shells (Fig. 6).

Residual water vapor may provide a mechanism for the formation of carbon monoxide molecules, which in turn allows two carbon monoxide molecules to decompose on particle surfaces to produce a carbon deposit and the evolution of carbon dioxide gas. Usually, however, these reactions occur at higher temperatures ($\sim 600°C$) and higher water vapor pressures (~ 1 Torr) [9]. The TEM water vapor pressure for these experiments was less than 2×10^{-8} Torr.

In conlusion, we have a working in-situ UHVTEM system to characterize nanocrystals under clean conditions. We have observed room temperature sintering, the effects of oxygen, and the interaction of copper particles with graphite and amorphous carbon supports. In an upcoming paper, we will detail the effects of oxygen and its implications for copper nanocrystal processing.

Acknowledgments

References

[1] J. Horvath, R. Birringer and H. Gleiter, *Solid State Commun.*, *62* (1987) 319.

[2] S.M. Klotsman, *Defect and Diffusion Forum*, *99–100* (1993) 25.

[3] H. Gleiter, in *Deformation of Polycrystals: Mechanisms and Microstructures*, Proc. 2nd RIS0 Int. Symp, 1981, p. 15.

[4] S. Iijima, *Exploratory Research and Advanced Technology Organization (ERATO) Promotes the Growth of Ultrafine Particles*, JRDC Project Research Report, 1984, p. 3, 1985, p. 10 (in Japanese).

[5] J.E. Bonevich and L.D. Marks, *J. Mater. Res.*, *7* (1992) 1489.

[6] M.L. McDonald, J.M. Gibson and F.C. Unterwald, *Rev. Sci. Instrum.*, *60* (1989) 700.

[7] M.J. Stowell, in J.W. Matthews (ed.), *Epitaxial Growth*, vol. 1. Academic Press, New York, 1975, p. 437.

[8] J. Rankin and L.A. Boatner, *J. Am. Ceram. Soc.*, *77* (1994) 1987.

[9] R.T.K. Baker and J.J. Chludzinski, Jr., *Carbon*, *19* (1981) 75.

Surface characterization of nanostructured metal and ceramic particles

P. Luo,[a,*] T.G. Nieh,[a] A.J. Schwartz,[a] T.J. Lenk[b]

[a]*Lawrence Livermore National Laboratory, Livermore, CA 94550, USA*
[b]*Raychem Corporation, 300 Constitution Drive, Menlo Park, CA 94025, USA*

Abstract

In the present study, nanocrystalline Al, TiN and SiC particles produced by different techniques were examined using X-ray diffraction analysis, scanning electron microscopy (SEM), and transmission electron microscopy (TEM). The average particle size and size distribution were measured for these nanoparticles. In addition, the surfaces of these particles were characterized by X-ray photoelectron spectroscopy (XPS) and high resolution transmission electron microscopy. An amorphous layer was normally found to form on the surface of the nanocrystalline particles. The layer thickness, depending upon the material, is sometimes non-uniform. The chemical states of the surface atoms on Al, TiN, and SiC were also determined by XPS.

Keywords: Ceramic particles; Surface characterization; Metal particles

1. Introduction

Much current materials research is focused on the design, synthesis, and processing of ultrafine material microstructures, extending into the nanoscale (< 100 nm) regime [1]. This research has been inspired by the realization that significant beneficial changes in the properties of materials can be achieved by reducing the scale of their microstructure while maintaining chemical and microstructural uniformity [1,2]. As a result of a large surface to volume ratio, nanocrystals have been suggested for use in applications such as energy storage, catalysis, and membranes [3,4]. These applications are clearly dependent on the surface characteristics of the nanocrystals.

It has been recognized that the presence of gaseous species, water vapor, and other electrolytes in air often causes oxidation and adsorption on the surfaces of non-oxide particles either during material preparation or storage [4]. The oxidized surface may further prohibit the densification of a sample during consolidation (e.g. sintering and hot pressing) [5]. In the present work, the surfaces of structural nanocrystalline particles of Al, TiN and SiC are examined and their structure and chemistry are discussed.

2. Experiment

Al and TiN nanoparticles were received from Ultram International. They were produced by a super-high-frequency (SHF) plasma chemical process [6]. In this method, a microwave generator was used to create a plasma which causes the reaction of selected chemicals and gases and produces the nanocrystals. In the case of SiC, β-SiC nanoparticles were made by a chemical synthesis process. Specifically, the particles were produced by spray drying an aqueous solution followed by thermochemical conversion under an argon gas environment [2]. All powders were stored in jars for about 6 months.

Analytical methods used to characterize these powders include X-ray diffraction (XRD) using Cu Kα radiation, scanning electron microscopy (SEM), and transmission electron microscopy (TEM). Surface morphology is determined by high resolution transmission electron microscopy (HRTEM). Sample powders were initially de-agglomerated in an ultrasonic bath filled with ethanol for 5 min and then collected using a TEM grid coated with a carbon film. The sample was cleaned and dried; then loaded on the TEM stage. The surface structure of the sample was subsequently examined. In addition, the chemical states of the particle surface were characterized by X-ray photoelectron spectroscopy (XPS) using a non-monochromatic Al Kα source. Sam-

---

* Corresponding author.

ple powders were mounted as thick layers on double-sided adhesive tape. The sample stubs were then tapped to remove excess powder and expose a fresh surface for examination. The measured XPS peaks were fitted using Gaussian–Lorentzian peaks with a Gaussian fraction of 0.75. Peak widths were typically 1.7–1.9 eV. Compositions of the surface layers were analyzed, both qualitatively and quantitatively.

3. Results and discussion

3.1. General characterization

Scanning electron microscopy (SEM) reveals that all of the nanopowders are agglomerated in a spherical geometry, especially the TiN and SiC ceramic powders
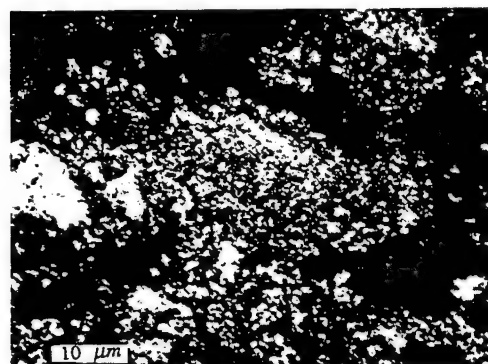
Al particles
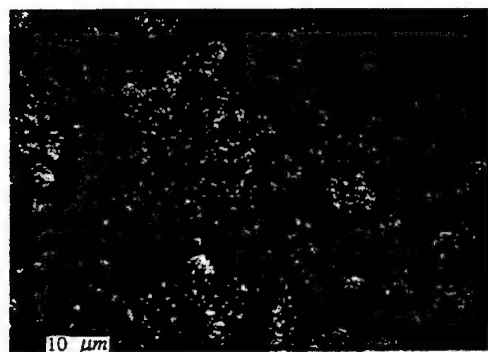
TiN particles

SiC particles

Fig. 1. Scanning electron microscopy reveals agglomeration of Al, TiN and SiC nanoparticles.
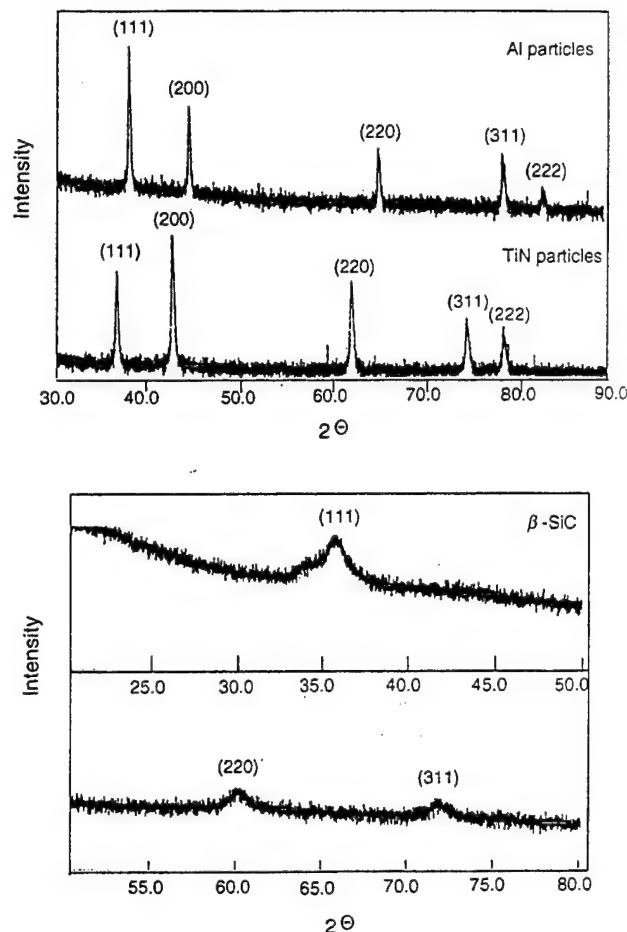
Fig. 2. Structural analysis of Al, TiN and SiC nanoparticles using X-ray diffraction.

(Fig. 1). SiC particles are agglomerated tightly into perfect spheres, as compared with the loosely agglomerated Al and TiN particles. X-ray diffraction results for these powders are shown in Fig. 2. Both Al and TiN are found to be face center cubic, but β-SiC is of diamond cubic structure. A small shoulder on the low angle side of the (111) diffraction plane of β-SiC is observed. This suggests that a small amount of α-SiC is contained in β-SiC powders. However, no other significant impurity peaks are detected in these three spectra, indicating the absence of any crystalline oxide phases in these samples.

TEM micrographs showing the morphology of de-agglomerated particles are presented in Fig. 3. It is readily observed that the majority of the Al particles are spherical, and the TiN particles are cubic. In contrast, SiC has both platelets and fiber-like particles. The average sizes of Al spheres, TiN squares and platelets, and SiC fiber-like and platelet particles are 50 nm, 20 nm, and 20 nm wide, respectively. However, the size distributions of these particles are found to be quite broad, up to 500 nm. Corresponding electron diffraction patterns show the polycrystalline nature of these particles with preferred orientations. The diffraction pattern of β-SiC

powders does not show any sign of α-SiC, but TEM shows only the local composition in a small area. However, no impurities are observed by indexing rings of these diffraction patterns. This indicates the absence of any crystalline oxide phases, consistent with the results obtained from X-ray diffraction analysis.

3.2. TEM

3.2.1. Al particles

High resolution transmission electron microscopy was performed on the three nanocrystals. An approximately 5 nm thick surface layer was noted on the Al particles (Fig. 4(a)). This surface layer is apparently quite uniform. Close examination (Fig. 4(b)) indicates that the layer is amorphous, in contrast to the Al grain which is crystalline, showing its (110) lattice image. The amorphous layer can be further divided into two sublayers. The outer sublayer is about 1 nm thick and appears to be more loosely packed than the inner sublayer. The difference may be related to the stoichiometry of the oxide layer, and suggests that the surface layer contains more than one type of chemical species and varies in composition from top to bottom. This needs further investigation.

(a)

(b)

Fig. 4. (a) Surface morphology of a typical Al particle. (b) High resolution TEM shows the amorphous surface layer of an Al particle.

Fig. 3. Transmission electron microscopy shows nanocrystalline Al, TiN and SiC with corresponding diffraction patterns.

3.2.2. TiN particles

In the case of TiN, a non-uniform surface layer thickness (2–5 nm) is observed, particularly at the sites where two particles come into contact (Figs. 5(a) and (b)). They are high resolution electron micrographs of some cubic TiN particles. Crystalline lattice fringes are readily seen. The two particles make close contact and appear to be epitaxial. The epitaxy may be related to the covalent nature of TiN, which produces strong anisotropy. The contour of the surface layer does not follow the boundary of the particle exactly. In fact, the contour appears to be determined by its equilibrium chemical potential, in particular at the sites where two particles impinge. It is further pointed out that the surface layer may be partly crystalline, as revealed by the appearance of some lattice fringes (indicated by arrows). In contrast to Figs. 5(a) and (b), Fig. 5(c) is a TiN particle showing the absence of any surface layer; lattice fringes extend to the outermost surface. In summary, the nature of the surface layer on nano-TiN particles is complex and varied.

3.2.3. SiC particles

In the case of SiC, the nano-particles exhibit a homogeneous surface layer, as shown in Fig. 6(a). The layer has a uniform thickness of about 3 nm and is amorphous. This is in contrast to the crystalline SiC which
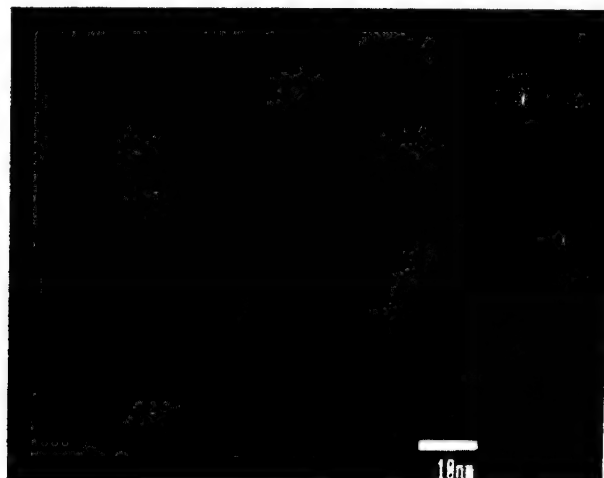
(a)

(b)

(c)

Fig. 5. (a) Surface morphology of typical TiN particles. (b) Surface morphology of the contact corner of two TiN particles. (c) Clean surface of a typical TiN particle.
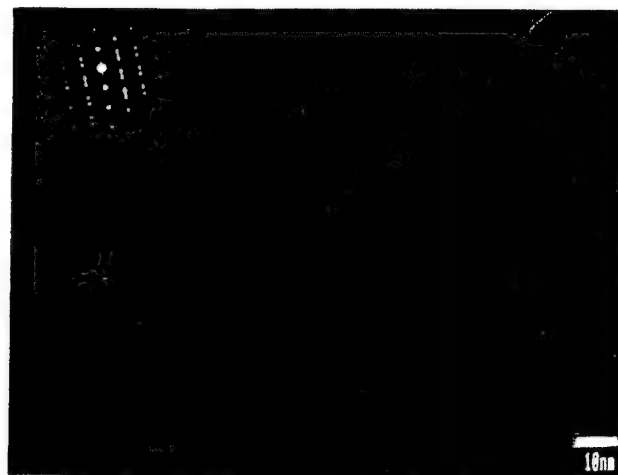
(a)
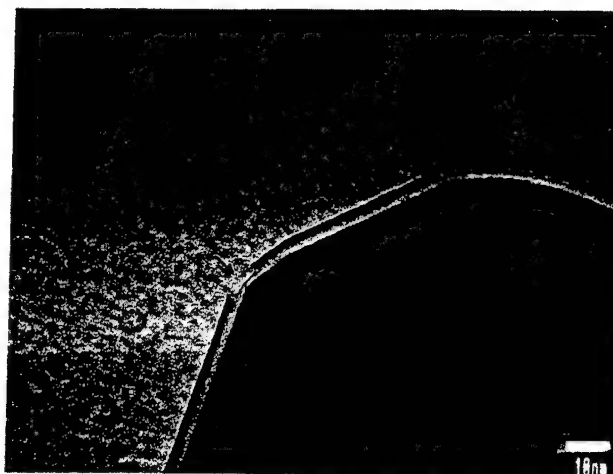
(b)

Fig. 6. (a) High resolution TEM of a SiC particle shows the surface layer structure contrasted with the twinning structure of the particle. (b) SiC surface layer shows 'chip-off' regions.

has (110) planes and a substantial amount of twinning (Fig. 6(a)). Fig. 6(b) shows a SiC particle with a multi-layered surface. Noted in the micrograph are 'chip-off' regions of the surface layer at some locations, particularly near the corner of the particle (indicated by arrows) suggesting a brittle surface layer.

3.3. XPS

The elemental composition of the surfaces of the Al, TiN and SiC particles is shown in Table 1. The effective

Table 1
Surface atomic compositions of Al, TiN and SiC particles

	Al	Ti	O	C	Si	N	Cl
Aluminum	21		54	22	3.0		
Titanium nitride		29	39	11	0.3	21	0.5
Silicon carbide			18	61	19	1.8	

The aluminum 2p region.

chisq = 3.285; chi = 1.813

The titanium 2p region.

chisq = 19.67; chi = 4.435

Silicon 2p region of silicon carbide powder.

chisq = 12.01; chi = 3.466

Peak fitting results for the Al2p region.

Peak	Binding Energy (eV)*	Assignment	Percent of Total
1	73.4	Aluminum Metal	75
2	76.2	Aluminum Oxides	25

*Corrected to C1s at 284.8 eV.

Peak areas and assignments for the titanium 2p region.

Peak Number	Peak	Binding Energy*	Percent of Total	Assignment (Percentage)
1	$2p_{3/2}$	456.4	47.7	TiN
2	$2p_{1/2}$	462.1	15.8	(63.5)
3	$2p_{3/2}$	459.4	27	TiO_2
4	$2p_{1/2}$	465.2	9.6	(36.6)

* Corrected to C1s at 284.8 eV.

Peak fitting results for the Si2p region of the silicon carbide powder.

Peak	Binding Energy (eV)	Assignment	Percent of Total Silicon
1	101.2	Carbide	79
2	102.7	—Si-O—	21

Fig. 7. XPS analysis of aluminum, titanium and silicon 2p regions.

analysis depth for XPS is about 10 nm. For the particles studied, this means that much of the signal will come from the surface layer (2–5 nm, see the Subsection 3.2), but that there will also be a significant contribution from the bulk material.

The Al and TiN particles have about 10–20 at.% carbon, consistent with contamination levels from typical laboratory handling and storage. The carbon on the Al is primarily hydrocarbon, a common contaminant. The carbon on the TiN appears to be primarily in the form of ethers or amines, which is more unusual, but is consistent with the high oxygen and nitrogen concentrations on these particles. The surface of the SiC particles is about 60% carbon, and about 30% of this is in the form of carbides. The excess organic material is most likely due to incomplete conversion of precursors into SiC.

Detailed scans of the Al, Ti (TiN), and Si (SiC) regions are shown in Fig. 7. Significant amounts of oxides are seen on the Al (about 25% oxidized forms, 75% metal) and TiN (about 35% titanium oxides, 65% titanium nitride) particles. Coupled with the structural observations from TEM, this suggests that the surface layers may be primarily oxides (the spectra include the surface layer plus several nanometers of the 'bulk' material). The SiC particles have about 80% of the surface silicon present as SiC. The binding energy of the remaining silicon is consistent with the presence of silanes (which are intermediate products in the particle synthesis).

4. Conclusions

(1) The morphologies of nanocrystalline particles of

Al, TiN and SiC are characterized. Al, TiN, and SiC are in the geometry of spheres, squares, and short fibers with platelets, respectively. The average particle sizes of Al, TiN, and SiC are 50 nm, 20 nm, and 20 nm, respectively.

(2) High resolution electron microscopy indicates that the surface layers of all these particles are mainly amorphous. The layer thicknesses are about 5 nm and 3 nm for Al and SiC particles, respectively. In contrast, the layer thickness of TiN is non-uniform; some areas show an agglomeration of surface products, but some exhibit a clean crystalline surface. Also, there exists some evidence indicating that the surface layers may, in fact, consist of more than one sublayer on SiC and Al particles.

(3) XPS analysis shows the presence of significant oxides on the surfaces of all three particles. The TiN surface is more heavily oxidized than the Al and SiC, and titanium oxides account for most of the oxygen seen on the surface. It is not known how much of this oxidation occurred during the synthesis process and how much during storage, but it seems likely that the observed surface layers for the Al and TiN particles are primarily oxides. The binding energy of the oxygen species present on the SiC particles is consistent with the presence of organic intermediate products (carbonyls and ethers) with some contribution (about 20%) from silicon oxides.

References

[1] H. Gleiter, *Prog. Mater. Sci.*, *33* (1989) 223.
[2] P. Luo, P.R. Strutt and T.D. Xiao, *Mater. Sci. Eng.*, *B17* (1993) 126–130.
[3] R.W. Siegel, *Nanostructured Materials*, *4(1)* (1994) 121–138.

[4] N. Ichinose, Y. Ozaki and S. Kashu, *Superfine Particle Technology*, English edition, Springer, London, 1992.
[5] T. Wang, L. Zhang, X. Fang, J. Hu and C. Mo, *J. Appl. Phys.* 74 (1993).
[6] *Advances in Nanophase Ceramics*, Advanced Materials and Processes, October 1994.

Synthesis and nitridation of nanocrystalline silicon produced via a tubular forced flow reactor

Darren T. Castro,[a] Jackie Y. Ying[b,*]

[a]*Department of Materials Science and Engineering, Massachusetts Institute of Technology, Cambridge, MA 02139, USA*
[b]*Department of Chemical Engineering, Massachusetts Institute of Technology, Cambridge, MA 02139, USA*

Abstract

The design and operation of a novel, continuous reactor for scaling-up the production of nanocrystalline materials is outlined. The reactor operates using a replenishable thermal evaporation source in a forced gas flow. This alternative reactor design overcomes many of the production limitations of the batch reactor inert gas condensation process used widely in nanocrystalline synthesis. By achieving gas flow velocities of 12.5–40 m s^{-1}, particle size is kept in the nanometer range by quickly removing the particles from the hot growth zone and minimizing their agglomeration during synthesis. The effects of processing parameters on Si particle size and morphology are presented. Nanocrystalline Si_3N_4 was produced by subsequent nitridation and heat treatment. Complete nitridation of the Si was achieved by 1050°C. Upon moderate heat treatment (1600°C for 3 h), the SiO_x present in the material crystallized.

Keywords: Nitridation; Silicon; Forced gas flow

1. Introduction

1.1. Motivation for synthesizing nanocrystalline Si_3N_4

Due to its high strength and resistance to oxidation, thermal shock, wear and corrosion, Si_3N_4 has great potential for applications such as advanced heat engine components and ball bearings. However, in order to densify conventional Si_3N_4, sintering additives such as MgO, Al_2O_3, and Y_2O_3 are typically needed. The oxide additive reacts with the SiO_2 surface layers to form a liquid phase at sintering temperatures. Upon solidification, this oxide phase is retained at the grain boundaries. If this intergranular phase is glassy, it can soften at moderately elevated temperatures leading to a degradation of the mechanical properties of the nitride component [1]. Additionally, the reliability of components is directly connected to the starting Si_3N_4 powder. The final grain and flaw sizes in a densified ceramic material are directly related to the particle size of the starting powder [2].

Several potential benefits may be achieved by using a nanocrystalline Si_3N_4 powder to produce Si_3N_4 compo-nents. A nanocrystalline ceramic powder (particle size ~ 10 nm) can lead to a greatly increased sintering rate compared with conventional powder (particle size $\sim 0.1-1$ μm). This size effect as well as the large volume fraction of grain boundaries and enhanced grain boundary diffusion coefficients in nanocrystalline materials can lead to improved sintering kinetics and the potential for lower temperature sintering with less or no sintering additive. For instance, nano-TiO_2 has been sintered at temperatures 400–600°C lower than conventional sintering temperatures and without the need for sintering aids [3]. Some work has been done on sintering nano-Si_3N_4 produced by a laser-induced chemical vapor deposition process [4,5]. The group from China reported sintering nano-Si_3N_4 at 1500–1600°C without additives and without significant grain growth [4]. The Rutgers group compared the sinterability of nano-Si_3N_4 that was exposed to air with that which was handled in a glove box environment (unexposed to air). With hot isostatic pressing and no additives, the air-exposed powders rapidly achieved $\sim 91\%$ densification [5].

The gas condensation method [6,7], by which a number of nanocrystalline materials are produced, typically yields a narrow log-normal size distribution of particles

---

* Corresponding author.
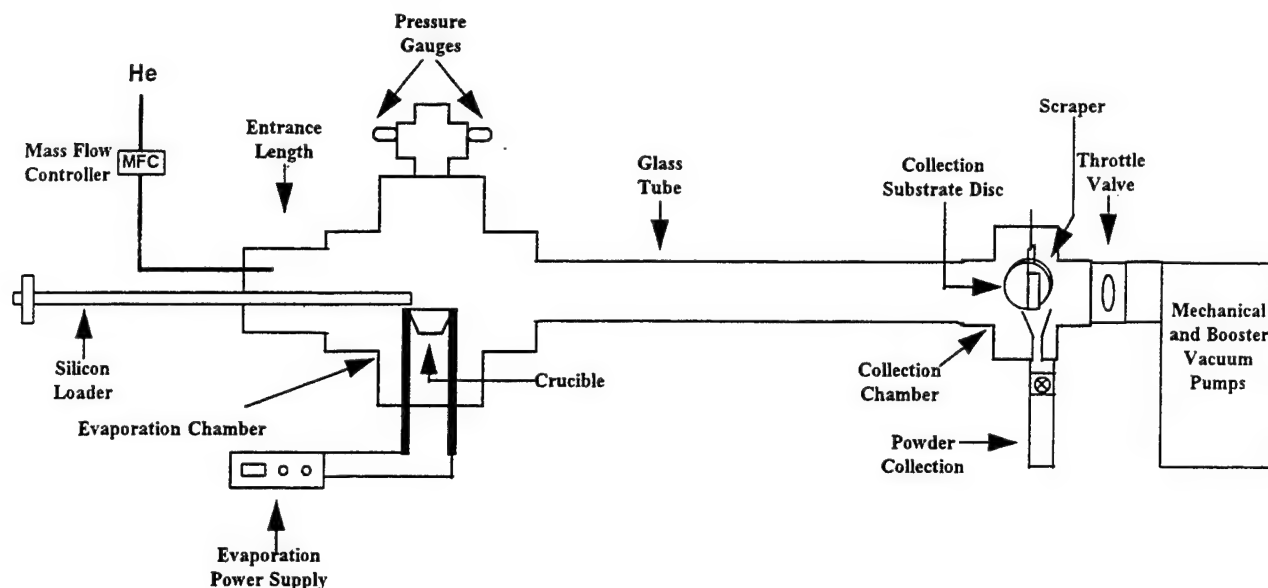
Fig. 1. Schematic of the tubular forced flow reactor for nanocrystalline synthesis.

[8]. This type of distribution has led to good green body packing and normal grain growth [3]. Such a starting powder could also prevent the formation of large internal flaws [9]. Finally, due to the well-controlled environment of nanocrystalline material synthesis by gas condensation, it is possible to control both impurities and additive introduction during processing for engineering of the grain boundaries. Thus, the advantages to pursuing a nanocrystalline Si_3N_4 powder through such a processing approach are clear.

1.2. Motivation for a forced flow reactor design

Due to inherent limitations in the traditional nanocrystalline synthesis approach of gas condensation, a forced flow reactor has always been recommended to facilitate scale-up such that one can synthesize significantly larger amounts of material than the few hundred mg per day that are normally produced by the conventional batch-type reactors [10]. The motivation for examining an alternative reactor design comes from the two drawbacks of the existing inert gas condensation process. First, rather than forming larger quantities of nanocrystals, increasing the rate of evaporation leads to increased particle size due to the presence of more coalescence partners. Second, a scale-up is difficult since collection efficiency is low due to loss of sample to the cold surrounding chamber wall in natural convective flow [11]. Therefore, the rate of nanocrystalline powder production with the natural convection method (gas velocities ~ 1 m s^{-1}) is limited. The application of a forced flux has been used to produce nanocrystalline metals (Cu, Pd, Ag) by removing the nanocrystals quickly from the hot growth zone over the evaporation

source [11,12]. By using high gas velocities (10 m s^{-1} or greater) particle coalescence is limited and the production rate of nanocrystalline materials may be significantly increased.

2. Experimental details

2.1. Nanocrystal synthesis in forced flow reactor

A novel tubular forced flow reactor for nanocrystalline synthesis has been custom designed and constructed. A schematic of the reactor is shown in Fig. 1. The incoming gas flow rate is set with a mass flow controller. Helium (He) enters at one end of the reactor and flows over the crucible where silicon (Si) is evaporating. The silicon supply is continually replenished with a magnetically coupled loader. A pumping system (Leybold) consisting of a roots blower (booster pump) backed by a single-stage mechanical pump continuously removes the Si particles in the He gas stream from the growth zone over the evaporation source. The particles entrained in the gas stream are deposited on a liquid nitrogen cooled disc mounted parallel to the gas flow in the center of the collection chamber, located at the other end of the tubular reactor. The pressure in the reactor is controlled by a throttle valve with a capacitance manometer input. Knowing the reactor pressure, reactor cross-sectional area and incoming gas flow rate, one may determine the gas (and particle) velocity [12]. The particles can be scraped off the rotating disc and collected. Following a production run, the reactor is controllably backfilled with air, exposing the material to oxygen.

In order to characterize the reactor's operation, the effect of reactor pressure and gas velocity on the particle size and morphology was examined. The reactor was operated at pressures ranging from 0.5 mbar to 11.3 mbar. He gas velocities ranged from 12.5 to 40 m s^{-1}. Particle size and morphology characterizations were performed by transmission electron microscopy (TEM). In some cases, particles were directly deposited on carbon grids mounted on the collection disc. In other instances, collected or heat-treated particulates were ground and suspended in isopropanol, and then deposited on TEM grids. An Akashi-002B operating at 200 kV was used for all TEM studies.

2.2. Nitridation experiments

The B.E.T. surface area of the as-prepared nanocrystalline Si produced in the reactor was determined by nitrogen adsorption (Micromeritics ASAP 2000). The as-prepared nanocrystalline Si was nitrided in both a thermal gravimetric analyzer (Perkin–Elmer TGA7) and a differential thermal analyzer (Perkin–Elmer DTA7) to follow nitridation and crystallization kinetics. The flowing nitrogen gas used was purified with an oxygen trap and a liquid nitrogen trap. Heating rates for all experiments were 5°C min^{-1} while the final temperature varied from 1100 to 1600°C with various soak times. For DTA experiments the samples were run in an alumina cup and covered with alumina powder. The samples were placed loosely in an alumina pan liner in the TGA analysis.

The as-prepared and nitrided materials (after various heat treatments) were examined by X-ray diffraction (XRD) using a Rigaku 300 with Cu-Kα radiation for $2\theta = 10°–70°$. The α-Si$_3$N$_4$ resulting from the nitridation/heat treatments was studied by TEM to determine particle size and morphology.

3. Results and discussion

3.1. Effect of reactor synthesis parameters

The as-synthesized material consists of approximately spherical, crystalline particles. The powder removed from the reactor has a dark brown appearance. Shown in Fig. 2 is a plot of particle size vs. reactor pressure. The gas (particle) velocity was kept constant at 12.5 m s^{-1} for these experiments. By varying the pressure, average particle sizes ranging from 5.7 to 9.5 nm were obtained. As has been reported by others previously, particle size increased with increasing reactor pressure due to confinement of the particles in the growth region above the evaporation source [13]. Fig. 3 is a TEM micrograph of representative Si particles ~ 7 nm in diameter obtained at 7 mbar and a gas velocity
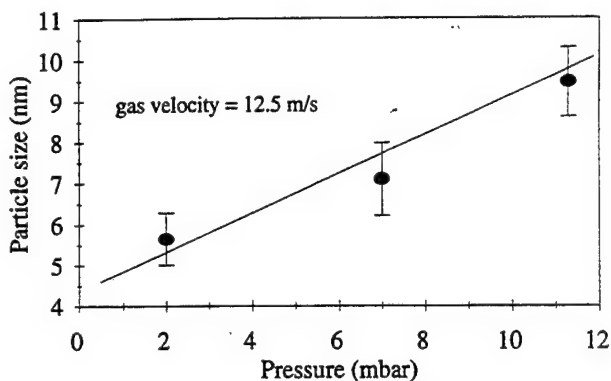
Fig. 2. Particle size as a function of reactor pressure at a gas velocity of 12.5 m s^{-1}.

of 12.5 m s^{-1}. Their lattice fringes are clearly visible. The crystalline nature of the as-prepared material is also shown by the Si TEM diffraction pattern in Fig. 4.

There was no significant difference in size or morphology of particles produced at gas velocities of 12.5, 15 and 25 m s^{-1}, with a reactor pressure of 2 mbar. Discrete crystalline particles of ~ 6 nm were seen in all cases. At a gas velocity of 40 m s^{-1}, an amorphous film was deposited on the collection substrate. The product consisted of thin flakes rather than individual particles. This is likely due to the more rapid quench rate of the Si (on the order of 4.1×10^4 K s^{-1}) and the fact that

Fig. 3. Nanocrystalline silicon particles produced at 7 mbar pressure and a gas velocity of 12.5 m s^{-1}.
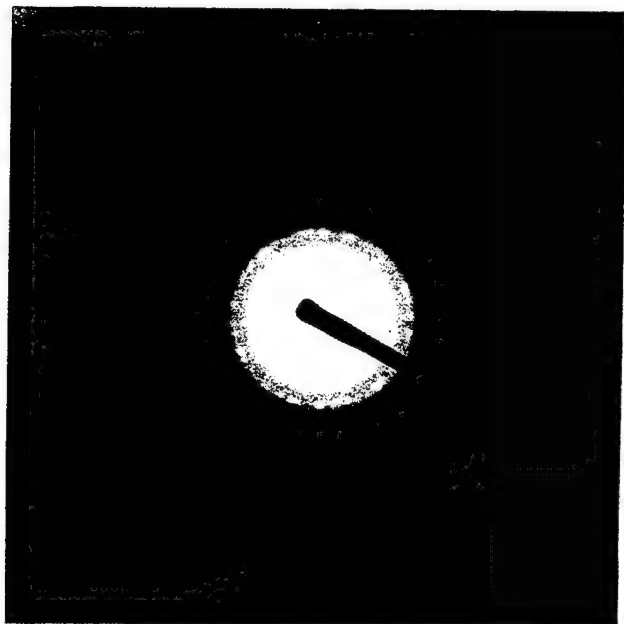
Fig. 4. TEM diffraction pattern of the as-prepared material shown in Fig. 3.

the Si atoms could not coalesce and order before they reached the liquid nitrogen cooled collector. A similar effect in a flow reactor has been observed by Iwama and Hayakawa in their synthesis of ultrafine metal particles [12]. They found that, depending on the distance from the evaporation point to the collection point and the He gas velocity, materials produced fall into either a 'film formation region' or a 'particle growth region'. On the basis of the size of our reactor and their data, the transition from particle to film formation in our reactor should occur at ~ 30 m s^{-1}.

The current Si evaporation rate is ~ 6 g h^{-1}. The current thermophoretic collection design is not highly effective. Much of the material synthesized is pulled into the vacuum pumping system due to the high gas flow velocity rather than gathered thermophoretically on the cooled collection disc. The collection efficiency is on the order of 5%–10%. The micrographs illustrate that nanocrystallites are effectively produced by this
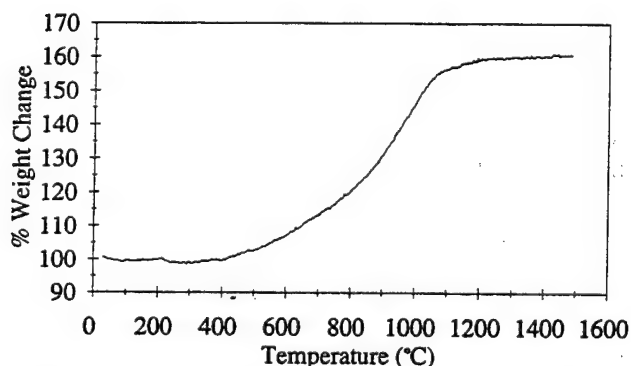
Fig. 5. TGA data showing Si-to-Si$_3$N$_4$ conversion by 1050°C.
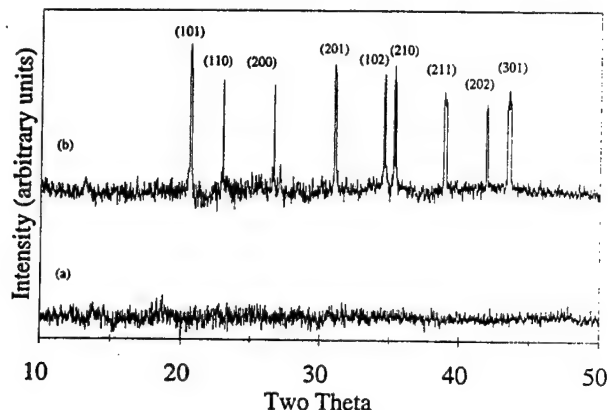
Fig. 6. (a) XRD data showing that as-prepared material is X-ray amorphous. Following heat treatment at 1600°C for 1 h in a flowing nitrogen atmosphere, α-Si$_3$N$_4$ peaks (indexed) are well developed (b).

reactor design despite the higher evaporation rate. Initial efforts to do in situ nitridation of the Si particles in a flowing gas stream of helium and nitrogen were complicated by nitridation of the evaporation source. The reactor is being modified to introduce nitrogen just beyond the evaporation crucible. A downstream microwave plasma applicator adjacent to the evaporation chamber will be used to ionize the nitrogen and lead to effective nitridation of the nanocrystalline Si particles passing through the N$_2$ plasma.

3.2. Nitridation results and discussion

On the basis of the study of reactor synthesis parameters, a pressure of 2 mbar and a gas velocity of 12.5 m s^{-1} were selected for continuous production of nanocrystalline Si. The as-prepared material has a B.E.T. surface area of (154.1 ± 1.6) m^2 g^{-1}. Its high
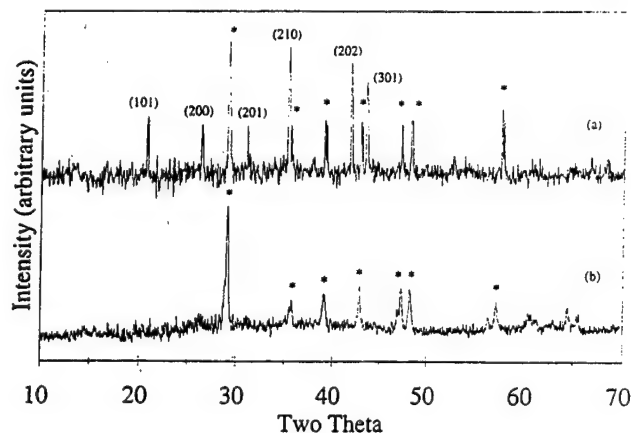
Fig. 7. (a) XRD data showing material heat treated at 1600°C for 3 h in a flowing nitrogen atmosphere developed additional peaks (*) unrelated to the α-Si$_3$N$_4$ peaks (indexed). These additional peaks were similar to the diffraction peaks of a crystalline, non-stoichiometric SiO$_x$ produced when the reactor had air leakage during the synthesis (b).

Fig. 8. TEM micrograph of α-Si$_3$N$_4$ particles formed during heat treatment to 1600°C for 1 h in a flowing nitrogen atmosphere.

Fig. 9. TEM micrograph of α-Si$_3$N$_4$ particles formed during heat treatment to 1600°C for 1 h in a flowing nitrogen atmosphere.

surface reactivity enabled nitridation and conversion to Si$_3$N$_4$ at relatively low temperatures. Nitriding temperatures for conventional Si range from $\sim$ 1200°C to 1450°C [14]. Ultrafine Si powder of diameter 20–50 nm produced by an arc-plasma method could be nitrided at 1100°C if unexposed to air, or at 1200°C if exposed to air [15]. As shown in Fig. 5, nitridation of our nanocrystalline Si was initiated at a low temperature of $\sim$ 500°C and was completed by $\sim$ 1050°C.

The as-prepared Si material is X-ray amorphous (see Fig. 6(a)). The first evidence of X-ray crystallinity is found in a sample held at 1500°C under N$_2$ gas flow for 30 min. The diffraction pattern indicated the formation of an α-Si$_3$N$_4$ phase in the sample. DTA reflects a major exothermic peak at 1490–1560°C, which may be attributed to crystallization of Si$_3$N$_4$. This suggests that the nitride formed between 500°C and 1050°C is amorphous. After a 1 h hold at 1600°C, the peaks for crystalline α-Si$_3$N$_4$ became well-defined (Fig. 6(b)). This material has the typical grayish white color of α-Si$_3$N$_4$.

After a 3 h soak at 1600°C in a flowing nitrogen atmosphere, an additional set of diffraction peaks, unrelated to Si$_3$N$_4$, was also observed (Fig. 7(a)). The additional diffraction peaks were similar to those of a crystalline, non-stoichiometric silicon oxide (SiO$_x$) produced earlier in the construction of this reactor when air leaks were a problem such that substantial oxygen was present during the Si nanocrystal synthesis (Fig.
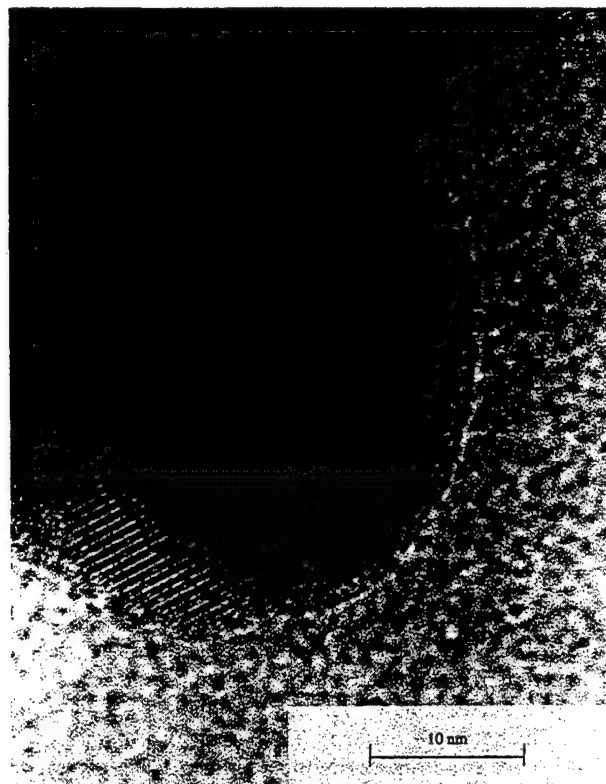
7(b)). This suggests that the amorphous silicon oxide on the surface of our Si$_3$N$_4$ material may be crystallized relatively easily.

TEM micrographs of the crystalline α-Si$_3$N$_4$ particles formed during heat treatment to 1600°C for 1 h in a flowing nitrogen atmosphere are shown in Figs. 8 and 9. The particles varied in size and shape with an average crystallite size of 70 nm. While many crystallites were nearly spherical, others were oblong and needle-like. The interconnected network-like appearance of the particles in Fig. 8 is most likely due to sintering that may have taken place between adjacent particles which were in contact with one another during the elevated temperature soak.

4. Conclusions

A continuous tubular forced flow reactor has been constructed for a high production rate of nanocrystalline materials. The effects of reactor parameters such as pressure and gas velocity on the particles produced were studied. Silicon nanocrystallites were produced with a high surface area (154 m^2 g^{-1}) and were nitrided easily at low temperatures (1050°C) with no special handling precautions. The surface silicon oxide on this material could be crystallized upon a moderate heat treatment.

Acknowledgments

References

[1] O. Unal, J.J. Petrovic and T.E. Mitchell, *J. Mater. Res.*, *8(3)* (1993) 626.

[2] E. Barringer, N. Jubb, B. Fegley, R.L. Pober and H.K. Bowen, in L.L. Hench and D.R. Ulrich (eds.), *Ultrastructure Processing of Ceramics, Glasses, and Composites*, Wiley, New York, 1984.

[3] R.W. Siegel, S. Ramasamy, H. Hahn, L. Zongquan, L. Ting and R. Gronsky, *J. Mater. Res.*, *3(6)* (1988) 1367.

[4] L. Zhang, C. Mo, T. Wang and C. Xie, in *Nanophase and Nanocomposite Materials*, Mater. Res. Soc. Symp. Proc., 286 MRS, Pittsburgh, PA, 1993, pp, 107–112.

[5] S.C. Danforth, W. Symons, K.J. Nielsen and R.E. Riman, in J.G.P. Binner (ed.), *Advanced Ceramic Processing and Technology*, vol. 1, Noyes Publications, NJ, 1990.

[6] R. Birringer, H. Gleiter, H.-P. Klien and P. Marguardt, *Phys. Lett.*, *A, 102* (1984) 365.

[7] J.Y. Ying, *J. Aerosol Sci.*, *24(3)* (1993) 315.

[8] R.W. Siegel, *Ann. Rev. Mater. Sci.*, *21* (1991) 559.

[9] H. Hahn, J. Logas and R.S. Averback, *J. Mater. Res.*, *5(3)* (1990) 609.

[10] R.W. Siegel and J.A. Eastman, in *Multicomponent Ultrafine Microstructures*, Mater. Res. Soc. Symp. Proc., 132, MRS, Pittsburgh, PA, 1989, pp. 3–14.

[11] V. Hass, H. Gleiter and R. Birringer, *Scr. Metall. Mater.*, *28* (1993) 721.

[12] S. Iwama and K. Hayakawa, *Nanostructured Mater.*, *1* (1992) 113.

[13] C.G. Granqvist and R.A. Buhrman, *J. Appl. Phys.*, *47* (1976) 2200.

[14] F.L. Riley, in F.L. Riley (ed.), *Progress in Nitrogen Ceramics*, Martinus Nijhoff, The Hague, Netherlands, 1983, pp. 121–133.

[15] K. Ishizaki, S. Yumoto and K. Tanaka, *J. Mater. Sci.*, *23* (1988) 1813.

Size distribution of Ni precipitates in Ag–Ni alloys determined by maximum entropy analysis of magnetization curves

Howard G. Zolla, Frans Spaepen

Division of Applied Sciences, Harvard University, Cambridge, MA 02138, USA

Abstract

Supersaturated Ag–Ni solutions containing approximately 5 at.% Ni are produced by electron-beam co-evaporation onto cold glass substrates. The magnetization of samples annealed to various temperatures is measured at room temperature as a function of applied field in a vibrating sample magnetometer. The magnetization curves of as-deposited samples show superparamagnetic behavior. On annealing, the Ni precipitates completely and coarsens. The volume distribution function of these superparamagnetic Ni particles is extracted from the magnetization curve by applying the maximum entropy method in which the magnetization is modeled as a weighted superposition of Langevin functions. The results are consistent with direct observations in the transmission electron microscope.

Keywords: Silver; Nickel; Magnetization curves

1. Introduction

Historically, nucleation, growth and coarsening of precipitates in alloys have been studied largely through direct observation by optical metallography and transmission electron microscopy (TEM). These methods, while widely applicable, can be tedious, especially in dilute systems where large specimen areas must be studied to acquire accurate statistics on volume fraction and particle size. They also have limitations at very small particle sizes.

Ferromagnetic precipitates in a weakly magnetic matrix can be studied by simpler means. Composition- and size-dependent magnetic [1] and electrical [2] properties of such alloys have long been used as probes of precipitation. We concentrate on the determination of the size distribution of nanocrystalline precipitates from their magnetic properties.

2. Magnetic granulometry

The assertion that a small ferromagnetic particle consists of a single domain was first made by Frenkel and Dorfman [3]. Elmore [4] experimentally verified

Montgomery's [5] prediction that the smallest of such single-domain particles obey Langevin's [6] equation for the magnetization of a paramagnet:

$$\frac{I}{I_s} = L(\alpha) = \coth(\alpha) - \frac{1}{\alpha} \quad \alpha = \frac{v M_s H}{kT} \quad (1)$$

where I and I_s are respectively the net and saturation magnetization of the system, M_s is the spontaneous magnetization per unit volume of the particle, v is the particle volume, H is the applied field, and k is the Boltzmann's constant. Bean [7,8] subsequently described these particles as exhibiting "super-paramagnetism" (SPM). Fig. 1 shows calculated values of Eq. (1) for SPM Ni particles of several volumes. If these particles are presumed to be spherical their diameters would range from 1 nm to 8 nm. Of note is the strongly size-dependent initial susceptibility. Many investigators (for a review see Ref. [9]) have since used Eq. (1) to estimate the size of ferromagnetic particles in catalysts, colloids, alloys and ferrofluids.

The need to determine I_s of the entire sample and the presence of a distribution of volumes complicate direct application of Eq. (1) to experimental measurements, since the measured magnetization is the superposition of the magnetization of particles of different volumes.

Kneller [10] has presented an analytical solution for the magnetization of a "top hat" distribution of SPM particles with an average volume v_0 and width $2bv_0$:

$$\frac{I}{I_s} = \frac{1}{2b\alpha} \ln\left\{\frac{(1-b)\sinh[\alpha(1+b)]}{(1+b)\sinh\lceil\alpha(1-b)\rceil}\right\} \quad \alpha = \frac{v_0 M_s H}{kT} \quad (2)$$

Eq. (2) adequately describes the magnetization of narrow, monomodal distributions of SPM particles and has been successfully applied to the determination of the size of magnetic particles. Most generally, the total magnetization can be modeled as a superposition of Langevin functions weighted by a volume fraction distribution function $f(v)$:

$$\frac{I}{I_s} = \int_0^\infty f(v) L\left(\frac{v M_s H}{kT}\right) dv \quad (3)$$

By discretizing volume space into N bins, one can attempt to solve P equations in $f(v_j)$, one for each data point $I(H_i)$ where the coefficients are Langevin functions $L(H_i, v_j)$ evaluated at each applied field and volume point. In index notation this can be expressed as

$$I_i = I_s L_{ij} f_j \quad (4)$$

where summation is implicit for i over $\{1 \ldots P\}$ and for j over $\{1 \ldots N\}$. Simply put, the problem at hand is the determination of $f(v_j)$ given a set of measurements $I(H_i)$ and a model $L(v_j H_i)$.

Methods of solution include the use of a specific functional form, such as a lognormal distribution for $f(v_j)$, direct matrix inversion, and a non-linear inversion computation based on Marquardts' adaptation of the Newton–Raphson method, as reviewed by Richardson [11]. All are limited by the determination of I_s of the

entire sample, which requires low temperature, ultra high field, or both, to saturate the magnetization of the specimen. As Fig. 1 demonstrates, for precipitate sizes less than about 2 nm direct determination of I_s is difficult. In addition, there is often no physical basis to pick one functional form for $f(v_j)$ over another as a starting place for a fit by any of the traditional methods.

Potton et al. [12–14] circumvented these diffculties through application of the maximum entropy (MaxEnt) method using the algorithm developed by Skilling [15]. The MaxEnt method permits solution to positive, linear superposition problems without requiring an initial choice of the functional form of the distribution or its absolute magnitude. The MaxEnt solution is the one that makes even use of all the data that is consistent with the uncertainties of the measurements. It maximizes the entropy

$$S = -\sum_{j=1}^N f_j \ln\left(\frac{f_j}{b_j}\right) \quad (5)$$

where b_j is the blank or starting level subject to the constraint

$$P = \sum_{i=1}^P \frac{(I_i - y_i)^2}{\sigma_i^2} \quad (6)$$

I_i are the actual measurements, y_i are the values given by Eq. (4) and σ_i are the standard deviations of each data point. Thus to solve Eq. (4) for f, one needs the physical model, a measure of the uncertainties, and magnetization data. There is no need to know I_s of the entire sample or to assume a form of f. I_s of the entire sample is easily determined by normalizing the integral of f to unity.

In this investigation, we apply Potton's method of magnetic granulometry to characterize the early stages of precipitation and growth of nanoscale Ni precipitates from a supersaturated solid solution of Ni in Ag.

3. Experimental procedure

Supersaturated Ag–Ni solid solutions are prepared as thin films, approximately 10 μm thick, by electron beam co-evaporation from two separate sources (99.99% Ag Canadian "Maple Leaf" coins and 99.99% Ni from Johnson Mathey/Alfa) onto commercial float glass substrates in high vacuum. The Ag and Ni deposition rates are controlled by a pair of quartz crystal deposition monitors at 60 and 3 nm min^{-1} respectively. The substrates are cleaned prior to deposition with an Ar ion sputtering gun to aid adhesion, and are cooled to minimize Ag–Ni segregation during deposition by a dry ice–ethanol mixture maintained at approximately 233 K. The composition is determined after deposition with a Cameca MBX electron microprobe with wavelength dispersive spectrometers (WDS).
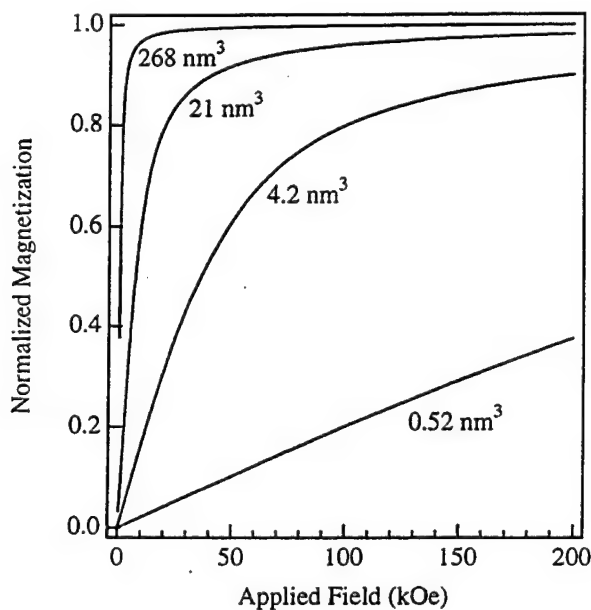
Fig. 1. Normalized room temperature magnetization for Ni particles of indicated volumes calculated with Eq. (1).

After deposition the films are scraped off their substrates and heated in a graphite boat at a rate of 80 K min^{-1} in He to a series of maximum temperatures in the 400 K to 750 K range and cooled rapidly (more than 100 K min^{-1}) back to room temperature. This causes nucleation, growth and coarsening of Ni precipitates from the supersaturated Ag–Ni solutions.

The magnetization at room temperature is measured as a function of applied magnetic field in heat treated alloys by a vibrating sample magnetometer (VSM) [16]. Measurements below 10 kOe are made in our laboratory between the poles of a standard electromagnet. Measurements up to 200 kOe are made at the Francis Bitter National Magnet Laboratory in a Bitter magnet. The magnetization of the diamagnetic sample holder is determined separately in the same geometry, and is subtracted from the raw data. The apparatus is calibrated with a bulk Ni standard and is accurate to within 2%.

Ni particle volume distributions are determined from magnetization data through application of the MaxEnt technique. To ensure that the distribution went to zero at high volume, it was necessary to interpolate a few points linearly between zero and the lowest measured magnetization. The MaxEnt algorithm is described by Skilling [15] and we used a code provided by Daniell [13]. The physical model is that given by Eqs. (1) and (3). Saturation moments are determined by normalizing the calculated volume distribution functions. For comparison, saturation moments are also determined by extrapolating the high field portion of each magnetization curve to zero with 1/H.

4. Results and discussion

Fig. 2 displays the room temperature magnetization of four samples from the same evaporation annealed to four successively higher temperatures and their MaxEnt fits.

Results are normalized with respect to overall Ni concentration which was in the range 5.6 ± 0.5 at.% Ni. Fig. 3 shows the normalized Ni precipitate size distribution calculated with MaxEnt for each sample displayed in Fig. 2.

Fig. 4 shows the saturation moment determined from MaxEnt and from extrapolation with 1/H for several maximum annealing temperatures including the four samples in Figs. 2 and 3. The intercepts of the extrapolated lines in Fig. 5 are calculated based on the slope from 160 kOe to 190 kOe and are each based on over 100 data points. The sample annealed to 750 K is not analyzed using maximum entropy since the magnetization curve displays a remanence. Non-zero remanence indicates that some of the particles have reached the critical size so that Eq. (1) no longer applies, as dis-
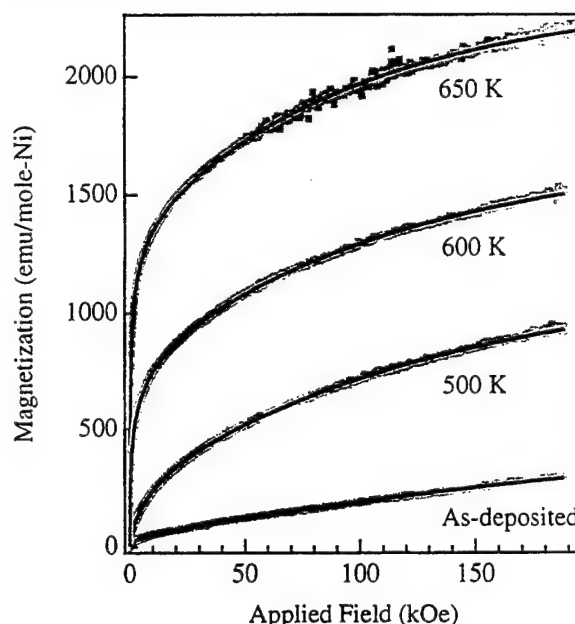
Fig. 2. Normalized magnetization curves for Ag–5at.%Ni alloys annealed up to different temperatures. The solid line is a fit to an Ni particle size distribution by the maximum entropy method.

cussed by Bean [7]. The fraction precipitated is estimated by dividing the specific saturation moment by the bulk Ni value of 3193 emu mol^{-1}. Several authors [17–19] have addressed the validity of the assumption that SPM particles in the size range under study still maintain a specific saturation moment equal to the bulk value. The uncertainty associated with this question is most significant in samples with lowest annealing tem-
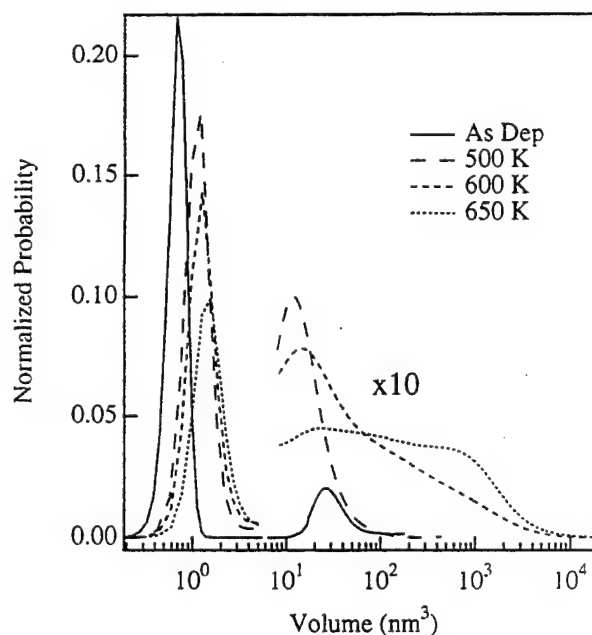
Fig. 3. Volume fraction distribution functions of the Ni particles, calculated from the magnetization curves of Fig. 2 by the maximum entropy method. Above 6 nm^3, the vertical scale is magnified by a factor of 10 for all four curves.
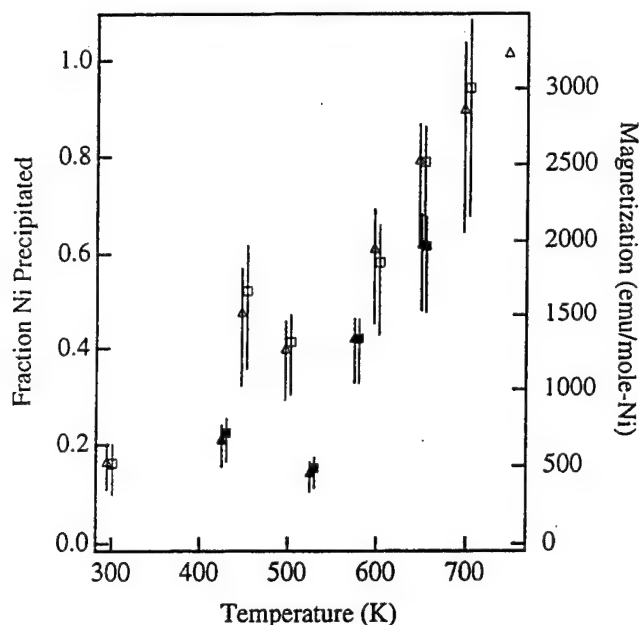
Fig. 4. Saturation moment and fraction precipitated determined from the maximum entropy fits (squares) and from extrapolation with $1/H$ (triangles, see Fig. 5) for two sets of Ag–5at.% films, prepared in separate depositions (open, closed symbols). The saturation moment of bulk Ni is 3193 emu mol^{-1}. Uncertainties indicated are for the fraction precipitated.

peratures, as they have the smallest precipitates. While it is established that the saturation moment is enhanced at small sizes, the magnitude of this effect will vary with the environment of the precipitate. Thus the effect of size-dependent saturation moments has been estimated from the data of Cale et al. [18] and is included in the
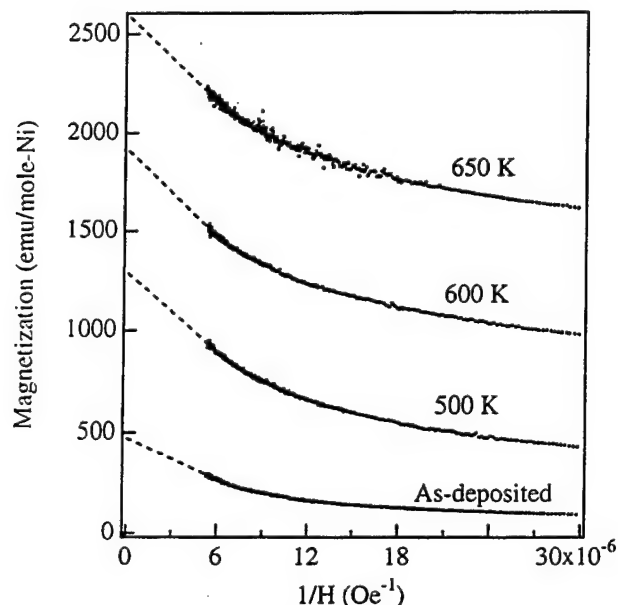
Fig. 5. Extrapolation (dashed lines) of the magnetization curves (dots) of Fig. 2 with $1/H$ to zero. The intercept with the moment axis is the saturation magnetization I_s of the entire sample.
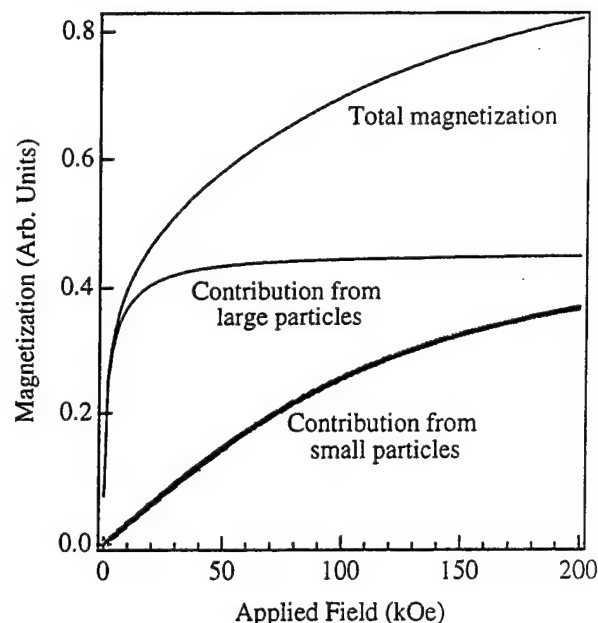
Fig. 6. Contributions to the magnetization from the Ni particles at high and low volume in an Ag–5at.% alloy annealed up to 650 K. The broad line is a fit with the Kneller function.

uncertainty shown. The presumption that Ni dissolved in Ag is magnetically inactive is consistent with the results of Tammann [1] and with results reported for Ni dissolved in Au, Cu and Al [20].

The magnetization curve of the unannealed sample shown in Fig. 2 exhibits a small initial susceptibility. Thus, as shown in Fig. 1, few particles of large volume are expected, and, indeed few are found in the results of Fig. 3. Most of the precipitated Ni is in particles with volume around 0.7 nm^3. Most of the informatioin about the size of these particles is contained in the ultra high field portion of the magnetization curve. Even at 190 kOe, they are still less than 60% saturated. The saturation moment for this sample determined from MaxEnt normalization is 530 emu mol^{-1} which is close to the value determined through $1/H$ extrapolation of 500 emu mol^{-1}.

The samples annealed to 500, 600 and 650 K exhibit increasingly higher initial susceptibilities. This manifests itself in the size distributions of Fig. 3, which each show a peak at high volume of increasing average size and higher integrated volume, while the magnitude and volume of the lower volume peak become progressively smaller. In addition, the saturation magnetization increases steadily as indicated in Figs. 4 and 5. In the sample annealed to 650 K approximately 80% of the Ni has precipitated.

The peaks at high volume in Fig. 3 are not insignificant as demonstrated in Fig. 6. The total magnetization for the 650 K sample is calculated using Eq. (4) from the entire size distribution curve shown in Fig. 3. The contributions to the magnetization from the two por-

tions of the distribution below and above a volume of 5.7 nm (which is at the lowest point of the valley between the two peaks) are indicated. The peak at high volume contributes more than the peak at low volume. The contribution to the magnetization of the peak at low volume is fit well by Eq. (2), Kneller's function. The fit gives an average volume v_0 of 1.55 nm^3 and a width $2bv_0$ of 0.67 nm^3, similar to those on the MaxEnt peak. Satisfactory fits with the Kneller function could not be found for the high volume contribution nor for the total magnetization. Kneller's function is appropriate for calculating the magnetization of a narrow distribution of volumes, not for one three orders of magnitude wide.

Our dark field TEM observations [21] cannot resolve particles below 0.8 nm, which is greater than the peaks at low volume in Fig. 3. However, at higher volumes, the agreement is satisfactory. For example, in the sample annealed to 650 K a distribution of particles with average size 352 nm^3, median size 55 nm^3 and standard deviation 874 nm^3 was measured.

5. Conclusion

Potton's maximum entropy (MaxEnt) method of magnetic granulometry has been successfully applied to Ni precipitates in Ag–Ni alloys. MaxEnt is a convenient way to study the nucleation, growth and coarsening process in these alloys. More importantly, the magnetic technique provides information about ultra-small magnetic precipitates which are not easily characterized by other means, including TEM.

Acknowledgments

References

[1] G. Tammann and W. Oelsen, *Z. Anorg. Allg. Chem., 186* (1930) 257.
[2] I.S. Servi and D. Turnbull, *Acta Metall., 14* (1966) 161.
[3] J. Frenkel and J. Dorfman, *Nature, 126* (1930) 274.
[4] W.C. Elmore, *Phys. Rev., 54* (1938) 1092.
[5] C.G. Montgomery, *Phys. Rev., 38* (1931) 1782.
[6] P. Langevin, *Ann. Chim. Phys., 5, Ser. 8* (1905) 70.
[7] C.P. Bean, *J. Appl. Phys., 26* (1955) 1381.
[8] C.P. Bean and J.D. Livingston, *J. Appl. Phys., 30* (1959) 120.
[9] P.W. Selwood, *Adsorption and Collective Paramagnetism*, Academic Press, New York, 1962.
[10] E. Kneller, *Z. Phys., 152* (1958) 574.
[11] J.T. Richardson, *J. Appl. Phys., 49* (1978) 1781.
[12] J.A. Potton, G.J. Daniell, A.D. Eastop et al., *J. Magn. Magn. Mater., 39* (1983) 95.
[13] J.A. Potton, G.J. Daniell and D. Melville, *J. Phys. D., 17* (1984) 1567.
[14] J.A. Potton, *Thesis*, University of Southampton, 1983.
[15] J. Skilling and R.K. Bryan, *Mon. Not. R. Astron. Soc., 211* (1984) 111.
[16] S. Foner, *Rev. Sci. Instrum., 30* (1959) 548.
[17] I.M.L. Billas, A. Chatelain and W.A. de Heer, *Science, 265* (1994) 1682.
[18] T.S. Cale, J.T. Richardson and J. Ginestra, *Appl. Phys. Lett., 42* (1983) 744.
[19] F.E. Luborsky and P.E. Lawrence, *J. Appl. Phys., 32* (1961) 231.
[20] N.W. Ashcroft and N.D. Mermin, *Solid State Physics*, Saunders, Philadelphia, PA, 1976, p. 686.
[21] H.G. Zolla and F. Spaepen, in preparation.

ELSEVIER

Computer simulation of the structure and dynamical properties of grain boundaries in a nanocrystalline model material

S.R. Phillpot[a], J. Wang[a], D. Wolf[a], H. Gleiter[b]

[a]Materials Science Division, Argonne National Laboratory, Argonne, IL 60439, USA
[b]Forschungszentrum Karlsruhe, D-76021 Karlsruhe, Germany

Abstract

Molecular dynamics simulations have been used to synthesize and characterize a fully dense, three-dimensional nanocrystalline material with an average grain size of 43 Å by crystallization from the melt. The structures and energies of the highly constrained grain boundaries in this material are found to be more isotropic than those of extended boundaries in bicrystals. Based on this observation, a simple structural model that combines a realistic treatment of the grain boundaries with a finite grain size—and yet permits a comparison with the structures of unconstrained boundaries in bicrystals—is developed. The low temperature thermal behavior of such a model material is shown to be dominated by low frequency phonon modes due to the grain boundaries and grain junctions.

Keywords: Grain boundaries; Computer simulation; Molecular dynamics; Nanocrystalline materials

1. Introduction

The atomic structure of grain boundaries (GBs) and its effect on the properties of nanocrystalline materials (NCMs) have been the subject of extensive discussion ever since the first ultrafine-grained polycrystals were synthesized over a decade ago by consolidation of small clusters formed via gas condensation [1,2]. The key issue is whether a novel state of matter exists in polycrystals with a grain size of typically 1–10 nm [3,4] or whether the structure and properties of NCMs can be extrapolated from those of coarse-grained polycrystals and bicrystals. The suggestion of a "frozen-gas"-like structure of the GBs in extremely constrained, small-grained polycrystals [3,4] appears plausible given that up to 50% of the atoms in such a material may be situated in the highly distorted and defected environments provided by the GBs and grain junctions; such structural environments are not found in glasses (with short-range order) or crystals (with long-range order).

In spite of much experimental work concerned with the structure and properties of NCMs performed to date, the often contradictory reports of "unusual" structures and "anomalous" properties have rendered it impossible to formulate a structural model that is consistent with the observations and permits the properties of these materials to be predicted. Although some observations involving Raman spectroscopy [5], atomic resolution transmission electron microscopy (TEM) combined with image simulations [6] and X-ray diffraction [7] indicate that the atomic structures of GBs in NCMs are in fact rather similar to those determined for coarse-grained polycrystalline or bicrystalline materials, other observations involving Mössbauer spectroscopy [8], atomic resolution [9] and conventional TEM [10] and X-ray diffraction [10,11] suggest the presence of non-equilibrium GBs in NCMs with structures and properties that differ significantly from those of coarse-grained materials. At present it therefore appears that without additional information coming, for example, from computer simulations, the formulation of a structural model for NCMs based on experiments alone may not be possible.

Our simulations of nanocrystalline materials discussed here involve two fundamentally different types of approaches for the synthesis of a dense, space-filling polycrystal. In the first, molecular dynamics (MD) simulations are used to crystallize from the melt a fully

dense, three-dimensional NCM with random grain orientations and an average grain size of 43 Å [12]. In the second a structural model consistent with the MD results is developed and tailored to capture what we believe to be the two essential structural features of NCMs, namely geometrical constraints (i.e. a finite grain size) and structural inhomogeneity (due to the GBs and grain junctions), while still permitting the connection with bicrystalline GBs to be made [13]. The comparison of the simulated structure and dynamical properties of this simple model material with those of the MD-grown material permits some important conclusions to be drawn as to the structural origin of the observed physical behaviour.

2. Synthesis and characterization of a nanocrystalline material by molecular dynamics

The simulation geometry used for the MD synthesis consists of a cubic volume of liquid periodically repeated in all three dimensions. The simulation cell is $24a_0 = 86.7$ Å on a side and contains a total of 55 296 atoms. A small ($6a_0$ diameter) crystalline truncated octahedral seed with {100} and {111} faces is placed near the center of each octant of the cube; thus approximately 10% of the atoms are initially crystalline. The seeds are preoriented so that the 24 grain boundaries in the final polycrystal consist of two (310) symmetric tilt grain boundaries (STGBs), two (111) STGBs, two (210) STGBs, two (001)(447) asymmetric tilt GBs and 16 general boundaries; the latter have both twist and tilt components.

Since we are not interested in the properties of any specific material, the Lennard-Jones (LJ) potential was used to describe the interatomic interactions. The potential was fitted to the melting point $T_m = 1356$ K and zero-temperature lattice parameter $a_0 = 3.616$ Å of Cu with a cohesive energy $E_{id} = -1.0378$ eV atom^{-1}.

Beginning with the simulation cell geometry described above, the NCM was grown by MD at a temperature of 1075 K (i.e. well below T_m) and at the density of the crystalline solid at 1075 K, with the atoms in the perfect crystal seeds initially fixed to ensure crystallization of the atoms in the liquid on to the seeds. After about 66 ps of simulation time the energy of the system stopped decreasing and the crystalline regions stopped growing (as indicated by the number of miscoordinated atoms ceasing to decrease). At this point the temperature was reduced in a stepwise manner to 900, 700 and 500 K at the perfect crystal lattice parameter appropriate to each temperature. The temperature was then further reduced consecutively to 300, 200, 100 and 1 K, at which temperatures the atoms in the seeds were allowed to move and the stresses on the system were reduced to zero by allowing the dimen-

sions of the simulation cell to change. This structure was then subjected to a zero-temperature iterative energy minimization (lattice statics) calculation until the total energy, the atomic forces and the stresses were suitably converged.

The radial distribution function (RDF) of the resulting NCM shows well-defined peaks characteristic of crystalline order, broadened by the presence of disorder due to the presence of GBs and grain junctions and slightly shifted from the perfect crystal positions. In particular the mean peak position of the first-nearest-neighbor peak is shifted upward by 0.06% to $0.7075a_0$. The lower density of the polycrystal associated with this lattice expansion is 97.5% of that of the perfect crystal.

To investigate the structure of the NCM at the atomic level, Fig. 1 shows the positions of the atoms in an x–y cross-section of thickness $0.5a_0$ through the center of the upper half of the equilibrated system. In Fig. 1 the normals to the (310) and (111) STGBs lie along the x axis of the upper and lower halves respectively. The atoms in Fig. 1 are distinguished by their miscoordinations M, i.e. by the number of nearest neighbors greater than 12 ($M > 0$) or less than 12 ($M < 0$). It is clear from these miscoordinations that the perfect crystal seeds have acted as nucleation centers for the growth of extended regions of highly ordered material. The presence of fairly localized GBs can be seen in the form of chains of miscoordinated atoms
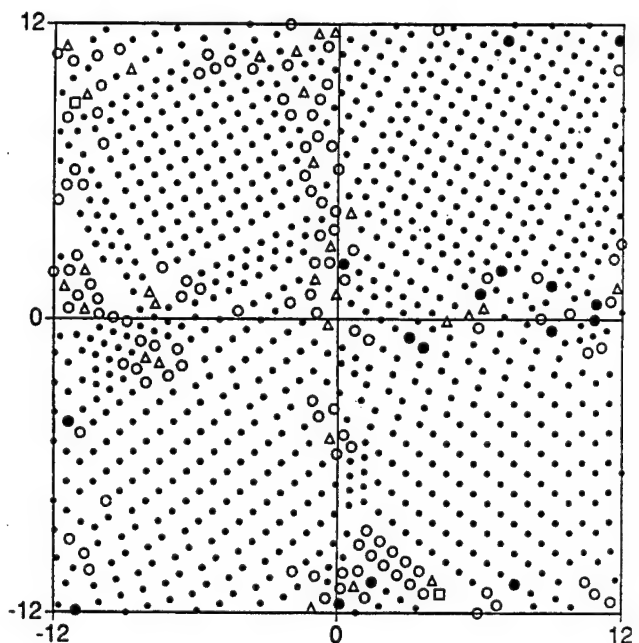
Fig. 1. Cross-section of thickness $0.5a_0$ through the center of the top half of the equilibrated polycrystal showing four of the eight grains. Atoms with miscoordination $M = 0$ (i.e. having 12 nearest neighbors) are denoted by small dots. Atoms with $M \leqslant -3$ ($M \geqslant 3$) are denoted by open (full) squares. Atoms with $M = -2$ ($M = 2$) are denoted by open (full) triangles. Atoms with $M = -1$ ($M = 1$) are denoted by open (full) circles.
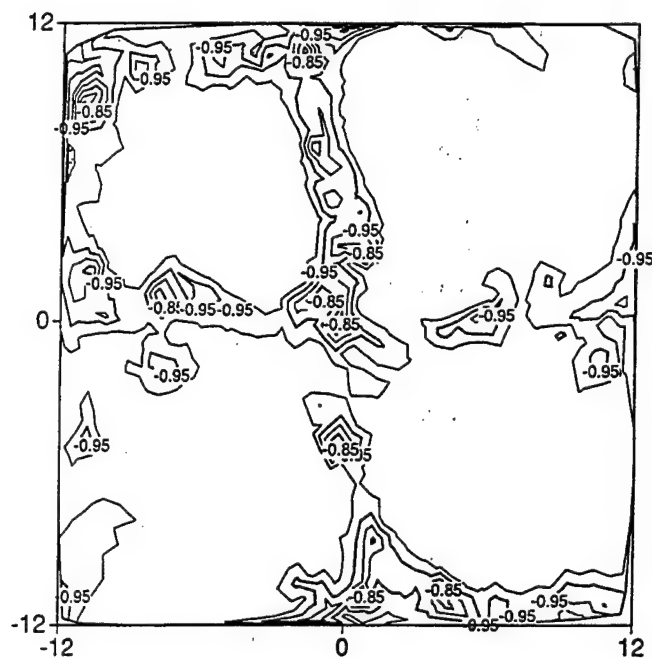
Fig. 2. Contours of equal energy, with 0.1 eV atom^{-1} between contours, for the cross-sections in Fig. 1.

approximately parallel to the edges of the simulation cell. Fig. 1 also shows growth defects in the perfect-crystal-like regions away from the GBs, the most obvious of which are point defects and clusters of point defects. A close examination of the atomic structures also shows the presence of dislocations formed during crystal growth.

Fig. 2 shows contours of equal energy for the structural cross-section in Fig. 1. Evidently there are large regions centered about the seeds where the energy is close to that of the perfect crystal (less than -1.0 eV), the higher energy regions being mainly localized in the relatively narrow GBs. A comparison of Figs. 1 and 2 shows that, not surprisingly, these high energy regions coincide with the miscoordinated atoms. A GB energy $\langle E_{GB} \rangle = 730$ mJ m^{-2}, averaged over the whole NCM was estimated from the total energy of the system, assuming that all GBs grow parallel to the simulation cell edges and are of equal energy. This value for $\langle E_{GB} \rangle$ represents a reasonable average for many twist and tilt GBs on high index planes determined for this potential [14].

To determine the effect of the constraints on the GBs in the NCM due to the presence of other nearby GBs, Fig. 3 shows the mean energy per atom across two $3a_0 \times 3a_0$ sections of the (310) STGB at the center of the panel of Fig. 2. These energy distributions can be compared with that for an infinitely extended, unconstrained (310) STGB in a bicrystal produced by lattice statics simulation, also shown in Fig. 3. While they are largely the same, each showing that the excess energy is localized in the GB regions, there are two significant

differences. First, because of the growth defects seen in Fig. 1, the energy in the interior of the grains of the polycrystal does not reach the perfect crystal value. Second, the excess energy associated with the GBs in the polycrystal is spread over a wider region. Defining the GB width as the width of the region with $E > -1.0$ eV, we obtain $\delta_{GB} \approx 2.8a_0$ and $3.5a_0$ for the two different sections of the (310) STGB in the NCM; by comparison, we find $\delta_{GB} \approx 1.6a_0$ for the bicrystalline GB. Sections through the other GBs in the polycrystal show that a thickness of $2.5a_0-3.5a_0$ is typical.

Examining the energies for the 24 GBs in the NCM as a whole, we see that in the severely constrained NCM the rigid body translations parallel to all the GBs cannot be optimized simultaneously, resulting in significantly increased energies of the lowest energy bicrystalline GBs [12]. For example, the energies of the (111) STGBs are considerably higher (200 and 630 mJ m^{-2}) than the value of 1 mJ m^{-2} for the (111) STGB in the bicrystal. By contrast, GBs already with very high energies in the bicrystal have similar or even slightly lower energies in the NCM, suggesting that bicrystalline GBs that are already very disordered cannot be disordered further even under the severe microstructural constraints. Based on these effects, one can expect a much narrower distribution of the GB energies in the NCM than in bicrystals and a relatively uniform GB width.

Finally, despite having only eight grains and 24 grain boundaries, we find the thermal expansion and elastic moduli of our model polycrystal to be almost isotropic [12].
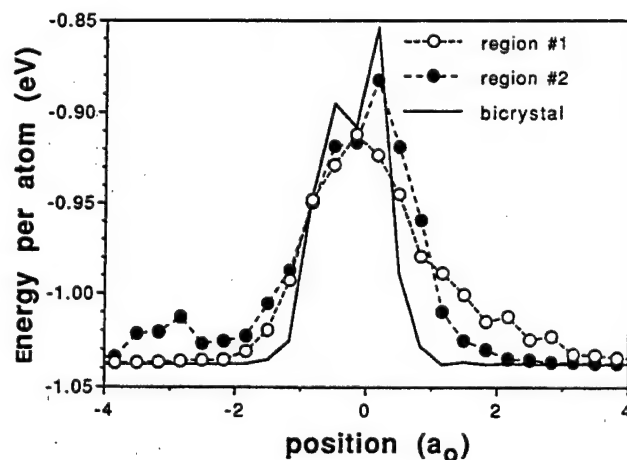
Fig. 3. Plane-by-plane mean potential energy per atom as a function of position through two $3a_0 \times 3a_0$ sections of the (310) symmetric tilt boundary between the top two squares in Figs. 1 and 2, compared with energy profile from a lattice statics simulation on the same GB in a bicrystal.

3. Model of a monodisperse nanocrystalline material

The rather isotropic structures and energies of the GBs observed in the above NCM suggest that it may be possible to formulate a simple structural model that is consistent with the MD simulations. In addition to isotropic GB properties, such a model has to capture, as a minimum, two additional essential structural features of NCMs, namely geometrical constraints (i.e. a finite grain size) and structural inhomogeneity (due to the GBs and grain junctions). Apart from incorporating a finite grain size, this type of model is designed to focus less on microstructural features than on a realistic physical description of the nature of the GB-induced inhomogeneities in the material.

It is widely recognized that the task of relating the structure and properties of GBs in a polycrystal to those of bicrystalline GBs is extremely difficult as it requires three types of microstructural averages to be performed either explicitly or implicitly. These arise from the geometrical constraints present in a polycrystal and involve averages over (a) the five macroscopic degrees of freedom (DOFs) that each individual GB contributes to the total number of DOFs of the polycrystal, (b) the various grain shapes and (c) the distribution of grain sizes invariably present in polycrystals.

In order to address as directly as possible the relationship between the highly constrained GBs in NCMs and the entirely unconstrained GBs in bicrystals, we pose the following question: As far as the total number of GB DOFs, grain shapes and grain sizes are concerned, what is the conceptually simplest polycrystal that one can, at least in principle, construct? In other words: What is the smallest number of geometrically distinct types of GBs, grain shapes and grain sizes that a polycrystal has to contain and still be space filling?

Fig. 4 shows that it is geometrically possible to construct a space-filling, three-dimensional polycrystal with a uniform (and unique) rhombohedral grain shape in which all GBs are crystallographically equivalent, i.e. a monodisperse polycrystal with exactly the same number of macroscopic degrees of freedom (at most five) as the corresponding bicrystal, the only difference being represented by the finite (and variable) grain size. Having thus eliminated the distributions in the types of grain boundaries and the grain shapes, our simulations of this model will focus entirely on the effect of the grain size (defined as the distance between the GBs), i.e. on the role of the geometrical constrains in the atomic structure and physical properties of a well-defined GB.

The simulation cell in Fig. 4 contains two sets of distinct rhombohedral grains, each set delimited by crystallographically equivalent surfaces, $(hkl)_1$ or $(hkl)_2$, and therefore forming 24 crystallographically equivalent asymmetric tilt boundaries (ATGBs; for details see Ref. [13]). For our simulations we have constructed a
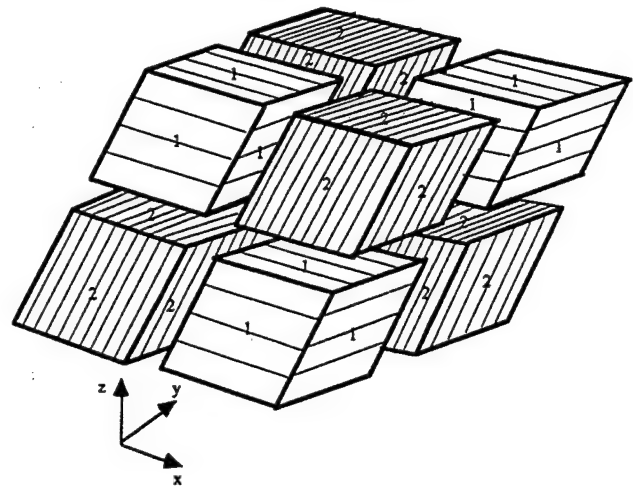
Fig. 4. Idealized space-filling polycrystal model. The 3D-periodic simulation cell shown here contains eight identically shaped rhombohedral grains delimited by two sets of crystallographically distinct surfaces (indicated by 1 or 2), forming a total of 24 crystallographically equivalent asymmetric tilt GBs.

series of such model nanocrystals of increasing size ($D = 8.2$, 14.4, 20.6 and 26.9 Å) in which one rhombohedron is bounded by (111) and the other by (115) planes; all GBs are therefore (115)(111) ATGBs.

Lattice statics simulations were used to determine the equilibrium structure of the NCMs. Throughout we use the same LJ potential as in the MD simulations reported above. The distribution of potential energies for our model NCMs shows three peaks, indicating three distinct types of crystal environments experienced by the atoms. The lowest energy peak centered very close to the perfect crystal cohesive energy corresponds to the grain interiors which, although slightly distorted, are essentially monocrystalline. The second peak is due to the GBs while the third peak arises from the grain junctions (i.e. the lines where four grain edges and the points where eight grain corners meet). As the grain size is reduced, the area under the perfect crystal peak decreases until it disappears completely for the smallest grain size, indicating overlapping GBs; simultaneously the areas under the two remaining peaks increase.

The GBs in our monodisperse model NCMs are clearly identifiable, with an atomic structure, energy, volume expansion and width (of about $1.5a_0$) which differ remarkably little from those of the two stable rigid body translational states determined for the related bicrystalline (115)(111) ATGB [13]. However, this width is somewhat smaller than that observed for the MD-grown polycrystal.

The radial distribution function (RDF) for the largest grain size is shown in Fig. 5 indicating excellent crystallinity of the material; similar plots were obtained even for the two smallest grain sizes. Corresponding to the reduced density of this material (94.2% of that of the perfect crystal), the mean peak positions are shifted

to slightly larger values with respect to the δ function peaks in the perfect f.c.c. crystal at $T = 0$ K. The RDF in Fig. 5 differs remarkably little from that obtained for the bicrystal (for the atoms within a distance of $\pm a_0$ from the GB) [15]. More importantly, the broadened peaks and the shift of the peak centers toward larger distances are generic features observed for virtually all GBs [15–17], suggesting that as far as structural disorder is concerned the particular GB considered here is reasonably representative. Indeed, this RDF is very similar to that of the MD-grown polycrystal which contains a variety of different GBs [12].

4. Phonon-induced specific heat

The monodisperse model of an NCM in Fig. 4 is based on the premise that its properties are primarily determined by the presence of crystalline regions separated by highly inhomogeneous, relatively narrow GBs, the detailed structures of which are only of secondary importance. While this premise is supported by the structural analyses presented above, the comparison of the temperature dependence of the excess specific heats of both the MD-grown NCM and the (115)(111) monodisperse model NCM provides further support.

Using the fully relaxed zero-temperature structures as starting points, lattice dynamics simulations were performed to determine the phonon spectrum, from which the low temperature thermodynamic properties of the material can be determined [18]. Fig. 6 compares the phonon density of states (DOS) for the smallest (115)(111) model NCM with that of a perfect (500-atom) f.c.c. crystal. Notice that, in agreement with the recent Raman [19] and neutron scattering [20] experiments, the DOS of the NCM exhibits low and high
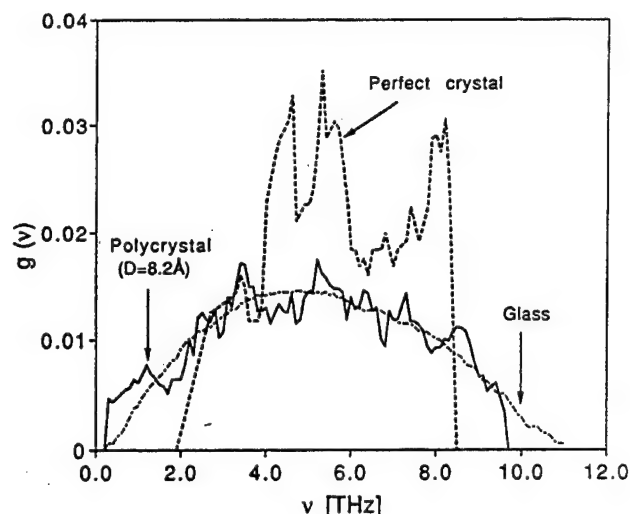
Fig. 6. Comparison of the vibrational density of states, $g(\nu)$, for the (115)(111) model NCM with the smallest grain size $D = 8.2$ Å (full curve) and for a perfect f.c.c. crystal containing 500 atoms in the 3D-periodic simulation cell (broken curve); ν is the phonon frequency.

frequency tails not present in the perfect crystal. A detailed analysis of the eigenvectors associated with these new modes shows that most are localized at the GBs and grain junctions, although there are also modes associated with collective vibrations of entire grains against each other.

The tails in the DOS in Fig. 6 originate from the broadening and shift of the peaks in the RDF which are known to also dominate the anomalous elastic behavior of multilayered materials [15]. Distances shorter than in the perfect crystal give rise to higher phonon frequencies while larger distances lead to lower phonon frequencies [15,17].

Fig. 7 shows the excess specific heat for the four model NCMs determined from the DOS in Fig. 6. In the context of lattice dynamics it is well known that only the lower frequency modes in Fig. 6 should contribute significantly to the thermodynamic properties. This is confirmed by the complete disappearance of the anomaly when the lower frequency modes are excluded. By contrast, the omission of the high frequency modes has no effect [13]. Fig. 7 also shows that the MD-grown polycrystal exhibits a pronounced peak in the specific heat at essentially the same temperature as the monodisperse NCMs. The peak height is lower, however, because the grain size of the MD-grown polycrystal is considerably larger (43.3 Å) than in the largest monodisperse model NCM.

The appearance of a pronounced low temperature peak in the specific heat, with a height that decreases with increasing grain size, is in qualitative agreement with the experimental results [21,22]. It has been suggested that these anomalies may be due either to in-
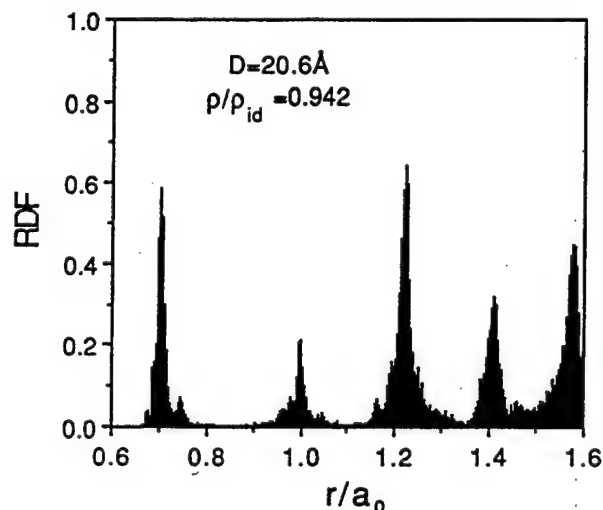

Fig. 5. Radial distribution function for the fully relaxed (115)(111) model NCM with a grain size of 20.6 Å.

creased anharmonicity at the GBs or to the presence of light element impurities [21]. While we cannot rule out any additional effects due to impurities, the above results demonstrate that an anomaly originates from the low frequency phonon modes associated with the disorder in the system.

5. Conclusions

In the molecular dynamics study we synthesized a three-dimensional, space-filling nanocrystalline material by growth from the melt into which, more or less randomly oriented crystalline seeds were inserted. The structure of the eight-grain polycrystal, which has an average grain size of 43 Å, exhibits large, nearly perfect crystalline regions separated by relatively narrow grain boundaries. In spite of the relatively small number of grains, the thermal expansion and elastic moduli of this model polycrystal are virtually isotropic.

The near isotropy in the structures and energies of the grain boundaries indicates that the detailed geometries and atomic structures of individual grain boundaries are relatively unimportant. We have therefore developed a highly idealized but conceptually simple model of a nanocrystalline material that combines the severe geometrical constraints associated with a small grain size with the strong inhomogeneity present in the grain boundaries and grain junctions. The comparison of some of the thermal properties obtained for this idealized model material with those of the more realistic MD-grown nanocrystalline material provides insights not readily obtained from experiments. Most notably, the model demonstrates the existence of a specific heat anomaly in nanocrystalline materials originating from the low frequency phonon modes associated with the atoms in the grain boundaries and grain junctions; a qualitatively identical peak is seen in the excess specific heat of the polycrystal grown by molecular dynamics.

References

[1] H. Gleiter, in N. Hansen, T. Leffers and H. Linholt (eds.), Proc. Second Risø Int. Symp. on Metallurgy and Materials Science, Risø National Laboratory, Roskilde, 1981, p. 15.
[2] R. Birringer, H. Gleiter, H.P. Klein and P. Marquardt, Phys. Lett. A, 102 (1984) 365.
[3] X. Zhu, R. Birringer, U. Herr and H. Gleiter, Phys. Rev. B, 35 (1987) 9085.
[4] H. Gleiter, Prog. Mater. Sci., 33 (1989) 223.
[5] C.A. Melendres, A. Narayanasamy, V.A. Moroni and R.W. Siegel, J. Mater. Res., 4 (1989) 1246.
[6] G.J. Thomas, R.W. Siegel and J.A. Eastman, Scr. Metall., 24 (1990) 201.
[7] J.A. Eastman, M.R. Fitzsimmons and L.J. Thompson, Philos. Mag. B, 66 (1992) 667.
[8] J. Jiang, S. Ramasamy, R. Birringer, U. Gonser and H. Gleiter, Solid State Commun., 80 (1991) 525; U. Herr, J. Jing, R. Birringer, U. Gonser and H. Gleiter, Appl. Phys. Lett., 50 (1987) 472.
[9] W. Wunderlich, Y. Ishida and R. Maurer, Scr. Metall., 24 (1990) 403.
[10] V.Y. Gertsman, R. Birringer, R.Z. Valiev and H. Gleiter, Scr. Metall. Mater., 30 (1994) 229.
[11] L. Löffler, J. Weissmüller and H. Gleiter, Nanostruct. Mater., 6 (1995) 367. J. Löffler and J. Weissmüller, Phys. Rev. B., 52 (1995) 7076.
[12] S.R. Phillpot, D. Wolf and H. Gleiter, J. Appl. Phys, 78 (1995) 847.
[13] J. Wang, D. Wolf, S.R. Phillpot and H. Gleiter, Philos. Mag. B., in press.
[14] D. Wolf, Scr. Metall., 23 (1989) 1913.
[15] D. Wolf and J.F. Lutsko, Phys. Rev. Lett., 60 (1988) 1170.
[16] D. Wolf and K.L. Merkle, in D. Wolf and S. Yip (eds.), Materials Interfaces: Atomic-Level Structure and Properties, Chapman and Hall, New York, 1992, p. 87.
[17] D. Wolf and J. Jaszczak, J. Comput. Aided Mater. Design, 1 (1993) 111.
[18] A.A. Maradudin, E.W. Montroll, G.H. Weiss and I.P. Ipatova, Solid State Phys., Suppl. 3, Academic Press (1971).
[19] E.D. Obraztsova, K.G. Korotushenko, S.M. Pimenov, V.G. Ralchenko, A.A. Smolin, V.I. Konov and E.N. Loubnin, Nanostruct. Mater., 6 (1995) 827.
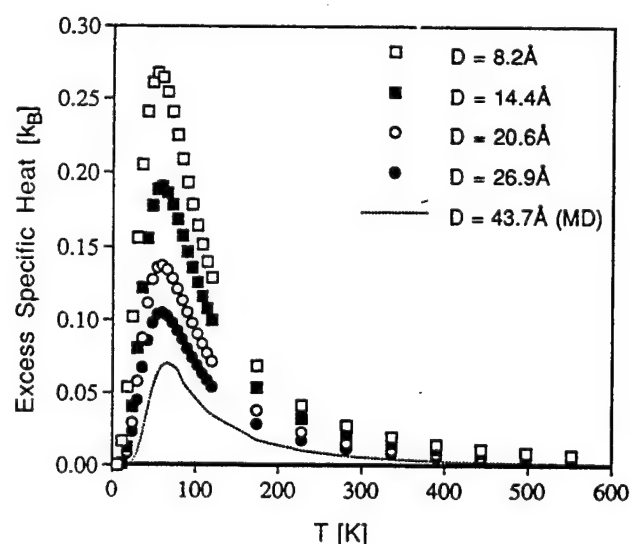
Fig. 7. Comparison of the temperature and grain size dependence of the excess specific heat (in units of Boltzmann's constant k_B) for the idealized (115)(111) model NCM with that for the MD-grown material with a grain size of 43 Å.

[20] J. Trampeneau, K. Bauszus, W. Petry and U. Herr, *Nanostruct. Mater.*, 6 (1995) 551.

[21] J. Rupp and R. Birringer, *Phys. Rev. B, 36* (1987) 7888; A. Tschöpe and R. Birringer, *Acta Metall. Mater.*, 41 (1993) 2791; *Philos. Mag. B, 68* (1993) 2223.

[22] H.G. Klein, *Diplom Thesis*, Universität des Saarlandes, 1992.

Modeling densification during sinter-forging of yttria-partially-stabilized zirconia

Douglas C. Hague, Merrilea J. Mayo

Department of Materials Science and Engineering, The Pennsylvania State University, University Park, PA 16802, USA

Abstract

A model to predict the densification and microstructural development of a nanocrystalline ceramic powder compact during sinter-forging has been developed. In the model, densification is predicted by superimposing stress-assisted densification mechanisms with a plastic-strain-controlled pore closure mechanism. During densification, grain growth is modeled with pore-controlled grain growth during intermediate stage sintering and combination of normal (static) grain growth and dynamic grain growth during final stage sintering. Applied stress and strain are allowed to vary as a function of time, so that widely varying experimental conditions can be modeled.

The model predictions are compared with experimental data for the sinter-forging of 3 mol% yttria-stabilized tetragonal zirconia polycrystals (3Y-TZP) at 1050 and 1100 °C. These predictions are made assuming a bimodal pore size distribution where pores smaller than the grain size are not allowed to be closed by strain. The model predicts that large pores are efficiently closed only by plastic strain but that small pores are easily eliminated by diffusional mechanisms. It is shown that grain size is minimized as a function of density under conditions that promote high strain rates, so that large pores are quickly eliminated while small pores are still available to control grain growth.

Keywords: Modeling densification; Sinter forging; Ceramic powder compact

1. Introduction

In the past several years a plethora of techniques have been shown to be capable of producing large quantities of nanocrystalline powder [1,2]. The next logical stage in the development of nanocrystalline materials is to consolidate these powders into fully dense materials without incurring significant grain growth. Early experiments in pressureless sintering did not appear to be able to fully densify powder compacts while retaining a nanocrystalline grain size [3,4]; however, sinter-forging has been shown to be quite effective in this regard [3,5]. Sinter-forging is the simultaneous densification and deformation of a porous ceramic at elevated temperature under the action of a uniaxial stress. Currently there are no models for this operation capable of predicting densification and grain growth. Several models exist for the densification of a compact by either stress-assisted diffusion [6,7] or strain-controlled elimination of pore volume [8,9]; however, predicting the densification of nanocrystalline materials requires the superposition of both these densification mecha-

nisms as well as the inclusion of grain growth in the model. The current study was undertaken in order to develop a more rigorous understanding of the sinter-forging process in nanocrystalline materials. A model has been constructed and is based on probable mechanisms of densification and microstructural evolution. Its predictions are compared with experimental data for the sinter-forging of nanocrystalline 3Y-TZP (3 mol% yttria-stabilized tetragonal zirconia polycrystals).

2. Modeling sinter-forging

The present model is constructed such that the densification and grain growth kinetics for any set of experimental conditions, including those where stress and strain rate are not constant, can be predicted. The approach this model takes is to superimpose independent densification mechanisms in a manner similar to that of Ashby and coworkers in the development of mechanism maps [6,10,11]. For sinter-forging, two mechanisms are assumed to be controlling densifica-

tion: stress-assisted diffusion and plastic-flow-induced closure of pores. Because of the different stress state involved, the power law creep mechanism previously developed for hot isostatic pressing model (isostatic stress state) [12,13] does not apply during sinter-forging (uniaxial stress state). Instead, a mechanism for densification during plastic flow under a uniaxial stress has been developed. Grain growth, as well as the evolution of the pore size and pore size distribution, has also been included in the modeling.

2.1. Densification equations

2.1.1. Diffusional densification

Many of the original derivations for diffusional densification mechanisms [7,14] involve assumptions that do not apply for nanocrystalline materials. For example, in nanocrystalline materials both diffusion due to the applied stress σ and that due to the intrinsic sintering stress are important. The intrinsic sintering stress arises from the curvature κ of the pore surface and is equal to $2\gamma/r$ for spherical pores, where γ is the surface energy and r is the pore radius. In submicron- and larger-grained materials the sintering stress term is generally ignored since it is less than 1 MPa, which is small compared with conventional levels of applied stress (10–300 MPa). However, in nanocrystalline materials the sintering stress is much greater and cannot be ignored, e.g. $2\gamma/r \approx 400$ MPa for a spherical pore with $r = 5$ nm. It therefore is included in the driving force of the present model. Another assumption in sintering models that becomes questionable is the mathematical approximation of an exponential driving force to a linear function [7,14]. Though valid when the sintering stress is small (i.e. less than 5 MPa), the approximation is not accurate when the sintering stress is large. Thus the simplified driving force

$$P = \frac{\sigma\Omega}{kT\rho} - \frac{\gamma\Omega}{kT}\kappa \tag{1}$$

is more correctly

$$P = \exp\left(\frac{\sigma\Omega}{kT\rho}\right) - \exp\left(\frac{\gamma\Omega}{kT}\kappa\right) \tag{2}$$

where ρ is the relative density, Ω is the atomic volume, k is Boltzmann's constant and T is the absolute temperature. Note that the two terms in Eq. (2) represent the different driving forces for diffusion: applied stress and pore curvature. In the present study Eq. (2) has been combined with densification equations developed by Ashby and coworkers [6] for intermediate stage sintering, i.e.

$$\frac{\delta\rho}{\delta t} = \frac{43(1 - \rho_0)^2}{(\rho - \rho_0)^2}\frac{D_{\mathrm{app}}}{kTg^2}\Omega P \tag{3}$$

and final stage sintering, i.e.

$$\frac{\delta\rho}{\delta t} = 54\frac{\Omega D_{\mathrm{app}}P}{kTg^2}5(1 - \rho)^{1/2} \tag{4}$$

where ρ_0 is the initial relative density and g is the particle size. The apparent diffusivity is defined as

$$D_{\mathrm{app}} = \frac{\delta D_{\mathrm{gb}}}{G} + D_{\mathrm{vol}} \tag{5}$$

where δD_{gb} is the grain boundary diffusivity, D_{vol} is the volume diffusivity and G is the grain size. The above formulation of the apparent diffusivity simplifies Ashby's original equations [6] so that it adheres to the usual expression for combined diffusivity along grain boundary and lattice paths [15].

2.1.2. Strain-controlled densification

Aside from the diffusional models of densification, plastic deformation has also long been considered to be a mechanism of densification for powder compacts [16]. Deformation-controlled pore closure is essentially the flow of the matrix adjacent to a pore such that material will flow into the pore (hydrostatic strain state) or flatten the pore (uniaxial strain state) [9]. To determine the densification that is caused by plastic strain during sinter-forging, a model for a uniaxial stress state is needed. In the case of sinter-forging of submicron-grained ceramics, the model of Kuhn and Ferguson [8] appears to be better able to predict densification than other models (e.g. that of Budiansky et al. [9]) [17]. Kuhn and Ferguson (who have studied powdered steel and aluminum) have shown that densification during deformation can be described by [8]

$$\frac{\mathrm{d}\varepsilon_r}{\mathrm{d}\varepsilon_z} = v = -\tfrac{1}{2}\rho^2 \tag{6}$$

where v is a pseudo-Poisson ratio, ε_r is the radial strain and ε_z is the axial strain. Starting with Eq. (6), the pore volume as a function of plastic strain ε_p has been derived for the present model as

$$\frac{V}{V_0} = \left(\frac{\rho}{\rho_0}\right)^{1/3}\frac{1 + \rho_0}{1 + \rho}\exp(-2\varepsilon_p) \approx \exp(-2\varepsilon_p) \tag{7}$$

where V_0 and V are the initial and current pore volumes respectively. Thus, by calculating the shrinkage in pore volume due to diffusion from Eq. (3) or (4) and adding that to the shrinkage in pore volume determined from Eq. (7), the densification for an interval of time in which a known strain occurs can be calculated.

2.2. Model assumptions

2.2.1. Densification

The microstructure of the powder compacts is assumed to be that of an agglomerated nanocrystalline compact. Thus the computer program which contains the sinter-forging model is written to accommodate any number of pore size categories. However, the pore size

distribution can be assumed to be bimodal with two types of pores: "small" intercrystallite pores (less than or approximately equal to the grain size) and "large" interagglomerate pores. The densification mechanisms are assumed to operate independently on each pore size class. This assumption precludes any interaction between pore sizes (e.g. differential shrinkage). The microstructure is also assumed to experience perfect thermal conductance (i.e. no thermal gradients exist in the material) and homogeneous densification (within the limits of the bimodal pore size distribution).

Pores are assumed to move through a geometric shape progression during sintering. The pores are approximated as cylinders during intermediate stage and spheres during final stage densification. The transition between intermediate and final stage sintering is based upon the Rayleigh instability-of-jets criterion [18]. Based on this criterion, the cylindrical pores become unstable and will break down into spheres when

$$L > 2\pi r \qquad (8)$$

where L is the length and r the radius of the cylindrical pore. The grain shape throughout densification is modeled as a tetrakaidecahedron. The length of a cylindrical pore is assumed to be equal to the length of an edge of the grain. Thus, as grains grow, the length of the pore increases. For a compact with a single pore size the transition from cylindrical to spherical pores occurs at a density of about 92%. For a multimodal pore size distribution the transition occurs at a slightly lower density which depends upon the nature and volume of each pore size class and related particle size.

2.2.2. Microstructure–deformation interactions

Because of the empirical nature of Kuhn and Ferguson's model [8] (Eq. (6)), interactions between porosity and deformation are not considered. The details of these interactions may become important when the porosity becomes on the scale of the deformation. In metals, for example, the scale of the deformation is the distance between dislocation glide planes. This is usually the distance between close-packed planes (i.e. less than the unit cell size). Thus all pores will be closed by strain. However, when considering the deformation of ceramics, the deformation is often considered to occur by grain boundary sliding [19]. Since the scale of the deformation for grain boundary sliding is approximately the grain size, plastic flow will not be capable of eliminating pores that are smaller than the grain size. Another way to view this concept is that during grain boundary sliding a grain cannot slide into a pore smaller than the grain. In this case the size of a pore will determine whether it interacts with a particular deformation mechanism. In the current study, where grain boundary sliding (superplastic flow) is dominant, only the large interagglomerate pores were allowed to be eliminated by strain.

2.2.3. Grain growth

Although grain growth is generally ignored in most densification models, it occurs throughout sintering. Owing to the large change in grain size during sintering of nanocrystalline materials as well as the desire to predict and optimize density–grain size relationships, inclusion of grain growth in the densification model was considered necessary. Since grain growth is assumed to be controlled by the porosity during intermediate stage sintering and the experimental grain size increases approximately linearly with overall density, the grain size is assumed to be of the form

$$G = A\rho + B \qquad (9)$$

during intermediate stage sintering of small pores, where A and B are constants. This assumption is consistent with earlier work on grain growth during intermediate state sintering [20–22]. During final stage sintering the grain growth becomes a combination of static grain growth [23]

$$G_s = [k(t - t_o) - G_o^3]^{1/3} \qquad (10)$$

and dynamic grain growth [24,25]

$$G = CG_s(\varepsilon_p - \varepsilon_{p_o}) + G_s \qquad (11)$$

In Eqs. (10) and (11), C is a constant independent of temperature (T), t_o, ε_{p_o} and G_o are the time, plastic strain and grain size respectively when the sample enters final stage sintering and t and ε_p are the current time and plastic strain respectively. The static grain growth constant k is a constant which is an Arrhenius function of temperature [23]:

$$k = k_0 \exp\left(\frac{-Q_{gg}}{kT}\right) \qquad (12)$$

where k_0 is an experimentally determined constant and Q_{gg} is the activation energy for grain growth. Note that for samples that are not undergoing strain, $G = G_s$.

2.2.4. Material constants and input

Most of the material constants necessary for predicting densification during sinter-forging can be found in the literature. The constants used in the current work on 3Y-TZP are listed in Table 1. Since no grain boundary diffusion coefficients were available for 3Y-TZP, the values for 12Ce-TZP (also tetragonal ZrO_2) are used.

For the modeling of a sinter-forging experiment it is necessary for the program user to supply time, stress and plastic strain in array form. The initial pore radii and associated volumes and particle sizes are also needed as inputs. In this way an initial microstructure is entered into the model. Finally the sinter-forging temperature is needed. The program calculates a change in volume and radius for each pore size category for a given time increment. Subsequently the density is calcu-

lated as well as a new grain size. The program then cycles to the next time increment where the shrinkage due to each mechanism is again calculated. In this way the density, grain size and pore volumes are determined as a function of time.

3. Experimental details

Sinter-forging was accomplished in air using an Instron 1332 loading apparatus. A design similar to Raj and coworkers' [30,31] experimental apparatus was implemented in order to measure the height and diameter continuously during sinter-forging. Load and extension were controlled in one of three manners: (1) constant cross-head speed, (2) constant loading rate or (3) constant loading rate to a set load after which the load is held constant ("constant-load" testing). Constant-cross-head-speed testing was performed at rates from 0.005 to 0.5 mm min^{-1}. Loading rates varied from 0.005 to 0.1 kN s^{-1} and loads were not allowed to exceed 30 kN during all tests. Sinter-forging temperatures were 1050 or 1100 °C. The heating rate for both pressureless sintering and sinter-forging was 10 °C min^{-1}. After reaching the required temperature, the samples were equilibrated for 15 min before applying a load. Stress and strains (axial, radial and plastic) were calculated by methods previously developed for sinter-forging [32] and are briefly given as

$$\varepsilon_z = \ln\left(\frac{l}{l_0}\right), \qquad \varepsilon_r = \ln\left(\frac{R}{R_0}\right) \tag{13}$$

where l and R are the instantaneous height and radius respectively and l_0 and R_0 are the height and radius when the load was applied. The plastic strain ε_p and volume strain ε_v were then calculated by

$$\varepsilon_p = \tfrac{2}{3}(\varepsilon_z - \varepsilon_r) \tag{14}$$

$$\varepsilon_v = \ln\left(\frac{v}{v_0}\right) = \varepsilon_z + 2\varepsilon_r \tag{15}$$

Table 1
3Y-TZP material constants used during modeling of sinter-forging

Material constant	Value
D_{vol} [26]	0.3 m^2 s^{-1}
Q_{vol} [26]	623 kJ mol^{-1}
$\delta D_{0_{gb}}$ [26]	2.9 × 10^{-7} m^3 s^{-1}
Q_{gb} [26]	506 kJ mol^{-1}
Atomic volume Ω derived from [27]	1.12 × 10^{-29} m^3
Solid–vapor energy γ [28]	1.428−(0.000431) T (J m^{-2})
A and B at 1100 °C, Eq. (9)	100 nm, 0
A and B at 1050 °C, Eq. (9)	22.2 nm, 42.8 nm
C, Eq. (11)	1.4
Grain growth k_0 [29]	3.37 × 10^{-10} m^3 s^{-1}
Grain growth Q_{gg} [29]	400 kJ mol^{-1}
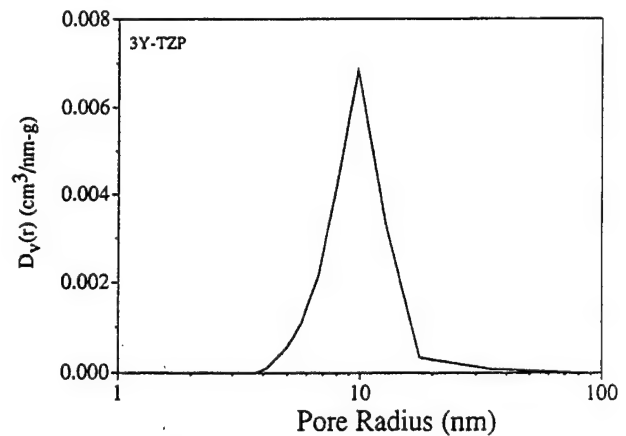
Fig. 1. Pore size distribution of pores less than 100 nm for 3Y-TZP compact sintered at 1100 °C for 15 min (ie. the initial starting point for sinter-forging at 1100 °C), $\rho = 71.9\%$. These intercrystallite pores are represented in the model as pores of 10 nm radius with a volume of 0.04088 cm^3 g^{-1}. The interagglomerate pores are much larger and cannot be observed by N$_2$ adsorption porosimetry.

where v_0 and v are the initial and final volumes of the sample respectively.

Green bodies were compacted by die pressing 3Y-TZP powders produced by co-precipitation [33]. Samples were 12.7 mm in diameter and about 5 g in mass. The green density varied between 32% and 40% of the theoretical density (6.08 g cm^{-3}). Final dimensions and densities were confirmed by caliper measurements and the Archimedes technique using water as the buoyancy medium. X-Ray diffraction was used to determine grain sizes less than 125 nm (Scherrer method) [34], while scanning electron microscopy (SEM) and the mean linear intercept ($\mathscr{L}$) technique were used for samples with grain sizes greater than 125 nm:

$$G = 1.56\mathscr{L} \tag{16}$$

Nitrogen adsorption porosimetry was used to monitor the pore size distribution below 100 nm [35]. The volume of pores below 100 nm (obtained from porosimetry) was then subtracted from the total open-pore volume to determine the volume of open pores greater than 100 nm.

4. Results and discussion

Since the initial microstructure of the compacts is critical to the model predictions, the initial pore radii and volumes were carefully monitored. For the nanocrystalline 3Y-TZP green compacts the grain size was 20 nm and the initial intercrystallite pore radius was 9 nm. After furnace equilibration the grain size was 55 nm at 1050 °C and 70 nm at 1100 °C. At both temperatures the intercrystallite pore radius grew to 10 nm (Fig. 1). For modeling, the "small" intercrystallite pore

sizes were simplified to a single pore size of radius 10 nm with a volume equivalent to that measured for all pores less than 100 nm. This approximation worked well because of the narrow size distribution of pore sizes centered on 10 nm (i.e. there were very few pores smaller than 5 nm or larger than 18 nm; see Fig. 1). By subtracting this volume of small pores from the total porosity present in the sample, the volume of "large" pores was determined. This large-pore volume (i.e. $V_{large} = V_{total} - V_{small}$) was found to be approximately constant over a wide range of green density, $\rho < 0.50$, and sintered (not sinter-forged) density, $\rho > 0.50$ (Fig. 2). Scanning electron microscopy of partially sintered samples showed that these large pores were approximately 5 µm or larger in diameter. Since these large pores were unlikely to shrink during pressureless sintering (i.e. furnace equilibration) at the temperatures studied, a volume of 0.021 cm³ g⁻¹ was used throughout the modeling as the initial volume of large pores.

Pressureless sintering was first modeled and compared with experimental data at 1050 and 1100 °C (Fig. 3). The model appears to satisfactorily predict the densification kinetics. An apparent limiting density of about 89% is due to the inability of diffusional mechanisms to shrink the large pores. Thus the agreement between prediction and experimental data has shown the ability of the model to accurately predict the densification kinetics for purely diffusional conditions and served to confirm that an appropriate starting microstructure was assumed.

To determine the appropriate densification mechanisms during sinter-forging (i.e. whether a strain-controlled pore closure mechanism was necessary), the prediction of densification was accomplished by applying either (1) the stress-assisted diffusional mechanisms alone (Eq. (3) or (4)) or (2) both the stress-assisted

Fig. 3. Modeling of densification during pressureless sintering at 1050 and 1100 °C (constant temperature). Assuming a bimodal distribution of pores, the model accurately predicts the densification kinetics as well as a limiting density of about 89%.

diffusional and strain-controlled pore closure mechanisms (Eq. (3) or (4) and Eq. (7)). As can be seen in Fig. 4, stress-assisted diffusion is not sufficient to predict the enhanced densification observed during sinter-forging at 1100 °C and a cross-head speed of 0.1 mm min⁻¹. In fact, for all predictions, stress-assisted diffusion consistently underestimated the observed densification kinetics. Thus it appears that the superposition of stress-assisted diffusion and strain-controlled pore closure is necessary to accurately predict densification during sinter-forging of agglomerated nanocrystalline compacts. The contribution of each mechanism can also be clearly seen by tracking the way in which different pore size classes are eliminated. Small pores are eliminated at a rate that is consistent with stress-assisted diffusion mechanisms, while the elimination of large pores can only be predicted by the strain-con-

Fig. 2. Pore volumes as a function of density. The small-pore volume measured by porosimetry is always less than the total pore volume calculated from the density. The difference, assumed to be due to large pores, is approximately constant (0.021 cm³ g⁻¹) in the density range measured.

Fig. 4. Modeling of sintering-forging at 1100 °C. The model predictions are shown with and without the strain-controlled pore closure densification mechanisms. Stress-assisted diffusion alone appears to be incapable of predicting the densification kinetics observed during sinter-forging.
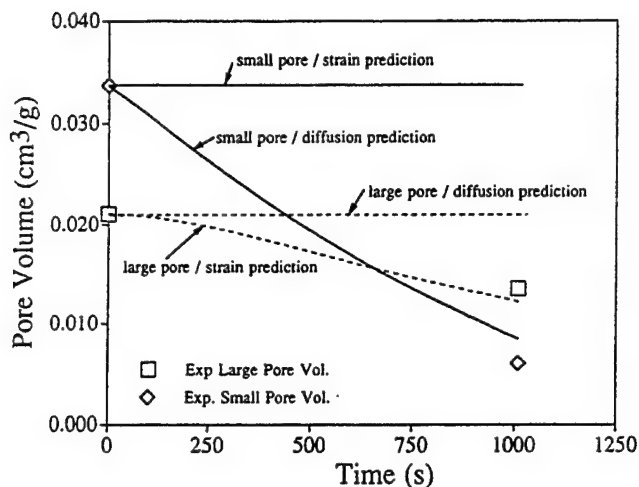
Fig. 5. Comparison of experimental small- and large-pore volumes with model predictions with either stress-assisted diffusion or strain-controlled pore closure mechanisms. The modeling shows that stress-assisted diffusion can explain the shrinkage of the small pores, while strain-controlled pore closure is responsible for the elimination of the large pores.

Fig. 7. Comparisons of model predictions with experimental results at 1100 °C for average plastic strain rates of $0-10^{-3}\,\mathrm{s}^{-1}$. The model begins to underpredict the densification at the highest strain rates.

trolled pore closure mechanism (Fig. 5). Thus the reduction in total pore volume cannot be accounted for unless both mechanisms are taken into account.

To test the versatility of the integrated model, sinter-forging experiments were conducted under widely varying strain rate and loading conditions. The model was able to predict the densification kinetics very well for most conditions (Figs. 6 and 7), though at 1100 °C the model began to underpredict the kinetics at the highest strain (and loading) rates. The el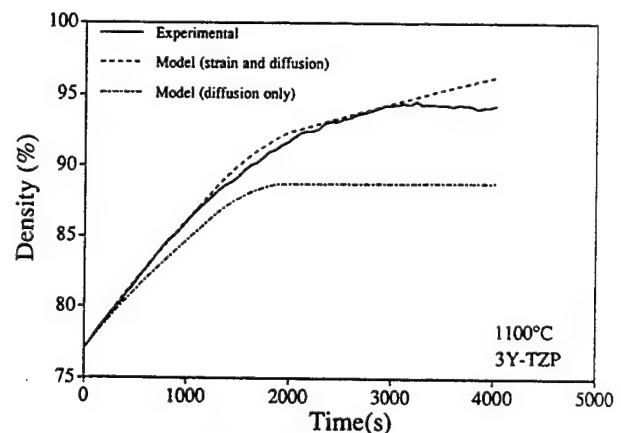imination of the remaining volume of large pores would cause the predictions to be much better. Microscopy of 1100 °C, high strain rate samples did not show any remaining large pores, leading to the conclusion that plastic deformation may be even more effective than the Kuhn and

Ferguson model predicts for strain-controlled pore closure (at least at high strain rates). However, there are several other factors which could cause this discrepancy: (1) the small pores may be susceptible to closure by strain at high stresses (dislocation activity?); (2) as suggested above, the mathematical description of the densification mechanisms may not be totally accurate; (3) another densification mechanism may be becoming active. At this point the reason for the underprediction is unclear.

The model appears to do an adequate job of predicting grain growth during sinter-forging (Fig. 8). For experimental conditions in which the model underpredicts the rate of densification ($\dot{\varepsilon}_p = 7 \times 10^{-4}\,\mathrm{s}^{-1}$, $T = 1100$ °C), the predicted grain size is too small (prediction not shown in Fig. 8). However, in most cases the predicted grain size compares fairly well with the measured grain size. Furthermore, the trends are clear:

Fig. 6. Comparisons of model predictions with experimental results at 1050 °C for average plastic strain rates of $0-10^{-3}\,\mathrm{s}^{-1}$. The model appears to be capable of predicting the densification very well.

Fig. 8. Prediction of grain size as a function of density for sinter-forging at 1100 °C. Higher strain rates are able to eliminate large pores before the smaller pores enter the final stage of densification and allow grain growth. Therefore density is increased while grain growth is minimized.

increased strain rates lead to better density–grain size combinations in both experiment and theory.

The reasons why maximum density and minimum grain size are produced under high strain rate conditions are explained by the model. Under high strain rate conditions, large pores shrink quickly (by strain-controlled pore closure), leading to fast densification. In these high strain rate cases the small pores also shrink faster owing to the high stresses; however, they are actually shrinking slower relative to the large pores. Thus the small pores are present at higher densities and are able to control grain growth during sinter-forging until they close. Once they are closed, the small pores are also eliminated more quickly at high strain rates, resulting in less time for the grains to grow by traditional static and dynamic grain growth mechanisms. Thus for sinter-forging at 1100 °C the best experimental grain size–density combination was produced at a strain rate $7 \times 10^{-4} \, \text{s}^{-1}$ (higher rates cracked the samples): a 121 nm grain size resulted with 98% density.

5. Conclusions

Modeling of densification and grain growth during sinter-forging of nanocrystalline ceramics has been accomplished. The model superimposes stress-assisted diffusional mechanisms with an experimentally based, strain-controlled pore closure mechanism. It has been shown that the superposition of the two mechanisms is necessary in order to accurately predict the densification of agglomerated 3Y-TZP powder compacts. The model predicts that in order to obtain a maximum sample density with minimum grain growth, high strain rates are necessary to eliminate large pores quickly before the small pores, which control grain growth during intermediate stage sintering, are eliminated.

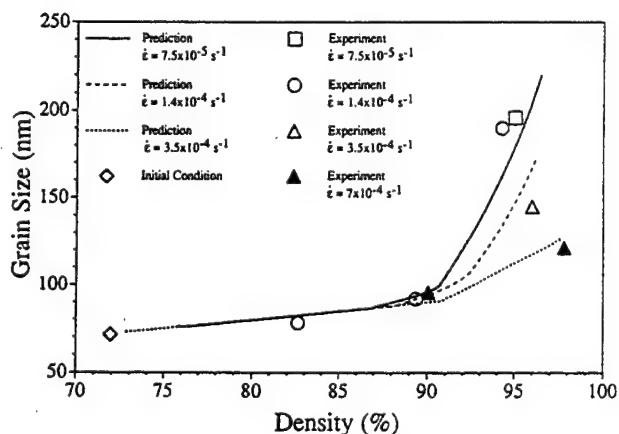## References

[1] Proc. 1st Intern. Conf. on Nanostructured Mater., Cancun, Mexico, 22–26 Sept. 1992, *Nanostruct. Mater.*, *3* (1993).

[2] Proc. 2nd Intern. Conf. on Nanostructured Mater., Stuttgart, Germany, 3–7 October, 1994, *Nanostruct. Mater.*, in press.

[3] H. Hahn, J. Logas and R.S. Averback, *J. Mater. Res.*, *5* (1990) 609.

[4] M.J. Mayo, D.C. Hague and D.-J. Chen, *Mater. Sci. Eng.*, *A166* (1993) 145.

[5] D.C. Hague and M.J. Mayo, in M. Nastasi, D.M. Parkin and H. Gleiter (eds.), *Mechanical Properties and Deformation Behavior of Materials Having Ultra-Fine Microstructures*, Kluwer, Boston, MA, 1993, p. 539.

[6] A.S. Helle, K.E. Easterling and M.F. Ashby, *Acta Metall.*, *33* (1985) 2163.

[7] R.L. Coble, *J. Appl. Phys.*, *41* (1970) 4798.

[8] H.A. Kuhn and B.L. Ferguson, *Powder Forging*, MPIF, Princeton, NJ, 1990, p. 59.

[9] B. Budiansky, J.W. Hutchinson and S. Slutsky, in H.G. Hopkins and M.J. Sewell (eds.), *Mechanics of Solids: The Rodney Hill 60th Anniversary Volume*, Pergamon, New York, 1982, p. 13.

[10] D.S. Wilkinson and M.F. Ashby, in G.C. Kuczynski (ed.), *Proc. 4th Int. Conf. on Sintering and Related Phenomena, Sintering and Catalysts*, Plenum, New York, 1975, p. 473.

[11] H.J. Frost and M.F. Ashby, *Deformation Mechanism Maps. The Plasticity and Creep of Metals and Ceramics*, Pergamon, New York, 1982.

[12] D.S. Wilkinson and M.F. Ashby, *Acta Metall.*, *23* (1975) 1277.

[13] J.M. Duva and P.D. Crow, *Acta Metall. Mater.*, *40* (1992) 31.

[14] R.L. Coble, *J. Appl. Phys.*, *32* (1961) 787.

[15] Ref. [11], p. 15.

[16] R.M. Spriggs and L. Atteraas, in *Ceramic Microstructures— Their Production*, Wiley, New York, 1968, p. 701.

[17] M.J. Mayo and D.C. Hague, in T.G. Langdon (ed.) *Superplasticity in Advanced Materials*, ICSAM-94 Materials Science Forum 170–172, Trans Tech, Aedermannsdorf, 1994, p. 141.

[18] Lord Rayleigh, *Scientific Papers by Lord Rayleigh*, Vol. 1, Dover, New York, 1964, p. 361.

[19] A.H. Chokshi, A.K. Mukherjee and T.G. Langdon, *Mater. Sci. Eng.*, *R10* (1993) 237.

[20] T.K. Gupta, *J. Am. Ceram. Soc.*, *55* (1972) 276.

[21] S.C. Samanta and R.L. Coble, *J. Am. Ceram. Soc.*, *55* (1972) 583.

[22] C.P. Cameron and R. Raj, *J. Am. Ceram. Soc.*, *71* (1988) 1031.

[23] R.J. Brook, in F.F.Y. Wang (ed.), *Treatise on Materials Science and Technology*, Vol. 9, *Ceramic Fabrication Processes*. Academic, New York, 1976, p. 331.

[24] Y.-I. Yoshizawa and T. Sakuma, *Eng. Fracture Mech.*, *40* (1991) 847.

[25] Y.-I. Yoshizawa and T. Sakuma, in S. Hori, M. Tokizane and N. Furushiro (eds.), *Superplasticity in Advanced materials*, JSRS, Osaka, 1991, p. 251.

[26] Y. Sakka, Y. Oishi, K. Ando and S. Morita, *J. Am. Ceram. Soc.*, *74* (1991) 2610.

[27] K. Tsukuma, Y. Kubota and T. Tsukidate, in N. Claussen, M. Rühle and A.H. Heuer (eds.), *Advances in Ceramics*, Vol. 12, American Ceramic Society, Columbus, OH, 1984, p. 382.

[28] D. Sotiropoulou and P. Nikolopoulos, *J. Mater. Sci.*, *26* (1991) 1395.

[29] D.-J. Chen, *Master's Thesis*, The Pennsylvania State University, University Park, PA, 1994.

[30] K.R. Venkatachari and R. Raj, *J. Am. Ceram. Soc.*, *69* (1986) 499.

[31] P.C. Panda, J. Wang and R. Raj, *J. Am. Ceram. Soc.*, *71* (1988) C507.

[32] R. Raj, *J. Am. Ceram. Soc.*, *65* (1982) C46.

[33] M. Çiftçioglu and M.J. Mayo, *MRS Symp. Proc.*, *196* (1990) 77.

[34] B.D. Cullity, *Elements of X-Ray Diffraction*, Addison-Wesley, Reading, MA, 2nd edn., 1978, p. 99.

[35] S. Lowell and J.E. Shields, *Powder Surface Area and Porosity*, Chapman and Hall, New York, 3rd edn., 1991, p. 52.

Growth of elongated nanostructures

D.G. Vlachos

Department of Chemical Engineering, University of Massachusetts, Amherst, MA 01003, USA

Abstract

Growth of elongated nanostructures from the gas phase on a masked substrate is modeled using the continuous time Monte Carlo method with the solid-on-solid approximation. We have found that the masked substrate imposes anisotropy on the growth of elongated nanostructures. Thus growth occurs either by nucleation of a single cluster in the short direction and wave propagation in the long direction or by formation of multiple nuclei followed by propagation of waves along the long direction. The growth rate of nanostructures depends significantly on their size. Narrow nanostructures grow about two orders of magnitude slower and there is a size-dependent critical supersaturation for growth to occur. This behavior is explained in terms of the thermal stability of nanostructures.

Keywords: Growth; Elongated nanostructures; Thermal stability

1. Introduction

Nanophase materials are encountered in many applications, including supported catalysts, ceramics and semiconductors. There has been a continuous need for structures of smaller dimensions and it may not be long before structures of atomic dimensions are synthesized in a reproducible and systematic way. The use of zeolite cages, for example, has opened new horizons for synthesis of materials of small size in confined geometries. Structures of small dimensions have recently been synthesized including quantum dots and wires.

The problem of crystal growth and crystal morphology has been studied since the pioneer work of Burton et al. [1]. An understanding of crystal growth at the molecular level has been pursued mostly for simple cubic crystals using Monte Carlo simulations for adsorption and desorption of growth units (homoepitaxial systems) [2,3]. These studies were subsequently extended to incorporate surface diffusion and dislocations [4].

Structures of atomic demensions exhibit finite size effects and magic numbers may be found [5]. These magic number structures have distinctly different properties from structures close in size. Such properties may include thermodynamic properties [5], selectively and reactivity [6], etc. The properties of small structures may be different from these of bulk materials. It is expected that sufficiently large three-dimensional particles and epitaxial thin films will behave like bulk materials. Despite static simulations on clusters [7], the critical size where the transition of bulk-like properties occurs is still an open question.

Understanding nucleation and growth of nanophase materials is central for miniaturization of structures with desired properties. Formation on a substrate of elongated nanostructures which are almost one-dimensional is of importance to catalysis, quantum wires and interconnecting lines for electronic devices [8,9]. Deposition on patterned and masked substrates is also of considerable interest for selective deposition.

Here we examine the morphology and growth rates of elongated nanostructrues growing from an adjacent fluid by employing the continuous time Monte Carlo method. Emphasis is placed on the role of finite size in growth rates, surface morphology, nucleation and dynamics.

2. Model and Monte Carlo simulations

Growth of elongated nanostructures on a masked substrate is modeled. A schematic illustration of the model is shown in the inset of Fig. 1 (see Section 3). The sticking coefficient on the masked substrate is taken to be zero. Thus incorporation into the nanos-

tructure occurs directly from the adjacent fluid phase. Adsorption and desorption are modeled and the resistance to transport in the adjacent fluid phase is considered to be small. For simplicity a simple cubic lattice is employed with first-nearest-neighbour interactions of strength ε. For the simulations reported here, $\varepsilon = 0.23$ eV and the temperature is taken to be $T = 1000$ K ($\varepsilon/kT = 2.669$, where k is the Boltzmann constant). The lattice size representing a growing nanostructure is $80 \times w$, where w is the width of the nanostructure and is a parameter of the model. The effect of length has been examined in the simulations. We have found that this size of 80 atoms gives results for the growth rate and surface morphology which are, within the accuracy of the simulations, independent of the length.

According to the kinetic theory, the adsorption probability per unit time per site is

$$p_a = \frac{s_0 P}{\eta_0 (2\pi m k T)^{1/2}} \tag{1}$$

where P is the gas phase pressure, s_0 is the sticking coefficient, which is assumed to be independent of the local environment of a surface site, η_0 is the density of sites and m is the mass of an atom.

The desorption probability per unit time of an atom with n first-nearest neighbors is

$$p_d(n) = v_0 \exp\left(-\frac{n\varepsilon}{kT}\right) \tag{2}$$

where v_0 is the pre-exponential factor. For an ideal gas in contact with a solid the difference in chemical poten-

tial between the two phases is

$$\Delta\mu = kT \ln\left(\frac{P}{P_e^\infty}\right) \tag{3}$$

where P_e^∞ is the equilibrium crystal vapor pressure of an infinite surface. The relative supersaturation with respect to an infinite surface is here defined as

$$\sigma_\infty = \frac{P}{P_e^\infty} - 1 \tag{4}$$

From Eqs. (1), (3) and (4), p_a becomes

$$p_a = p_{a,e} \exp\left(\frac{\Delta\mu}{kT}\right) = p_{a,e}(1 + \sigma_\infty) \tag{5}$$

where $p_{a,e}$ is the adsorption transition probability of a gas in equilibrium with the solid phase. Equilibrium occurs when the adsorption rate equals the average desorption rate. The two rates are equal at "kink" sites with exactly half the neighbors present [10], i.e. $p_d(3) = p_{a,e}$.

The continuous time Monte Carlo method [11] is employed which is an extension of the n-fold method proposed by Bortz et al. [12]. Every trial is successful and the time is updated by a continuous amount determined from the average lifetime of the surface configuration. A priori probabilities of various events are calculated before rather than after choosing an event. The efficiency of simulations increases by putting the atoms in classes of the same transition probability. For example, in the case of an adsorption event all sites are equivalent and belong to the same class. For desorption the activation energy depends on the local environment of an atom. The probability per unit time of choosing a particular desorption class is then $N_d(n)p_d(n)$, where $N_d(n)$ is the number of atoms with n first-nearest neighbors. The total probability per unit time is then

$$p^{tot} = p_{a,e} \sum_{surface} \left[\exp\left(\frac{\Delta\mu}{kT}\right) + \exp\left(\frac{(3-n)\varepsilon}{kT}\right)\right] \tag{6}$$

After selecting a class, a site from this class is randomly chosen and the event is executed. The time is then incremented by [11]

$$\Delta t = -\frac{\ln(\xi)}{p^{tot}} \tag{7}$$

where ξ is a random number ($0 < \xi < 1$).

The size of the nanostructure in one direction is sufficiently long so that periodic boundary conditions are used. The width in the other direction is short and free boundary conditions are employed. Since the sticking coefficient on the mask is taken to be zero, creeping of material from the nanostructure to the mask is not considered here. Runs with 10^6 up to 2×10^8 successful Monte Carlo trials have been performed. Longer runs were done for slow-growing stripes and shorter runs for fast-growing stripes.
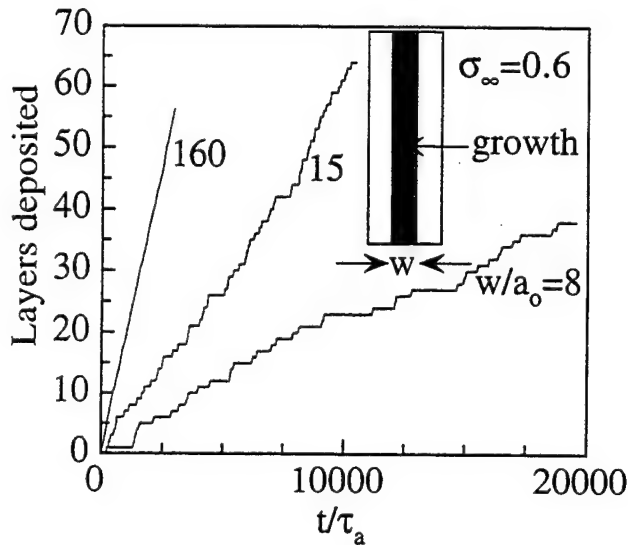

Fig. 1. Number of layers deposited vs. time for various nanostructure widths with $\sigma_\infty = 0.6$. The inset is a schematic illustration of an elongated nanostructure growing on an inert substrate. For narrow stripes, nucleation barriers exist and the growth oscillates between low and high values.

3. Results and discussion

Fig. 1 shows the number of layers deposited vs. time for various nanostructure widths at a relative supersaturation $\sigma_\infty = 0.6$. The time is made dimensionless by dividing t by the characteristic time for adsorption of an atom, $\tau_a = 1/p_{a,e}$. The width w is made dimensionless by the lattice constant a_0, and its numerical value indicates the number of rows of atoms in the stripe.

The first noticeable feature is that the average slope of the curves decreases as the width of a nanostructure decreases. Thus the growth rate of wide stripes is much higher than that of narrow nanostructures. For the case of $w/a_0 = 160$ the height of the nanstructures changes smoothly with time. In contrast, step-like curves are obtained for $w/a_0 = 15$ and 8. This behavior is reminiscent of nucleation barriers.

At relatively low supersaturations, growth on flat surfaces proceeds slowly by two-dimensional nucleation. There is some time elapsed before a critical size nucleus is formed on a surface. This is indicated by a horizontal line with small fluctuations in Fig. 1. Two-dimensional growth of a critical nucleus then occurs rapidly to complete one monolayer. This is indicated by an almost vertical line connecting horizontal lines in Fig. 1. During the time needed for cluster formation the growth rate is very low (a small slope in the height–time curve). In contrast, during two-dimensional growth of a supercritical cluster the growth rate is high (a large slope in the height–time curve). Thus the growth rate oscillates between low and high values for sufficiently narrow nanostructures but is almost constant (a constant slope in the height–time curve) for wide nanostructures.

Our simulations indicate that for a certain pressure (supersaturation) and temperature, nucleation times may be very short on large surfaces but very long on small size structures, which creates the difference in growth rates among structures of various widths. In contrast, when the supersaturation is high, the probability of formation of a critical nucleus is high. Under these conditions, kink sites are available at the periphery of growing clusters and growth proceeds rapidly, resulting in smooth height–time curves.

Fig. 2 shows the growth rate vs. the width of nanostructures for $\sigma_\infty = 0.6$. The points are obtained from Monte Carlo simulations and the full curve connects the points. The growth rate is an average of at least 10 independent runs generated from various sequences of random numbers. Larger uncertainties occur for narrow nanostructures, because the number of layers deposited during a simulation is not large and times for nucleation of a new layer are long. Longer and more runs are then required for narrow stripes to obtain good statistics.
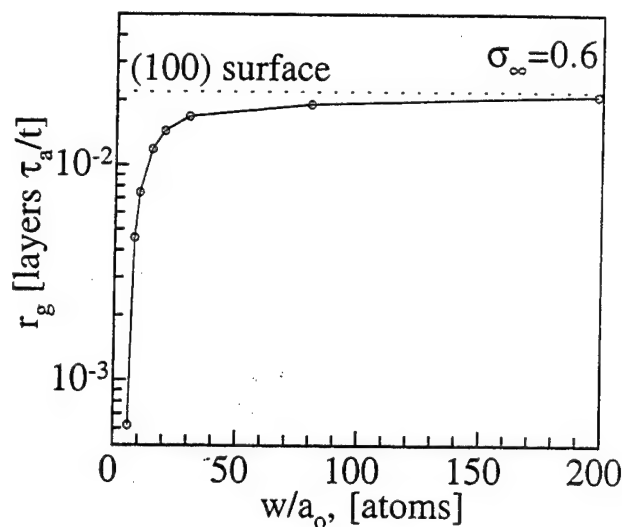
It is found that narrow nanostructures exhibit a

Fig. 2. Time average growth rate vs. width of nanostructures for $\sigma_\infty = 0.6$. The broken line shows the growth rate of the (100) surface. The growth rate decreases very rapidly with decreasing stripe width. Periodic boundary conditions overestimate the growth rate of relatively small structures.

considerably low growth rate as compared with wide nanostructures. The growth rate increases very sharply with nanostructure width and at sufficiently large widths it increases slightly with w approaching an asymptote. The broken line shows the growth rate of the (100) plane obtained from an 80×80 lattice using periodic boundary conditions in both directions. This value is a theoretical upper bound for the growth rate of elongated nanostructures. The asymptote is approached slowly, because even for wide stripes there are always edge effects. Atoms at edges have fewer bonds as compared with an infinite surface where atoms at edges have nearest neighbors through the use of periodic boundary conditions. As an example of a material with a lattice constant of 3 Å and $w/a_0 = 150$, the width of the nanostructure is 450 Å. Fig. 2 indicates that the growth rate of stripes of this size is overestimated by more than 10% when periodic boundary conditions are employed in both directions as compared with free boundary conditions in the short dimension.

The growth rate of narrow nanostructures can be lower than that of large films by as much as two orders of magnitude. In fact, for a certain supersaturation there may be a critical width below which growth of nanostructures is impossible. Instead, etching of more narrow nanostructures occurs. For the conditions shown in Fig. 2, $w/a_0 = 6$ is the minimum size for which growth occurs. This is at first surprising, because for a positive supersaturation one would expect growth of stripes of all sizes but not etching.

The supersaturation is the driving force for growth; conversely, undersaturation is the driving force for etching. At equilibrium of an infinite crystal with the gas phase the supersaturation is zero ($\sigma_\infty = 0$) and no

growth occurs. For gas phase pressure above the equilibrium pressure, $P > P_c^\infty$ ($\sigma_\infty > 0$), growth occurs and the growth rate increases with σ_∞. Based on a dislocation model of crystal growth, the growth rate exhibits a linear and a quadratic dependence on the driving force for high and low supersaturations respectively [1]. On the other hand, for gas phase pressure below the equilibrium pressure, $P < P_c^\infty$ ($\sigma_\infty < 0$), etching of crystals occurs.

When the critical nucleus size is sufficiently large, its probability of formation is very low. Nucleation then controls the growth rate, which is low. The probabilities of formation and disappearance of a critical nucleus are equal. From a thermodynamic point of view, clusters of different shape may have a different free enegy. Thus the critical nucleus size may depend also on its shape. In particular, the contribution of line tension to the free energy plays a central role in affecting critical nucleus size. The anisotropy of the substrate imposes an anisotropy in the critical nucleus, which must be elongated. Such an elongated nucleus has an increased line free energy as compared with a square nucleus and is thermodynamically less stable. Consequently, nucleation of such elongated nanoclusters is more difficult, requires longer times and results in lower growth rates as the width decreases. Sufficiently narrow nanostructures are unstable and disappear. We have found that the critical value of supersaturation below which growth is impossible decreases as w decreases.

The surface of stripes examined here is flat without dislocations and steps from misorientation for which the model of Burton et al. holds. Steps appear only at the periphery of growing clusters. For narrow nanostructures, clusters first grow along the short dimension and then along the long dimension to produce a critical nucleus size as shown in Fig. 3. That is, clusters perco-

Fig. 4. Square root of time average growth rate vs. supersaturation for various stripe widths. The growth rate depends in a quadratic way on the supersaturation. There may be a critical supersaturation for every stripe width below which etching occurs.
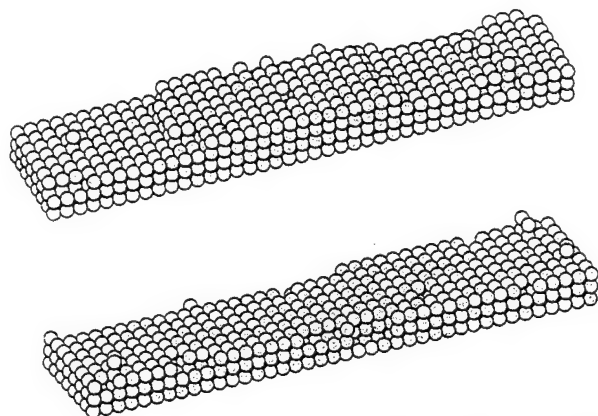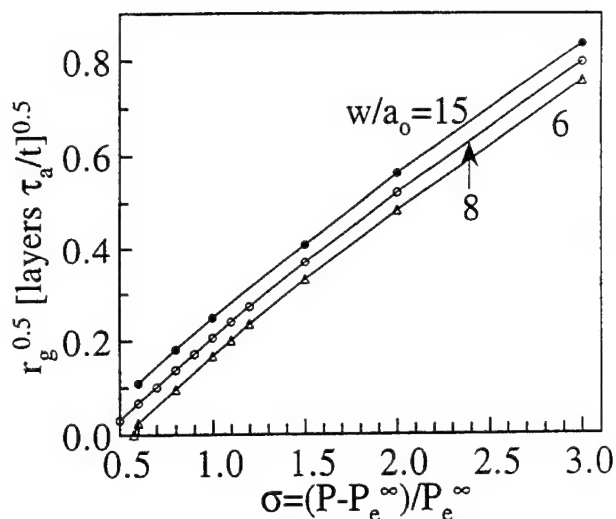

Fig. 3. Snapshots of the top four layers during growth of a 40×8 stripe. The top snapshot shows a nucleus which has formed in the short dimension and subsequently grown in the long dimension. The bottom snapshot shows the surface morphology after a layer has just been completed. Defects at the edges of the nanostructure are observed.

late fast in the short dimension but grow slowly along the long dimension until a critical size nucleus is formed. Under these circumstances, clusters possess steps for atom incorporation only along the short dimension. Thus the anisotropic growth results in propagation of waves along the long dimension. When the stripe is short, we found that only one nucleus forms and two one-dimensional waves propagate in opposite directions to produce one monolayer. When the stripe is long, such as 80 atoms, multiple nuclei form in a layer and waves propagate and annihilate as they collide.

Fig. 4 shows the square root of the growth rate of a nanostructure vs. the supersaturation for various widths of nanostructures. The points correspond to Monte Carlo simulations and the curves are interpolations of the points. An almost straight line is obtained, indicating that the growth rate has an almost quadratic dependence on the driving force defined with respect to an infinite surface. The distance between curves corresponding to different widths is slightly reduced with increasing supersaturation. This indicates that there is only one dominant mechanism for all supersaturations which creates the difference in growth rates between various widths. It is expected that in the limit of fast growth the dependence of growth rate on size will be weak. For example, the growth rate of $w/a_0 = 15$ is higher than that of $w/a_0 = 8$ by about 160%, 1.5% and 1.0% for $\sigma_\infty = 0.6$, 20 and 50 respectively.

Atoms at edges of nanostructures are energetically unfavorable and thus the vapor pressure of narrow nanostructures is enhanced compared with an infinite surface. This reduces the growth rate, because desorption rates near the edges are locally high. Desorption of

atoms at the edges creates energetically unfavorable atoms next to the edges. This situation propagates subsequently toward the axis of symmetry of a nanostructure. When a nanostructure is very narrow, desorption occurs quickly compared with the time required for nucleation of an elongated critical nucleus. Thus clusters of small length are rapidly destroyed owing to edge effects and the probability of formation of a critical nucleus is low.

To examine the interplay of thermal stability and nucleation in the observed growth rates, the critical supersaturation needed for growth has been calculated vs. the nanostructure width. The critical supersaturation determines the pressure at which the nanostructure is in equilibrium with the gas phase. Growth and etching are very slow near equilibrium, i.e. as the supersaturation approaches the critical value. In addition, during growth of narrow nanostructures near the critical supersaturation, large fluctuations are observed. Typically a few layers are deposited followed by etching and subsequent growth. To determine the critical supersaturation, the growth and etching rates have been determined sufficiently close to the critical value. An interpolation has then been used to find the critical supersaturation for which the growth rate is zero. The error in calculating the critical supersaturation is bounded by the difference between the data obtained on either side of zero rate. The inset in Fig. 5 shows an example of this calculation. The points are obtained from Monte Carlo simulations and the full curves are interpolations of the points. The rate r_g of growth (positive sign) and etching (negative sign) and the square root of r_g are plotted vs. the supersaturation for
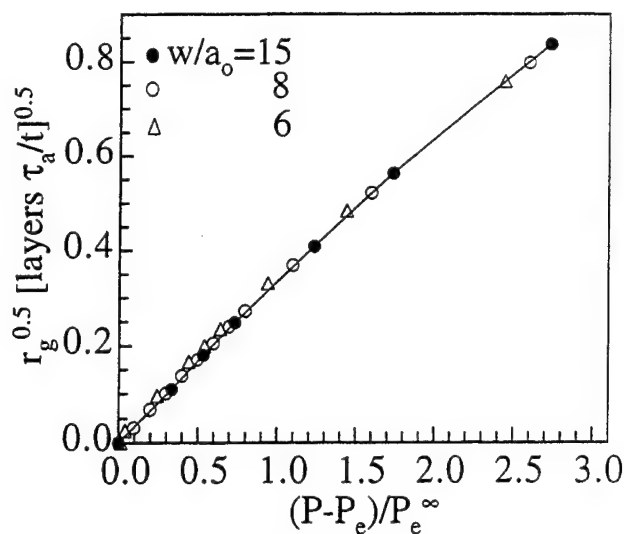
Fig. 6. Square root of time average growth rate vs. acutal supersaturation for various stripe widths. The dominant mechanism for the low growth rates of narrow nanostructures is due to the reduced thermal stability manifested by their low vapor pressure.

$w/a_0 = 8$. The intersection of the two curves with the horizontal axis at $r_g = 0$ provides the critical supersaturation $\sigma_c = P_e/P_e^\infty - 1$ separating the growth from the etching conditions for a certain nanostructure.

Fig. 5 shows the critical supersaturation (equilibrium pressure) vs. the inverse of the width of the nanostructure. The points are obtained from an analysis similar to that shown in the inset and the line is a least-squares fit to the points. A linear dependence is found with a good correlation coefficient. This indicates that the vapor pressure is inversely proportional to the width of the nanostructure for the conditions examined.

For finite size nanostructures the vapor pressure is higher than that of an infinite surface. As a result the actual driving force for growth of nanostructures is lower than that of an infinite (100) surface. The growth rate is then replotted vs. the actual driving force made dimensionless with the equilibrium pressure of a reference size (in this case of an infinite (100) surface) for various widths in Fig. 6. The points correspond to Monte Carlo simulations and the curve is an interpolation of the points obtained for $w/a_0 = 15$. When the growth rate is plotted vs. the actual supersaturation, most of the finite size effects disappear. Within the accuracy of the simulations, points collapse on a single curve, especially at high supersaturations. This indicates that to a large extent the strong dependence of growth rate on size is due to the variation in vapor pressure with finite width. However, some small deviations are still observed at small supersaturations among different widths. Since simulations are more inaccurate at low supersaturations because of slow nucleation, our conclusions cannot be more definite. However, our simulations indicate that the strong dependence of growth rate
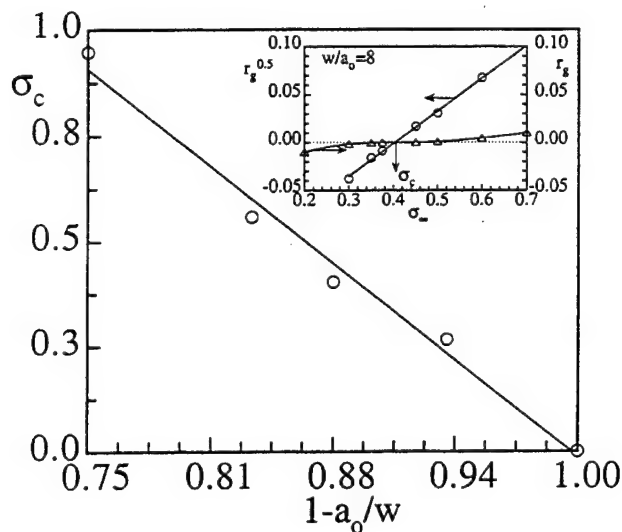

Fig. 5. Critical supersaturation vs. inverse of stripe width. The vapour pressure of a nanostructure is inversely proportional to the width of the nanostructure. The inset shows the growth rate and the square of the growth rate vs. supersaturation for $w/a_0 = 8$ for an estimation of the equilibrium vapor pressure.

on finite size is primarily due to the finite size dependence of the vapor pressure.

Here we examined adsorption and desorption without migration. Surface diffusion results in establishment of local equilibrium at a solid–fluid interface. Adatoms migrate on a surface to reach energetically favorable positions such as steps and kinks where they get incorporated. The activation energy for desorption and surface diffusion from such positions is considerably high and as a result the probability of adatoms escaping the nanostructure is low. It is thus expected that surface diffusion will reduce the desorption rate and increase the growth rate as also happens with large cyrstals [4].

4. Conclusions

We have examined the growth of elongated nanostructures from a fluid phase using the continuous time Monte Carlo algorithm and the solid-on-solid approximation. We have found that the growth rate is considerably low for narrow nanostructures and tends to an asymptote for a few hundred angstroms under the conditions studied. Low growth rates are attributed to the reduced thermal stability of narrow nanostructures manifested by low vapor pressures. Nucleation is observed for sufficiently narrow structures under conditions where fast growth occurs for large surfaces. This results in alternation of the growth rate between high and low values (oscillations). The time average growth rate changes almost in a quadratic way with the relative supersaturation. The anisotropy of the initial surface imposes an anisotropy in the growth of elongated structures. Clusters first nucleate along the short dimension and then propagate along the long dimension. For long nanostructures, multiple nuclei are formed and merge, whereas for short nanostructures only one nucleus is formed and propagates to create one monolayer. Our simulations here indicate that growth of small nanostructures including stripes and three-dimensional clusters can be profoundly slower than growth of thin films and large particles respectively.

Acknowledgements

References

[1] W.K. Burton, N. Cabrera and F.C. Frank, *Philos. Trans. R. Soc. Lond. A, 243* (1951) 299.

[2] J.P. van der Eerden and P. Bennema, *Prog. Cryst. Growth Charact., 1* (1978) 219.

[3] G.H. Gilmer and K.A. Jackson, in E. Kaldis and H.J. Scheel (eds.), *Crystal Growth and Materials*, North-Holland, Amsterdam, 1977, p. 79.

[4] G.H. Gilmer and P. Bennema, *J. Appl. Phys., 43*(4) (1972) 1347.

[5] D.G. Vlachos, L.D. Schmidt and R. Aris, *J. Chem. Phys., 96* (1992) 6880.

[6] E.K. Parks, B.H. Weiller, P.S. Bechthold, W.F. Hoffman, G.C. Nieman, L.G. Pobo and S.J. Riley, *J. Chem. Phys., 88* (1988) 1622.

[7] B. Raoult, J. Farges, M.F. De Feraudy and G. Torchet, *Philos. Mag. B, 60* (1989) 881.

[8] I. Zuburtikudis and H. Saltsburg, *Science, 258* (1992) 1337.

[9] J. Tersoff and R.M. Tromp, *Phys. Rev. Lett., 70* (1993) 2782.

[10] G.H. Gilmer, *Science, 208* (1980) 355.

[11] D.G. Vlachos, L.D. Schmidt and R. Aris, *Phys. Rev. B, 47* (1993) 4896.

[12] A.B. Bortz, M.H. Kalos and J.L. Lebowitz, *J. Comput. Phys., 17* (1975) 10.

Molecular dynamics simulations of densification processes in nanocrystalline materials

Huilong Zhu[a], R.S. Averback[a,b]

[a]*Materials Research Laboratory, University of Illinois at Urbana-Champaign, Urbana, IL 61801, USA*
[b]*Department of Materials Science and Engineering, University of Illinois at Urbana-Champaign, Urbana, IL 61801, USA*

Abstract

Molecular dynamics computer simulations were employed to investigate the dynamic processes of diffusion, grain growth, sintering, and consolidation in nanocrystalline copper (n-Cu). At room temperature, fully dense n-Cu was found to be stable. At 1100 K, a large fraction of atoms in the n-Cu became amorphous which provides a new mechanism of grain growth and recrystallization. Atomic mobility in dense n-Cu decreased with time as the grain boundaries relaxed. The initial configurations of the grains were shown to have a strong influence on pressureless sintering. Both hydrostatic pressure and uniaxial stress loading accelerrated the process of densification on porous n-Cu. The latter, however, was found more efficient due to grain boundary sliding.

Keywords: Molecular dynamics; Nanocrystals; Copper

1. Introduction

Nanocrystalline materials have become of great interest in recent years owing to their interesting properties and potential for technical applications [1]. An important step for continued progress in this new field, particularly in the area of structural applications, is learning how to consolidate these materials into dense bodies. Although substantial progress has been made in developing models of consolidation and deformation, it is not clear whether these models are relevant for nanocrystalline materials [2–5]. For example, the macroscopic models that are currently available are based on the kinetic and thermodynamic properties of solids that are close to equilibrium, which is not the case for nanocrystals. For them, it is likely that a more atomistic approach will be necessary to describe kinetic processes. This need to examine processes on the atomic scale has hampered experimental investigations as well. Molecular dynamics (MD) simulation, however, provides a powerful means to probe the atomic motion that takes place during sintering and consolidation of nanocrystals, and because of the small number of atoms in each grain, it becomes a practical means as well.

The aim of the present work, therefore, was to test the feasibility of using atomistic simulations of the kinetic processes that occur during the early stages of sintering and pressure assisted compaction of nanocrystals. The influences of initial packing configuration, temperature, and applied stresses on densification processes were examined.

2. Method

One method to simulate the consolidation process of nanocrystals by MD is by reducing the dimensions of the modeling cell with a constant speed [6]. With this method, an arbitrary factor, the speed of the moving boundary, is introduced into the problem, which would seemingly cause artificial effects. To avoid this problem, we have devised a reasonable algorithm [7], which is a modification of the Parrinello–Rahman method (PR MD) [8], to simulate the sintering and consolidation processes of nanocrystals under constant stress. Essentially, our algorithm, which is incorporated in DYNAMO [9], divides the atoms of the modeling cell into two coupling groups: a boundary group, which consists of the atoms near boundary, and a bulk group which includes the rest of the atoms. The motion of the bulk atoms is described by regular Newton equations. For

the boundary atoms, the motion is governed by a set equations modified, but similar to those given by PR MD. Unlike the previous theories, the boundary mass obtained by our method is independent of the size of computational cell, which means that the physical dynamic processes creating pressure in the interior of the cell are determined only by the positions and interactions of bulk atoms.

The modeling cells were octahedrons, containing between 4,688 and 9,136 atoms. Periodic boundary conditions were employed to reduce surface effects. The grains were assumed to be infinitely long (periodic) cylinders with initial diameters of $6.20a_0$, $8.28a_0$ and $15.10a_0$, where a_0 ($=0.362$ nm) is the lattice constant of Cu. The choice of cylindrical grains for these initial simulations was motivated by the ease of viewing and analyzing this geometry. The axes of all cylinders were $\langle 001 \rangle$, which has been chosen as the z-axis in our computational cells. At the beginning of the simulation, each cylinder is rotated randomly around its $\langle 001 \rangle$ axis. The repeat length of the cylinders is $6a_0$ which is large enough to avoid self-interaction caused by the periodic boundary. Temperatures ranging from 300 to 1 100 K, and external pressures, from 0.0 to 4.0 GPa, were chosen for the simulation of the sintering and consolidation processes. For each simulation event, the temperature and external stress were maintained constant from the beginning to the end. For the simulations of sintering, the external stresses were set to zero. Two initial arrays of cylinders, corresponding to high and low density n-Cu, were set up to examine the influences of packing configurations on the deformation of nanocrystals. The embedded atom potential of Sabochick and Lam, which was proven reliable in earlier studies [10], was employed to represent the forces in copper.

3. Results

It is illuminating to view the positions of the atoms in various instants of time to gain a qualitative understanding the densification process in nanocrystalline materials. Fig. 1 shows the projections of all atoms in the x–y plane at several instants of time. This simulation event, called S1, illustrates pressureless sintering of Cu at 300 K. The initial configuration of the four cylinders is closed-packed, which yields a relative atomic density of $\approx 84\%$. All cylinders at the beginning have the same diameter, $d = 8.28a_0$. By 5 ps, the cylinders have moved together due to the surface attraction among them. This attraction produces a few GPa negative pressure in the sample. Some regions of the grain boundaries appear amorphous, which was probably caused by the large stresses in the grain boundaries. The densification process was completed in remarkably

short time for sintering at 300 K, within 20 ps. Several tilt grain boundaries were formed among the cylinders. The deformation of the central cylinder, see Fig. 1(b), indicates that the grain was being subjected to a very high shear stress. Finally, stable, fully dense, n-Cu was achieved. Although it might appear surprising that complete sintering of Cu can take place within 20 ps, we believe this is due to the initial close packing of the cylinders and the high stresses on the boundary contacts, which approach (or exceed) the theoretical strength of Cu.

It is well-known that temperature, relative to the melting temperature, is an important processing variable that controls the rates of densification, grain growth, and creep. In addition, experimental data show that the melting temperature of a nanocrystal is size dependent [11]. Thus, the behavior of a nanocrystal at high temperature is both scientifically and technologically important. To examine the effect of temperature, we repeated the simulation event just described, but with the sample temperature held at 1 100 K. This event is denoted as S2. Projections similar to those in Fig. 1 for S1 are shown in Fig. 2 for S2. It can be seen that at 5 ps, the aggregate of cylinders has fully densified and that the amorphous region is much larger than that in S1. By 20 ps, the amorphous region grew into the cylinder, C1, at the lower right corner (note the periodic boundary) and at 60 ps C1 lined up with the cylinder, C3, at the lower left corner. By 120 ps, the cylinders in S2 almost became a single crystal with the original orientation of C3. From these simulations, it is seen that if the temperature is high, in this case $T/T_m \approx 0.8$, grain boundary amorphization, or melting, provides an unexpected mechanism of densification and grain growth in nanocrystalline materials.
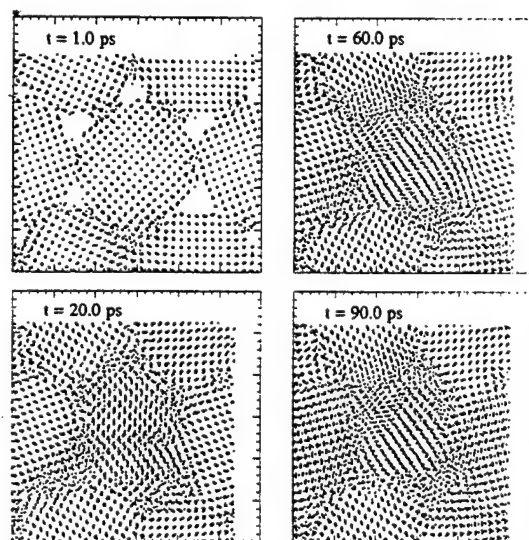

Fig. 1. Positions of atoms during pressureless sintering at $T = 300$ K for several instants.
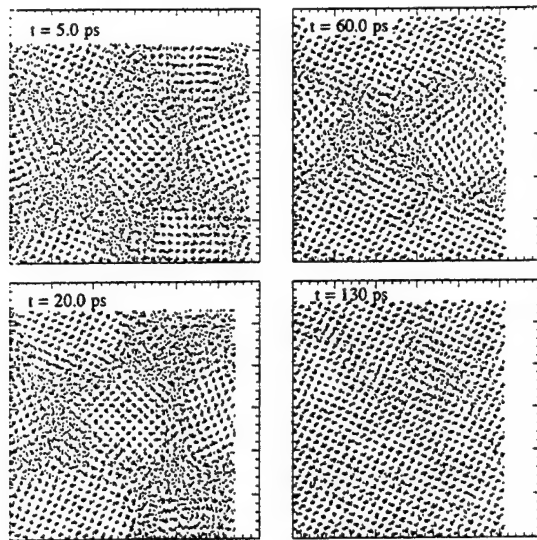
Fig. 2. Atom positions during pressureless sintering at $T = 1\,100$ K for several instants.

Fig. 4. Positions of atoms during sintering at $T = 300$ K under a hydrostatic pressure of 4.0 GPa, for several instants. The initial configuration is shown in Fig. 3(b).

The initial configuration of nanocrystalline particles plays a central role in the densification process [5]. Actually, porous nanocrystals will shrink during sintering but sintering alone, or even hot isostatic pressing, may not result in full densification [12]. In addition, the rate of sintering and grain growth is known to depend on the relative sizes and packing of grains[13]. We have considered these possibilities. Fig. 3 shows the atom positions during pressureless sintering of a new sample, event S3, at $T = 300$ K. S3 uses three cylinders: two of them with $d = 15.10a_0$ and one with $d = 6.20a_0$ at the corners. The starting configuration is shown in Fig. 3(a). After sintering for 50 ps, Fig. 3(b), a pore still remains and the smaller cylinder has recrystallized on the nearby large ones. This illustrates that unless the cylinders are initially close-packed, Cu will not fully sinter at room temperature under zero applied stress, which agrees with experimental observation [14].

Since a nanocrystal may not fully densify during pressureless sintering, an external pressure or stress is generally applied to help eliminate the remaining pores.
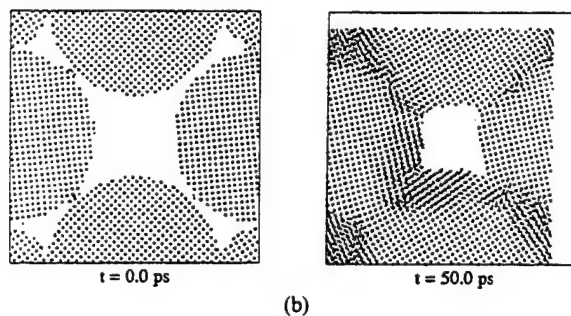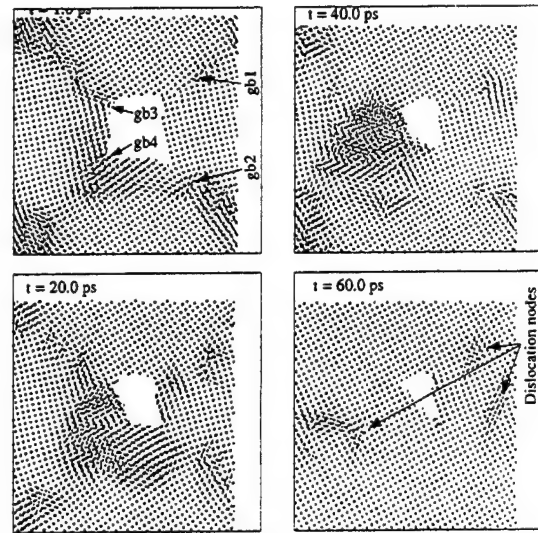

Fig. 3. Positions of atoms during pressureless sintering at $T = 300$ K for several instants. The particle packing is less dense than that in Fig. 1.

Simulations of these processes are straightforward. We focus here on studying the consolidation of S3 at room temperature, since this configuration of grains did not reach full density during the pressureless sintering just described. First, a hydrostatic pressure of 4.0 GPa was applied to the sample in S3 after it had undergone pressureless sintering for 50 ps; the projections of the atom sites at several instants of time are shown in Fig. 4. By 20 ps, a large change in the lattice structure took place in the region to the left of the pore, as grain boundary motion can be observed. More explicitly, the grain boundary, gb1, in the upper-right corner has moved down and one in the lower-right corner, gb2, moved up, indicating the shrinkage of the aggregate. Between 20 and 40 ps, the grain boundary, gb3, at the upper-left corner moved down and one, gb4, at the lower-left corner, moved up. The positions of gb1 and gb2 did not change much during this latter time interval. Grain boundary dislocations in gb3 move to the region on the left-side of the pore and eventually disappeared. At 60 ps a single crystal formed with a pore at the center and three dislocation nodes. Two of the four dislocations terminated in the pore, which indicates a dislocation node may form in the location of a pore as the pore closes during consolidation. The dislocation density in this structure at 60 ps corresponds to $\approx 8 \times 10^{16}\,\text{m}^{-2}$. Experimental data suggest that the lower limit of dislocation density in n-Cu is $10^{15}\,\text{m}^{-2}$ [15].

The application of a uniaxial stress is widely implemented in the experimental research of nanocrystal densification and consolidation [16,17]. Thus, an event was simulated with an external, constant, uniaxial stress of 4.0 GPa applied to the configuration of event S3 in the y-direction, σ_{yy}. The other stresses, σ_{zz} and σ_{xx} were
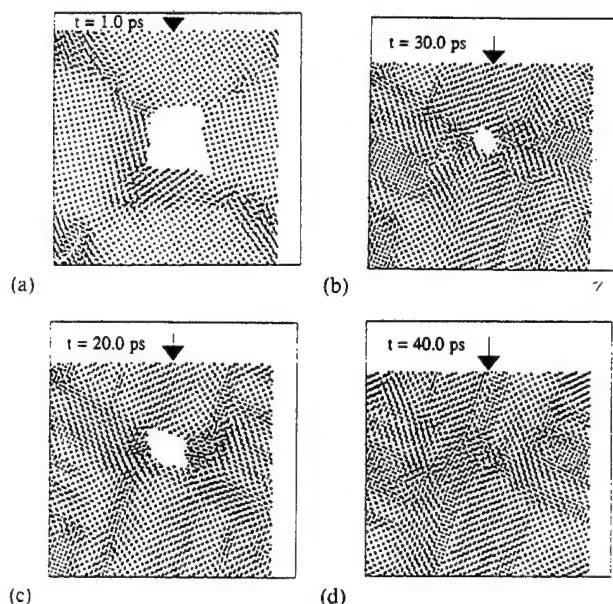
(a) (b) (c) (d)

Fig. 5. Positions of atoms during sintering at $T = 300$ K under a uniaxial stress of 4.0 GPa, for several instants. The initial configuration is shown in Fig. 3(b). The arrows show the direction of the loading stress.

set to zero. The projections of the atom positions for this event are illustrated in Fig. 5. The densification rate is observed to be faster in this case than that under hydrostatic pressure (see Fig. 3); the configurations of S3 has been fully densified by uniaxial stress before 40 ps, as shown in Fig. 5(d). In order to examine the relative motion of the nano-cylinders, some atoms were marked at $t = 0$ (shown by open circles) and followed to 40 ps (by solid circles), as shown in Fig. 6. A clockwise rotation of the cylinders of $\approx 18°$, and grain boundary sliding, indicated by the arrows in Fig. 6, took place; these motions are believed to facilitate the densification of S3. A more detailed analysis, which will be reported elsewhere [7], showed that the speed of grain boundary sliding is about $v_s/300$, where $v_s = 5\,000$ m s^{-1} is the speed of sound in Cu. No obvious grain boundary sliding is observed in the simulation using hydrostatic loading.

The events qualitatively described above, were also analyzed quantitatively. The normalized densities (D_n)
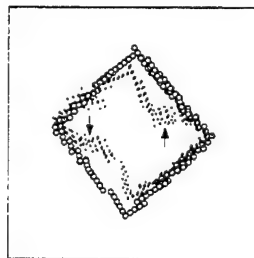

Fig. 6. Grain boundary sliding during consolidation under an uniaxial stress of 4.0 GPa. Sliding is indicated by the arrows.
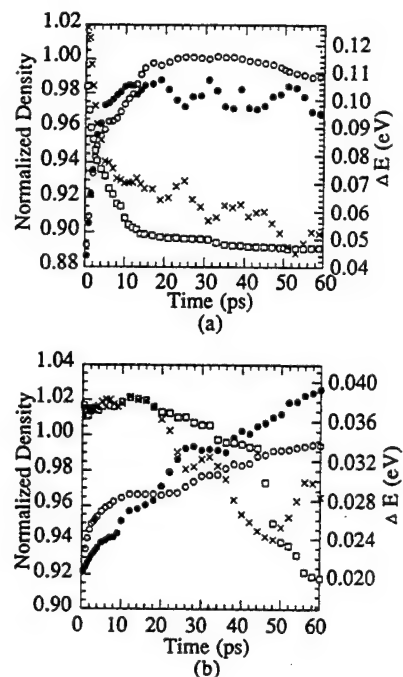

Fig. 7. Normalized densities, D_n, and relative potential energies per atom, ΔE, as a function of time. (a) For S1, $\bigcirc$ is D_n and $\square$ is ΔE: for S2, $\bullet$ is D_n and x is ΔE: (b) For hydrostatic pressure, $\bigcirc$ is D_n and $\square$ is ΔE; for uniaxial stress loading, $\bullet$ is D_n and x is ΔE.

and relative potential energies per atom (ΔE) for S1 and S2 are illustrated in Fig. 7 as a function of time. D_n is the relative density; i.e. the density normalized by the density of perfect lattice at the relevant temperature. ΔE is the difference between the potential energies per atom in a nanocrystal and in a perfect lattice at the same temperature. The reason for using ΔE is to focus on the influence of temperature on the grain boundaries. As shown in Fig. 7(a), D_n for S1 and S2 increase very fast, while ΔE decreases during the first 4 ps, owing to the shrinkage of the surfaces. After 4 ps, the curves of D_n and ΔE for S2 fluctuate relatively more than for S1. Actually, S2 is structurally unstable on the time scale of the simulation, which was discussed above and shown in Fig. 2. This causes fluctuations in ΔE [7]. For the consolidation processes of S3 under pressure of 4.0 GPa, D_n increased relatively slowly since S3 has been sintered for 50 ps before the starting of the consolidations. Comparing ΔE of S3 under hydrostatic pressure with the event under uniaxial stress, the lattice condition causes larger fluctuations than the former. This implies that the uniaxial stress drove S3 further from an equilibrium state than the hydrostatic pressure, even though the full densification of S3 has been achieved by uniaxial stress.

The role of grain boundaries for enhancing atomic diffusion is important for nearly all kinetic processes in nanocrystalline materials and was examined here. Due to the deformation of nanocrystals in the sintering or

consolidation, the determination of diffusion coefficients is not straightforward. Rather than computing the simple mean square displacement of atoms, which includes drift diffusion, the relative displacement of atoms was used instead for determining the 'true' migration of atoms. The definition of the relative displacement, $\Delta r_i(t, t')$, of the ith atom from time t' to t is

$$\Delta r_i(t, t') = \left[\left(\vec{r}_i(t) - \vec{r}_i(t') - \frac{1}{n'} \sum_{k=1}^{n'} (\vec{r}_k(t) - \vec{r}_k(t'))^2 \right) \right]^{1/2} \tag{1}$$

where $\vec{r}_k(t)$ is the position vector of the kth atom at time t and n' is the number of the neighbors of the ith atom. The sum in the brackets on the right-hand of Eq. (1) is over the first 12 neighbors of the ith atom at time t'. Furthermore, the total square displacement (TSD) in a sample from t' to t can be written as $\Delta R^2(t, t') = \Sigma_i \Delta r_i^2(t, t')$, where the sum is over all atoms whose relative displacement is larger than half the distance of nearest neighbors in a Cu crystal. The total square displacements are plotted in Fig. 8 as a function of temperature, and at several times. All data plotted in Fig. 8 were obtained from samples starting with the same configuration as S1 after it had densified. It is seen that at relatively low temperatures, such as 300–900 K, TSD decreases with increasing sintering time. This implies that grain boundary relaxation reduces the mobility of the atoms in the boundaries. From 40 to 90 ps, at $T = 300$ K, the averaged TSD is about 78.2 Å^2 which is close to that at the time of 35 ps. Relaxation of atoms in the grain boundaries, therefore, is very slow after 40 ps. Consequently, the activation energy of diffusion for atoms in the grain boundaries in the equilibrium state, in the region of temperature of 300–700 K, can be estimated by the slope of the curve at time 35 ps. This yields an activation enthalpy of diffusion of ≈ 0.8 eV, which agrees with experiments on n-Cu [18]. Above 700 K, the atoms migrate very fast since the large amorphous zones are formed in the region of the grain boundaries.
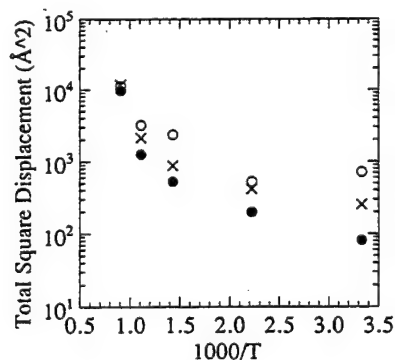
4. Summary

The consolidation of nanocrystalline copper was studied using molecular dynamics simulations. The initial configurations of grains were shown to have a strong influence on pressureless sintering effects. For closed packed grains, stable n-Cu formed during pressureless sintering at room temperature. At the temperature of 1 100 K, n-Cu is unstable and an amorphous state nucleates on the boundaries. This mechanism plays an important role in grain growth and recrystallization. Relaxation of the grain boundaries with time reduces the mobility of atoms in the boundaries. Both hydrostatic pressure and uniaxial stress loading accelerate the processes of densification in porous n-Cu, but the latter is more efficient due to grain boundary sliding.

Acknowledgments

References

[1] R.W. Siegel, *Mater. Sci. Eng. A, 204* (1995) 7–11.
[2] M.F. Ashby and R.A. Verrall, *Acta Metallurgica, 21* (1973) 149–163.
[3] A.G. Evans and T.G. Langdon, *Prog. Mater. Sci., 21* (1976) 171–441.
[4] E. Arzt, *Acta Metall., 30* (1982) 1883.
[5] W.J. Soppe, G.J. Janssen, B.C. Bonekamp, L.A. Correia and H.J. Veringa, *J. Mater. Sci., 29* (1994) 754.
[6] Z. Chen, Q. Yuan and J. Ding, *Chinese Phys. Lett., 10* (1993) 103.
[7] H. Zhu and R.S. Averback, unpublished results.
[8] M. Parrinello and A. Rahman, *Phys. Rev. Lett., 45* (1980) 1196.
[9] M.S. Daw, M.I. Basker and S.M. Foiles, personal communication.
[10] M.J. Sabochick and N.Q. Lam, *Phys. Rev., B43* (1991) 5243.
[11] F.G. Shi, *J. Mater. Res., 9* (5) (1994).
[12] J. Kellett and F.F. Lange, *J. Am. Ceram. Soc.,* (1989).
[13] F.F. Lange, *J. Am. Ceram., 72* (1989) 3.
[14] See for example H.J. Höfler, R.S. Averback, H. Hahn and H. Gleiter, *J. Appl. Phys., 74* (1993) 3832.
[15] R.Z. Valiev, E.V. Kozlov, Yu. F. Ivanov, J. Lian, A.A. Nazarov and B. Baudelet, *Acta Metall. Mater., 42* (1994) 2467.
[16] K.R. Venkatachari and R. Raj, *J. Am. Cer. Soc., 70* (1987) 514.
[17] R.S. Averback, H.J. Höfler and R. Tao, *Mater. Sci. Eng. A, 166* (1993) 169.
[18] J. Horvath, R. Birringer and H. Gleiter, *Sol. State Comm., 62* (1987) 319.

Fig. 8. Total square displacement as a function of temperature for several instants. $\bigcirc$, in the time interval 10–20 ps; x, 20–30 ps and $\bullet$, 30–40 ps.

Atomic model of a palladium nanostructure

M. Celino, G. D'Agostino, V. Rosato

ENEA, CRE Casaccia, Dipartimento Innovazione, CP 2400, I-00100 Roma, Italy

Abstract

We report on the atomistic modelling and molecular dynamics simulation of several palladium nanostructures characterized by grains of various sizes. The atomistic modelling is based on the "simulated cluster condensation" technique, which allows the design of a nanostructure by the aggregation of atomic clusters of various sizes. The phase obtained upon thermal relaxation shows a density close to that resulting from the experimental "gas condensation" technique. The structural analysis has focused on the features induced by the presence of heterogeneous regions (grain boundaries and cavities) and on the resulting stress localization

Keywords: Palladium nanostructure; Atomic model; Stress localization

1. Introduction

The increasing interest in nanostructured materials (called n-phases hereinafter) is mainly related to their novel and enhanced properties due to the high number of grain boundaries (GBs) and interfaces. Among the features that make these systems particularly appealing are their anomalously high diffusivity [1] and high reactivity [2,3], which enable them to be employed in catalytic applications. They also show a more ductile behaviour with respect to the parent microcrystalline phase (m-phase hereinafter) and an increased thermal expansion [4]. Moreover, several insoluble or low soluble elements can be alloyed by various means and the resulting phases exhibit n-phase structures [5]. The elastic constants of n-phases have been measured by a variety of methods and found to be reduced by 30% or less [6–8] with respect to m-phases. The most significant changes in the elastic behaviour is the increase in yield strength and hardness with temperature [9]. Although being one of the most relevant issues, the latter is also the least understood and thus the most controversial [10–12].

The extreme structural heterogeneity of n-phases on the atomic scale is the primary reason for their peculiar behaviour. In ordinary m-phases the fraction of atoms in the (homogeneous) bulk regions greatly overwhelms that in the interfacial (heterogeneous) regions. By contrast, in n-phases the disordered regions contain a similar number of atoms to the bulk. In this respect the

n-phase can be thought of as a transition state between the m-crystal and the amorphous phase, in which the spatial coherence of the crystalline lattice has totally disappeared. Indeed, the close resemblance between amorphous and n-phases have been pushed further. It has been suggested that GB structures in n-phases look more like a disordered phase (glassy or gas like) than do the corresponding ones in coarse-grained m-phases [13]. The controversy on this point seems to have survived despite clear transmission electron microscopy (TEM) evidence for ordinary structures of GBs in metallic n-phases [14]. It is, however, a paramount importance to establish to what extent the structure of the "disordered" regions is responsible for the behaviour of most of the thermoelastic properties in n-phases.

In this scenario the study via molecular dynamics (MD) of a "realistic" n-phase model on the atomic scale assumes a definite relevance, since it constitutes a unique tool to probe the extent and amount of structure–property correlations. The availability in the same framework of simulation models of bulk crystalline and amorphous phases allows quantitative and qualitative comparisons between average and local properties in those systems.

The state of the art of the MD approach to the physics of n-phases is focused on the separate evaluation of the contributions of the various regions present in the n-structures. This implies the evaluation of the contributions coming from GBs and multiple-junction

Table 1
Values of the potential parameters for Pd. Some predicted relevant quantities for the bulk structure are reported together with the corresponding experimental data (second row). Here T_m is the melting point, ΔH_m is the latent heat of melting, α is the linear expansion coefficient at room temperature and c_p is the constant-pressure specific heat

A (eV)	ξ (eV)	p	q	T_m (K)	ΔH_m (cal g-atom^{-1})	α (10^{-5} K^{-1})	c_p (cal K^{-1} g-atom^{-1})
0.1746	1.718	10.867	3.742	1580	3824	1.7	6.26
				1825	4197	1.2	6.21

regions, free surfaces and crystalline regions. However, it has been recently pointed out that the properties of multidimensional defects in n-phases do actually depend on the grain size [15]. As a consequence, only direct simulations of the entire n-phase structures may allow a correct reproduction of the particular properties observed in these systems.

The purpose of this work is twofold. First we introduce a method to reproduce the formation of n-structures via the aggregation of atomic clusters. We will then perform classical MD on the resulting n-phases to evaluate the relevant thermodynamic properties which will be directly related to the peculiar structural features. Palladium has been selected as a test case, since, owing to the variety of different studies, one has access to a large set of experimental data [16,17].

The present work is thus divided as follows. We first show the main features of the interatomic potential employed for computations. We then recall some recent results on cluster stability as a function of dimension in order to motivate the choice of the size of the Pd cluster employed in the aggregation process. We will then introduce the proposed simulation process to design n-phases, called "simulate cluster condensation" (SCC). A critical discussion of the relevant results will finally summarize the major achievements of the work while providing new insights for further studies.

2. Computational details and the potential scheme

As many-body potential scheme based on the second-moment approximation of a tight-binding hamiltonian (SMTB) has been successfully applied to study the thermodynamic and structural properties of most transition metals and several alloys in the bulk crystalline [18,19] and amorphous [20,21] phases. It has also been recently applied to the study of metallic clusters [22,23].

In this scheme the cohesive energy of a system of N atoms of a given species can be written as

$$E_c = \sum_{i=1}^{N} \left[\sum_{j=1}^{N} A \exp\left[-p\left(\frac{-r_{ij}}{r_0 - 1} \right) \right] \right.$$
$$\left. - \left\{ \sum_{j=1}^{N} \xi^2 \exp\left[-2q\left(-r_{ij}r_0 - 1 \right) \right] \right\}^{1/2} \right] \tag{1}$$

where r_0 is the nearest-neighbour distance in the lattice at $T = 0$. The parameters A, ξ, p and q are determined by fitting the experimental values of cohesive energy, lattice parameter, bulk modulus and shear elastic constants and by taking the equilibrium condition into account. It has been shown [19] that the introduction of the fifth-neighbour interaction cut-off produces a close reproduction of the relevant thermodynamic quantities. In Table 1 we give the parameters of Eq. (1) and some calculated thermodynamic quantities compared with the experimental data for palladium (second row).

3. Simulated cluster condensation

It is generally recognized that the properties on n-phases also depend on the particular preparation technique. The most widely used experimental technique is "gas condensation" [2], which allows the production of samples of high chemical purity. However, the possibility of obtaining metallic nanostructures by mechanical attrition of m-phase powders has been recently demonstrated [24]. At least on general grounds, the structures resulting from such processes can be thought of as different from the phases obtained by cluster compaction. In fact, in the former case, externally imposed strain fields are likely to affect the in-grain microscopic structure and to enhance stress localization and presistence.

In the context of modelling for MD simulations, the problem of "sample preparation" has been recently discussed [16,17,25]. In a previous study we have compared the various types of aggregation processes [25]. In the present paper we shall focus on the description of one of the proposed techniques, namely "simulated cluster condensation", which reproduces the low temperature cohesion of metallic clusters originally in a gas-like phase. We intend to study the process of nanostructure preparation by fragmentation of an m-phase, since this is expected to occur in the mechanical attrition preparation.

When two clusters of very small size are kept at a sufficiently short distance so that they interact, their cohesive energy quickly increases. If the system is isolated, this induces a temperature increase which brings clusters of very small size to their melting point. Upon

Table 2
Relevant thermodynamic and structural quantities for the simulated samples. Data relative to free clusters (c-309, c-586 and c-923), bulk and amorphous system are given for comparision. Here ρ is the density of the n-phase relative to the crystalline bulk, U/N is the cohesive energy per atom, r_1 is the average first-neighbour distance, σ^2 is the variance of the first peak of $g(r)$ integrated up to half-way between the first and second-neighbour distances, δp is the standard deviation of the local average pressure distributions of Fig. 2 and N_{bulk}/N is the ratio of bulk-like atoms (evaluated by means of Voronoi polyhedra) to the total number of atoms

	ρ	U/N (eV)	r_1 (Å)	σ^2 (10^{-3} Å^2)	δp (kbar)	N_{bulk}/N
c-309		−3.653	2.719	9.9	45	0.48
c-586		−3.714	2.728	9.2	38.2	0.54
c-923		−3.729	2.731	9.2	39.7	0.61
n-309	0.83	−3.810	2.762	20.8	23.5	0.38
n-586	0.92	−3.854	2.758	13.0	17.2	0.75
n-923	0.83	−3.813	2.754	15.3	22.0	0.59
Bulk	1	−3.896	2.761	8.4	0.6	1
Amorphous	0.97	−3.819	2.782	30.2	16.0	

further cooling, one is left with a larger cluster [26] and the individual cluster identity is lost. In order to prevent such a phenomenon, we have selected clusters of size larger than about 300 atoms, where the "approaching energy" is not enough to induce melting. To correctly sample the various local structures which occur in an n-phase, we have condensed a sufficiently large number of clusters. As a consequence we have been forced to limit the size of the initial clusters to the range from 300 up to about 1000 atoms, thus keeping the total number of particles to a convenient value around 10^4.

The most stable f.c.c.-based closed-shell configurations of Pd clusters in the range $300 < N < 1000$ are $N_1 = 309$ (cubo-octahedron), $N_2 = 586$ (tronco-octahedron) and $N_3 = 923$ (cubo-octahedron). If we disregard the icosahedral clusters, these are the most tightly bound and they also exhibit the smallest volume, as can be evaluated by means of a Voronoi polyhedra summation [27]. Their thermodynamic behaviour has been reproduced by classical MD based on the potential scheme described in Eq. (1). The potential energy curves for these clusters as a function of temperature show the presence of the well-known "extended" melting region [28] at temperatures substantially below the bulk melting point [27]. In this context we have ascertained that the structures of the selected clusters are stable up to their respective melting temperatures (i.e. no structural phase occurs).

We have thus chosen to reproduce the SCC of three different monodisperse gases of clusters of N_1, N_2 or N_3 atoms respectively. In the following the obtained n-phases will be referred to as n-309, n-586 and n-923 according to the building blocks employed.

The SCC process consists of two steps.

(1) During the early stages, to avoid huge computational requirements, we have introduced "effective" interactions between the clusters seen as point-like particles without any internal degrees of freedom. This assumption is justified because of the slow dynamics of the only weakly interacting particles where the internal degrees of freedom are practically frozen in. The starting point of the simulation consists of introducing the desired number of point-like particles within a "computational periodic box" in a gas-like configuration. The process of condensation of the point-like particles is then simulated by means of an effective interaction which has been defined by averaging the complete interaction energy over many different (10^4) mutual orientations of the clusters. The obtained values of the energy as a function of the centre-of-mass distance r have been interpolated by a Morse potential

$$V_{eff}(r) = B\{ \exp[-2\alpha(r - \lambda_0)] - 2 \exp[-\alpha(r - \lambda_0)]\} \quad (2)$$

The value of λ_0 for a given cluster dimension is thus related to the cluster diameter. The condensation process has been carried out via a classical constant-pressure, constant-temperature MD scheme with a small, fictitious external pressure added to speed up the aggregation dynamics. A repeated simulated annealing procedure has produced the room temperature ground state characterized by the smallest volume and the highest cohesive energy.

(2) The second step of the SCC consists of replacing each point-like particle with a randomly oriented cluster centred at the equilibrium position of its "effective" particle. The relaxation process following the replacement of the point-like particles with the clusters has been performed by means of a constant-pressure, constant-temperature MD simulation generated by the Nosè–Parrinello–Rahman hamiltonian. As in the preceding step, periodic boundary conditions have been applied. The equations of motion have been integrated by a fifth-order Gear algorithm with a time step of 10^{-15} s. The final values of density and cohesive energy after relaxation at room temperature are reported in the first two columns of Table 2.

4. Results and discussion

The SCC technique described above does not mimic the actual process of cluster condensation, since the internal degrees of freedom are kept frozen during the early stage of the process. However, the result of the SCC process is a soft n-phase ($\rho \approx 0.8-0.9$ relative to the crystalline bulk density) similar to the "as-prepared" samples obtained in a gas condensation apparatus after ordinary rough compaction at room temperature. The sizes of grains in the final samples almost coincide with those of the initial clusters. As a consequence, SCC allows the control of the n-phase grain size. The resulting density derives from the presence of empty regions (or cavities) of various extents that may be considered stable at room temperature over the simulation duration (typically 1 ns). Moreover, the presence of a large amount of "interfacial" regions further contributes to the decrease in the overall density.

At the end of the SCC process the structure can be regarded as in a (deep) metastable phase. From this structure we have estimated all the thermodynamic and structural properties which have been further related to each other and compared with those of the bulk and the simulated amorphous state.

Several properties of Pd n-phases have been recently reported by Fitzsimmons et al. [16]. They are mainly related to (1) a lattice parameter almost independent of the average grain size, (2) a mean square relative displacement (MSRD) enhanced with respect to bulk crystals owing to the increased static displacements in the disordered regions and (3) a broad strain distribution (as determined by the width of diffraction peaks).

In order to ascertain the presence of the above properties in our simulated nanostructures, we have evaluated the radial distribution functions $g(r)$ for all
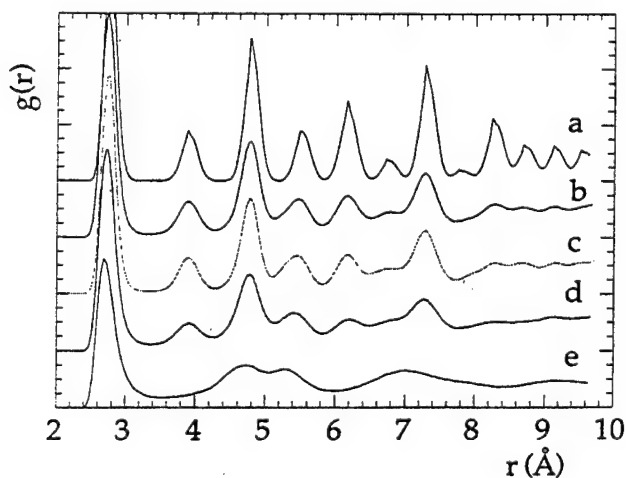

Fig. 1. Radial distribution functions $g(r)$ for several simulated systems at $T = 300$ K and $P_{ext} = 0$ after complete relaxation: a, crystalline bulk; b, n-923; c, n-586; d, n-309; e, amorphous.

the stable structures. In Fig. 1 we show the n-phase $g(r)$s compared with those pertaining to a bulk single crystal and an amorphous structure at the same temperature. The n-phase $g(r)$s have well-defined crystalline peaks at small distances. The first peaks exhibit a slight asymmetry which progressively increases as the grain size decreases, thus assuming the typical shape of the amorphous structure.

Analysis of the first-neighbour peak positions (Table 2) shows that the huge contraction of average first-neighbour distance detected in free clusters almost disappears. Therefore, despite the difference in grain dimensions, the average first-neighbour distances resulting from the various nanostructures are very similar.

The behaviour of the MSRD on going from one structure to another is related to the variation in the mean square amplitude of atomic vibration, $\langle u^2 \rangle$, and, more relevantly, to the static atomic displacement with respect to the f.c.c.-like equilibrium position. This information can be achieved via analysis of the width of the first-neighbour peaks. This parameter seems to be more sensitive to the final density of the nanostructure (see Table 2) since it increases with decreasing system density. While the average first-neighbour distance is not strictly related to the average density, the MSRD is much more sensitive to the local environment, thus indicating the presence of extended disordered regions (interfaces, free surfaces, etc.).

In order to investigate in more detail the structure-property correlations, we have performed stress analysis at the atomic level [29–32]. IWe have thus first evaluated the local pressure p_i and then attempted to relate it to the various n-phase regions. In the present context the pressure on particle i simply refers to the trace of its stress tensor σ, i.e.

$$p_i = \frac{1}{3} \sum_\alpha \sigma_i^{\alpha\alpha} \tag{3}$$

where

$$\alpha_i^{\alpha\beta} = -\frac{1}{\Omega_i} \sum_{j=1}^{n_i} (F_{ij}^\alpha r_{ij}^\beta + m_i V_i^\alpha v_i^\beta) \tag{4}$$

is the ordinary definition of the stress tensor, with Ω_i the atomic volume evaluated as [31]

$$\Omega_i = \frac{4}{3} \pi \left[\frac{\sum_{j=1}^{n_i} r_{ij}^{-1}}{\sum_{j=1}^{n_i} r_{ij}^{-2}} \right]^3 \tag{5}$$

Fig. 2 shows the distribution of the average values of single-particle pressure, $\langle p_i \rangle$, mediated over a significant time interval (10^4 time steps). The average pressure histograms are compared with those pertaining to bulk crystal and amorphous phase at the same temperature. as expected, the dispersion of the distributions is a decreasing function of the cluster size (see Table 2 for the value of the dispersion of the pressure distibutions).
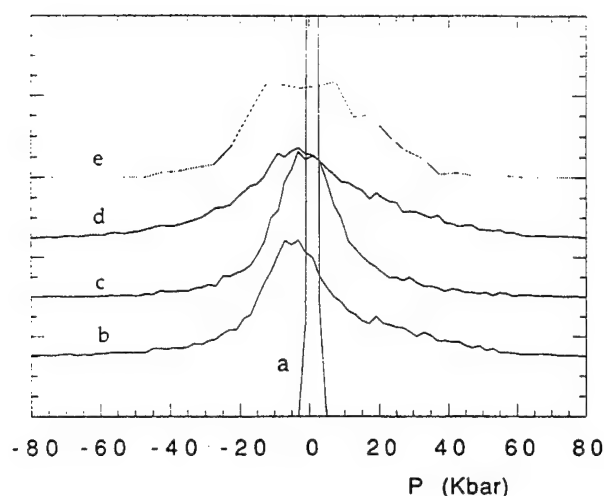
Fig. 2. Single-particle average pressure distributions for the same systems as Fig. 1.
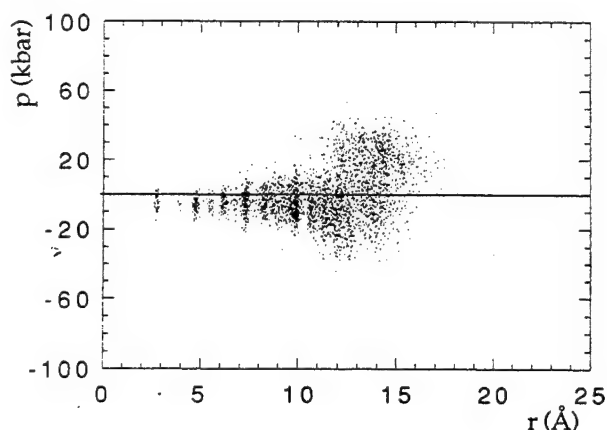

Fig. 3. Single-particle average pressure as a function of distance from grain centres for sample n-923.

As has been shown in a previous paper [25], the first-neighbour coordination is a good parameter for classifying the various structural regions in an n-phase. Atoms at free surfaces are expected to have a coordination less than 12 (typically 7–9), whereas atoms at GBs show a spread in the range 10–13 as in the amorphous phase.

In order to illustrate the pressure localization in our n-structures, we report the pressure distribution of atoms as a function of their distance from the centre of the grains to which they belong (Fig. 3). The dispersion of the average pressure of atoms belonging to the inner part of the grins is narrower than that pertaining to atoms of outer shells (i.e. interfacial regions and free surfaces).

5. Conclusions

In the prsent paper we have introduced a simulation technique which allows the efficient condensation of a gas of clusters to obtain a "soft" n-phase at low temperatures. MD simulations on the resulting n-phases have enabled us to establish the following.

(1) The average first-neighbour spacing is almost independent of the grain size. Small fluctuations of the average value are due to the presence of highly disordered regions that particularly affect the sample with the smallest grain size.

(2) The MRSD values are half-way between those of bulk crystalline solids and those pertaining to a simulated amorphous system.

(3) the local pressure distribution is even wider than that of a simulated amorphous system, despite the fact that n-phases do exhibit well-defined crystalline regions. This implies the presence of large strained regions localized at the interfaces, as can be inferred by the correlation between local pressures and distance from the grain centres (see Fig. 3). Moreover, the appearance of a strong strain field can be ultimately related to the "potential" driving force towards grain growth and cavity annihilation.

The average total thermodynamic and structural quantities evaluated for these systems exhibit a correct stationary behaviour over a long relaxation period (about 10^5 time steps). However, it has been remarked that the atomic pressures are inhomogeneously distributed. Although the global pressure is vanishingly small, there seems to occur a stationary pressure balance within various regions of the n-structures: bulk regions at a slightly negative pressure; interfacial regions with a resulting small positive pressure characterized by a large dispersion.

In principle, the comparison of the various simulated samples may provide a means to outline the effect of grain size on the relevant physical quantities. In fact, the grain size is just one of the parameters that characterize the samples: the global density of the aggregate and the shape of the grains (i.e. the GB geometry) also greatly influence the properties of the simulated samples. One of the methods that may allow us to isolate the grain size effect consists of designing different systems composed of the same number of clusters placed at given initial positions and orientations but with different sizes [33]. In the present paper only the n-923 and n-309 samples can be compared since they share the grain structure and termination. As expected, the system with the smaller grain size exhibits a larger MRSD and a lower cohesive energy.

However, the grain size does not seem to be the most relevant parameter to understand the n-phase behaviour. For instance, sample n-923 exhibits enhanced levels of strain and local pressure dispersion (see Table 2) with respect to sample n-586 which has a smaller grain size. In the former case both the density and fraction of bulk-like atoms seem to be more directly related to the presence of disorder and the pressure distribution.

One of the further steps of this work will be to anlayse the thermal stability of the n-phase in order to verify whether simple thermal annealing can bring the density up to $\rho = 1$, thus providing complete void annihilation. Preliminary results have indicated that the obtained dense n-phases are stable up to elevated temperatures ($T \approx 800$ K), where they do not exhibit any significant density increase. In this temperature range, owing to the short duration of the computer simulation, we have no appreciable grain growth, as would be expected [24]. Other important forthcoming results will be related to the response of the simulated n-phase to external stresses at room temperature.

Future applications on parallel computers will allow the simulation of larger systems whose grain sizes will be comparable with realistic samples. This breakthrough will certainly allow us to better compare simulation results with experimental data.

Acknowledgements

References

[1] W. Dickenscheid, R. Birringer, H. Gleiter, O. Kanert, B. Michel and B. Gunther, *Solid State Commun.*, 79 (1991) 683.

[2] G.W. Nieman, J.R. Weertman and R.W. Siegel, *J. Mater. Res.*, 6 (1991) 1012.

[3] V. Krstic, U. Erb and G. Palumbo, *Scr. Metall. Mater.*, 29 (1993) 1501.

[4] J.A. Eastman, M.R. Fitzsimmons and L.J. Thompson, *Philos. Mag. B*, 66 (1992) 667.

[5] J. Eckert, J.C. Holtzer and W.L. Johnson, *Scr. Metall. Mater.*, 27 (1992) 1105.

[6] R.W. Siegel, *Ann. Rev. Mater. Sci.*, 21 (1991) 559, and references cited therein.

[7] C. Suryanarayana and M. Fhroes, *Metall. Trans. A*, 23 (1992) 1071.

[8] G.W. Nieman, J.R. Weertman and R.W. Siegel, *Scr. Metall.*, 23 (1989) 2013.

[9] G.W. Nieman, J.R. Weertman and R.W. Siegel, *Scr. Metall. Mater.*, 24 (1990) 145.

[10] J.S.C. Jang and C.C. Koch, *Scr. Metall. Mater.*, 24 (1990) 1599.

[11] A.H. Chokshi, A. Roseu, J. Karch and H. Gleiter, *Scr. Metall. Mater.*, 23 (1989) 1679.

[12] T.G. Nieh and J. Wadsworth, *Scr. Metall. Mater.*, 25 (1991) 955.

[13] T. Haubold, R. Birringer, B. Lengeler and H. Gleiter, *Phys. Lett. A*, 135 (1989) 461.

[14] R.W. Siegel, in D. Wolf and S. Yip (eds.), *Material Interfaces*, Chapman and Hall, London, 1992.

[15] J. Wang, D. Wolf, S.R. Phillpot and H. Gleiter, *Proc. 2nd Int. Conf. on Nanostructured Materials*, Stuttgart, October 1994.

[16] M.R. Fitzsimmons, J.A. Eastman, M. Muller-Stach and G. Wallner, *Phys. Rev. B*, 44 (1991) 2452.

[17] W. Wunderlich, Y. Ishida and R. Maurer, *Scr. Metall. Mater.*, 24 (1990) 403.

[18] V. Rosato, M. Guillope and B. Legrand, *Philos. Mag. A*, 59 (1989) 321.

[19] F. Cleri and V. Rosato, *Phys. Rev. B*, 48 (1993) 22.

[20] C. Massobrio, V. Pontikis and G. Martin, *Phys. Rev. Lett.*, 62 (1989) 1142.

[21] C. Massobrio and V. Rosato, *Solid State Phenom.*, 28 (1992) 147.

[22] G. D'Agostino, *Philos. Mag. B*, 68 (1993) 903.

[23] G. D'Agostino, A. Pinto and S. Mobilio, *Phys. Rev. B*, 48 (1993) 14 447.

[24] J. Eckert, J.C. Holtzer, C.E. Krill III and W.L. Johnson, *J. Mater. Res.*, 7 (1992) 1751.

[25] M. Celino, G. D'Agostino and V. Rosato, *Proc. 2nd Int. Conf. on Nanostructured Materials*, Stuttgart, October 1994.

[26] V. Paillard, P. Melinon, V. Dupuis, J.P. Perez and B. Champagnon, *Phys. Rev. Lett.*, 25 (1993) 4170.

[27] G. D'Agostino, *Ph. D. Thesis*, University of Rome "La Sapienza", 1991.

[28] J. Jellinek, T.L. Beck and R.S. Berry, *J. Chem. Phys.*, 84 (1986) 2783.

[29] V. Vitek and T. Egami, *Phys. Status Solidi B*, 144 (1987) 145.

[30] T. Egami, K. Maeda and V. Vitek, *Philos. Mag. A*, 41 (1980) 833.

[31] D. Srolovitz, K. Maeda, V. Vitek and T. Egami, *Philos. Mag. A*, 44 (1981) 847.

[32] V. Rosato and F. Cleri, *J. Non-Cryst. Solids*, 144 (1992) 187.

[33] S.R. Phillpot, personal communication.

Processing of nano-scaled silicon powders to prepare slip cast structural ceramics

C. Bossel[a], J. Dutta[a,*], R. Houriet[a], J. Hilborn[b], H. Hofmann[a]

[a]*Laboratoire de Technologie des Poudres, Département des Matériaux, Ecole Polytechnique Fédérale de Lausanne, 1015 Lausanne, Switzerland*
[b]*Laboratoire des Polymères, Département des Matériaux, Ecole Polytechnique Fédérale de Lausanne, 1015 Lausanne, Switzerland*

Abstract

For slip casting of ceramic powders it is necessary to have a well-defined and thus disagglomerated colloidal suspension. Proper selection of the solvent is required in order to achieve separation of the particles to obtain a homogenous mixture of the powders which is necessary for shaping complex geometrical structures, often used in structural ceramics. Here we report a preliminary investigation of the deagglomeration phenomena of nano-scaled silicon powders obtained by plasma induced dissociation of silane and compare it with silicon nitride powders prepared by laser induced condensation reactions and a commercial product (UBE SE E-10). The size dispersion of aggregates in colloidal suspensions, determined by photon correlation spectroscopy and sedimentation particle size analysis techniques, varies from 20 to 500 nm. Variation in the deagglomeration properties of the particles in different solvents depends on the surface property of the powders, and on the inter-particle interactions. These are studied with respect to the variations in the surface property of the powders in different solvents. Ethanol was found to be a suitable solvent for the colloidal suspension as the average aggregate radii of the silicon powders could be reduced to 80 nm.

*Keywords:* Silicon powders; Ceramic powders; Nano

1. Introduction

Nano-structured materials are of interest as they show the potential for making ceramics with enhanced mechanical properties due to the fine microstructures. It is thus important to control the processing of the powders to be able to make ceramics with a controlled microstructure [1]. Silicon based advanced ceramics are being studied in great detail for mechanical and opto-electronic applications. In ceramic processing a good control of the processing parameters can be achieved through slip casting of the powders. Slip casting permits the homogeneous consolidation of powder and the realisation of complex shapes with a high density green body. The processing of nanometric powders hardly allows green body densities over 40%, as the high specific surface leads to the formation of hard agglomerates in the colloid [2]. As synthesized nanoparticles can be completely deagglomerated as long as the primary particles are merely held together by surface forces rather than being partially sintered by neck formation, which are usually referred to as hard agglomerates. In this work we report on the dispersion behaviour of nano-structured silicon powders in various solvents and examine the conclusions which can be drawn from it.

2. Experimental methods

Silicon nano-powders (a-Si:H) were prepared by gas phase reaction of silane in a capacitively coupled radio-frequency plasma-enhanced chemical vapour deposition (rf-PECVD) system and collected from the electrodes after the synthesis, in Balzers's laboratories (Balzers SA, Palaiseau, France) and CRPP (EPFL, Lausanne, Switzerland) [3]. Silicon nitride (Si_3N_4) powders were synthesized by laser induced reaction between silane and ammonia (as shown in reaction (1)) at ENEA (Area Innovazione, CR Frascati, Italy) [4].

$$3SiH_4 + 4NH_3 = Si_3N_4(s) + 12H_2 \qquad (1)$$
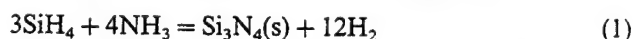
Commercial Si_3N_4 (UBE SN E-10) from UBE (Japan) was also studied for comparison.

* Corresponding author.

Mass loss and heat flow as a function of increasing temperature were recorded in a thermogravimetric differential analysis system (TGA/DTA Setaram 680), allowing estimation of the phase transformations of the powders. The use of different atmospheres, namely oxygen and Forming gas ($92\%N_2-8\%H_2$), gave valuable information on the oxidation behaviour of the powders.

The gas adsorption technique using nitrogen (BET method) and helium picnometry were carried out to determine, respectively, the specific surface and the density of the powders. Crystallinity and crystallite sizes were evaluated from XRD [5].

High resolution transmission electron microscopy (HRTEM) was carried out in a Phillips EM 430 on samples sprayed on the carbon coated copper grids. Estimation of the particle size was made from the TEM measurements. Bonding and chemistry of the surface was monitored by a Nicolet 510 FTIR spectrometer from pellets made by mixing the powders with potassium bromide. Electron spectroscopy for chemical analysis (ESCA) was used to determine the atomic stoichiometry of the powder surface.

Colloids were prepared with a powder concentration between 15 and 50 vpm (0.03 and 0.1 g l^{-1}). All samples were dispersed for 10 min in an ultrasonic water bath. Solvents used were: distilled water, ethanol, isopropanol, ethylene glycol, methyl ethyl ketone, acetyl acetone, acetone, triethylamine and dimethyl acetyl acetate.

The agglomerate or aggregate sizes in the colloids were determined by two methods. The first method was by sedimentation (Horiba Capa 700), which is based on the attenuation of transmitted light during sedimentation and which can measure particles larger than 100 nm. The second method used was photo correlation spectroscopy (PCS, on a Malvern Zetasizer 4 or BrookHaven Instrument), based on scattering of light by particles, which allows the estimation of particles as small as 5 nm.

3. Results and discussion

3.1. Morphological analysis

A typical transmission electron micrograph showing the particle aggregation in a-Si:H powders is shown in Fig. 1. It can be observed that the particles are aggregated into larger blocks, probably due to the electrostatic interactions (Fig. 1). XRD allows the estimation of the average crystallite diameter [6] by the use of the Debye–Scherrer law (not considering any strain effects), from the broadening of the crystalline peaks. Crystallites form a small part of the primary particles, mostly amorphous, which grow into larger sizes after

heat treatment at elevated temperatures [6]. The crystallite size estimated from XRD for the as synthesized a-Si:H powders (~ 3 nm) is at the limit of thermodynamic equilibrium between the amorphous and the crystalline states. Short range ordering of the bond angles in the silicon matrix of the a-Si:H powders was interpreted from Raman spectroscopic measurements [3].

BET gives information on the specific surface of the powder, which can be utilised to calculate the average diameter of the primary particles if we suppose that they are spheres with regular surfaces. These assumptions are justified from the observations made in TEM [6]. The specific surface area was 160 m^2 g^{-1} for the a-Si:H powders, which corresponds to primary particle sizes of 20 nm, comparing well with the particle sizes determined by TEM (20–30 nm).

3.2. Chemical analysis

a-Si:H powder was heated at low temperatures (between 80 and 200 °C) in a thermogravimetric analyser (TGA) system, in air and in a reducing atmosphere. Aggregate sizes after annealing were measured by PCS, to check the influence of oxidation and adsorbed moisture on the surface chemistry and the aggregation phenomena. The loss of water around 100 °C was observed but no difference in aggregate sizes was observed. This suggests that the surface is oxidized, and that the adsorbed water has no influence on colloidal dispersion.
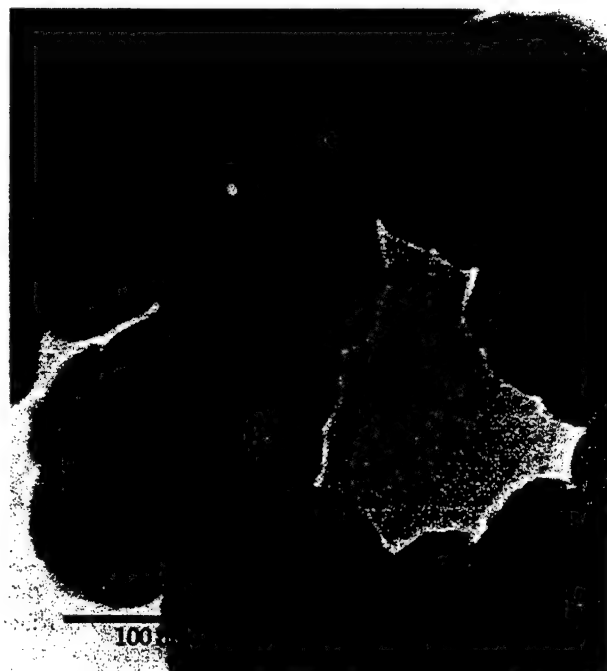

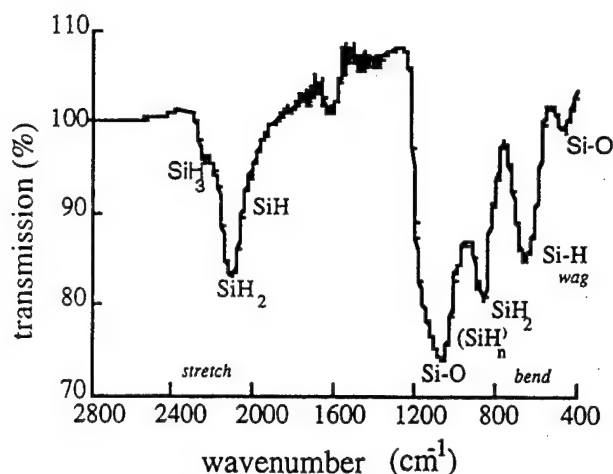Fig. 1. TEM micrograph showing the microstructure of the powder.

Fig. 2. Infrared spectrum of the silicon powder.

Heating at higher temperatures showed exothermic peaks at 350 and 620 °C, which are believed to be the signature of the loss of weakly bonded hydrogen and the beginning of crystallization, respectively.

The chemistry of the surface controls the colloidal properties. Post-oxidation analysis of silicon nitride in TGA suggests that the powder contains about 6% oxygen, presumably at the surface as silicon suboxides. ESCA measurements further confirm that oxygen accounts for 30 at.% of the superficial layers of a-Si:H powders, and 25% of Si_3N_4 powders. Carbon is present as carbides or as carbonates in the surface as well, 1.5% in a-Si:H powders, and 6% in Si_3N_4, evidently due to the contamination from exposure to the atmosphere. Also, due to the synthesis from silane the a-Si:H powders contain about 20 at.% hydrogen. In Fig. 2 a typical infrared spectrum of the silicon powder studied here is presented. Since the small particles are very reactive due to their large specific areas, exposure to atmosphere immediately oxidizes the powders, as can be observed from the Si–O absorption band centered at 1100 cm^{-1}. The oxygen is mostly bonded to the surface of the powders, as can be interpreted from the presence of Si–O$_3$ absorption at 2240 cm^{-1}. Silicon and hydrogen are bonded in clusters, as can be observed from the absorption peaks at 880 cm^{-1}, 2080 cm^{-1} and 2100 cm^{-1}, which are attributed to Si–H$_2$ bending, Si–H$_2$ stretching and (Si–H$_2$)$_n$ stretching, respectively. Furthermore, the presence of Si–O absorbtion at 1100 cm^{-1} suggests bridging-type oxygen bonding on the surface.

The characteristics of the oxygenated surface would be different for different amounts of oxygen in the powder. This can strongly influence the dispersion characteristics and so the results obtained in these experiments cannot necessarily be extrapolated to oxygen free samples.

3.3. Ultrasonic dispersion

In dry powder an agglomeration of primary particles is almost inevitable. In the colloidal state, several binding forces have to be counteracted in order to achieve an acceptable disagglomerated state. The major binding forces which are experienced by the particles in a low viscosity solvent are: (1) binding by adhesion forces between the particles, essentially due to Van der Waals interaction; (2) binding by wetting liquids: these boundary forces are in addition to the capillary under-pressure in the liquid bridges and they are stronger than the adhesion forces but less influenced by the surface roughness.

Dispersion of the powders essentially requires counteracting these two forces by physico-chemical and mechanical means to an extent that minimizes the aggregate sizes. In order to achieve this situation, it is absolutely essential to achieve good wetting of the solid particles by the liquid, deagglomeration of the aggregates and stabilization of the suspension to prevent renewed agglomeration.

Ultrasonic dispersion was used to disperse the aggregates from the agglomerates. Above a power level of 1 W, ultrasonic waves in liquid form cavities which implode, producing an intense pressure gradient (20 GPa cm^{-1}) [7]. We monitored the size of agglomerates in the suspension after various time delays of ultrasonic dispersion in the bath at a constant power. The agglomerate size decreases during the first 3 min of ultrasonic dispersion, and then reaches a minimum value which is believed to be the best dispersion possible under the present conditions. For all the samples we carried out the ultrasonic dispersion for 10 min. It has been reported that if ultrasonic dispersion is carried out for a longer time, aggregation of particles during implosions is observed, which we did not see under our present conditions.

3.4. Choice of the solvent

To obtain non-agglomerated sterically stabilized suspensions, strongly attached and dense layers of dispersant molecules are required on the powder surface. A strong adsorption is obtained by the interfacial Lewis acid–base interactions between dispersant and surface site of the powder [8]. Another condition to obtain a stabilized suspension requires a solvent of low surface energy so as to wet the surface, which essentially means that the solvent must have a low dipolar moment. For example, distilled water could not be used to disperse our powders because of its high polarity, even after changing the polarity in pH or ionic content. Organic additives such as polyoxyethylene (Tween 80) had to be added in water to achieve wetting. But these additives create bubbles during the ultrasonic dispersion process, sometimes adversely influencing the PCS measurements.

A parameter F is often used to characterize the suitability of dispersing solvents, where F is given by [9]

$$F = \frac{\eta \epsilon}{\mu}$$

where η (cP) is the viscosity, ϵ is the dielectric constant and μ (D) the dipolar moment.

A solvent with a low F is characterized by the tendency to create electrical charges on an initially uncharged surface to electrostatically stabilize the particles. Without this stabilization the particles would tend to re-agglomerate after the ultrasonic dispersion process. We measured the mean diameter of particles in several colloids (Fig. 3) with the same amount of a-Si:H powder, but different solvents, and monitored the re-agglomeration phenomenon as a function of time. The mean diameter of agglomerates was not proportional to F, which might mean that the surface was already charged before the wetting treatment.

One of the best solvents to achieve nearly total deagglomeration seems to be ethanol. We studied the mixtures ethanol + MEK (methyl ethyl ketone) and ethanol + water with the powders a-Si:H and Si₃N₄ (Fig. 4). From this study it appears that the best stabilization is achieved when the ethanol content in the solvent is maximum, essentially thus motivating our choice of ethanol as the solvent for dispersing this type of powder. The measured diameter of the aggregates in all the powders considered in this study after the ultrasonic dispersion is shown in Table 1.

The ultrasonic treatment of the colloidal suspension leads to the rupture of weak bonds between aggregates but stronger chemical bonds between primary particles are difficult to break. The estimated particle size in the colloids is then the size of the strong aggregates between primary particles. Knowing the diameter of primary particles, d_{prim}, and the diameter of aggregates, d_{agg}, we can calculate the maximum number of particles

Fig. 4. Diameter of a-Si:H and Si₃N₃ aggregates in a mixture of varying amount of ethanol and MEK or water.

per aggregate or the fractal dimension of aggregate by using [10]

$$N = \left(\frac{d_{agg}}{d_{prim}} \right)^3$$

The average diameter in the colloid, as measured for a-Si:H, is 150 nm, which means that no more than 420 primary particles are contained per aggregate. Following similar reasoning, we estimate that no more than 1400 particles of Si₃N₄ form an aggregate. The particles are necked to each other rather than sintered into one mass; thus the particles are obviously smaller in number in the aggregates. Observation by HRTEM confirms these estimations (Table 2).

3.5. Formation of the aggregates

In the rf-plasma, large hydrogenated silicon clusters are formed by condensation reactions resulting in negatively charged clusters having highly cross-linked three-dimensional structures [11]. The formation of small clusters, at least up to about 40 atoms of silicon, arises from negative ion polymerization in low pressure silane discharges, while anion–neutral and neutral–neutral condensation leads to homogeneous nucleation that ultimately results in the formation of the powders. The growth of the clusters is limited and when they get larger they may get ejected and attach to one of the
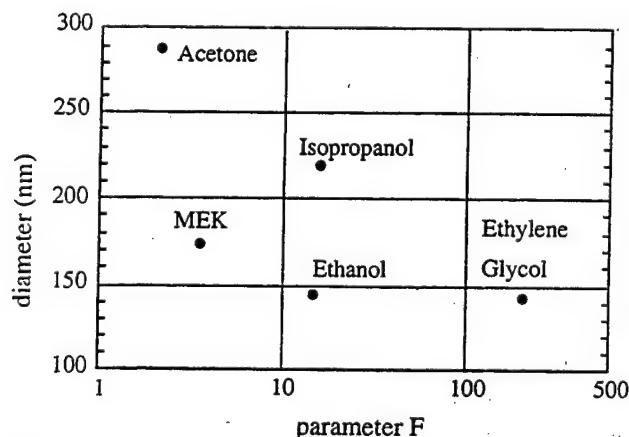

Fig. 3. Diameter of a-Si:H in various solvents. No correlation is observed between the standard $F = \eta \epsilon / \mu$ and the agglomerate diameter.
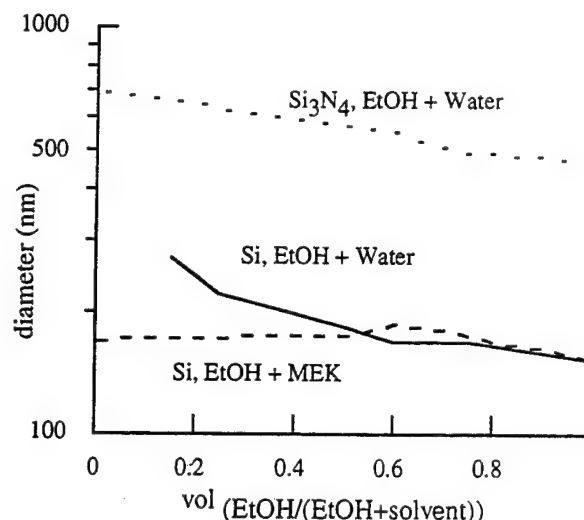
Table 1
Diameter (nm) of particle agglomerates in three different solvents

	EtOH	Water	MEK
a-Si:H	146 ± 11	–	162 ± 15
Si₃N₄ (ENEA)	470 ± 30	720 ± 50	530 ± 50
Si₃N₄ (UBE E-10)	650	630	

Table 2
Morphological sizes observed by different analytical methods

	XRD	BET	PCS	TEM
Observed object	crystallites	primary particles	aggregates	all
a-Si:H, average diameter	3 nm	20 nm	150 nm	20–150 nm
a-Si$_3$N$_4$ (ENEA), average diameter	1 nm	40 nm	450 nm	40–450 nm

electrodes where they are eventually collected. As the larger clusters are in continuous motion in the plasma they have a high probability of collision, which might lead to larger chemically bonded clusters. The overall mechanism of agglomeration is shown in Fig. 5. The charged clusters create an electrostatic repulsion between the particles, and in addition, face the gravitational force, drag due to gas flow, along with the force due to the electrical field across the electrodes [12]. Above a given size, the balancing forces are disturbed and the aggregates can no longer be sustained by the plasma; thus they get ejected. In the case of laser driven reactions, the primary agglomeration phase occurs in the gas phase and once the balancing forces consisting of the thermophoretic forces, the drag due to gas flow and the gravitational forces are overcome, the agglomerates are ejected from the reactor for collection.

observed in amorphous silicon as determined by photocorrelation spectroscopy. The silicon nitride powders obtained by laser driven reactions form aggregates of about 250 nm radii, while the commercial UBE powders are dispersed in aggregates of 300 nm sized radii, which agrees well with the literature. The smaller aggregate sizes of the powders synthesized by plasma processing could be due to the inherent properties of the plasma. Detailed study of the cluster growth and the development of the powder in the plasma will add more light to this observation. The a-Si:H powders obtained by the plasma reaction of silane qualify well for slip cast because of the uniform shape to the spherical aggregates. However, further studies have to be carried out to verify the advantages of small sized agglomerates of powders obtained by plasma induced condensation reactions, and to clarify whether these conclusions are universally true for the other silicon alloys.

4. Conclusions

The properties of the colloidal suspensions necessary to prepare slip cast ceramics depend upon the solvents used. Ethanol was found to be a suitable universal solvent for the powders studied here as it dispersed the agglomerates into the smallest aggregates when compared with suspensions made in other solvents. Particle size measurements of the dispersion of nano-sized a-Si:H powders obtained by plasma driven reactions of silane, and Si:N powders obtained by laser driven reactions of silane and ammonia suggest that the primary particles form chemically bonded aggregates, which are difficult to separate. Aggregate sizes of 80 nm radii were

References

[1] F.F. Lange, B.V. Velamakanni, J.C. Chang and D.S. Pearson, Proc. 11th Riso Int. Symp. on Metallurgy and Material Science, 1990, pp. 57–78.
[2] I.A. Aksay, G.C. Tangle and M. Sarikaya, Ceramic Powder Processing Science, Proc. 2nd Int. Conf., Berchesgaden, FRG, 1988, p. 463.
[3] J. Dutta, W.S. Bacsa and C. Hollenstein, J. Appl. Phys. (1995) in press.
[4] E. Borsella, S. Botti, M.C. Cecile and A. Nesterenko, US–Italy Workshop on Advanced Materials, 1993.
[5] J. Dutta, I.M. Reaney, C. Bossel, R. Houriet and H. Hofmann, Nanostruct. Mater. (1995) in press.
[6] B.D. Cullity, Element of X-Ray Diffraction, Addison-Wesley, New York, 1978, p. 289.
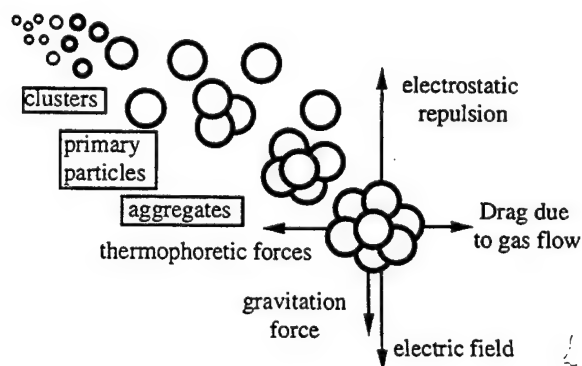[7] L.D. Rozenberg, High Intensity Ultrasonic Fields, Plenum Press, New York, 1972, p. 263.

Fig. 5. Model of powder agglomeration during synthesis in plasma.

[8] F.M. Fowkes, in K.L. Mitttal (ed.), *Surface and Colloidal Science in Computer Technology*, Plenum Press, New York, 1987, pp. 3–25.

[9] M. Lihrmann, in Duran and Fernandez (eds.), *Third Euro-ceramics VI*, Faenza Edice Iberica, Spain, 1993, pp. 27–32.

[10] P.J. Van der Put, R.A.Bauer and J.Schooman, in G.L. Messing (ed.), *Ceramic Powder Science III*, American Ceramic Society, Westerville, OH, 1990, pp. 259–266.

[11] C. Hollenstein, J.-L. Dorier, J. Dutta, L. Sansonnens and A.A. Howling, *Plasma Sources Sci. Technol.*, 3 (1994) 278–285.

[12] J.-L. Dorier, C. Hollenstein and A.A. Howling, *J. Vac. Sci. Technol. A*, (1995) in press.

Particle structure control in nanoparticle synthesis from the vapor phase

Richard C. Flagan, Melissa M. Lunden

California Institute of Technology, Pasadena, CA 91125, USA

Abstract

Nanostructured materials have generally been synthesized by condensation from the vapor phase in an inert carrier gas, most often in a buoyant plume above a hot vapor source. Particles form by homogeneous nucleation as the gases cool and grow by Brownian coagulation. Previous studies have shown that the size of the smallest structures is reduced with decreasing pressure, so most nanoparticle synthesis is performed at low pressures. The crystallites produced by this method are subunits of larger agglomerate particles, often with substantial neck formation that interferes with consolidation. Examination of the theory of particle growth under such conditions reveals that, once agglomerate particles begin to form, particle growth rapidly accelerates. The crystallite size is, therefore, determined by the growth prior to the onset of agglomeration. From this analysis, it is seen that the rate of production of nanoparticles can be increased dramatically if the synthesis reactor is operated at higher pressure, with correspondingly shorter growth times. The growth time is determined by the effective cooling rate in the growth region of the reactor. Short growth times are achieved by rapid cooling. Neck formation in those agglomerate particles that do form is diminished by starting the growth process at a high initial temperature.

Keywords: Vapour phase; Synthesis

1. Introduction

The predominant technology for laboratory synthesis of nanoparticles from the vapor phase is the so-called inert gas condensation method with which Gleiter and coworkers [1,2] first generated the materials that demonstrated the exciting properties of nanostructured materials. The roots of this technology are generally traced back to the pioneering work of Granqvist and Buhrman [3], although the extensive investigations of the thermodynamically stable and metastable crystals by Uyeda and coworkers [4,5] over 20 years were based on the technique. Much earlier, Pfund [6] employed this basic approach for the synthesis of bismuth fumes. Earlier yet, carbon black and lamp black were produced by methods that differ from the methods of Gleiter primarily in their execution at atmospheric pressure with a chemical reaction source for the particulate material. Indeed, carbon particles produced as a fume from the vapor phase have nanometer-scale fine struc-

tures and form the basis of a large volume nanocomposite, namely rubber that has been reinforced with carbon black to improve the wear properties of tires. Our interest here focuses on extensions of the modern incarnation of this technology for the synthesis of nanostructured metals, ceramics, and semiconductors.

In the inert gas condensation method, a metal is vaporized into a low density gas, typically helium. Typically, the temperature required for vaporization is achieved by Joule heating, although thermal plasmas [7], laser ablation [8] and spark ablation sources [9] operate in essentially the same manner. Vapors migrate from the hot source into a cooler gas by a combination of convective flows and diffusion. Although dilution resulting from the latter transport mechanism decreases the partial pressure of the vapor from the saturation condition at the source, the decreasing temperature leads to a far more rapid decrease in the equilibrium vapor pressure and correspondingly high supersaturation. This effect is amplified by using helium, which has

a very high thermal conductivity. At high supersaturation, the vapors rapidly nucleate, forming very large numbers of extremely small particles. The particles then grow by Brownian coagulation as they are advected away from the source in the thermal plume or forced flow. Ultimately, the particles are collected for subsequent consolidation. The particles are generally collected by thermophoretic deposition on a cold surface [3,4], the same technology that has been used since ancient times in the production of carbon black. Most applications of the inert gas condensation method carry this approach to extremes by cooling the deposition substrate with liquid nitrogen to enhance the deposition efficiency.

Particles collected in this manner are highly concentrated on the deposition substrate. While the particles deposited on the substrate have a complex aggregate morphology, the material is generally described in terms of the size of the crystallites that make up the larger structures. However, the crystallite size is only part of the picture. Kaito [10] demonstrated quite clearly that the nature of these particles could be altered by heating the plume above the source. When the plume was not heated, MoO_3 crystallites only grew within about 30 mm of a 0.5 mm diameter Mo wire. A range of particle sizes and structures was seen above that height, depending upon the position relative to the center of the smoke plume, but the sizes on any streamline did not appear to change appreciably. If, however, a second heater was placed above the source wire so that the plume passed between heated grids, the crystallite size did increase. This was attributed to the coalescence of the crystallites that make up the complex aggregate particles present in the plume. While such aggregate particles are useful in some applications, notably in structure blacks that are used for reinforcing rubber and other polymers, hard agglomerates severely hinder the consolidation of metal and, especially, ceramic powders.

Some definitions are required for the work that follows. By "particle" we mean the entity that moves as a unit in the aerosol phase, although it is the size of the crystallite subunit that has received the greatest attention in the literature on nanostructured materials. Measurements of crystallite size by electron microscopy frequently yield estimates that severely underestimate the total particle volume or mass. Nguyen and Flagan [11] compared transmission electron microscopy (TEM) estimates of the sizes of particles with measurements based on the migration of singly charged particles in an electric field for particles synthesized by thermal degradation of dilute silane gas in a nitrogen carrier. The TEM-determined sizes are in the 10 to 20 nm range and decrease with increasing silane concentration. Measurements based on the mi-

gration velocity of singly charged particles in an electric field, on the other hand, suggest a much larger particle size, ranging from 40 nm to nearly 200 nm at the highest silane concentrations. This mobility size is closely related to the projected area of the particle. The difference between these two size estimates reveals a substantial deviation of the particle structure from the dense, roughly spherical particles that TEM analysis might suggest. The small subunits that comprise the particles are the so-called "primary particles" that coagulated to form the larger agglomerate. The primary particles may be strongly bound together as a result of neck growth, forming a "hard agglomerate" or "aggregate", or they may be weakly bound together by Van der Waals forces to form a "soft agglomerate".
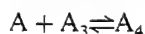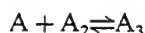
The strength of the bonds between the primary particles that comprise an agglomerate may vary widely, depending on the material properties, the atmosphere, and the temperature–time history that the particle has experienced subsequent to collision with other primary particles due to Brownian motion. Coagulation is a general term that is used to describe particle combination by Brownian motion or other mechanisms, and it is generally applied to particle combination with complete coalescence. Agglomeration refers to the combination of particles in which the primary particles remain identifiable, and may be applied to the formation of either soft van der Waals or hard, sintered agglomerates. Soft agglomerates, being formed at temperatures too low for significant coalescence, may be separated into their component primary particles with relative ease, facilitating subsequent consolidation. Consolidation of powders containing hard agglomerates, on the other hand, is much more difficult, frequently resulting in densities well below the theoretical limit.

In this paper, we seek to understand the dynamics of nanoparticle synthesis reactors sufficiently well to facilitate the production of nanoparticles with minimal hard agglomerates. Although it is the major technology being used in the development of nanostructured materials technology and provides most of the data on the relationship between operating parameters and material properties, the inert gas condensation system is far from optimal for large-scale production of nanoparticles. In the discussion that follows, we focus on the particle dynamics that must be understood to achieve the needed control over particle properties. While we shall examine the consistency of the models developed with the existing database, we do not attempt to model the complex, buoyancy-driven flows of inert gas condensation systems. Instead, we develop one dimensional models that highlight the processes that dominate particle growth and structural evolution in nanoparticle synthesis.

2. Particle formation and growth

2.1. Particle inception and vapor deposition

Vaporization of a refractory material from a hot source, be it produced by Joule heating, by a thermal plasma, or by any other method, into low pressure gas leads to rapid and extreme supersaturation as the vapors cool. High supersaturation favors the growth of small clusters. Initially, the clusters grow by monomer addition,

$$A + A \rightleftharpoons A_2$$

$$A + A_2 \rightleftharpoons A_3$$

$$A + A_3 \rightleftharpoons A_4$$

$$\cdots$$

$$A + A_{g-1} \rightleftharpoons A_g$$

$$\cdots$$

The addition of monomers to the growing clusters can be estimated from the kinetic theory of gases, but the reverse term is not known a priori. The frequency of evaporation of monomers from the cluster is estimated by application of the principle of microscopic reversibility, equating the rates of condensation and evaporation at full thermodyamic equilibrium. Unfortunately, the free energy of the small clusters is not well understood, so estimates are generally required. The classical derivation employs the so-called capillarity approximation in which the free · energy of a cluster containing g molecules is modeled as equivalent to g molecules of bulk material (usually taken to be liquid) with an additional surface free energy term. In the absence of more detailed information, the surface free energy is generally approximated by that of the bulk liquid, introducing a large uncertainty into the calculated nucleation rate. If one further assumes that a steady-state cluster distribution persists during the period when most of the new particles are formed, the nucleation rates becomes

$$J = \frac{p_v v_1}{\sqrt{2\pi m_v kT}} \sqrt{\frac{\sigma}{kT}} N_1 \exp\left[-\frac{16\pi\sigma^3 v_1^2}{3(kT)^3 \ln^2 S}\right] \quad (1)$$

Although predicted nucleation rates frequently deviate from measured rates by many orders of magnitude, this expression clearly predicts the observed strong dependence of the rate of particle formation on the saturation ratio, $S = p_{vap}/p_{sat}(T)$, and the surface tension, σ, and yields reasonable predictions of the value of S at which the nucleation rate becomes appreciable. For the refractory materials that have been the focus of most nanostructured material synthesis and for the extreme variations in temperature that occur in the inert gas condensation system, nucleation usually begins very abruptly and proceeds at a very high rate. The particles

thus produced serve as sinks for additional vapor, quickly reducing the supersaturation and quenching additional nucleation. Large numbers of extremely fine particles are generated in this brief nucleation burst. Although the particles grow somewhat by condensation, the vapor partial pressure is quickly depleted. The particles then grow by Brownian coagulation.

While the process outlined above is typical of present nanoparticle synthesis systems, nucleation can be slowed if the supersaturation is limited. Allowing nucleation to occur at relatively low supersaturation, the rate of particle formation is reduced, leading to lower initial number concentrations. These particles can then be grown to larger size as additional material is deposited on the surfaces of the growing particles. This approach has been demonstrated most effectively in particle synthesis by gas phase chemical reactions in which the reaction rate was gradually accelerated as the initial nuclei grew, producing a much narrower size distribution of nanometer sized particles than resulted from reaction at a higher temperature in an isothermal reactor [12,13]. The rate of vapor deposition on a nanoparticle is directly proportional to the particle's projected area. Assuming that all molecules that arrive at the particle surface contribute to particle growth, the time rate of change in the particle radius is

$$\frac{da}{dt} = \frac{N_1 \bar{c}}{4} \quad (2)$$

If the nucleation burst produces particles ranging in size from a_0 to $a_0 + \Delta a$, the upper and lower bound sizes will increase due to vapor deposition, but the range of sizes will not change. Thus, the relative range of particle sizes, $\Delta a/a$, will decrease as the particles grow, leading to a narrower distribution as observed by Okuyama et al. [13]. This phenomenon has been used effectively in nanoparticle synthesis by Bowles et al. [14], who generated clusters of controlled size, i.e., dimers, and then grew them by vapor deposition, leading to a very narrow particle size distribution. These methods have generally been applied to laboratory investigations of particles and clusters rather than to the production of the quantities of materials needed for studies of nanostructured materials.

2.2. Coagulation and agglomeration

In most refractory particle synthesis systems, very large numbers of small particles are produced during the nucleation burst. Their growth by condensation is limited by the amount of vapor in the system. The particles continue to grow, however, due to Brownian coagulation. While the particles are small and the gases relatively hot, particles coalesce quickly after agglomeration. Later, however, due to decreasing mobility of the atoms in the small particles and decreasing excess sur-

face free energy driving forces, the coalescence slows, and the particles grow as low density agglomerates. Although the fine structure of the resulting particles may be on the desired nanometer scale, the particles are actually much larger and may be quite rigid, hindering consolidation of the powder. To understand the competing processes that govern the structure of nanoparticles, we must examine each of the mechanisms involved in the particle growth.

We seek to understand the evolution of the particle size distribution due to Brownian coagulation. Systems of interest for nanoparticle synthesis generally involve substantial temperature variations. To avoid confusion with temperature effects on the particle concentration, it is convenient to express the particle concentration on a mass rather than a volumetric basis, i.e., we define the total number of particles per unit mass of gas in the system at time t as $N(t)$. The number of particles per unit mass with volumes between v and $v + dv$ is $dN(t) = n(v,t)dv$, where $n(v,t)$, the continuous representation of the particle size distribution, is related to the conventional volumetric size distribution function $\tilde{n}(v,t)$ by

$$n(v, t) = \rho \tilde{n}(v, t) \tag{3}$$

and ρ is the gas density. The growth of aerosol particles by coagulation is described by an integro-differential equation,

$$\left(\frac{\partial n(v, t)}{\partial t}\right)_{\text{coag}} = \frac{1}{2}\int_0^v \rho K(v - u, u)n(v - u, t)n(u, t)\,\mathrm{d}u$$

$$- n(v, t)\int_0^\infty \rho K(v, u)n(u, t)\,\mathrm{d}u \tag{4}$$

where $K(v,u)$ is the rate coefficient for Brownian collisions between particles of volumes u and v. The first term on the right-hand-side describes the formation of particles of volume v by coagulation of smaller particles. The second term describes the loss of such particles by coagulation with particles of any size. Although the particle sizes of interest are small, the numbers of atoms involved are sufficiently large that the continuous representation of the particle size distribution is an excellent approximation that leads to some simplifications for predicting the performance of nanoparticle synthesis systems.

Even at atmospheric pressure, nanoparticles remain small compared to the mean-free-path of the gas molecules λ throughout their growth. The appropriate collision frequency function for modeling nanoparticle synthesis is, therefore, that for coagulation of free molecular particles, i.e.,

$$K(v, u) = A_{\text{collision}} \frac{\bar{c}_{uv}}{4} \tag{5}$$

The mean relative thermal speed of the two particles is

$$\bar{c}_{uv} = \sqrt{\frac{8kT}{\pi \rho_p}}\left(\frac{1}{v} + \frac{1}{u}\right)^{1/2} \tag{6}$$

and $A_{\text{collision}}$ is the collision cross-sectional area. Early in the growth process, the particles coalesce rapidly and may, therefore, be assumed to be spherical, so that

$$A_{\text{collision,s}} = 4\pi\left(\frac{3}{4\pi}\right)^{2/3}(v^{1/3} + u^{1/3})^2 \tag{7}$$

The collision frequency function for spherical particles thus becomes

$$K_s(v, u) = \kappa(v^{1/3} + u^{1/3})^2\left(\frac{1}{v} + \frac{1}{u}\right)^{1/2} \tag{8}$$

where

$$\kappa = \left(\frac{3}{4\pi}\right)^{1/6}\sqrt{\frac{6kT}{\rho_p}} \tag{9}$$

Late in the growth process, coalescence slows and the particles take on complex agglomerate structures that are fractal-like. For mass-fractal particles, the volume of particulate material contained within a region of radius r scales as

$$v \approx v_0\left(\frac{r}{r_0}\right)^{D_f} \tag{10}$$

where

$$v_0 = \tfrac{4}{3}\pi a_0^3$$

is the volume of the so-called primary particles (radius a_0) that comprise the agglomerate, and D_f is the mass-fractal dimension of the particle. For a wide range of aerosol systems, the fractal dimension for solid particles grown by coagulation at temperatures sufficiently low that coalescence does not appreciably alter the particle shape, the fractal dimension is approximately $D \approx 1.8$. The collision radius for a particle of volume v thus scales as

$$r \approx a_0\left(\frac{v}{v_0}\right)^{1/D_f} \tag{11}$$

The collisional area for free molecular coagulation of mass-fractal particles of volumes u and v is thought to scale as [15]

$$A_{\text{collision,a}} \sim \phi(v^{1/D_f} + u^{1/D_f})^v \tag{12}$$

where $v = \text{Min}(D_f, 2)$. The parameter ϕ has been introduced for dimensional consistency. If we require that $A_{\text{collision,a}}(v_0,v_0) = A_{\text{collision,s}}(v_0,v_0)$, we find

$$\phi = 4\pi\left[\frac{3}{4\pi}\right]^{2/3} 2^{2 - v} v_0^{2/3 - v/D_f} \tag{13}$$

and the collision frequency function becomes

$$K_a(u, v) = 2^{2 - v}\kappa v_0^{2/3 - v/D_f}(u^{1/D_f} + v^{1/D_f})^v\left(\frac{1}{u} + \frac{1}{v}\right)^{1/2} \tag{14}$$

This expression reduces to $K_s(u,v)$ for $D_f = 3$ and $v = 2$.

Examination of the two forms of the collision frequency function reveals some important features of the transition from coalescent coagulation to agglomeration. Consider first the coagulation coefficients for particles of equal volumes, i.e., $K_s(v,v)$ and $K_a(v,v)$. The ratio of these two rate parameters is

$$\frac{K_a(v, v)}{K_s(v, v)} = 2^{2-v}\left(\frac{v}{v_0}\right)^{v/D_f - 2/3} \tag{15}$$

For a typical fractal dimension of 1.8, the exponent on v becomes 1/3. We see that, as particles grow beyond a starting volume, v_0, the rate constant for growth of agglomerate particles accelerates beyond that for spheres. Hence, once particles begin to agglomerate, growth accelerates. This is illustrated in Fig. 1 for a typical fractal dimension of 1.8, showing that agglomerate particles will coagulate much faster than spheres of equal volume. The range of volumes examined here is large, but recall that an increase in volume of 10^3 results in an increased radius for spherical particles of a factor of 10.

The effect of agglomerate structure on coagulation is even more pronounced for particles of different sizes. We consider the coagulation of particles of volumes v and βv. The ratio of the coagulation rate coefficient for spherical particles of different volumes to that for particles of equal volumes is

$$\frac{K_s(v, \beta v)}{K_s(v, v)} = (1 + \beta^{1/3})^2\left(1 + \frac{1}{\beta}\right)^{1/2} \tag{16}$$

while that for agglomerate particles is

$$\frac{K_a(v, \beta v)}{K_a(v, v)} = (1 + \beta^{1/D_f})^v\left(1 + \frac{1}{\beta}\right)^{1/2} \tag{17}$$

These ratios are compared in Fig. 2. In both cases, the collision frequency function increases as β increases, but the rate of increase is greater for agglomerate particles. Thus, once a range of particle sizes is present in the aerosol, particles of differing sizes will coagulate more rapidly than large or small particles of comparable size. The fast increase in the coagulation rate con-

Fig. 2. Variation of the coagulation rate coefficient with relative particle volume for particles of different volumes. Solid line, aggregate particles with fractal dimension D_f; dashed line, spherical particles.

stant for agglomerates arises from the rapid increase in the collision area of the agglomerate particles. The large particles present a large target for impingement of the more mobile smaller particles. This reinforces the conclusion that once agglomerates begin forming, they will grow more rapidly than dense particles, often at the expense of dense particle growth.

2.3. Population dynamics

The collision frequency function is said to be homogeneous of degree γ if

$$K(\beta\eta, \beta\tilde{\eta}) = \beta^\gamma K(\eta, \tilde{\eta}) \tag{18}$$

Both of the collision frequency functions presented above are homogeneous. The degree of homogeneity for spheres is $\gamma = 1/6$, while that for agglomerates is $\gamma = \dfrac{v}{D_f} - \dfrac{1}{2}$. When the collision frequency function is homogeneous, the particle size distribution of a coagulating aerosol asymptotically approaches a self-preserving form that can be expressed in terms of the dimensionless particle volume [15–17]

$$\eta = \frac{v}{\bar{v}(t)}$$

$$\psi(\eta) = \frac{n(v, t)}{\mathcal{N}(t)}\bar{v}(t) \tag{19}$$

where

$$\bar{v}(t) = \frac{V}{\mathcal{N}(t)} \tag{20}$$

Fig. 1. Ratio of the coagulation rate coefficients of agglomerate and spherical particles with particle size for particles of equal volume.

and V is the total volume of particulate material per unit mass. Substituting the self-preserving particle size distribution into Eq. (4) and integrating both sides over all particle volumes yields a rate equation for the total particle volume per unit mass of gas in the aerosol system,

$$\frac{d\mathcal{N}}{dt} = -2^{1-\nu}\alpha\kappa\rho\bar{v}_0^{2/3 - \nu/D_f}V^{\nu/D_f - 1/2}\mathcal{N}^{5/2 - \nu/D_f} \qquad (21)$$

where

$$\alpha = \int_0^\infty \int_0^\infty \left(\frac{1}{\eta} + \frac{1}{\tilde{\eta}}\right)^{1/2}(\eta^{1/D_f} + \tilde{\eta}^{1/D_f})^\nu \psi(\eta)\psi(\tilde{\eta}) \, d\tilde{\eta} \, d\eta \qquad (22)$$

must be determined by numerical solution of the coagulation equation. For free-molecular coagulation of spherical particles, $\alpha = 6.67$ [16]. The self-preserving particle size distribution for free molecular coagulation of spherical particles is approximately log-normal, with a geometric standard deviation of $\sigma_G \approx 1.35$. The value of α for agglomerate particles should, at least, be of the same order of magnitude.

Assuming that the total particle volume V is constant throughout the coagulation growth process, the mean particle volume $= V/N(t)$ thus obeys

$$\frac{d\bar{v}}{dt} = 2^{1-\nu}\alpha\kappa\rho\bar{v}_0^{2/3 - \nu/D_f}V\bar{v}^{\nu/D_f - 1/2} \qquad (23)$$

Integrating Eq. (23) over time subject to an initial condition of $\bar{v}(0) = \bar{v}_0$, e.g., the size of particle produced by homogeneous nucleation, yields

$$\bar{v}(t) = \bar{v}_0\left[1 + 2^{1-\nu}\left(\frac{3}{2} - \frac{\nu}{D_f}\right)\frac{\alpha\kappa_0\rho_0 V}{\bar{v}_0^{5/6}}\int_0^t \frac{\kappa\rho}{\kappa_0\rho_0} dt\right]^{1/((3/2)-(\nu/D_f))} \qquad (24)$$

Assuming ideal gas, constant pressure, and noting that $\kappa \sim T^{1/2}$,

$$\frac{\kappa\rho}{\kappa_0\rho_0} = \sqrt{\frac{T_0}{T}} \qquad (25)$$

The integral in Eq. (24) allows application of the expression to variable temperature systems.

We see from Eq. (24) that the rate of particle growth depends on the total volume of particulate material per unit volume of gas, ρV, the fractal dimension of the particles, D_f, the sizes of the primary particles from which the agglomerates are assembled, and, through Eq. (25), the temperature-time history of the aerosol system. Because the particles of interest are much smaller than the mean-free-path of the gas molecules, there is no explicit dependence on the total pressure in the reactor. Instead, the dependence on $\rho V = P_v/R_{gas}T$ indicates an influence of the partial pressure of the vapor precursor, P_v. Experimental observations in inert gas condensation reactors, on the other hand, show a strong dependence of the primary particle size on the system pressure [3]. This apparent contradiction can be resolved by examining the complex vapor source commonly used in IGC systems. For a system with uniform composition and starting from thermal equilibrium with a hot vapor source, particle growth would be independent of the overall pressure. However, diffusion of the vapors from the hot source into the surrounding low density gas varies inversely with overall pressure. Hence, lowering the pressure increases vapor dispersion and dilution, thereby lowering the volume concentration of particulate material produced by condensation and slowing their growth by coagulation. The complex interplay between heat and mass transfer in the vicinity of the vapor source is beyond the scope of this paper. Rather than attempt to model this complex source in detail, we assume that the initial vapor partial pressure is a constant fraction of the overall system pressure. The resulting model captures the essential features of particle growth in these systems without the complexity of modeling the buoyancy-driven flows in the IGC system and is more applicable to forced flow systems that will probably dominate in large-scale nanoparticle production.

For isothermal coagulation of spherical particles, the particle growth equation (Eq. (24) can be rewritten as

$$\bar{v} = \bar{v}_0\left[1 + \frac{t}{\tau_{cs}}\right]^{6/5} = \bar{v}_0[1 + \theta]^{6/5} \qquad (26)$$

where

$$\tau_{cs}^{-1} = \frac{5}{12}\frac{\alpha\kappa_0\rho_0 V}{\bar{v}_0^{5/6}} \qquad (27)$$

is the characteristic time for coagulation of spherical particles, and

$$\theta = \frac{t}{\tau_{cs}} \qquad (28)$$

Allowing for fractal particles, isothermal coagulation yields

$$\bar{v} = \bar{v}_0\left[1 + 2^{2-\nu}\frac{6}{5}\left(\frac{3}{2} - \frac{\nu}{D_f}\right)\theta\right]^{1/((3/2)-(\nu/D_f))} \qquad (29)$$

For spheres at long time, increases as $\theta^{6/5}$, while for agglomerate particles with a fractal dimension of $D_f = 1.8$, $\bar{v} \sim \theta^2$. Thus, as expected from the collision frequency function, we again see that agglomerate particles will grow more rapidly than will spheres. Allowing for both fractal particles and variable temperature, the more general result is

$$\bar{v} = \bar{v}_0\left[1 + \frac{1}{\tau_{ca}}\int_0^t \frac{dt}{\sqrt{T/T_0}}\right]^{1/((3/2)-(\nu/D_f))} \qquad (30)$$

where

$$\tau_{ca} = \frac{\tau_{cs}}{\frac{6}{5} 2^{2-\nu} \left(\frac{3}{2} - \frac{\nu}{D_f} \right)} \qquad (31)$$

is the characteristic time for agglomerate coagulation.

Nanoparticle synthesis systems are characterized by rapid cooling of the vapors and product particles. Generally, the temperature is initially sufficiently high that the particles coalesce quickly after coagulation so that each collision event involves pairs of spheres. After sufficient cooling, the coalescence will slow to the point that necks between the coagulated particles grow only to a limited extent between collision events. From that time forward, the particles will grow as agglomerate particles, developing dendritic fractal-like structures that coalesce on a time scale that is much longer than the time between collision events. In rapidly cooled gases, we expect this transition to be quite abrupt. Consider the extreme case of instantaneous cessation of coalescence at a time θ^*. For $\theta < \theta^*$ the particles are assumed to grow as dense spheres ($D_f = 3$), while for $\theta > \theta^*$ the particles are assumed to grow as agglomerate particles with $D_f = 1.8$. The primary particle size of the agglomerates is assumed to be the sphere volume at time θ^*. Fig. 3 shows effects of this abrupt transition on the evolution of the particle volume. The transition has arbitrarily
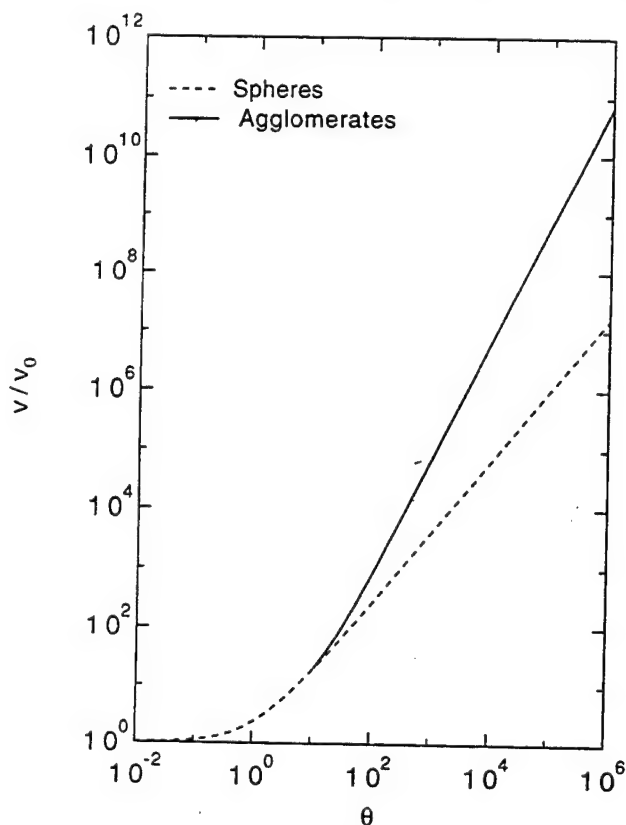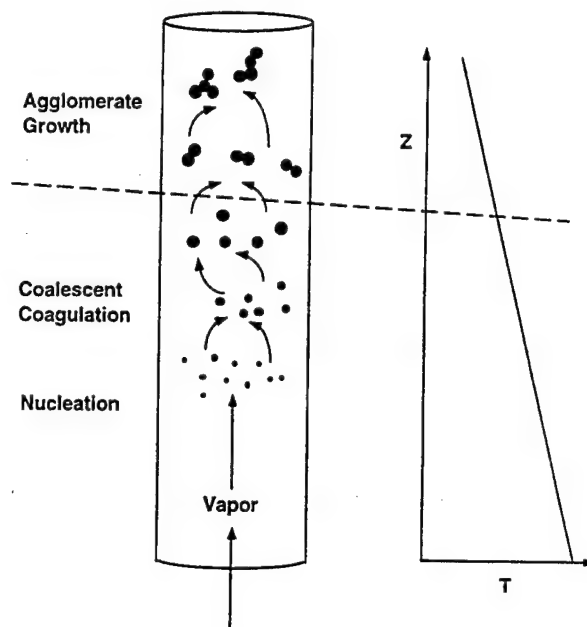
Fig. 4. Schematic illustration of the processes that contribute to particle growth in nanoparticle synthesis.

been set at $\theta^* = 10$ for these calculations. Following the onset of agglomeration, the agglomerate volume rapidly outpaces that for spheres.

The processes that determine the growth dynamics of nanoparticles are summarized in Fig. 4. Initially, the temperature is high enough that agglomerated particles coalesce before additional particle collisions, so the particles remain spherical. As the temperature drops and the particles grow, the coalescence rate slows, leading to agglomerate formation. The objective in most nanoparticle synthesis is to grow dense nonagglomerated nanoparticles. Only the early stage of growth when the particles are still approximately spherical contributes to the production of such particles. Once agglomeration begins, continued growth of nonagglomerated nanoparticles is unlikely. A number of important features of nanoparticle synthesis systems are revealed with a simple model. We assume that vapor is uniformly distributed throughout the volume of a forced flow reactor. As noted above, particle evolution depends on the partial pressure of the vapor precursor but not on the total system pressure. Fig. 5 presents an operating map for spherical particle growth by coagulation, showing isopleths of constant final particle size and mass production rate as a function of the precursor partial pressure the time available for particle growth. The solid lines show how particle size varies with operating pressure and growth time. The broken lines are isopleths of constant mass production rate per unit of active reactor volume, i.e.,

$$\frac{p_v \mathcal{M}_p}{RT\tau_{res}}$$

Fig. 3. Particle volume increase for spherical particles (broken line) that transition to agglomerate formation ($D_f = 1.8$) at $\theta = 10$ (solid line).

where M_p is the molecular weight of the product material and τ_{res} is the residence time available for coalescent particle growth in the reactor. As one increases the operating pressure at constant growth time, both the size of the product particles and the mass throughput increase. Thus, increasing the system pressure has two effects, one desirable and one undesirable for nanoparticle synthesis.

The operating map shows that, to produce particles of a given size, the residence time must be increased as the pressure is decreased, leading to a decrease in the mass production rate. To increase the mass throughput of particles of a given size, the pressure could be increased, but the residence time would have to be decreased to limit growth. In the Gleiter-type inert gas condensation reactor operated at 1000 Pa, 5 nm radius particles are produced in about 0.1 s at a rate of about 1 mg cm^{-3} h^{-1}. A higher pressure source, such as a thermal plasma reactor operated at atmospheric pressure, could produce such particles in times as short as 1 ms. This thousand-fold reduction in the growth time is accompanied by a comparable increase in the mass production rate. Of course, neither of these systems is operated in an isothermal mode as we have modeled here, but the comparison is qualitatively valid. If one wants to increase the production rate of a reactor in which the primary growth mechanism is coagulation, operation at elevated pressures and short growth times is very beneficial. The time for growth of the primary particles is determined by the time during which the temperature is high enough for particles to coalesce
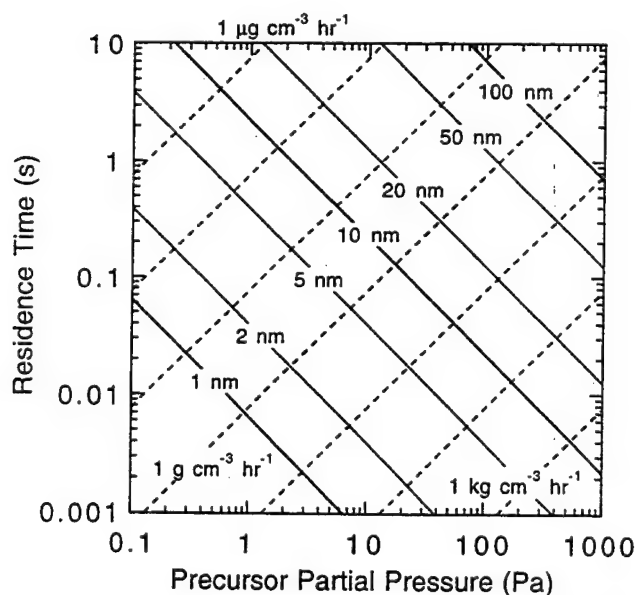
Fig. 5. Operating map of nanoparticle synthesis system performance. Isopleths of constant mean particle size and reactor throughput are plotted as functions of system operating pressure and residence time. Particles are assumed to be spherical, with a reactor temperature of 1600 K.

completely. Once the temperature has dropped below that point, either hard or soft agglomerates may be generated, but primary particle growth will be severely limited. To understand this transition, we must examine the competition between coagulation and coalescence.

3. Particle coalescence

A number of condensed phase transport mechanisms contribute to the coalescence of agglomerates produced by coagulation. Our interest is in the time required for complete coalescence of the bisphere that is produced when two spherical particles coagulate. The excess surface area of the bisphere provides the driving force for interdiffusion of the two particles. Viscous flow and diffusion through the particle volume, grain boundaries, or surfaces may contribute to the coalescence depending on the material properties and growth conditions. The early phase of this process is described in classical sintering models [18–21] in terms of the growth of the radius of the neck between the spheres relative to the sphere radius by a single mechanism, i.e.,

$$\left(\frac{x}{a_i}\right)^n = \frac{B(T)}{a_i^m} t \qquad (32)$$

where a_i is the initial radius of the spherical particle and m and n depend upon the individual mechanism. These expressions are based upon simplified geometries for the growing neck that limit their applicability to a neck radius below about $x/a_i \approx 0.3$. Although they do not describe the complete coalescence that we seek to understand, the early stage sintering models do provide an estimate for the time required for sintering. That characteristic time for neck growth is

$$\tau_s = \frac{a_i^m}{B(T)} \qquad (33)$$

A number of investigators have applied such models of neck growth to the description of the structural evolution of aerosol particles. Ulrich [22] observed that the sizes of silica particles produced in a flame synthesis process grew much more slowly than coagulation calculations would suggest. He later attributed the slow growth to slow viscous coalescence of agglomerate particles, and attempted to model the process by tracking the number of primary particles that make up the agglomerates [23]. He characterized the rate of assimilation of one primary particle into another one in terms of the characteristic time for viscous coalescence [18],

$$\tau_{sv} = \frac{\mu a}{\gamma} \qquad (34)$$

where γ is the surface free energy of the material and μ is its viscosity.

More recently, Koch and Friedlander [24] expressed the relaxation of the particle structure in terms of its surface area. They suggested that a rate equation should be written for the decay of the particle surface area and that the decay could be modeled as a first order process, i.e.,

$$\left(\frac{\mathrm{d}s}{\mathrm{d}t}\right)_{\text{coalescence}} = -\frac{s - s_s}{\tau_s} \tag{35}$$

where s_s is the surface area of the fully coalesced particle, i.e., that of a sphere with the same volume as that of the agglomerate, and τ_s is the characteristic time for coalescence that was estimated using classical sintering models. Although there is no rigorous basis for this model, calculations of Hiram and Nir [25] suggest that the approach surface area to that of a dense sphere size in viscous coalescence is approximately exponential for $t \gg \tau_s$. Based on the long time limit, they estimated τ_s based on the final size of the fully densified spherical particle. Although the model was developed to describe nearly dense particles undergoing viscous coalescence, Koch and Friedlander [24] applied their model to the entire evolution of the aerosol, extending from early times when particles coalesce quickly to later times when large agglomerates are the dominant structures.

From this beginning, both approximate and detailed predictions of the size and surface area distribution function have evolved [24,26–31]. The use of a simple parameter such as the agglomerate surface area or the number of primary parameters is cogent; however, although considerable effort has been invested in developing and solving representations of the coupled coagulation/sintering problem, remarkably little attention has been given to the form of the sintering term itself. We may anticipate the development of sintering models that more precisely follow the approach to complete coalescence by writing the rate equation for the surface area evolution in the form,

$$\left(\frac{\mathrm{d}s}{\mathrm{d}t}\right)_{\text{coalescence}} = f(s, T, t) \tag{36}$$

This formulation will allow the incorporation of more quantitative models of the neck geometry and of multiple transport mechanisms.

For the present, however, we limit our analysis to probing the transition from coalescent coagulation to agglomerate formation by comparing the characteristic times for coagulation with that for coalescence. We note that, once τ_s/τ_c exceeds a value near unity, complete coalescence is unlikely. From that time on, particles may be expected to grow as agglomerates. Some sintering may continue, but this will generally lead to undesired neck growth resulting in hard agglomerates rather than complete coalescence. Only by increasing the temperature as the particles grow, thereby accelerat-

ing sintering and reducing τ_s, can particles continue to grow beyond this transition point. More commonly, the temperature will decrease as growth progresses, accelerating the transition.

Thus, the key to the production of dense, nonagglomerated particles when coagulation is the dominant growth mechanism is to quench coagulation before the onset of agglomeration, i.e., while τ_s/τ_c is still less than unity. In the discussion that follows, particle growth is followed only until $\tau_s/\tau_c = 1$. Throughout the growth phase, the particles coalesce on a time scale that is short by comparison with the time between collision events. Hence, for the present purposes it is sufficient to consider only the coagulation of spherical particles.

We consider first the onset of agglomeration in isothermal particle growth. For the self-preserving particle size distribution, isothermal growth yields

$$\bar{a} = \bar{a}_0[1 + \theta]^{2/5} \tag{37}$$

The ratio of characteristic times becomes

$$\frac{\tau_s}{\tau_c} = \frac{\tau_{s0}(1 + \theta)^{2m/5}}{\tau_{c0}(1 + \theta)} = \frac{\tau_{s0}}{\tau_{c0}}(1 + \theta)^{(2m/5) - 1} \tag{38}$$

This result reveals some interesting trends in the coalescence dynamics of coagulating aerosols. For $m < 5/2$ and synthesis conditions that allow coalescence of the smallest clusters ($\tau_{s0}/\tau_{c0} < 1$), coagulation will not lead to agglomerate formation under isothermal conditions. Even for $m > 5/2$, the coalescence time will increase only slightly faster than that for sphere coagulation, so the transition might not occur within the residence time in the synthesis reactor. This is suggested by the characteristic times for isothermal particle growth in Fig. 6 using a silicon aerosol and surface diffusion, $m = 4$, as the sintering mechanism. Moreover, if the transition is passed, the slow increase in the coalescence time means that substantial neck growth can be expected following any coagulation events that subsequently occur. However, isothermal growth is an idealized case that would only be expected in carefully controlled laboratory experiments.

The inert gas condensation system and most other fine particle synthesis technologies employ a high temperature source, but allow substantial cooling of the aerosol after particles are formed. Indeed, in the inert gas condensation method and thermal plasma reactors, the temperature drop is responsible for particle formation in the first place. To examine the role of cooling on the transition from coalescent growth to agglomeration, we consider the particle dynamics when the aerosol is cooled at a constant rate,

$$\frac{\mathrm{d}T}{\mathrm{d}t} = -\frac{T_0}{\tau_T} \tag{39}$$

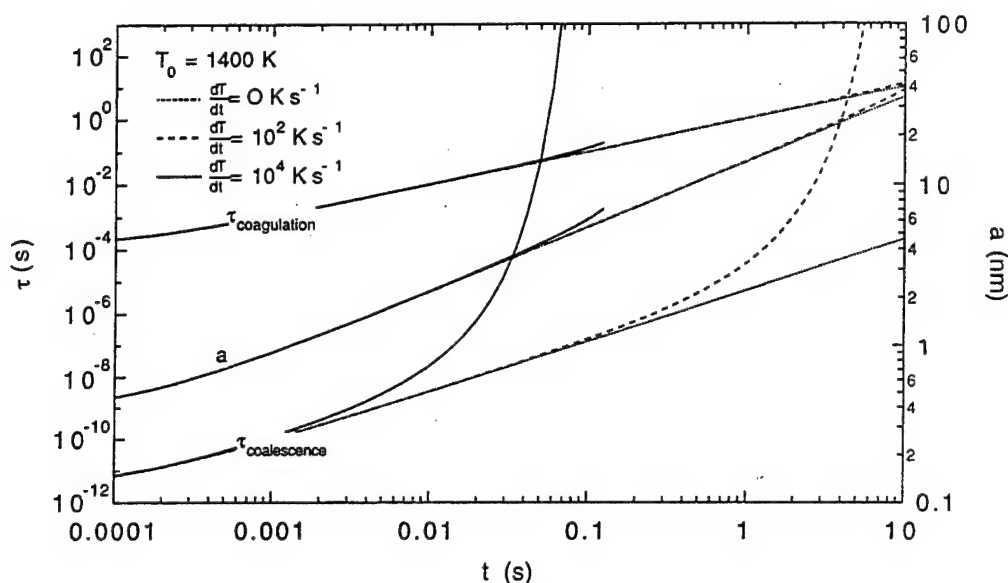The particle growth is then described by

Fig. 6. Variation of the characteristic times for coagulation and coalescence of silicon nanoparticles and the product particle radius with growth time. The initial reactor temperature was 1400 K. Results for isothermal growth and for growth at cooling rates of 10^2 K s^{-1} and 10^4 K s^{-1} are shown.

$$\bar{v} = v_0 \left[1 + \frac{1}{\tau_{c0}} \int_t^{t_0} \frac{dt'}{\sqrt{T/T_0}} \right]^{6/5} = \bar{v}_0 [1 + 2\lambda(1 - \sqrt{1 - \theta/\lambda})]^{6/5} \tag{40}$$

where

$$\lambda = \frac{\tau_T}{\tau_{c0}} \tag{41}$$

Given this growth trajectory, the characteristic time for sintering varies with time according to

$$\tau_s = \frac{a^m}{B(T)} = \frac{a^m}{AT^{\gamma}} \exp\left[\frac{E}{RT}\right]$$

$$= \frac{\tau_{s0}[1 + 2\lambda\sqrt{1 - \theta/\lambda}]^{2m/5}}{[1 - \theta/\lambda]^{\gamma m}} \exp\left[\frac{\epsilon\theta}{\lambda - \theta}\right] \tag{42}$$

where $\varepsilon = E/(RT_0)$. Fig. 6 shows the influence of the cooling rate on the variation of the characteristic time for coalescence of a silicon aerosol formed at an initial temperature of 1400 K and subjected to cooling rates of 10^2 K s^{-1} and 10^4 K s^{-1}. In both cases, cooling causes the characteristic time for coalescence to increase dramatically. The low cooling rate allows a longer time for growth before the coalescence time surpasses that for coagulation. In both cases, the two characteristic times rapidly diverge, although the divergence is more rapid at the higher cooling rate. The divergence will be greater than indicated here because the more rapid growth of the agglomerate particles is not considered in Fig. 6.

The rapid reduction in the sintering rate essentially freezes the structure of the primary particles. Ideally, neck growth would be terminated abruptly by rapid cooling, so that agglomerates formed after the desired product particle size is reached would be held together

only by Van der Waals forces. Unfortunately, necks may continue to grow between agglomerated particles after τ_s exceeds τ_c. This will depend upon the rate of divergence of the characteristic times. This divergence is not always as large as the ones shown in Fig. 6. The initial temperature also influences the transition from coalescent growth to agglomeration as is illustrated in Fig. 7. If the initial growth temperature is low enough that the coalescence time is only slightly smaller than that for coagulation, the rate of divergence is reduced dramatically. The lower divergence rate will allow greater neck formation of agglomerates formed shortly after the onset of agglomeration. Reactor operation
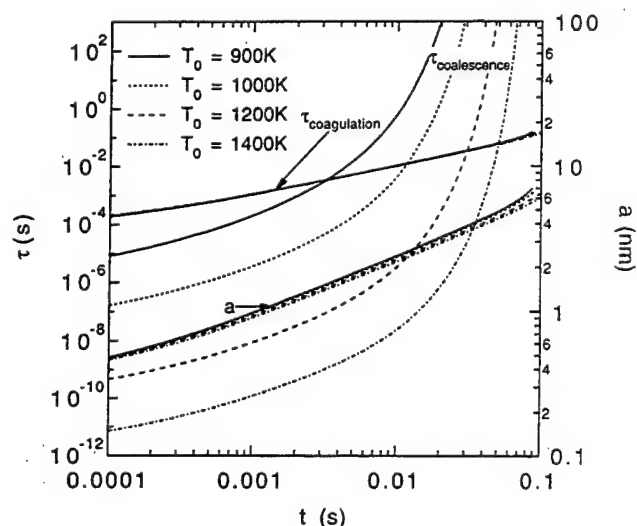
Fig. 7. Characteristic times for coagulation and coalescence of silicon nanoparticles as a function of growth time for a cooling rate of 10^4 K s^{-1} and various initial reactor temperatures.
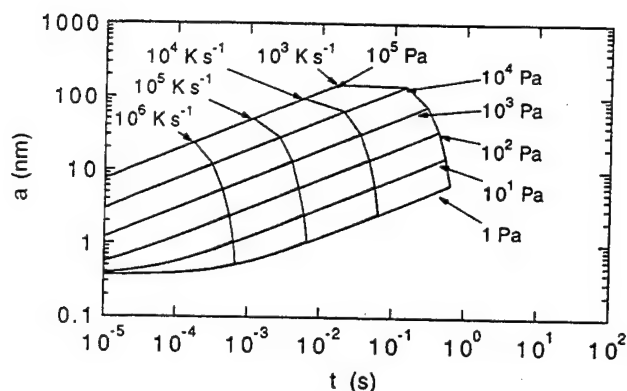
Fig. 8. Variation of particle size with temperature for silicon nanoparticles for various initial Si partial pressures and constant cooling rates. Growth curves for various cooling rates are terminated at the point where $\tau_s = \tau_c$.

with a higher temperature in the primary growth region will, therefore, inhibit the formation of strongly necked agglomerates.

Fig. 8 shows the influence of operating pressure on the growth of silicon nanoparticles for a constant initial mole fraction of Si vapor of 10%. As the initial vapor partial pressure is increased, the particle growth is accelerated. Because of the strong temperature dependence of the sintering rate, the time at which the particle coalescence is quenched for a given cooling rate is nearly independent of the pressure, although the particle size at that time increases dramatically with pressure. The growth time required to produce a given particle size decreases with increasing pressure, and is controllable through the cooling rate. Thus, the key parameters governing the size of the product particles are the initial partial pressure of the vapor or precursor material, and the cooling rate. Because the mass throughput per unit of reactor volume is proportional to the pressure and inversely proportional to the growth time, increasing the system pressure dramatically increases the rate of production of the nanoparticles.

4. Conclusions

The mechanism of nanoparticle growth from the vapor phase has been examined with emphasis on coagulation and coalescence, since those mechanisms dominate in the inert gas condensation method of synthesis. Particles are generally formed at high enough temperatures that coalescence is rapid at first. As the aerosol ages, the temperature drops and the coalescence rate slows, so that after some time agglomerate particles begin to grow. Because of their larger collision cross-sections, agglomerate particles coagulate more rapidly than do spheres of equal mass. As a result, once

agglomerates begin to form, particle growth accelerates dramatically. Because the coalescence rate is decreasing at the same time, growth beyond the onset of agglomeration does not contribute to the growth of the primary particles.

The size of nanoparticles synthesized from the vapor phase is, therefore, the size the dense particles grow to before agglomeration. Particle size increases with the amount of vapor available for particle growth, and with the time available for growth before the onset of agglomeration. As the initial vapor partial pressure is increased, the time required to grow particles to a given size decreases and the mass production rate per unit of active reactor volume increases. Although research quantities of material have been effectively generated using low pressure inert-gas-condensation reactors, efforts to produce technologically significant quantities of nanoparticles will benefit from higher synthesis pressures.

The rate of decrease of the coalescence rate following the onset of agglomeration depends on the cooling rate and on the initial growth temperature. If the initial operating temperature is low enough that the coalescence time is comparable to the coagulation time, the coalescence time will increase only slightly faster than that for coagulation. Strong neck formation and hard agglomerates can then be expected. On the other hand, if the initial operating temperature is much higher so that coalescence is initially very rapid, the transition will occur much more abruptly. Neck growth within the first agglomerates to form will be decreased as a result, and agglomerates will be more amenable to dispersion. Although the energy cost will behigher, a better product will result.

Acknowledgement

References

[1] R. Birringer, H. Gleiter, H.P. Klein and P. Marquardt, Phys. Lett., 102A (1984) 365–369.
[2] R. Birringer, Mater. Sci. Eng., A117 (1989) 33–43.
[3] C.G. Granqvist and R.A. Buhrman, Ultrafine metal particles, J. Appl. Phys., 47 (1976) 2200–2219.
[4] K. Kimoto, Y. Kamiya, M. Nonoyama and R. Uyeda, An electron microscope study on fine metal particles in argon gas at low pressure, J. Appl. Phys., 2 (1963) 702–713.
[5] R. Uyeda, Growth of polyhedral metal crystallites in inactive gas, J. Crystal Growth, 45 (1978) 485–489.
[6] A.H. Pfund, Bismuth black and its applications, Rev. Sci. Instrum., 1 (1930) 398–399.
[7] S.L. Girshick, C.P. Chiu and P.H. McMurry, Plasma Chem. Plasma Process., 8 (1989) 145–157.

[8] E. Werwa, A.A. Seraphin, L.A. Chiu, C.X. Chou and K.D. Kohlebrander. *Appl. Phys. Lett.*, *64* (1994) 1821–1823.

[9] W.A. Saunders, P.C. Sercel, R.B. Lee, H.A. Atwater, K.J. Vahala and R.C. Flagan. *Appl. Phys. Lett.*, *63* (1993) 1549–1551.

[10] C. Kaito, Coalescence growth of smoke particles prepared by a gas-evaporation technique, *Jap. J. Appl. Phys.*, *17* (1978) 601–609.

[11] H.V. Nguyen and R.C. Flagan, Particle formation and growth in single-stage aerosol reactors, *Langmuir*, *7* (1991) 1807–1814.

[12] M.K. Alam and R.C. Flagan, Controlled nucleation aerosol reactors – production of bulk silicon, *Aerosol Sci. Technol*, *5* (1986) 237–248.

[13] K. Okuyama, Y. Kousaka, N. Tohge, S. Yamamoto, J.J. Wu, R.C. Flagan and J. H. Seinfeld, Production of ultrafine metal oxide aerosol particles by thermal decomposition of metal alkoxide vapors, *AIChE J.*, *32* (1986) 2010–2019.

[14] R.S. Bowles, S.B. Park and R.P. Andres, Generation of supported metal clusters of controlled size, *J. Mol. Catal*, *20* (1983) 279–287.

[15] R.D. Mountain, G.W. Mulholland and H. Baum, *J. Colloid Interface Sci.*, *114* (1986) 67–81.

[16] F.S. Lai, S.K. Friedlander, J. Pich and G.M. Hidy, The self-preserving particle size distribution for brownian coagulation in the free-molecule regime, *J. Colloid Interface Sci.*, *39* (1972) 395.

[17] T. Matsoukas and S.K. Friedlander, *J. Colloid Interface Sci.*, *146* (1991) 495.

[18] J. Frenkel, *J. Phys.*, *9* (1945) 385–396.

[19] G.C. Kuckynski, Self-diffusion in sintering of metallic particles, *Trans. AIME*, *185* (1949) 169–178.

[20] W.D. Kingery and M. Berg, Study of the initial stages of sintering solids by viscous flow, evaporation-condensation, and self-diffusion, *J. Appl. Phys.*, *26* (1955) 1205–1212.

[21] D.L. Johnson, New method of obtaining volume, grain-boundary, and surface diffusion coefficients from sintering data. *J. Appl. Phys.*, *40* (1069) 192–200.

[22] G.D. Ulrich, Theory of particle formation and growth in oxide synthesis flames, *Combust. Sci Technol.*, *4* (1971) 47–57.

[23] G.D. Ulrich and N.S. Subramanian, Particle growth in flames iii. coalescence as a rate-controlling process, *Combust. Sci. Technol.*, *17* (1977) 119–126.

[24] W. Koch and S.K. Friedlander, The effect of particle coalescence on the surface area of a coagulating aerosol, *J. Colloid Interface Sci.*, *140* (1990) 419–427.

[25] Y. Hiram and A. Nir, *J. Colloid Interface Sci.*, *95* (1983) 462–470.

[26] W. Koch and S.K. Friedlander, Particle growth by coalescence and agglomeration, *Part. Part. Syst.*, *8* (1991) 86–89.

[27] M.K. Wu and S.K. Friedlander, Controlled synthesis of nano-sized particles by aerosol processes, *Aerosol Sci. Technol.*, *19* (1993) 527–548.

[28] A. Kobata, K. Kusakabe and S. Morooka, Growth and transformation of tio_2 crystallites in aerosol reactor, *AIChE J.*, *37* (1991) 347–359.

[29] F.E. Kruis, K.A. Kusters, S.E. Pratsinis and B. Scarlett, A simple model for the evolution of the characteristics of aggregate particles undergoing coagulation and sintering. *Aerosol Sci. Technol.*, *19* (1993) 514–526.

[30] Y. Xiong and S.E. Pratsinis, Formation of agglomerate particles by coagulation and sintering. 1. a 2-dimensional solution of the population balance equation, *J. Aerosol Sci.*, *24* (1993) 283–300.

[31] Y. Xiong and S.E. Pratsinis, Formation of agglomerate particles by coagulation and sintering. 2. the evolution of the morphology of aerosol-made titania, silica, and silica-doped titania powders, *J. Aerosol Sci.*, *24* (1993) 301–313.

Nanocomposites for high temperature applications

V. Provenzano[a], R.L. Holtz[b]

[a]*Physical Metallurgy Branch, Code 6323, Materials Science and Technology Division, Naval Research Laboratory, Washington, DC 20735-5343, USA*
[b]*Geo-Centers, Inc., 10903 Indian Head Highway, Fort Washington, MD 20744, USA*

Abstract

This paper reviews the research that has been conducted at the Naval Research Laboratory during the past few years on nanocomposites for high temperature applications. The research was inspired by a strengthening theory proposed by N.P. Louat (*Acta. Metall.*, *33* (1985) 59). The theory sought to take advantage of the high strength and toughness of fine-grained metals while at the same time avoiding, through use of composites, the inherent thermal instability of these materials at high temperatures due to thermally activated processes such as creep, grain boundary sliding and grain coarsening. To test this idea, both microcomposites and nanocomposites were synthesized and processed at the Naval Research Laboratory by different techniques that included liquid infiltration, electroless plating, chemical vapor deposition fluidized-bed, inert gas condensation, and ball milling. In all cases, the composites consisted of a hard reinforcing phase embedded in a softer metal matrix phase in which both phases are nearly immiscible. For the case of copper–niobium and brass–niobium microcomposites, both strength enhancement and high temperature strength retention were demonstrated. For physical-vapor deposited copper–niobium nanocomposites, very large increases were observed in the microhardnesses with a peak in the microhardness values around 63 vol.% niobium. Suppression of grain growth at temperatures close to the melting point of copper were demonstrated, as well. Similar results were obtained for silver–nickel nanocomposites. Processing nanocomposite metals has proven to be plagued with two principal challenges: consolidation and oxidation. These two problems with nanostructured metals suggest alternative research directions designed to take advantage both of the strong reactivity and of the large grain boundary surfaces of the nanostructured materials.

Keywords: High temperature applications; Nanocomposites

1. Introduction

In this paper we summarize some research effects that have been conducted at the Naval Research Laboratory during the past few years in the development of nanocomposite materials for high temperature applications. This research is based on a strengthening theory developed by Louat and described in detail elsewhere [1]. In essence, the requirements of the Louat theory for high temperature strength retention are for a nanoscale composite with hard particles in a soft matrix, a volume fraction of the reinforcing phase above 50%, good bonding between the matrix and the reinforcement, and immiscibility of the two phases.

Our first attempts in making composite model materials that satisfied the basic requirements of the strengthening theory involved the use of liquid metal infiltration of commercially available fine metal powders. To this end, hot isostatic pressing (HIP) was used to liquid infiltrate and subsequently to consolidate nearly immiscible metal phases that involved the use of a refractory metal, such as tungsten or niobium, as the reinforcing phase, and a softer metal, such as copper or iron, as the matrix phase. Limited results were also obtained by infiltrating aluminium into oxide particles. The liquid infiltration techniques employed to produce the composite specimens has been amply described in previous papers [2–4].

Besides liquid infiltration, other methods have been used to coat the reinforcing particles with a suitable metal and then consolidate the coated particles by conventional processing. These methods include coating the particles by electroless plating or through a fluidized-bed chemical vapor deposition (CVD) technique [5]. Because of some inherent problems associated with each technique, these two methods did not produce promising results. Electroless plating coated the particles unevenly and the deposited metal converted
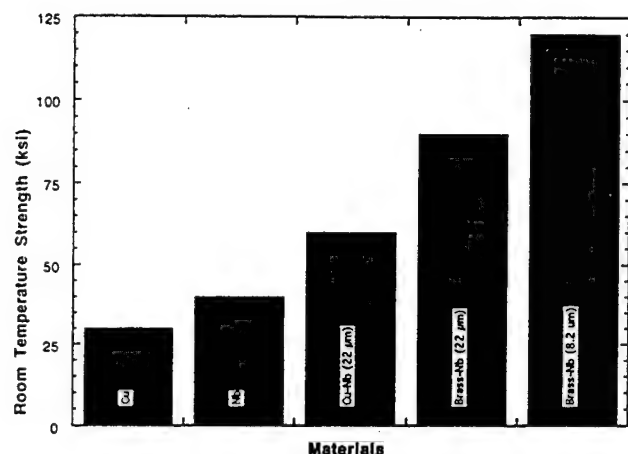
Fig. 1. Room temperature tensile strength of niobium particles infiltered with copper or brass compared with pure copper and niobium strengths. Data for brass–niobium with 8.2 μm particles show a more than threefold increase with respect to the rule of mixtures prediction.

into an oxide which on compaction, caused the composite samples to be brittle. The CVD method can only successfully coat relatively large particles (larger than 10 μm in diameter) and, further, the coated particles were contaminated with a carbon residue that could not be eliminated.

In order to produce contamination-free materials and

have better control both of the composition and of the resulting microstructure, nanocomposites were synthesized by the inert gas condensation-physical vapor deposition (PVD) method, using sputtering for vapor sources. Following the deposition, the nanosize powders were compacted by various means including cold pressing, HIPing, and sintering. Details of the deposition method as well as details of the processing steps are given elsewhere [6]. The combinations investigated have included copper–niobium, copper–chromium, copper–iron, and silver–nickel. In this paper, however, we only review the results obtained for the copper–niobium system and present some results on the silver–nickel system; some limited results obtained by ball milling are also included.

Research on nanocomposites for high temperature applications has produced some interesting results, but has presented some serious challenges. In the concluding section of this paper we discuss the rationale used for choosing the new research directions.

2. Copper–niobium composites

The bargraph presented in Fig. 1 as well as the tensile testing data presented in Fig. 2 summarize the key results obained on composite samples produced by the
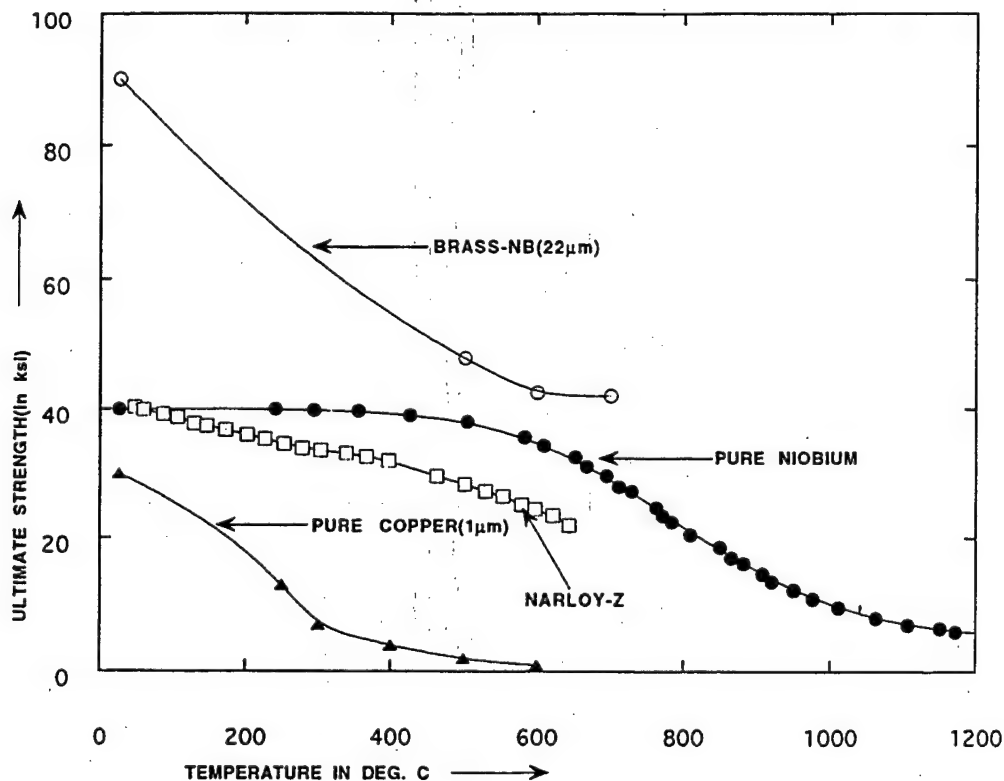
Fig. 2. Tensile strength as a function of temperature for niobium powder infiltrated with brass compared with pure copper and niobium, and Naraloy-Z Cu alloy. Data show that the brass–niobium composite retains 50% of its strength at temperatures close to the melting temperature of the brass matrix.
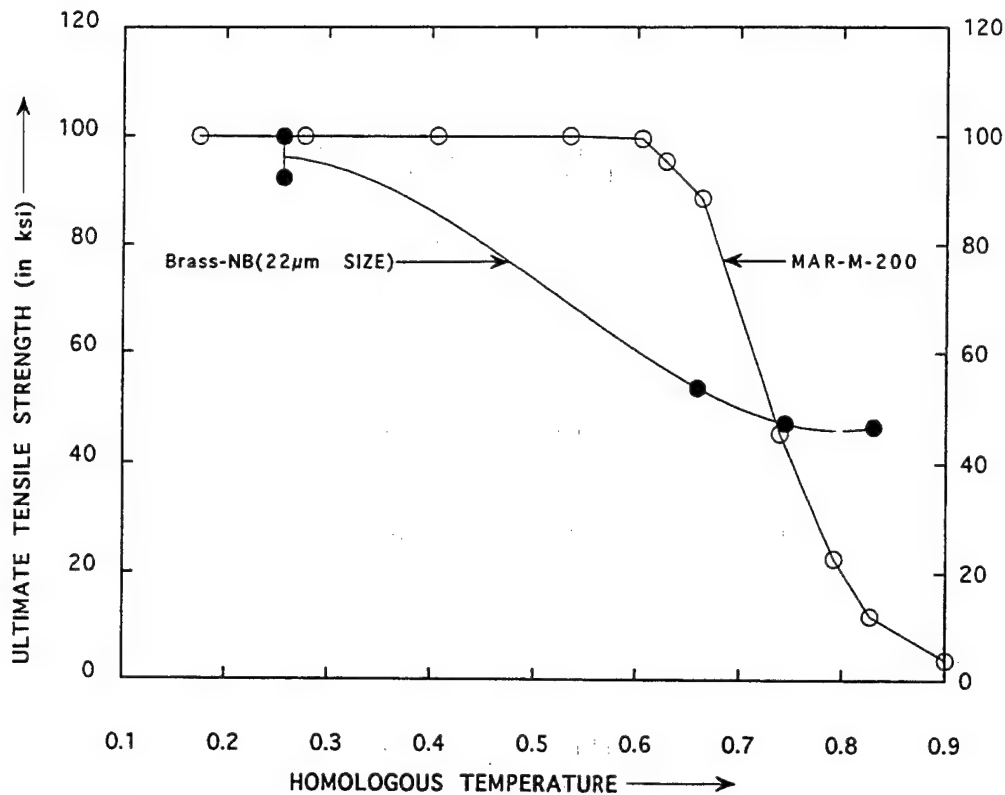
Fig. 3. Tensile strength vs. homologous temperature for MAR-M-200 superalloy and brass-infiltrated niobium particles (22 μm size). The composite exhibits superior strength retention (approximately 50% at 85% of the matrix melting temperature).

liquid infiltration method. In all cases, the niobium content was between 50 and 60 vol.% in a matrix of copper or brass. Brass was used because better 'wetting' of the niobium was achieved. Fig. 1 shows that the room temperature strengths of both copper–niobium and brass–niobium are significantly enhanced with respect to that of pure copper or pure niobium. In fact, the strength increment for the case of brass–niobium with an average particle size of 8.2 μm is more than three times the value predicted by the rule of mixtures. Fig. 2, referring to the case of 22 mm niobium particles in brass, shows that the composite retains approximately 50% of its room temperature strength at about 85% of the melting temperature of brass. By contrast, at the same temperature, pure copper, pure niobium, and Naraloy-Z (a copper-base alloy used in the space shuttle main engine) start losing most of their strength. Fig. 3 compares the brass–niobium with MAR-M-200 superalloy, a typical turbine blade alloy, and shows that the composite retains strength to a higher homologous temperature (relative to the melting point). These results are consistent with the general predictions of the Louat model, and suggested that it would be reasonable to look for enhanced properties in nanostructured copper–niobium.

Details of the synthesis, processing, and microstructure of nanocrystalline copper–niobium are given in a previous publication [6] and are only summarized here. The specimens were made by PVD and were cold

compacted prior to sintering in either vacuum or hydrogen. As-deposited, the particle sizes of the nano-composite and pure copper are roughly the same (40–60 nm). However, after a vacuum heat treatment for 4 h at 400 °C the nanocrystalline copper experienced a factor of ten increase in grain size, whereas the nanocomposite did not experience noticeable grain growth. Finally, for a 4 h vacuum treatment at 1000 °C, the average grain growth of the copper–niobium nanocomposite was only increased by a factor of two, compared with a factor of 200 for nanocrystalline copper.

This thermal grain growth suppression displayed by the copper–niobium nanocomposite is reflected in the microhardness results shown in Fig. 4. For a given heat treatment, the microhardness values display a peak around 63 vol.% niobium (incidentally, this is the random close packing fraction for equisized hard spheres). However, the microhardness values of the as-deposited, cold-pressed powder are roughly the same for different volume fractions of niobium. The decrease in the microhardness with heat treatment observed in pure copper is consistent with the large grain coarsening resulting from the high temperature sintering. In contrast, the increased microhardness observed in pure niobium after the various heat treatments is the result of the better consolidation after sintering. It should be noted, however, that the niobium-rich specimens were all brittle after heat treatments. As is discussed later, the brittle
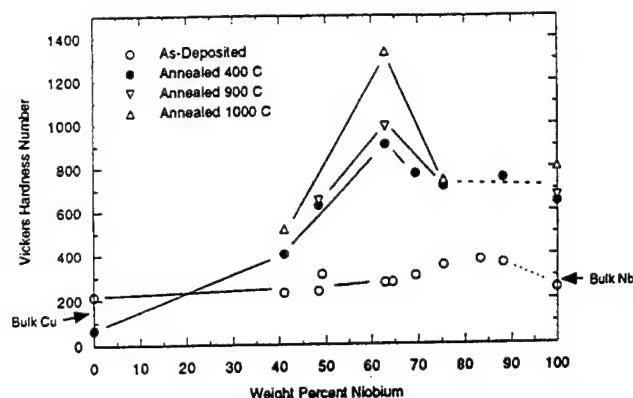
Fig. 4. Vicker's microhardness values of copper–niobium nanocomposites vs. weight per cent niobium for various sintering temperatures. Note a maximum in the hardness values around 63 wt.% niobium for all the sintering treatments.

behavior is thought to be associated with the formation of oxides during the high temperature exposures. Even when sintered in a highly reducing atmosphere of pure hydrogen, niobium oxides are formed and are easily seen via X-ray diffraction [6].

The microhardness of copper–niobium nanocomposite (approximately 45 vol.% niobium) shows a substantial, approximately linear decrease with increasing temperature, shown in Fig. 5 [7]. In contrast to the results for liquid-infiltrated microcomposites described above, this behavior is not at all suggestive to high-temperature strength retention. Subsequent X-ray diffraction and SEM examination of the specimen after the high-temperature hardness testing showed it to be heavily oxidized.

Another consequence of oxide contamination is apparent with some material prepared by ball milling [8]. The SEM image in Fig. 6(a) shows the as-milled material, which has the form of flakes consisting of a mixture of nanocrystalline copper–niobium particles. Although the corresponding X-ray diffraction data show no obvi-

ous oxide present, the presence of oxidation is suggested by the fact that this material could not be consolidated at all either by uniaxial cold-pressing to over 1 GPa, or by CIPing at 600 MPa. Some degree of consolidation was achieved by HIPing at 600 °C at 200 MPa held for 2 h, and a respectable Vicker's microhardness of 420 was obtained. However, the material was quite brittle, there were significant variations in hardness ($\pm 30\%$ in HV), and the materials was obviously not compacted very well. The corresponding X-ray diffraction spectra show the presence of niobium oxide. Presumably, the high surface area of nanoscale niobium particles is easily oxidized even by traces of oxygen present in HIPing bags and vacuum sintering ovens.
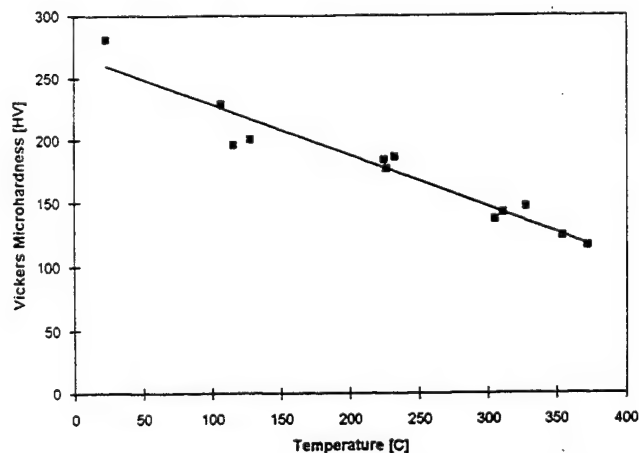
Another possible approach to copper–niobium composite synthesis that was explored was recrystallization of amorphous copper–niobium thin films deposited by sputtering onto a liquid nitrogen cooled substrate. The material was subsequently HIPed at 1000 °C at 200 MPa for 2 h. This route offered a possibility of producing the nanocomposites by in situ reactions so as to lessen the oxidation problem. The as-deposited structure is shown in Fig. 7(a), showing a typical columnar thin film microstructure, while the corresponding X-ray spectrum shows the amorphous structure. HIPing crystallized the microstructure and resulted in a dense microstructure of niobium particles embedded in copper, shown in Fig. 7(b) (polished specimen). However, the average niobium grain sizes of 5 μm shows that nanoscale phase separation is not achieved by this approach. The fracture surface of the crystallized specimen, Fig. 7(c), indicates a decohesive rupture failure with the copper matrix debonded from the niobium particles. Again, the corresponding X-ray pattern shows the presence of oxides, presumably from the residual air left in the HIPing bag.

From the data presented on copper–niobium it is clear that the nanocomposite route, through the PVD of nearly immiscible binary metals, leads to a thermally stable microstructure with little grain growth even at temperatures close to the melting temperature of the copper matrix. Grain growth suppression is a basic requirement of the Louat strengthening theory. Also of significance is that a large enhancement in the microhardness was observed in the consolidated nanocomposite specimens, with a peak value around 63 vol.% niobium. However, high temperature processing necessary to consolidate these materials leads to the formation of niobium oxide, which has the detrimental effects of making the nanocomposite brittle and prone to failure by debonding at the particle–matrix interface.

3. Silver–nickel composites

The difficulties encountered in processing copper–niobium nanocomposites, particularly the oxidation

Fig. 5. Vicker's microhardness of HIPed Cu–45 wt.% Nb as a function of temperature.

As-Received

Particle size 3-10 nm

CIPed 88ksi

Particle size 3-10 nm

HIPed 600 °C, 30ksi
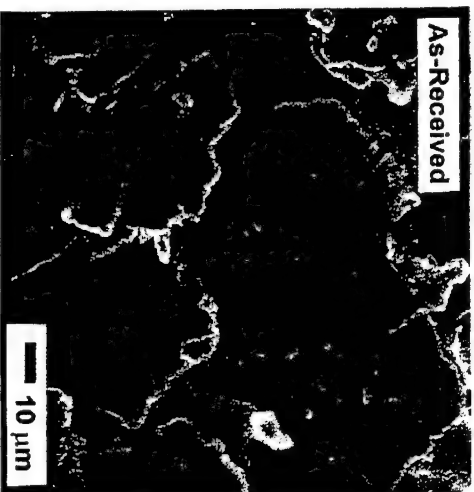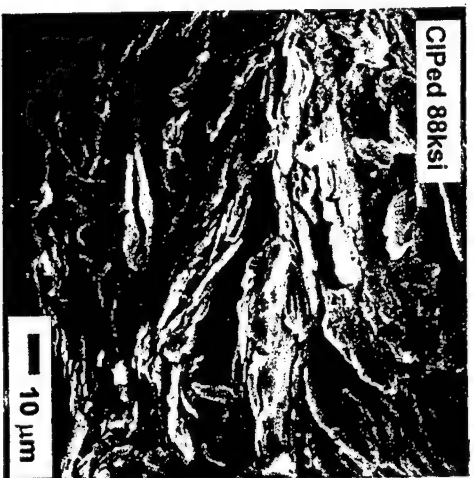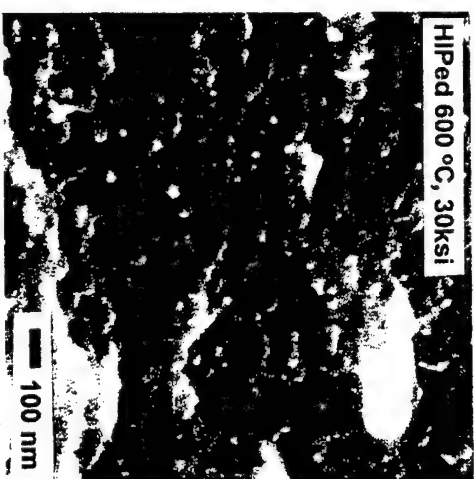
Particle size 20-40 nm

HV = 420 +/- 140

10 µm

10 µm

100 nm
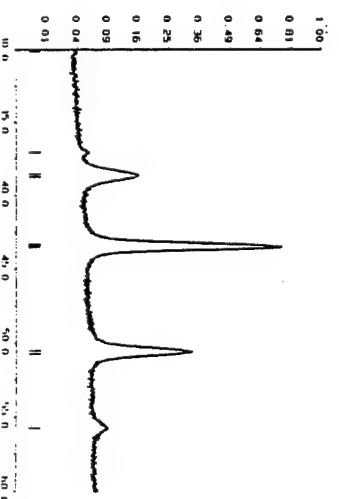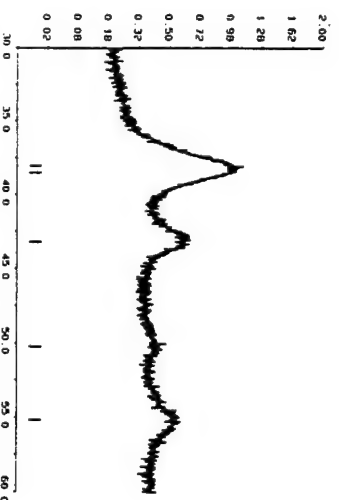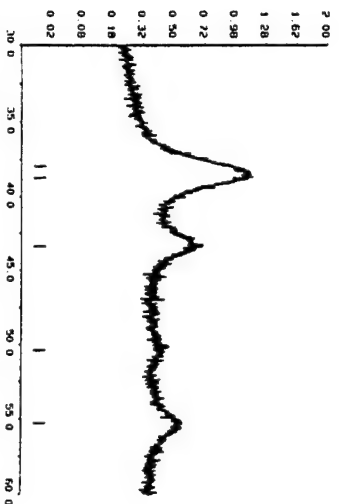
Fig. 6. Microstructural evolution of ball milled copper–niobium nanocomposite as a function of consolidation treatment together with corresponding X-ray diffraction scans.
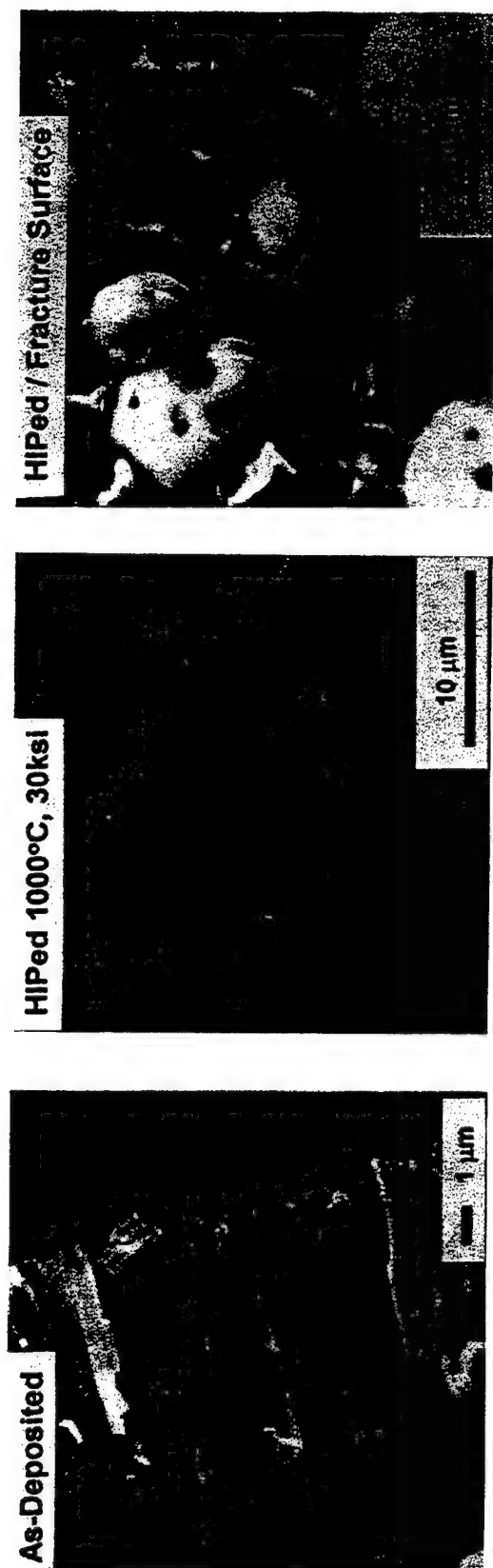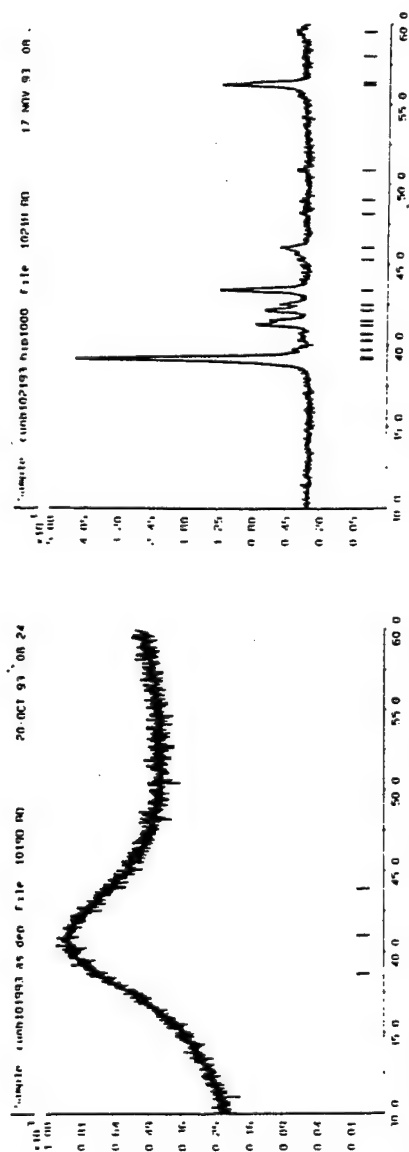
Fig. 7. SEM images showing microstructural evolution of amorphous Cu–55 wt.% Nb with consolidation treatment and the fracture surface of the HIPed specimen fractured at room temperature. The figure also includes corresponding X-ray diffraction scans.
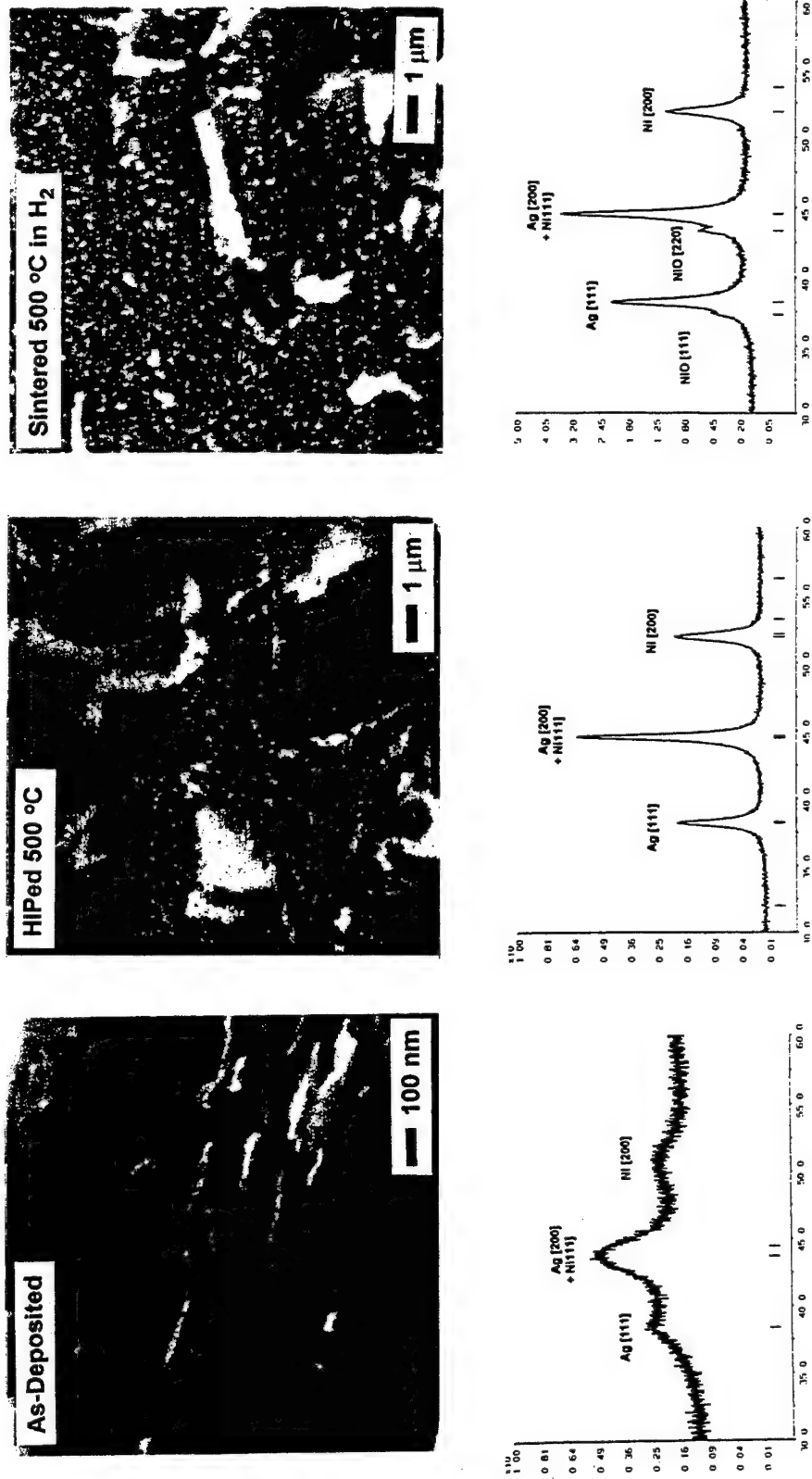
Fig. 8. SEM images and X-ray diffraction scans of Ag–64 wt.% Ni nanocomposite showing the microstructural evolution as a function of consolidation treatment.
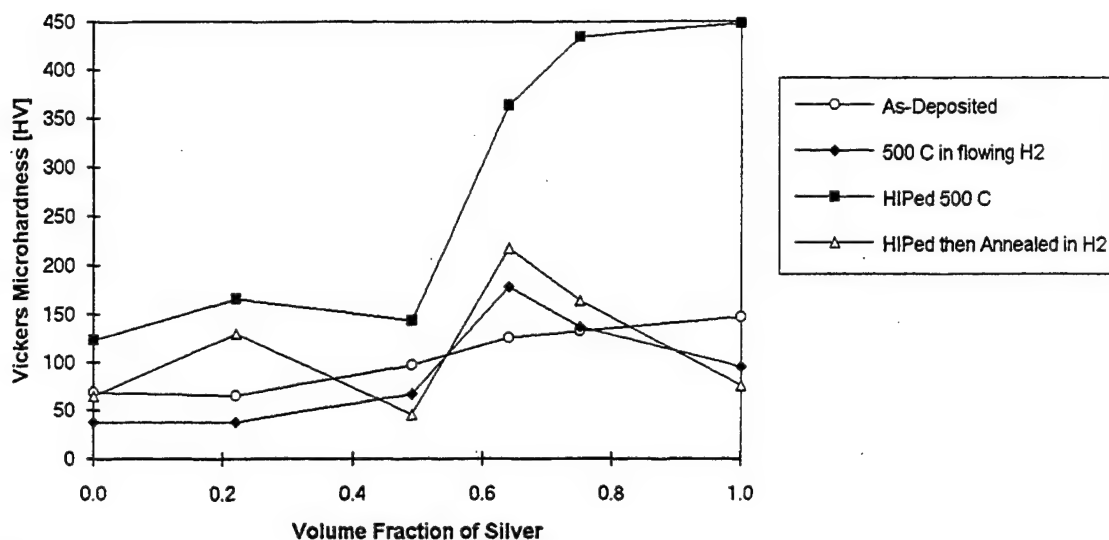
Fig. 9. Vicker's microhardness of silver–nickel nanocomposites as a function of consolidation treatment and volume per cent nickel.

problems, led us to consider other immiscible combinations of ductile metals. For obvious practical reasons, certain materials were eliminated from consideration: (1) any constituents more costly than gold, (2) those that are particularly hazardous, toxic, or carcinogenic, and (3) any constituents that could not be reduced easily in hydrogen below 1000 °C. In addition, combinations with more than a few per cent mutual solubility were not considered, as that can be expected to result in excessive grain growth at high temperature. Given these restrictions, there are only about 14 candidate systems: Ag–Co, Ag–Cr, Ag–Fe, Ag–Mo, Ag–Ni, Co–Cu, Co–Mo, Cr–Cu, Cu–Fe, Cu–Mo, and Fe-Mo. Considering constraints imposed by our synthesis equipment, the list was reduced further to just seven combinations: Ag–Co, Ag–Cr, Ag–Ni, which have similar phase diagrams; Ag–Mo, Cu–Mo, and Cu–Cr, which we expected to be similar to Cu–Nb which we had already tried; and Cu–Co. We decided to explore Ag–Ni, because materials with similar phase diagrams have not been studied before, it was expected on the basis of the free energy of formation of oxides to be the least oxidation prone, and it would be softer and consequently easier to consolidate at moderate temperature and pressures. Furthermore, some silver-coated nickel powders were available commercially for comparison with the physical-vapor deposited nancomposites. Consideration of prospective applications was not a factor in this selection.

Deposition and processing of the silver–nickel was essentially the same as used for the copper–niobium [6]. In Fig. 8 we illustrate the microstructural evolution and the corresponding X-ray diffraction spectra of a silver–nickel nanocomposite of about 64 vol.% nickel as a function of processing. The as-deposited and cold-pressed powder shows a fine but poorly consolidated microstructure (30–40 nm particle size) typical of nanocomposites produced by this method. Sintering the material for 2 h at 500 °C in flowing hydrogen produced a phase-separated microstructure with some grain growth. Some of the silver segregated into relatively large islands, resulting in a porous and poorly consolidated microstructure. HIPing the nanocomposite at 500 °C produced a microstructure similar to that of the sintered specimen, that is, silver segregation and a porous structure. The corresponding X-ray diffraction patterns show nickel oxide in the HIPed specimen, although no evidence of oxides in the as-deposited or hydrogen-sintered specimens.

Fig. 9 shows the microhardenss behavior of silver–nickel as a function of processing treatment and nickel content. As with the case of copper–niobium, the sintered specimen shows a peak in the hardness value near 60 vol.% nickel. The HIPed samples have high hardness when the nickel content is greater than 60 vol.%, and a minimum value at about 50% nickel.

For comparison, silver–nickel microcomposite samples were produced from commercially available silver-coated nickel particles (6–10 μm). Since the silver coating on the nickel particles was thin, corresponding to only 15% silver, enough excess silver powder (3–7 μm) was added to the mix to make an overall composition of about 60 vol.% nickel. The mixed and blended powders were first uniaxially cold pressed at about 500 MPa, and then HIPed at 500 and 200 MPa for 1 h. The consolidated microstructure, shown in Fig. 10(a), shows silver segregating around the nickel particles and some sintering together of the nickel particles. The other two SEM images in Fig. 10 illustrate the fractographic features of two silver–nickel specimens that were tensile tested at room temperature and at 345 °C respectively [9]. In both cases the failure appears to be
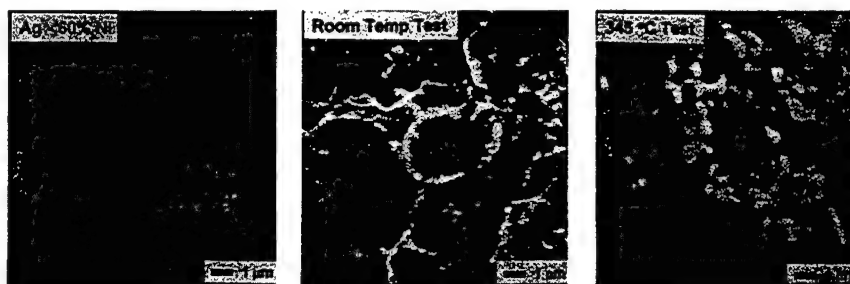
Fig. 10. SEM images showing microstructural details of compacted Ag–60 vol.% Ni microcomposites prepared from commercially available silver and silver coated niobium powders.

by decohesive rupture at the silver–nickel interface. The room-temperature tensile strengh was 330 MPa. For comparison, pure bulk silver and nickel have measured room temperature tensile strengths of 150 and 390 MPa respectively, so the strength value of the microcomposite approximately corresponds to that predicted from simple rule of mixtures. At the 345 °C testing temperature, however, the strength of the composite, 90 MPa, is significantly lower than a rule of mixture prediction based on the measured pure bulk silver and nickel strengths of 76 and 345 MPa.

To summarize the silver–nickel results, as in the case of copper–niobium, grain growth suppression was observed in the silver–nickel nanocomposite. Also similar to copper–niobium, the sintered nanocomposite shows a peak in microhardness around 60% nickel. In addition, silver–nickel is very difficult to process without forming nickel oxide; the formation of oxide probably increases the segregation of silver, embrittles the material; and prevents full consolidation. Finally, baseline study of silver–nickel microcomposites produced from commercially available micrometer size powders displayed poor elevated tensile strength and evidence of failure at the matrix–particle interface.

4. Discussion

Two important implications that can be drawn from this study are as follows. (1) A significant hardness peak was observed in sintered copper–niobium nanocomposite around 60–65 vol.% niboium and similar effects in silver–nickel, suggesting a dilatancy (wetstand) effect consistent with Louat's strengthening theory. (2) These nanocomposite are stable against grain growth even at temperatures close to the melting temperature of the matrix, also consistent with Louat's postulates for high tempreature strength retention. However, other observations bring into question another key requirement of theory. The need for strong particle–matrix interface bonding may be incompatible with the criterion of immiscibility of the two phases required to prevent grain growth. This consideration

leads us to conclude that, in practice, no technologically relevant phase-separated pure metals are available in nature to make nanocomposites for high temperature applications. Generally, our study has shown that, with few exceptions (specifically, the noble metals), nanocrystalline metals are difficult or impossible to handle and process without oxidation occurring and, further, that nanocomposites are difficult to consolidate by conventional methods.

Research over recent years has demonstrated certain obvious problems that generally apply to most nanostructured metals; that is, oxidation, thermal instability, and difficulty in consolidation. The need for a shift of focus on the presumed technological merits of nanostructured metals away from structural applications, particularly involving elevated temperatures, is apparent. Single-phase nanocrystalline metals are not thermally stable, which indicates that nanocomposites must be used instead to preserve nanosize grains above room temperature. Further, nanostructred metals, because of their very small size and large grain boundary surfaces, are very reactive. It is clear that processing steps especially those involving high temperature treatments, usually lead to the formation of oxides and other reactive compounds such as carbides and nitrides. Oxide formation weakens the interface between the matrix and the reinforcing particles in the composites, and prevents full densification. Poor interface bonding and incomplete consolidation usually result in a brittle compact with particle–matrix debonding as the most common mode of failure.

From what we have learned and have stated above, it is clear that realistic structural nanocomposites will take advantage of the reactivity of nanostructured metals by producing composite systems through in situ reaction processing. That is, the reinforcing phase, both for microstructural thermal stability and for mechanical property enhancement, will be a reactive product, such as an oxide, a carbide, a nitride, or an intermetallic phase. This approach not only may avoid the contamination problem that we encountered in the past, but will also produce a strong coherent interface between the matrix and the reinforcing phase. Another main

area of promise is non-structural applications that uti-
lize both the strong reactivity and the large grain
boundary surfaces of the nanostructured materials.
These include nanostructured coatings, for wear resis-
tance and for thermal barrier coatings, and nanostruc-
tural metals and alloys for gaseous getters and sensors
and for hydrogen storage.

References

[1] N.P. Louat, *Acta Metall.*, 33 (1985) 59.
[2] V. Provenzano, N.P. Louat, K. Sadananda, M.A. Imam, C.J. Skowronek, J. Calvert and B.B. Rath, in T.S. Sudarshan and D.G. Bhat (eds.), *Symp. on Surface Modification Technologies II.* The Minerals, Metals, and Materials Society, Warrendale, PA, 1989, p. 313.
[3] V. Provenzano, N.P. Louat, M.A. Imam and K. Sadananda, *Scri. Metall. Mater.*, 24 (1990) 2065.
[4] V. Provenzano, N.P. Louat, M.A. Imam and K. Sadananda, *Nanostruct. Mater.*, 1 (1993) 89.
[5] B.E. Williams, J.J. Stiglich and R.B. Kaplan, CVD coated tung-sten powder composites: processing and characterization, pre-sented at the *1991 TMS Annual Meet., New Orlands, LA, 17–21 February 1991.*
[6] R.L. Holtz and V. Provenzano, *Nanostruct. Mater.*, 4 (1994) 41.
[7] C.J. Youngdahl and J.R. Weertman, Northwestern University, unpublished, 1994.
[8] K. Koch and R.A. Vaughn, North Carolina State University, unpublished, 1993.
[9] J. Wolla, Naval Research Laboratory, unpublished, 1994.

Variations in nanostructure and composition for controlling the interfacial properties of metal matrix composites and ceramic matrix composites

J.T. McGinn[a], B. Singh[a], T. Mukherji[b]

[a]David Sarnoff Research Center, CN 5300, Princeton, NJ, USA
[b]Allied Signal Engines, 550 Main Street, Stratford, CT 06497, USA

Abstract

Interface properties are critical to the strength and toughness of metal matrix composites and ceramic matrix composites. These interfaces provide both diffusion barriers and load transfer functions. The nanostructure across the interface was varied to fulfill conflicting diffusion and load transfer demands. The deposition conditions developed allow nanostructure control of TiN fiber coatings. The TiN coating varied from a dense, diffusion-limiting layer to a columnar bond–debond layer. TiN was deposited in a reel-to-reel, cylindrical magnetron coater. The fiber bias and gas flow rates were the dominant deposition parameters controlling the nanostructure. Nanostructure changes were examined after consolidation in a Ti matrix and additional heat treatments at 1000 °C.

Keywords: Interfacial properties; Titanium; Heat treatments

1. Introduction

High temperature performance demands placed on advanced metal matrix composites (MMCs) and ceramic matrix composites (CMCs) have centered significant attention on the fiber interface. It is generally accepted that interface control is critical to mechanical success under extreme conditions. Three generic attributes demanded of a fiber–matrix interface are (1) preventing deleterious fiber–matrix interactions, (2) controlling fiber–matrix debonding characteristics, and (3) diminishing the negative effects of mismatch between the fiber and matrix coefficients of thermal expansion (CTE).

Limiting mass transport across the interface prevents deleterious fiber–matrix interactions by slowing interdiffusion and undesirable phase formation. Often associated with embrittlement and fiber depletion, such phases form during high temperature consolidation or extended periods under lower temperature operating conditions.

Proper bonding insures crack deflection along the fiber–matrix interface rather than shearing the fiber in the crack plane. This is particularly true of CMCs where strong fiber–matrix bonding results in a single fracture plane through fiber and matrix. Fracture surface deflection increases the crack propagation energy. Additional energy required to pull debonded fibers from matrix cavities further toughens the material.

The effects of CTE mismatch arise owing to abrupt changes in material properties at the fiber–matrix interface. Finite element modeling has shown hoop stresses are displaced from the interface by coatings with properties that vary gradually between the fiber and the matrix [1].

These demands are in conflict. Limiting fiber–matrix interactions requires a high temperature barrier with low diffusivity. Suitable materials typically contain few internal diffusion paths (e.g. voids, grain boundaries and dislocations), have close packed structures, and often display covalent bonding. Conversely, crack deflecting layers benefit from high densities of stress-risers and crack-initators. CTE mismatch layers containing materials foreign to the interface increase the chemical complexity.

Multilayer coatings represent a solution to those conflicting demands. Typical multilayer coatings containing distinct chemical layers add to interface com-

plexity and increased manufacturing cost. An alternative, that has received little attention, is the use of nanostructure to alter the properties of successive coating layers. In this approach, deposition would vary, forming a dense, low-defect density diffusion barrier and a porous, crack-deflecting layer in a single coating. Columnar grain removal from diffusion barriers is important. These grains are commonly formed by many deposition processes. The associated grain boundaries offer rapid diffusion paths.

Loosely packed grains and voids offer the possiblity of modifying the bond strength across the crack-deflecting layer. Additional compatibility can be introduced if coating layers incorporate transition regions with material properties varying gradually from fiber-like to matrix-like. This requires coating-material properties that vary continuously with composition over an extended phase field. Titanium nitride possesses such an extended phase field with a Ti-to-N ratio varying from 28 to 55 at.%. Our goal was to develop a single material coating with nanostructure variation suitable to accomplish the three functions of a fiber–matrix interface. This work demonstrates the ability to change the nanostructure by depositing symmetric coatings with layers varying from columnar to equiaxed and back to columnar. This symmetry insures that a layer's nanostructure is not predetermined by the structure of the preceding layer.

A cylindrical magnetron, shown schematically in Fig. 1, was used to deposit all coatings. The cylindrical mangetron was developed at Sarnoff specifically to coat fibers. The procedure to control the nanostructure and vary the coating composition has not previously been demonstrated on fiber-like substrates.
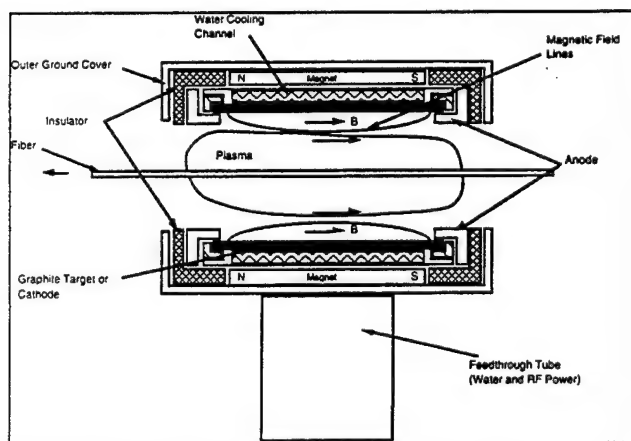
Fig. 1. Cylindrical PECVD reactor module used for deposition of multi-layer coatings onto moving SCS fibers. Three of these source modules were installed in the base of the vacuum chamber.
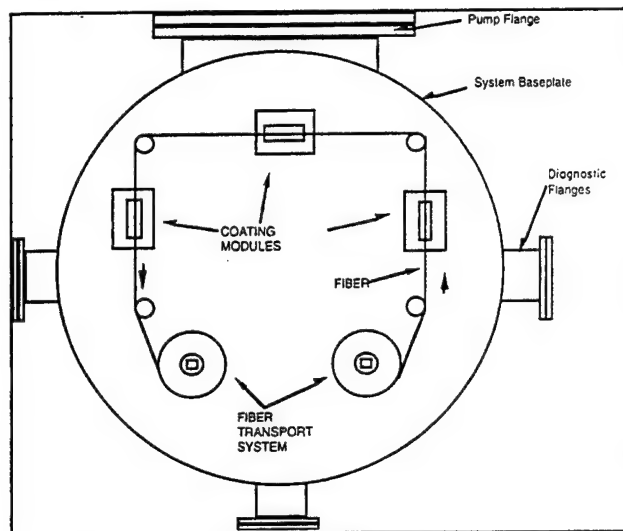
Fig. 2. Top view of the reel-to-reel system developed for coating long fiber lengths.

2. Experimental details

2.1. Experimental system

Although variations in nanostructure and composition have applications to both MMCs and CMCs, only MMC matrix materials was explored. The composite studied for this work was a Ti-1100 matrix with embedded SCS-6 fibers from Textron Specialty Materials. Rhodes characterized the interface formed in this system, and strong fiber–matrix interactions were found [2]. Titanium nitride was chosen as the coating. Titanium nitride has strong covalent bonds and a resultant low self diffusion coefficient. It is a highly effective diffusion barrier for integrated circuits (ICs) [3]. Our choice of this system was guided by previous experience and the large literature base relating deposition conditions and nanostructure.

2.2. Coating deposition, cylindrical magnetron

Coatings were applied to SCS fibers using a specially designed cylindrical magnetron sputtering source shown in Fig. 1. The system has three modules that can deposite multiple layers or undertaken fiber pre-cleaning. Fig. 1 shows a cross-section of a sputtering module and Fig. 2 is a top view of the deposition system.

The cylindrical magnetron provides uniform, high-rate coating capability for SCS-6 fibers. The fiber is centered in each module by the fiber transport system. The sputtering target is cylindrical and arranged as shown in Fig. 1. Plasma is generated using r.f. (13.56 MHz) excitation and a capacitively coupled "L" type impedance matching network. Commerically available Plasma Therm, Inc., r.f. power supplies and matching networks were also used.

The source configuration in Fig. 1 embodies some unique construction features enabling the cathode or "target" to be water cooled and rapidly changed. The sputtering module's diameter is 2.0 inches and the active region's length is approximately 3.0 inches. The device employs an auxiliary anode and a proprietary fiber biasing capability.

Fig. 2 shows the top view of the coating system. Computerized gas flow meters and pressure controllers are used to introduce and control the process gas mixture, flow rate, and pressure in real time. The specially designed, in situ reel-to-reel fiber transport system is computer controlled. The control algorithm enables selection of fiber speed, duration of specific fiber sections in the coating zone, number of repeated back and forth steps, etc. A stepper motor is used for the transport movement. The combination of the stepper motor and the computerized control system enables selected fiber sections to be positioned accurately in the coating zone.

To ensure reliable operation of the transport, the tension and synchronization of the take-up and source spools had to be carefully controlled. Thus the fiber transport system required considerable development and optimization to make it suitable for monofilament SCS fibers.

2.3. Parameter space explored

Graded titanium nitride coatings were achieved by varying the N_2 flow during deposition. A single fiber pass through the coater was made at a fixed N_2 flow rate. The N_2 flow rate was then altered and a subsequent pass made. This process continued until the desired structure was achieved. A pure titanium layer was deposited in initial and final passes to promote adhesion. Argon was used as a carrier gas.

The coatings were deposited using multiple sources. The parameters used for the experiments are shown in Table 1. Since the SCS fiber are sufficiently conductive, a d.c. bias can be employed. The d.c. bias effects the composition of the TiN films. This requires calibrating the deposition conditions for each bias used. Calibration runs were analyzed for composition and nanostructure

Table 1
Parameter space investigated

	Range explored	High density coating	Columnar coating
Bias (V)	0–400	−80	−40
Power (W)	100–700	400	400
Pressure (μm Hg)	5–20	20	20
Flow (Ar + N_2) (standard $cm^3 min^{-1}$)	100	100	100
N_2 flow (standard $cm^3 min^{-1}$)	0.5–5	2	0.5–2

Table 2
Gas flow rates and resultant Ti:N ration for deposited film

Ar flow (standard $cm^3 min^{-1}$)	N_2 flow (standard $cm^3 min^{-1}$)	Ti-to-N ratio
99.5	0.5	0.90
99.0	1.0	0.57
98.0	2.0	0.52

Cylindrical magnetron processing parameters, shown in Table 1, are similar to traditionally planar magnetron values.

2.4. Consolidation

A standard consolidation procedure was used to embed both coated and uncoated SCS-6 fibers in a Ti-1100 matrix. Sheets of Ti-1100 was etched in 0.5% HNO_3 1.0% HF, 98% H_2O, rinsed in double distilled H_2O with a final rinse in ethyl alcohol. A foil–fiber–foil consolidation scheme was used with a consolidation frame providing lateral confinement. Frame and sample were evacuated to 5×10^{-6} Torr and heated to 1000 °C. The system was brought to atmospheric pressure under argon flow. The consolidation force and temperature were raised slowly to 7000 psi and 1000 °C respectively. Consolidations continued for 2 h. Subsequently, the consolidation force was removed slowly and the sample cooled under argon. Strips were cut from the consolidated coupon for separate anneals of 3 and 9 h at 1000 °C.

3. Results

The effects of various magnetron and process variables on thin film nanostructure and compositon were studied. The selected range for each parameter was based on previous experience. The parameter's ranges and the optimum value for a titanium nitride film with a compact nanostructure and a golden-yellow color, typical of a stoichiometric TiN, are given in Table 1. Table 2 gives the titanium-to-nitrogen ratios for coatings deposited at −80 V bias as determined by electron microprobe analysis.

Fiber bias was the dominant parameter controlling the coating's nanostructure. Columnar or densely packed nanostructures could be deposited over a wide range of nitrogen flow conditions by fixing the fiber bias. The most equiaxed coatings were deposited with a bias of −80 V. With increasingly positive bias, intermediate and eventually columnar nanostructures resulted. The equiaxed and columnar structures are shown in Fig. 3(a) and (b). Biases more negative than −80 V caused a decrease in deposition rate. The coating adhesion deteriorated with increasing negative bias. Coatings deposited

(a)

(b)
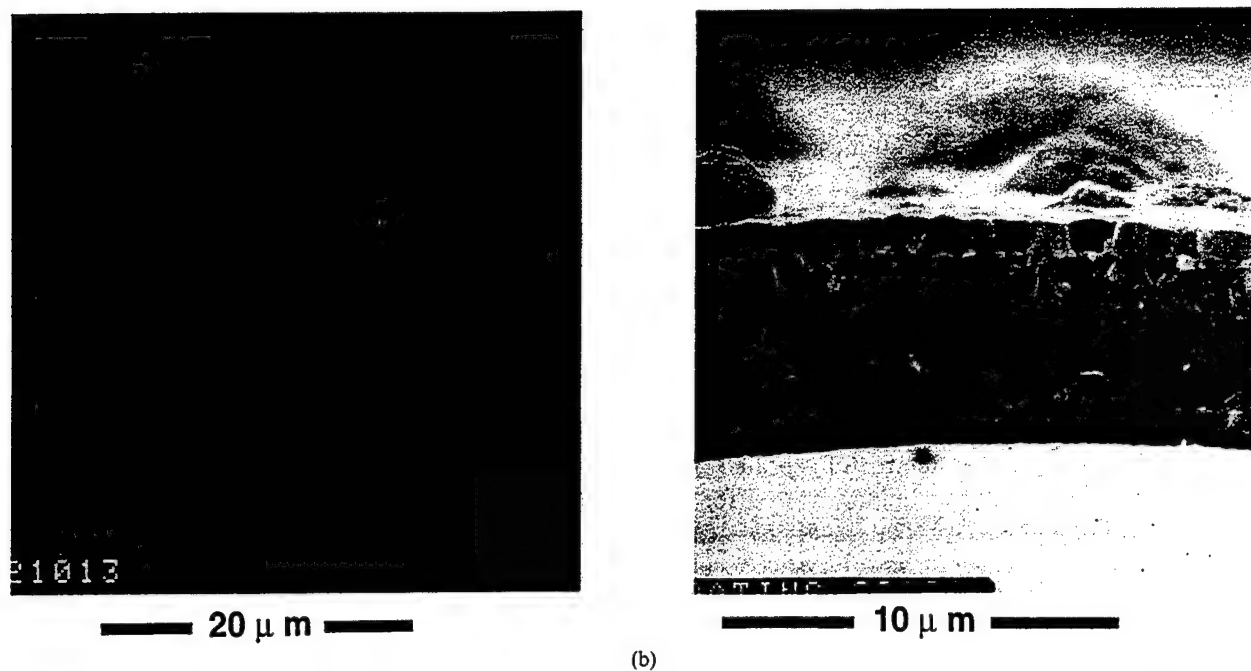
Fig. 3. With increasingly negative bias, the deposited titanium nitride's nanostructure changes from columnar to equiaxed: (a) bias −40 V, columnar nanostructure with grain boundaries passing through the layer and acting as rapid diffusion path; (b) −80 V bias, equiaxed grain boundary structure.

with a −80 V bias lacked sufficient adhesion to survive consolidation. Fiber–coating adhesion was improved by depositing the first nitride layer with a −40 V bias. To retain coating symmetry, the final nitride layer was also deposited at −40 V bias. All internal layers were deposited at −80 V bias.

Titanium-to-nitrogen ratios are shown in Table 2. All coatings were deposited with a −80 V bias. Compositions near stoichiometric TiN are deposited at the lowest nitrogen flow rate. At the highest nitrogen flow rate, the composition approaches stoichiometric Ti_2N. Crystalline phases were identified by X-ray diffraction. Graphite, α-SiC, and β-SiC, from the SCS-6 fiber, were always detected. Coating phases associated with a −80 V bias and various flow rates are listed in Table 3. Oxides, when observed, were associated with residual gaseous oxygen in the sputtering chamber. TiN was found for all gas flow conditions while Ti_2N was observed sporadically.

The final coating contained eight layers differing in titanium-to-nitrogen ratio and bias. To improve the adhesion further, an initial layer of titanium was deposited. Coating symmetry was maintained with the final four layers deposited in reverse order to the first four. Deposition conditions for each layer are given in Table 4 and the resultant structure is shown in Fig. 4.

As-consolidated samples demonstrated good protection of the fiber–matrix interface. Etching of polished sections revealed a complex structure around coated fibers after consolidation. Fig. 5 shows a cross-section after a 3 min etch in 1% HNO_3, 2% HF, 97% H_2O. Qualitative Auger analysis indicated interdiffusion across the titanium–graphite and TiN–matrix interfaces. TiC had formed at the titanium–graphite interface. The trend seen in Fig. 5 was too thin for Auger analysis but from its etching characteristics it is surmised to be unreacted titanium.

Table 3
Crystalline phases identified by X-ray diffraction, all layers deposited under −80 V bias

Flow rate (standard cm^3 min^{-1})	TiN	Ti_2N	TiO_2
0.5 N_2, 99.5 Ar	X		X
1.0 N_2, 99.0 Ar	X	X	
2.0 N_2, 98 Ar	X		

Table 4
Deposition parameters for symmetric coating layers

Layer	Bias (V)	N_2 flow (standard cm^3 min^{-1})	Ar flow (standard cm^3 min^{-1})
1	0	0	100
2	−40	0.5	99.5
3	−80	1	99
4	−80	2	98
5	−80	2	98
6	−80	1	99
7	−40	0.05	99.6
8	0	0	100
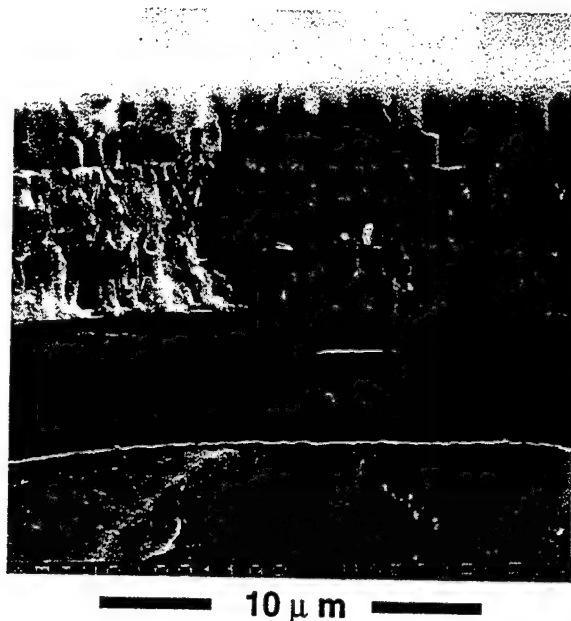
Fig. 4. Symmetric coating showing variation in the nanostructure and composition of titanium nitride layers. The first and last layers of the deposition are pure titanium.

Fig. 5. SEM image of coated fiber after consolidation.

4. Discussion and conclusions

Simultaneous nanostructure and composition control of a single-phase system deposited onto cylindrical fiber surfaces has been demonstrated. This capability offers the possibility of a single material system meeting multiple coating demands. While nitrogen diffusion into the matrix clearly indicates that titanium nitride is unsuitable as a coating in the SCS-6/Ti-1100 system, the principles demonstrated can serve as a useful step in designing a system that possesses the required coating attributes.

Fiber bias is the principle parameter for controlling the deposition nanostructure. Coatings change from columnar to equiaxed as the fiber bias is changed from 0 V to −80 V. It is believed the bias supplies additional energy to arriving ions and promotes local rearrangment of the ions into the deposited film. Extensive work on ion-assisted deposition of very high performance coatings has shown optimum properties for films bombarded with reative species having energies of a few tens of electronvolts [4,5]. It appears the key role of ion bombardment during growth is imparting adatom mobility to the condensing species. This enhances epitaxial growth, increases film density by eliminating columnar growth, reduces film stress, and improves many other desirable film properties [5]. Typically, it is desirable that impinging ions have energies approximately equal to the growth material's chemical bond strength. Ener-

gies in excess of few hundred electronvolts, however, can cause structural and crystalline imperfections in the deposited layers. An optimum bias or ion energy bombardment level must be determined empirically.

Varying the coating composition from fiber-like to matrix-like allows tailoring mechanical properties across the fiber–matrix interface. Matching CTE and elastic properties across the coating are attractive possibilities. Clearly titanium nitride is not suitable for the SCS-6/Ti-1100 system owing to the rapid diffusion of nitrogen in Ti-1100. The work does demonstrate simultaneous nanostructure and composition modification for fiber coatings using a cylindrical magnetron and standard sputtering practices.

References

[1] M.E. Labib, H. Merrick, L.S. Hu, C.-Y. Lai and B. Singh, Graded composition fiber coatings for intermetallic matrix composits, *NASA Conf. Publ. Proc. HITEMP Review 1991*, Advanced High Temperature Engineering Materials Technology Program, Westlake Holiday Inn, Cleveland, OH, October 1991.

[2] C.G. Rhodes, Study of titanium-matrix composites, *Technical Report SC5288, iFR*, 1982 (Rockwell-International Science Center, Thousand Oaks, CA).

[3] N. Kumar, K. Pourrezaei, J.T. McGinn, B. Lee and E.C. Douglas, TEM study of brown golden titanium nitride thin films in VLSI diffusion barriers, *J. Vac. Sci. Technol. A*, 6 (1988) 1602.

[4] P.J. Martin, H.A. Macleod, R.P. Netterfield, E.G. Packey and W.G. Sainty, Assisted deposition of optical films, *App. Opt.*, 22 (1983) 178.

[5] R. Messier and Y.E. Yehoda, Investigation of film microstructures in thin films, *J. App. Phys.*, 58 (1985) 3739.

ELSEVIER

Nanostructured palladium membrane synthesis by magnetron sputtering

Kenneth J. Bryden, Jackie Y. Ying*

Department of Chemical Engineering, Massachusetts Institute of Technology, Cambridge, MA 02139, USA

Abstract

Palladium membranes are of technological interest since they show a very high selectivity for hydrogen. Diffusion through the palladium is often the rate-limiting step in hydrogen transport through the membrane. Hydrogen flux can be improved by reducing the membrane thickness and increasing the hydrogen diffusivity. Nanostructured palladium has a higher hydrogen diffusivity than conventional palladium due to its large volume fraction of grain boundaries. They were generated as ultrathin membranes by d.c. magnetron sputtering onto porous Vycor® glass substrates in an argon atmosphere. The nanostructured films exhibited no cracks on the submicron scale when examined with environmental scanning electron microscopy. The membranes delaminated from the substrates when exposed to hydrogen at room temperature, owing to the $\alpha \rightarrow \beta$ phase transition. Heating the ultrathin nanostructured palladium membranes to 200 °C led to some grain growth. Stabilization against the phase transition and grain coarsening is critical to applications of nanostructured membranes in hydrogen separations, and can be achieved by the alloying of palladium with another metal.

Keywords: Nanostructures; Palladium; Inorganic membranes; Magnetron sputtering

1. Introduction

Inorganic membranes have attracted considerable interest since they can be used for high-temperature separations and also in high-temperature membrane-assisted catalytic reactions [1–3]. In a membrane reactor the equilibrium is shifted by selectively removing one of the products or adding one of the reactants. Membranes produced from hydride-forming metals are one class of inorganic membranes. As non-porous membranes, these metals provide high permselectivity for hydrogen. Hydrogen passes through metal membranes by a solution-diffusion mechanism: it adsorbs on the surface of the metallic membrane, dissociates, diffuses through the bulk metal, and then recombines to form molecular hydrogen, which desorbs from the membrane surface [1].

Metal membranes can be used to separate hydrogen in a gas mixture. They can also be employed in membrane reactions involving hydrogenation or dehydrogenation. By selectively adding or removing hydrogen

from a reaction, the steady-state concentration of reactants and products can be shifted to a more favorable equilibrium conversion [4]. For example, continuous hydrogen removal in a membrane reactor enabled 99.7% conversion of cyclohexane to benzene, compared to the closed-system equilibrium conversion of 18.7% [5]. By changing the equilibrium conditions, it may also be possible to suppress undesirable side-reactions in certain cases to increase product selectivity.

Metallic membranes have the disadvantages that they are expensive and that the flux through them is low. They can be improved if the metallic layer can be made thinner. A thinner metal layer, however, has lower mechanical strength in a self-supporting metal membrane application. In order to meet the challenge of attaining both high selectivity and good mechanical strength, metal membranes have been deposited on inorganic supports such as glass, ceramics and metals.

Several different methods have been used to deposit the metal onto the porous support: electroless plating [6–9], spray pyrolysis [10] and sputtering [11–13]. Sputtering has several advantages: (a) synthesis of ultrathin films with minimal impurity, (b) greater flexibility for

---

* Corresponding author.

synthesizing alloys, (c) easily controllable process parameters, and (d) the ability to generate nanostructured films. At high sputtering pressures (10–100 Pa) the metal atoms collide with argon atoms and lose energy. This cooling leads to a high supersaturation of metal atoms which can cause homogenous nucleation to form nanocrystalline particles in the gas phase [14]. As the gas pressure is lowered, thermalization decreases, and the metal atoms are more likely to deposit directly onto the substrate, forming granular thin films with grain sizes in the nanometer range [15]. Nanostructured materials have been investigated with a great deal of interest because of their unique size-dependent properties [16]. They are polycrystalline solids made up of grains of up to 10 nm diameter. Due to the small crystal size, a nanostructured material has 20–50% of its atoms located in the grain boundaries. Consequently, this material can be thought of as composed of two structural components: a crystalline component made up of nanometer-sized grains, and a grain-boundary component that has a lower packing density than a crystalline structure [16].

The rate-limiting step in membrane applications is hydrogen diffusion through the bulk material. Diffusion through the crystalline lattice is determined by the atomic structure and the chemical nature of the material. Compared to lattice diffusion, grain-boundary diffusion is significantly faster owing to the excess free volume in the grain boundaries. Nanocrystalline materials have the benefit of a substantial grain-boundary component which acts as a network of fast diffusion pathways. The overall diffusivity of the nanocrystalline material can be as much as about 10 times higher than that of conventional polycrystalline material [16].

Previous research provides evidence for the structure-sensitive diffusion coefficients in nanocrystalline Pd. Fig. 1 [17] illustrates that at very low hydrogen concentrations the diffusivity of hydrogen is smaller in nanocrystalline Pd than in a Pd single crystal. However, the diffusion coefficient increases with hydrogen concentration for nanocrystalline Pd and becomes significantly higher than the constant diffusion coefficient in single-crystal Pd [17]. The hydrogen diffusivity is thought to be initially lower in nanocrystalline materials due to the filling of hydrogen in low-energy sites. Once these sites are occupied, hydrogen can move quickly along the interfaces, producing a much higher diffusivity than in conventional materials. Thus, a nanostructured Pd ultrathin membrane would be very attractive, due to the increase in the hydrogen flux from increasing the hydrogen diffusivity and reducing the film thickness.

For depositing thin nanostructured metallic films, a substrate with pores larger than 20 Å is needed to prevent mass-transfer resistance. However, to provide proper support for the deposition of a crack-free film,

the substrate should have pores less than 100 nm. The substrate should also be thermally stable and defect-free. Corning Vycor® porous silica glass was tested as the substrate.

2. Experimental details

The nanostructured thin films were synthesized in a custom-designed ultrahigh vacuum system with d.c. magnetron sputtering (3 inch diameter gun, US Inc.) [18]. Pd was sputtered at a power of 100 W and argon pressures between 0.1 and 7 Pa. Before sputtering, the system was pumped down to a base pressure of 5×10^{-3} Pa. The Pd films were sputtered onto porous Vycor® glass disks (Corning 7930) mounted a distance of 13 cm from the metallic target. The film thickness and deposition rate were measured in situ by a film thickness monitor (Sycon Instruments STM-100/MF).

The grain size and microstructure of the deposited films were examined by transmission electron microscopy (TEM). Copper grids with silicon monoxide films were placed in the same location as the glass substrates. The samples collected on the copper grids were studied with a JEOL 200CX TEM operating at 200 kV.

The glass substrates were characterized by nitrogen adsorption for B.E.T. surface area and pore size distribution. The thickness and morphology of the films deposited on the Vycor® were examined by environmental scanning electron microscopy (ElectroScan ESEM).

The helium and hydrogen fluxes through the membrane packages were measured in a membrane perme-
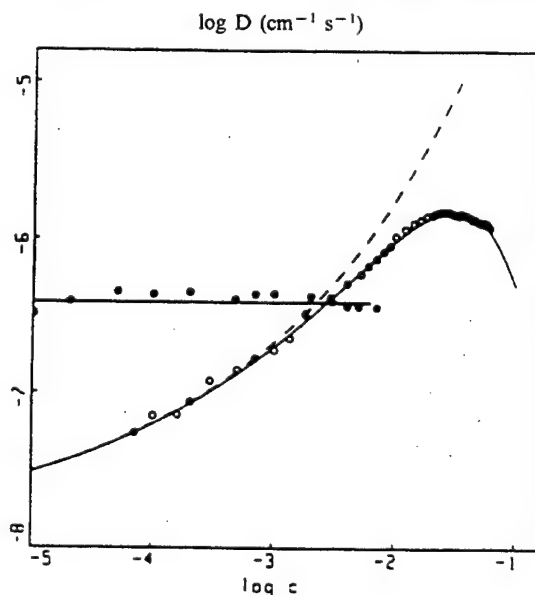
Fig. 1. Diffusion coefficient of hydrogen at 293 K as a function of hydrogen concentration in single-crystal palladium (●) and nanocrystalline palladium (○) [17].
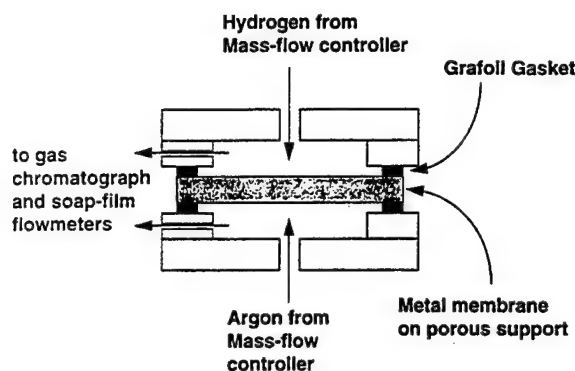
Fig. 2. Schematic of the membrane permeation cell.

ation cell (Fig. 2). The metal film supported on the porous glass was sealed between two flexible Grafoil® graphite gaskets. Each half of the permeation cell was equipped with gas inlets and outlets. Thermocouples were used to measure the temperature on both sides of the permeation cell. Pure hydrogen was introduced over the top of the membrane package, and pure argon was used as a sweep gas on the other side of the membrane package. The entering flow rates were measured by mass-flow controllers, and the flow rates of the exiting streams were measured with soap-film flow-meters. The compositions of the entering and exiting streams were determined using a gas chromatograph (Hewlett–Packard 5710A) equipped with a thermal conductivity detector.

3. Results and discussion

3.1. Effect of sputtering pressure on film morphology

Studies were first conducted at different pressures to determine the effect of sputtering pressure on film morphology. Transmission electron micrographs of Pd films on copper TEM grids are presented in Fig. 3. At an Ar pressure of 7 Pa, a film with a discontinuous "island" morphology and large cracks was produced. As the pressure was lowered to 2 Pa, a granular film with many fine pores and pinholes was obtained. This material would not provide sufficient hydrogen selectivity. When the pressure was further decreased to 0.7 Pa, a dense, continuous nanocrystalline granular film was achieved. A high-density, crack-free, non-porous film of finer grain size was achieved at 0.1 Pa.

3.2. Examination of porous glass substrates

The pore size distribution of Vycor®-brand porous glass is presented in Fig. 4, showing the average pore diameter of 40 Å. The thermal stability of the porous glass substrates was characterized by heating the glass
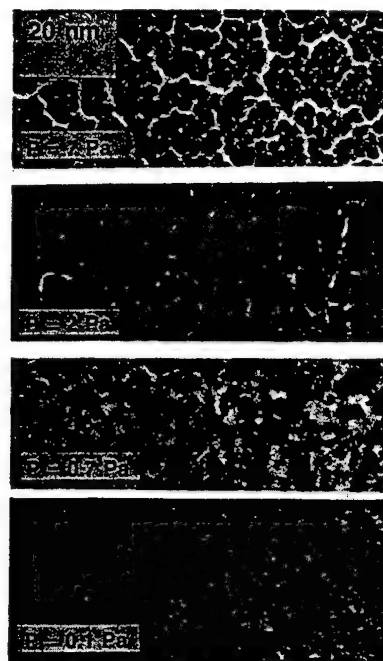
Fig. 3. TEM images showing the effect of sputtering pressure on palladium film morphology.

in air for 10 h in a series of treatments of increasing temperatures. The results are presented in Fig. 5. This glass substrate remained unchanged in microstructure below 600 °C, and decreased in surface area and microporosity above that temperature. The thermal stability to 600 °C is acceptable for most membrane-assisted reactions which operate at temperatures between 200 and 600 °C [19].

Vycor® brand glass is available with ground surface, rolled surface, and ground-and-polished surface. ESEM investigation revealed that ground surface glass has large pores (about 20 μm in diameter) which would make it impossible to deposit a crack-free film of a desirable thickness of about 1 μm. Glasses with rolled surface and ground-and-polished surface are both shown by ESEM to have much smoother morphology (Fig. 6). These two forms of Vycor® brand glass were chosen as substrates for Pd film deposition.
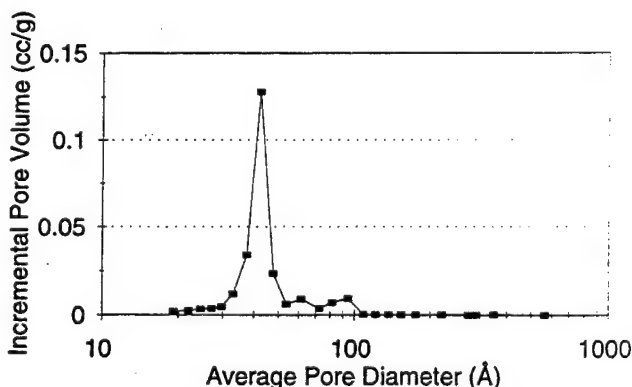
Fig. 4. Pore size distribution in porous Vycor® glass.
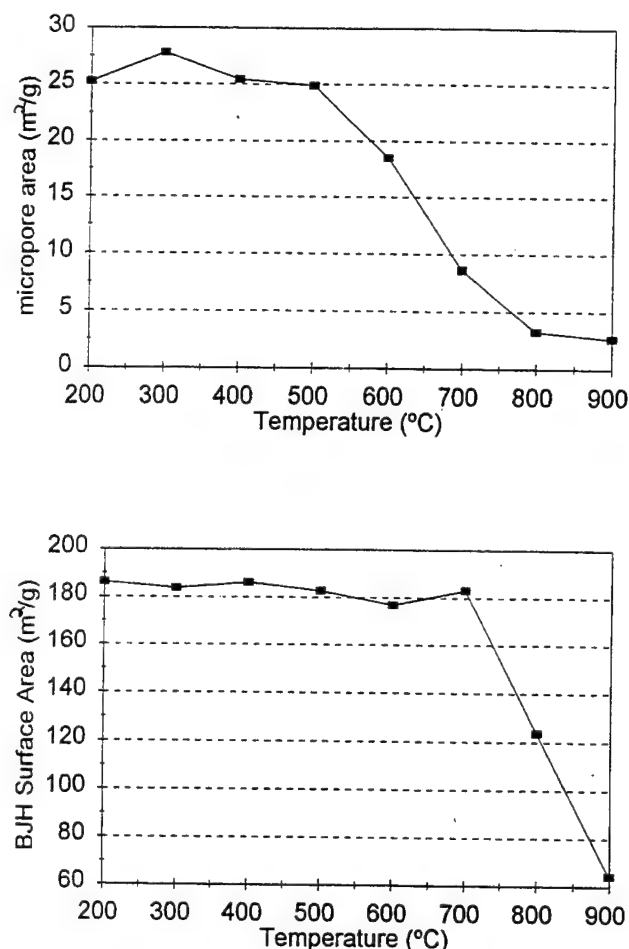
Fig. 5. Plots of microporosity and surface area vs. heating temperature for porous Vycor® glass.

3.3. Synthesis and characterization of supported metal membranes

Sputtering was used to produce ultrathin Pd films on the glass substrates. It was carried out at a pressure of 0.3 Pa. This sputtering pressure would yield a dense, nanocrystalline film at a reasonable deposition rate of 4–5 Å s^{-1}. The glass substrates were mounted 13 cm from the target, and sputtering was carried out at a power of 100 W. Films with thicknesses of 0.05 μm, 0.5 μm, 1 μm and 5 μm were obtained. Examination of the as-prepared membrane packages with ESEM showed that the Pd films were continuous and had no cracks that were visible at the resolution limit of ESEM (about 100 nm). Edge-on examination showed that the film thickness was uniform (Fig. 7).

After examination with ESEM, the membrane packages were loaded into the gas permeation cell to determine their hydrogen permselectivity. Leak-checking with helium revealed some leakage in the Pd films, possibly due to pinholes in the film that were too small to see with ESEM. These pinholes were most likely related to submicron-sized surface defects in the Vy-

cor®-brand glass substrates, which would require "caulking", for example, by aqueous colloidal silica deposits [20]. When the films were exposed to hydrogen at room temperature, they delaminated owing to the $\alpha \rightarrow \beta$ phase transition. Examination with ESEM after membrane exposure to hydrogen revealed the presence of many fine cracks caused by the expansion and contraction of the Pd from the phase transformation. Temperatures greater than 310 °C and pressures above 2.0 MPa would move the range of operation out of the two-phase region and avoid any phase transition in Pd [1]. However, grain growth might occur at high operating temperature.

The nanostructured Pd thin film was found to be less thermally stable than a bulk nanostructured Pd compact. Previous studies indicate that a nanostructured Pd compact undergoes only minor grain growth from 6 nm to 20 nm when heated to 750 K (477 °C) [21]. The thermal stability of a nanostructured Pd film 0.05 μm thick on porous glass was examined at 200 °C in air. As illustrated in the ESEM micrographs in Fig. 8, grain growth has occurred in these films, resulting in some grains as large as 100–200 nm. Thus, with heating, the high volume fraction of grain boundaries in the pure Pd nanostructured thin film would be lost, and with it the desired high hydrogen diffusivity. This grain growth is consistent with the work of others who found that pure gold deposited on SiO$_2$ had grain growth occurring at 20% of its melting temperature [22]. Grain growth in thin-film samples is different from that in bulk samples
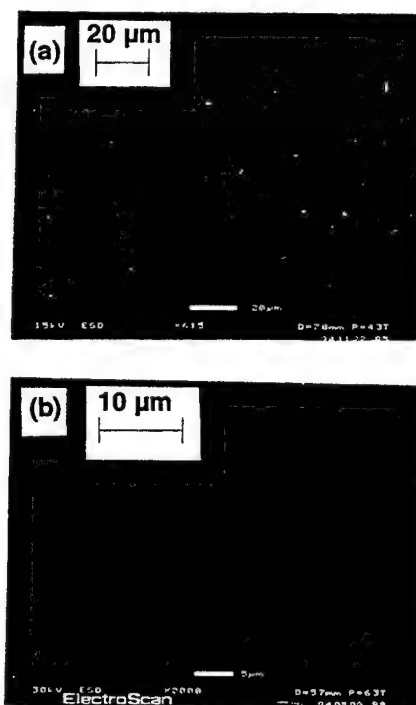
Fig. 6. ESEM images of the surface of untreated porous glass: (a) rolled surface; (b) ground-and-polished surface.
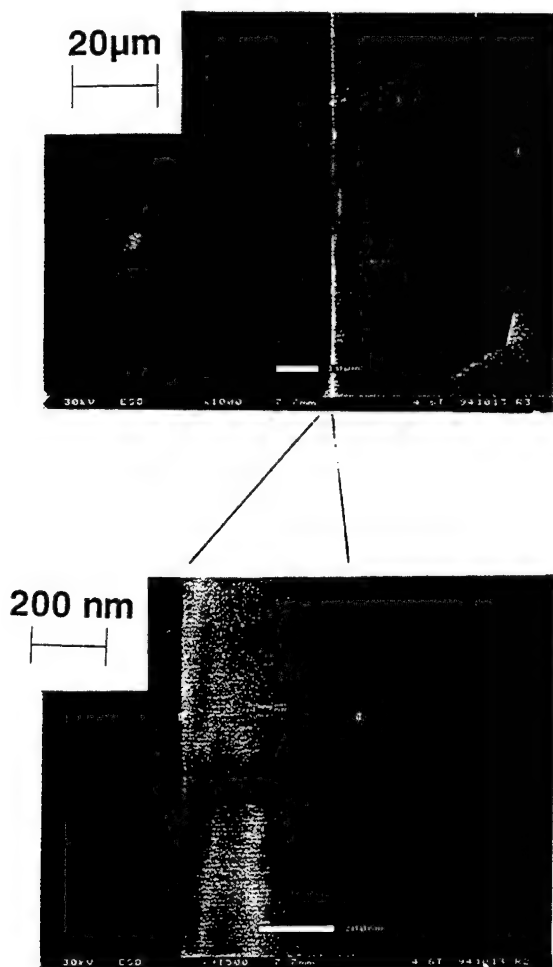
Fig. 7. ESEM image showing edge-on view of palladium film 470 nm thick on porous glass.

due to the presence of the interface with the substrate and the top surface of the film [23].

In order to suppress grain growth and the $\alpha \to \beta$ phase transition, doping of Pd with another element will be performed. Krill et al. found that a 20at.%Zr-80at.%Pd alloy with 7 nm diameter grains synthesized by high-energy ball milling could be significantly stabilized against grain growth due to the thermodynamic effect of solute segregation to the grain boundaries in this supersaturated solution [24]. On the other hand, alloying Pd with Ag, Ru, Rh and other metals has been found to suppress the $\alpha \to \beta$ phase transition at room temperature [1,19]. With the proper choice of dopant, a material can be designed to avoid both grain-growth and phase-transition problems. Sputtering would be ideally suited to preparing a uniform multicomponent material, since it can maintain the composition of the sputtering target in the film deposited.

4. Conclusions

Nanostructured Pd films were produced on porous Vycor®-brand glass supports by d.c. magnetron sputtering in an argon atmosphere. Ultrathin, crack-free films may be produced under controlled sputtering conditions. To achieve successful nanostructured membrane development, further research is needed to tackle challenges in substrate preparation, and thermal and mechanical stability of thin films. The former involves modification of the substrate through materials processing strategies that will provide a microdefect-free surface morphology, such as by plugging the microdefects with colloidal silica. Alloys need to be developed to stabilize the nanostructured thin film against grain growth at high temperatures, and against delamination and cracking from the $\alpha \to \beta$ phase transition. Further research is also needed in understanding the thermodynamics and kinetics of nanostructured thin films for advanced membrane reaction applications.
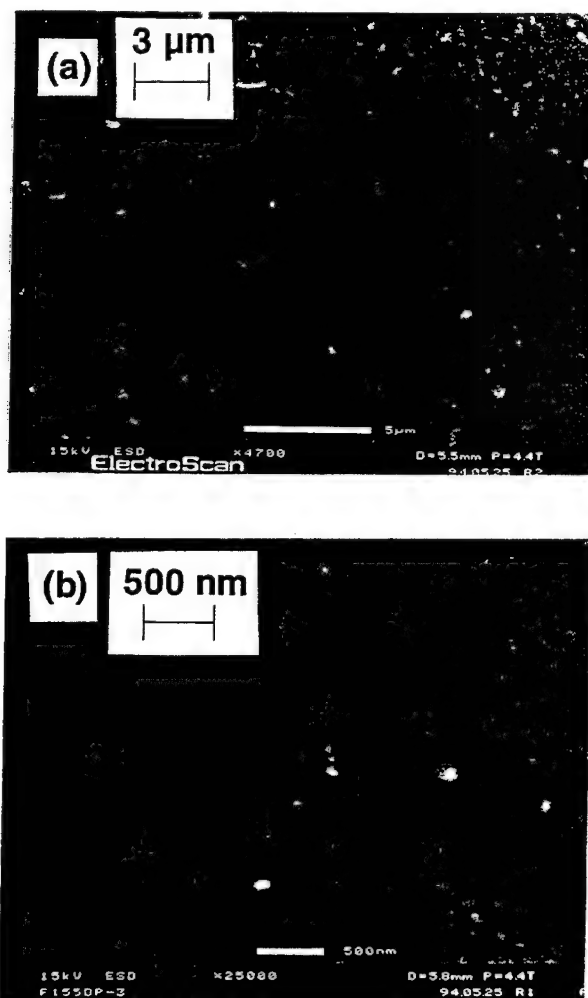
Fig. 8. ESEM images of 500 Å Pd films heated to 200 °C on porous glass: (a) rolled surface; (b) ground-and-polished surface.

Acknowledgments

References

[1] J. Shu, B.P.A. Grandjean, A. van Neste and S. Kaliaguine, *Can. J. Chem. Eng.*, *69* (1991) 1036.
[2] J. Zaman and A. Chakma, *J. Mem. Sci.*, *92* (1994) 1.
[3] G. Saracco and V. Specchia, *Catal. Rev. — Sci. Eng.*, *36* (1994) 305.
[4] J.N. Armor, *Appl. Catal.*, *49* (1989) 1.
[5] N. Itoh, *AIChE J.*, *33* (1987) 1576.
[6] S. Uemiya, T. Matsuda and E. Kikuchi, *J. Mem. Sci.*, *56* (1991) 315.
[7] R. Govind and D. Atnoor, *Ind. Eng. Chem. Res.*, *30* (1991) 591.
[8] J. Shu, B.P.A. Grandjean, E. Ghali and S. Kaliaguine, *J. Mem. Sci.*, *77* (1993) 181.
[9] J.P. Collins and J.D. Way, *Ind. Eng. Chem. Res.*, *32* (1993) 3006.
[10] Z.Y. Li, H. Maeda, K. Kusakabe, S. Morooka, H. Anzai and S. Akiyama, *J. Mem. Sci.*, *78* (1993) 247.
[11] S. Ilias and R. Govind, *AIChE Symp. Series*, *268*, *85* (1989) 18.
[12] V.M. Gryaznov, O.S. Serebryannikova, Yu. M. Serov, M.M. Ermilova, A.N. Karavanov, A.P. Mischenko and N.V. Orekhova, *Appl. Catal. A*, *96* (1993) 15.
[13] E. Gobina and R. Hughes, *J. Mem. Sci.*, *90* (1994) 11.
[14] J.Y. Ying, *J. Aerosol Sci.*, *24* (1993) 315.
[15] V. Haas and R. Birringer, *Nanostr. Mater.*, *1* (1992) 491.
[16] H. Gleiter, *Prog. Mater. Sci.*, *33* (1989) 223.
[17] R. Kirchhiem, T. Mütschele, W. Kieninger, H. Gleiter, R. Birringer and T.D. Koblé, *Mater. Sci. Eng.*, *99* (1988) 457.
[18] A. Tschöpe and J.Y. Ying, *Nanostr. Mater.*, *4* (1994) 617.
[19] J.N. Armor, *Chemtech* (Sept. 1992) 557.
[20] M. Trocha and W.J. Koros, *J. Mem. Sci.*, *95* (1994) 259.
[21] J. Rupp and R. Birringer, *Phys. Rev. B*, *36* (1987) 7888.
[22] C.C. Wong, H.I. Smith and C.V. Thompson, *Appl. Phys. Lett.*, *48* (1986) 335.
[23] C.V. Thompson, *Annu. Rev. Mater. Sci.*, *20* (1990) 245.
[24] C.E. Krill, R. Klein, S. Janes and R. Birringer, *Mater. Sci. Forum*, *179–181* (1995) 443.

Fast consolidation of ceramic powders

Subhash H. Risbud*, Chien-Hua Shan[1]

Division of Materials Science and Engineering, Department of Chemical Engineering and Materials Science, University of California at Davis, Davis, CA 95616, USA

Abstract

Very fast densification of ceramic powders (alpha-alumina, aluminum nitride, and YBCO superconducting oxides) using prior electric discharge before resistance sintering leads to microstructures that retain the particle size of the starting powders. The time taken to achieve near-theoretical density can be as little as 5 min and usually not more than 15 min. The short time is the principal reason for arresting possible grain growth and the electric discharge step may perhaps be responsible for sweeping off impurities from powder surfaces, thus giving clean grain boundaries in the sintered material. In the YBCO powders the surface effect appears to create a filamentary layer that gives unexpectedly high (240 to 300 K) resistivity onsets and diamagnetic behavior.

Keywords: Ceramic powders; Densification

1. Introduction

The development of advanced materials has created many opportunities for synthesis of nanometer size (less than about 50 to 75 nm) ceramic, metallic, and composite powders for use in critical technological applications. Specially important in most future applications is the synthesis of powders with known size distributions and high chemical purity. For example, nanosize powders of ceramics such as alumina, silicon nitride, or carbides are starting to become available in reasonable quantities. Some exciting research areas using nanosize powders include sintering, coatings, and creation of nanostructures in bulk materials, with attendant effects on high temperature plasticity, optical transparency, electronic properties and perhaps even superconducting transitions.

Once powder particles of a well defined distribution are synthesized it is crucial to have processing methods to fabricate dense components by techniques that can retain the particle size in the final microstructure. From an engineering production perspective it would be very desirable to have processing protocols that can have near-net shape manufacturing potential. In the present paper we show results obtained with a process that consolidates ceramic powders to near-theoretical density in a mattter of 10 to 15 min often at temperatures well below normal sintering temperatures. This plasma activated sintering (PAS) process [1–6] applies an electric discharge to the loosely filled powders contained in a die and then later completes the sintering step by normal resistance heating.

2. Experimental procedure

An overall view and a closeup of the densification chamber of the plasma activated sintering equipment is shown in Fig. 1. This equipment performs two major functions. In the first electric discharge step, a cyclic on/off pulse of electric current is applied for a short duration of about a minute. Following this, the powder is heated resistively to the sintering temperature and after densification for a few minutes the solid sample is cooled to room temperature within a few minutes. Our earliest experimental work was performed with commercial aluminum nitride powders [1] from Tokuyama Soda Co. in Japan. The powder was high purity AlN with a particle size of about 0.44 μm. PAS processing was performed in a 2 cm diameter graphite die cavity using as-received powders without any additives. Similarly, in the case of the alpha alumina powders, 10 g of a commercial powder (Baikowski Chimie, Annecy

* Corresponding author.
[1] Present address: Applied Materials Inc., Santa Clara, CA 95054, USA.

Cedex, France; agglomerate size = 300 to 500 nm) were loaded into graphite dies (2 cm in diameter) without any prior cold compaction. Chemical analysis of the powders indicates (oxides of each element in ppm): 457 Mg, 101 Fe, 83 Si, 38 Ga, 38 Zn, 33 Ti, 17 Na, 16 Mn, 5 Zr, less than 4 Mo and Cr, 3 Ca, and less than 1 Li and Ni. The electric discharge and sintering were then performed using a typical activation step consisting of 30 to 60 ms on/off electrical discharge pulses lasting a total duration of 1 min. Following this activation step the powders in the die were heated resistively using a 1500 A d.c. current to about 1150 °C. Another process variation was as follows: 90 s of plasma activation pulses (each pulse of 60 ms duration) at room temperature followed by heating to 200 °C, repeating the 90 s of 60 ms pulses, heating to 1150 °C, holding for 10 min and furnace cooling the sample to room temperature.

In the case of the YBCO ceramic samples, powders corresponding to the well known 123 (Y:Ba:Cu) stoichiometry were obtained from a commercial supplier (SSC, Inc, Woodinville, WA). Their synthesis method consisted of microscale mixing, atomization, and dehydration of nitrate precursor solutions by a spraying technique. The particle size distribution of the 123 phase powder was approximately 2 to 5 μm, and X-ray diffraction in our laboratory reconfirmed the presence of the "123" orthorhombic phase with no unreacted or secondary phases. All the experimental data were obtained on samples made from this single lot of powder to eliminate any possible batch to batch variation in the starting materials. The processing of the YBCO to dense pellets was performed using a processing cycle shown schematically in Fig. 2. Ten grams of the 123 powder were filled into the graphite die cavity and subjected to a high current electric discharge (750 A, 25 V). Following about 90 s of pulsed (60 ms cycles) current application, the die was heated to the consolidation temperature of approximately 900 °C (using a 1500 A d.c. current) while simultaneously applying a moderate uniaxial pressure of about 15 MPa. After holding at this temperature for about 15 min, the samples were removed from the die and cooled to room temperature. Resistivity–temperature data were obtained on samples (approximately $3 \times 3 \times 6$ mm^3) using the standard 4-probe method with an applied current of 0.1, 1, and 3 mA. A.c. susceptibility and d.c. magnetization data were obtained on a Model 7225 a.c./d.c. system configured with a 5 tesla magnet (Lakeshore Cryotronics, Westerville, Ohio).

3. Results and discussion

AlN powders were densified to better than 99.8% of the theoretical density using PAS processing at temperatures from 1600 to 1800 °C for times varying from 4 to 15 min. Pellets 2 to 5 mm thick were usually prepared

(a)

(b)
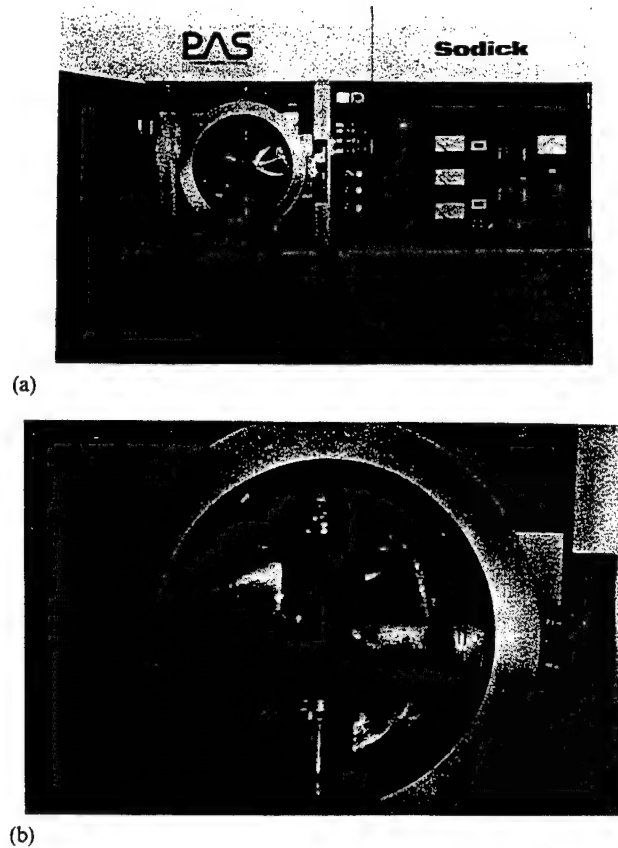
Fig. 1. (a) Overall view of the Plasma Activated Sintering Equipment showing consolidation chamber, power controls and panels. (b) Close-up view of the densification chamber used in PAS showing the graphite die and rams as well as the thermocouple for temperature measurements.

with a diameter of 2 cm and the microstructure was analyzed by milling TEM specimens from a 3 mm diameter core drilled segment from the center of the bulk disk. The average grain size measured by TEM was about the same as the starting particle size of about 0.4 μm. Particularly significant was the observation of clean grain boundaries and direct grain-to-grain contact
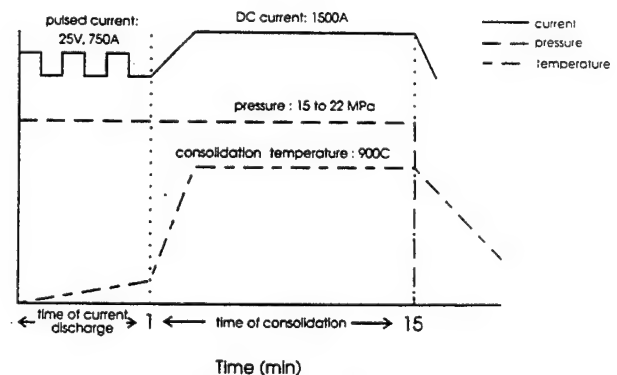
Fig. 2. Typical processing schedule used in the preparation of bulk samples from 123 phase powders. Note the electric discharge for 1 min (60 ms pulsed cycles) that precedes consolidation by heating to 900 °C, 15 min. Dense solid samples of > 99% of theoretical density were obtained by this process.
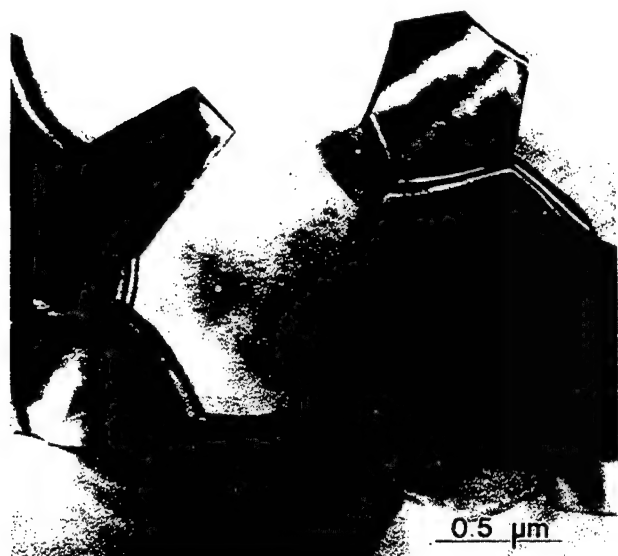
Fig. 3. Bright field TEM image of the densified alpha-alumina sample. The structure is submicrometer and shows very little grain growth in comparison with the starting powder particle size. A very few voids were seen inside some grains but most of the microstructure was dense alpha-alumina. Amorphous or crystalline phases were not seen at any of the boundaries or at triple points.

in almost the entire microstructure [1]. The absence of an amorphous or second phase layer at the boundary is equally important. Electron energy loss spectroscopy also showed no oxygen enrichment at the boundaries or at triple points and no evidence of any oxide formation.

In PAS sintered alpha-alumina, densities of about 99.2% of the theoretical value (3.986 g cm^{-3}) were measured in an average of three measurements. Fracture surfaces examined by scanning electron microscopy showed a grain size of 500 to 600 nm with virtually no porosity. This shows that after sintering the grain size of the solid material was almost the same as the starting powder size of 300 to 500 nm. The structure and interface between grains was examined by high resolution electron microscopy. TEM specimens were again prepared by mechanical thinning and dimpling and final thinning to electron transparency was done by argon ion-beam milling. Fig. 3 shows a bright field TEM image of the consolidated alpha-alumina sample. The image reveals a structure with an average grain size of about 650 nm. A very small number of voids were also observed within a few grains. The grain boundaries were examined by HREM imaging to determine whether or not thin amorphous regions existed between boundary surfaces. Fig. 4 shows a typical HREM image of the grain boundary in PAS consolidated alpha-alumina. The observed grain boundary is in edge-on orientation with respect to the incident electron beam direction. The upper grain is in [2$\bar{2}$01] zone axis orientation and the bottom one is in [1$\bar{1}$01] zone axis orientation. The structural width of the boundary is about

0.4–0.5 nm. The boundary appears to be very clean even at this fine scale of resolution, similar to the grain boundaries in AlN processed by plasma activated sintering. In both alpha-alumina and in AlN we did not see evidence of an amorphous or impurity phase layer at any of the grain boundary regions. Pressureless sintering and hot pressing of alumina powders with similar particle sizes has been studied in recent work [7,8]. Pressureless sintering at 1500 °C for 1 h often gives alumina samples with a density of about 96.3%. Hot pressing has been shown to give samples with a density of 99.4% using a temperature of 1400 °C and a pressure of 50 MPa. By comparison, our PAS densities after sintering at 1150 °C for just 10 to 15 min are comparable to or better than the above values, indicating the considerable promise of the process for retention of fine nanostructures. Surface diffusion enhancement during the plasma activation step might be a possible cause of this very rapid consolidation. By way of comparison of the present data, studies on hot pressed samples of MgO doped alumina fabricated at 1400 °C under a 50 MPa pressure show abnormal grain growth with the grain size increasing from 0.45 μm to 5 μm within just 10 min [7].

In the YBCO superconducting 123 composition, pellets (20 mm in diameter and 3 mm in thickness) obtained by our rapid consolidation process had measured densities of 6.3 g cm^{-3} (greater than 99% of the theoretical density of 6.34). Scanning electron microscopy of the fracture surfaces of the pellets showed an average grain size of about 3 to 4 μm and virtually no porosity. Lattice parameters obtained from X-ray diffraction patterns of the pellets matched the orthorhombic "123" phase structure. Samples of the YBCO pellets prepared from the same powder batch by routine furnace sintering gave the expected 92 K transition to the zero resistivity condition and a TEM mi-
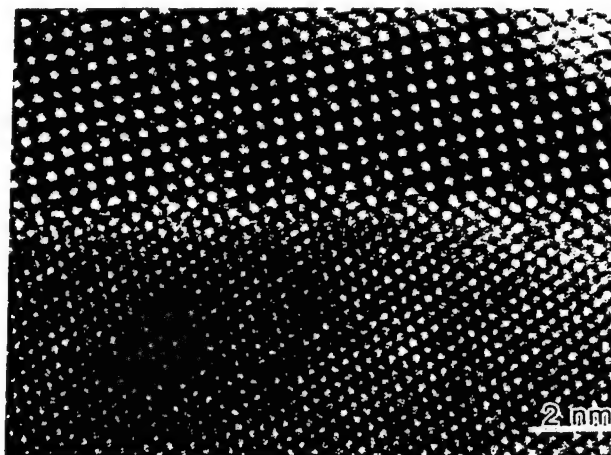
Fig. 4. High resolution TEM image of a grain boundary area in the PAS densified alpha-alumina sample. Excellent grain to grain contact and a structurally clean boundary is evident.
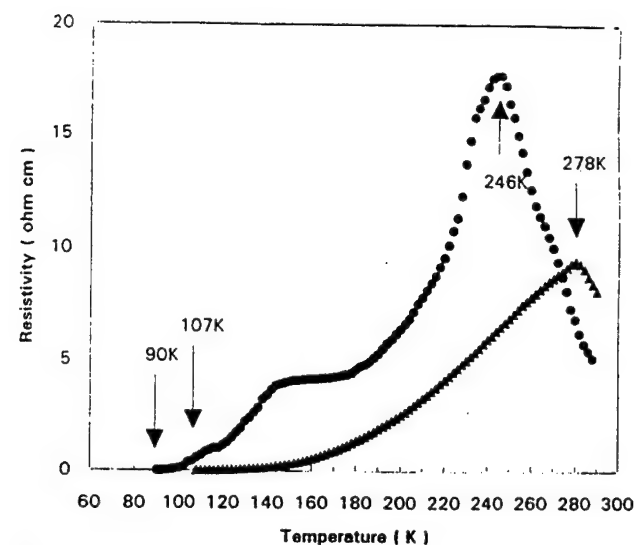
(a)
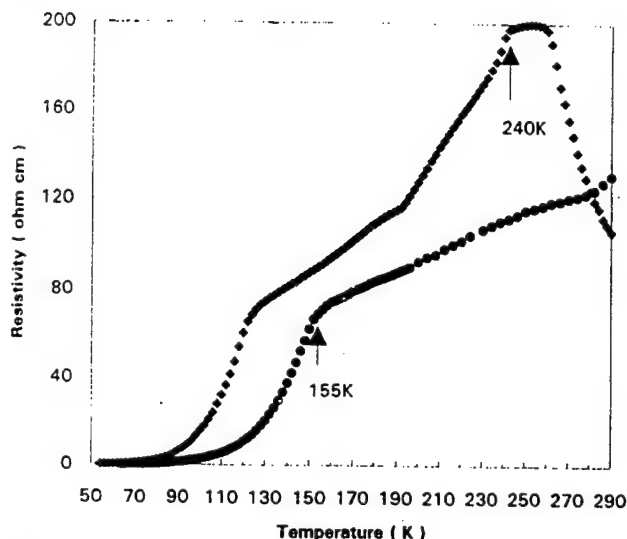
(b)

Fig. 5. (a) Resistivity–temperature for as-consolidated samples 1 and 2 showing the onsets for sample 1 at 246 K (zero = 90 K) and onset at 278 K for sample 2 (zero = 107 K). An additional transition at about 145 K is also seen in sample 1. These data were reproducible on the same sample within hours and after up to 4 weeks of storage in a laboratory dessicator. (b) Resistivity–temperature for as-consolidated sample 3 showing an onset at 240 K (top curve) and the same sample after air annealing at 350 °C for 1 h showing an onset at 155 K (lower curve).

crostructure showing the usual lath like elongated grain structure. The resistivity–temperature data for two different as-consolidated samples, shown in Fig. 5(a), reveal transition onsets at temperatures of 246 K for sample 1 and 278 K for sample 2; the resistivity reaches zero values at 90 K and 107 K, respectively. Similar data for sample 3 are shown in Fig. 5(b), where the as-consolidated sample shows an onset temperature of 240 K (top curve in Fig. 5(b)). After annealing this sample in air at 350 °C for 1 h, the resistivity–temperature data showed an onset at 155 K (Fig. 5(b), lower

curve). These transitions were repeatedly observed on literally the same set of samples in several different measurements taken successively after time intervals of days, 1 week, 2 weeks and 1 month. Fig. 6 shows the a.c. susceptibility data, with corrections for diamagnetic contributions from the sample holder. Diamagnetic transitions commencing at about 150 K for sample 1 (Fig. 6(a)) and at about 200 K for sample 2 (Fig. 6(b)) can be seen in these data. Fig. 6(c) shows the a.c. susceptibility data for sample 3 (the one annealed in air at 350 °C for 1 h and with the T_c onset at 155 K shown in the lower curve of Fig. 5(b)). Once again a diamagnetic regime (negative susceptibilities) is clearly seen in the temperature range 160 to 300 K (both uncorrected and sample holder corrected data are deliberately shown in Fig. 6(c)). These data for all three samples were reproducible in several separate measurements performed over a period of about 2 weeks and provide convincing evidence for the existence of a diamagnetic regime in these samples in the temperature range 150 to 300 K. To the best of our knowledge, this is the first time that diamagnetic behavior (i.e. negative a.c. susceptibilities) has been observed in YBCO at such high temperatures although other evidence for possible superconductivity at 240 K has been reported in the literature in the past [9–11].The physical or magnetic phenomena associated with these transitions are unknown but a predominantly diamagnetic species must be a constituent of the material at these temperatures. It is difficult to link this observed diamagnetic behavior to bulk superconductivity specially if unknown surface effects during the current discharge step alter the particle surfaces either structurally or chemically.

It is tempting, on the basis of the consistently reproducible negatively valued a.c. susceptibility at temperatures between 160 and 300 K, to think that we have a superconducting YBCO material at such high temperatures by PAS processing. However, magnetization and Meissner effect measurements on these same samples show no evidence for bulk superconductivity. One possible explanation is that the bulk of the sample has the usual 90 K phase with the possibility that a very small fraction of some higher T_c phase co-exists at grain interfaces. Alternatively, the current discharge applied to the powder surfaces prior to densification creates surface states that are responsible for the resitivity drops at > 240 K and the negative susceptibilities upto 300 K. The accumulation of electronic charge on the particle surfaces during the pulsed electric discharge step in our processing schedule must play a crucial, and not yet fully understood, role in the microstructural evolution and properties. It may be very interesting to consolidate nanometer size powders of YBCO and other superconductors to see if unusual effects occur in nanostructures comparable to the coherence length of the superconductor. From a mechanical processing

(a)

(b)

(c)
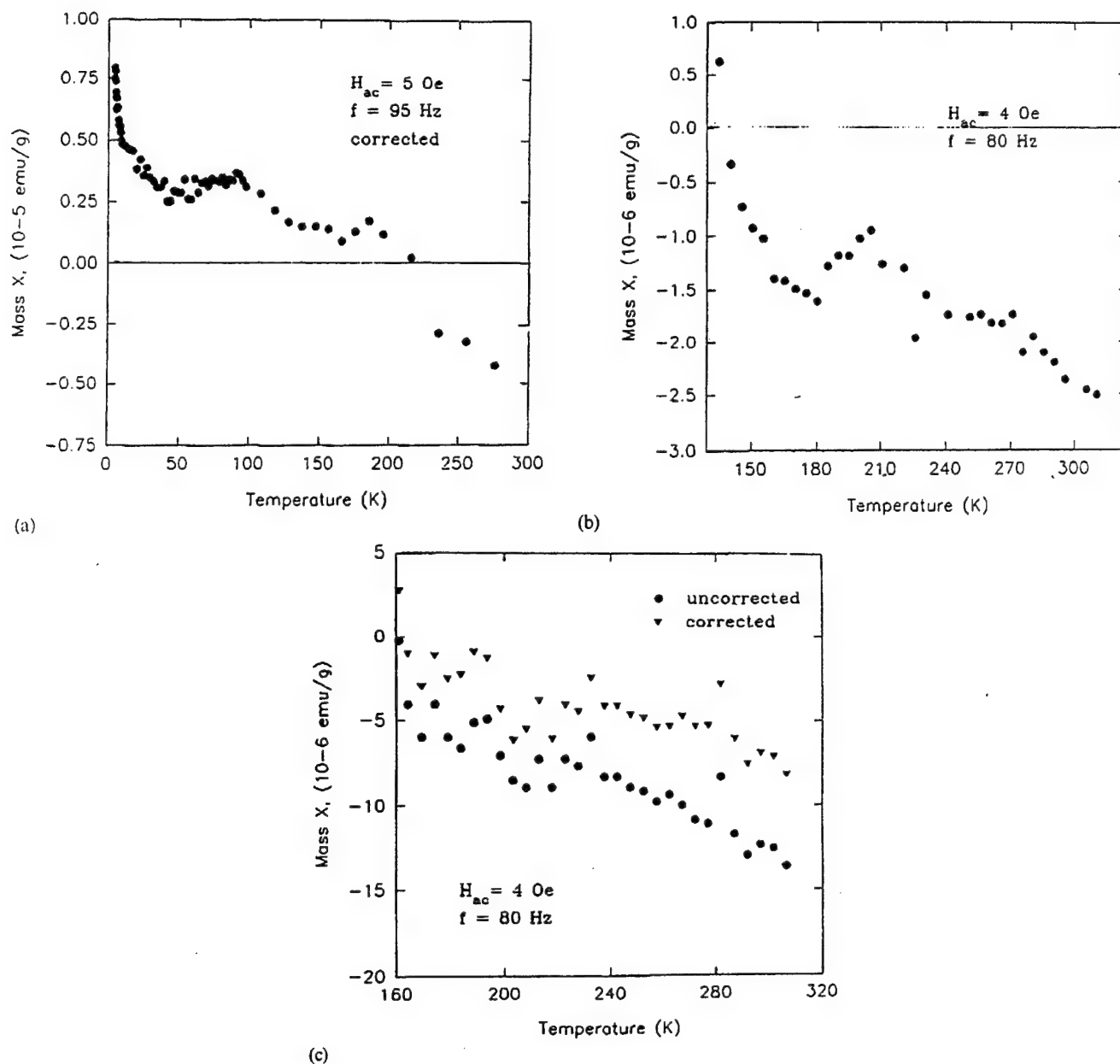
Fig. 6. (a) A.c. susceptibility of sample 1 as a function of temperature. Note the negative susceptibilities from 150 to 300 K. These data were corrected for sample holder contributions and were repeatable in several measurements. (b) A.c. susceptibility for sample 2 over the temperature range 160 to 300 K showing negative values of susceptibility (these data are again corrected for sample holder contributions). (c) A.c. susceptibility for sample 3 from 160 to 300 K. Both uncorrected and corrected data are shown and reveal once again negative susceptibilities. Data for all three samples show a diamagnetic regime in susceptibility measurements.

point of view ductility could be perhaps induced in these nanostructures with an impact on the shaping and forming of these and other ceramic materials.

4. Summary

Rapid densification of nanometer size ceramic powders to near theoretical density was achieved by using an electric discharge step prior to sintering in a new

process called Plasma Activated Sintering (PAS). Results obtained on aluminum nitride, aluminum oxide, and YBCO superconducting ceramic show the unique ability of PAS processing to create nanostructures with little or no grain growth of the starting powder particles simultaneous with the attainment of full densities. Microstructures obtained by high resolution electron microscopy provide proof of clean grain boundaries with excellent grain to grain contact in the sintered materials.

Acknowledgements

References

[1] S.H. Risbud, J.R. Groza and M.J. Kim, *Phil. Mag. B*, 69 (1994) 525.
[2] S.H. Risbud and C.H. Shan, *Mater. Lett.*, 20 (1994) 149.
[3] C.H. Shan, S.H. Risbud, K. Yamazaki and K. Shoda, *Mater. Sci. Eng. B*, 26 (1994) 55.
[4] J.R. Groza, S.H. Risbud and K. Yamazaki, *J. Mater. Res.*, 7 (1992) 2643.
[5] J. Hensley, C.H. Shan, S.H. Risbud and J.R. Groza, in *Powder Metallurgy in Aerospace, Defense and Demanding Applications*. MPIF, Princeton, NJ, 1993, pp. 309–315.
[6] S.H. Risbud, C.H. Shan, M.J. Kim and A.K. Mukherjee. *J. Mater. Res.*, 1995, 10 (1995) 237.
[7] J.F. Roy, M. Descemond, C. Brodhag and F. Thevenot, *J. Eur. Ceram. Soc.*, 11 (1993) 325.
[8] T. Nishida, H. Nakano and K. Urabe, *J. Eur. Ceram. Soc.*, 11 (1993) 193.
[9] C.Y. Huang, L.J. Dries, P.H. Hor, R.L. Meng, C.W. Chu and R.B. Frankel, *Nature*, 328 (1987) 403.
[10] J.T. Chen, L.E. Wenger, C.J. McEwan and E.M. Logothetis. *Phys. Rev. Lett.*, 58 (1987) 1972.
[11] C.S. Pande, M.S. Osofsky, A.K. Singh, L.E. Richards. R. Ashoka, V. Letourneau and S.A. Wolf, *Phys. Rev. B*, 37 (1988) 1594.

ELSEVIER

High pressure and low temperature sintering of bulk nanocrystalline TiO$_2$

Shih-Chieh Liao[a], Kook D. Pae[b], William E. Mayo[a]

[a]*Department of Mechanics and Materials Science,* [b]*Department of Mechanical and Aerospace Engineering, Rutgers University, Piscataway, NJ 08855, USA*

Abstract

Bulk n-TiO$_2$ samples with a relative density as high as 95% and a grain size less than 50 nm were fabricated by hot-pressing at temperatures as low as 400 °C and at pressures up to 1.5 GPa. During hot-pressing, the anatase phase transformed to the rutile phase and the amount of transformation increased with sintering pressure. The grain size in both the anatase and the rutile phase increased with sintering pressure at a constant temperature but the grain size of the transformed phase is always smaller than that of the starting material. We believe that the smaller grain size of the rutile phase is related to multiple nucleation events in the anatase phase during sintering at very high pressure. The average grain size increased from 27 nm in the original powder to only 45 nm in the compact after hot-pressing. Analysis of the grain size and closed porosity by transmission electron microscopy suggested that closed pores at grain boundary triple junctions might also retard the grain boundary migration and thus prevent grain growth. A competing mechanism is also proposed in which the rate of grain growth is controlled by the pressure effect on the bulk diffusion rate and interface energy.

Keywords: Hot pressing; Grain boundary; Competing mechanism

1. Introduction

Nanocrystalline materials were first synthesized by Gleiter and co-workers [1] in 1984 and have since become a major focus of many researchers. Because of the small grain size in nanocrystalline materials, a large fraction of the atoms lie near the grain surface or internal boundaries. Such surfaces or internal boundaries represent a special state of solid matter owing to the fact that the atoms near the surface are subjected to the different potential fields of the atoms on either side of the interface. As a result, the atomic arrangements on the surfaces or internal boundaries differ from both the glassy and crystalline states. To illustrate the importance of the interface, some [2] have proposed that nanocrystalline materials be considered two-phase materials composed of distinct interfacial and crystalline phases. In addition, when considering nanocrystalline ceramics, pores are also an important element of the structure that must be considered. For the purposes of our dicussion we assume that the upper limit of grain size for nanocrystalline materials is about 100 nm [3,4].

It is common knowledge that the sintering temperature of an ultrafine powder is substantially below that of common powders. This difference of up to several hundred degrees is due to increased capillary forces based on the Gibbs–Thomson effect and more favorable particle structure. Interest in nano-grained ceramic powders for processing of ceramics is motivated by the promise of improved sinterability at low temperature below (0.5T_m), an increase in toughness due to a reduction in flaw size, and low-temperature superplastic deformation. However, it is well known that consolidation of ultrafine powder is very difficult because of its low apparent denisty, low flow rate, high contents of absorbed gases and admixtures, high surface area relative to its weight, and severe interparticle friction. All of the common powder processing methods such as hot (isostatic) pressing, extrusion, injection molding, sinter-forging, etc., may be used for ultrafine powder processing. However, unless grain growth during processing is controlled, the prospects for production of nanocrystalline compacts will be seriously hampered. Therefore, control of the grain growth is one of the most important tasks for all consolidation techniques.

Most early studies of nanomaterials were limited to metals [1,5,6]. However, Karch et al. [7] produced nanocrystalline TiO_2 and CaF_2 and reported remarkable results illustrating that these materials showed superplastic behavior at room temperature. Subsequent work has also demonstrated that enhanced sintering [8,9] and superplastic deformation [10,11] are possible in nanocrystalline ceramics (n-TiO_2), but not without significant grain growth. Hahn et al. [12] studied the sintering and deformation kinetics of n-TiO_2. It was found that pressureless sintering yielded densities above 95% of the theoretical value with a modest increase in grain size, whereas pressure-assisted sintering (1 GPa) resulted in high density samples without grain growth. They also conducted creep tests in compression and observed that true strains up to 0.6 could be achieved at 810 °C with fracture.

Averback et al. [13] studied sintering and grain growth in nanocrystalline ceramics. They observed that the green density of these materials varied greatly with compaction pressure and temperature. Densities greater than 90% of the theoretical value could be achieved without grain growth in n-TiO_2 using pressure-assisted sintering at about 500 °C. Their study showed that the grain size varied as a function of $t^{1/3}$. Moreover, the grain growth in denser materials was greatly accelerated compared with that in less dense materials, suggesting pore stabilization of the grain size. The grain size could be partially stabilized by suitable doping or by pressure-assisted sintering.

Mayo and Hague [14] studied the porosity–grain growth relationships in sintering of n-TiO_2. Porosimetry data revealed that pore growth and pore shrinkage adhered well to Kingery's [15] predictions based on a critical pore size-to-grain size ratio. In addition, it appeared that open pores severely limited grain growth during stage II sintering. This was demonstrated by the observation that the grain was correlated with the average spacing between open pores so that instantaneous grain sizes could be calculated directly from the pore size distributions.

Hague and Mayo [16] also studied the effect of crystallization and phase transformation on the grain growth of n-TiO_2. They found during sintering that the presence of inter-agglomerated pores served to prevent an individual anatase grain from growing beyond the perimeter of the host agglomerate. As sintering continued, the anatase phase transformed to the rutile phase. They attributed the post transformation rutile grain growth (to 185 nm compared with the pre-transformation anatase grain size (50 nm)) to the low number of rutile nucleation events.

Sinter-forging has been studied for n-TiO_2 by Uchic et al. [17]. They found that full density could be achieved at temperatures below $0.5T_m$ and that the grain growth could be limited to 50–60 nm as the

density increased to greater than 96%. They showed that the stress dependence of the creep rate was an indication of grain boundary sliding accommodated by large pores.

Nanocrystalline TiO_2 shows great promise for possible applications requiring superplastic deformation and much effort has been expended to make bulk samples from nanocrystalline powder. The aim of the present work was to investigate the sintering characteristics of bulk n-TiO_2 fabricated by hot-pressing. The effects of sintering pressure on density, grain size, porosity, and anatase-rutile phase transformation are presented.

2. Experimental procedure

2.1. Material

Nanocrystalline TiO_2 powder made by a gas phase condensation method was purchased from Nanophase Technologies Corporation. The powder consisted of 95.8 wt.% anatase phase and 4.2 wt.% rutile phase with an average grain size of 27 nm, as determined by X-ray diffraction and line broadening methods respectively.

2.2. Consolidation

Hot-pressing of the n-TiO_2 powders was carried out in a piston-cylinder apparatus as shown in Fig. 1. The mold (Fig. 2) is made of a maraging steel (VascoMax 350, Teledyne Vasco Corporation). Prior to hot-pressing, the powder was first pressed in the mold at room temperature at a relatively low pressure. Then the mold containing the pressed powder was placed in the piston-

Fig. 1. Schematic diagram of the apparatus for hot pressing.

Fig. 2. Details of the maraging steel mold for hot pressing.

2.3. Characterization

2.3.1. X-ray diffraction

X-ray diffraction was used to determine the identity, quantity, and crystallite size of the phases present in the samples. These tests were carried out on a Siemens D5000-RA diffractometer operated at a voltage of 40 kV and a current of 50 mA with Cu Kα radiation. The scanning step size and the collection time for each step were set at 0.01° and 30 s, respectively. To determine the quantity of each phase, the intensity of the (110) rutile and (101) anatase peaks was used by an internal reference method using reported $I/I_{corundum}$ values for the rutile and anatase phases.

The as-received n-TiO$_2$ powder consists of about 95.8 wt.% anatase phase and 4.2 wt.% rutile phase, both of which have tetragonal crystal structure. The density of the rutile phase ($\rho_r = 4.23$ g cm^{-1}) is larger than that of the anatase phase ($\rho_a = 3.90$ g cm^{-3}) and the anatase to rutile phase transformation is irreversible.

The crystallite size was determined by Scherrer's method based on the measurement of diffraction peak broadening given by

$$B(2\theta) = 0.9\lambda/L \cos\theta \tag{1}$$

where $B(2\theta)$ is the full width at half-maximum intensity (FWHM) of a diffraction peak, λ is the X-ray wavelength, L is the crystallite size, and θ is Bragg's angle.

In addition to the broadening due to small crystallite size, there is always additional broadening due to slit widths, sample size, penetration into the sample, imperfect focusing, and non-monochromaticity of the beam (α_1 and α_2 for example). All of these broadening sources are grouped together under the name "instrumental broadening". To correct for the instrumental broadening, standard peaks were run using a silicon standard in which the crystal size is large enough to eliminate all crystal-size broadening. These standards peaks ((111) at $2\theta = 28.47°$ and (311) at $2\theta = 56.17°$) were run under instrumental conditions identical with those for the test samples. By assuming Gaussian shapes for the diffraction peaks, the corrected FWHM without instrumental broadening $B_c(2\theta)$ can be obtained by the following equation

$$B_c^2(2\theta) = B_h^2(2\theta) - B_s^2(2\theta) \tag{2}$$

where $B_h(2\theta)$ is the broadening from samples containing both the desired broadening and the instrumental broadening and $B_s(2\theta)$ is the instrumental broadening obtained from the standard. Once the value of $B_c(2\theta)$ is known, the crystal size can be easily determined using Scherrer's formula, Eq. (1). In the present study, we used the lines (110) at $2\theta = 27.45°$, (211) at $2\theta = 54.32°$ and (220) at $2\theta = 56.64°$ of the rutile phase; and the line (101) at $2\theta = 25.28°$ of the anatase phase to determine the crystal size of both phases.

cylinder apparatus. The pressure was raised to approximately 0.50, 0.75, 1.00, 1.25, or 1.50 GPa respectively, and then the temperature was raised to 400 °C by two band heaters. To measure the sintering temperature of the nanopowder, a chromel-alumel thermocouple was inserted into a hole in the bottom plug (see Fig. 2) close to the powder. The sintering time was kept constant at 7 h for all samples, except sample 5 ($t_s = 1$ h). The hot-pressing conditions for each sample are summarized in Table 1. Following the pressure-assisted sintering, the mold was cooled to about 200 °C where the pressure was released and the sample removed. The sintered cylindrical samples were 1.27 cm in diameter and 1.27 cm in height. The color of the samples varied from a dark gray on the surface to a light gray at the center. This change in color from the original white powder is believed to be caused by oxygen depletion. A similar phenomenon has been found by others in the processing of n-TiO$_2$ powder [18–21]. The non-stoichiometry in the bulk n-TiO$_2$ samples might be a result of the reaction of oxygen in n-TiO$_2$ with the surface of the steel mold during hot-pressing.

Table 1
Test conditions and results of hot pressing n-TiO$_2$ powder

Sample	Pressure (GPa)	Temperature (°C)	Time (h)	Rutile grain size[a] (nm)	Anatase grain size[a] (nm)	Density[b] (g cm^{-3})	Density (% of theoretical)	Open porosity (vol.%)	Rutile phase[c] (wt.%)
Powder				27	27				4.2
1	0.50	400	7	32	32	2.89	74	25.5	6.8
2	0.75	400	7	34	35	3.34	85	14.4	9.9
3	1.00	400	7	35	36	3.44	88	11.6	10.2
4	1.25	400	7	38	41	3.84	94	0.1	35.6
5	1.50	400	1	44	59	4.01	95	0	95.1

[a] Measured by the Scherrer method.
[b] Measured by the Archimedes method.
[c] Weight fraction of phases determined by X-ray diffraction with the (110) peak of the rutile phase and the (101) peak of the anatase phase.

2.3.2. Density and porosity measurement

The density and open porosity of the samples were determined by Archimedes' method. Before being weighed in air, samples were dried in vacuum at room temperature for 24 h to eliminate all moisture in the samples. To determine the open pore volume in the samples, the following steps were taken: (1) weigh a sample in air W_{air}, (2) put a sample in boiling water for 2 h to fill the open pores completely with water, and (3) after cooling, weigh the saturated piece suspended in water W_{sus} and in air W_{sat}. The difference between these last two values permits calculation of the density. The difference between the saturated and dry weights gives the open pore volume.

2.3.3. Transmission electron microscopy (TEM)

The microstructure of both n-TiO$_2$ powder and the bulk n-TiO$_2$ samples was studied by TEM. TEM samples of n-TiO$_2$ powder were obtained by first putting a very small amount of the powder into methanol and then vibrating the suspension by an ultrasonic oscillator to disintegrate any agglomerates. A 3 mm copper grid holder was dipped into this suspension and then dried in air. A TEM sample of the bulk n-TiO$_2$ was obtained by cutting off a thin slice from the bulk samples using a diamond saw, followed by conventional grinding, dimpling, and ion-milling. The samples were ion milled in a rotation stage cooled with liquid nitrogen using an ion beam current of 0.5 mA and a voltage of 6 keV. All samples were examined with an ISI-002B high-resolution transmission electron microscopy operated at 200 kV.

3. Results and discussion

The grain size of the as-received n-TiO$_2$ powder, measured by TEM, was found to be in the range of 5 nm to 50 nm, as shown in Fig. 3. By using X-ray diffraction techniques previously described, the average grain size of the starting n-TiO$_2$ powder, which consists of about 95.8 wt.% anatase phase and 4.2 wt.% rutile phase, was determined to be 27 nm. Figs. 4(a) and 4(b) show the X-ray diffraction profiles of the starting powder along with the pressure-assisted and sintered bulk samples. Shown in this figure are the (110) peak of the rutile phase and the (101) peak of the anatase phase. Note the relative changes in these peak heights, indicating the relative extent of the transformation.

The test conditions and results of hot-pressing n-TiO$_2$ powder are summarized in Table 1. It can be seen from Table 1 and Fig. 5 that the density increases with sintering pressure to 95% of the theoretical value while the grain size remains small. This is the first time that n-TiO$_2$ powder has been sintered successfully to 95% relative density at only 400 °C without significant grain growth. This sintering temperature of 400 °C (673 K) is less than a third of the melting point of titania (T_m of TiO$_2$ is 1870 °C or 2143 K). It is known that hot-pressing increases the driving force for densification through the expression,
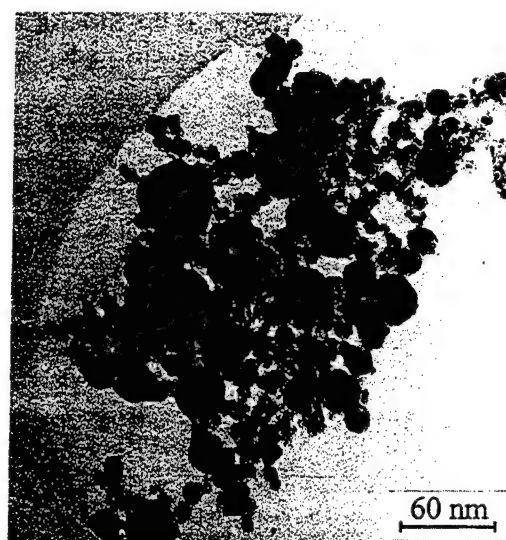
Fig. 3. Transmission electron micrograph of n-TiO$_2$ powder.

(a)

(b)
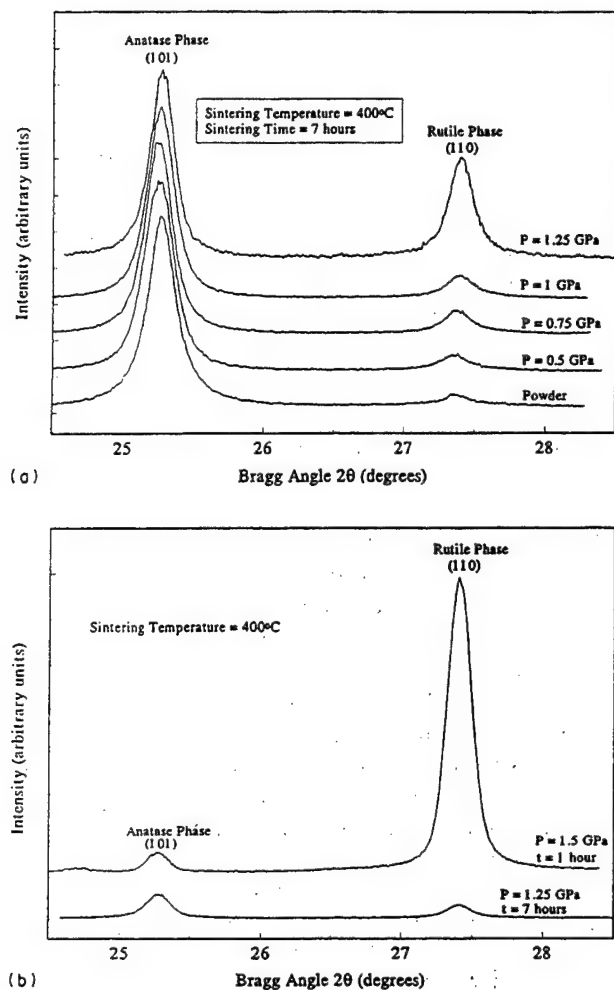
Fig. 4. (a) (b) X-ray diffraction profiles of the starting n-TiO$_2$ powder and the bulk n-TiO$_2$ samples hot-pressed at 400 °C and at various pressures.

$$\sigma_s = 2\gamma/r + \sigma_e \qquad (3)$$

where σ_s is the total sintering stress, γ is the surface energy, r is the pore radius and σ_e is the effective stress. It is clear from the results of the present study that the
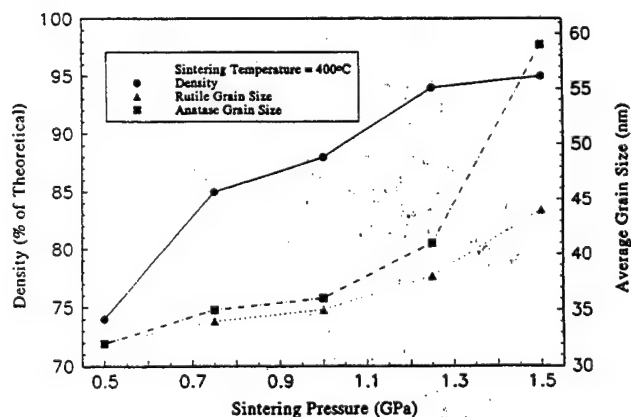
Fig. 5. Relative density and grain size of both the anatase and rutile phases as a function of sintering pressure.

applied high pressure can significantly decrease the densification temperature and in doing so limits grain growth.

We also observed in our study that the grains grew slightly from 27 nm to 35 nm at 1 GPa and to 44 nm at 1.5 GPa for the rutile phases. The corresponding data for the anatase phase are from 27 nm to 36 nm at 1 GPa and to 59 nm at 1.5 GPa. It is known that grain growth is affected not only by the sintering pressure but also by the porosity among other things. For example, the sintering process is accompanied by pore shrinkage, pore coalescence, and grain growth. During the second stage of solid-state sintering, the microstructure of a powder compact is characterized by a complex network of tubular pores that are open to the external surface. Most densification of a ceramic material takes place during this stage. This second stage sintering is followed by the final state in which the interconnected necks between pores disappear and only isolated pores appear. Gupta [22] found a strong correlation (usually linear) between increasing density (or decreasing pore volume) and increasing grain size in stage two sintering for large-grained ceramic materials. In addition, for nanocrystalline ceramics, it has been shown [13,14] that pores, especially open pores at grain boundaries can retard the migration of a grain boundary and thus reduce the rate of grain growth. Averback et al. [13] found in sintering of n-TiO$_2$ that grain growth in a denser material was greatly accelerated compared with that in a less dense material, suggesting pore stabilization of grain size. Mayo and Hague [14] found that grain growth was also linked to densification in stage two. However, the amount of grain growth which occurred was small compared with the amount of densification which took place. They also found a strong correlation between the closure of open porosity and the onset of accelerated grain growth for pressureless sintering. They attributed this to the fact that open pores present in stage two sintering were strong grain boundary pinning sites but that the closed pores were less effective.

In the present study, the average grain size of both phases was found to increase slightly when the bulk density increases from 74% to 94% of theoretical value during stage two sintering, as shown in Fig. 5. Moreover, the open porosity (volume per cent) decreased with sintering pressure and was nearly completely eliminated when the sintering pressure reached 1.25 GPa. Simultaneously, the grain size (volume average of grain sizes for the two phases) increased from 32 to 40 nm, as shown in Fig. 6. It appears that the effect of open pores on grain growth was reduced with decreasing pore volume which occurred with increasing sintering pressure. As a consequence, minor grain growth with increasing sintering pressure was seen because of the disappearance of the retarding force represented by the
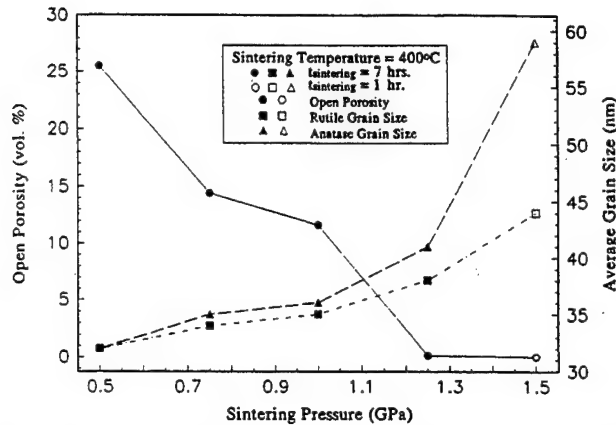
Fig. 6. Open porosity and grain size of both the anatase and rutile phases as a function of sintering pressure.

pores. Accelerated grain growth corresponding to the complete closure of open porosity was not seen. Sample 5 (Table 1) still contained about 5 vol.% closed pores. TEM of the pore structure of this sample revealed that almost all the closed pores were located at grain triple junctions, as shown in Fig. 7. It has been suggested [23,24] that closed pores sitting on a triple junction can effectively prevent grain boundary migration. It appears in the present study that the closed pores on triple junctions of sample 5 might have helped to retard grain boundary migration, so that the grain growth was effectively limited. In addition, the grains of the anatase phase grew larger than the grains of the rutile phase (Table 1 and Fig. 5). In other words, the transformed product (rutile) has a smaller grain size than the start-

Fig. 7. Transmission electron micrograph of the closed pore structure of sample 5. Note that almost all the pores are located at grain boundary triple junctions.

ing phase (anatase). This is probably due to an increased nucleation rate brought on by the high sintering pressure. This effect is most pronounced at the highest pressure, and may be even more important at pressures above 1.5 GPa.

In addition to the effect of porosity on grain growth proposed above, a second mechanism is also possible. Consider, for example, the rate of grain growth $\dot{g}$ proposed by Uhlmann et al. [25]

$$\dot{g} = \left(\frac{f}{a_0}\right) D \left[1 - \exp\left(-\frac{\Delta G}{RT}\right) \right] \qquad (4)$$

where f is the fraction of sites at the interface where atoms can be added or removed, a_0 is the jump distance, D is the diffusion coefficient for atoms across an interface, and ΔG is the free energy difference across the interface. We know that D decreases with pressure with the following relationship

$$\left[\frac{\partial \ln D}{\partial P}\right]_T = -\frac{\Delta V}{RT} \qquad (5)$$

where ΔV is the activation volume for atom transport across the interface. Assuming that the Gibbs-Thomson effect is the controlling mechanism for nanograin growth, we obtain

$$\Delta G \approx \frac{2\gamma V_m}{r} \qquad (6)$$

where γ is the interface energy, r is the radius of curvature of the interface, and V_m is the molar volume. Also, from the fundamental thermodynamic relationship,

$$\left(\frac{\partial \gamma}{\partial P}\right)_T = V \qquad (7)$$

where V is the excess volume and is positive in the present case, we know that the interface energy increases with pressure at constant temperature. Thus, ΔG will increase with pressure. Therefore, the overall growth rate may be written as

$$\dot{g} = \left(\frac{f}{a_0}\right) D_0 \exp\left(-\frac{P\Delta V}{RT}\right) \left[1 - \exp\left(-\frac{2\gamma V_m}{rRT}\right) \right] \qquad (8)$$

where D_0 is the diffusion coefficient at atmospheric pressure. The first part, $\exp(-P\Delta V/RT)$, of this equation decreases rapidly with pressure while the second part, $1 - \exp(-2\gamma V_m/rRT)$, increases rapidly with pressure. The product, however, shows a maximum at a critical pressure, as shown schematically in Fig. 8. The overall effect of pressure on the growth rate is thus seen to depend on the balance between the change in the diffusion coefficient D and the change in interface energy with pressure. At low pressures on the one hand, the rapid increase in the interface energy outweighs the effect of D and thus the growth rate will increase with pressure. At sufficiently high pressures, on the other
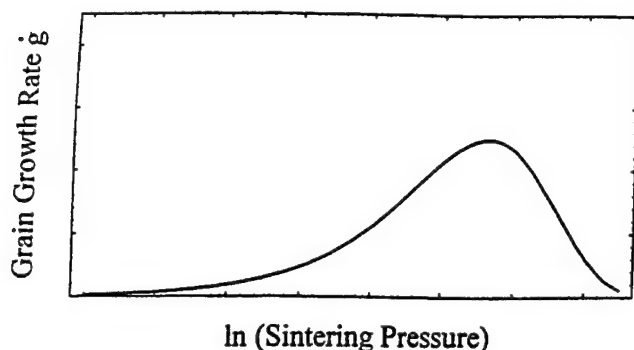
Fig. 8. Plot of the growth rate equation $\dot{g} = A \exp(-k_1 P)[1 - \exp \times (-k_2 P)]$ showing the general form of the grain growth rate as a function of sintering pressure.

hand, the effect of D should dominate and the growth rate should decrease. In other words, there exists a threshold critical pressure below which the growth rate will increase with pressure, which is in agreement with our experimental observations. A similar phenomenon has been seen in the zirconia system by Skandan et al. [26].

Phase transformation from the anatase to the rutile phase occurred during hot-pressing and the amount of transformation increased with sintering pressure, as shown in Fig. 9. This is not unexpected because the applied hydrostatic pressure would enhance the transformation from the less dense metastable anatase phase to the denser structure of the rutile phase. The amount of phase transformation, however, was not linearly related to the sintering pressure. Instead, most material transformed only when the pressure exceeded 1 GPa. In addition, it is known from the present results that on applying high pressure during sintering, the phase transformation occurs at significantly lower temperature. It is also believed that the applied high pressure can result in an increased nucleation rate of the rutile phase. The combination of low sintering temperature
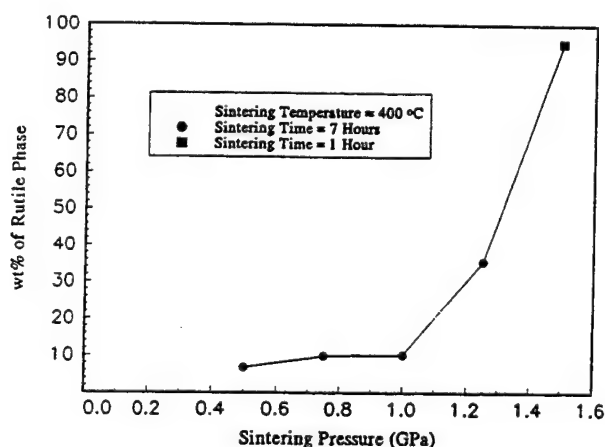
Fig. 9. Pressure-induced phase transformation (anatase to rutile) of n-TiO₂ during hot pressing. The graph shows the weight per cent of the rutile phase as a function of sintering pressure.

and high nucleation rate limited the grain growth of the rutile phase. The average grain size of the rutile phase (95.1 wt.%) of sample 5 is only 44 nm, compared with the average grain size of 27 nm for the rutile phase (4.2 wt.%) in the original powder. It is worthwhile comparing our result with the recent results from a pressureless process, in which an anatase phase powder was heated to 900 °C for 1 h. Nearly all material transformed to the rutile phase but the average grain size of the rutile phase grew to 264 nm [27].

The phase transformation from the anatase to the rutile phase in the present study did not increase the rutile grain size. In contrast, Hague and Mayo [16] found a linear relationship between increasing rutile grain size and increasing weight per cent of rutile phase. They proposed that the presence of inter-agglomerate pores served during sintering to prevent an individual anatase grain from growing beyond the perimeter of the host agglomerate. As sintering continued, the anatase phase began to transform to the rutile phase and the rutile grain grew to 185 nm which was significantly larger than the pre-transformation anatase grain size (50 nm). The model proposed by Hague and Mayo [16] appears not to apply to the present study at much higher pressures insofar as the rutile grain size is concerned. It should be noted that the sintering conditions (the sintering pressure and the sintering temperature) used in the present study were very different than those of Hague and Mayo.

4. Conclusions

The following conclusions may be drawn from the present experimental results.

(i) It is possible to achieve nearly fully sintered bulk samples of n-TiO₂ at a temperature as low as 400 °C under high pressure.

(ii) The phase transformation from the metastable anatase phase to the denser rutile phase occurred during sintering at various pressures and at 400 °C. The maximum extent of the phase transformation was 95%, which was achieved at $P_s = 1.5$ GPa and $T = 400$ °C.

(iii) The relative density of the compact increased with sintering pressure under constant temperature (400 °C) from 74% at 0.5 GPa to 95% at 1.5 GPa.

(iv) Open porosity was found to decrease with sintering pressure and was nearly eliminated when the sintering pressure reached 1.25 GPa at 400 °C.

(v) The average grain size of both phases (anatase and rutile) increased with pressure. The average grain size of the rutile phase increased from 27 nm in the original powder form, to 32 nm at 0.5 GPa, to 35 nm at 1 GPa, and to 44 nm at 1.5 GPa, while the average grain size of the anatase phase grew from 27 nm in the original powder, to 32 nm at 0.5 GPa, to 36 nm at

1 GPa, and to 59 nm at 1.5 GPa. A new mechanism for grain growth with sintering pressure is proposed. According to the proposed theory, the grain growth rate is controlled by the presure effect on bulk diffusion rate and interface energy. It predicts that the rate of grain growth will increase with pressure until the pressure reaches a critical value and then decrease thereafter.

(vi) The grain size of the transformation product (rutile) was found to be always less than the grain size of the pre-transformation phase (anatase) under the same processing conditions. We believe this to be the result of an increased nucleation rate brought on by the high sintering pressure. This effect was most pronounced at the highest pressure, and may be even more important at pressures above 1.5 GPa. This suggests that pressure-assisted low temperature sintering may ultimately produce an even finer grain size.

(vii) Transmission electron micrographs showed the nanocrystals were well formed and most of the closed pores appeared to be at the grain boundary triple junctions. In addition, anlaysis of the grain size and closed porosity with transmission electron microscopy suggested that closed pores at grain boundary triple junctions could retard grain boundary migration and thus prevent grain growth.

Acknowledgements

References

[1] R. Birringer, H. Gleiter, H.P. Klein and P. Marquardt, *Phys. Lett. A*, *102* (1984) 365.

[2] X. Zhu, R. Birringer, U. Herr and H. Gleiter, *Phys. Rev. B*, *35* (1987) 9085.

[3] R.W. Siegel, in M. Nastasi, D.M. Parkin and H. Gleiter (eds.), *Proc. NATO-ASI Conf. on Mechanical Properties and Deformation Behaviour of Material Having Ultra-Fine Microstructures*, Kluwer Academic, Dordrecht, 1993, p. 509.

[4] R.A. Andrievski, *J. Mater. Sci.*, *29* (1994) 614.

[5] R. Birringer, U. Herr and H. Gleiter, *Trans. Jpn. Inst. Met. Suppl.*, *27* (1986) 43.

[6] T. Mütschele and R. Kirchheim, *Scr. Metall.*, *21* (1987) 1101.

[7] J. Karch, R. Birringer and H. Gleiter, *Nature (London)*, *330* (1987) 556.

[8] R.W. Siegel, S. Ramasamy, H. Hahn, Li Zongquan, Lu Ting and R. Gronsky, *J. Mater. Res.*, *3* (1988) 1367.

[9] H. Hahn, J. Logas and R.S. Averback, *J. Mater. Res.*, *5* (1990) 609.

[10] H. Hahn and R.S. Averback, *J. Am. Ceram. Soc.*, *74* (11) (1991) 2918.

[11] M. Guermazi, H.J. Höfler, H. Hahn and R.S. Averback, *J. Am. Ceram. Soc.*, *74* (10) (1991) 2672.

[12] H. Hahn, J. Logas, H.J. Höfler, P. Kurath and R.S. Averback, *Mater. Res. Soc. Symp. Proc.*, *196* (1990) 71.

[13] R.S. Averback, H.J. Höfler, H. Hahn and J. Logas, *Nanostruct. Mater.*, *1* (1992) 173.

[14] M.J. Mayo and D.C. Hague, *Nanostruct. Mater.*, *3* (1993) 43.

[15] W.D. Kingery, H.K. Bowen, and D.R. Uhlmann, *Introduction to Ceramics*, Wiley, New York, 1976, p. 486, 2nd edn.

[16] D.C. Hague and M.J. Mayo, *Nanostruct. Mater.*, *3* (1993) 61.

[17] M. Uchic, H.J. Höfler, W.J. Flick, R. Tao, P. Kurath and R.S. Averback, *Scr. Metall.*, *26* (1992) 791.

[18] Z.-Q. Li, S. Ramasamy, H. Hahn and R.W. Siegel, *Mater. Lett.*, *6* (1988) 195.

[19] C.A. Melendres, A. Narayanasamy, V.A. Maroni and R.W. Siegel, *J. Mater. Res.*, *4* (1989) 1246.

[20] J.C. Parker and R.W. Siegel, *Appl. Phys. Lett.*, *57* (1990) 943.

[21] C.D. Terwilliger and Y.M. Chiang, *Nanostruct. Mater.*, *2* (1993) 37.

[22] T.K. Gupta, *J. Am. Ceram. Soc.*, *55* (5) (1972) 276.

[23] C.H. Hsueh and A.G. Evans, *Acta Metall.*, *30* (1982) 1269.

[24] M.A. Spears and A.G. Evans, *Acta Metall.*, *30* (1982) 1281.

[25] D.R. Uhlmann, J.F. Hays and D. Turnbull, *Phys. Chem. Glass*, *7* (5) (1966) 159.

[26] G. Skandan, H. Hahn, B.H. Kear, M. Roddy and W.R. Cannon, *Mater. Lett. 20* (1994) 305.

[27] The powder processed and characterized by Nanophase Technolgies Corporation, private communication, 1994.

Aerosol synthesis of nanoscale clusters using atmospheric arc evaporation

W. Mahoney, R.P. Andres

School of Chemical Engineering, Purdue University, West Lafayette, IN 47907-1283, USA

Abstract

A gas aggregation source that operates at atmospheric pressure and is capable of producing grams per hour of unaggregated, equiaxed metal clusters with diameters in the nanometer range is described. A controlled current d.c. arc is employed to evaporate metal atoms from a liquid metal pool. These evaporated atoms are entrained in a flowing stream of inert gas and quickly transferred to a quench region where the hot stream from the arc plasma is mixed with a second quench stream of cold inert gas. The quench gas provides rapid cooling and immediate dilution, both initiating cluster growth and suppressing cluster aggregation. Cluster size is controlled by varying the metal atom density and residence time in the arc plasma, in the quench region and in the flow downstream from the quench region.

Keywords: Aerosol synthesis; Nanoscale clusters; Arc evaporation

1. Introduction

Methods for producing bulk quantities of size selected, nanometer diameter metal clusters are essential if these intriguing materials are to serve as precursors to nanostructured materials. Most current methods for synthesizing nanoscale clusters are hindered by either low production rates or minimal control of the cluster size.

One of the most flexible methods for producing nanoscale metal clusters is by means of gas aggregation. This technique proceeds by evaporating the metal in the presence of an inert gas and then condensing the metal atoms by cooling the inert gas stream. Gleiter developed a simple source based on this technique that is capable of producing gram quantities of consolidated nanoscale clusters [1]. In this source the metal is evaporated from a resistively heated boat into a low pressure background of inert gas. The metal atoms are cooled by collisions with the inert gas atoms, and this induces homogeneous nucleation and growth of small metal clusters. The resulting clusters are driven by thermophoretic forces to a cold collection surface where they consolidate as a loose powder which can be compacted and sintered to form a nanostructured solid. The variables used to control cluster size in this source are evaporation rate, inert gas pressure and molecular weight of inert gas. An increase in any of these variables results in an increase in the mean cluster size and broadening of the size distribution.

A gas aggregation source designed to give better control over the cluster size distribution and permit molecular beam sampling of unconsolidated clusters is the multiple expansion cluster source (MECS) developed by Andres and his students [2,3]. This source employs forced convective flow of an inert gas to control cluster nucleation and growth. Metal is evaporated from closed crucibles placed inside a resistively heated carbon oven that is pressurized by helium [3]. The superheated mixture of metal atoms, diatoms and inert gas is sonically expanded through a hole in the oven into a quench region where it is mixed with a stream of cold inert gas (either Ar or He). This supersaturated mixture is further expanded into a tubular fast flow reactor in which the clusters grow via accretion of metal atoms onto clusters initially present as diatoms in the oven. By adjusting the metal atom densities and residence times in each section of the MECS, good control over mean cluster size and a tight size distribution can both be achieved. The classical MECS is operated below atmospheric pressure so that a sample of the cluster aerosol can be easily sampled by

expansion into a vacuum chamber as a molecular beam. Owing to materials and pumping speed limitations this source is limited to fairly unreactive metals and to milligram per hour production rates.

The goal of the present research was to develop a cluster source capable of (1) producing crystalline, equiaxed clusters of almost any metal, (2) producing clusters with controlled mean diameters in the nanometer size range and with a narrow size distribution, and (3) achieving gram per hour production rate.

2. Arc evaporation cluster source (AECS)

To accomplish this task, we utilize a controlled d.c. arc discharge for metal evaporation coupled with forced convective flow and rapid quenching at 1 atm to control cluster size and limit cluster aggregation. Fig. 1 shows a schematic diagram of this apparatus along with the associated processes that occur during operation. The important processes are (1) metal evaporation, (2) cluster nucleation and growth, (3) cluster transport, and (4) cluster capture.

Evaporation is achieved by establishing a d.c. arc discharge between two electrodes, an upper electrode fabricated from a tantalum tube which also serves as the inlet to the quench region and a lower electrode which is a heavy gage tungsten wire basket that contains the metal to be vaporized. This lower electrode is attached by means of tantalum foil to a stainless steel tube which serves as a port for introducing gas into the evaporation region. In most cases this gas is argon which serves two purposes; it facilitates arc ignition and acts as a carrier gas transporting the metal vapor into the quench region. Arc ignition is achieved by touching
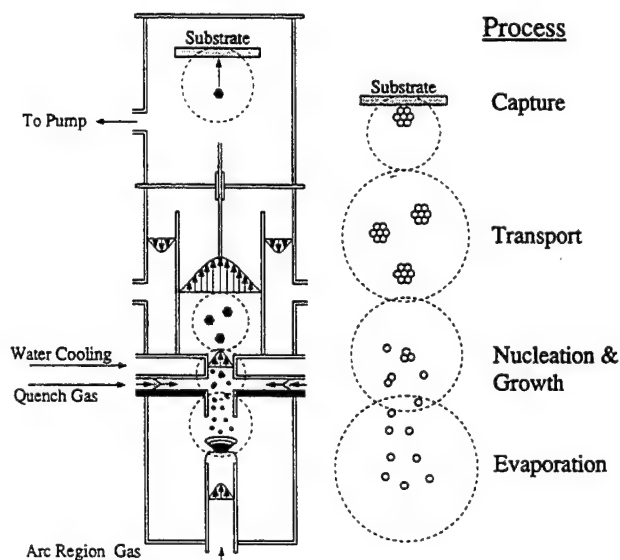
Table 1
Typical operating parameters

Pressure (atm)	1
Energy input (kW)	0.1–1
Arc voltage (V)	8–13
Arc current (A)	10–70
Efficiency (%)	$\approx 10\%$
Polarity	Anode
Evaporation rate (g h^{-1})	1–50
Arc gas flow (Ar) (cm^3 s^{-1})	90–160
Quench flow (Ar) (cm^3 s^{-1})	0–200
Growth time (ms)	10–90
Transport time (s)	0.2–0.7

the electrodes momentarily and then separating them to establish a gap of approximately 1 cm. After ignition, the temperature of the tungsten basket rises rapidly, the metal evaporant quickly melts, and evaporation proceeds from molten metal in the tungsten basket.

Hot vapor from the evaporation region is transferred directly into the quench region where it is mixed with a stream of room temperature gas, typically argon. The role of this quench gas is to cool the hot vapor coming from the arc, thereby initating cluster nucleation and growth, and to dilute the aerosol mixture, suppressing cluster aggregation. The quench region is defined by a graphite flange, which supports the tantalum electrode, and a water cooled flange fabricated from stainless steel (see Fig. 1). The gas mixture in the quench region is cooled both by the cold quench gas and by heat transfer to the water cooled flange.

Downstream of the quench region, the cluster aerosol expands into a laminar flow transport tube. In order to sample the cluster aerosol, the center-line flow near the exit of this tube is expanded through a capillary into a pumped chamber held at approximately 1 Torr. In this chamber the cluster are deposited onto thin, electron transparent films for offline analysis of cluster size, size distribution, and degree of aggregation using a JEOL 2000FX transmission electron microscope.

3. Relevant variables and typical operating conditions

Table 1 lists typical operating conditions. We have found that we are able to keep growth times small and produce clusters in the 1–100 nm diameter range at atmospheric pressure. Evaporation rates are controlled by controlling the arc current. Neglecting any variations in the heat losses due to radiation and convection, increases in arc power are dissipated as enthalpy of evaporation. Experimental evaporation rates are typi-

Fig. 1. Schematic diagram of the arc evaporation cluster source (AECS), illustrating the cluster formation process.
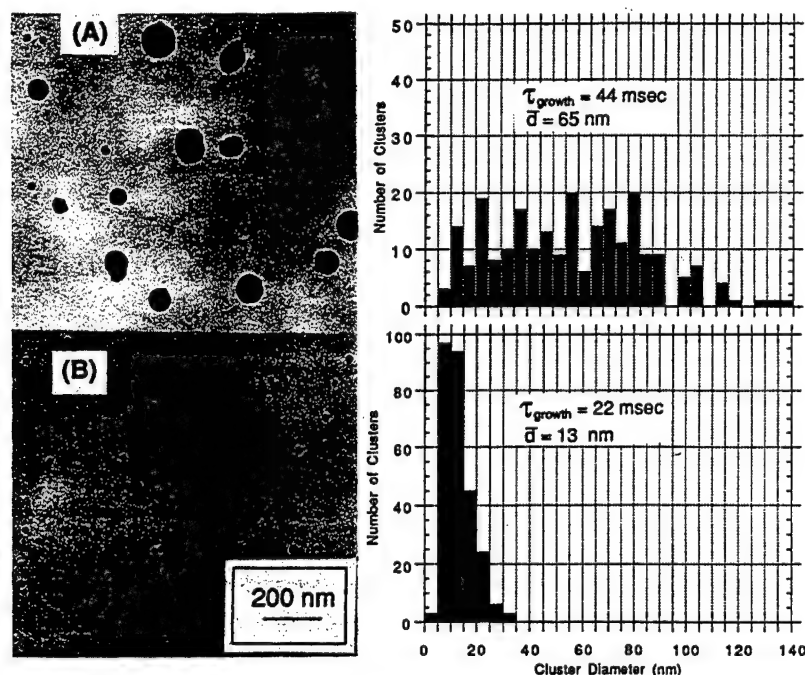
Fig. 2. Bright field transmission electron micrographs and diameter distributions for indium clusters: (A) no quench gas and (B) 160 cm³ s⁻¹ argon quench flow. The arc gas flow was 160 cm³ s⁻¹ argon in both cases.

cally 20–30 g h⁻¹ for arc currents in the 20–40 A range with the metal pool as the anode in the arc circuit. It is important to maintain this polarity and to evaporate from a molten source in order to avoid microdroplet formation commonly encountered in arc evaporation processes. Calculated energy efficiencies based on the ratio of the rate of metal vaporization to the arc power input are on the order of 10%. Arc evaporation region gas flows are typically 90–160 cm³ s⁻¹. Arc stability places a maximum constraint on this gas flow rate. This maximum increases with increasing arc current. Exceeding the maximum flow rate at a given arc current leads to unstable arc operation characterized by fluctuating arc voltages and a tendency of the arc to self extinguish. The arc characteristics are independent of quench gas flow rate. Quench gas flow rates have been varied from 0–200 cm³ s⁻¹. The arc region gas flow and quench gas flow determine the residence times in the source. Growth times in the quench region are typically a few tens of milliseconds and transport times to the sampling capillary are on the order of half a second.

4. Cluster size control: quench effect

Fig. 2 illustrates the effect of quench rate on cluster growth. These data are for indium clusters produced at an evaporation rate of approximately 20 grams per hour. The top electron micrograph and particle diameter distribution correspond to no gas being introduced into the quench region. The flow of argon in the

evaporation region was 160 cm³ s⁻¹. The clusters are unaggregated and crystalline and posses a broad size distribution with a mean diameter of approximately 65 nm. The bottom electron micrograph and diameter distribution correspond to identical conditions but with a 1/1 ratio of evaporation region to quench region gas flows. The effect of the added quench gas is to reduce the mean cluster diameter to approximately 13 nm with a corresponding sharpening of the size distribution. This result holds in general. Holding all other variables constant, increasing the quench flow serves to reduce the mean cluster size while sharpening the size distribution. Similar evaporation rates and cluster size distributions have been achieved with copper, silver and titanium metals.

5. Production of metal (oxide, nitride) clusters

The arc plasma can also be used to react metal atoms with oxygen or nitrogen in order to produce metal oxide or metal nitride clusters. The reactive gas can be introduced into the high temperature arc region or into the cooler quench region. As an example, we illustrate formation of TiN and TiO_2 clusters. Fig. 3 shows a TEM bright field image accompanied by a corresponding TED pattern for TiN particles formed by evaporation of Ti using nitrogen as the gas introduced into the arc. The clusters formed were loosely aggregated crystallites with a crystal structure corresponding to TiN as evidenced by the TED pattern. Adding argon quench
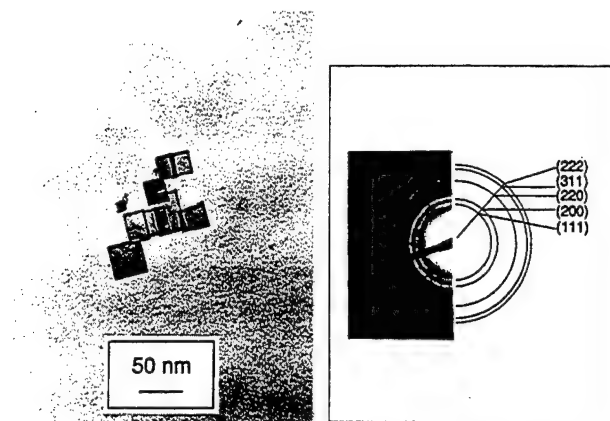
Fig. 3. Bright field TEM and TED pattern of TiN clusters formed by evaporation of Ti using nitrogen as the arc region gas.

gas had the general effect of reducing the primary cluster size and reducing the mean aggregate size.

TiO$_2$ clusters were synthesized by evaporating Ti using argon in the arc region and quenching with air. Fig. 4 shows TEM bright field images of TiO$_2$ clusters formed at two different quench ratios. Fig. 4(A) shows clusters formed by quenching with 50 cm^3 s^{-1} air whereas Fig. 4(B) shows clusters quenched with 150 cm^3 s^{-1} air. The argon flow in the evaporation region for these experiments was 160 cm^3 s^{-1}. The larger clusters formed in the first case are unaggregated with a mean diameter of approximately 52 nm. Increasing the quench flow rate to 150 cm^3 s^{-1} results in a reduction of mean cluster diameter to 26 nm and a

sharpening of the diameter distribution. Electron diffraction shows these particles to be crystalline; however, the relative amounts of the rutile and anatase phases have not been determined. Of interest is the absence of TiN when air is used as quench gas.

6. Summary

We have developed a new type of gas aggregation cluster source for producing nanoscale clusters of metals and metal-based ceramics. Evaporation of the desired metal is achieved by d.c. arc evaporation from a liquid metal pool into a flowing gas stream. Rapid mixing of this vapor with a second stream of room temperature quench gas serves to cool and dilute the metal vapor, initiating cluster growth and suppressing cluster aggregation. The source operates at atmospheric pressure. Evaporation rates are controlled by controlling the arc current and have been varied from 1 to 50 g h^{-1}. Cluster size and size distribution are influenced strongly by the gas flow rates in the arc region and in the quench gas region. Controlled mean cluster diameters in the 1–100 nm size range have been achieved. Increasing the quench flow serves to reduce the mean particle size and sharpen the size distribution. Metal oxide and metal nitride clusters can be formed by addition of reactive gas. TiN clusters have been formed by introducing N$_2$ in the arc region. TiO$_2$ clusters have been formed by introducing air in the quench region.
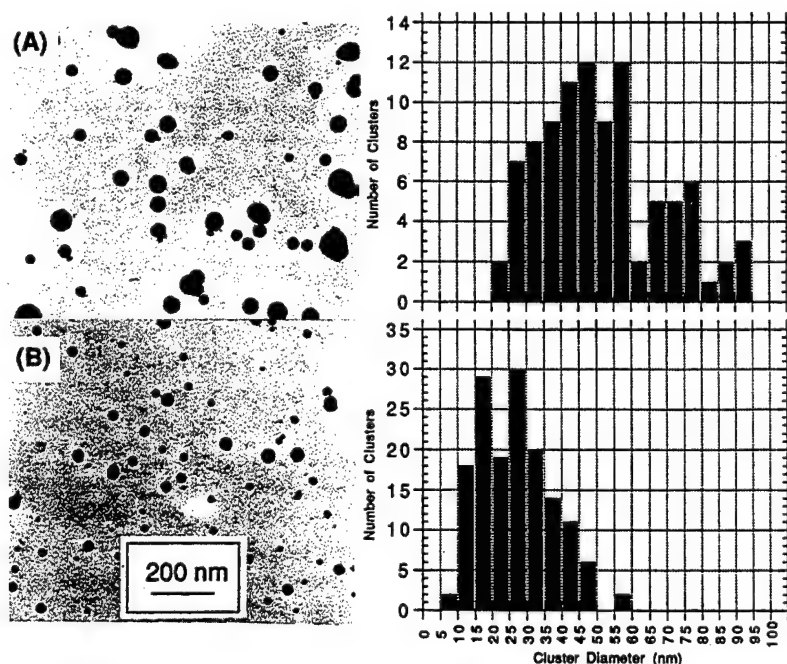
Fig. 4. TEM bright field images and size distributions of TiO$_2$ clusters formed by Ti evaporation in argon (160 cm^3 s^{-1}) using air as quench gas: (A) 50 cm^3 s^{-1} air and (B) 150 cm^3 s^{-1} air.

Acknowledgements

References

[1] H. Gleiter, *Nanostruct. Mater.*, *1* (1992) 1, and references cited therein.

[2] R.S. Bowles, J.J. Kolstad, J.M. Calo and R.P. Andres, *Surf. Sci.*, *106* (1981) 117.

[3] S.B. Park, *PhD Thesis*, Purdue University, 1988.

ELSEVIER

Synthesis and characterization of amorphous $Fe_{80-x}Cr_xB_{20}$ nanoparticles

D. Fiorani[a], H. Romero[a], L. Suber[a], A.M. Testa[a], M. Vittori[b], A. Montone[b], J.L. Dormann[c], J. Maknani[c]

[a]ICMAT, CNR, Area della Ricerca di Roma, C.P. 10, 00016 Monterotondo Stazione, Roma, Italy
[b]ENEA, Settore Nuovi Materiali, C.R.E. Casaccia, C.P. 2400, 00100 Roma, Italy
[c]Lab. de Magnetisme et Materiaux Magnetiques, CNRS, 1 Place A. Briand, 92195 Meudon Cedex, France

Abstract

We report the preparation of amorphous $Fe_{80-x}Cr_xB_{20}$ nanoparticles by chemical reduction, their morphological and structural characterization and the study of their magnetic properties by means of Mössbauer and magnetization measurements. The results show that the mean particle size is composition dependent, decreasing with increasing x. The magnetic properties, determined by the chemical composition and by the particle size distribution, change with increasing x from a ferromagnetic character to a state characterized by the coexistence of Fe–Cr–B ferromagnetic particles with a growing fraction of antiferromagnetic (partially oxidized) and paramagnetic (oxidized) particles.

Keywords: Synthesis; Chemical reduction; Magnetic properties

1. Introduction

Among the methods for preparing fine particles, the chemical ones usually present the advantage of leading to more homogeneous products in a larger composition range. In particular for preparing ternary transition metal–boron, $Fe_{80-x}M_xB_{20}$, amorphous alloys, the chemical reduction of aqueous solutions of metal salts with $NaBH_4$ has proved to be a very successful method [1–4], producing ultrafine powders suitable for compaction in samples of various shapes for different kinds of technological applications. It has been reported that the composition of the particles, their size and shape can be carefully controlled by varying the preparation parameters, such as borohydride concentration [4], temperature [6], pH [7], starting metals salts, way of mixing the liquids (salts and reductant aqueous solutions) and their addition rates [5,8]. Consequently the magnetic properties can be strongly modified by the preparation conditions.

Within this context we report the preparation, by a chemical reduction route, of $Fe_{80-x}Cr_xB_{20}$ ($5 \leq x \leq 70$) fine particles, their morphological and structural char-

acterization and an investigation on their magnetic properties.

2. Experimental

2.1. Material preparation

Fine $Fe_{80-x}Cr_xB_{20}$ ($5 \leq x \leq 70$) particles were prepared by reducing aqueous solutions of $FeSO_4$ and $CrCl_3$ with aqueous solutions of $NaBH_4$ (typical molecular ratio 8:100). The reactions were carried out in an atmosphere of high purity nitrogen. The reductant solution was added to the metal salts solution maintaining the reaction vessel in an alcohol bath at $T = -10\ °C$. The black fine powder was washed thoroughly with water to remove residual ions from the reaction mixture and with acetone to remove water. The sample was then dried overnight under vacuum. Finally air was introduced in the vessel in a controlled way in order to passivate the fine particles, which are pyrophoric. Materials with the following compositions x were prepared: 5, 10, 20, 25, 40, 60.

The material with $x = 40$ was also prepared starting from $FeCl_3 \cdot 6H_2O$, instead of $FeSO_4$, and changing the method of mixing of liquids, i.e. adding the metal salts aqueous solution to the reductant solution.

With the aim of covering the particles with a SiO_2 layer, to reduce the interparticle interactions, tetraethoxysilane was added to a suspension of $Fe_{80-x}Cr_xB_{20}$ in a mixture of isopropylic alcohol and water (20:1) with NH_3 at 50 °C. The mixture was stirred for 5 days and finally the ultrafine grey powder was filtered, washed with isopropylic alcohol and dried under vacuum.

2.2. Material characterization

The morphology, the chemical composition and the structure of the powder specimens were examined by TEM, SEM and X-ray diffraction measurements. The TEM instrument was a Jeol 4000 FX, equipped with an Ultra Thin Window (UTW) X-ray detector and operated at 400 kV. To this purpose the powders were dispersed with an ultrasonic bath and a drop of the resulting suspension was allowed to dry on a microscope grid coated with a thin carbon film.

The magnetic properties were investigated by Mössbauer and magnetization measurements. Mössbauer spectra were recorded in the temperature range 4.2–600 K using a conventional spectrometer operating in the constant acceleration mode. The source was ^{57}Co in Rh. Magnetization measurements were performed in the temperature range 4.2–300 K by a commercial (Quantum Design) SQUID magnetometer ($H_{max} = 5.5$ T).

3. Results and discussion

3.1. Morphological and structural characterization

X-ray and electron diffraction show that the particles are amorphous. TEM measurements show that the series of samples with variable composition x consist of agglomerates or long chains of spherical particles of different sizes. The mean particle diameter and the width of size distribution depends on the composition x (e.g. for $x = 40$, the diameter ranges from few nanometers to 200 nm, with a mean value $\phi = 110$ nm and with the width at half heigth in the distribution curve $\Gamma_{1/2} = 50$ nm; for $x = 60$, $\phi_{max} = 90$ nm, $\phi = 50$ nm, $\Gamma_{1/2} = 40$ nm). Within each sample there is a chemical composition distribution also, related to the size distribution, the smallest particles being richer in chromium. This indicates that the nucleation process in this system is controlled by the chemical composition, a higher chromium content promoting an easier nucleation, whereas the subsequent growth occurs in a solution enriched in iron.

The sample with $x = 40$, prepared starting from $FeCl_3$ instead of $FeSO_4$ and adding the solution of metal salts to the reductant solution, consists of agglomerated particles of irregular shape. The particle sizes, ranging from $\cong 20$ nm to $\cong 50$ nm, are smaller than in the previous sample with the same composition x.

The sample prepared with the aim of covering particles with SiO_2 shows agglomerates containing Fe, Cr and Si. However, despite the presence of a Si peak in the X-ray spectrum from the agglomerates, it is difficult from TEM images to detect the SiO_2 layers around the particles.

3.2. Magnetic properties

(a) Mössbauer spectra

Mossbauer spectra consist of a broad sextuplet, revealing a large distribution of hyperfine fields, characteristic of an amorphous structure, and a central paramagnetic doublet. An example of the hyperfine field distribution is reported in Fig. 1 for $x = 16$ at $T = 4.2$ K. An example of the variation with temperature of the hyperfine patterns is shown in Fig. 2 for $x = 25$. At the highest temperature ($T = 590$ K) the sample appears to be crystallized. The crystallization temperature increases with x (e.g. for $x = 25$, $T_{cr} \cong 550$ K). For the particles rich in iron, in a first step the crystallization product is almost pure metallic iron.

The spectra confirm the existence, within each sample, of both particle size and chemical composition distribution and their close relationship. The analysis of the spectra reveals the presence of three types of particles, their relative fraction depending on the composition x:

(i) paramagnetic particles (P), at least down to 4.2 K. They would correspond to particles very rich in
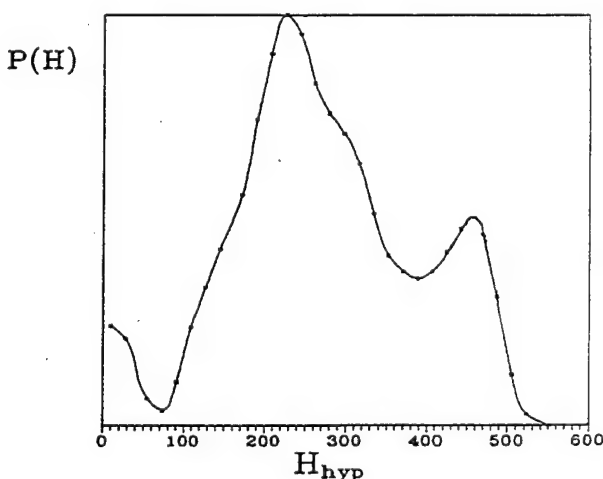
Fig. 1. Hyperfine field distribution at $T = 4.2$ K for $x = 16$.
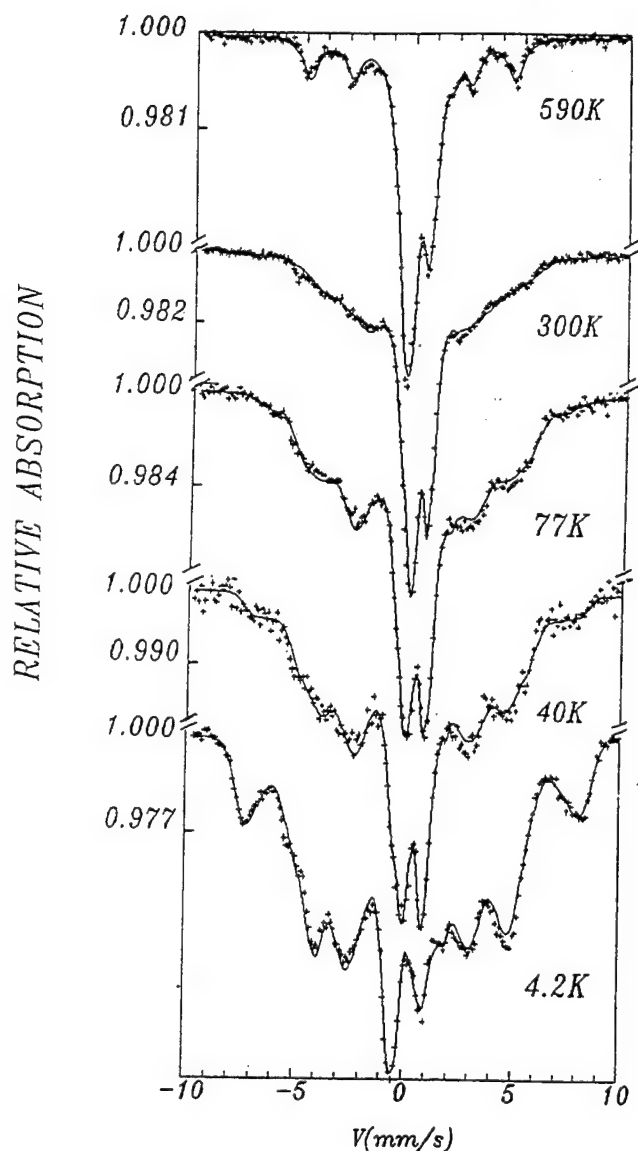
Fig. 2. Mossbauer spectra at different temperatures for $x = 25$.

chromium, which are the smallest ones. In these particles iron is fully oxidized (Fe^{3+}).

(ii) antiferromagnetically ordered particles (AF), with Neel temperature $20\ K < T_N < 77\ K$. They are richer in chromium than the nominal composition. These particles are partially oxidized (both Fe^{2+} and Fe^{3+} ions are present).

(iii) ferromagnetically ordered particles (F), with a large distribution of Curie temperature (e.g. for $x = 25$, the maximum T_c value is about 450 K, corresponding to $x = 7$ in the bulk). Most of these particles are richer in iron than the nominal composition and some of them have a composition close to the nominal one. This type of particle, being the biggest ones and corresponding to metallic Fe–Cr–B metallic particles, represent the main part of the spectra.

As an example of how the relative fraction of the three types of particles evolve with composition: for $x = 5$, F = 88%, AF = 11%, P = 1%; for $x = 40$, F = 74%, AF = 15%, P = 11%.

Preliminary studies on SiO_2 covered particles show a clear decrease of the isomer shift (about $0.15\ mm\ s^{-1}$) and an increase of the width of the quadrupole splitting distribution in the paramagnetic state, indicating a change in the electronic states due to surface modification.

(b) Magnetization measurements

Magnetization measurements, performed as a function of the magnetic field at $T = 5\ K$, show a progressive change with the composition x [9]. This reflects the change of the relative fraction of the different types of particle. For low x values ($x \leq 25$) typical ferromagnetic hysteresis cycles are observed (Fig. 3(a,b)). The magnetization saturates (e.g. for $x = 5$, $M_s = 108$ emu g^{-1}) and the coercive field is very low (e.g. for $x = 20$, $H_c = 20$ Oe). This behaviour reflects the large predominance of the Fe–Cr–B metallic particles, which are soft ferromagnets in the bulk state.

For $x > 25$ the behaviour of the magnetization curves progressively moves away from a typical ferromagnetic one: they do not show saturation and clearly reveal the coexistence of ferromagnetic, antiferromagnetic and paramagnetic particles, the fraction of the last two increasing with increasing x (Fig. 3(c,d)).The contribution of the two non-ferromagnetic components to the magnetization curve is clearly shown by the linear increase in the high field region observed for high x values.

Hysteresis is observed in the low field region for each sample, with a coercive field increasing with x (e.g. for $x = 40$, $H_c = 70$ Oe; for $x = 60$, $H_c = 300$ Oe). This could be due in principle to particle size as well as to chemical composition effect, leading to an increase of anisotropy. Preliminary measurements performed on the SiO_2 covered particles show an increase of the coercive field with respect to the uncovered particles (e.g. for $x = 70$, at $T = 5\ K$, $H_c = 500$ with SiO_2 and $H_c = 200$ Oe without SiO_2), indicating that the surface modification leads to an increase of the surface and shape anisotropy, which represent the most important contribution to the total anisotropy, as the magnetocrystalline anisotropy is very weak in the amorphous particles.

4. Conclusions

We have reported the preparation, by a chemical reduction route, of amorphous $Fe_{80-x}Cr_xB_{20}$ fine particles, their morphological and structural characterization and the study of their magnetic properties. The
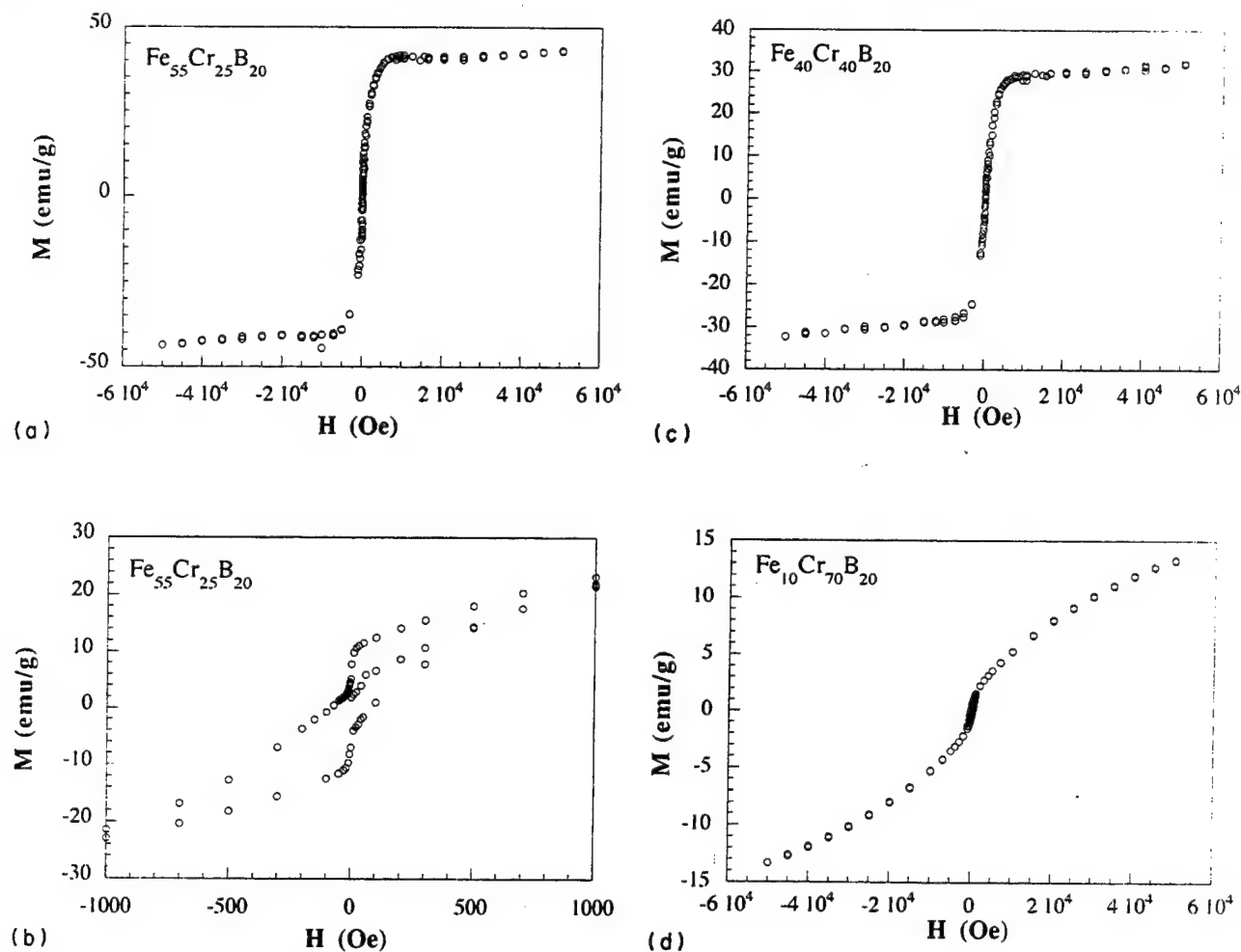
Fig. 3. Magnetization vs. H at $T = 5$ K: (a,b) $x = 25$; (c) $x = 40$; (d) $x = 70$.

results indicate that changes in the preparation parameters (e.g. the type of starting metal salts, the way of mixing the solutions) lead to different particle shapes (spherical or irregular), to a different particle size distribution and to different kinds of aggregation (in chains or in agglomerates), producing important modifications of the magnetic properties. Moreover, the covering of particles with SiO_2 layers is found to increase the surface anisotropy, as detected by an increase in the coercive fields. The composition dependence of the magnetic behavior is found to be mainly determined by the change, within a series of samples prepared in the same conditions, of the relative ratio between metallic ferromagnetic particles (largely predominant), partially

oxidized antiferromagnetic and oxidized paramagnetic particles.

References

[1] S. Linderoth et al., *J. Magn. Magn. Mater.*, *81* (1989) 138
[2] J. Rivas et al., *J. Magn. Magn. Mater.*, *122* (1993) 1
[3] A. Carrias et al., *Chem. Mater.*, *2* (1990) 363
[4] L. Yiping et al., *J. Magn. Magn. Mater.*, *79* (1989) 321
[5] S. Wells et al., *J. Phys. Cond. Matter*, *1* (1989) 8199
[6] J. Jiang et al., *J. Non-Cryst. Solids*, *124* (1990) 139
[7] S. Linderoth and S. Morup, *J. Appl. Phys.*, *67* (1990) 4472
[8] C.B. Koch et al., *MRS Symp. Proc.*, *206* (1991) 327
[9] D. Fiorani et al., *J. Magn. Magn. Mater.*, in press.

Effect of hydrolysis on the colloidal stability of fine alumina suspensions

J. Liu, L.Q. Wang, B.C. Bunker, G.L. Graff, J.W. Virden, R.H. Jones

Department of Materials Science, Pacific Northwest Laboratory, Battelle Boulevard, Box 999, Richland, WA 99352, USA

Abstract

This paper investigates the effect of hydrolysis and the formation of hydrated polycations on the colloidal stability and rheological properties of fine alumina suspensions. This is an important phenomenon in colloidal processing of advanced ceramic materials and nanocomposite materials from fine particles. The aging process and the formation of large polycations in the solution are monitored by nuclear magnetic resonance, and the aggregation rate and viscosity of the suspension are measured under similar conditions. It is observed that aging under acidic conditions increases colloidal stability against aggregation in dispersed suspensions, and reduces the viscosity in flocculated suspensions. This behavior corresponds well to the formation of large polynuclear species through hydrolysis. It is suggested that the hydrated polycations significantly modify the total interaction energy between two particles at short separation distances.

Keywords: Hydrolysis; Colloidal stability; Fine alumina suspensions

1. Introduction

Colloidal processing methods have been widely used to prepare advanced ceramic materials and nanocomposite materials [1–5]. The packing density and microstructure of the green body are mainly determined by the interactions between the colloidal particles and the conditions under which the suspension is prepared and consolidated. Three mechanisms to control colloidal stability are well documented [6]: electrostatic repulsion due to charge development on particle surfaces, van der Waals attraction through dipole–dipole interactions, and steric interaction from polymers adsorbed onto the particles. These interaction energies can be estimated using a DLVO (Derjaguin–Landau–Verwey–Overbeek) theory [6]. Strong electrostatic or steric repulsion will produce a well-dispersed suspension and high packing density. On the other hand, a flocculated suspension in the absence of long-range repulsion will result in poor consolidation and low packing density.

The stability, rheology, and consolidation of some common oxide materials, such as alumina, have been extensively studied in the literature [7–11]. However, many ceramic suspensions, especially those made of fine particles, exhibit time-dependent colloidal properties through aging and hydrolysis [12,13]. The effect of such phenomena on the colloidal stability has not been well studied. For example, metal oxides can undergo extensive hydrolysis in an aqueous solution and produce a variety of solution species, depending on pH, temperature, electrolyte concentrations, mechanical stirring, and reaction time [14]. It has been suggested that the hydrolyzed polynuclear species may have an effect on the colloidal stability of peptized beohmite [15]. Petroff and Sayer have purposely introduced zirconium hydrogel to zirconia, alumina, and titania suspensions to modify the surface chemistry and enhance colloidal stability [16]. There are several recent studies related to "non-DLVO" forces in ceramic suspensions [9–11,17,18]. Because these non-DLVO forces are generally attributed to the short-range hydration forces [19–22], a better understanding of the influence of surface hydrolysis is important.

The purpose of this study is to examine the hydrolysis process of suspensions of fine alumina particles, and

its correlation with colloidal stability and rheological properties. The solution species is studied by magnetic resonance, and the aggregation rate and viscosity of the suspension are monitored at the same time. It is concluded that the hydrolysis process greatly affects the colloidal properties of fine particles: the increased colloidal stability and reduced viscosity can be directly related to the dissolution and formation of large polynuclear species through aging under acidic conditions. These hydrated polycations can significantly modify the total interaction energy between two particles at short separation distances.

2. Experimental procedure

Aqueous suspensions of unagglomerated α-alumina powder (AKP 53, 0.2 μm median particle size obtained from Sumitomo Chemical Co., New York) were studied. Nuclear magnetic resonance (NMR) was used to study the hydrolyzed polycation species. The aggregation rates, viscosity, and electrokinetic mobility were measured under controlled experimental conditions.

2.1. Nuclear magnetic resonance spectroscopy

^{27}Al solid-state NMR was used to identify chemical species in the colloidal aging processes through chemical shifts and line shape of NMR signals. No effort was made to measure the absolute concentration of the soluble species in this study. ^{27}Al NMR experiments were carried out with a Chemagnetics spectrometer (300 MHz, 89 mm wide bore Oxford magnet) using a CP-MAS probe. Suspensions of 15 vol.% Al_2O_3 were prepared with initial pH 1.49, 2.00, 2.57, and 3.79. The suspension was pipetted into 5 mm plastic cylinders, which were then put in the 7 mm zirconia PENCIL™ rotors. NMR measurements were performed during the aging process. Samples were spun at 3–4 kHz; spectra were collected by using a single-pulse Block decay method with a 5 ms aluminum pulse and a 500 ms relaxation delay. For all experiments, 40 ms acquisition times and a 50 kHz spectral window were employed. The number of transients was 500 to 1000.

The approach employed in this study is designed to maximize the signal from the dissolved Al species and minimize the signal from the alumina particles. Because samples were submicrometer Al_2O_3 colloidal particles suspended in water, a broad NMR signal was observed for the Al_2O_3 particles due to large quadruple moments of Al, having FWHM (full width at half maximum) of 8 to 9 kHZ at nonspin and 1 to 2 kHz at 3 kHz spinning. Both magic angle spinning (MAS) and static Block decay measurements were taken. It was found that static measurements (without spinning) resolved narrow peaks (FWHM of 100 to 200 Hz). Although

with spinning the peaks from Al_2O_3 particles were greatly narrowed, those narrow peaks were embedded in the Al_2O_3 main peak and its side bands. Thus, all aluminum spectra were taken at nonspin and without decoupling because no changes in spectra were observed with and without decoupling.

2.2. Aggregation study of dilute suspensions

Aggregation studies were conducted at pH 2 for diluted suspensions. The samples were aged for different times to study the effect of hydrolyzed clusters formed during aging. A 15 vol.% suspension was made with 11.88 g of AKP 53 powder added to 17 ml deionized water; the pH was preadjusted to 2.00 with dilute HNO_3. The suspensions were sonicated for 20 min and pH was readjusted to 2 by dilute HNO_3. The samples were then aged for different times: no aging, aged 1 day, and aged 21 days. The pH of the suspension increased slowly with time; therefore, it was necessary to readjust pH to 2 before measuring the particle and aggregate size. About 0.2 ml of the suspension was diluted to 10 ml of 0.1 M $NaNO_3$ solution, with pH preadjusted to 2. The particle size and the aggregate size distribution of the dilute suspension was measured at different times by a Microtrac Series 9200 Ultrafine Particle Analyzer using the Doppler shift laser light scattering principle. The initial particle size distribution was also measured by diluting the suspension with pure deionized water at pH 2.

2.3. Viscosity

Shearing experiments were performed at pH 4. Suspensions of 15 vol.% were prepared with initial pH of 2.00 and 3.79. After the samples had been aged for different times, the suspensions were sonicated for 20 min, and pH of all the suspensions was readjusted to 4. Then $NaNO_3$ was added to the suspension to make a 0.3 M electrolyte solution. The stress–shearing rate relationship was measured by a Haake Viscometer with an SVI sensor. The apparent viscosity was obtained by dividing the stress by the shearing rate.

2.4. Transmission electron microscopy (TEM)

Transmission electron microscopy was used to study the morphology of the particles before and after aging. Similar suspensions of aged and nonaged suspensions of 15 vol.% solid loading were prepared and 0.3 M $NaNO_3$ was added. A TEM copper grid coated with carbon thin film was gently introduced into the suspension and pulled out. A drying paper was used to remove the excess suspension and liquid. TEM imaging was performed on a Philips 400 TEM at 120 kV.
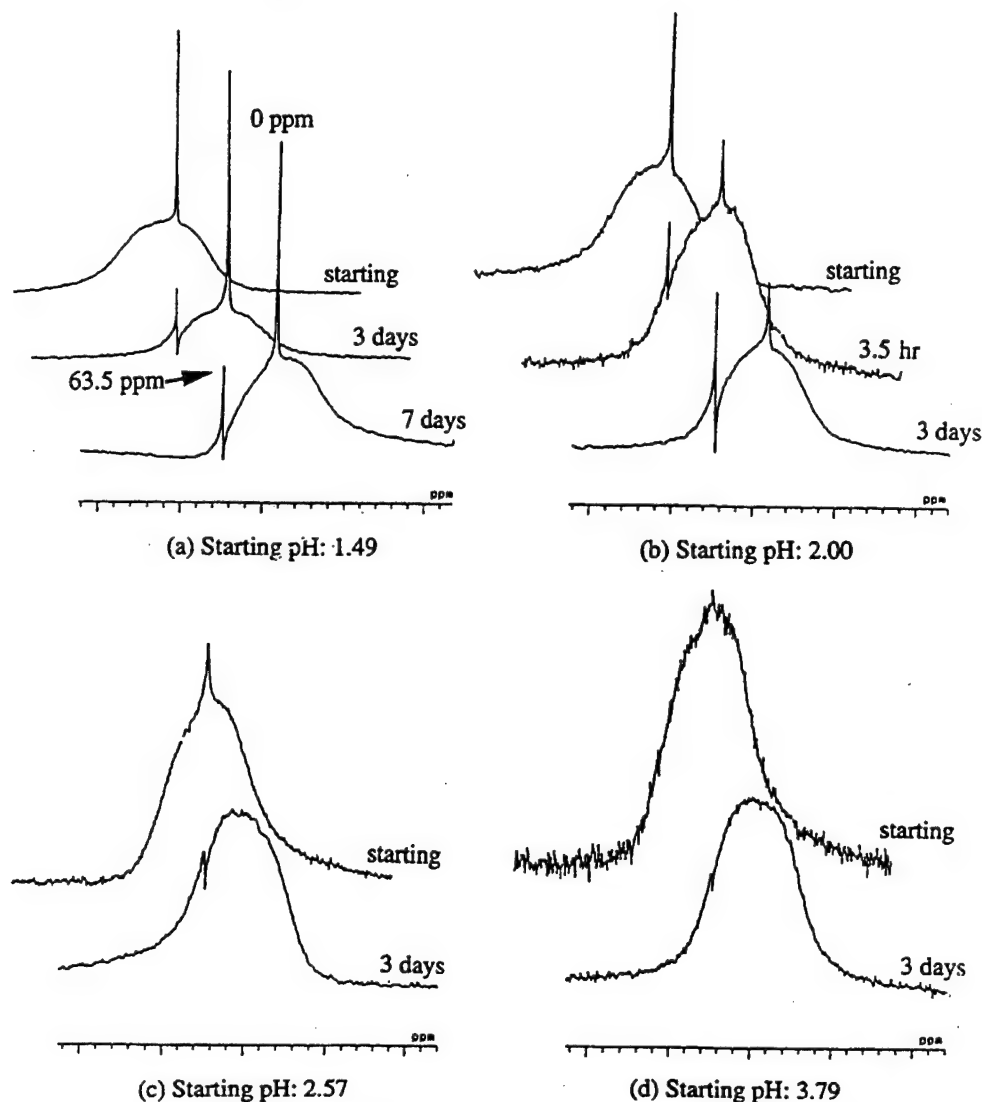
Fig. 1. NMR results on alumina suspensions aged for different times at different pH. The peak at 0 ppm corresponds to the single Al^{3+} ions, and the peak at 63.5 ppm corresponds to the Al_{13} clusters; the broad peak comes from the alumina particles themselves. The peak height at 63.5 ppm increased with aging at low pH (a and b), suggesting that the concentration of polycations increases during aging. At a higher pH both the dissolution and formation of the polyclusters were sluggish (c and d).

3. Results

The NMR study provided direct information on the hydrolysis process in the suspension. Four suspensions were prepared with an initial pH of 1.49, 2.00, 2.57, and 3.79. During aging, the pH of all the suspensions shifted to a higher value due to hydrolysis. After aging for 3 days, the pH values became 4.05, 4.40, 4.64, and 4.75, respectively. The NMR results are summarized in Fig. 1. Only one sharp peak was observed at 0 ppm for fresh suspensions. This peak corresponds to the single $Al(H_2O)_6^{3+}$ ions. At a lower pH, this peak was higher, indicating fast dissolution kinetics; at a higher pH, the peak was broad and small, indicating slow dissolution kinetics.

After some time of aging, a second peak appeared at 63.5 ppm at low pH, corresponding to the $\langle Al_{13}O_4(OH)_{24}(H_2O)_{12}\rangle^{7+}$ (Al_{13} polycation) [15,24]. The Al_{13} cluster contains 12 AlO_6 octahedra joined by common edges. The tetrahedron of the four oxygens surrounds the aluminum atom at the center. This tetrahedrally coordinated aluminum produces a narrow Al NMR resonance at 63.5 ppm (relative to $\langle Al(H_2O)_6\rangle^{3+}$). Because this is one of the most stable and prominent poly species in the solution [15,24], this narrow resonance can be used as a probe to study the forming of hydrated polycations in the solution. Fig. 1(a,b) illustrates how this peak grew with time at low pH, suggesting that the concentration of the polycation increases with time during aging at low pH. The figure also shows that at pH 2.00 the peak height at zero ppm

decreased after aging while at the same time the peak at 63.5 ppm grew. This occurred because the dissolved Al^{3+} ions combined to form the polyclusters at a later stage. On the other hand, Fig. 1(c,d) shows that both the dissolution and the formation of the polyspecies were not significant at a higher pH. Only a small peak at 63.5 ppm was detected in Fig. 1(c) after 3 days of aging; at even a higher pH, there is only a tiny shoulder (Fig. 1(d)).

These results from alumina suspensions are consistent with those reported in the literature [14,23] concerning the hydrolysis and condensation process of aluminum ions:

(1) The solubility of aluminum ions is highest at low pH, reaches a minimum at pH 6.5, and increases again at high pH.

(2) The mononuclear species forms rapidly and reversibly, while polycation species, such as $\langle Al_2(OH)_2(H_2O)_8\rangle^{4+}$ and $\langle Al_3(OH)_4(H_2O)_9\rangle^{5+}$, form slowly. Larger hydrated polyclusters, $\langle Al_{13}O_4(OH)_{24}(H_2O)_{12}\rangle^{7+}$ (Al_{13} cluster), will take longer to grow.

(3) The distribution of the polymeric species is pH-sensitive. Under acidic conditions (pH < 4) the large clusters, especially Al_{13} clusters, dominate, while at a higher pH, most aluminum ions exist as mononuclear species.

From this discussion, it is clear that the alumina suspension consists not only of the alumina particles, but also of hydrolyzed polycations. The hydrated polynuclear clusters will certainly have an effect on the colloidal stability and rheological properties of the suspension. Like other organic processing additives (surfactant, polymers), these charged polycation clusters can modify the interaction potentials between the particles when the range of the interaction being considered is comparable to the dimension of these polycations, and can influence the colloidal properties of the suspensions through electrostatic, steric, electrosteric or other mechanisms.

The aggregation experiments were conducted on suspensions aged at pH 2 for different times. As discussed in the previous sections, aging at low pH will increase the concentration of polycation clusters. The nonaged sample (fresh sample) has no polycation clusters, the sample aged for 1 day has some polycation clusters, and the sample aged 21 days has more polycation clusters. These experiments will then tell whether the hydrated polycations have any effect on the colloidal stability. The particle size distributions of all the suspensions were first measured to ensure that the starting conditions were the same. As shown in Fig. 2, these suspensions do have the same initial particle size distribution. The mean particle size of 0.2 μm agrees with the supplied literature data. In Fig. 3 the particle and aggregate size distribution is plotted 1 min, 8 min, and

22 min after the dispersed suspension was placed into 0.1 M $NaNO_3$ solutions at pH 2 to start aggregation. Fig. 3(a) shows that significant aggregation had already occurred in the nonaged suspension after 1 min in 0.1 M $NaNO_3$, while the suspensions aged 1 day and 21 days remained mostly dispersed. After 8 min, the suspension aged 1 day also aggregated. After 22 min all the particles in the nonaged suspension were flocculated, yet the samples aged 21 days were only partially aggregated. In all the cases, the nonaged suspension with least amount of polycation clusters always had a size distribution on the right, indicating large agglomerate size; the suspension aged 21 days with more hydrolyzed polycation clusters had a size distribution on the left, indicating smaller agglomerate sizes. The suspension aged for 1 day was between the two. These experiments prove that aging at low pH makes the suspension more stable. Because it was shown earlier that aging under acidic conditions produces a high concentration of hydrolyzed polycations, these results then suggest that these hydrated polycations help stabilize the suspension.

The rheological experiment further illustrated the effect of hydrolyzed polycation clusters on the viscosity of the suspension. All the experiments were conducted at pH 4, with some suspensions first aged at pH 2 to create hydrolyzed clusters, and other suspensions prepared fresh. Fig. 4 shows that aging at pH 2 greatly reduced the shearing stress and viscosity. This can be attributed to the existence of hydrolyzed polyclusters to create a weak interaction potential. The fresh suspension prepared at pH 4 had much higher shearing stress and viscosity because the hydrated polycations were not present. Aging under this condition led to even higher
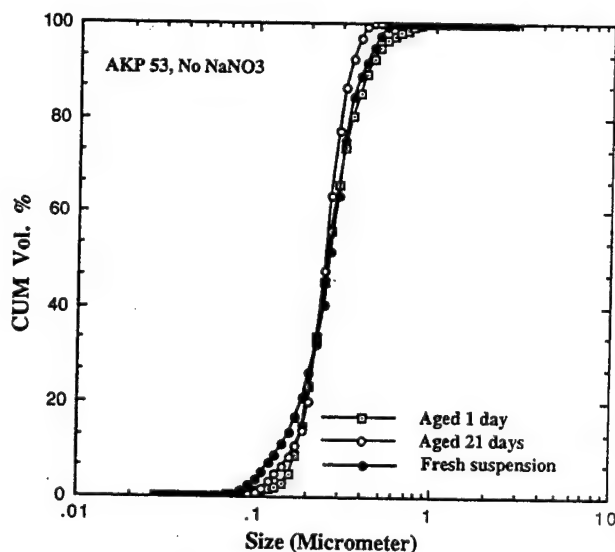
Fig. 2. Particle size distribution before aggregation. The nonaged sample and the samples aged 1 and 21 days had similar size distribution.

Fig. 4. Comparison of the viscosity for flocculated suspensions with and without hydrolyzed clusters at about pH 4. The suspension aged at pH 2 first had significantly lower viscosity. On the other hand, aging at pH 4 did not create more hydrolyzed clusters and increased the viscosity.

Fig. 3. Aggregate size distribution in 0.1 M $NaNO_3$ solution at pH 2 after 1 min (a), 8 min (b), and 20 min (c) after the aggregation was initiated. The suspension without the hydrated polycations (nonaged sample) aggregated faster than the suspensions with polycations (aged samples).

shearing stress and viscosity due to a stronger bonding between particles created during aging. On the other hand, aging at pH 2 improved the rheological properties and reduced the viscosity.

TEM was also used to show the morphological difference between the aged and nonaged alumina particles. Fig. 5(a) shows the nonaged alumina particles, and Fig. 5(b) shows the aged alumina particles. Comparison between 5(a) and 5(b) shows that the nonaged suspension consisted of relatively clean particles and particle surfaces; yet the aged suspension had particles with rough surfaces due to dissolution and formation of hydrolyzed clusters. Very fine aluminum hydroxide particles can be observed in the background. Usually fine particles are also seen between larger alumina particles. These very small particles are assumed to be aggregated and condensed products of the polycation clusters in the solutions.
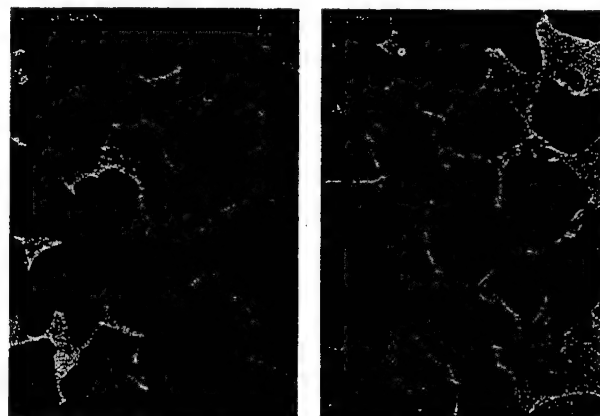
Fig. 5. Comparison of the morphology of aged and nonaged alumina particles. The nonaged particles had smooth clean surfaces; the aged particles showed rough surfaces, and ultrafine particles in the solution and between the particles.

Fig. 6. Estimated interaction energies for 0.2 mm alumina particles in 0.2 M NaNO$_3$ aqueous suspension. Va, van der Waals attraction; Vr, electrostatic repulsion; V(total), total interaction. If the net interaction can be truncated at about 5 Å separation, the particles will have a weak attraction potential.

4. Summary and discussion

This paper has shown that hydrated polycations greatly affect the colloidal stability and rheological behavior of fine alumina suspensions. Under conditions when the polycations can form, such as aging at low pH, the suspension becomes more stable against aggregation, and has a low viscosity if flocculated. The aggregation rate, rheological properties, and morphological changes are all consistent with this conclusion. It can also be expected that the hydrolysis process will play a more important role for even finer particles (nanometer-sized particles) because of the increased surface area and the range of interactions that need to be considered.

In the literature, short-range hydration forces have been used to prepare weakly flocculated alumina suspensions with desirable rheological properties for near-net-shape forming [9–11]. Such suspensions are produced by the addition of electrolytes into dispersed colloids and subsequent pressure filtration. This procedure produces suspensions with high packing density (58 vol.%), and low viscosity required of plastic forming. The hydration forces are attributed to the absorption of anions (Cl$^-$, Br$^-$, I$^-$, NO$_3^-$ etc.) on the positively charged particle surface under acidic conditions. Then the questions are why the unusual colloidal behavior in alumina is only observed at pH below 4, not observed at higher pH, and why the short-range forces are more effective in alumina suspensions and less effective in nonoxide suspensions [17]. In latex suspensions and in mica systems [21], the hydration forces are only detected at high pH (above the isoelectric point) with the adsorption of hydrated cations. Below the isoelectric point, the effect of hydration forces on the colloidal stability is not observed since only unhydrated NO$_3^-$ adsorbs to the positively charged surface.

Apparently the behavior of the hydration forces discussed in the literature [9–11] is somewhat similar to the hydrolysis and formation of the polycations in alumina suspensions discussed in this paper, which would only have a significant effect at low pH range. Therefore, it is reasonable to speculate that the hydrated polycations formed through aging may have contributed to the hydration forces [9–11] in such oxide suspensions. A better understanding of the origin of such short-range interactions and the effect of surface hydrolysis will be achieved with the application of advanced surface characterization techniques.

To evaluate the influence of the polycations on the interaction potential between the particles, the interaction energies between 0.2 mm alumina particles in 0.2 M NaNO$_3$ solutions were estimated through the DLVO theory [6,24] using constant potential approximation. The surface potential was taken as 60 mV, a typical number for fully charged oxide particles, and the effective Hamaker constant was taken as 11.9 kT [7,8]. The final results are plotted in Fig. 6. The net interaction energy remains slightly negative (attractive) over a wide range until the separation distance between the particle surface is less than 5 Å or so, below which the attraction energy increases rapidly with decreasing distance. However, if the net interaction is intercepted at about 5 Å separation, the total attraction will be small. The radius of the most common aluminum polycation, the Al$_{13}$ cluster, is about 3.75 to 3.9 Å. These hydrated polycations on the particle surface or between the particles can change colloidal interactions and produce a repulsive potential at about twice their dimensions, as schematically shown by the straight line. This phenomenon will provide an effective steric barrier at close distance similar to adsorbed organic polymers [25] and therefore will reduce the attraction energy between particles and increase the colloidal stability. Due to the steep repulsion from the steric interaction, a shallow energy minimum is introduced to the total energy potential. Unfortunately, the NMR technique used in the current study is not sensitive to the structures on the particle surfaces; therefore the exact conformation on the surface and the adsorption behavior of the hydrated species cannot be studied.

References

[1] R.G. Horn, *J. Am. Ceram. Soc.*, *73* (1990) 1117.
[2] I.A. Aksay, in J.A. Mangels and G.L. Messing (eds.), *Advances in Ceramics*, *9*, *Forming of Ceramics*, American Ceramic Society, Westerville, OH, 1984, p. 94.
[3] F.F. Lane, *J. Am. Ceram. Soc.*, *72* (1989) 3.
[4] J. Liu, M. Sarikaya, W.Y. Shih, W.-H. Shih and I.A. Aksay, *Mat. Res. Soc. Symp. Proc.*, *175* (1990) 30.
[5] Y. Hirata, I. Haraguchi and Y. Ishihara, *J. Mater. Res.*, *58* (1992) 408.
[6] J.T.G. Overbeek, *J. Colloid. Interface Sci.*, *58* (1977), 408.
[7] L. Bergstrom, *J. Chem. Soc. Faraday Trans.*, *88* (1992) 3201.
[8] L. Bergstrom, C.H. Schilling and I.A. Aksay, *J. Am. Ceram. Soc.*, *75* (1992) 3305.
[9] B.V. Velamakanni, J.C. Chang, F.F. Lange and D.S. Pearson, *Langmuir*, *6* (1990) 1323.
[10] W.A. Ducker, Z. Xu, D.R. Clarke and J.N. Israelachvili, *J. Am. Ceram. Soc.*, *77* (1994)437.
[11] B.V. Velamakanni, F.F. Lange, F.W. Zok and D.S. Pearson, *J. Am. Ceram. Soc.*, *77* (1994) 216.
[12] L. Bergstrom and R.J. Pugh, *J. Am. Cer. Soc.*, *72* (1989)103.
[13] L. Bergstrom and E. Bostedt, *Coll. Surf.*, *49* (1990) 183.
[14] C.F. Baes and R.E. Mesmer, *The Hydrolysis of Cations*, Krieger Publishing Co., Malabar, FL, 1986.
[15] T. Assih, A. Ayral, M. Abenoza and J. Phalippou, *J. Mater. Sci.*, *23* (1988) 3326 .
[16] T.E. Petroff and M. Sayer, *Colloids Surface*, *78* (1993) 235.
[17] E.P. Luther, T.M. Kramer, F.F. Lange and D.S. Pearson, *J. Am. Ceram. Soc.*, *77* (1994) 1047.
[18] K. Higashitani, M. Kondo and S. Hatade, *J. Colloid. Interface Sci.*, *142* (1991) 204.
[19] J.N. Israelachvili and R.M. Pashley, *J. Colloid. Interface Sci.*, *97* (1984) 446.
[20] J. Israelachvili, *Intermolecular and Surface Forces*, Academic Press, San Diego, 1991, p. 275.
[21] V.E. Shubin and P. Kekicheff, *J. Colloid. Interface Sci.*, *155* (1993) 108.
[22] P.M. Pashley, *J. Colloid. Interface Sci.*, *83* (1981) 531.
[23] C.J. Brinker and G.W. Scherer, *Sol-Gel Science*, Academic Press, San Diego, 1990, p. 60.
[24] D.J. Shaw, *Introduction to Colloid and Surface Chemistry*, Butterworths, Boston, 1980, p. 186.
[25] D.H. Napper, *Polymeric Stabilization of Colloidal Dispersions*, Academic Press, London, 1983.

Nanocomposites containing nanoclusters of Fe_2P or γ-Fe_2O_3

C.M. Lukehart*,[a], Stephen B. Milne[a], S.R. Stock[b], R.D. Shull[c], James E. Wittig[d]

[a]*Department of Chemistry, Vanderbilt University, Nashville, TN 37235, USA*
[b]*School of Materials Science and Engineering, Georgia Institute of Technology, Atlanta, GA 30332, USA*
[c]*National Institute of Standards and Technology, Gaithersburg, MD 20899, USA*
[d]*Department of Applied and Engineering Sciences, Vanderbilt University, Nashville, TN 37235, USA*

Abstract

Covalent incorporation of an organoiron complex into a silica xerogel matrix affords a single-source precursor for two different nanocomposite materials. Thermal treatment of this molecularly doped xerogel under hydrogen produces a nanocomposite containing nanocrystals of Fe_2P (barringerite). Thermal treatment of this doped xerogel under oxidizing conditions gives a nanocomposite containing nanocluster of γ-Fe_2O_3 (maghemite-Q). The latter result is unique in that thermal treatment of silica xerogels doped with ferric ions under similar thermal conditions affords an undesired iron silicate, Fe_2SiO_4 (fayalite), as the principle product. Preliminary magnetization measurements indicate that both nanocomposites exhibit interesting magnetic properties.

Keywords: Organoiron complexes; Magnetization measurements

1. Introduction

Silica xerogel, formed by a conventional sol–gel method in the presence of the organoiron complex $(MeO)_3SiCH_2CH_2Ph_2PFe(CO)_4$, is obtained as an amber solid. The organoiron compound is presumed to be covalently incorporated into the xerogel matrix through hydrolysis and subsequent condensation reactions of the silicate ester group on the bifunctional phosphine ligand. This molecularly doped xerogel serves as a precursor in the formation of two different nanocomposite materials.

Subjecting this doped xerogel to 900 °C in a hydrogen atmosphere produces a silica xerogel containing nanocrystals of Fe_2P, syn-barringerite. Metal phosphides are a well known class of solid materials [1] that are technologically important as semiconductors and as phosphorescent or electronic materials [1,2]. Conventional synthesis of metal phosphides has entailed direct reaction of the elements for prolonged periods at high temperature, reaction of phosphine with metals or metal oxides under similar conditions, reduction of metal phosphates with carbon at high temperature,

electrolysis of molten phosphates, chemical vapor deposition, or solid-state metathesis reactions [3]. Property measurements of bulk Fe_2P have been complicated by the presence of impurities and by a lack of compositional homogeneity. Recently, however, the magnetic properties of crystalline Fe_2P have been examined [4–6]; this bulk material exhibits a ferromagnetic to paramagnetic transition at $T_C = 217$ °C. The synthesis of nanocrystalline Fe_2P dispersed throughout a silica xerogel matrix offers a unique opportunity to measure magnetic properties of this substance as a nanophase. To our knowledge, this is the first report of the preparation of Fe_2P as nanocrystals.

Heating the molecularly doped silica xerogel described above in air at 950 °C produces an ochre nanocomposite containing nanoclusters of γ-Fe_2O_3 (maghemite-Q). This result is unexpected since previous attempts to prepare γ-Fe_2O_3 in a silica xerogel host matrix have proved unsuccessful owing to preferential formation of other iron phases. For example, thermal treatment of silica xerogels doped with inorganic ferric salts under reducing conditions at temperatures greater than 400 °C leads to preferential formation of fayalite (Fe_2SiO_4) which cannot be converted to the elemental iron oxides. Thermal treatment of this Fe(III)-doped silica xerogel under reducing conditions at temperatures

---
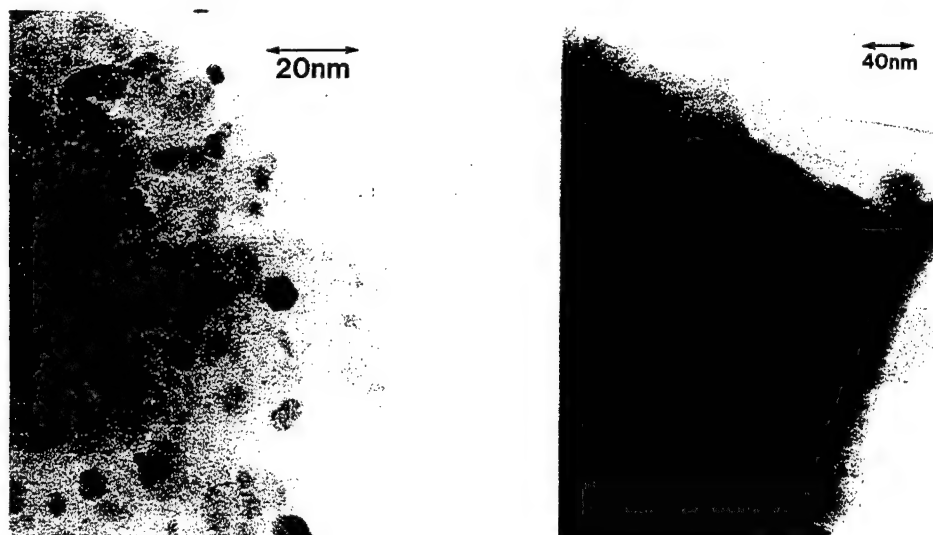
Fig. 1. TEM images of silica xerogel nanocomposites containing nanoclusters of Fe$_2$P (a) or nanoclusters of γ-Fe$_2$O$_3$ (b).

less than 400 °C leads to the formation of α-Fe; however, oxidation of this composite material gives iron oxides other than γ-Fe$_2$O$_3$ [7–9]. Nanocrystalline γ-Fe$_2$O$_3$ has been successfuly prepared recently in matrices other than silica xerogel by precipitation and oxidation of Fe(II) ion in a polymer ion-exchange resin [10] and by the thermal decomposition and oxidation of Fe(CO)$_5$ within glass beads [10,11]. Preliminary magnetization measurements of silica xerogel nanocomposites containing nanoclusters of Fe$_2$P or γ-Fe$_2$O$_3$ are also discussed.

2. Experimental details

The synthesis of the organoiron complex (MeO)$_3$SiCH$_2$CH$_2$Ph$_2$PFe(CO)$_4$, and the preparation of a silica xerogel matrix doped with this molecular precursor followed previously reported procedures [12]. Chemical microanalysis of the molecularly doped xerogel indicated elemental weight percentages of 4.02 for Fe and 27.38 for Si giving an Si-to-Fe atomic ratio of ca. 13:1.

A sample of the molecularly doped silica xerogel in an alumina boat was placed inside a tube furnace and was heated at 900 °C for 30 min in a hydrogen atmosphere to give a deep maroon xerogel product. Chemical microanalysis of this powder indicated elemental weight percentages of 5.82 for Fe and 41.33 for Si giving an Si-to-Fe atomic ratio of ca. 14:1. TEM analysis of this sample revealed nanocrystals of Fe$_2$P uniformly dispersed throughout a silica xerogel host matrix.

A sample of the molecularly doped silica xerogel in an alumina boat was placed inside a tube furnace and was heated in air at 950 °C for 2 h to give an ochre xerogel product. Chemical microanalysis of this power

indicated elemental weight percentages of 5.61 for Fe and 42.21 for Si giving an Si-to-Fe atomic ratio of ca. 15:1. TEM analysis of this sample revealed nanoparticulates of γ-Fe$_2$O$_3$ highly dispersed throughout a silica xerogel host matrix.

Techniques used to characterize these nanocomposites included transmission electron microscopy (TEM) using a Philips CM20T microscope operating at 200 kV and equipped for selected area electron diffraction and energy dispersive spectroscopy (EDS), X-ray diffraction (XRD) using a Philips PW1800 $\theta/2\theta$ automatic powder diffractometer equipped with a Cu target and a post-sample monochromator, and magnetization measurements recorded as a function of field strength and temperature using a vibrating sample magnetometer.

Bulk chemical microanalyses were performed by Galbraith Laboratories, Inc., Knoxville, TN.

3. Results and discussion

TEM images of the Fe$_2$P and γ-Fe$_2$O$_3$ nanocomposites are shown in Fig. 1. The micrograph of the Fe$_2$P nanocomposite reveals nanocrystalline particulates highly dispersed throughout the xerogel host matrix. The particulate features exhibit sharp edges and corners, and some particles are oriented properly to give a hexagonal projection, as expected for nanocrystals of hexagonal Fe$_2$P (syn-barringerite). A histogram of Fe$_2$P particle sizes gives a monomodal distribution of particle diameters ranging in value from 2 to 8 nm with an average particle diameter of 4.7 nm. EDS spectra of this nanocomposite reveal the presence of Fe, P, and Si (the Kα emission of all three elements plus the Kβ emission of Fe). On-particle EDS spectra reveal an Fe:P ratio of 2.12.

Table 1
Selected area electron diffraction d-spacings (in Å) obtained from ring patterns for nanocomposites containing nanoclusters of Fe_2P or γ-Fe_2O_3 in comparison with standard data

d (standard)	hkl	d (observed)	Error (%)
Fe_2P nanocomposite (JCPDS No. 27-1171)			
2.23	1 1 1	2.25	0.89
2.05	2 0 1	2.04	0.49
1.92	2 1 0	1.94	1.04
1.69	3 0 0	1.68	0.59
1.40	3 1 0	1.40	0
1.30	3 1 1	1.29	0.77
1.10	—	1.09	0.91
γ-Fe_2O_3 nanocomposite (JCPDS No. 25-1402)			
2.95	206	2.99	1.36
2.64	109	2.62	0.68
2.51	119	2.55	1.59
2.23	316	2.22	0.45
1.70	2 2 12	1.72	1.17
1.60	1 1 15	1.61	0.63
1.47	4 0 12	1.45	0.67
1.32	2 0 18	1.32	0

Particulates are also evident in the micrograph of the γ-Fe_2O_3 nanocomposite. These features are nearly speheroidal in shape, and a histogram of particle sizes reveals a monomodal distribution of particle diameters ranging in value from 7.5 to 22.5 nm with an average particle diameter of 14.6 nm. EDS spectra of this nanocomposite shows Fe ($K\alpha$ and $K\beta$ emissions) and Si ($K\alpha$ emission) along with a small amount of P ($K\alpha$ emission). The presence of residual phosphorus in the sample is not unexpected because air oxidation of the

molecularly doped xerogel leads to incomplete loss of the phosphorus present in the molecular precursor (presumably owing to phosphate formation).

The results of selected area electron diffraction ring patterns are presented in Table 1. The observed d-spacings match well with those published for standard samples of Fe_2P or γ-Fe_2O_3. These data clearly identify the Fe_2P crystalline phase and distinguish this composition from other known iron phosphides. A spot pattern obtained by electron diffraction from one nanocrystal of Fe_2P could also be interpreted using the known cell parameters of hexagonal barringerite (Fe_2P).

Verification of the γ-Fe_2O_3 crystalline phase is complicated by the large number of known iron oxides. Electron diffraction data for this nanocomposite (shown in Table 1) clearly indicate a close match between all of the observed rings to those known for γ-Fe_2O_3 (maghemite-Q). By comparing these diffraction data with those known for other iron phases, it is evident that the diffracting phase is not α-Fe_2O_3. In addition, the observed rings at d-spacings of 2.64 and 2.23 Å distinguish the observed phase from the common iron oxide Fe_3O_4 (magnetite). Electron diffraction data indicate the absence of any of the known iron silicates. The ochre color of this nanocomposite is also characteristic of γ-Fe_2O_3.

An XRD scan obtained from the Fe_2P nanocomposite is shown in Fig. 2. The observed peaks match well in 2θ values and in relative intensities with the corresponding 111, 201, and 210 diffraction peaks of standard Fe_2P. Measurements of the full width at half-maximum of each of these three peaks and application of Scherrer's equation [13] gives a volume-averaged mean particle diameter of 10 nm. The discrepancy be-
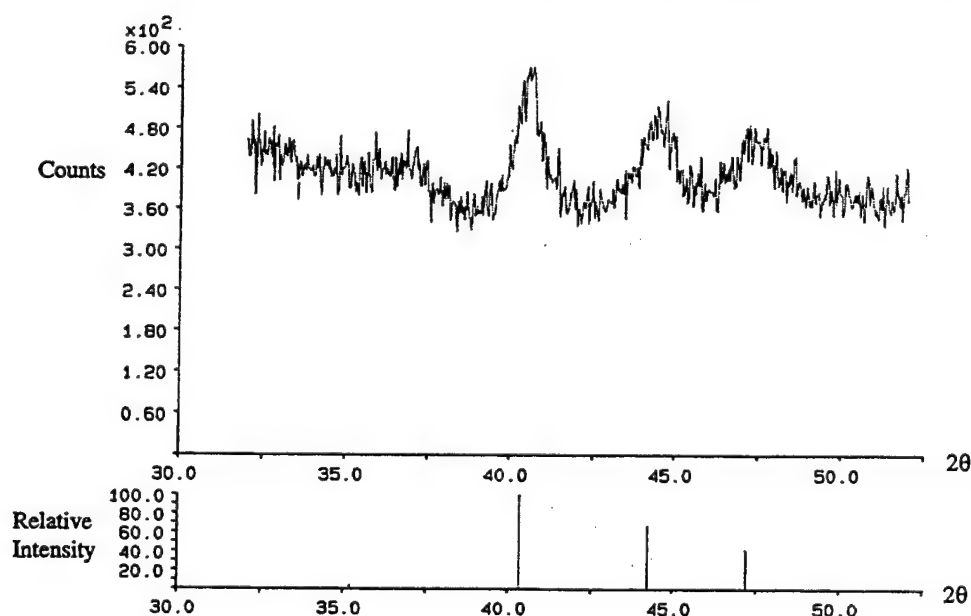
Fig. 2. An XRD scan of the Fe_2P nanocomposite showing the observed and reference (syn-barringerite, JCPDS No. 33-670) diffraction peaks.
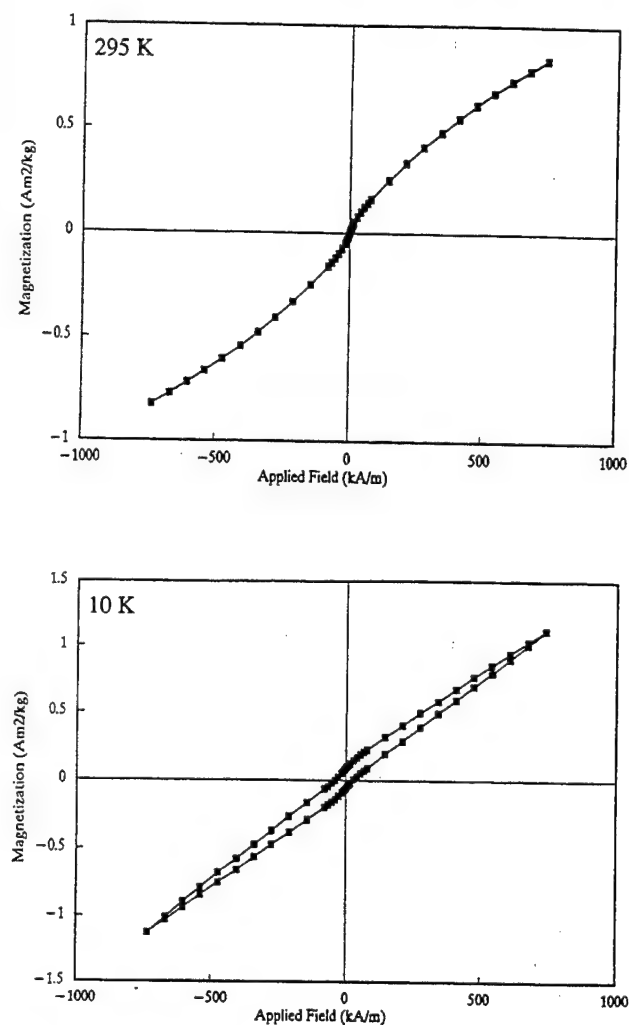
Fig. 3. Magnetization vs. applied field for the Fe_2P nanocomposite at 295 K and 10 K.

tween this diameter and the number-average mean diameter obtained from direct TEM measurements implies that a small fraction of the Fe_2P particles had diameters significantly larger than 4.7 nm. XRD scans of the γ-Fe_2O_3 nanocomposite reveal several peaks of low intensity and have, at present, precluded unambiguous interpretation. The high temperature under which this sample was prepared leads to the formation of cristobolite which also complicates interpretation of the XRD scan.

An interesting property of both nanocomposites is that they are sufficiently magnetic that they adhere to an $SmCo_5$ permanent magnet. Preliminary magnetization measurements for the Fe_2P and γ-Fe_2O_3 nanocomposites at 10 K and 295 K are shown in Fig. 3 and 4 respectively. The magentic properties of the Fe_2P nanocomposite are much as expected for a small-particle system. At room temperature, this material is superparamagnetic (curved M vs. H isotherms and no remanence) and has a relatively low magnetization of $0.8\ Am^2\ kg^{-1}$ at 1 T. On cooling to 10 K, its magnetiza-

tion increases (to $1.2\ Am^2\ kg^{-1}$ at 1 T) and a measurable width to its hysteresis develops. The sample appears ferromagnetic with a large susceptibility ($1.5 \times 10^{-6}\ m^3\ kg^{-1}$ or $1.2 \times 10^{-4}\ emu^{-1}\ g\ Oe^{-1}$) and has a coercivity near $34\ kA\ m^{-1}$ (430 Oe) and a remanence of $0.075\ Am^2\ kg^{-1}$ ($0.075\ emu\ g^{-1}$). The sample is also very far from saturation at a field strength of 1 T. The rather unusual shape of this hysteresis loop possibly indicates this material is comprised of a combination of paramagnetic and ferromagnetic constituents. Resolution of this complexity will result from more detailed measurements of the temperature dependence of the sample magnetization.

The magnetization of the γ-Fe_2O_3 nanocomposite is linear with the applied magnetic field at both room temperature and 10 K, implying it is paramagnetic between these temperatures (see Fig. 4(a)). As expected for a paramagnet, the magnetic susceptibility χ also increases with decreasing temperature. For this particular material, χ increased from $1.47 \times 10^{-7}\ m^3\ kg^{-1}$ ($1.1 \times 10^{-5}\ emu\ g^{-1}\ Oe^{-1}$) at 300 K to $6.6 \times 10^{-7}\ m^3\ kg^{-1}\ Oe^{-1}$) at 10 K. The full temperature dependence
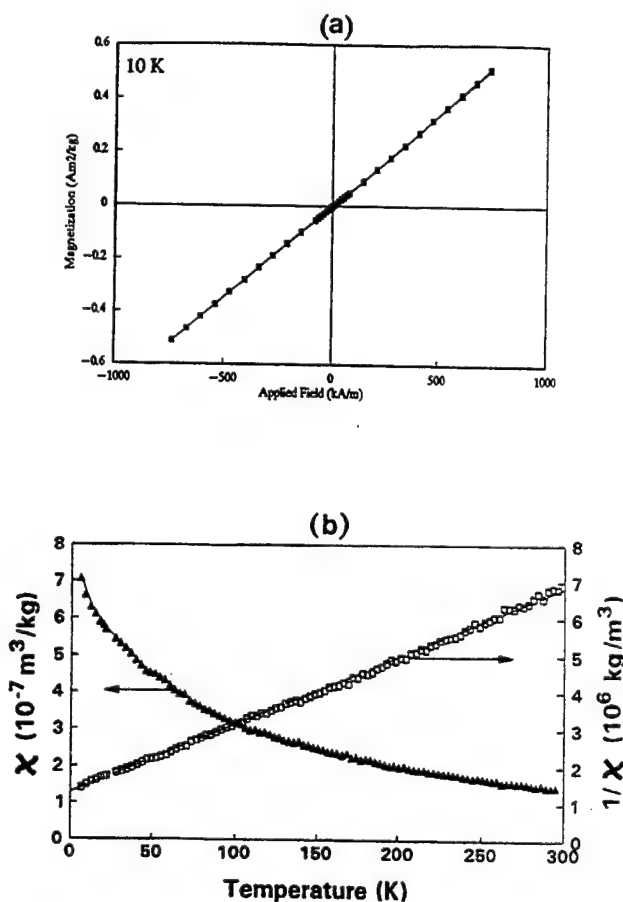
Fig. 4. (a) Magnetization vs. applied magnetic field at 10 K and (b) magnetic susceptibility (filled symbols) and reciprocal susceptibility (open symbols) vs. temperature for the γ-Fe_2O_3 nanocompostie. The dashed line in (b), $1/\chi = 10^4(128 + 1.85T)$, is a linear least-squares fit to the reciprocal susceptibility data.

of both the susceptibility and the inverse susceptibility for this nancomposite is shown in Fig. 4(b). The linear $1/\chi$ vs. T curve illustrates that Curie–Weiss behavior is followed by this nanocomposite to low temperatures. The extrapolation of this linear dependence to $1/\chi = 0$ indicates a negative intercept (-69.5 K) of the temperature axis, implying antiferromagnetic interactions between the Fe spins. This behavior is similar to that observed in silica aerogels doped with inorganic ferric salts [9].

4. Conclusions

Thermal treatments of a silica xerogel covalently doped with an organoiron complex under either reducing or oxidizing conditions gives nanocomposites containing nanoclusters of Fe_2P or γ-Fe_2O_3, respectively. This synthetic strategy provides a unique route for the preparation of bulk nanocomposites containing a nanocrystalline metal phosphide phase. For unknown reasons, the organoiron precursor is oxidized to give nanocrystalline γ-Fe_2O_3, whereas elevated temperature oxidation of silica xerogels doped with ferric ion under similar conditions gives undesired iron silicate formation. Preliminary magnetization measurements indicate that both of these nanocomposite materials exhibit interesting magnetic properties.

Acknowledgements

References

[1] H.G. von Schnering and W. Honle, *Encyclopedia of Inorganic Chemistry*, Vol. 6, Wiley, Chichester, 1994, p. 3106.

[2] B. Arinsson, T. Landstrom and S. Rundquist, *Borides, Silicides and Phosphides*, Wiley, New York, 1965.

[3] A.L. Hector and I.P. Parkin, *J. Mater. Chem.*, *4* (1994) 279.

[4] H. Fujii, Y. Uwatoko, K. Motoya, Y. Ito and T. Okamoto, *J. Phys. Soc. Jpn.*, *57* (1988) 2143.

[5] S. Ishida, S. Asano and J. Ishida, *J. Phys. F*, *17* (1987) 475.

[6] R. Wappling, L. Haggstrom, T. Ericsson, S. Devanarayanan. B. Carlsson and S. Rundquvist, *J. Solid State Chem.*, *13* (1975) 258.

[7] R.D. Shull, J.J. Ritter and L.J. Swartzendruber, *J. Appl. Phys.*, *69* (1991) 5144.

[8] R.D. Shull and J.J. Ritter, *Mater. Res. Soc. Symp. Proc.*, *195* (1990) 435.

[9] R.D. Shull, J.J. Ritter, A.J. Shapiro, L.J. Swartzendruber and L.H. Bennet, *Mater. Res. Soc. Symp. Proc.*, *132* (1989) 179.

[10] J.K. Vassiliou, V. Mehrotra, M.W. Russell, E.P. Giannelis, R.D. McMichael, R.D. Shull and R.F. Ziolo, *J. Appl. Phys.*, *73* (1993) 5109.

[11] R.F. Ziolo, E.P. Giannelis and R.D. Shull, *Nanostruct. Mater.*, *3* (1993) 85.

[12] K.J. Burnam, J.P. Carpenter, C.M. Lukehart, S.B. Milne, S.R. Stock, R. Glosser and B.D. Jones, *Mater. Res. Soc. Symp. Proc.*, *351* (1994) 21.

[13] H.P. Klug and L.E. Alexander, *X-Ray Diffraction Procedures for Polycrystalline and Amorphous Materials*, Wiley, New York. 1974, 2nd edn.

Thermal chemical synthesis of nanostructured chromium carbide cermets

P. Luo, P.R. Strutt[1]

Institute of Materials Science, University of Connecticut, Storrs, CT 06269, USA

Abstract

Nanocrystalline cobalt chromium carbide and nickel chromium carbide cermets are synthesized using the solution spray methodology followed by thermal chemical conversion. This newly developed synthesis approach is compared with traditional methods which have been used in carbide cermet industries. Characterization of as-synthesized materials is conducted by X-ray diffraction. Phase formations vs. processing temperatures are investigated. The structure and morphology of these materials are revealed by scanning electron microscopy and transmission electron microscopy.

Keywords: Thermal chemical synthesis; Chromium carbide cements; Scanning electron microscopy; Transmission electron microscopy

1. Introduction

As is well known, nanocrystalline materials can display unusual hardness combined with good fracture toughness characteristics. This is an especially intriguing combination of properties for cutting tool industries. The nanostructured WC/Co cermet material [1,2] has been already successfully synthesized at Rutgers University. The method involves solution spray drying followed by thermal conversion in an environment of reactive gases. Based on this methodology, a composite material of silicon carbide and chromium silicide has been successfully synthesized at the University of Connecticut [3]. A modification has been made in this synthesis route which involves using an inert gas atmosphere instead of a reactive gas species. Another advantage of this method is that a "water-soluble carbon" compound is selected, which allows carbon to be homogeneously mixed, in situ, prior to spray drying. This paper describes a similar approach for synthesizing nanocrystalline chromium carbide cermets.

2. Processing methodology

Traditional industrial methods for synthesizing chromium carbide cermets involve crushing, grinding, blending and consolidation of the constituent powders [4,5]. A limitation of this approach is that the scale of the morphological and compositional variation in the cermet material is determined by the size of the phases in the blended powder. An additional shortcoming is the introduction of impurities during processing. In Fig. 1 a comparison of the traditional method and the advanced thermochemical method is illustrated. The thermochemical synthesis approach begins with precursor (precomposite) compounds in which the elements A, B, and C (the constituent elements of the ternary two-phase composite) are mixed at the molecular level. The precursor compounds are made using aqueous solution chemistry and then transformed into nanostructured AC/B followed by thermochemical conversion. In this work elements A, B and C are chromium, cobalt or nickel and carbon respectively.

3. Experiment

The first step in the experimental method involved spray drying an aqueous solution (via atomization)

---

[1] Present address: Precision Manufacturing Center, University of Connecticut, Storrs, CT 06269, USA.

Traditional carbide cermet synthesis processing
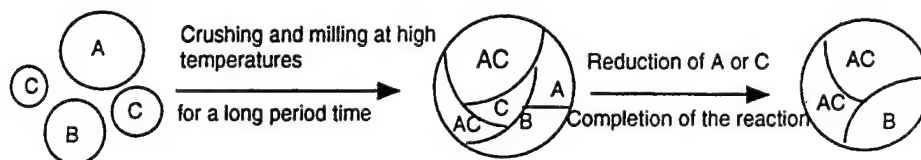
Advanced thermal chemical solution method of synthesizing carbide cermet materials
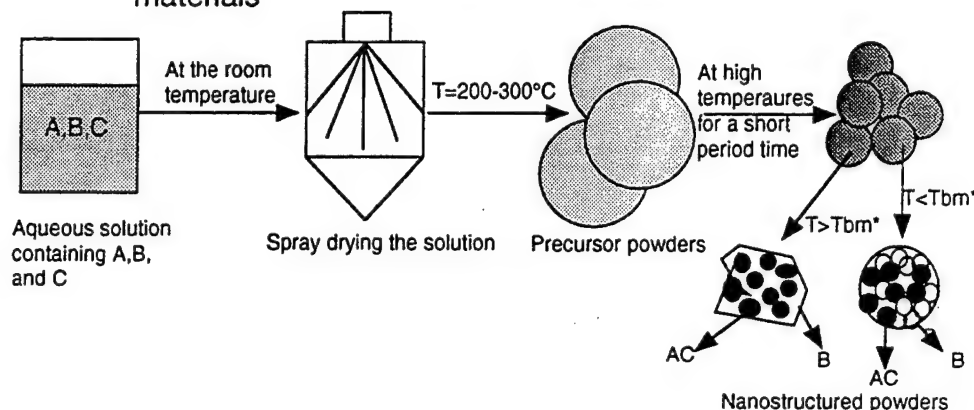
*Tbm: the melting point of the second phase material B

Fig. 1. Comparison of traditional processing and advanced chemical processing.

containing appropriate quantities of Cr, Co/Ni and C to synthesize the desired end product materials such as Cr_7C_3/Co and Cr_3C_2/Ni cermets. Experiments were performed in a unit manufactured by Yamato Scientific Co., Ltd., Tokyo, Japan. The precursor solution contained $CrCl_3$, $C_6H_{12}O_6$ and $NiCl_3$ or $CoCl_3$, with concentration ratio corresponding to the composition of the desired end product. This solution was pumped from a feed tank into the spray nozzle (type 1A) at a selected speed. Atomization was achieved using compressed air, which was delivered to the nozzle at a pressure of $3.5\,kgf\,cm^{-2}$. The atomized liquid was rapidly dried by a coaxial flow of air heated to a temperature above 200 °C and supplied at a rate of $1.0\,m^3\,min^{-1}$. The resulting powder was cyclone separated from the flowing gas stream. This process produced relatively large particles (1–5 μm) which were of a convenient form for the subsequent processing operations. Spray-dried precursor powders were then placed in an alumina boat and heated at 1100, 1250 and 1300 °C in a tube furnace for 5 h in an inert argon gas environment. This thermal treatment allowed solid state chemical reactions to occur for conversion of the spray-dried powder into a nanostructured form.

As-synthesized sample powders were characterized using X-ray diffraction (XRD) and scanning electron microscopy (SEM). Transmission electron microscopy (TEM) was conducted to study the nature of the syn-

thesized $Ni/Cr–Cr_3C_2$ nanocrystalline material, which existed in the form of dense chromium particle agglomerates, due to melting of the Ni/Cr phase during 1300 °C heat treatment. Since this material was too thick to be transparent in the electron beam it was thinned using dilute acetic acid etchant. These precipitates were then examined by TEM.

4. Results and discussion

X-Ray diffraction analysis revealing the formation of cobalt and chromium carbide produced by post synthesis thermal treatment is shown in Fig. 2. As can be seen, chromium oxide is the major intermediate product during this process. By increasing the thermal conversion temperature from 1100 to 1250 °C, chromium oxide is partially converted to chromium carbide and together with an increase in the amount of cobalt. In addition, the unconverted carbon from the precursor powder is converted into graphitic carbon, as shown by the peak in the diffraction spectrum labeled " # ". The following chemical reaction has therefore occurred:

$$7Cr_2O_3 + 27C \rightarrow 2Cr_7C_3 + 21CO\uparrow \qquad (1)$$
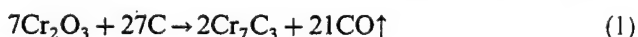
Well delineated chromium carbide peaks exist in material treated at 1300 °C, see Fig. 2 and the above reaction goes to completion. Cobalt metal is decomposed
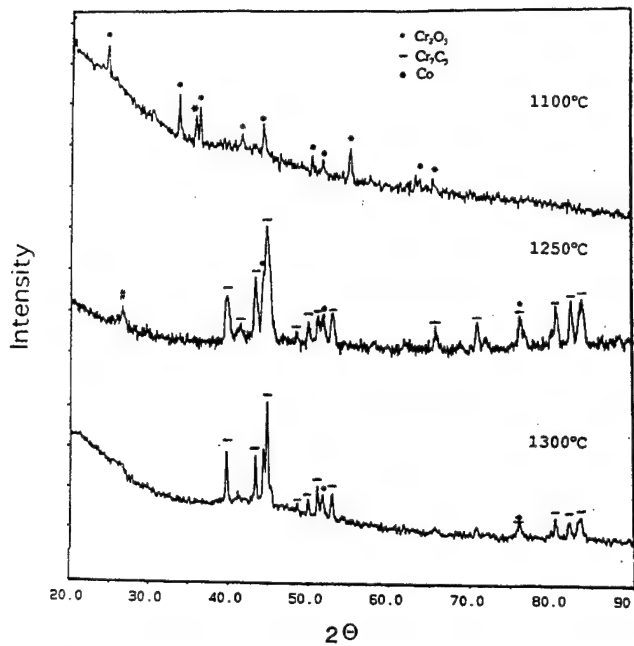
Fig. 2. X-Ray analysis of chromium carbide formation vs. processing temperature.

Fig. 4. Example of submicron features of as-synthesized chromium carbide and cobalt cermet material at 1250 °C.

directly from the precursor complex without formation of its oxide form. The lack of cobalt oxide might be due to its instability.

Scanning electron microscopy reveals the Ni/Cr–Cr_3C_2 particle agglomerates in material thermally treated at 1250 and 1300 °C, as seen in Fig. 3 thsee agglomerates are 1 mm in diameter. Careful examination (Figs. 4 and 5) however, reveals the sub-micron features in these agglomerates, where in Fig. 5 the carbide particles are of irregular shape. In studying how the final structure forms it is interesting to note that fine spherical nanoparticles agglomerates actually exist in the intermediate precursor material processed at 500 °C, see Fig. 6.

Fig. 5. Morphology of as-synthesized chromium carbide and nickel cermet material at 1300 °C.

Fig. 3. Morphology of as-synthesized chromium carbide and cobalt cermet material at 1250 °C.
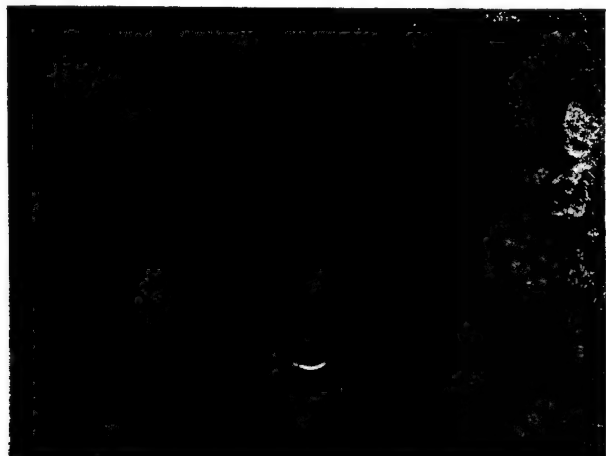
Fig. 6. Morphology of intermediate product powders of chromium carbide and nickel cermet material at 500 °C.
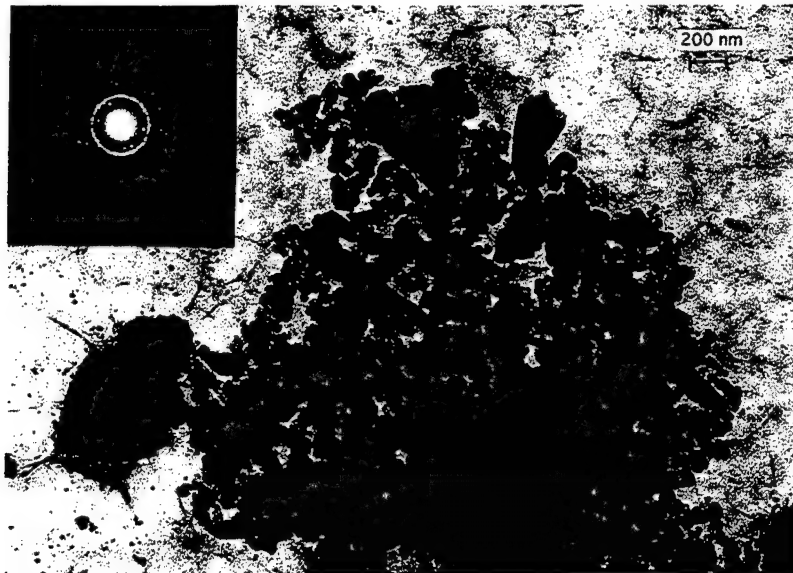
Fig. 7. TEM observation of as-synthesized chromium carbide Cr_3C_2 nanoparticles at 1300 °C for 7 h.

A transmission electron micrograph of chromium carbide nanoparticles (Ni was removed by an acid wash), together with the corresponding diffraction pattern, is shown in Fig. 7. Most of the particles are in the size range from 50 to 100 nm, but there are also some particles bigger than 200 nm.

A structural analysis of nickel chromium carbide cermet was performed using X-ray diffraction. As shown in Fig. 8, hexagonal chromium carbide in the form of Cr_3C_2 and an Ni–Cr metallic phase were observed after processing the spray-dried precursor at 1300 °C for 7 h. This spectrum agrees with that of commercially available nickel chromium carbide cermet, which is also shown in Fig. 8 for comparison.

Phase evolution during the synthesis process was revealed by X-ray diffraction analyses on intermediate products and final products up to 1300 °C; see Fig. 9. Increasing the processing temperature to 500 °C causes
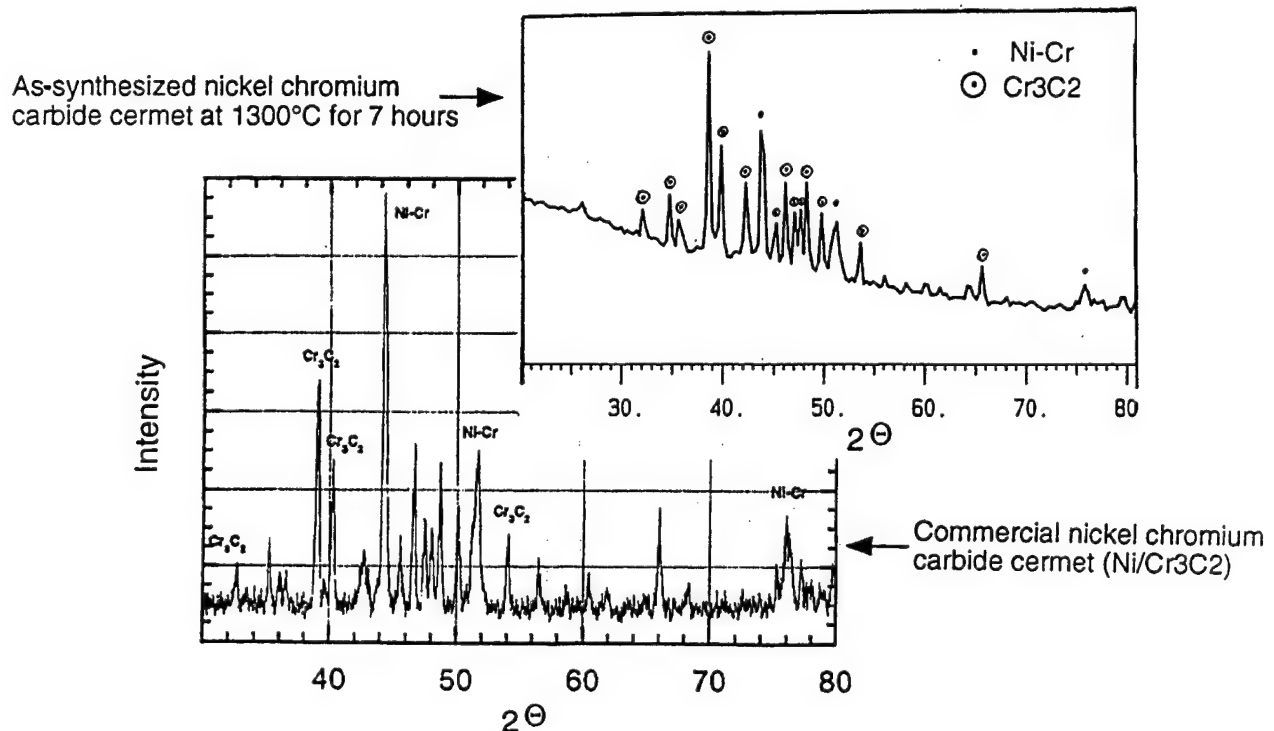
Fig. 8. Structural analysis of as-synthesized nickel chromium carbide Ni–Cr/Cr_3C_2 cermet material (compared with commercial product).
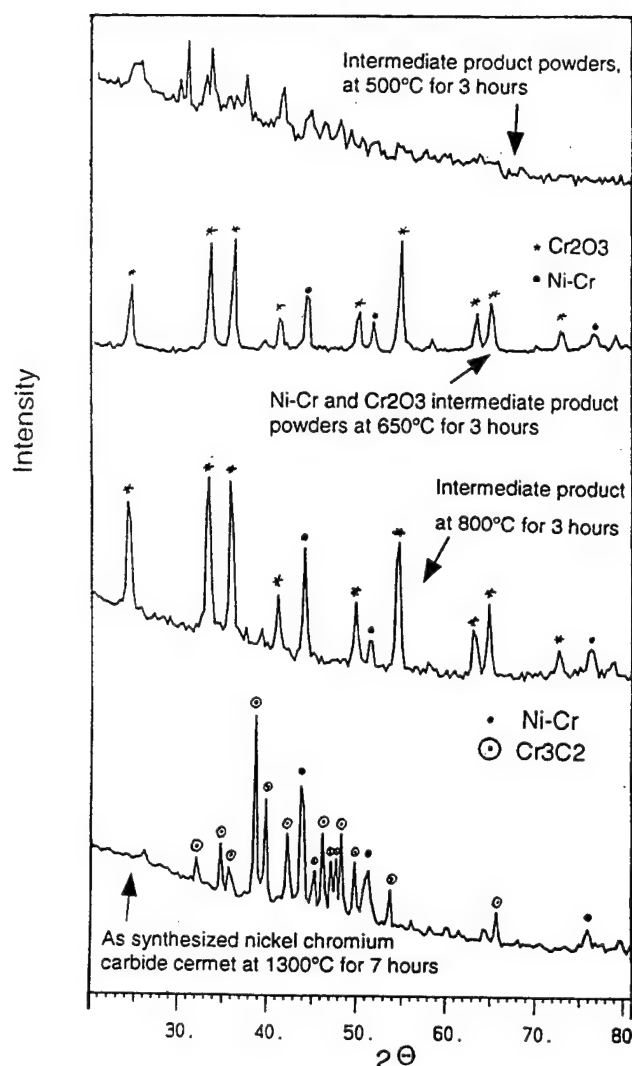
Fig. 9. Analysis of chromium carbide phase formation vs. processing temperature.

the precursor powder to be converted into an intermediate crystalline compound; at 650 °C it becomes a mixture of chromium oxide and nickel–chromium crystalline phases. Up to 800 °C there is no evidence of a chromium carbide phase. Complete conversion to the chromium carbide phase (Cr_3C_2) is finally observed at a temperature of 1300 °C. The following reaction is suggested:

$$3Cr_2O_3 + 13C \rightarrow 2Cr_3C_2 + 9CO\uparrow \qquad (2)$$
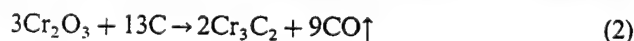
The type of chromium carbide end product observed depends on the initial concentration ratio of carbon to chromium. In other words, the Cr_7C_3 variant of the nickel cermet can be obtained by adding a smaller amount of carbon according to Eq. (1). The complete

reaction mechanism of nanocrystalline carbide formation is not clear and needs to be studied in the future.

5. Conclusions

(1) A methodology of solution spray drying followed by thermal chemical conversion provides a unique route for synthesizing nanostructured chromium carbide cermets such as cobalt chromium carbide and nickel chromium carbide. The advantage of this synthesis route is that it uses simple water-soluble salts resulting in a homogeneous mixture of carbon.

(2) Morphological characterization is conducted by scanning electron microscopy and transmission electron microscopy. Intermediate products have a morphology of spherical agglomerates. Final products have an irregular geometry at high temperatures. This geometry may be due to the melting of Co or Ni phases in the cermets. TEM observation shows the nanostructured nature of the chromium carbide phase with a crystallite size of 50–100 nm. There are also some bigger crystals present in these cermets. A broad range of agglomeration is observed.

X-Ray analysis shows chromium oxide formation in the intermediate synthesis steps. Complete conversion from the oxide to the carbide occurs at 1250 °C and above. Therefore a high temperature reaction (1250 °C) is required in this synthesis route.

References

[1] L.E. McCandlish, B.H. Kear and B.K. Kim, *Mater. Sci. Technol.*, 6 (1990) 953.
[2] B.H. Kear and L.E. McCandlish, *Nanostruct. Mater.*, 3 (1993) 19–30.
[3] P. Luo, P.r. Strutt and T.D. Xiao, *Mater. Sci. Eng.*, B17 (1993) 126–130.
[4] T.Ya. Kosolapova, *Carbides: Properties, Production, and Applications*, Plenum, New York, 1971.
[5] M. Rhodes, *Principles of Powder Technology*, Wiley, New York, 1990.

Sonochemical synthesis of nanostructured catalysts

Kenneth S. Suslick*, Taeghwan Hyeon, Mingming Fang, Andrzej A. Cichowlas

School of Chemical Sciences and Materials Research Laboratory, University of Illinois at Urbana-Champaign, 505 S. Mathews Avenue, Urbana, IL 61801, USA

Abstract

Sonochemistry arises from acoustic cavitation; the formation, growth, and collapse of bubbles in a liquid. The implosive collapse of a bubble generates a localized hot spot; a temperature of ~ 5000 K and pressure of ~ 1800 atm, with cooling rates that exceed 10^9 K s^{-1}. Using these extreme conditions, we have developed a new synthetic technique for the synthesis of nanostructured inorganic materials. When irradiated with high intensity ultrasound in low volatility solvents under argon, volatile organometallic precursors produce high surface area solids that consist of agglomerates of nanometer clusters. These sonochemically produced nanostructured solids are active heterogeneous catalysts for hydrocarbon reforming and CO hydrogenation. For Fe and Co, nanostructured metals are formed; for Mo and W, metal carbides (e.g., Mo_2C) are produced. Using polymeric ligands (e.g., polyvinylpyrrolidone) or oxide supports (alumina or silica), the initially formed nanoscale clusters can be trapped as colloids or supported catalysts, respectively.

Keywords: Sonochemical synthesis; Nanostructured catalysts

1. Introduction

The preparation of nanostructured materials has been the recent focus of intense study in materials science [1,2]. A variety of chemical and physical preparative methods have been applied to produce materials with nanometer structure, including metal evaporation [3], decomposition of organometallic compounds [4], and the reduction of metal salts [5,6]. Sonochemical decomposition of transition metal carbonyl compounds has also been proven to be a useful technique to generate nanophase transition metals [7,8].

In sonochemical reactions, there is no direct coupling of the ultrasound with chemical species on a molecular level. Instead, the chemical effects of ultrasound originate from transient hot spots formed during acoustic cavitation (the formation, growth and collapse of bubbles in a liquid) [9,10]. The temperature reached during bubble collapse in a cavitating bubble field is approximately 5000 K with a sub-microsecond lifetime [11]. Consequently, acoustic cavitation creates not only extreme temperatures, but also extraordinary cooling rates (above 10^9 K s^{-1}). These exceptional local conditions can be used to generate nanostructured materials.

Sonochemical rates depend on a variety of experimental parameters. In order to achieve good sonochemical yields, precursors should be volatile, since the primary sonochemical reaction site is the vapor inside the cavitating bubbles [12]. In addition, the solvent vapor pressure should be low at the sonication temperature, because the solvent vapor inside the bubble reduces the collapse efficiency.

Scheme 1. Sonochemical synthesis of various forms of nanostructured materials.

Fig. 1. Transmission electron micrograph of nanostructured Fe–PVP, obtained on a Phillips 420 electron microscope.

The sonochemical synthesis of nanophase materials has the advantage that various classes of materials can be generated simply by changing the reaction medium. When precursors are sonicated in high boiling alkanes such as decane or hexadecane, nanostructured, high porosity metal powders are formed. Using a polymeric ligand (e.g. polyvinylpyrrolidone (PVP)) or inorganic support (silica, alumina, etc.), the initially formed nanometer clusters can be intercepted and nanophase metal colloids and nanostructured supported metal catalysts are respectively synthesized (Scheme 1). A transmission electron micrograph of the nanocolloid Fe–PVP is shown in Fig. 1.

We report here the sonochemical synthesis and heterogeneous catalytic studies of nanostructured Fe on silica, nanostructured Fe–Co alloys and nanostructured Mo_2C catalysts.

2. Experimental details

2.1. General procedures

All manipulations for the preparation of samples were performed using Schlenk vacuum line and inert atmosphere box (Vacuum Atmospheres, < 1 ppm O_2) techniques. Pentane was distilled over sodium benzophenone. Decane and hexadecane were distilled over sodium. Ultrasonic irradiation was accomplished with a high intensity ultrasonic probe (Sonics and Materials, model VC-600, 1 cm Ti horn, 20 kHz, 100 W cm^{-2}).

X-ray powder diffraction data were collected on a Rigaku D-max diffractometer using Cu Kα radiation ($\lambda = 1.5418$ Å). Scanning electron micrographs were taken on a Hitachi S800 electron microscope. Trans-

mission electron micrographs were taken on a Phillips CM-12 electron microscope. Samples for elemental analysis were submitted in sealed vials without exposure to air.

Hydrogen (99.99%, Linde), methane (99.97%, Matheson) and CO (99.0 + %, Linde) were further purified through 5A molecular sieves and oxy-traps (Alltech). Cyclohexane (99 + %, Fischer) was dried over molecular sieves prior to use. In the catalytic reactions with cyclohexane, a MKS mass flow controller maintained the flow of hydrogen at 27.5 cm^3 (STP) min^{-1} to carry the cyclohexane vapor at a constant partial pressure of 0.1 bar through the catalyst. A quartz reactor was used for both adsorption and gas–solid catalytic studies. The catalysts were transferred from an inert atmosphere box to the catalytic rig without exposure to air. Surface areas were calculated by applying the BET equation to the N_2 adsorption isotherm measured at 77 K. The gas products obtained during the temperature-programmed desorption (TPD) and temperature-programmed reaction (TPR) experiments were analyzed by a quadrupole mass spectrometer (Spectra Instruments). The catalytic reaction products were analyzed by gas chromatography (Hewlett-Packard 5730A) on an n-octane/Porasil C column with flame ionization detector.

2.2. Synthesis of nanostructured catalysts by sonochemical decomposition

2.2.1. Nanostructured Fe–SiO$_2$ catalyst

Silica gel (Universal Scientific Inc., 63–100 mesh) was pretreated at 450 °C under vacuum (1×10^{-5} torr) for 10 h before use. To this, a solution of Fe(CO)$_5$ in dry decane was added, and the slurry was irradiated at 20 °C with a high-intensity ultrasonic probe for 3 h under argon. After irradiation, the black powder was filtered and washed with dry pentane in an inert atmosphere box.

Conventional silica-supported crystalline iron catalysts were prepared using the standard incipient wetness impregnation method by dissolving Fe(NO$_3$)$_3$·9H$_2$O in an aqueous solution containing silica gel [13]. These samples were dried at 120 °C for 12 h, and calcined at 450 °C under an O_2 flow for 1 h. Reduction of iron supported on silica was carried out in a flow of hydrogen at 200 °C for 1 h, at 300 °C for 1 h, and finally at 450 °C for 2 h.

2.2.2. Nanostructured Fe–Co alloy catalysts

A solution of Fe(CO)$_5$ and Co(CO)$_3$(NO) in dry decane was irradiated at 0 °C with a high-intensity ultrasonic probe for 3 h under argon. After irradiation, a black powder was formed, which was filtered and washed with dry pentane in the glove box.

Sonochemical synthesis of nanostructured catalysts

Kenneth S. Suslick*, Taeghwan Hyeon, Mingming Fang, Andrzej A. Cichowlas

School of Chemical Sciences and Materials Research Laboratory, University of Illinois at Urbana-Champaign, 505 S. Mathews Avenue, Urbana, IL 61801, USA

Abstract

Sonochemistry arises from acoustic cavitation; the formation, growth, and collapse of bubbles in a liquid. The implosive collapse of a bubble generates a localized hot spot; a temperature of ~ 5000 K and pressure of ~ 1800 atm, with cooling rates that exceed 10^9 K s^{-1}. Using these extreme conditions, we have developed a new synthetic technique for the synthesis of nanostructured inorganic materials. When irradiated with high intensity ultrasound in low volatility solvents under argon, volatile organometallic precursors produce high surface area solids that consist of agglomerates of nanometer clusters. These sonochemically produced nanostructured solids are active heterogeneous catalysts for hydrocarbon reforming and CO hydrogenation. For Fe and Co, nanostructured metals are formed; for Mo and W, metal carbides (e.g., Mo_2C) are produced. Using polymeric ligands (e.g., polyvinylpyrrolidone) or oxide supports (alumina or silica), the initially formed nanoscale clusters can be trapped as colloids or supported catalysts, respectively.

Keywords: Sonochemical synthesis; Nanostructured catalysts

1. Introduction

The preparation of nanostructured materials has been the recent focus of intense study in materials science [1,2]. A variety of chemical and physical preparative methods have been applied to produce materials with nanometer structure, including metal evaporation [3], decomposition of organometallic compounds [4], and the reduction of metal salts [5,6]. Sonochemical decomposition of transition metal carbonyl compounds has also been proven to be a useful technique to generate nanophase transition metals [7,8].

In sonochemical reactions, there is no direct coupling of the ultrasound with chemical species on a molecular level. Instead, the chemical effects of ultrasound originate from transient hot spots formed during acoustic cavitation (the formation, growth and collapse of bubbles in a liquid) [9,10]. The temperature reached during bubble collapse in a cavitating bubble field is approximately 5000 K with a sub-microsecond lifetime [11]. Consequently, acoustic cavitation creates not only extreme temperatures, but also extraordinary cooling rates (above 10^9 K s^{-1}). These exceptional local conditions can be used to generate nanostructured materials.

Sonochemical rates depend on a variety of experimental parameters. In order to achieve good sonochemical yields, precursors should be volatile, since the primary sonochemical reaction site is the vapor inside the cavitating bubbles [12]. In addition, the solvent vapor pressure should be low at the sonication temperature, because the solvent vapor inside the bubble reduces the collapse efficiency.

Scheme 1. Sonochemical synthesis of various forms of nanostructured materials.

---

* Corresponding author.

Fig. 1. Transmission electron micrograph of nanostructured Fe–PVP, obtained on a Phillips 420 electron microscope.

The sonochemical synthesis of nanophase materials has the advantage that various classes of materials can be generated simply by changing the reaction medium. When precursors are sonicated in high boiling alkanes such as decane or hexadecane, nanostructured, high porosity metal powders are formed. Using a polymeric ligand (e.g. polyvinylpyrrolidone (PVP)) or inorganic support (silica, alumina, etc.), the initially formed nanometer clusters can be intercepted and nanophase metal colloids·and nanostructured supported metal catalysts are respectively synthesized (Scheme 1). A transmission electron micrograph of the nanocolloid Fe–PVP is shown in Fig. 1.

We report here the sonochemical synthesis and heterogeneous catalytic studies of nanostructured Fe on silica, nanostructured Fe–Co alloys and nanostructured Mo_2C catalysts.

2. Experimental details

2.1. General procedures

All manipulations for the preparation of samples were performed using Schlenk vacuum line and inert atmosphere box (Vacuum Atmospheres, < 1 ppm O_2) techniques. Pentane was distilled over sodium benzophenone. Decane and hexadecane were distilled over sodium. Ultrasonic irradiation was accomplished with a high intensity ultrasonic probe (Sonics and Materials, model VC-600, 1 cm Ti horn, 20 kHz, 100 W cm^{-2}).

X-ray powder diffraction data were collected on a Rigaku D-max diffractometer using Cu Kα radiation ($\lambda = 1.5418$ Å). Scanning electron micrographs were taken on a Hitachi S800 electron microscope. Trans-

mission electron micrographs were taken on a Phillips CM-12 electron microscope. Samples for elemental analysis were submitted in sealed vials without exposure to air.

Hydrogen (99.99%, Linde), methane (99.97%, Matheson) and CO (99.0 + %, Linde) were further purified through 5A molecular sieves and oxy-traps (Alltech). Cyclohexane (99 + %, Fischer) was dried over molecular sieves prior to use. In the catalytic reactions with cyclohexane, a MKS mass flow controller maintained the flow of hydrogen at 27.5 cm^3 (STP) min^{-1} to carry the cyclohexane vapor at a constant partial pressure of 0.1 bar through the catalyst. A quartz reactor was used for both adsorption and gas–solid catalytic studies. The catalysts were transferred from an inert atmosphere box to the catalytic rig without exposure to air. Surface areas were calculated by applying the BET equation to the N_2 adsorption isotherm measured at 77 K. The gas products obtained during the temperature-programmed desorption (TPD) and temperature-programmed reaction (TPR) experiments were analyzed by a quadrupole mass spectrometer (Spectra Instruments). The catalytic reaction products were analyzed by gas chromatography (Hewlett-Packard 5730A) on an *n*-octane/Porasil C column with flame ionization detector.

2.2. Synthesis of nanostructured catalysts by sonochemical decomposition

2.2.1. Nanostructured Fe–SiO2 catalyst

Silica gel (Universal Scientific Inc., 63–100 mesh) was pretreated at 450 °C under vacuum (1×10^{-5} torr) for 10 h before use. To this, a solution of $Fe(CO)_5$ in dry decane was added, and the slurry was irradiated at 20 °C with a high-intensity ultrasonic probe for 3 h under argon. After irradiation, the black powder was filtered and washed with dry pentane in an inert atmosphere box.

Conventional silica-supported crystalline iron catalysts were prepared using the standard incipient wetness impregnation method by dissolving $Fe(NO_3)_3 \cdot 9H_2O$ in an aqueous solution containing silica gel [13]. These samples were dried at 120 °C for 12 h, and calcined at 450 °C under an O_2 flow for 1 h. Reduction of iron supported on silica was carried out in a flow of hydrogen at 200 °C for 1 h, at 300 °C for 1 h, and finally at 450 °C for 2 h.

2.2.2. Nanostructured Fe–Co alloy catalysts

A solution of $Fe(CO)_5$ and $Co(CO)_3(NO)$ in dry decane was irradiated at 0 °C with a high-intensity ultrasonic probe for 3 h under argon. After irradiation, a black powder was formed, which was filtered and washed with dry pentane in the glove box.

2.2.3. Nanostructured molybdenum carbide catalyst

A slurry of molybdenum hexacarbonyl in hexadecane was sonicated at 90 °C for 3 h under argon to yield a black powder. Hexadecane was chosen as a solvent because its vapor pressure is low at the sonication temperature. The powder was filtered inside a dry box, washed several times with purified, degassed pentane.

3. Results and discussion

3.1. Synthesis and catalytic studies of nanostructured silica-supported Fe

Ultrasonic irradiation of decane solutions of iron pentacarbonyl, $Fe(CO)_5$, in the presence of silica gel produces a silica-supported material with nanometer-sized clusters of amorphous iron deposited on the silica surface. The iron loading on the SiO_2 can be easily varied by changing the initial concentration of the $Fe(CO)_5$ solution. Elemental analysis reveals Fe, Si, O and a trace amount of carbon (< 1%) to be present. The origin of carbon most likely arises from the decomposition of CO or the alkane solvent during ultrasonic irradiation.

The amorphous nature of these supported iron particles has been confirmed by several different techniques, including differential scanning calorimetry (DSC), X-ray powder diffraction, and electron-beam microdiffraction. Differential scanning calorimetry shows one exothermic transition at 335 °C corresponding to a disorder–order transition (crystallization) of the amorphous iron. Initial X-ray powder diffraction shows no diffraction peaks; after heat treatment under He at 400 °C (sufficient to induce crystallization) for 4 h, the line characteristic of α-iron metal (d spacings of 2.03, 1.43, 1.17 and 1.04 Å) are observed. After crystallization, the X-ray powder diffraction pattern contains no peaks attributable to iron oxide, iron carbide or other iron-based phases. Electron microdiffraction with a transmission electron microscope confirms these observations and shows only a diffuse ring characteristic of amorphous iron particles.

The transmission electron micrograph showed that the iron particles produced by sonolysis of $Fe(CO)_5$ were highly dispersed on the SiO_2 surface. The iron particles range in size from 3 to 8 nm. Chemisorption of carbon monoxide allowed measurement of the dispersion and the average particle size of the iron supported on the silica surface [14]. CO chemisorption measurement data at − 78 °C show the average iron particle size to be ≈ 7.3 nm, which agrees well with TEM data.

The catalytic activity of the silica-supported nanostructured iron was examined for the commercially important Fischer–Tropsch synthesis reaction (i.e.,

hydrogenation of CO). Fig. 2 compares the activity (in terms of turnover frequency of CO molecules converted per catalytic site per second) of silica-supported nanophase iron and conventional silica-supported iron, prepared by the incipient wetness method, as a function of temperature. These catalytic data were obtained at high iron loading and low dispersion to minimize the effects of support and dispersion. The sonochemically produced iron on silica catalyst is an order of magnitude more active than a comparable conventional supported iron catalyst. Moreover, the silica-supported nanostructured iron catalyst exhibits high activity at low temperatures (< 250 °C), whereas the silica supported conventional iron catalyst has no activity. We hypothesize that the dramatic difference in activity between the two samples below 300 °C may be due to the amorphous nature of iron and the inherently highly-defected surface formed during sonolysis of $Fe(CO)_5$ when the amorphous state of iron is preserved. Above that temperature some decline in activity could be observed, which we believe is due to the iron crystallization process, surface annealing, and deactivation of the catalyst as a result of surface carbon deposition.

Differences between the catalytic properties of the nanostructured iron and of conventional supported catalysts are also observed in selectivities of hydrocarbon synthesis. Under our conditions, the major reaction products for both catalysts are short chain (C_1 to C_4) hydrocarbons and CO_2. Product distribution of hydrocarbons showed that at temperatures lower than 275 °C, the silica-supported nanostructured iron catalyst shows higher selectivity towards long chain hydrocarbons (C_{5+}), whereas the conventional supported iron shows no activity at these temperatures. At temperatures higher than 275 °C (where crystallization can
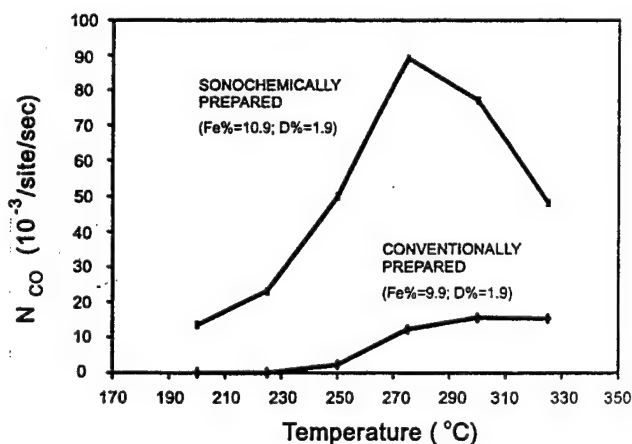
Fig. 2. The catalytic activity of SiO_2 supported amorphous nanostructured iron prepared sonochemically from $Fe(CO)_5$ and SiO_2 slurry (iron loading wt.% = 10.94, and dispersion, $D\%$ = 1.85) and SiO_2 supported crystalline iron prepared by the incipient wetness method (Fe wt.% = 9.91, $D\%$ = 1.86) as a function of temperature for Fischer–Tropsch synthesis (H_2/CO = 3.48, 1 atm, 25 °C).

occur), the reaction product distributions are similar for both types of catalyst.

3.2. Synthesis and catalytic studies of nanostructured Fe–Co alloys

Fe(CO)$_5$ and Co(CO)$_3$(NO) were chosen as precursors because of their high vapor pressures at modest bulk solution temperatures where they are still thermally stable. The composition of the Fe–Co alloys can be controlled simply by changing the ratio of the vapor pressures (via solution concentrations) of the precursors; alloy compositions ranging from pure Fe to pure Co are readily obtained.

The solid-solution nature of the alloys was confirmed by TEM-EDX results, from multiple locations on the polycrystalline alloy powders. The EDX results show that the alloys are homogeneous on the few-nanometer scale. The original Fe, Co, and Fe–Co alloys produced by ultrasound are amorphous, as determined by XRD, electron-beam microdiffraction, and DSC. After heat treatment under H$_2$ gas flow at 400 °C for 2 h, all samples underwent crystallization. The XRD results show no peaks attributable to iron/cobalt oxide, iron/cobalt carbide or other iron/cobalt impurity phases. Pure Fe crystallizes to cubic (bcc) structure, pure Co crystallizes to cubic (fcc) and hexagonal (hcp) mixed structures. All the alloys that we have tested so far crystallize in the bcc structure, which is consistent with the known Fe–Co equilibrium phase diagram [15]. Elemental analysis results show that nearly pure metal and alloys are produced (<1% impurity). SEM at high magnification indicates that these materials are porous aggregates of small clusters of 10–20 nm particles, as shown in Fig. 3. Surface electronic structures and surface compositions of the sonochemically prepared Fe–Co alloys were also examined by using X-ray photoelectron spectroscopy (XPS). The XPS measurements were performed on heat treated samples before catalytic reactions. The electronic structures of the surfaces of these samples appear to be the same as the pure metals. The surface compositions of the alloys demonstrate some small enrichment of Fe over Co. Similar trends towards an iron-enriched surface have been reported by other researchers with other preparations using coprecipitation methods [16].

The catalytic studies of the sonochemically prepared Fe–Co alloys were continued on cyclohexane dehydrogenation and hydrogenolysis reactions. All catalysts were treated under H$_2$ gas flow at 400 °C for 2 h before the catalytic studies. The catalytic activity (in terms of turnover frequency of cyclohexane molecules converted to benzene per surface Fe/Co atom per second) as a function of temperature is shown in Fig. 4. Two kinds of product were formed during the cyclohexane reaction: benzene was the only dehydrogenation reaction
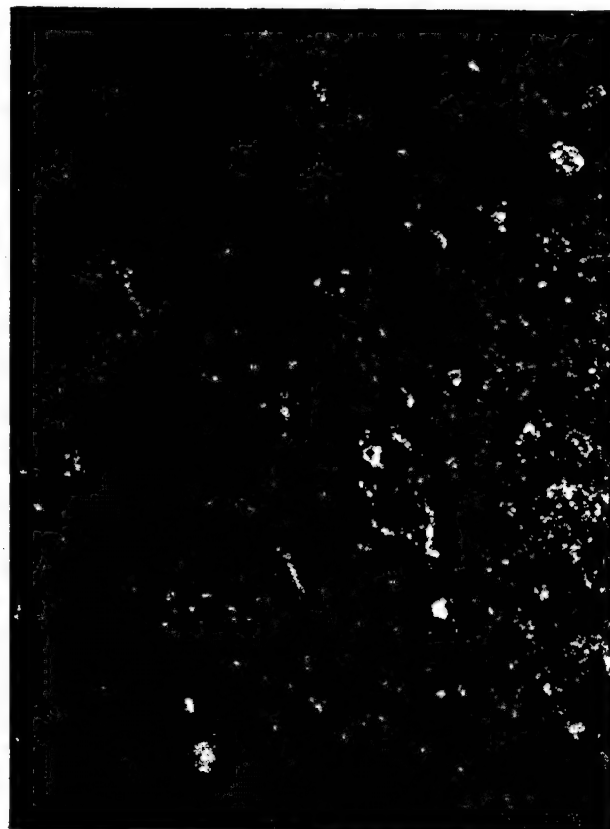
Fig. 3. Scanning electron micrograph of nanostructured 1:1 Fe:Co alloy, obtained on a Hitachi S800 electron microscope.

product and aliphatic hydrocarbons (mostly methane) were the hydrogenolysis reaction products. The catalytic selectivity (in terms of the percentage of benzene among all the reaction products) as a function of temperature is shown in Fig. 5. The catalytic properties of the sonochemically prepared Fe, Co and Fe–Co alloys in the cyclohexane reaction exhibit interesting trends. First, they are all active catalysts for cyclohexane conversion: pure Co has the highest activity (albeit primarily for hydrogenolysis), pure Fe has the lowest activity, and Fe–Co alloys have intermediate activity between pure Fe and pure Co. Second, Fe–Co alloys
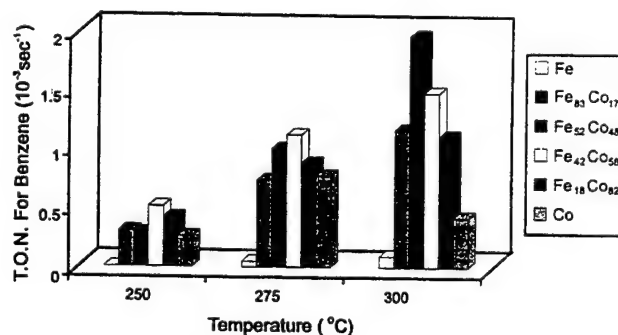
Fig. 4. The catalytic activity of Fe, Co, and Fe–Co alloys for dehydrogenation of cyclohexane to benzene as a function of temperature.
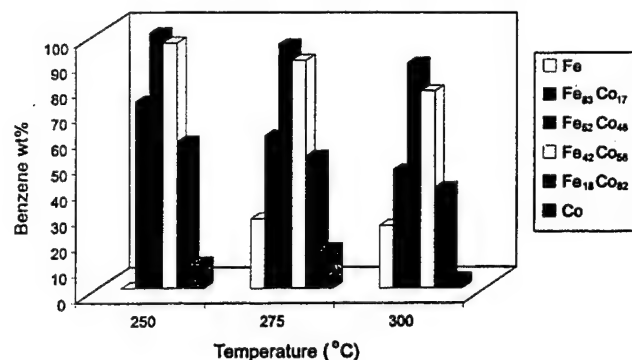
Fig. 5. The catalytic selectivity of Fe, Co, and Fe–Co alloys for dehydrogenation versus hydrogenolysis of cyclohexane as a function of temperature.

Fig. 6. X-ray powder diffraction patterns of sonochemically produced Mo_2C (a) after synthesis, (b) after heat treatment under He, 450 °C, 12 h.

generate much more dehydrogenation product (benzene) than pure Fe or Co. Third, the 1:1 Fe–Co alloy has both much higher dehydrogenation activities and selectivities at all reaction temperatures (250 to 300 °C) than the other alloys or pure metals. To our surprise, in the best cases, the selectivity for dehydrogenation approaches 100%. The origin of this high selectivity is currently under further investigation.

3.3. Synthesis and catalytic studies of nanostructured molybdenum carbide

Recently, molybdenum and tungsten carbides have been explored as heterogeneous catalysts because the activity of these carbides is similar to that of the platinum group metals [17–19]. For catalytic applications, high surface area materials are generally needed. The preparation of interstitial carbides of molybdenum and tungsten with high surface areas, however, is very difficult. Boudart and Volpe prepared carbides of molybdenum and tungsten with high surface areas by the temperature programmed carburization of the corresponding nitrides [20]. We present here a simple sonochemical synthesis of nanophase molybdenum carbide from the ultrasonic irradiation of molybdenum hexacarbonyl.

Sonochemical decomposition of molybdenum hexacarbonyl in hexadecane produced a black powder. X-ray powder diffraction (XRD) showed extremely broad peaks centered at a d spacing of 2.4 Å, 1.5 Å and 1.3 Å, which do not match body centered cubic (bcc) lines of molybdenum metal. After the heat treatment at 450 °C under helium flow for 12 h, sharper peaks in the XRD were observed at d spacing values of 2.39 Å, 1.49 Å and 1.27 Å, which match very well with face centered cubic (fcc) molybdenum carbide, Mo_2C (Fig. 6). Elemental analysis also confirmed the stoichiometry of 2Mo/C, but with some oxygen as discussed below. The formation of molybdenum carbide can be explained by the disproportionation of carbon monoxide on the ac-

tive metal surface to form carbon and carbon dioxide [21].
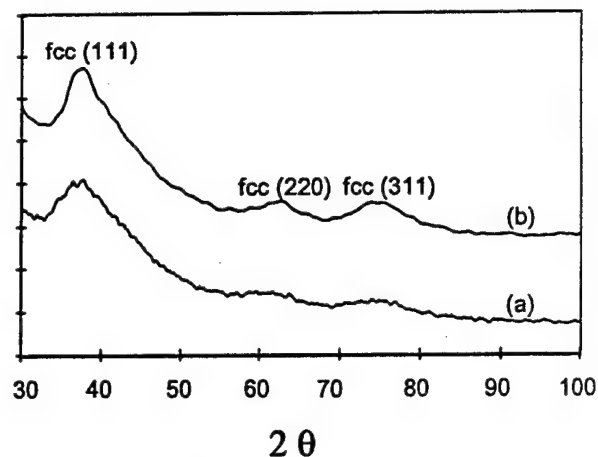
The SEM showed that the surface is extremely porous. The high resolution TEM showed that the solids were made up of aggregates of 2 nm sized particles (Fig. 7). Consistent with this, the particle size calculated from the line broadening of X-ray powder diffraction was 1.6 nm. Surface area, determined by BET gas adsorption isotherms, was found to be 188 m^2 g^{-1}.

Even after heat treatment at 450 °C under helium, the sample still contained about 4 wt.% of oxygen. Since the presence of oxygen could poison the catalytic activity, it was removed before catalytic studies by
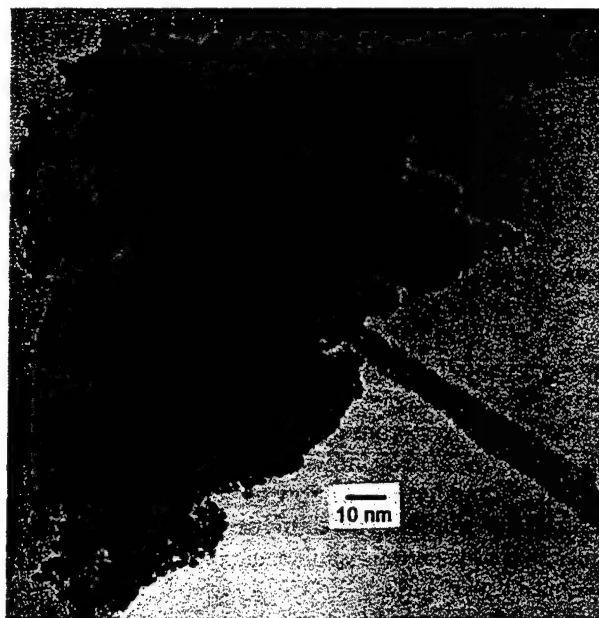
Fig. 7. Transmission electron micrograph of sonochemically produced Mo_2C, obtained on a Phillips CM-12 electron microscope.
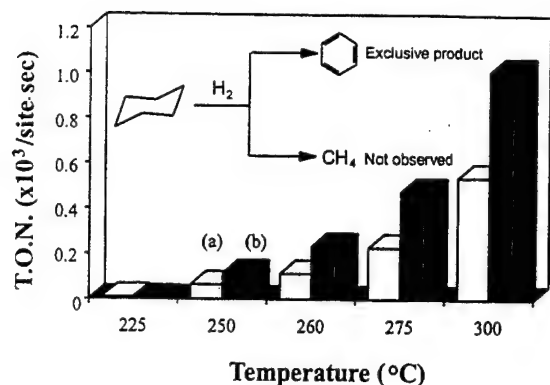
Fig. 8. Catalytic activity of sonochemically produced Mo$_2$C for dehydrogenation of cyclohexane: (a) sample heat treated under helium at 450 °C for 12 h; and (b) sample heat treated under CH$_4$/H$_2$ at 500 °C for 48 h.

heating in a flowing 1:1 CH$_4$/H$_2$ mixture at 300 °C for 1 h, then at 400 °C for 1 h, and finally at 500 °C for 48 h. The flow rate of the CH$_4$/H$_2$ mixture was 27.5 cm^3 (STP) min^{-1}. After the heat treatment, the elemental analysis results showed the sample was pure Mo$_2$C; oxygen, excess carbon, and hydrogen had been removed. Electron micrographs showed that the material was still porous and was composed of particles of 3 nm in diameter. The BET surface area decreased slightly to 130 m^2 g^{-1}.

The catalytic activity of the sonochemically produced molybdenum carbide was tested for the dehydrogenation of cyclohexane. Fig. 8 shows the catalytic activity (in terms of turnover frequency of cyclohexane molecules converted per site per second) as a function of temperature for the sample pretreated under CH$_4$/H$_2$ at 500 °C for 48 h and for the sample pretreated under helium at 450 °C for 12 h.

At all the reaction temperatures, benzene was the only product formed for either sample. No hydrogenolysis products were detected. Compared to the sample heat treated under CH$_4$/H$_2$, the sample heat treated under helium (i.e., with oxide impurity) had the same selectivity (benzene is the only product), but with somewhat lower activity. These results demonstrate that the sonochemically prepared molybdenum carbide is an excellent dehydrogenation catalyst and a rather poor hydrogenolysis catalyst. This is also confirmed by the lack of activity for ethane hydrogenolysis: during 28 h reaction with ethane and H$_2$ at 300 °C, no methane was detected.

The catalytic properties of Mo$_2$C (fcc) and Mo$_2$C (hcp) have been studied intensively in recent years [17–24]. CO hydrogenation, olefin hydrogenation, and hydrocarbon isomerization and hydrogenolysis have been investigated. Few reports, however, mention Mo$_2$C as an active dehydrogenation catalyst. As a precedent for our studies, carburization of Mo is known to temper Mo metal for dehydrogenation of hydrocarbons [25]. Bell et al. show there is some catalytic activity for ethane

hydrogenolysis using Mo$_2$C (fcc) prepared by reduction and carburization of MoO$_3$ under similar conditions (300 °C, H$_2$/C$_2$H$_6$ = 5) [17]. It seems the sonochemically prepared Mo$_2$C (fcc) has different and more selective catalytic behavior than the molybdenum carbides generated by the other methods.

4. Conclusions

Sonochemical decomposition of volatile organometallic precursors in high boiling solvents produces nanostructured materials in various forms with high catalytic activities.

Sonication of iron pentacarbonyl with silica in decane at 20 °C generated supported amorphous nanostructured Fe–SiO$_2$ catalyst. The nanostructured Fe–SiO$_2$ catalyst showed higher catalytic activity for the Fischer–Tropsch synthesis compared to the conventional Fe–silica catalyst prepared by the incipient wetness method.

Sonochemical decomposition of Fe(CO)$_5$ and Co(CO)$_3$(NO) in decane at 0 °C generated nanostructured Fe and Co metals and Fe–Co alloys. The sonochemically prepared Fe–Co alloys have large surface areas relative to bulk metal even after heat treatment. We find very high catalytic activity for these Fe, Co, and Fe–Co powders for the dehydrogenation and hydrogenolysis of cyclohexane. The sonochemically prepared Fe–Co alloys show high catalytic activity for the dehydrogenation of cyclohexane to benzene, with 1:1 ratio Fe–Co alloys having selectivities as high as 100%.

Ultrasonic irradiation of molybdenum hexacarbonyl in hexadecane at 90 °C gave nanometer-sized powder of face centered cubic molybdenum carbide. The material was extremely porous with a high surface area and consisted of aggregates of ≈ 2 nm sized particles. The catalytic properties of the sonochemically prepared fcc Mo$_2$C have been studied on dehydrogenation and hydrogenolysis of cyclohexane and hydrogenolysis of ethane. The catalytic results showed the molybdenum carbide generated by ultrasound is a good dehydrogenation catalyst and a poor hydrogenolysis catalyst.

References

[1] H. Weller, *Adv. Mater.*, 5 (1993) 88.
[2] G.A. Ozin, *Adv. Mater.*, 4 (1992) 612.

[3] S.C. Davis and K.J. Klabunde, *Chem. Rev.*, *82* (1982) 152.

[4] A.S. Lisitsyn, A.V. Golovin, A.L. Chuvilin, V.L. Kuznetsov, A.V. Romanenko, A.F. Danilyuk and Y.I. Yermakov, *Appl. Catal.*, *55* (1989) 235.

[5] H. Boennemann, W. Brijoux R. Brinkmann and T. Joussen, *Angew. Chem.*, *Int. Ed. Engl.*, *129* (1990) 273.

[6] K.-L. Tsai and J.L. Dye, *J. Am. Chem. Soc.*, *113* (1991) 1650.

[7] K.S. Suslick, S.B. Choe, A.A. Cichowlas and M.W. Grinstaff, *Nature*, *353* (1991) 414.

[8] M.W. Grinstaff, M.B. Salamon and K.S. Suslick, *Phys. Rev. B*, *48* (1993) 269.

[9] K.S. Suslick, *Science*, *247* (1990) 1439.

[10] K.S. Suslick, in K.S. Suslick (ed.), *Ultrasound: Its Chemical, Physical, and Biological Effects*, VCH Press, New York, 1988, p. 123.

[11] E.B. Flint and K.S. Suslick, *Science*, *253* (1991) 1397.

[12] K.S. Suslick, R.E. Cline and D.A. Hammerton, *J. Am. Chem. Soc.*, *106* (1986) 5641.

[13] D. Bianchi, L.M. Tan, S. Borcar and C.O. Bennett, *J. Catal.*, *84* (1983), 358.

[14] J.A. Dumesic, H. Topsøe and M. Boudart, *J. Catal.*, *37* (1975) 513.

[15] T. Nishizawa and K. Ishida, *Bull. Alloy Phase Diagrams*, *5* (1984) 250.

[16] M. Nakamura, B.J. Wood, P.Y. Hou and H. Wise, in *Proc. 4th Int. Cong. on Catal.*, *Tokyo*, Kodansha Ltd., Tokyo, 1981, p. 432.

[17] G.S. Ranhotra, G.W. Haddix, A.T. Bell and J.A. Reimer, *J. Catal.*, *108* (1987) 40.

[18] J.S. Lee, S.T. Oyama and M. Boudart, *J. Catal.*, *125* (1990) 157.

[19] M.J. Ledoux, C. Pham-Huu, J. Guille and H. Dunlop, *J. Catal.*, *134* (1992) 383.

[20] L. Volpe and M. Boudart, *J. Solid State Chem.*, *59* (1985) 332.

[21] N.M. Rodriguez, M.S. Kim and R.T.K. Baker, *J. Catal.*, *144* (1993) 93.

[22] J.S. Lee, L. Volpe, F.H. Ribeiro and M. Boudart, *J. Catal.*, *112* (1988) 44.

[23] G.S. Ranhotra, G.W. Haddix, A.T. Bell and J.A. Reimer, *J. Catal.*, *108* (1987) 24.

[24] C. Pham-Huu, M. Ledoux and J. Guille, *J. Catal.*, *143* (1993) 249.

[25] E.I. Ko and R.J. Madix, *Surf. Sci.*, *100* (1980) L449, L505.

ELSEVIER

Sonochemical synthesis of nanocrystalline molybdenum disilicide (MoSi₂)

Timothy J. Trentler[a], R. Suryanarayanan[b], Shankar M.L. Sastry[b], William E. Buhro[a,*]

[a]*Department of Chemistry, Washington University, St. Louis, MO 63130-4899, USA*
[b]*Department of Mechanical Engineering, Washington University, St. Louis, MO 63130-4899, USA*

Abstract

Sonochemical co-reduction of $MoCl_5$ and $SiCl_4$ with NaK alloy in a hexane dispersion using 600 W, 20 kHz irradiation, followed by annealing at 900 °C produces nanocrystalline $MoSi_2$ powders with $\approx 90\%$ yield. Consolidation by hot pressing at 1170 °C, 140 MPa for 4 h gives a 78%-dense compact with 31 nm average grain sizes and a Vickers microhardness of 1484 (10% kg/mm². Consolidation by hot pressing at 1200 °C, 100 MPa for 10 min. followed by hot isostatic pressing at 1100 °C, 200 MPa for 4 h gives a 83%-dense compact with 41 nm average grain sizes and a Vickers microhardness of $1587 \pm 10\%$ kg mm^{-2}. The second compact exhibits a compressive yield strength of 2875 MPa, and fractures without significant plastic deformation. The microhardness values and compression strengths are 50–70% higher in nanocrystalline $MoSi_2$ than in conventional, coarse-grained $MoSi_2$.

Keywords: Sonochemical synthesis; Molybdenum disilicide; Ultrasound; Intermetallics

1. Introduction

Herein we describe the preparation of nanocrystalline $MoSi_2$ by a novel, low-temperature, chemical method. Nanocrystalline powders produced by sonochemical processing were consolidated by a combination of hot pressing and hot isostatic pressing at 1100–1200 °C. The resulting densified samples retained grain sizes in the nanometer regime, and exhibited substantially higher Vickers microhardness and compressive yield strength than exhibited by coarse-grained $MoSi_2$. This is one of the first reports of the production of nanocrystalline $MoSi_2$ [1], and to our knowledge the first report of the consolidation and mechanical properties of nanocrystalline $MoSi_2$.

The intermetallic compound $MoSi_2$ is a candidate material for applications in aerospace structural components because of its low density, high-temperature strength, and oxidation resistance [2]. However, like other intermetallics conventional coarse-grained $MoSi_2$ is brittle at normal environmental temperatures [2].

Refinement of grain sizes to nanometer dimensions is predicted [3,4] to improve the ductility, fracture toughness, and strength of intermetallics by inducing fundamental changes in strengthening and deformation mechanisms [5]. Indeed, nanocrystalline aluminide intermetallics exhibit higher Vickers microhardness than their coarse-grained counterparts, indicative of increased strength [4,6–9]. A few studies of nanocrystalline aluminides have also shown decreasing microhardness with decreasing grain size in the range of ca. 10–30 nm, which may reflect the onset of low-temperature ductility [4,6,7]. Prior to the present work related measurements on nanocrystalline silicide intermetallics were unavailable. We now report that grain-size reductions into the nanometer regime improve the strength of $MoSi_2$; however, evidence for low-temperature ductility has not yet been obtained.

2. Chemical synthesis

The initial step was the sonochemical co-reduction of molybdenum and silicon chlorides in a hexane dispersion as shown in Eq. (1). Reaction mixtures were

---

* Corresponding author.

heterogeneous because of the immiscibility of the liquid-metal reducing agent, sodium potassium alloy (NaK), and the insolubility of $MoCl_5$ in the reaction solvent. Consequently, the procedure was performed in the presence of high-intensity ultrasonic irradiation, which is known to effectively promote chemical reactions among such heterogeneous mixtures [10,11]. In the present synthesis ultrasonic irradiation formed a fine emulsion of the liquid NaK alloy, which maximized the interfacial contact between it and the other reactant phases. Dramatic rate enhancements resulted such that Eq. (1) was generally conducted within 30 min to a few hours with sonochemical promotion, but required days without it (and $MoSi_2$ was never obtained from such reactions). Related co-reduction strategies have been reported by Ritter for the synthesis of TiB_2, SiC, B_4C, SiC/TiC, and SiC/TiN, in which high-speed, high-shear stirring was used to maximize interfacial contact between the immiscible reactant phases [12].

$$MoCl_5 + 2SiCl_4 + 13/2NaK \xrightarrow[\text{hexane}]{))))))} $$

$$MoSi_2 + 13/2NaCl + 13/2KCl \quad (1)$$
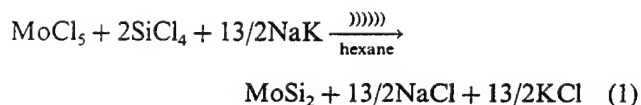
Eq. (1) was conducted to produce 1–6 g of $MoSi_2$ in the apparatus shown in Fig. 1, according to the following sequence. The apparatus was charged with hexane, $SiCl_4$, and $MoCl_5$, and was placed in an ice-water bath. A $SiCl_4$:$MoCl_5$ molar ratio of 3:1 was employed to minimize formation of a byproduct silicon-deficient phase, Mo_5Si_3. (The stoichiometric excess of $SiCl_4$ employed was balanced by a corresponding excess of NaK reductant.) Ultrasonic irradiation (600 W, 20 kHz) of the reaction mixture was initiated via a direct-immersion (13 mm diameter) titanium horn. While irradiation continued, the NaK alloy was slowly added dropwise from a pressure-equalizing addition funnel through a neck of the reaction flask. (**Caution:** NaK is a hazardous, highly reactive, flammable material that must be handled in environments free of halogenated solvents, oxygen, water, or other protic substances [13].) An exothermic reaction ensued, which produced a brown precipitate consisting of an amorphous precursor to $MoSi_2$ and salts (NaCl and KCl).
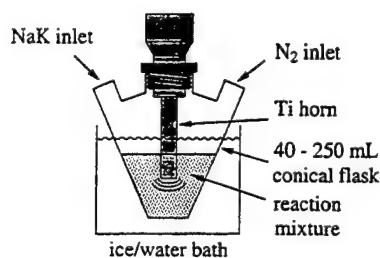
Fig. 1. Sonochemical reaction apparatus with direct-immersion titanium horn.
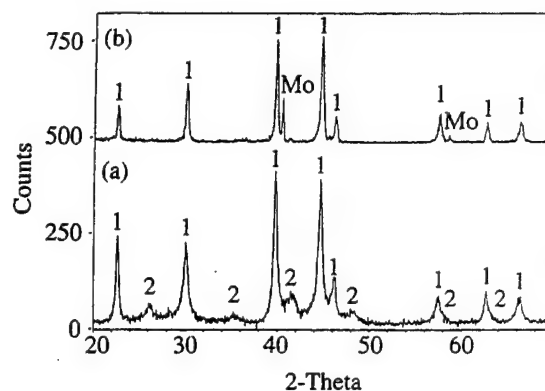
Fig. 2. (a) XRD pattern of nanocrystalline $MoSi_2$ powder annealed at 900 °C for 5 min. The phases present are α-$MoSi_2$ (1, low-temp. phase) and β-$MoSi_2$ (2, high-temp. phase). The crystallite coherence length calculated by the Scherrer equation using reflections from α-$MoSi_2$ was 16 nm. (b) XRD pattern of the hot-pressed $MoSi_2$ compact (see text); the crystallite coherence length was 31 nm. The minor reflections assigned to Mo metal are the result of extrinsic surface contamination of the compact by partial degradation of the TZM punch.

Nanocrystalline $MoSi_2$ was isolated and characterized as follows. The brown precipitate was annealed at 900 °C, 10^{-3} torr to crystallize the $MoSi_2$ and to remove the byproduct salts by sublimation. (This step required between 5 min and a few hours, depending on reaction scale.) Nanocrystalline $MoSi_2$ was collected as a black powder with $\approx 90\%$ yields. X-ray diffraction (XRD) patterns of the powders revealed both the α (low-temperature) and β (high-temperature) phases of $MoSi_2$ to be present, and indicated average crystallite coherence lengths in the range 16–31 nm, depending on annealing time (see Fig. 2(a)). Minor reflections corresponding to the byproduct silicon-deficient phase Mo_5Si_3 were often detected in the XRD patterns (although not in Fig. 2(a)), particularly in the larger-scale reactions. We attribute the presence of the Mo_5Si_3 impurity to a lack of thorough mixing and therefore incomplete reaction during sonochemical processing. A second byproduct observed in some cases was the Nowotny phase, Mo_5Si_3C [14]. This impurity was traced to exposure of the powders to organic (carbon-containing) vapors during annealing, and was avoided by preventing such exposure. Transmission-electron-microscopy (TEM) images of the powders comprised ≈ 20 nm $MoSi_2$ crystallites immersed in a finer matrix (see Fig. 3). Consolidation of the nanocrystalline powders was conducted as described below.

3. Consolidation and mechanical properties

Two sets of consolidation conditions were examined. The first compact was consolidated by hot pressing a cold compact of nanocrystalline $MoSi_2$ powder at 1170 °C, 140 MPa for 4 h in a tungsten die between TZM

Fig. 3. Dark-field TEM image of nanocrystalline MoSi₂ powder on holey carbon film.

punches. The resulting black, disc-shaped specimen measured ≈ 10 mm in diameter by 1 mm in thickness, and had 78% of the theoretical density of MoSi$_2$ as determined by the Archimedes method. An XRD pattern confirmed the material to be α-MoSi$_2$ having an average crystallite coherence length of 31 nm (see Fig. 2(b)), consistent with minimal grain growth. Scanning-electron-microscopy (SEM) images of a polished surface of the compact showed cusp-shaped interaggregate pores having average sizes of the order of 100–300 nm,

Fig. 4. SEM image of the hot-pressed MoSi$_2$ compact after surface polishing and etching (see text).
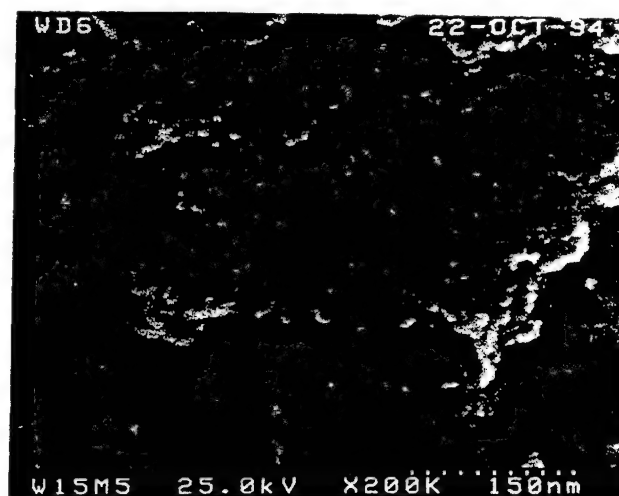
Fig. 5. SEM image of the hot-pressed and hot-isostatically-pressed MoSi$_2$ compact after surface polishing and etching (see text).

and rounded intergranular pores having sizes of 30–45 nm. SEM images of a polished and etched (HF/HNO$_3$, lactic acid) surface revealed a fine nanostructure, with smoothly textured 50–75 nm features comprising even smaller grains (see Fig. 4). Note that the apparently large porosity in the etched sample (Fig. 4) is misleading because the etchant attacks the nanocrystalline surface vigorously at the grain boundaries and about the pre-existing smaller pores. The greater magnification necessary to resolve the nanometer grain sizes also enhances the appearance of porosity. The average room-temperature Vickers microhardness determined for the compact was $1484 \pm 10\%$ (kg mm^{-2}), which was significantly higher than the value of $1045 \pm 10\%$ determined under identical testing conditions for a fully dense compact of conventional, coarse-grained MoSi$_2$.

The second compact was consolidated by first hot pressing a cold compact of nanocrystalline MoSi$_2$ powder at 1200 °C, 100 MPa for 10 min, and then hot isostatically pressing the hot-pressed compact at 1100 °C, 200 MPa for 4 h in a sealed (in vacuo) titanium can. The resulting specimen was 10 mm in diameter by 10 mm in length, and was determined to be 83% dense. The XRD pattern was comparable to Fig. 2(b) except that Mo$_5$Si$_3$ was present as a minor component. An average crystallite coherence length of 41 nm was calculated from the XRD lines for the α-MoSi$_2$ phase. Further evidence for the retention of the fine nanostructure was found in SEM images of a polished and etched surface of the compact (see Fig. 5). In Fig. 5 extremely fine features of ≈ 10–20 nm are readily evident; the reasons for the apparent differences between Fig. 4 and Fig. 5 (in view of the similar XRD crystallite coherence lengths in the two compacts) are not understood at present. The average room-temperature Vickers micro-hardness of the second compact was determined to be

$1587 \pm 10\%$ (kg mm^{-2}), similar to the value determined for the first compact.

A $3 \times 3 \times 4$ mm cuboidal section was cut from the second compact for compressive-strength testing at room temperature. A compressive yield strength of 2875 MPa was measured, as compared to 770–1550 MPa for fully dense, coarse-grained $MoSi_2$ [15]. The nanocrystalline sample fractured at the yield point, indicating that the specimen possessed little room-temperature ductility. Consolidated nanocrystalline $MoSi_2$ was therefore shown to be significantly harder and stronger than conventional $MoSi_2$ in three separate experiments; the relative ductilities remain to be established.

4. Summary and conclusions

(1) The sonochemical co-reduction strategy afforded a convenient means of producing nanocrystalline $MoSi_2$ powders in batches of up to ≈ 5 g. Procedures conducted on larger scales (to date) have suffered from the incorporation of minor amounts of the silicon-deficient byproduct phase Mo_5Si_3.

(2) Consolidation of the nanocrystalline powders by hot pressing or by a combination of hot pressing and hot isostatic pressing yielded compacts having 1.5-times the Vickers microhardness and 1.9-times the compression strength of conventional, coarse-grained $MoSi_2$.

(3) Work is in progress to determine the temperature-dependence of the compressive and flexural strengths and ductilities, and fracture toughness of nanocrystalline $MoSi_2$. The low-temperature ductilities of the present samples were probably limited by their high residual porosities of $\approx 20\%$.

(4) Efforts are under way to increase the synthetic scale

to a more useful level, and to reduce the residual porosity of the compacts through optimization of powder-packing and consolidation conditions.

Acknowledgments

References

[1] E. Gaffet and N. Malhouroux-Gaffet, *J. Alloys Comp.*, 205 (1994) 27.

[2] A.K. Vasud⊖van and J.J. Petrovic, *Mater. Sci. Eng.*, A155 (1992) 1.

[3] C. Suryanarayana and F.H. Froes, *Adv. Mater.*, 5 (1993) 96.

[4] R. Bohn, T. Haubold, R. Birringer and H. Gleiter, *Scripta Metall. Mater.*, 25 (1991) 811.

[5] J. Karch, R. Birringer and H. Gleiter, *Nature*, 330 (1987) 556.

[6] H. Chang, C.J. Altstetter and R.S. Averback, *J. Mater. Res.*, 7 (1992) 2962.

[7] T. Haubold, R. Bohn, R. Birringer and H. Gleiter, *Mater. Sci. Eng.*, A153 (1992) 679.

[8] T. Itsukaichi, K. Masuyama, M. Umemoto, I. Okane and J.G. Caba ± as-Moreno, *J. Mater. Res.*, 8 (1993) 1817.

[9] T. Christman and M. Jain, *Scripta Metall. Mater.*, 25 (1991) 767.

[10] K.S. Suslick, *Science*, 247 (1990) 1439.

[11] K.S. Suslick (ed.), *Ultrasound: Its Chemical, Physical, and Biological Effects*, VCH, New York, 1988.

[12] J.J. Ritter, *Adv. Ceram.*, 21 (1987) 21.

[13] D.F. Shriver, *The Manipulation of Air-sensitive Compounds*, Wiley, New York, 1986, pp. 206–207.

[14] E. Parthé, W. Jeitschko and V. Sadagopan, *Acta Crystallogr.*, 19 (1965) 1031.

[15] R.M. Aikin, Jr., *Mater. Sci. Eng.*, A155 (1992) 121; and *Ceram. Eng. Sci. Proc.*, 12 (1991) 1643.

Chemical synthesis and characterization of nanosized titanium aluminide

Stuart. T. Schwab*, Partha. P. Paul, Yi-Ming Pan

Southwest Research Institute, Materials and Structures Division 6220 Culebra Road, San Antonio, TX 78228-0510, USA

Abstract

Titanium aluminides are among the more promising intermetallics for use in aerospace and automotive applications; however, their acceptance has been hampered by their lack of ductility. Significant improvement in ductility may be obtained from nanostructured intermetallics. Reaction of $Ti[N(SiMe_3)_2]_3$ with excess alane produces a precursor (Compound 1) to titanium aluminide. We propose compound **1** to be a loose cluster (or family of clusters) in which titanium and aluminum atoms are both bonded directly and bridged by imidosilanes. This chemically synthesized precursor, when heated to 1000 °C, produces nanosized particles of $TiAl_3$. Nanosized $TiAl_3$ has been characterized by chemical analysis, solid-state NMR, X-ray diffraction, energy dispersive spectroscopy, and high-resolution electron microscopy.

Keywords: Chemical precursors; Intermetallics; Nanoparticles

1. Introduction

Although plagued by a lack of ductility, titanium aluminides are among the more promising intermetallics under development [1–5]. Of the three compounds in Ti–Al system, $TiAl_3$ exhibits the lowest density and the best oxidation resistance, but is the least ductile [1–5]. Nanostructured materials are currently the focus of intense investigation because they exhibit novel properties or dramatic improvements in properties over materials with conventional microstructures [6–10]. Gleiter [11] has proposed that substantial improvements in ductility may be observed in nanostructured intermetallics.

Researchers have traditionally relied on vapor phase or mechanical attrition techniques that are not amenable to industrial scale production [12]. Because of deficiencies in these methods, there is growing interest in chemical techniques of producing nanostructured materials [13,14]. Borohydride reduction [15–17] and co-reduction of metal chlorides with lithium triethylborohydride ("Super-Hydride") [18,19] are known to yield nanosize particles of metals and alloys. We report here the solution chemical synthesis and microstructural characterization of nanosize $TiAl_3$.

2. Experimental

2.1 General

The chemical synthesis and handling of Compound **1** were carried out under anhydrous and anaerobic conditions using common synthetic techniques in combination with an inert atmosphere/vacuum manifold system or an argon-filled drybox [20].

2.2. Preparation of nanosized TiAl₃

Titanium tris[bis(dimethylsilyl)amide)] (1.2 g, 2.25 mmol) was dissolved in 60 ml of hexanes. A 0.32 M diethyl ether solution of AlH_3 (25 ml, 8 mmol excess) was added slowly to the blue solution. The mixture was stirred for 18 h. A steel gray solid formed which was isolated by filtration and washed, first with 50 ml of hexanes and then with 50 ml of diethyl ether. Drying the solid under vacuum yielded 0.8 g of Compound **1** as a powder. Compound **1** (1.5 g) was pressed (using a KBr pellet press and hand pressure) into a small billet

* Corresponding author.

and heated in a quartz crucible under vacuum at 1000 °C for 0.5 h. The furnace was cooled to room temperature and the fragile pellet was crushed to yield a fine black powder (Compound **2**, 0.85 g).

2.3. Characterization

Characterization of the heat treated powder (**2**) was performed with solid-state nuclear magnetic resonance (NMR) spectroscopy and X-ray powder diffraction (XRD). The solid-state spectra were recorded on a Brooker AM-600 NMR spectrometer operating at 156.4 MHz for ^{27}Al. Powder X-ray diffraction (XRD) analyses were conducted with the aid of a Siemens D-500 X-ray diffractometer. The microstructure characterization and phase identification of Compound **2** were performed at the atomic level, using high resolution electron microscopy (HREM) including a JEM-4000EX HREM and a VG HB501 energy dispersive spectroscopy (EDS) microanalysis. A small portion of Compound **2** was dispersed on perforated carbon-coated copper grids for HREM analysis. The lattice images were digitized and optical techniques were used to determine lattice spacing.

3. Results and discussion

3.1. Synthesis and characterization of Compound 1

Co-reduction of metal halides with lithium triethylborohydride is known to produce pure metal alloys in some cases [18]. Our attempts to co-reduce an equimolar mixture of $TiCl_4$ and $AlCl_3$ with seven equivalents of lithium triethylborohydride yielded a very reactive solid that, upon heat treatment at 1000 °C under inert conditions, converted to microcrystalline Ti_3Al, as observed by XRD. Unfortunately, substantial impurities (primarily LiCl) were also present. Salt impurities, such as LiCl, are particularly bothersome because they are not readily removed through sublimation or reactive atmosphere pyrolysis.

In an attempt to produce salt-free Ti_xAl_y, a dilute hexane solution of $Ti[N(SiMe_3)_2]_3$ [21] was combined with an excess of AlH_3 [22] in ether at ambient temperature, according to Eq. (1). A very fine, intractable, steel-gray powder precipitated from the dark solution. This pyrophoric powder was washed with ether and dried under vacuum to produce Compound **1** (elemental analysis: C 12.0; H 3.2; N 0.8; Al 28.5; Cl 32; O 4.9; Si 0.5; Ti 17.1) in 60–65% yield, based on Ti.

$$Ti[N(SiMe_3)_2]_3 + AlH_3 \xrightarrow{25°C} Compound\ \mathbf{1} \qquad (1)$$
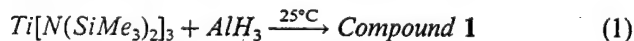
The solid-state ^1H NMR (CRAMPS, 360 MHz) spectrum of Compound **1** consists of resonances at 0.3 ppm and 7.3 ppm, which can be assigned to $-Si(CH_3)_3$ and

$-NH$ protons, respectively [23]. The infrared spectrum (KBr pellet) of Compound **1** displays absorptions at ca. 3300 cm^{-1}, ca 3000 cm^{-1}, 1630 cm^{-1}, 1385 cm^{-1}, and 990 cm^{-1}. We assign the 3300 cm^{-1} and 3000 cm^{-1} absorptions to N–H and C–H stretching vibrations, respectively. The 1635 cm^{-1} absorption may be assigned to N–H bending, while the 1385 cm^{-1} and 990 cm^{-1} absorptions may be assigned to C–H bending and out of plane deformations.

While the assignments made to the infrared absorptions are consistent with the presence of the functions suggested by the CRAMPS analysis, the structure of **1** remains unclear. Nonetheless, we believe Compound **1** to be a loose cluster (or family of clusters) in which titanium and aluminum atoms are both bonded directly and bridged by imidosilanes. Based on preliminary electron spin resonance (ESR) analysis results, we further propose that this cluster (or family of clusters) contains a substantial number of unpaired electrons that may be considered nascent Ti–Al bonds.

3.2. Synthesis and characterization of nanosize TiAl₃

Compound **1** was pressed into a small billet and heated under vacuum to 1000 °C for 0.5 h. Upon cooling to room temperature, the resulting fragile pellet was crushed to produce a fine black powder (Compound **2**) in a yield of 60% by weight. Comparison of the XRD pattern obtained from Compound **2** (Fig. 1) with that obtained from a commercial sample of $TiAl_3$ confirms the identity of the crystalline product as $TiAl_3$ ($TiAl_3$ powder was purchased from CERAC, Inc., Milwaukee, WI). The XRD pattern also reveals the presence of small amounts of TiO and Ti_3Al. The TiO is probably produced through reaction with the atmosphere, and it may be possible to eliminate its formation through strict maintenance of anhydrous and anaerobic conditions. While the appearance of Ti_3Al is puzzling, it may be possible to control its formation through optimization of the reaction stoichiometry and/or the pyrolysis conditions. While small amounts of amorphous material are present, the XRD pattern (Fig. 1) shows little evidence of the "amorphous halo" that is indicative of the presence of substantial amorphous content.

Analysis of selected particles of Compound **2** by energy dispersive spectroscopy (EDS) indicated a Ti:Al ratio of 1:3, while bulk chemical analysis (elemental analysis: C 4.38; H 0.41; N 0.92; Al 42.5; O 14.5, Si < 0.5; Ti 38.0) indicated a Ti:Al ratio of 1:2. A lower bulk aluminum content is expected to result from the presence of the Ti_3Al and TiO impurities. The solid-state ^{27}Al MAS NMR spectrum (156.4 MHz) of Compound **2** presents a major absorption at 252 ppm that may be assigned to $TiAl_3$; the solid-state ^{27}Al MAS NMR spectrum (156.4 MHz) of the commercial $TiAl_3$ powder consisted of a single resonance at 256 ppm.
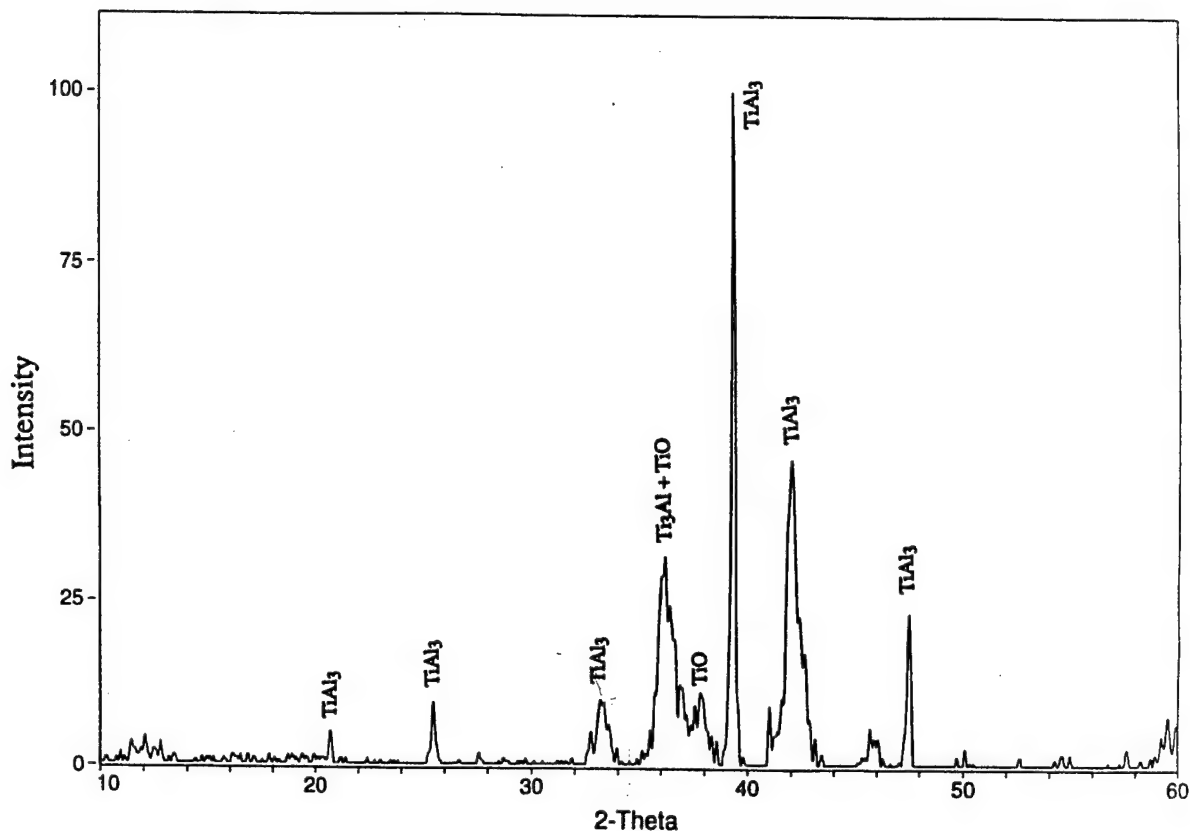
Fig. 1. Powder X-ray diffraction pattern of nanosize TiAl₃ (Compound 2).

The bright field micrograph presented as Fig. 2 reveals Compound 2 to be composed of agglomerated nanosize particles with a size distribution of approximately 5–25 nm. The crystals tend to be equiaxed, and their interfaces appear to be sharp at the grain boundaries. The HREM lattice image of two adjacent nanocrystalline grains presented as Fig. 3 reveals both grains as having a lattice spacing of 0.212 nm, which is consistent with that expected from the (004) plane of TiAl₃. EDS microanalysis of Compound 2 using a
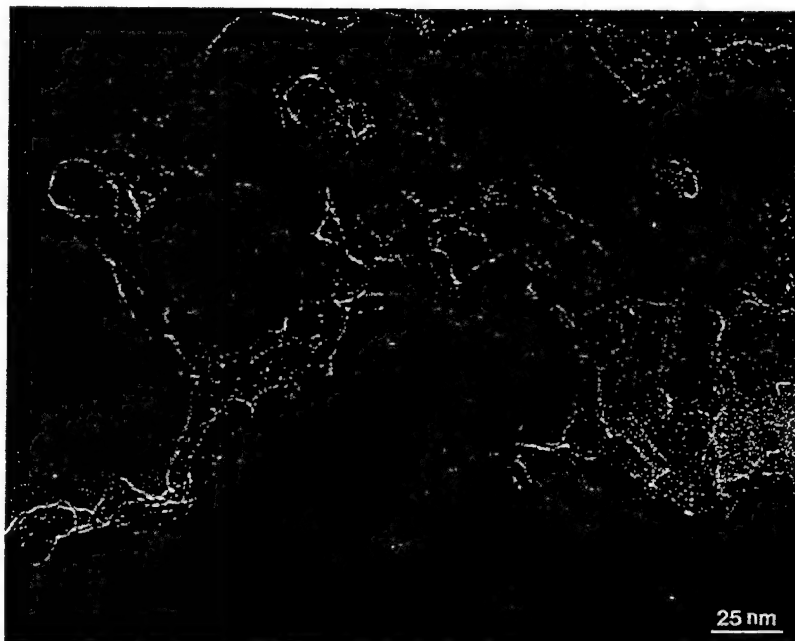
Fig. 2. Transmission electron micrograph of nanosize TiAl₃ powder (Compound 2).
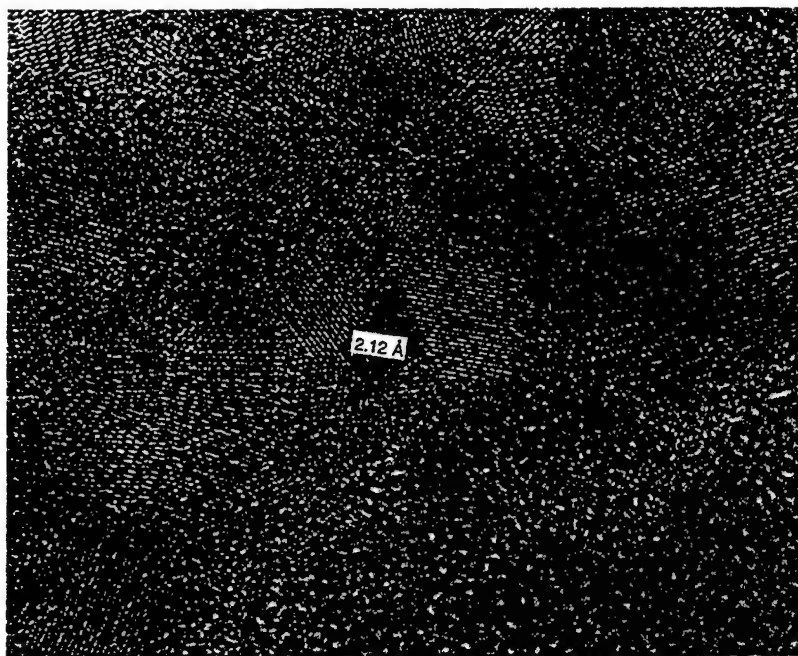
Fig. 3. High-resolution electron micrograph lattice fringes from (004) plane of nanosize TiAl₃ (Compound 2).

probe size of about 1 nm indicates an atomic ratio of Ti:Al of approximately 1:3, as expected for TiAl₃.

4. Conclusion

Pyrolytic decomposition of a chemical precursor has been found to produce nanostructured titanium aluminide (TiAl₃). Examination of bulk specimens of chemically derived TiAl₃ should enable us to determine whether the promise of improved properties is realized in this nanostructured material.

Acknowledgments

References

[1] F.H. Froes, C. Suryanarayana and D. Eliezer, *J. Mater. Sci., 27* (1992) 5113 .

[2] K.S. Kumar in R. Darolia et al. (eds.), *Structural Intermetallics*, The Minerals, Metals & Materials Society, Warrendale, PA, 1993, pp. 87–96.

[3] Z.L. Wu and D.P. Pope, in R. Darolia et al. (eds.), *Structural Intermetallics*, The Minerals, Metals & Materials Society, Warrendale, PA, 1993, pp. 107–116.

[4] M. Yamaguchi, *Mater. Sci. Tech., 8* (1992) 299.

[5] Y. Umakoshi et al., *J. Mater. Sci., 24* (1989) 1599.

[6] R.W. Siegel, *Annu. Rev. Mater. Sci., 21* (1991) 559.

[7] H. Gleiter, *NanoStruc. Mater., 1* (1992) 1.

[8] H. Gleiter, *Adv. Mater., 4* (1992) 474.

[9] R.D. Shull, *NanoStruc. Mater., 2* (1993) 213.

[10] R. Dagani, *Chem. Eng. News, 70(47)* (1992) 18.

[11] R. Bohn, H. Gleiter et al., *Scripta Metall. Mater., 25* (1991) 811.

[12] L.E. Brus et al., *J. Mater. Res., 4* (1989) 704.

[13] G.M. Whitesides, J.P. Mathias and C.J. Seto, *Science, 254* (1991) 1312.

[14] G.A. Ozin, *Adv. Mater., 4* (1992) 612.

[15] R.D. Reike, *Science, 246* (1989) 1260.

[16] J. van Wonterghem et al., *Nature, 322* (1986) 622.

[17] G.N. Glavee et al., *Inorg. Chem., 32* (1993) 474.

[18] H. Bonnemann, W. Brijoux and T. Joussen, *Angew. Chem. Int. Ed. Engl., 29* (1990) 273.

[19] D. Zeng and M.J. Hampden-Smith, *Chem. Mater., 5* (1993) 681.

[20] D.F. Shriver, M.A. Drezdzon, *The Manipulation of Air-Sensitive Compounds*, John Wiley, New York, 2nd edn., 1986.

[21] E.C. Alyea, D.C. Bradley and R.G. Copperwaite, *J. Chem. Soc., Dalton Trans.* (1972) 1580.

[22] A.E. Finholt, A.C. Bond and H.I. Schleisinger, *J. Am. Chem. Soc., 69* (1947) 1199.

[23] G.E. Maciel, C.E. Bronnimann and B.L. Hawkins, in W.S. Warren (ed.), *Advances in Magnetic Resonance*, Vol. 14, Academic, New York, 1990, pp. 125–150.

Nanostructure of polymer-derived silicon nitride

Stuart. T. Schwab*, Richard A. Page

Southwest Research Institute, Materials and Structures Division, 6220 Culebra Road, San Antonio, TX 78228-0510, USA

Abstract

Although silicon nitride (Si_3N_4) ceramics have considerable potential for use in high temperature applications such as engines, processing-related difficulties and associated high cost have hindered their acceptance. While chemical processing methods, such as those based on preceramic polymers, have the potential to overcome many of the difficulties inherent to traditional techniques, many features of polymer-derived Si_3N_4 are poorly understood. Transmission electron microscopy (TEM) has been used to characterize the nanostructure of polymer-derived Si_3N_4. The polymer-derived material is found to consist of large grains composed of very fine crystallites, as well as fibrils 40–50 nm in diameter. If the factors responsible for the formation of these structures were understood, the understanding could be harnessed to produce Si_3N_4 components with enhanced fracture resistance and other engineering properties.

Keywords: Nanostructures; Silicon nitride; Preceramic polymer

1. Introduction

Explosive growth has been forecast for advanced ceramics and ceramic composites for the last several years. This growth has not been realized in part because current, powder-based methods of producing ceramics are inefficient and expensive, and yield products prone to brittle failure. Chemical production of ceramics has the potential to enable development of more efficient and inexpensive manufacturing methods, and so much attention has been devoted to chemical routes to ceramics (e.g., sol–gel and preceramic polymers). In addition to gains in manufacturing costs, these chemical approaches offer the potential for producing microstructures that resist brittle fracture.

Silicon nitride (Si_3N_4) is being considered for a wide variety of high temperature applications because of its excellent strength at elevated temperature, resistance to thermal shock, resistance to oxidation and other properties [1]. Despite its potential, relatively little is known about the microstructure of chemically-derived Si_3N_4. A particularly useful family of polymeric precursors to Si_3N_4 has been developed at the Southwest Research Institute (SwRI). These polymers, known as perhydro-

polysilazanes (PHPS), contain only the elements silicon, nitrogen, and hydrogen, and so convert to carbon-free silicon nitride when fired. Although originally developed as binders for Si_3N_4 powder processing [2], these polysilazanes have demonstrated their utility in the repair of damaged oxidation protection coatings on carbon–carbon composites [3], and have been shown to be effective matrix precursors for the polymer infiltration/pyrolysis (PIP) of fiber-reinforced Si_3N_4 composites [4].

Characterization of the PHPS-derived Si_3N_4 by X-ray diffraction (XRD) revealed a relationship between phase composition, crystallite size and firing condition [5]. To characterize this material further, the microstructure of PHPS-derived Si_3N_4 was examined by transmission electron microscopy (TEM).

2. Experimental

2.1. Preparation of PHPS-derived Si_3N_4

Unless otherwise noted, all manipulations of uncured polysilazanes were carried out under anhydrous and anaerobic conditions using common synthetic techniques in combination with an inert atmosphere/vac-

---

* Corresponding author.

uum manifold system or an argon-filled drybox [6]. The polymer synthesis has been described previously [7]. To prepare a billet for TEM characterization, PHPS was fired to 1000 °F under nitrogen, the char product was ground with an agate mortar and pestle, and classified through a -140 inch mesh. After combination with additional PHPS, as described elsewhere [3], the mixture was pressed into a billet at room temperature and fired to 1500 °C under nitrogen.

2.2. Foil preparation and characterization

The porous PHPS-derived compacts were fractured at room temperature to reveal their internal microstructure. One half of the fractured specimen was coated with iridium and examined in the SEM. The other half of the fracture specimen was impregnated with epoxy under vacuum. Discs (3 mm diam.) were machined ultrasonically from thin slices obtained from the impregnated compact using a low speed diamond saw. These discs were ground by hand to a thickness of roughly 50 μm, thinned to perforation by ion-milling, and then coated with a thin carbon film. The thinned foils were mounted in a double tilt analytical goniometer and examined in a Philips EM420 TEM/STEM operated at 120 kV. Selected area and convergent beam diffraction techniques were used to identify the crystallographic nature of the constituents observed within the foil.

3. Results and discussion

Examination of the fracture surface in the SEM revealed a granular appearance with grains of a few to a few tens of microns in size, as shown in Fig. 1. In addition to the relatively coarse granular features, very

Fig. 2. Fracture surface of PHPS-derived ceramic showing fibrous material.

fine fibers or "fibrils", were observed throughout the fracture surface, as seen in Fig. 2. It was evident from the SEM examination that these fibrils were submicrometer in cross section and exhibited very large aspect ratios. Previously, XRD analysis had suggested an average crystallite size of approximately 30 nm for PHPS-derived ceramics produced at the same temperature as the material under study [5]. To resolve this discrepancy, thin foils of polymer-derived Si_3N_4 were prepared and studied by TEM.

The thin foils prepared from the pyrolyzed PHPS exhibited a very complex microstructure. The large few to a few tens of micrometer grains that were observed on the fracture surface in the SEM were also evident in the thin foils. The TEM examination, however, indicated that these large grains were composed of much smaller crystallites, whose size and morphology varied considerably. Equiaxed crystallites ranging from less

Fig. 1. Granular structure of PHPS-derived ceramic fracture surface.
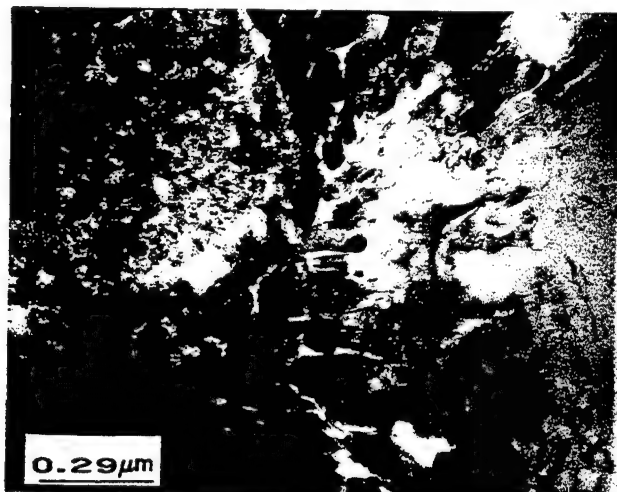
Fig. 3. Bright field TEM image showing range of crystallite size.
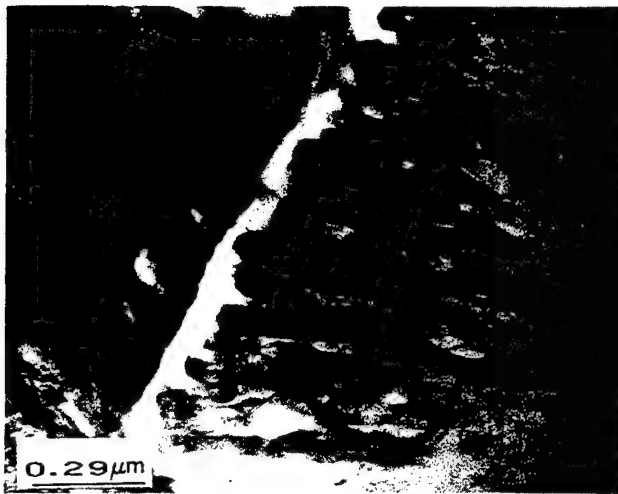
Fig. 4. Bright field TEM image of elongated crystallites.

than 10 nm to greater than 100 nm were evident (Fig. 3), as were elongated crystallites with widths of the order of 500 nm, as seen in Fig. 4. Selected area electron diffraction patterns showed the crystallites to be predominantly α-Si_3N_4, with small amounts of β-Si_3N_4 and elemental silicon present as well. The diffraction results also confirmed that the diffraction contrast observed in the bright field images was due to orientation differences between the individual crystallites.

The fibrils seen in the fracture surface were also observed in the thin foil TEM specimens. Their presence appeared to be limited to void spaces between the large Si_3N_4 grains and they were generally randomly oriented in loosely spaced clusters. Although considerable variation in fibril diameter existed, the average diameter appeared to be of the order of 40–50 nm. Convergent beam electron diffraction patterns taken from the fibrils (Fig. 5) indicate a crystalline Si_3N_4 composition.

It appears that the microstructure of the polymer-derived ceramic results from two mechanisms. The small, equiaxed crystallites are probably produced from the condensed phase during pyrolysis, while the fibrils are probably produced from the vapor phase. The polymer-derived ceramic is known to contain excess silicon that nitrides readily above roughly 1400 °C [5]. It is plausible that the observed fibrils are produced by nitridation of free silicon on or near the surface of voids. Additional study of the formation mechanisms is in progress.

4. Conclusion

The microstructure of polymer-derived Si_3N_4 has been found to consist of micrometer size grains, which are composed of sub-micron crystallites, as well as small, crystalline fibrils. While the mechanisms responsible for the formation of these features is unknown, if understood, such mechanisms could be harnessed to produce ceramics with enhanced ductility, fracture resistance, and other desirable engineering properties.
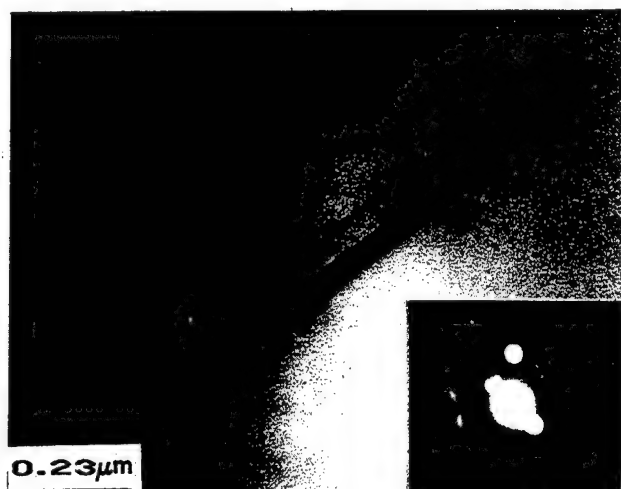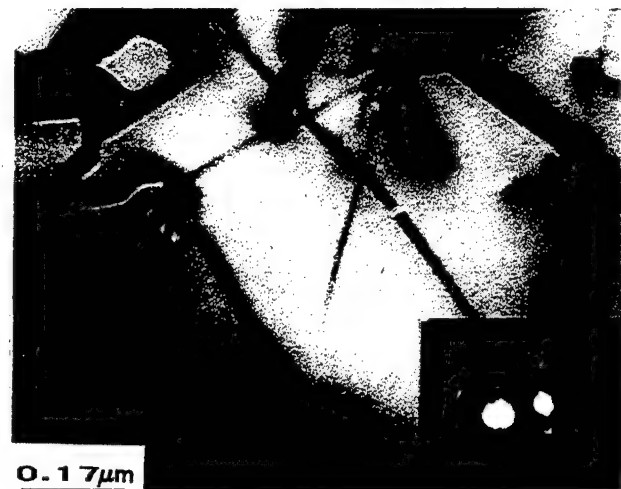
Fig. 5. (A,B) Bright field TEM image and convergent beam diffraction patterns of the Si_3N_4 fibrils observed in the thin foil.

References

[1] (a) G. Ziegler, J. Heinrich and G. Wötting, *J. Mater. Sci.*, *22* (1987) 3041–3086; (b) C. Boberski, R. Hamminger, M. Peuckert, F. Aldinger, R. Dillinger, J. Heinrich and J. Huber, *Angew. Chem. Int. Ed. Engl. Adv. Mater.*, *28* (1989) 1560–1569.

[2] (a) S.T. Schwab, R.C. Graef, D.L. Davidson and Y.-M. Pan, *Polymer Preprints*, *32* (1991) 556–558; (b) S.T. Schwab and C.R. Blanchard-Ardid, The use of organometallic precursors to silicon nitride as binders, *Mater. Res. Soc. Symp. Proc.*, *121* (1988) 581–587.

[3] (a) S.T. Schwab and R.C. Graef, Repair of oxidation protection coatings on carbon–carbon using preceramic polymers, *NASA-CP 3133, Part 2* (1991) 781–798; (b) S.T. Schwab, R.C. Graef and D.E. Lutfi, Repair of oxidation protection coatings on RCC-3 using preceramic polymers, *NASA-CP 3175, Part 2* (1992) 599–622.

[4] (a) S.T. Schwab, R.C. Graef, Y.M. Pan and D.L. Davidson, Infiltration/pyrolysis processing of SiC fiber-reinforced Si_3N_4 composites, *NASA-CP 3175, Part 2* (1992) 721–738.

[5] C.R. Blanchard and S.T. Schwab, X-ray diffraction analysis of the pyrolytic conversion of perhydropolysilazane to Si_3N_4, *J. Am. Cer. Soc.*, *77* (1994) 1729–1739.

[6] a) D.F. Shriver and M.A. Drezdzon, *The Manipulation of Air-Sensitive Compounds*, John Wiley, New York, 2nd edn., 1986; (b) A.L. Wayda and M.Y. Darensbourg, *Experimental Organometallic Chemistry*, ACS Symposium Series 357, American Chemical Society, Washington, DC, 1987.

[7] S.T. Schwab, Polysilazane precursors for silicon nitride and resultant products, U.S. Patent 5 294 425, (March 15, 1994).

Phase and size control of nanometer-size materials synthesized in supersonic jet expansions

Wenqing Lu, Jinfan Huang

Department of Chemistry, University of Michigan, Ann Arbor, MI 48109-1055, USA

Abstract

We present results of experimental studies to control the phase and size of nanometer-size materials generated in supersonic jet expansions. The effects of expansion conditions such as initial temperature, stagnation pressure, mole fraction of sample in the carrier gas, geometry of the nozzle, and location in the jet have been examined. The experimental results indicate that relatively larger nanometer-size particles may be obtained by using lower starting temperature, higher carrier gas pressure, relatively lower mole fraction up to a point where the release of the heat from condensation is no longer the dominant control factor, Laval nozzles instead of tubular nozzles, and by taking the materials from the central core of the supersonic jet.

Keywords: Synthesis; Supersonic jet expansions

1. Introduction

As a result of their interesting properties and potential applications, nanometer-size particles have attracted attention during the past decade. Various methods to synthesize the nanometer size materials, including consolidation from vapor [1–5], matrix-mediated synthesis [6], ball-milling [7,8], magnetic sputtering [9], electrochemical techniques [10] and arrested precipitation reactions in solutions [11,12], have been reported. Every method has its advantages and its limitations. Therefore, new approaches would be desirable. Since Becker and his coworkers [13] first reported H_2, Ar, and N_2 cluster beams formed from free jet expansions, such expansions have been widely used to generate clusters with sizes in the range from dimers to many thousands of molecules [14–17]. The diameters of clusters with several thousands of molecules reach the upper limit of quantum size effect; for instance the quantum size effect of CdS occurs if the crystallite diameter is comparable to or below the exciton diameter of 5–6 nm ($\sim$ 1500–2000 molecules) [18]. Therefore, the jet expansion method may be used to synthesize some interesting nanometer size materials.

Considerable attention has been devoted to the theory of cluster formation in supersonic expansions

[14,19–21]. No final and fully successful treatments exist, however, for predicting the size of particles generated in supersonic jets under arbitrary expansion conditions. Systematic experimental investigations are necessary to get insight into the effective control of the particles generated in supersonic flow. In the present paper we report results on the control over phases and sizes of nanometer size clusters of NH_3. Although crystalline ammonia is of little interest in material science, the technique can be used for materials with much higher melting points. Accordingly, the conclusions drawn from our experiments may be helpful in the production of nanometer size materials via condensation in supersonic expansions.

2. Experimental section

As shown in Fig. 1, our current apparatus to synthesize nanometer size particles through supersonic expansion consists of an expansion control system and a particle size probe system. The expansion control system is the combination of a pulsed nozzle, a temperature controlled sample holder, and a carrier/sample gas supply line. A General Valve Corporation Series 9 high
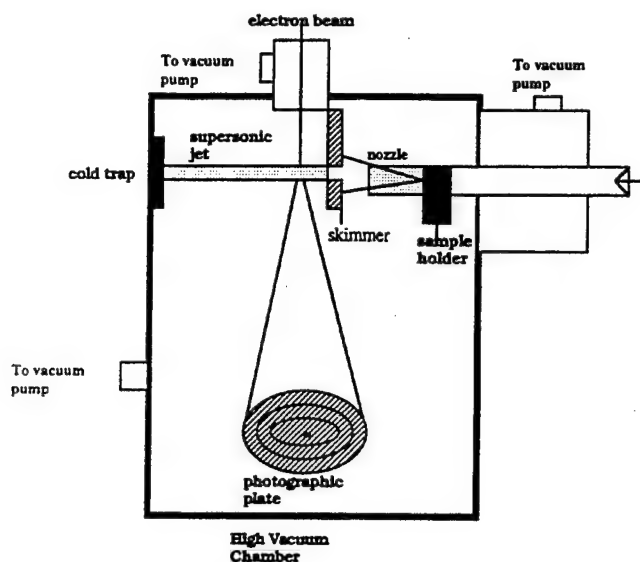
Fig. 1. Schematic drawing of the apparatus used to generate nanometer size materials through supersonic jet expansion.

speed solenoid valve was modified so that nozzles with different geometry can be easily mounted onto it. Pulses were generated through an IOTA ONE pulse driver (General Valve Corporation). The use of a pulsed nozzle ensures that supersonic jets do not build up magnificent background gas during the time they are probed by electrons. Initial sample temperatures can be controlled by means of a heating element surrounding the sample holder and nozzle. Therefore, experiments can be carried out on nonvolatile materials as well as volatile ones. When using gaseous samples the carrier/sample gas supply line is directly connected to the pressurized gas tank and the stagnation pressure is adjusted through regulators. When working with liquid or solid samples the subject mole fraction is controlled by adjusting the sample temperature and the stagnation pressure. Pulsed 44 KeV electron beams are used to probe the particles formed in the supersonic jet and the diffracted electrons are recorded on photographic plates. From the diffraction patterns can be determined the phases, structures, and sizes of particles. A Vee skimmer [22] mounted 2 mm before the electron beam is used to select a stream of particles at the desired radius of the supersonic jet. The distance between the nozzle tip and the electron beam can be adjusted during an experiment so that the time evolution of the synthesized particles downstream of the nozzle can be readily probed. A cold trap is used to condense the residual gas.

The chemicals used in present experiment were NH_3 gas (99.99% air products) and neon carrier (99.999%, air products). NH_3/Ne samples with four different mole fractions (neat NH_3 gas, $x = 0.5$, 0.25, and 0.125) were investigated under different initial temperatures and different stagnation pressures. A glass Laval nozzle (G No. 19) with the dimensions of 0.20 mm entrance i.d.,

2.02 mm exit i.d., and overall length of 20.08 mm was used in most of the experiments. A tubular nozzle with i.d. of 0.23 mm and length of 5.0 mm was also tested to compare the effect of nozzle geometry on particle size. The nozzles were operated at a frequency of 19 Hz and a duration time of 0.4 ms. Electron beams with the same frequency and duration time were used but a delay time of 0.6 ms allowed the steady-state portion of the pulsed jet to reach the electron beam. Kodak medium slide photographic plates were used to record the diffraction patterns, which are the sum of 300 to 1500 pulsed exposures in the present experiment. Experimental conditions including mole fractions, stagnation pressures, and initial temperatures are listed in Table 1.

3. Results

Typical electron diffraction patterns from expansions of NH_3/Ne samples through the Laval nozzle are given in Figs. 2 and 3. These diffraction patterns can be classified into pure solid diffraction, pure liquid diffraction, and mixed solid–liquid diffraction. Most of the patterns are from solid particles; for instance the diffraction pattern corresponding to curve c in Fig. 3 is in reasonable agreement with the calculated pattern from the crystal structural data [23] of the primitive cubic phase of NH_3 with a cell dimension of $a = 5.104(6)$Å, space group of $P2_13$, and particle diameter of 10.4 nm. Fig. 4 compares the calculated intensity curve with the experimental curve 3c. The features of curves f and g in Fig. 2 are similar to the reported X-ray diffraction patterns of liquid ammonia [24,25]. It is evident that the patterns like curves c to e in Fig. 2 correspond to a superposition of diffraction from solid and from liquid particles. By selecting proper expansion conditions it is sometimes possible to control the phase of nanometer size products.

Fig. 5 shows electron diffraction patterns of particles produced in neat NH_3 expansions at different distances beyond the Laval nozzle tip. A steady growth of Debye–Scherrer rings due to the solid phase frozen from the liquid can be seen.

The variation in particle size under different expansion conditions can be inferred from the breadths of diffraction peaks given in Figs. 2 and 3. Estimated particle sizes are listed in Table 1. By varying the expansion parameters within the range listed in Table 1 it is possible to generate NH_3 particles and to control their average diameters from ~ 3.8 to ~ 10.8 nm.

The distribution of particle size within a jet expanded from a Laval nozzle is not uniform. Larger size particles were observed to be concentrated in the center line of a jet and the particle diameters fall off with increasing radial distance. For instance, at a distance of 35 mm from the nozzle tip the average particle diameters

Table 1
Summary of selected experiments of NH_3 [a]

P [b]	Mole fraction	Stagnation pressure (bar)	Initial temperature (K)	Particle size [c] (nm)	Phase	Drop size [d] Expt.	Calcd.
G 19 nozzle							
932	1.0	2.75	295	8.3	s	8.9	
933	1.0	4.14	295	9.2	s	9.9	
934	1.0	5.51	295	9.5	s + l	10.3	
935	1.0	2.75	323	3.8	s + l	4.2	
936	1.0	4.14	323	4.7	s + l	5.1	
937	1.0	5.51	323	5.0	s + l	5.4	
938	1.0	2.75	348		l		
939	1.0	4.14	348		l		
940	1.0	5.51	348		l		
941	0.5	2.75	323	7.0	s	7.5	
942	0.5	4.14	323	9.0	s	9.7	
943	0.5	5.51	323	10.4	s	11.2	
944	0.5	2.75	348	6.6	s	7.1	
945	0.5	4.14	348	6.9	s	7.4	
946	0.5	5.51	348	8.8	s	9.5	
947	0.5	2.75	295	9.0	s	9.6	
948	0.5	4.14	295	10.2	s	11.0	
949	0.5	5.51	295	10.8	s	11.5	
950	0.25	2.75	295	8.2	s	8.9	
952	0.25	5.51	295	10.4	s	11.2	
953	0.25	2.75	323	7.1	s	7.6	
954	0.25	4.14	323	9.1	s	9.8	
955	0.25	5.51	323	9.3	s	10.0	
956	0.25	2.75	348	5.6	s	6.0	
957	0.25	4.14	348	8.7	s	9.3	
958	0.25	5.51	348	9.8	s	10.5	
959	0.125	2.75	348	7.6	s	8.1	8.3[e]
964	0.125	4.14	295	9.3	s	9.9	10.4[e]
966	0.125	5.51	323	9.8	s	10.5	11.3[e]
967	0.125	4.14	323	8.5	s	9.1	10.0[e]
968	0.125	2.75	323	8.3	s	8.9	8.5[e]
Tubular nozzle							
999	1.0	4.14	295	2.2	s	2.4	
1000	1.0	5.51	295	2.2	s	2.4	

[a] Distances to the nozzle tip for G 19 nozzle were set at 35 mm, for tubular nozzle at 9 mm. [b] Plate number. [c] Crystalline particles. [d] Droplets at the nozzle tip. [e] Calculated from numerical integration of Eq. (1) in the text.

in a jet of neat NH_3 expanded under 3.2 bar stagnation pressure and 295 K initial temperature are 8.9, 8.5, 8.0, and 7.6 nm for radial distances at 0.0, 1.3, 2.5, and 4.4 mm respectively. This observation provides another means of selecting the particle size generated in the supersonic jet method.

4. Discussion

The control of phases of nanometer size materials synthesized in supersonic jets has been one of the particular interests of this laboratory [16,17,26,27]. For some substances the phase produced depends upon the temperature of the flow at some critical stage of particle growth [27]. For other substances the kinetics of phase changes in the clusters during the cooling flow is cru-

cial. One consequence of the kinetic aspect is that new crystalline phases never seen in the bulk have been produced in the jets [17,27,28]. Metastable phases which are difficult to synthesize in the bulk can sometimes be readily generated in supersonic expansions. For example, the transition from metastable cubic ice to the stable hexagonal ice is irreversible. However, it is difficult to prepare cubic phase ice from the direct cooling of bulk water. The conventional approach [29] has been to condense water vapor onto a cold surface to obtain amorphous ice. Upon warming up to ~156 K cubic ice is produced. However, the product from supersonic expansions is highly supercooled liquid which quickly freezes to cubic ice [30,31,33,34]. Because only one crystalline phase of NH_3 is known under normal pressure, no new crystalline phase was observed in the present experiments.
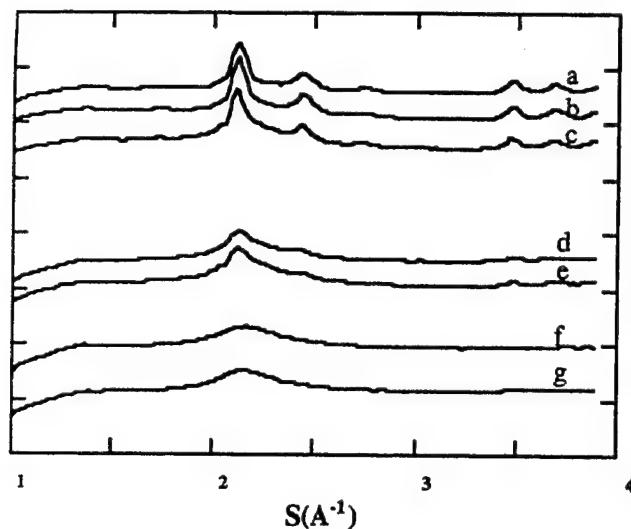
Fig. 2. Electron diffraction patterns of nanometer size particles from neat NH_3 expansions under different stagnation pressure and initial temperature. (a) $T = 295$ K, $P = 2.75$ bar; (b) $T = 295$ K, $P = 4.14$ bar; (c) $T = 295$ K, $P = 5.51$ bar; (d) $T = 323$ K, $P = 4.14$ bar; (e) $T = 323$ K, $P = 5.51$ bar; (f) $T = 348$ K, $P = 2.75$ bar; (g) $T = 295$ K, $P = 4.14$ bar.

Fig. 4. Electron diffraction patterns of nanometer size particles: (a) experimental; (b) calculated.

According to a computer modeling [21] based on the expansion conditions used in the experiment with diffraction curves shown in Fig. 5, liquid NH_3 droplets with diameter of ~ 10 nm exit the nozzle at about 155 K (40 K below the bulk melting point) after they have fully grown in the nozzle. When these droplets fly into the vacuum chamber evaporative cooling quickly reduces their temperatures. At a distance of 19 mm from the nozzle tip the temperature of droplets reaches

~ 122 K and they begin to freeze. The completion of freezing was observed ~ 30 mm after they exited the nozzle. The sizes of the final microcrystalline products listed in Table 1 depend on the sizes of liquid droplets generated inside the nozzle and the amount of evaporation to cool to the freezing temperature and the amount to dissipate the heat of fusion. A detailed procedure to estimate these loses was given in our previous paper [32]. The sizes of the liquid droplet listed in Table 1 were calculated from the crystal sizes by this procedure.

To understand the effects of the expansion conditions on the sizes of liquid droplets from our experiment we carried out calculations based on some simple theoretical models. One of the simplest and most easily applied is that of Weiel [19], who recently proposed a model of

Fig. 3. Electron diffraction patterns of nanometer size particles from NH_3/Ne ($x = 0.5$) expansion under different stagnation pressures and initial temperatures. (a) $T = 323$ K, $P = 2.75$ bar; (b) $T = 323$ K, $P = 4.14$ bar; (c) $T = 323$ K, $P = 5.51$ bar; (d) $T = 348$ K, $P = 2.75$ bar; (e) $T = 348$ K, $P = 4.14$ bar; (f) $T = 348$ K, $P = 5.51$ bar; (g) $T = 295$ K, $P = 2.75$ bar; (h) $T = 295$ K, $P = 4.14$ bar; (i) $T = 295$ K, $P = 5.51$ bar.
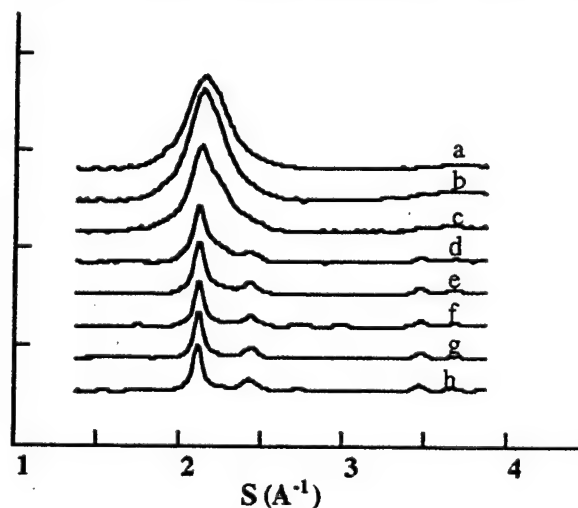
Fig. 5. Electron diffraction patterns indicate the freezing of NH_3 droplets into nanocrystals under initial temperature of 295 K and stagnation pressure of 3.2 bar beyond the nozzle tip. (a) Distance to the nozzle tip equals 9.0 mm; (b) 14.0mm; (c) 19.0 mm; (d) 24.0 mm; (e) 29.0mm; (f) 34.0 mm; (g) 39.0 mm; (h) 44.0 mm.

coagulation growth in a system with a very low ratio of sample to carrier gas. According to his model the upper limit of possible cluster sizes in expanding flows through a conical nozzle can be obtained by integrating the differential equation

$$dN(\delta)/d\delta = 4Dd_1^2[3\pi m_{gas}/(5m_1)]^{1/2}\ln2\, n_1(0)N^{16}(\delta)$$

$$\times [1 + (1/3)M^2(\delta)]^{-3/2}M^{-1}(\delta) \qquad (1)$$

where D is the nozzle throat diameter, $\delta = x/D$ and x is the distance to the throat, $N(\delta)$ is the cluster size as a function of δ, d_1 is the diameter of monomer, m_{gas} is the atomic mass of carrier gas, m_1 is atomic or molecular mass of the sample, and $M(\delta)$ is the Mach number which may be approximated as

$$M(\delta) = 1 + 2.8284\delta\,\tan(\alpha) \qquad (2)$$

for a conical nozzle with total opening angle 2α in the range of $\delta < 20$. NH_3/Ne samples with a mole fraction of 0.125 marginally satisfy the assumption of this model. Results from numerical integration of Eq. (1) under different expansion conditions are compared in Table 1. It is interesting to find that the calculated maximum droplet sizes reasonably reproduce observed trends of variation in droplet sizes on changing the stagnation pressure and temperature. To visualize the relationship between the cluster sizes and the expansion conditions from the Weiel model, Eq. (1) can be rewritten in the following form

$$N(\delta)^{5/6} = A \int d\delta/\{[1 + 2.8284\delta\,\tan(\alpha)]$$

$$[1.333 + 1.886\delta\,\tan(\alpha) + 2.667\delta^2\,\tan^2(\alpha)]^{3/2}\} \quad (3)$$

with

$$A = 3.265 \times 10^6 DPx_i m_{gas}^{1/2} m_1^{1/6}\rho^{2/3}/T \qquad (4)$$

where P is the stagnation pressure, x_i is the mole fraction of the sample gas, ρ is the density of bulk liquid sample and T is the initial temperature. According to Eqs. (3) and (4) it is clear that increasing the stagnation pressure or lowering the initial temperature should favor the generation of larger clusters. This implication is consistent with our experimental results listed in Table 1 for samples with $x_i = 0.125$. Even for samples with much higher mole fraction the effects of stagnation pressure and initial temperature on the sizes of particles are still roughly predictable by Eq (1).

Weiel's development was based on a very dilute system. From Eq. (4) the particle size increases with increasing sample mole fractions. Most of the samples used in our experiments have very high mole fractions. For such samples our experiments show that under the same expansion conditions the particle size increases with decreasing mole fractions. From our experiences the particle size starts to reduce when the sample is diluted to a certain point.

Numerical integration of Eq. (1) indicates that particle size decreases with the increasing of angle α, the decreasing of throat diameter, or the shortening of nozzle length. In our present experiment we did not examine these factors but only tested the difference between a Laval nozzle and a tubular nozzle with similar throat diameter. It is clear from Table 1 that particles generated from the Laval nozzle are much larger than those from the tubular nozzle under the same expansion conditions. Similar results have been observed in much previous work.

The fact that Weiel's equations account in order of magnitude for our results as well as they do, and in such a simple way, makes the model deserve attention. The physical mechanism upon which Weiel's model is based is that in which particle growth and ultimate particle size depend on particle–particle collisions rather than condensation of monomers upon cold particles. The importance of such particle–particle collisions has been questioned [35]. Another concern is that the model assumptions essentially ignore the process of nucleation and monomer growth that has been the basis of virtually all prior treatments of the formation of particles in supersonic expansions. These treatments are also able account for large cluster size, but are far less elementary to apply. Moreover, in the case of solid particles, they imply that the particles tend to be single crystals rather than Weiel's aggregates of many crystalline domains. Experimental evidence to date for particles formed in supersonic expansions is that the single crystal domains observed are quite as large as the polycrystalline particles implied by Weiel's equations. Nevertheless, the success of these equations in accounting semiquantitatively for the present results for liquid ammonia cannot be disregarded.

References

[1] H. Gleiter, in N. Hansen et al. (eds.), *Deformation of Polycrystals: Mechanism and Microstructures*, Riso Natl. Lab., Roskilde. Denmark, 1981, p. 15.

[2] R. Birringer, H. Gleiter, H.P. Klein and P. Marquardt, *Phys. Lett.*, A102 (1984) 365.

[3] R.W. Siegel and H. Hahn, in M. Yussouff (ed.), *Current Trends in the Physics of Materials*, World Scientific, Singapore, 1987, p. 403.

[4] R.W. Siegel, S. Ramasamy, H. Hahn, Z. Li, T. Lu and R. Gronsky, *J. Mater. Res.*, 3 (1988) 1367.

[5] M.S. Dresselhaus, G. Dresselhaus and P.C. Eklund, *J. Mater. Res.*, *8* (1993) 2054.

[6] E.P. Giannelis et al., *Science*, *257* (1992) 219.

[7] M.S. Boldrick, E. Yang and C.N.J. Wagner, *J. Non-Cryst. Solids*, *150* (1992) 478.

[8] P. Matteazzi and G.L. Caer, *J. Am. Ceram. Soc.*, *75* (1992) 2749.

[9] R.S. Averback and H. Hahn, *J. Appl. Phys.*, *67* (1990) 1113.

[10] L. Kavan, T. Stoto, M. Gratzel, D. Fitzmarice and V. Shklover, *J. Phys. Chem.*, *97* (1993) 9493.

[11] M.L. Steigerwald et al., *J. Am. Chem. Soc.*, *110* (1988) 3046.

[12] Y. Nosaka et al., *Chem. Lett.*, *1988* (1988) 605.

[13] E.W. Becker, K. Bier and W. Henkes, *Z. Phys.*, *146* (1956) 333.

[14] O.F. Hagena, *Surf. Sci.*, *106* (1981) 101.

[15] M.M. Kappes, *Chem Rev.*, *88* (1988) 369.

[16] L.S. Bartell, *Chem Rev.*, *86* (1986) 491.

[17] L.S. Bartell, L. Harsanyi and E.J. Valente, *J. Phys. Chem.*, *93* (1989) 6201.

[18] Y. Wang and N. Herron, *J. Phys. Chem.*, *95* (1991) 525.

[19] R. Weiel, *Z. Phys.*, *D27* (1993) 89.

[20] O.F. Hagena, *Z. Phys.*, *D4* (1987) 291.

[21] L.S. Bartell, *J. Phys. Chem.*, *94* (1990) 5102.

[22] L.S. Bartell and R. French, *J. Rev. Sci. Instrum.*, *60* (1989) 1223.

[23] I. Olovsson and D.H. Templeton, *Acta Crystallogr.*, *12* (1959) 832; J.W. Reed and P.M. Harris, *J. Chem. Phys.*, *35* (1961) 1730; A. Hewat and A. Riekel, *Acta Crystallogr.*, *35* (1979) 569.

[24] R.F. Kruh and J.I. Petz, *J. Chem. Phys.*, *41* (1964) 890.

[25] A.H. Narten, *J. Chem. Phys.*, *49* (1968) 1692.

[26] L. Harsanyi, L.S. Bartell and E.J. Valente, *J. Phys. Chem.*, *92* (1988) 37.

[27] L.S. Bartell and R.A. Machonkin, *J. Phys. Chem.*, *94* (1990) 6468.

[28] L.S. Bartell, J.W. Hovick, T.S. Dibble, P.J. Lennon and L. Harsanyi, *J. Phys. Chem.*, *97* (1993) 230.

[29] J.E. Bertie, L.D. Calvert and E. Whalley, *J Chem. Phys.*, *38* (1963) 840.

[30] L.S. Bartell and J. Huang, *J. Phys. Chem.*, *98* (1994) 7455.

[31] J. Huang and L.S. Bartell, *J. Phys. Chem.*, in press.

[32] J. Huang and L.S. Bartell, *J. Phys. Chem.*, *98* (1994) 4543.

[33] G.D. Stein and J.A. Armstrong, *J. Chem. Phys.*, *58* (1973) 1999.

[34] G. Torchet, P. Schwartz, J. Farges, M.F. de Feraudy and B. Raoult, *J. Chem. Phys.*, *79* (1983) 6197.

[35] O.F. Hagena, Personal communication, Karlsruhe, May, 1983.

The synthesis of nanocrystalline nickel boride powders by ball milling of elemental components

A. Corrias, G. Ennas, G. Marongiu, A. Musinu, G. Paschina*, D. Zedda

Dipartimento di Scienze Chimiche, Università di Cagliari, Via Ospedale 72, I-09124 Cagliari, Italy

Abstract

Solid state reaction induced by ball milling the elemental components has been investigated on $Ni_{60}B_{40}$ and $Ni_{80}B_{20}$ mixtures by means of transmission electron microscopy, X-ray diffraction and differential scanning calorimetry. The time evolution of the reaction is similar in the two samples, although slower in $Ni_{80}B_{20}$. Reaction begins with the formation of o-Ni_3B and of a disordered phase. The final products are nanocrystalline o-Ni_3B and unreacted nickel in $Ni_{80}B_{20}$ and nanocrystalline t-Ni_2B in $Ni_{60}B_{40}$. Different milling conditions, tested on the $Ni_{60}B_{40}$ sample, do not modify the path but affect the rate of the solid state reaction.

Keywords: Synthesis; Nickel boride powders; Ball milling

1. Introduction

Mechanical alloying was applied for the first time to obtain dispersion strengthened Ni-based superalloys [1]. Since then it has widely been applied to the preparation of amorphous metal–metal and metal–metalloid alloys starting either from mixtures of elemental powders or from intermetallic compounds [2–5]. Recently the interest in this technique has been extended to the synthesis of nanocrystalline alloy powders [6–10].

It is well known that ball milling of elemental powders induces a solid state reaction (SSR) through the atomic mixing of the components. SSR may lead to crystalline or amorphous phases (or a mixture of the two), depending on the physical and chemical characteristics of the starting elements [11] and on the milling conditions [12]. Because of the continuous fragmentation of the materials due to the ball milling action, final products may frequently be nanoamorphous or nanocrystalline powders.

We have recently reported the results of ball milling of Co–B mixtures [13,14]. We have shown that SSR leads to an amorphous phase which partially trans-

forms to crystalline t-Co_2B with further milling. The SSR rate and the amount of the crystalline phase formation depend on both mixture composition and milling conditions.

We report herewith the results of a study on the SSR of Ni–B mixtures.

2. Experimental

Mixtures of face centred cubic (fcc) nickel (Johnson Matthey 99.9%) and rombohedral boron (Ventron 99.7%) powders of atomic compositions $Ni_{60}B_{40}$ and $Ni_{80}B_{20}$ were milled in a planetary Fritsch Pulverisette 5 ball mill. Amounts of 20 g were sealed in 250 cm^3 steel vials together with stainless steel balls in argon atmosphere.

Overheating was prevented by a cold air jet and alternate milling and rest periods at 5 min intervals. Full/void volume ratio and ball/powder weight ratio inside the vials were kept equal to 1/10 and 10/1 respectively. In order to investigate the different possible paths of solid state reaction, the milling process was carried out on the $Ni_{60}B_{40}$ sample under different milling intensities by changing the ball diameter and the rotation speed of the mill.

* Corresponding author.
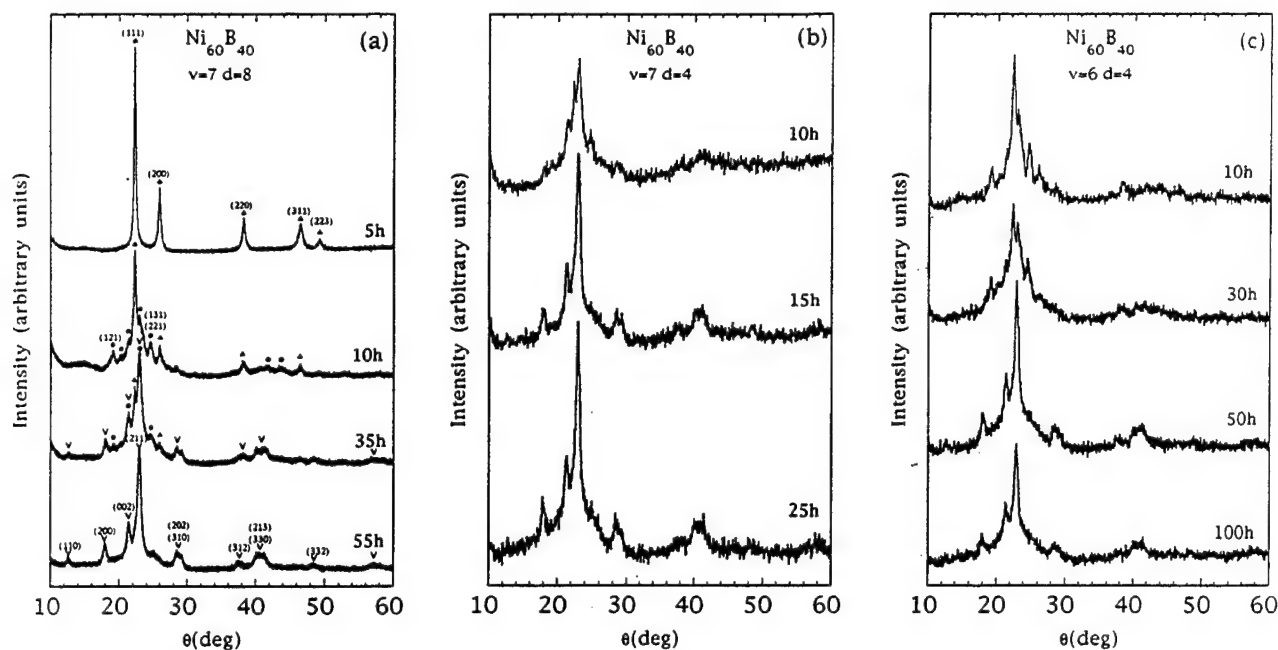
Fig. 1. XRD spectra of $Ni_{60}B_{40}$ at selected milling steps. (a) Milling speed 250 rpm ($v = 7$), ball diameter 8 mm ($d = 8$); (b) milling speed 250 rpm ($v = 7$), ball diameter 4 mm ($d = 4$); (c) milling speed 200 rpm ($v = 6$), ball diameter 4 mm ($d = 4$). ▲, fcc nickel; ●, o-Ni_3B; ∨, t-Ni_2B. Miller indexes are only reported for the most significant peaks.

X-ray diffraction (XRD), transmission electron microscopy (TEM) and differential scanning calorimetry (DSC) measurements were performed on small portions of the powders sampled at different milling times in argon atmosphere. XRD and TEM analyses were also carried out on thermally treated milled samples, rapidly cooled to room temperature after heating.

XRD spectra were recorded on a θ–θ Seifert diffractometer in the range $10° < \theta < 60°$ using Cu Kα radiation. TEM micrographs were taken on a JEOL 200CX microscope; powders were deposited on a carbon grid after being dispersed in octane. DSC measurements were carried out in a Perkin Elmer DSC-7 calorimeter with a heating rate of 10 °C min^{-1} in a inert atmosphere in the range from 20 to 580 °C and repeated after cooling down to room temperature in order to estimate DSC areas.

3. Results

3.1. XRD

Fig. 1(a) shows the diffraction spectra of the $Ni_{60}B_{40}$ sample at selected milling steps. Milling was performed at a speed of 250 rpm with balls of 8 mm diameter. The diffraction pattern after 5 h milling only shows the peaks of fcc nickel [15], although reduced in height and slightly broadened with respect to those of the unmilled mixture (not shown); boron peaks are not detectable because the scattering power of this element is much

lower than that of nickel. A significant change occurs after 10 h milling, when the peaks due to crystalline o-Ni_3B [16] and a broad halo centred at $\theta = 22°$ begin to appear. Crystalline nickel peaks, although further weakened, are still clearly evident. After 35 h milling the weakening of the (111) nickel peak is accompanied by the appearance of (110) and (200) t-Ni_2B peaks [17] and by an increase of the peak centred at $\theta = 22.9°$ where both (031) o-Ni_3B and (211) t-Ni_2B fall. The intensities of (121) and (131) o-Ni_3B peaks also suffer a significant reduction. They disappear after 55 h milling, when only peaks of the crystalline t-Ni_2B are present in the diffraction pattern.

Fig. 1(b,c) shows selected diffraction spectra of two $Ni_{60}B_{40}$ mixtures processed at different milling intensities. When the ball diameter is reduced to 4 mm the result after 15 h is very close to that previously reached after 55 h. Further milling, up to 25 h, does not cause any significant variation. When the mill rotation speed is reduced to 200 rpm, keeping the 4 mm balls, the time evolution of the diffraction spectra is close to that of Fig. 1(a).

Fig. 2 shows selected XRD spectra of an $Ni_{80}B_{20}$ sample milled under the same conditions used for $Ni_{60}B_{40}$, reported in Fig. 1(a). The spectra after 5 h milling are very similar in the two samples; then the behaviour of $Ni_{80}B_{20}$ begins to differentiate. The (121) and (131) peaks of crystalline o-Ni_3B appear only after 15 h when Ni peaks, although broadened, are still evident. o-Ni_3B peaks increase slowly with milling up to 45 h and are superimposed on a faint halo. Further

milling up to 75 h does not cause any appreciable variation in the XRD spectra. The presence of t-Ni_2B peaks has never been revealed.

3.2. TEM

The bright field micrograph of $Ni_{60}B_{40}$ after 5h milling (Fig. 3) shows a very broad crystallite size distribution; a similar situation occurs in $Ni_{80}B_{20}$. The dark field image obtained from the (022) spot of the [111] reciprocal lattice section of one particle is shown in Fig. 4; it reveals a layered structure with uniform layer thickness around 10 nm.

After 55 h crystallite size distribution is rather narrow and centred at 10 nm for $Ni_{60}B_{40}$ and 20 nm for $Ni_{80}B_{20}$ samples, as determined from TEM micrographs.

Fig. 3. Bright field image for $Ni_{60}B_{40}$ after 5 h milling ($v = 7$, $d = 8$).

3.3. DSC

DSC results of $Ni_{60}B_{40}$ and $Ni_{80}B_{20}$ samples at selected milling steps are shown in Fig. 5. Curves of both samples after 5 h milling exhibit an exothermic peak around 300 °C followed by a large band. In $Ni_{60}B_{40}$ a pronounced peak, superimposed on the band, is also present around 400 °C. The areas of the peaks and of the band decrease with milling and almost vanish at the final milling stages. Samples of the two mixtures at 5 h milling were thermally treated up to 310 °C and 580 °C and rapidly cooled to room temperature. XRD spectra of these samples are shown in Fig. 6. The XRD patterns of the samples heated up to 310 °C are very similar. They show peaks of o-Ni_3B accompanied by sharp Ni peaks. The XRD pattern of $Ni_{60}B_{40}$ heated up to 580 °C is dominated by the peaks of t-Ni_2B; peaks of o-Ni_4B_3 [18] are also present. On the other hand the XRD pattern of $Ni_{80}B_{20}$ heated up to 580 °C shows the peaks of o-Ni_3B and of metallic nickel.

Fig. 2. XRD spectra of $Ni_{80}B_{20}$ at selected milling steps. Milling speed 250 rpm ($v = 7$), ball diameter 8 mm ($d = 8$). ▲, fcc nickel; ●, o-Ni_3B. Miller indexes are only reported for the most significant peaks.
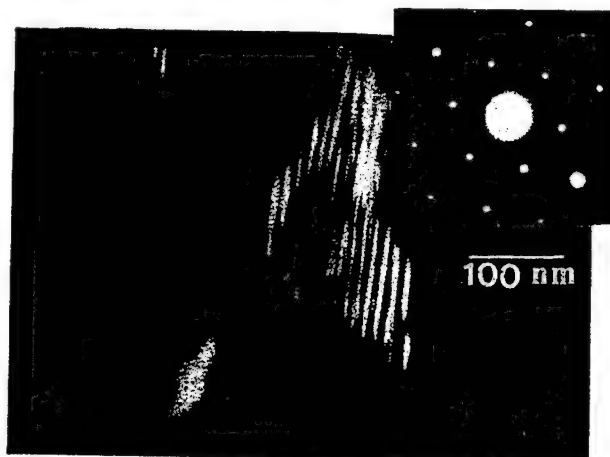
Fig. 4. Dark field image of a particle in $Ni_{60}B_{40}$ sample after 5 h milling, obtained from (0$\bar{2}$2) spot of the [111] reciprocal lattice section with its pertinent SAD.
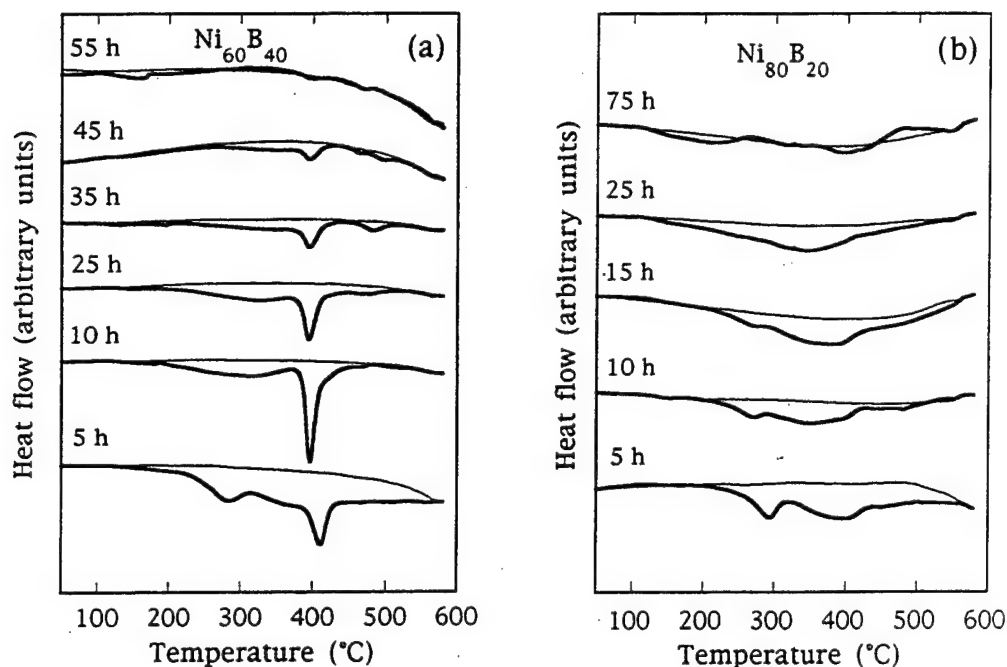
Fig. 5. DSC traces at selected milling steps for $Ni_{60}B_{40}$ (a) and for $Ni_{80}B_{20}$ (b) samples. Thicker lines correspond to first run, thinner ones to second run.

4. Discussion

The behaviour of the two mixtures at the beginning of the milling process seems to be independent of their stoichiometry, as suggested by the close resemblance of their XRD spectra and of their bright field micrographs after 5 h milling. During this interval the energy transfer from the balls to the powders leads to the formation of layered particles and to the grain size refinement of the metal crystallites, as shown by the TEM micrographs and by the peak broadening in XRD patterns. At this stage the elements have been brought into intimate contact and solid state reaction (SSR) begins to evolve with the formation of crystalline o-Ni_3B and a highly disordered phase. This fact is in agreement with the presence in DSC traces of the peak around 300 °C. This is due to the reaction of nickel and boron to give o-Ni_3B, as confirmed by XRD spectra of both samples after thermal treatment up to 310 °C (Fig. 6). The spectra of $Ni_{60}B_{40}$ and $Ni_{80}B_{20}$ compare with those of the milled samples in Fig. 1(a) at 10 h and in Fig. 2 at 15 h respectively; however, peaks are sharper because of the larger crystallite dimensions due to the increased diffusivity of the two elements with temperature.

The amounts of both crystalline and disordered phases keep increasing with milling until intermediate times and then the behaviour of the two mixtures begins to differentiate.

In $Ni_{60}B_{40}$ further milling leads to a decrease of the disordered material which feeds the formation of the crystalline phases. This growth is accompanied by a progressive transition from nickel rich o-Ni_3B to boron

richer t-Ni_2B, which is the final product of SSR after 55 milling hours (Fig. 1(a)). This evolution is evidenced by the trend of the area of the DSC peak around 400 °C, which is due to the formation of t-Ni_2B.

In $Ni_{80}B_{20}$ the reaction rate is slower, as shown by the fact that the o-Ni_3B peaks appear only after 15 h. Then the system reaches a steady state where crystalline o-Ni_3B, unreacted nickel and a disordered phase coexist in the mixture (Fig. 2).

The time evolution of SSR is also clearly evidenced by the trend of DSC traces with milling time. In both mixtures the areas of the peaks and the band have maximum values after 5 h milling, when the elements have been brought into intimate contact but they have not reacted yet. The areas decrease at longer times when milling induces the formation of the reaction products. DSC traces of the samples when the reaction has reached a steady state are almost flattened out since at this stage thermal treatment only induces the growth of the present crystallites.

The results of the three milling processes carried out on the $Ni_{60}B_{40}$ mixtures indicate that the different energy conditions affect the reaction rate but not its path. The reduction of ball size and the increase of their number significantly accelerate the reaction. This is due to the higher frequency of ball collisions with each other and with the vial walls, although the energy transfer at each hit is reduced because of the lower values of ball free path and of their momentum. In a previous work [13,14], Co–B mixtures were milled under the strongest energetic conditions used in this study. In that case a complete amorphization of the $Co_{60}B_{40}$
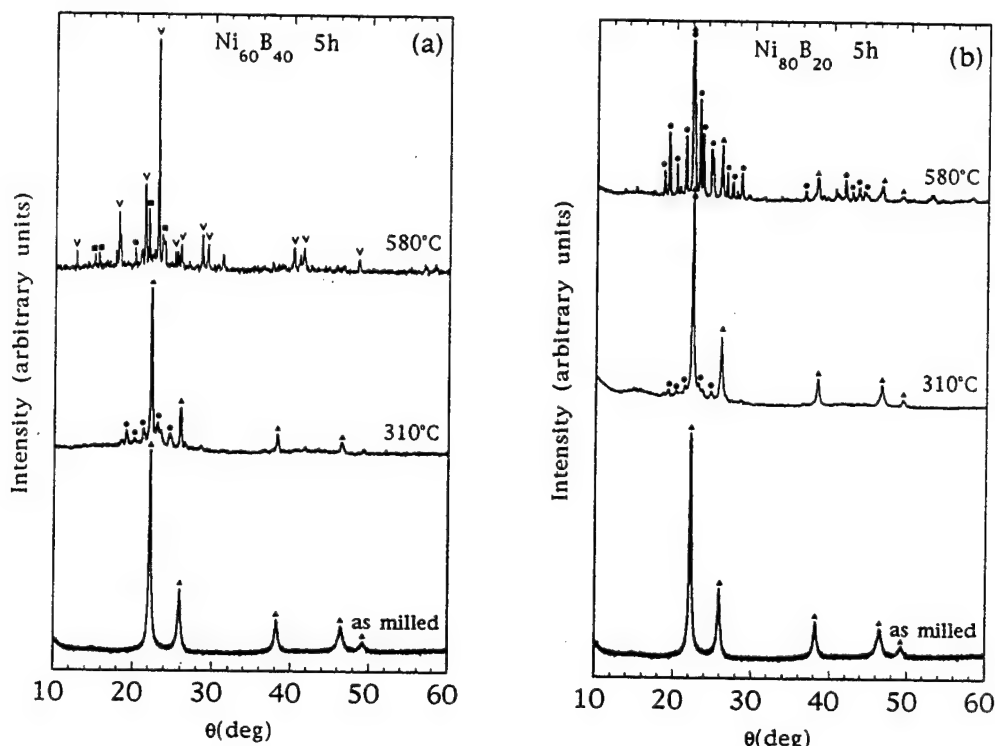
Fig. 6. XRD spectra of 5 h milled $Ni_{60}B_{40}$ (a) and $Ni_{80}B_{20}$ (b) samples after thermal treatment to 310 °C and 580 °C. ▲, fcc nickel; ●, o-Ni_3B; ∨, t-Ni_2B; ■, o-Ni_4B_3.

sample was reached without the formation of crystalline boride phases. These formed only after further milling probably because of their high activation energy. By contrast, in Ni–B mixtures, SSR occurs even under the mildest energetic conditions and o-Ni_3B is the first product that is formed under all the tested milling conditions. This phase is thermodynamically favoured among the nickel borides because its formation enthalpy (ΔH_f) is the most negative [19]. The fact that o-Ni_3B is also the compound with the lowest boron content suggests that SSR proceeds through the continuous diffusion of boron atoms into the nickel lattice, which is repeatedly distorted and made highly defective by milling.

The final product in the $Ni_{60}B_{40}$ sample is t-Ni_2B, which has a stoichiometry close to the starting mixture. The thermal treatment of this sample also leads to the formation of o-Ni_4B_3, which has never been identified among the milling products. o-Ni_4B_3 has a more negative ΔH_f than that of t-Ni_2B but, since o-Ni_4B_3 has a higher boron content, it needs a large diffusion of boron in the nickel lattice that can only be reached by thermal treatment.

5. Conclusions

Ball milling of elemental nickel and boron powders yields nanocrystalline o-Ni_3B and t-Ni_2B depending on mixture composition. o-Ni_3B, which always forms at the beginning of the solid state reaction, is the final product in the $Ni_{80}B_{20}$ mixture. In $Ni_{60}B_{40}$ the solid state reaction evolves to t-Ni_2B, whose composition is close to that of the starting mixture.

At the end of milling process the crystallite sizes are in the nanometric range in both systems.

Acknowledgements

References

[1] J.S. Benjamin, *Metall. Trans.*, *1* (1970) 2943.
[2] C.C. Koch, in R.W. Cahn, P. Haansen and E.J. Kramer (eds.), *Materials Science and Technology: A Comprehensive Treatment*. Vol. 15, VCH, Weinheim, Germany, 1991, pp. 194–245.
[3] E. Arzt and L. Schultz (eds.), *New Materials by Mechanical Alloying Techniques*, DGM Informationsgeselschaft, Oberursel, Germany, 1988.
[4] A.R. Yavari and P.J. Desré (eds.), *Multilayer Amorphisation by Solid State Reaction and Mechanical Alloying*, Les Editions de Physique, Les Ulis, France, 1990.
[5] J.J. deBarbadillo, F.H. Froes and R. Schwartz (eds.), *Mechanical Alloying for Structural Applications*, ASM International, Material Park, Ohio, 1993.

[6] E. Hellstern, H.J. Fecht, Z. Fu and W.L. Johnson, *J. Appl. Phys.*, *65* (1989) 305.

[7] J.S.C. Jang and C.C. Koch, *J. Mater. Res.*, *5* (1990) 498.

[8] C.C. Koch and Y.S. Cho, *Nanostruct. Mater.*, *1* (1992) 207.

[9] E. Gaffet and M. Harmelin, *J. Less-Common Met.*, *157* (1990) 210.

[10] J. Eckert, J.C. Holzer, C.E. Krill, III and W.L. Johnson, *J. Mater. Res.*, *7* (1992) 1751.

[11] R.B. Schwarz, R.R. Petrich and C.K. Saw, *J. Non-Cryst. Solids*, *76* (1985) 281.

[12] N. Burgio, A. Iasonna, M. Magini, S. Martelli and F. Padella, *Nuovo Cimento*, *13* (1991) 459.

[13] A. Corrias, G. Ennas, G. Marongiu and G. Paschina, *J. Mater. Sci.*, *26* (1991) 5081.

[14] A. Corrias, G. Ennas, G. Marongiu, A. Musinu and G. Paschina, *J. Non-Cryst. Solids*, *163* (1993) 35.

[15] PDF card 4-850, Int. Center for Diffraction Data, 1601 Park Lane, Swarthmore, PA.

[16] PDF card 19-834, Int. Center for Diffraction Data, 1601 Park Lane, Swarthmore, PA.

[17] PDF card 25-576, Int. Center for Diffraction Data, 1601 Park Lane, Swarthmore,. PA.

[18] PDF card 12-417, Int. Center for Diffraction Data, 1601 Park Lane, Swarthmore, PA.

[19] O. Teppo and P. Taskinen, *Mater. Sci. Technol.*, *9* (1993) 205.

Synthesis of nanocrystalline Fe–13at.%B–7at.%Si by mechanical alloying

Robert J. Perez, Benlih Huang, Paula J. Crawford, Adel A. Sharif, Enrique J. Lavernia

Department of Chemical Engineering and Materials Science, University of California-Irvine, Irvine, CA 92717-2575, USA

Abstract

The synthesis of nanocrystalline Fe–13at.%B–7at.%Si using mechanical alloying of elemental powders in a SPEX mill was investigated. Precise lattice parameter measurements provide insight into the dissolution of Si and B in the nanocrystalline Fe lattice. These data indicate that the complete dissolution of Si in the crystalline Fe matrix required 128 h milling. Only 35% of the total B content was estimated to be in solution after 128 h. Debris from vial and ball wear after this extended milling, however, is found to represent over 35 wt.% of the final composition, and to produce an increase in lattice parameter of approximately 3.7×10^{-7} nm per hour of milling. In addition, the present results indicate that the disappearance of Si peaks in the X-ray diffraction spectra may be related more directly to the low atomic scattering factor of Si than to its dissolution in Fe.

Keywords: Synthesis; Mechanical alloying; Milling

1. Introduction

Mechanical alloying is a technique by which novel materials may be synthesized from elemental or pre-alloyed powders via a high energy ball milling process. Although originally utilized for the synthesis of oxide dispersion strengthened materials [1], mechanical alloying has recently been reported to be capable of producing alloys, intermetallic compounds, and amorphous materials [2–4].

Alloys based on the Fe–B–Si system originally attracted attention owing to the useful magnetic properties obtained when they were quenched to an amorphous state using melt-spinning. Subsequently, some efforts were made to synthesize amorphous Fe–B–Si from elemental powders using ball milling [5–7]. From these studies, it was concluded that ball milling produced either no [5] or only partial [6,7] transformation to the amorphous state in this alloy system. Recent work, however, has demonstrated that outstanding magnetic properties may be obtained in nanocrystalline Fe–B–Si based alloys obtained through annealing of the amorphous phase [8]. This suggests that ball milled Fe–B–Si, although not fully amorphous, may prove useful. As a result, determination of the extent to which

B and Si are incorporated in the Fe crystallites during ball milling is of interest. One means of obtaining this information is through the use of precise lattice parameter measurements. The aim of the present work is to study the dissolution of B and Si in nanocrystalline Fe during mechanical alloying, and to provide insight regarding the effect of vial and ball contamination on the milled material. Finally, the significance of the disappearance of X-ray diffraction peaks, a phenomenon frequently assumed to indicate alloying is discussed.

2. Experimental

Powders of Fe (99.9 + %, below 75 µm), B (99.7%, below 250 µm) and Si (99.9%, below 150 µm) were milled in a SPEX model 8000D shaker mill. Each of the two 440C stainless steel vials contained two 12.7 mm diameter and four 6.35 mm diameter 440C balls. Each vial was loaded with a charge of the Fe–13.at.%B–7at.%Si elemental powder mixture sufficient to create a 5:1 ratio of ball to powder mass, and was sealed in a glovebox under an argon atmosphere. Scanning electron microscopy (SEM) was performed using a Hitachi

S-500 at 20 kV on powder specimens mounted in cross-section, polished and etched using a 10% Nital solution. Electron probe microanalysis (EPMA) results were obtained using a JEOL Superprobe 733 configured for wavelength spectrometry.

X-ray diffraction analysis was performed using Cu $K\alpha$ radiation in a Siemens D5000 diffractometer equipped with a graphite monochromator. The resultant diffraction spectra were corrected for $K\alpha_2$ effects prior to the collection of peak location and full width at half-maximum (FWHM) data using a Siemens peak-fitting algorithm. Following instrumental broadening correction, the FWHM data were separated into broadening components attributed to fine crystallite size and to plastic strain using a simplified Warren–Averbach approach employed by Fecht et al. [9]. This method utilized the least squares fit obtained from a plot of Δs vs. s, where $s = (2 \sin \theta)/\lambda$, $\Delta s = (\Delta \theta \cos \theta)/\lambda$, λ (nm) is the X-ray wavelength, while θ and $\Delta\theta$ are the Bragg angle and the corresponding FWHM of each peak respectively. The average crystallite size d (nm) was calculated using the Scherrer equation,

$$d = 0.92/\Delta s'$$

where $\Delta s'$ represents Δs at $(2 \sin \theta)/\lambda = 0$. For each milled powder sample, lattice parameter values were calculated from the high angle peak positions and were plotted as a function of $\cos^2 \theta/\sin \theta$. Subsequent linear regression and extrapolation to $\cos^2\theta/\sin\theta = 0$ produced a single lattice parameter value, effectively corrected for systematic error due to displacement of the powder sample from the diffractometer axis [10].

3. Results

X-ray diffraction analysis of the Fe–13at.%B–7at.%Si elemental powder blend, prior to milling, produced characteristic Fe and Si peaks, as shown in Fig.

Fig. 2. Crystallite size versus milling time of ball milled Fe–B–Si mixture.

1. No peaks representative of B were detected, owing to the low atomic scattering factor of B. As the milling process proceeded, evidence of continuous refinement of the microstructure with increasing milling time was provided by the increasing breadth of the X-ray diffraction peaks. Only 0.5 h milling was required to reduce the Fe crystallite size to below 90 nm and to produce the complete disappearance of the Si peaks from the X-ray spectra, leaving only those associated with Fe. Following a rapid decrease during the first 30 h milling, the crystallite size reached a minimum value of approximately 12 nm. This was maintained up to the maximum milling duration of 256 h, as shown in Fig. 2.

Although X-ray diffraction results exhibited only Fe peaks in the spectra after 0.5 h milling, EPMA analysis revealed that B and Si were inhomogeneously distributed throughout the Fe matrix, as shown in Figs. 3 and 4 respectively. The individual B fragments were

Fig. 1. X-ray diffraction of the Fe–B–Si elemental mixture after ball milling for 0, 0.5, 64 and 256 h.
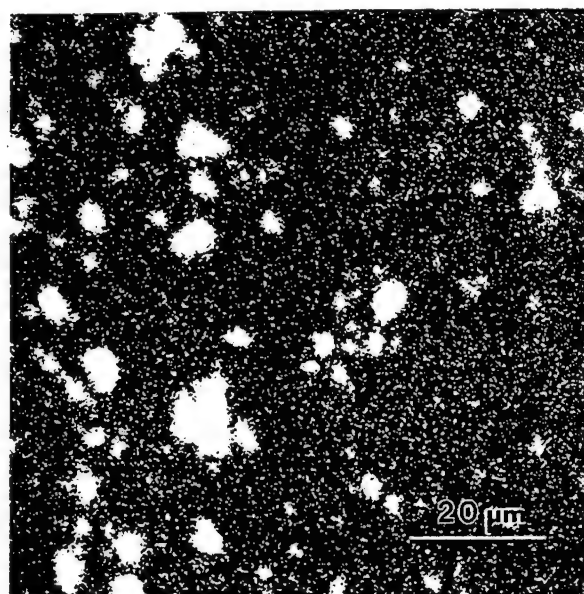
Fig. 3. B map of a Fe–B–Si powder particle after 0.5 h milling. Light areas represent B.
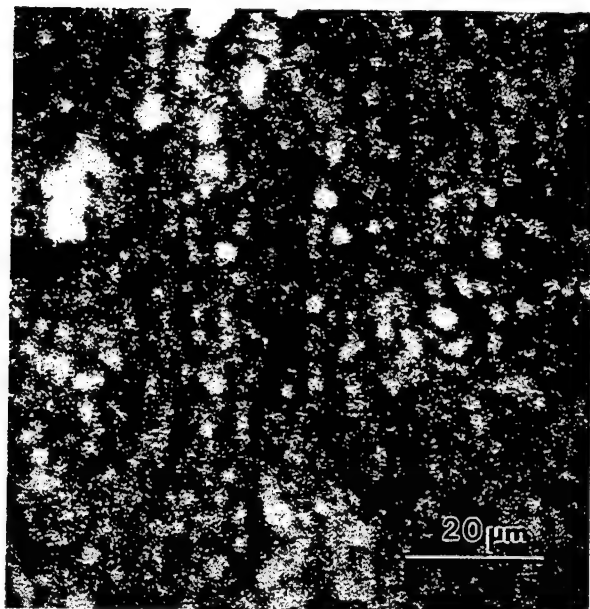
Fig. 4. Si map of a Fe–B–Si powder particle after 0.5 h milling. Light areas represent Si.

Fig. 6. B map of a Fe–B–Si powder particle after 64 h milling. Light areas represent B.

observed to decrease in size from 2–10 μm after 0.5 h milling to less than 4 μm after 64 h. These were clearly resolved by secondary electron SEM imaging, Fig. 5, as well as EPMA mapping, Fig. 6. In comparison, the Si was more rapidly dispersed in the Fe matrix, resulting in a distribution which, to the limit of EPMA resolution, appeared essentially homogeneous after 64 h milling. A similarly homogeneous distribution of B was observed by EPMA in powders milled for 256 h.

Precise lattice parameter measurements were performed on the milled Fe–B–Si mixture using the Fe diffraction peak positions. The resultant data, given in

Fig. 7, are accompanied by additional lattice parameter values obtained by milling pure Fe under identical conditions. From published lattice parameter data from quenched Fe–Si and Fe–B alloys, it is apparent that significant reductions are associated with dissolution of either Si or B in Fe [11,12]. For example, the addition of 7 at.% Si to Fe prior to quenching is reported to result in a lattice parameter reduction of 0.0005 nm over that of unalloyed Fe [12]. In light of this finding, it may be proposed that the surprising increase in lattice parameter observed after 256 h milling may be related primarily to the effect of contamination, as estimated from the milled Fe. This hypothesis is supported by measurements of the weight loss experienced by the milling balls and container following extended milling. Typical values, given in Table 1, indicate that

Fig. 5. Secondary electron SEM image of Fe–B–Si powders milled for 0.5 h. Arrows indicate B particles.
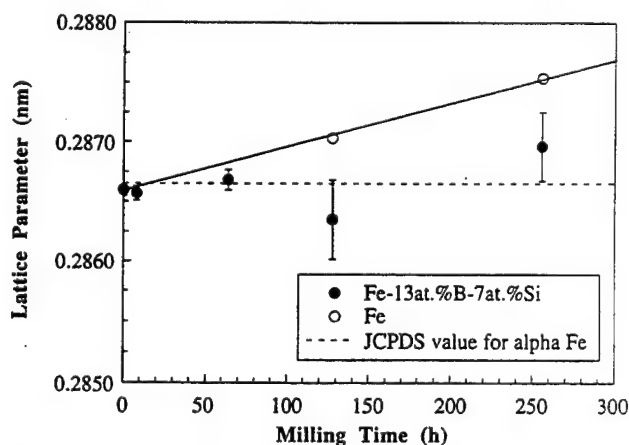
Fig. 7. Lattice parameter of milled Fe–B–Si and Fe versus milling time. The linear fit of the Fe data allows the effect of contamination with milling time to be approximated.

Table 1
Effect of vial and ball contamination on the composition and lattice parameter of milled Fe

Milling time (h)	Contamination (wt.% of final composition)	Lattice parameter (nm)
0	0	0.2866
128	38	0.2870
256	45	0.2875

the amount of wear debris generated over the course of a 128 h experiment was sufficient to make up approximately 38 wt.% of the final composition. By treating the resultant lattice expansion as a linear trend, as indicated by the solid line in Fig. 7, the lattice expansion due to contamination was estimated to occur at a rate of 3.7×10^{-6} nm per hour of milling time.

4. Discussion

4.1. Contamination due to wear debris

In this study, the effect of vial and ball wear debris on the Fe–B–Si lattice parameter, as estimated by milling pure Fe, was significant. Although the effect of contamination has been directly addressed in the case of some ball milled alloy systems [13,14], it is not typically considered in detail. Under the present experimental conditions, however, it is apparent that the effect of contamination may be large enough to overshadow the effect of Si or B dissolution on the lattice parameter. Although extended periods of high energy milling are frequently utilized in reasearch studies, it would appear that in the case of SPEX milling of Fe, greater than 64 h may be unacceptable for most practical purposes.

It has been proposed that one source of lattice expansion in milled Fe-alloy may be due to the refinement of crystalline grains [2]. From Figs. 2 and 7, however, it is apparent that although the grain size decreased rapidly during the initial 50 h milling, there was little significant change in lattice parameter. This implies that the effect of grain size reduction on the lattice parameter was negligible when compared with the effect of the dissolution of the milling debris in the Fe particles.

In order to separate the effects of the contamination from those of B and Si dissolution, it may be speculated that their respective contributions are superimposed, thereby allowing the effect of milling contamination to be eliminated through subtraction of an appropriate value. As a result, using the linear fit of milled Fe in Fig. 7, a set of "corrected" lattice parameter values have been calculated, as in Fig. 8. These corrected values, taken to represent only the effects of B and Si

dissolution, form the foundation for the following discussion.

4.2. Formation of Solid Solution

The corrected lattice parameter data presented in Fig. 8 suggest that the dissolution of Si and B in the matrix was only partially complete after 64 h milling, and had reached a steady state limit after 128 h milling, which was thereafter maintained up to 256 h. These observations agree with those obtained using EPMA. For example, after 64 h milling, B fragments of up to 4 μm in size were present in the milled powders, as shown in Fig. 6. EPMA mapping after 256 h, however, indicated a homogéneous distribution.

In order to separate the effects of Si from those of B on the Fe lattice parameter, experiments were performed on Fe–B and Fe–Si mixtures under identical milling conditions for 128 h, as indicated in Fig. 8. The degree of Si dissolution may be estimated quantitatively from studies performed on rapidly quenched Fe–Si alloys [11,12] which indicated a decrease in the Fe lattice parameter of approximately 0.000065 nm per atomic per cent Si in solution [12]. In the present study, the average lattice parameter after 128 h milling thereby represents 5 at.% Si in solution in Fe. Taking into account the additional Fe incurred owing to wear debris, this represents over 75% of the initial quantity of Si. Similarly, the lattice parameter obtained for milled Fe–B was estimated to represent 4 at.% B in solution, based on data for quenched Fe–B alloys [11]. This indicates dissolution of only 35% of the total amount of B present. These values suggest that 128 h milling produced essentially complete dissolution of Si in the Fe lattice, but only partial dissolution of B.
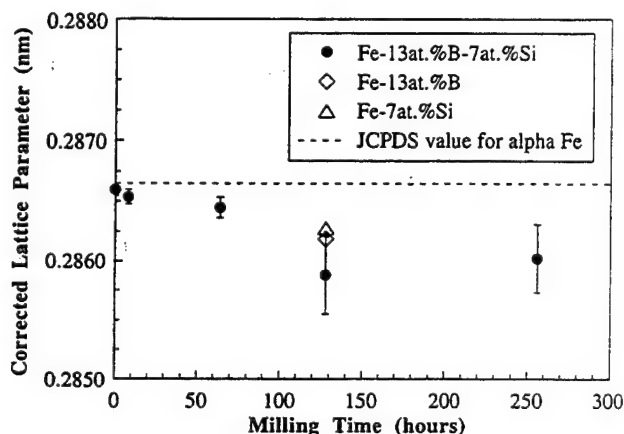
Fig. 8. Corrected Fe lattice parameter values obtained by subtracting the corresponding lattice expansion observed in milled Fe (see solid line, Fig. 7). This offers an idealized set of values in the absence of vial and ball contamination. Fe–B and Fe–Si error bars have been omitted for clarity, but are comparable in magnitude to that of Fe–B–Si at 128 h.

4.3. Disappearance of Si peaks in the X-ray diffraction spectra

It is evident from data presented in this study that the disappearance of the Si peaks in the X-ray diffraction spectra did not correspond to the complete dissolution of Si in Fe. Specifically, from Fig. 1, it is apparent that the X-ray diffraction peaks due to crystalline Si were no longer detectable after 0.5 h milling. From the corresponding EPMA map in Fig. 4, however it is observed that the Si was inhomogeneously distributed in regions of high concentration, typically of 10 µm or less in size. Furthermore, lattice parameter data from Fig. 8 indicate no detectable reduction, and therefore, no significant dissolution of Si after 0.5 h milling. This observation is significant owing to the fact that the disappearance of X-ray diffraction peaks corresponding to one constituent is often taken as primary evidence of the dissolution of that element. The present experimental results demonstrate that this is not reliable in the case of Si in Fe.

This is in agreement with more general observations drawn by Huang et al. [15]. In this work, examination of eleven equiatomic binary alloy systems indicate a consistent trend that the element with the higher atomic number persists in the X-ray spectra following milling, while the other does not. This was attributed primarily to the direct proportionality between atomic number and atomic scattering factor [15]. This led to the conclusion that the disappearance of peaks in the X-ray spectrum of mechanically alloyed powders is related more directly to the atomic scattering factor than to the actual dissolution of the element.

5. Conclusions

In summary, it was observed, first, that an Fe–13.%B–7at.%Si elemental powder mixture required nearly 128 h milling in a SPEX shaker mill in order to obtain a steady state concentration of B and Si in solution. Lattice parameter measurements indicated nearly complete (greater than 75%) dissolution of Si and only partial (approximately 35%) dissolution of B after 128 h. These values remained essentially constant up to 256 h milling.

Second, the effect of contamination due to vial and ball wear was significant. After 128 h milling the quantity of wear was sufficient to represent over 35 wt.% of the final powder composition. It appears that this debris combined with the starting powder so as to produce a 3.7×10^{-7} nm increase in lattice parameter per hour of milling time.

Third, the disappearance of the Si peaks from the X-ray diffraction spectra did not correspond to the complete dissolution of Si in Fe. Instead, this phenomenon may be related to the low atomic scattering factor of Si and the formation of a sub-micrometer structure of Si in the Fe matrix.

Acknowledgements

References

[1] J.S. Benjamin, in P.H. Shingu (ed.), *Mechanical Alloying*, Trans Tech, Aedermannsdorf, 1992, pp. 1–18.
[2] E. Gaffet, N. Malhouroux and M. Abdellaoui, *J. Alloys Comp.*, *194* (1993) 339–360.
[3] C.C. Koch, *Annu. Rev. Mater. Sci.*, *19* (1989) 121–143.
[4] C.C. Koch, *Nanostruct. Mater.*, *2* (1993) 109–129.
[5] L. Schultz, E. Hellstern and G. Zorn, *Z. Phys. Chem.*, *157* (1988) 203–208.
[6] S. Suriñach, M.D. Baró, J. Segura, M.T. Clabaguera-Mora and N. Clavaguera, *Mater. Sci. Eng.*, *A*134 (1991) 1368–1371.
[7] H. Okumura, K.N. Ishihara, P.H. Shingu, H.S. Park and S. Nasu, *J. Mater. Sci.*, *27* (1992) 153–160.
[8] Y. Yoshizawa and K. Yamauchi, Mater. Sci. Eng., *A133* (1991) 176–179.
[9] H.J. Fecht, E. Hellstern, Z. Fu and W.L. Johnson, *Metall. Trans. A21* (1990) 2333–2337.
[10] B.D. Cullity, *Elements of X-Ray Diffraction*, Addison-Wesley, Reading, MA, 1978, p. 359.
[11] W.B. Pearson, *A Handbook of Lattice Spacings and Structures of Metals and Alloys* Pergamon, Oxford, 1967, pp. 935, 1300.
[12] M.J. Tenwick and H.A. Davies, *Int. J. Rapid Solidif.*, *1* (1984–1985) 143–155.
[13] T.H. Courtney and Z. Wang, *Scr. Metall.*, *27* (1992) 777–782.
[14] N. Merk and L.E. Tanner, *Scr. Metall.*, *24* (1990) 309–313.
[15] B.-L. Huang, R.J. Perez, E.J. Lavernia and M.J. Luton, *Nanostruct. Mater.*, *5* (1995) in press.

Electronic and vibrational properties of Rb-intercalated MoS$_2$ nanoparticles

S. Bandow[a], Y. Maruyama[a], X.-X. Bi[b], R. Ochoa[c], J.M. Holden[c], W.-T. Lee[c], P.C. Eklund[c]

[a]*Institute for Molecular Science, Myodaiji, Okazaki 444, Japan*
[b]*Department of Electrical Engineering and Computer Science, MIT, Massachusetts Ave., Cambridge, MA 02139, USA*
[c]*Department of Physics and Astronomy and Center for Applied Energy Research, University of Kentucky, Lexington, KY 40506, USA*

Abstract

Nanoplatelets (diameter about 8 nm) synthesized by laser pyrolysis and bulk powder of MoS$_2$ have been intercalated with Rb to establish the metallic state. The properties of these powders are investigated by Raman scattering, X-ray diffraction, transmission electron microscopy and electron spin resonance (ESR). With increasing time of Rb intercalation the Raman-active interlayer A$_{1g}$ mode is observed to *red shift* in the nanoplatelet sample and *blue shift* in the micron-size bulk powder sample. In both samples the Rb doping eventually induces a metallic state and the Raman signal is lost. A broad ESR line was detected for the Rb-saturated MoS$_2$ bulk powder sample, also indicating the metallic character. Owing to the small particle size of the nanoplatelets, no broad line ESR signal was observed for the intercalated nanoplatelets. A low field (ESR) signal was used to search for superconductivity and a $T_c = 6.4$ K was observed in the bulk, in good agreement with the literature. However, no superconductivity down to 3.5 K was observed in the nanoplatelet sample.

Keywords: Electronic properties; Vibrational properties; Laser pyrolysis

1. Introduction

In this paper we discuss preliminary results of electron spin resonance and Raman studies of the effect of Rb intercalation on small (about 5 nm) "nanoplatelets" of MoS$_2$ produced by CO$_2$ laser pyrolysis [1]. The intercalation compounds M$_x$MoS$_2$, where M is an alkali metal or an alkaline earth, have been studied in detail in the bulk phase [2–4]. The purpose of our investigation is to search for interesting size-related effects in the electronic and vibrational properties of these intercalation compounds. Interplanar forces between adjacent MoS$_2$ layers (Fig. 1) have been shown to be sufficiently weak to allow the insertion or intercalation of ions (M$^+$) in the van der Waals gap between host layers. All such gaps are filled in the so-called "stage 1 compound" and $x \approx 0.3$–0.4, depending on the size of the intercalate species. Electrons are donated from the M intercalate layers to conduction band states associated with the MoS$_2$ layers, transforming the material from a semiconducting to a metallic system.

Furthermore, superconductivity has been observed in the M$_x$MoS$_2$ compounds for M$_x(T_c) \equiv$ Na$_x$(3.6 K), Ca$_x$(4.0 K), Sr$_x$(5.6 K), K$_{0.4}$(6.9 K), Rb$_{0.3}$(6.9 K) and Cs$_{0.3}$(6.9 K) [2], where T_c is the transition temperature.

2. Experimental details

Ultrafine MoS$_2$ particles were synthesized by the CO$_2$ laser pyrolysis (LP) method invented by Haggerty and coworkers in 1981 [5]. For comparison studies, bulk crystalline 2H-MoS$_2$ powder (diameter greater than 1 μm) was obtained from Aldrich (99%). Recently we have shown that LP is a versatile technique for the preparation of nanoparticles, producing a variety of binary transition metal sulfides, carbides, oxides and nitrides from a mixture of a metal carbonyl and a second reactant gas such as H$_2$S, C$_2$H$_4$, O$_2$ or NH$_3$.

The MoS$_2$ nanoparticles were produced in the LP apparatus using a mixture of an Mo carbonyl (Mo(CO)$_6$) and H$_2$S in the reactant gas steam. In
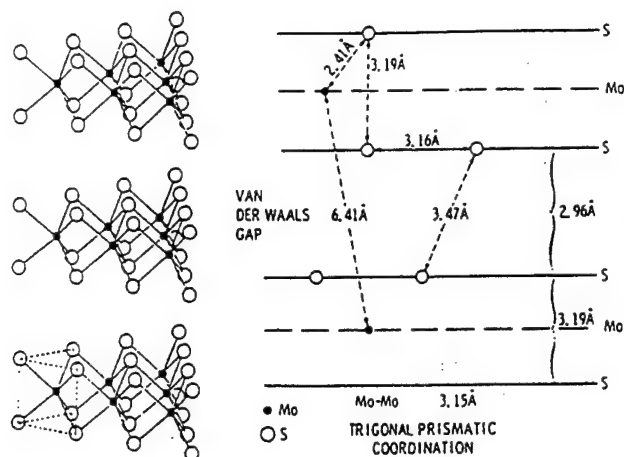
Fig. 1. Crystal structure of pristine MoS_2. (From Ref. [2].)

Fig. 2. Transmission electron micrograph of MoS_2 nanoparticles.

addition to these gases, C_2H_4 was added as an absorber for CO_2 radiation, thereby coupling the laser beam energy into the reaction. The reactant gases flow vertically upward out of a small stainless steel nozzle and are intersected by the horizontal laser beam, decomposing the carbonyl to Mo and CO. The Mo then reacts rapidly with the H_2S to nucleate and form MoS_2

nanoparticles which drift upward and out of the laser-heated region in about 1 ms, thereby terminating the particle growth at an effective diameter of about 8 nm.

Rb intercalation was accomplished by exposing the MoS_2 to hot Rb vapor in an evacuated (5 mm diameter) quartz tube. Bulk or ultrafine MoS_2 powder was
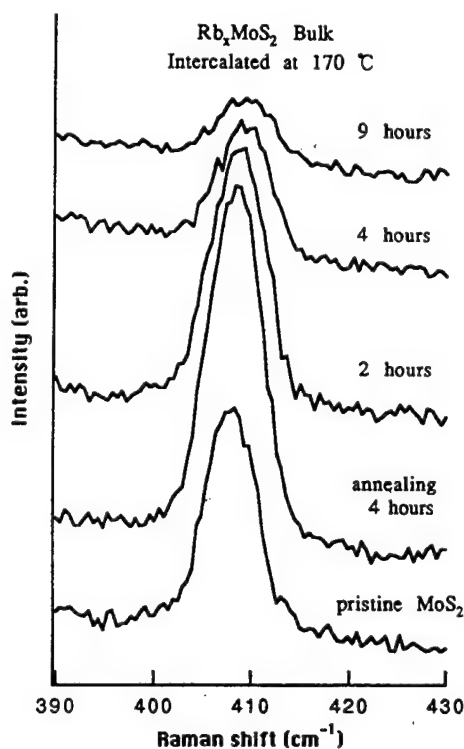
(a)
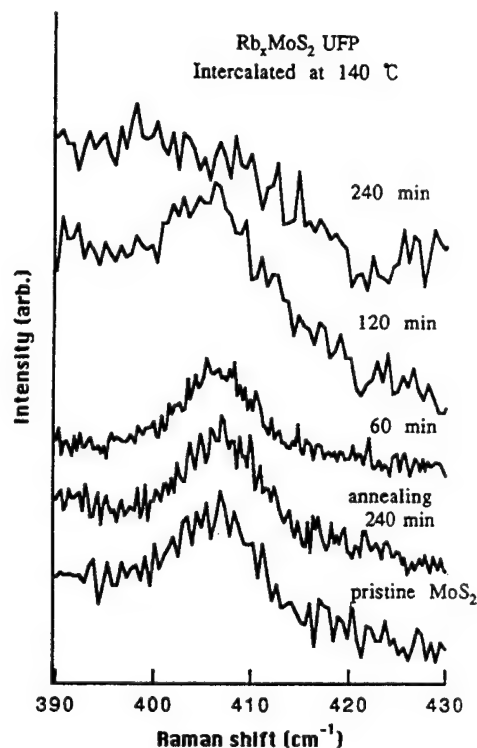
(b)

Fig. 3. Time evolution of Raman-active A_{1g} mode of MoS_2 with increasing Rb intercalation for (a) bulk and (b) UFP Rb_xMoS_2 samples respectively. In both (a) and (b) the label "annealing" should be taken to indicate that the sample was heated without being exposed to Rb vapor. A blue shift and a red shift of the Raman peak are observed for bulk and UFP samples respectively. The disappearance of the Raman band with increasing intercalation is evidence for the Rb-induced donation of conduction electrons to Mo-derived bands.
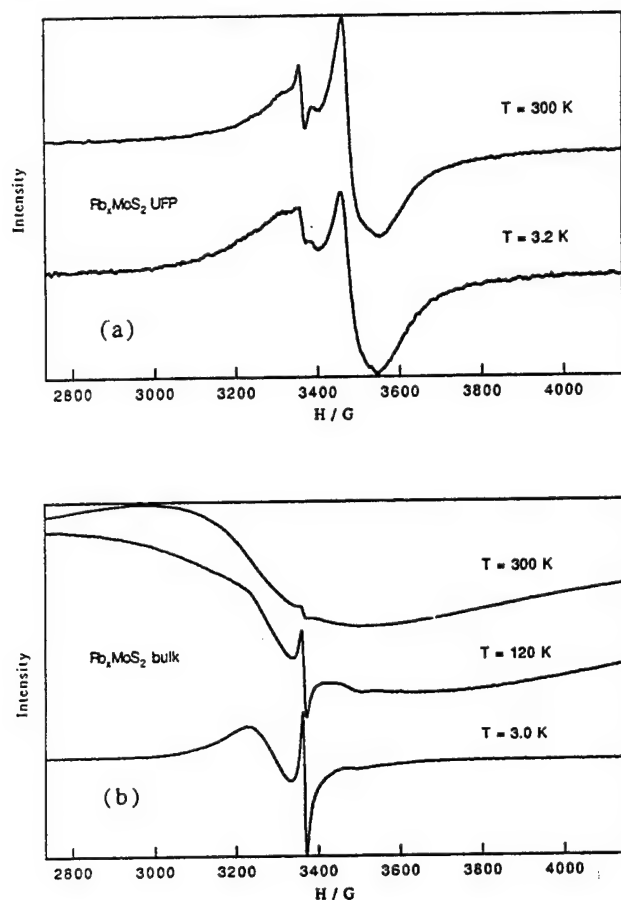
Fig. 4. ESR spectra from Rb-saturated MoS$_2$: (a) UFP sample; (b) bulk sample.

put at one end of the quartz ampoule and Rb at the other end. Intercalation was conducted in an isothermal environment at $T = 140$ °C (sample S # 140) and $T = 170$ °C (sample S # 170). The ampoule was removed from the oven at various times during the intercalation process and Raman scattering spectra were then collected at $T \approx 24$ °C using an Ar ion laser (488.0 and 514.5 nm). Electron spin resonance experiments were carried out on the Rb-saturated samples as a function of T in a Bruker ESP300E spectrometer operated at X band (9.4 GHz) with a magnetic field modulation frequency of 100 kHz.

3. Results and discussion

3.1. Transmission electron microscopy and X-ray diffraction

Transmission electron microscopy (TEM) and X-ray diffraction (XRD) were used to investigate the crystallinity and size distribution of the nanoparticles. A lattice image of the MoS$_2$ particles taken using a Phillips EM400 transmission electron microscope

(TEM) is shown in Fig. 2. The ultrafine particles (UFPs) have agglomerated to form a chain-like structure on the microscope grid and the image shows clearly the layer structure of the particles. Note that several of the particles appear to have curved or bend layers, which is expected to decouple the layers to some extent. Stacking faults are also evident in the figure. The XRD data exhibited broad diffraction lines consistent with the small particle size observed in the TEM (about 8 nm).

3.2. Raman scattering

MoS$_2$ in the 2H (hexagonal) phase exhibits four Raman-active modes: $A_{1g} + E_{1g} + 2E_{2g}$ [3]. The low frequency $E_{2g}(2)$ mode is the shear mode between weakly coupled MoS$_2$ layers and was observed at 32 cm^{-1} [2]. At higher frequency, two intralayer modes are observed, $E_{2g}(1)$ at 383 cm^{-1} and E_{1g} at 286 cm^{-1}, and also one interlayer mode, A_{1g}, is observed at 407 cm^{-1}. The Raman spectrum of the host MoS$_2$ nanoparticles revealed the two highest frequency modes at about 382 cm^{-1} ($E_{2g}(1)$, weak) and 407 cm^{-1} (A_{1g}, strong). Thus these mode frequencies are in very good agreement with observations in bulk MoS$_2$. In the bulk MoS$_2$ we obtained the value of 408 cm^{-1} for the A_{1g} mode, 1 cm^{-1} higher than the value reported in Ref. [3]. The other two intralayer modes were not observed in either the nanoplatelets or the bulk powder: the shear mode is obscured by stray laser light scattered from the powder surface and the E_{1g} mode is very weak in single experiments and even more difficult to detect in nanopowder samples.

In Figs. 3(a) (bulk) and 3(b) (UFP) we show the evolution of the A_{1g} mode observed at room temperature at various times during Rb intercalation. The ampoules were removed from the furnace to acquire the Raman spectrum. Contrasting the behavior between the bulk and nanoparticle forms, two forms of MoS$_2$ hosts are observed. Whereas the A_{1g} peak in the UFP host (Fig. 3(b)) *red shifts* by 1 cm^{-1} during intercalation ($T = 140$ °C) before the peak is lost owing to increasing metallic character of the sample, this phonon mode *blue shifts* by a similar amount in the bulk sample (Fig. 3(a)) when intercalated at a slightly higher $T = 170$ °C. This difference in the phonon behavior of the nanophase and bulk host MoS$_2$, although small, is unexpected and not understood at present. In general, small Rb-induced shifts in phonon frequency are expected owing to charge transfer.

3.3. Electron Spin Resonance

For the electron spin resonance (ESR) study, Rb-saturated bulk and nanopowder samples were prepared in an isothermal environment at 140 °C for 7 days. The
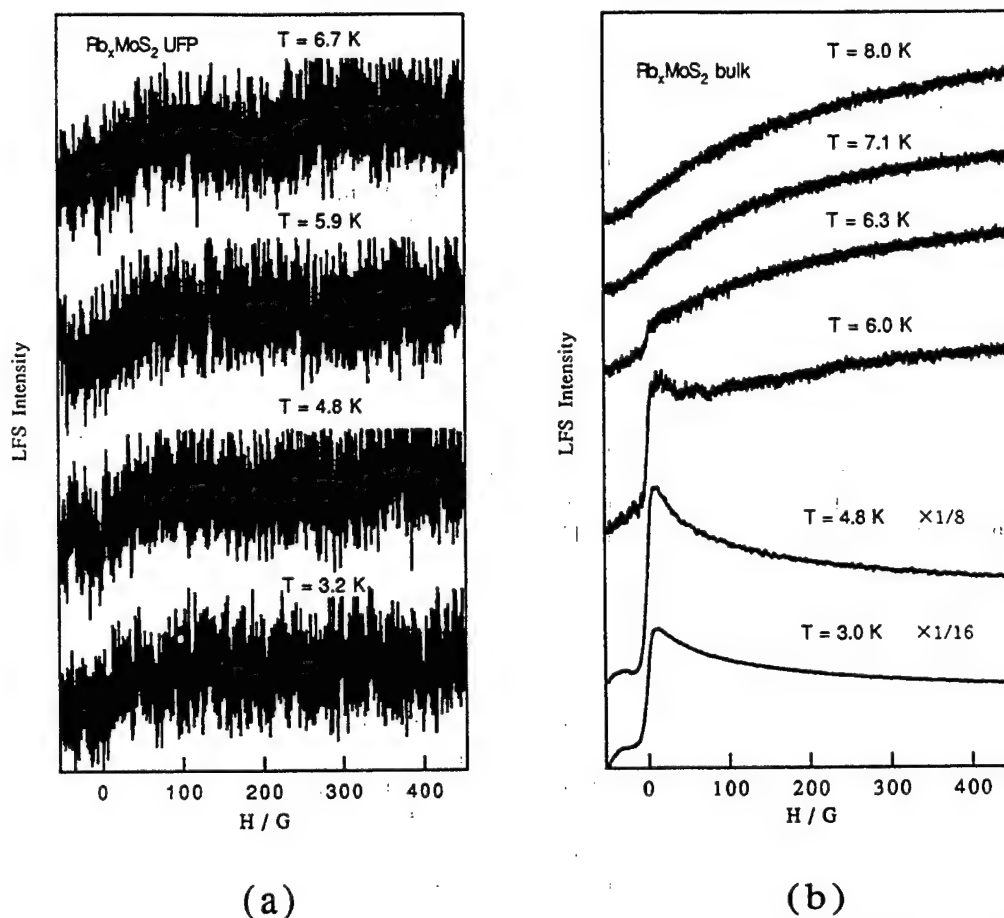
Fig. 5. Low field signal for increasing magnetic field form Rb-saturated MoS_2: (a) UFP sample; (b) bulk sample. The LFS due to the superconductivity can be seen at 6.3 K for the bulk sample. No LFS evidence for superconductivity in the UFP sample is detected down to 3.2 K.

A_{1g} mode in bulk $Rb_x MoS_2$ intercalated at 140 °C was observed at 410 cm^{-1}, consistent with the blue shift observed in the 170 °C intercalation. Past studies of the bulk material have found that a charge transfer occurs between the intercalant and host, giving rise to alternating positively (Rb) and negatively (MoS_2) charged layers in the intercalation compound and free electrons in the MoS_2-derived d-electron conduction band states [4]. The Rb-saturated MoS_2 bulk compound showed a broad ESR line at $T = 300$ K (Fig. 4(b)). Consistent with previous work, this ESR signal is identified with d-band conduction electrons of the host 2H-MoS_2 which have been donated to Mo-derived bands by the Rb intercalant. The line width ΔH of this ESR line broadens with decreasing temperature, as indicated in Fig. 4(b). The narrowest ΔH component is of spurious origin and is also observed in the pristine bulk MoS_2 powder. A second broad ESR line ($\Delta H \approx 300$ G) is observed in the bulk MoS_2 after Rb intercalation. However, a broad ESR signal could not be detected in the Rb-saturated MoS_2 UFP sample (Fig. 4(a)). In general, ΔH is inversely related to the conduction electron lifetime τ (or the inverse spin flip scattering rate).

The conduction electrons in a small particle will encounter the surface before being scattered by phonons. Hence τ for a UFP sample will be much shorter than that for a bulk sample and as a result ΔH becomes extremely broad, hiding the signal behind the detection limit of the ESR instrument. Both the UFP and bulk Rb-intercalated 2H-MoS_2 samples are therefore expected to be in the metallic state, consistent with the loss of Raman signal with increasing Rb intercalation. An in-depth analysis of the ESR data in Fig. 4 will be undertaken in the future.

In Figs. 5(a) and 5(b) we show the ESR low field signal (LFS) for the UFP and bulk forms of $Rb_x MoS_2$ respectively. The LFS is sensitive to the presence of a superconducting phase in the sample and exhibits a large signal due to microwave absorption near zero magnetic field in this case. We have used the technique to measure the superconducting transition temperature T_c in both the bulk and nanopowder forms. The LFS for the bulk sample indicates a superconducting transition at 6.3 K, as shown in Fig. 5(b), and the LFS increase with decreasing temperature. Only the data for increasing magnetic field are indicated in the figure. The data

for decreasing magnetic field are not shown; however, we observe the field hysteresis in the LFS data as expected. T_c for bulk Rb_xMoS_2 is estimated to be 6.4 K by extrapolating the LFS intensity to zero, in good agreement with the literature ($Rb_{0.3}MoS_2$, $T_c = 6.9$ K [2]). However, no LFS was observed for the UFP sample down to 3.2 K (Fig. 5(a)), i.e. superconductivity was not observed down to 3.2 K for UFP Rb_x. MoS_2.

4. Conclusions

Some of the nanophase MoS_2 particles produced by LP are observed in TEM lattice images to exhibit curved or bent layers. Similar to that observed for turbostratic graphite, the interlayer stacking sequence appears to be statistical in origin. The interlayer A_{1g} Raman-active mode exhibited a blue shift for the bulk powder sample with increasing Rb intercalation, but the UFP sample exhibited the opposite (red shift) behavior. The reason for this difference is not yet completely understood, but it may be tied to the stacking disorder in the nanoparticles. T_c was observed for the bulk sample at a value close to that reported earlier. However, no superconducting transition down to 3.2 K was detected for the UFP sample. Superconductivity is closely related to both the lattice vibrations and the conduction electron density of states. Therefore it is possible that a size effect in either the phonon or the electronic density of states is responsible for the depression of T_c.

Acknowledgements

References

[1] X.-X. Bi, Y. Wang, W. Lee, K. Wang, S. Bandow and P.C. Eklund, *MRS Symp. Proc.*, (1993).

[2] R.B. Somoano and J.A. Woollam, in F. Levy (ed.), *Intercalated Layered Materials*, Reidel, Dordreacht, 1979, p. 307.

[3] T. Sekine, C. Julien and M. Balkanski, in M. Balkanski (ed.), *Microionics–Solid State Intergrable Batteries*, Elsevier, Amsterdam, 1991, p. 373.

[4] R.B. Somoano, V. Hadek and A. Rembaum, *J. Chem. Phys.*, *58* (1973) 697.

[5] J.S. Haggerty, in J.I. Steinfeild (ed.), *Laser-Induced Chemical Process*, Plenum, New York, 1981.

[6] R. Kubo, *J. Phys. Soc. Jpn.*, *17* (1962) 975.

Study of grain growth in electrodeposited nanocrystalline nickel–1.2 wt.% phosphorus alloy

S.C. Mehta[a,1], D.A. Smith[a], U. Erb[b]

[a]Stevens Institute of Technology, Department of Materials Science and Engineering, Hoboken, NJ 07030, USA

[b]Queens' University, Department of Metallurgy and Materials Engineering, Kingston K7L 3N6, Canada

Abstract

The paper describes a transmission electron microscope study of the microstructural evolution of electrodeposited nanocrystalline Ni–1.2wt.%P and pure nickel during heating experiments performed in situ. The grain structure of the Ni–1.2wt.%P alloy was found to be stable up to a temperature of 360 °C. The grain growth was concurrent with Ni_3P precipitation, suggesting the important role of phosphorus in supersaturated solid solution in imparting the thermal stability to the microstructure. Normal grain growth was observed in Ni–1.2wt.%P at annealing temperatures up to 480 °C. Subsequent analysis revealed pinning of grain boundaries by Ni_3P precipitates. The value of activation energy for grain growth in Ni–P alloy (2.25 eV), obtained from continuous scan rate DSC experiments, is consistent with the above observation. Electrodeposited nanocrystalline nickel, on the other hand, showed abnormal grain growth at temperatures as low as 260 °C. At 320 °C, the microstructure had largely transformed from the nanocrystalline to the microcrystalline state.

Keywords: Grain growth; Electrodeposition; Phosphorus alloys

1. Introduction

Nanograined materials, owing to their ultra-fine grain sizes, manifest several physical and mechanical properties which are significantly different from their polycrystalline counterparts. The enhanced properties of these novel materials promise their usage for a number of applications. However, the inherent thermal instability of nanograined materials still poses a severe limitation on their widespread application. For example, Gunther et al. [1] reported abnormal grain growth at room temperature in as-compacted nanocrystalline (nc) palladium and copper produced by the inert gas condensation technique; abnormal grain growth was observed in pure nc Ag at 200 °C. Gertsman and Birringer [2] also observed abnormal grain growth at ambient temperature in nc copper prepared by the inert gas condensation method. Ganapathi et al. [3] measured the kinetic parameters for grain growth in nc

copper produced by the inert gas condensation technique. They obtained a significantly reduced value of the activation energy for grain growth in nc copper (30 ± 9 kJ mole^{-1} as against 80 kJ mole^{-1} for grain growth in conventional polycrystalline copper). Erb [4], in isothermal experiments, observed abnormal grain growth in electrodeposited nc nickel at 80 °C.

Attempts are being made to improve the thermal stability of nanocrystalline materials. The conventional approach of grain boundary pinning by solute additions and second phase precipitates is being commonly employed. Several studies of the effect of solute additions and second phase precipitates on grain growth kinetics have been reported. For example, Gunther et al. [1] obtained a value for the activation energy for grain growth in nc Ag–7at.%O which was twice as high as that of the pure nc Ag. Lu et al. [5], in their DSC measurements, found the activation energy for grain growth in a Ni–20at.%P alloy to be 182.3 ± 4.2 kJ mole^{-1}. Boylan et al. [6], in their in-situ isothermal grain growth experiments, showed the effectiveness of Ni_3P precipitates in inhibiting the grain growth in electrodeposited nc Ni–1.2wt.%P up to a temperature of

---
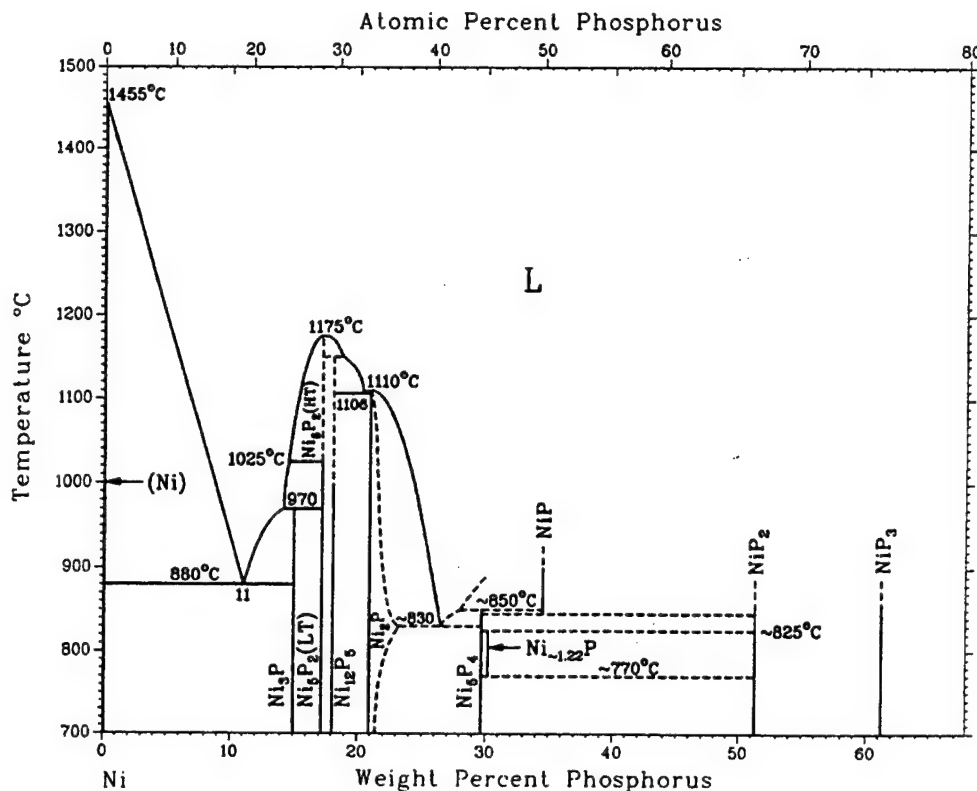
Fig. 1. Ni–P binary alloy phase diagram [9].

623 °C. However, despite the work cited above, the kinetics of grain growth and the role of solutes and second phase precipitates in grain growth inhibition in nanocrystalline materials are still not fully understood.

The present paper reports the results of in-situ annealing of electrodeposited nanocrystalline Ni–1.2wt.%P alloy. An in-situ grain growth study of electrodeposited nc nickel is also performed in order to provide a reference with respect to which the role of phosphorus in solid solution and Ni_3P precipitates in grain growth inhibition can be demonstrated. The activation energy for grain growth in Ni–1.2wt.% P is evaluated using DSC experiments.

2. Experimental

Nanocrystalline Ni and Ni–1.2wt.%P were prepared using the pulsed electrodeposition technique. A description of pulsed electrodeposition and the specific processing parameters are given elsewhere [7]. The as-deposited material was in the form of a sheet about 250 μm thick from which 3 mm discs were cut for TEM observation. These discs were made electron transparent using a FISCHIONE model 120 twin jet electropolisher. The electrolyte used for the polishing was a solution of concentrated HNO_3 and CH_3OH mixed in a 1:3 proportion. The electropolishing conditions for

nickel were −40 °C and 10 V while those for Ni–1.2wt.%P were −20 °C and 5 V. The microstructural characterization was performed using a Philips CM30 High Resolution Transmission Electron Microscope (HRTEM) at an operating voltage of 300 kV. The in-situ annealing experiments were performed using a single tilt resistive heating holder (Philips model PW6363/00 Heating Temperature Controller). A step heating profile was used for both Ni and Ni–1.2wt.%P. Nickel was heated from ambient temperature up to a maximum of 320 °C in steps of 20 °C with a hold for 15 min at each intermediate temperature to allow the microstructure to stabilize. Ni–1.2wt.%P was heated from ambient temperature up to a maximum temperature of 480 °C in steps of 20 °C with a hold for 10 min at each intermediate temperature. The DSC measurements were performed on the Ni–P alloy using a Perkin Elmer DSC-4 system in a continuous scanning mode. The samples were heated from ambient temperature up to a maximum temperature of 550 °C using heating rates of 10, 20, 40, 60 and 80 °C min^{-1}.

3. Results

Fig. 1 is a Ni–P binary alloy phase diagram. Note that the equilibrium solid solubility of phosphorus in nickel is negligible up to a temperature of 880 °C. The
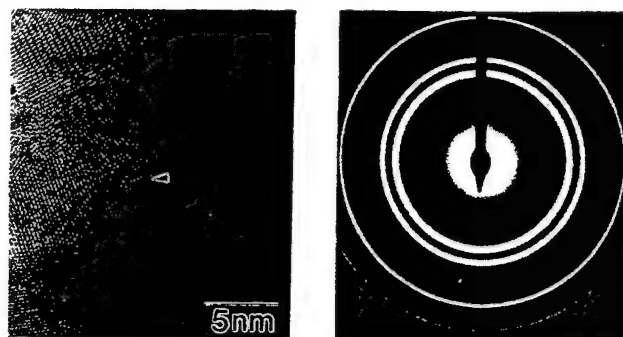
Fig. 2. (a) High resolution micrograph showing grain structure in electrodeposited nanocrystalline Ni–1.2wt.%P alloy. A coherent twin boundary is shown by an arrow in (a). Panel (b) is an electron diffraction pattern of as-deposited Ni–1.2wt.%P alloy.

grain structures of as-deposited nc Ni–1.2wt.%P and Ni were characterized using HRTEM. Fig. 2(a) is a high resolution micrograph showing the grain structure of Ni–1.2wt.%P alloy. Lattice cross fringes seen in several grains are of the {111} lattice planes observed in < 110 > projection. The average grain size of the as-deposited sample is approximately 10 nm. An independent study of grain size measurements in similarly processed nc Ni–1.2wt.%P suggests a lognormal grain size distribution [8]. The coherent twin boundary, indicated by an arrow in Fig. 2(a), shows apparent perfect matching of atoms along the interface. The density of lattice dislocations was very low. Multiple twinning was occasionally observed. The electron diffraction pattern of the as-deposited sample, shown in Fig. 2(b), shows fcc reflections characteristic of nickel, suggesting that phosphorus in the alloy is present either in the form of a solid solution or segregated along grain boundaries. The lattice parameters of the Ni–P alloy, calculated from the electron diffraction pattern, were the same as that for nickel.

Fig. 3 is a high resolution micrograph of electrodeposited nanocrystalline nickel. The average grain size of the as-deposited nickel sample is approximately 25 nm. Grain size inhomogeneity is quite evident from the micrograph. The smallest grain observed in the mi-

Fig. 3. High resolution micrograph showing grain size, shape and distribution in as-deposited nanocrystalline nickel.

crograph has a diameter of approximately 4 nm. No lattice dislocations were observed. However, low angle grain boundaries with misfit dislocations were quite abundant. Symmetrical tilt grain boundaries were also observed. The atomic arrangements at several symmetrical tilt boundaries were found to appear qualitatively very similar to those in corresponding boundaries in conventional polycrystals. Twinning (shown by an arrow in Fig. 3) was a quite common occurrence in the microstructure.

Fig. 4(a) is a series of micrographs showing the microstructural evolution as a function of temperature in nc Ni–1.2wt.%P alloy during in-situ annealing. Fig. 4(b) is a set of diffraction patterns corresponding to the microstructures shown in Fig. 4(a). Fig. 4(a) shows that the average grain size doubled as a result of heating to 300 °C. The most extensive grain growth was, however, observed above 360 °C. Diffraction patterns of the microstructure taken at various temperatures during the in-situ annealing show only fcc reflections up to 300 °C. However, extra diffraction spots corresponding to Ni_3P precipitates start appearing at 360 °C. There exists a correlation between Ni_3P precipitation and the onset of rapid grain growth in Ni–1.2wt.%P alloy. The average grain size of the sample heated to 480 °C has increased to approximately 100 nm. Fig. 5 shows an enlarged view of the microstructure at 480 °C. Ni_3P precipitates, identified by the Energy Dispersive Spectroscopy (EDS) and electron diffraction pattern, and shown by arrows in Fig. 5, are located at triple junctions and inside a few grains. Normal grain grain growth was observed in Ni–1.2wt.%P up to 480 °C. The DSC data measuring the shift in peak temperature of grain growth as a function of heating rates in Ni–P alloy are presented in Fig. 6 in the form of Kissinger's plot [10,11]. Kissinger's plot is a graph of $\ln(b/T_p^2)$ vs. $1/T_p$, where b is heating rate and T_p is the peak temperature in K. The two parameters are related by the following equation [11].

$$A'(b/T_p^2) = \exp(-Q/kT_p) \qquad (1)$$

where A' is a constant. The value of activation energy Q for the grain growth in Ni–P alloy is then calculated from the slope of Kissinger's graph in Fig. 6.

Fig. 7(a) shows a series of micrographs taken at several intermediate temperatures during the in-situ annealing of electrodeposited nanocrystalline nickel. The grain growth is not significant up to a temperature of 240 °C. However, abnormal grain growth sets in at annealing temperatures above 240 °C. At 320 °C, the microstructure completely transformed from the nanocrystalline to the microcrystalline state. Fig. 7(b) shows an enlarged view of the stages in microstructural evolution in nanocrystalline nickel in the temperature range 260–300 °C. As can be seen in Fig. 7(b), at 260 °C, several large grains, around 250 nm in diameter,
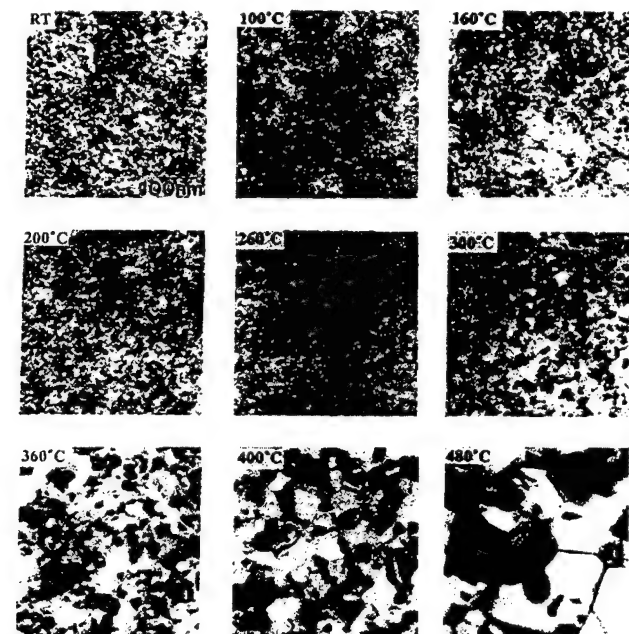
(a)
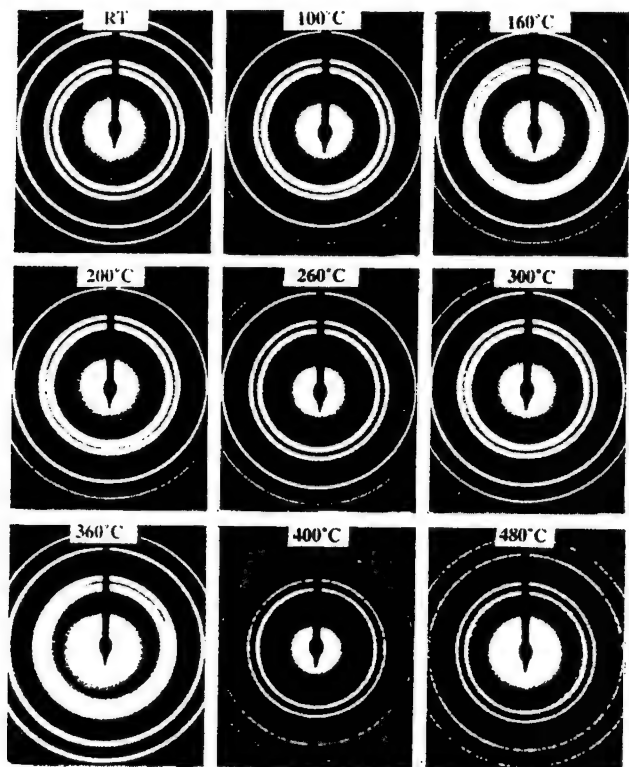
(b)

Fig. 4. (a) Microstructural evolution during in-situ annealing of electrodeposited nanocrystalline Ni–1.2wt.%P alloy. (b) Electron diffraction patterns of the microstructures corresponding to (a).

have nucleated in the matrix of nanometer sized grains. The rate of abnormal grain growth increases with increasing temperature. At 280 °C, approximately 50% of the volume fraction was occupied by large abnormally grown grains. Note the presence of a sizeable volume
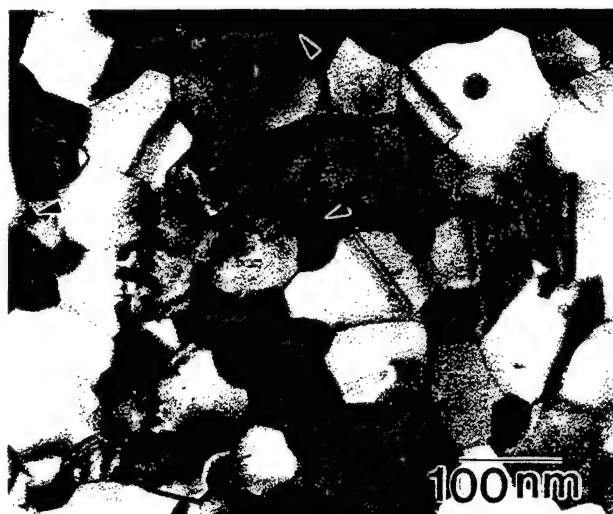
Fig. 5. Microstructure of Ni–1.2wt.%P after annealing at 480 °C. Ni_3P precipitates are shown by arrows.

fraction of nanometer sized grains in the microstructure even at 280 °C. At 300 °C, grain boundaries of large grains further migrated, increasing the average grain size to 500 nm. A few pockets of nanometer sized grains can still be seen. At 320 °C, the microstructure almost completely transformed from the nanocrystalline to the microcrystalline state with the average grain size reaching approximately a micrometer.

4. Discussion

The Ni–P equilibrium phase diagram (Fig. 1) shows that nickel and phosphorus are insoluble in the solid state and that fcc nickel and bct Ni_3P form the equilibrium phases for the composition of the Ni–P alloy
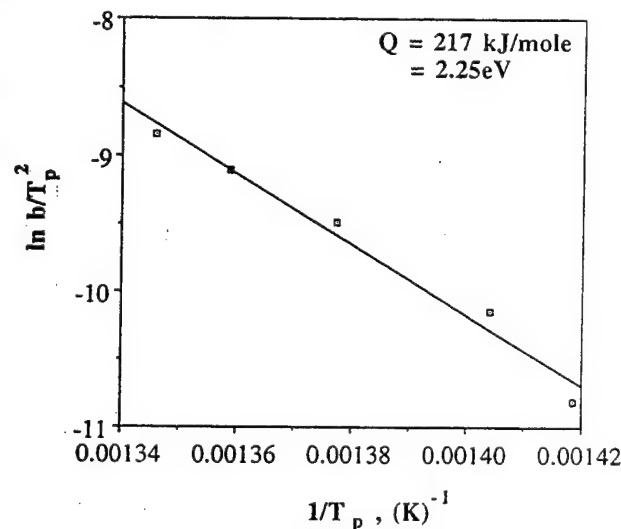
Fig. 6. Kissinger's plot for grain growth in electrodeposited nanocrystalline Ni–1.2wt.%P alloy.

(a)

(b)
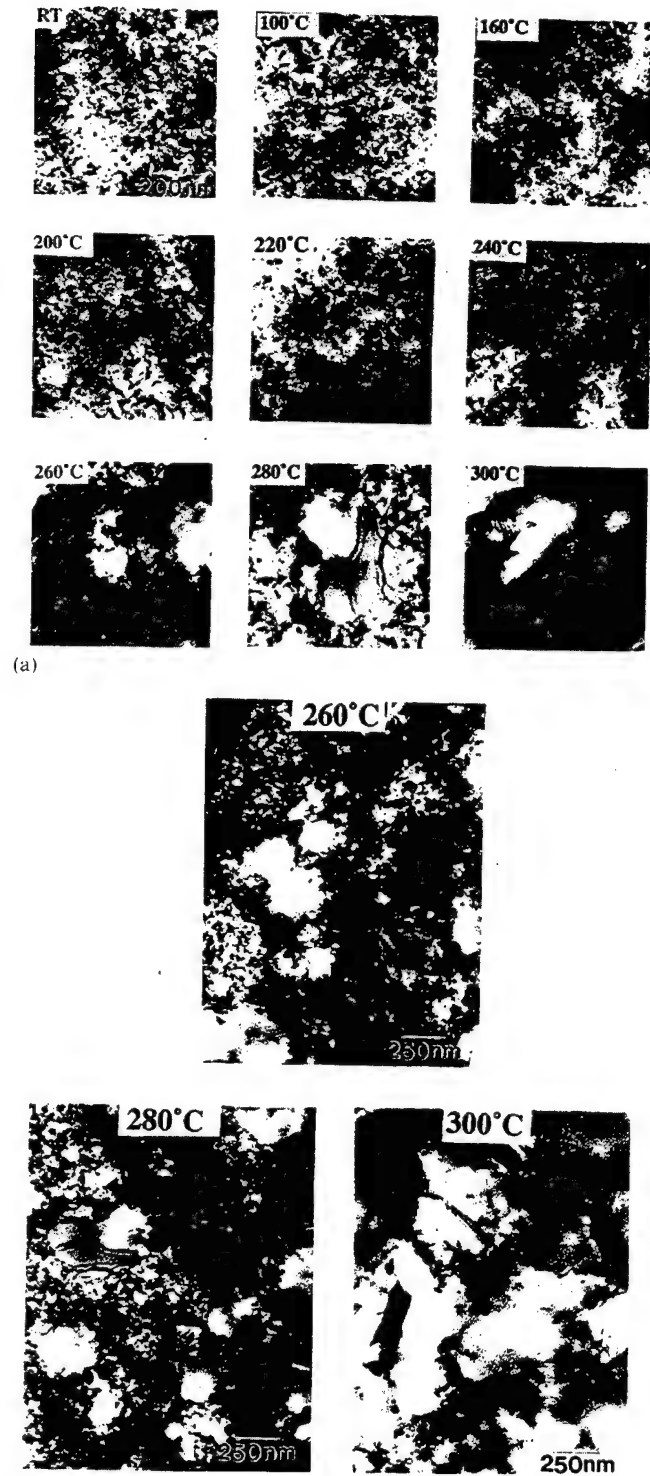
Fig. 7. (a) Microstructural evolution during in-situ annealing of electrodeposited nanocrystalline nickel. (b) Microstructures at 260 °C, 280 °C and 300 °C, showing abnormal grain growth as a function of temperature during in-situ annealing in electrodeposited nanocrystalline nickel.

used in the present work. The electron diffraction pattern of as deposited nc Ni–1.2wt.%P alloy (Fig. 2(c)), however, reveals no diffraction spots corresponding to

the Ni$_3$P phase, implying that phosphorus in the as-deposited alloy exists in the form of a supersaturated solid solution. Considering the positive enthalpy of mixing between nickel and phosphorus, phosphorus, under equilibrium conditions, would preferentially segregate along grain boundaries. A simple calculation suggests that if all the phosphorus were to segregate along grain boundaries, approximately 3 atomic percent of phosphorus would be required to cover the whole grain boundary area with a monolayer of phosphorus atoms. Since the amount of phosphorus in the Ni–P alloy is only 2.25 atomic percent, the grain boundary phosphorus segregation would be less than a monolayer in extent. The first order approximation to grain boundary dragging force exerted by phosphorus atoms can be obtained from the following equation [12]:

$$F = 4C_o \gamma / r \qquad (2)$$

where C_o is the average solute concentration, γ is the average grain boundary energy, and r is the phosphorus atom radius. On the other hand, the curvature induced boundary migration force is given as

$$F = 2\gamma / R \qquad (3)$$

where R is the average grain size. In equilibrium, the grain boundary pinning force due to solute drag cancels the curvature induced boundary migration force. It is in principle possible to estimate the equilibrium grain size by equating Eq. (2) and Eq. (3).

$$2\gamma / R = 4C_o \gamma / r \qquad (4a)$$

$$R = r / 2C_o \qquad (4b)$$

Taking the value for r, the atomic radius of phosphorus, and C_o as 0.123 nm and 0.0225 (assuming no segregation effect) respectively, the critical equilibrium grain size R to the first order approximation would be 3 nm. In fact, the grain size of the as-deposited material does not change significantly from the original value of 9 nm up to the temperature of 300 °C. At temperatures exceeding 360 °C, there is increasing competition between the solute drag effect and the grain boundary pinning due to Ni$_3$P precipitation, with the latter effect progressively increasing with increase in temperature as a result of the increase in the volume fraction of Ni$_3$P and decrease of C_o. The critical grain size in such a case is evaluated as follows [13].

$$2\gamma / R = 4C_o \gamma / r + 4f \gamma / r' \qquad (5a)$$

which simplifies to

$$R = 0.5[C_o / r + f / r']^{-1} \qquad (5b)$$

where f and r' represent the volume fraction and the average size of Ni$_3$P precipitates respectively. The rapid grain growth seen in Ni–P alloy above 360 °C (Fig. 4(a)) is therefore mainly due to a transition from the

solute induced drag effect to the weaker grain boundary pinning due to Ni_3P precipitates.

The electron diffraction pattern in Fig. 4(b) indicates the onset of Ni_3P precipitation at 360 °C. With increase in temperature, coarsening of Ni_3P precipitates, most likely mediated by grain boundaries, results in the reduction in the boundary pinning force. Grain coarsening is quite evident from the micrograph in Fig. 5, which shows the average grain size grown to 100 nm. The stability of microstructure in Ni–P alloy below the temperature of 360 °C and a concurrence of the rapid onset of grain growth and Ni_3P precipitation above 360 °C clearly suggests that phosphorus in supersaturated solid solution exerts a solute drag effect on grain boundaries, inhibiting the grain growth. Further, the value of activation energy for grain growth in Ni–P alloy, as measured from our DSC experiments, was 2.25 eV, which is considerably greater than 1.4 eV, the activation energy value for grain boundary self diffusivity of nickel in polycrystalline nickel [14], suggesting that Ni_3P effectively pins grain boundaries. The apparent discrepancy between the activation energy values evaluated in this study and that reported in Ref. [5] (1.83 eV) is attributed to the fact that samples used in Ref. [5] were prepared by crystallizing the amorphous Ni–P alloy so that these samples contained a mixture of fcc Ni and bct Ni_3P phases. The higher value of activation energy obtained in our study is possibly due to a combination of two processes, viz. the nucleation of Ni_3P precipitates and grain growth occurring simultaneously.

Abnormal grain growth observed in electrodeposited nc Ni is consistent with similar such observations made in inert gas condensed nc Cu, nc Pd and nc Ag [1,2] and electrodeposited nc Cu foils [15]. Abnormal grain growth in the nc Ni could be possibly connected to the presence of low angle grain boundaries in their microstructure, which could coalesce to give a mobile high angle grain boundary. The reason for abnormal grain growth in nc Ni could also be attributed to the grain size distribution effect, a theory proposed by Hillert [16]. The theory predicts that if the initial grain size range is wider than Hillert's distribution, those grains having a radius larger than 1.8 will be unstable and will grow abnormally, at the expense of the remainder, until they impinge on others developing in a similar fashion. This will then produce a relatively coarse grained microstructure with a narrow grain-size range. At this stage, growth can proceed uniformly within the new

structure, and Hillert's steady state grain size distribution is achieved asymptotically. The high resolution study of grain size distribution in electrodeposited nc Ni did show some evidence of wide grain size distribution. However, further experiments are required to clearly understand the mechanism of abnormal grain growth in pure nanocrystalline metals.

5. Conclusions

The stability of microstructure up to 360 °C and the concurrence of rapid grain growth with the onset of Ni_3P precipitation clearly revealed the stronger solute drag effect due to phosphorus atoms in controlling the stability of the microstructure in Ni–P alloy. The results of DSC measurements are in agreement with the direct in-situ TEM observations. Grain growth in electrodeposited nc Ni was, however, characterized by the onset of abnormal grain growth at 260 °C. These results are in concurrence with the other similar observations of abnormal grain growth in nc Cu, nc Pd and nc Ag.

References

[1] B. Gunther, A. Kumpmann and H.D. Kunze, *Scr. Metall. Mater.*, *27* (1992) 833.
[2] V.Y. Gertsman and R. Birringer, *Scr. Metall. Mater.*, *30* (1994) 577.
[3] S.K. Ganapathi, D.M. Owen and A.H. Chokshi, *Scr. Metall. Mater.*, *25* (1991) 2699.
[4] U. Erb, personal communication.
[5] K. Lu, W.D. Wei and J.T. Wang, *J. Appl. Phys.*, *69* (1991) 7345.
[6] K. Boylan, D. Ostrander, U. Erb, G. Palumbo and K.T. Aust, *Scr. Metall. Mater.*, *25* (1991) 2711.
[7] A.M. El-Sherik and U. Erb, *J. Mater. Sci.*, in press.
[8] D. Osmola, P. Nolan, U. Erb, G. Palumbo and K.T. Aust, *Phys. Stat. Sol. (a)*, *131* (1992) 569.
[9] T.B. Massalski, J.L. Murray, L.H. Bennett and H. Baker (eds.), *Binary Alloy Phase Diagrams*, Vol. 2, ASM International, Materials Park, Ohio, 1986, p. 1739.
[10] H.E. Kissinger, *Anal. Chem.*, *29* (1957) 1702.
[11] L.C. Chen and F. Spaepen, *J. Appl. Phys.*, *69* (1991) 679.
[12] F. Haessner (ed.), *Recrystallization of Metallic Materials*, Dr. Riederer Verlag GmbH, Stuttgart, 1978, p. 14.
[13] D.A. Smith, M. Small and C. Stanis, *Ultramicroscopy*, *51* (1993) 328.
[14] I. Kaur, W. Gust and L. Kozma (eds.), *Handbook of Grain and Interphase Boundary Diffusion Data*, Vol. 2, 1989, p. 1037.
[15] L. Delplancke, J. Charlier and R. Winand, presented at the MRS Fall meeting, Nov. 28–Dec. 1, 1994, Boston, MA.
[16] M. Hillert, *Acta Metall.*, *13* (1965) 227.

Engineering nanocrystalline materials from amorphous precursors

M.L. Trudeau

Materials Technology, Hydro-Québec Res. Inst., 1800 montée Ste-Julie, Varennes, Québec J3X 1S1, Canada

Abstract

Various processes have been developed for the production of nanocrystalline materials. One interesting technique is the "nano-crystallization" of amorphous precursors. For example, new soft magnetic nanocrystalline materials, with a composition such as $Fe_{87}Zr_7Cu_1B_5$, are based on the thermal crystallization of an amorphous ribbon. In this work, we show that with a sufficient understanding of the amorphous nature of an alloy we can design a specific crystallization process that will produce a unique nanostructured material. Two examples of such design are presented here. The first involves the possibilities of using mechanical energy to induce crystallization of an amorphous alloy. For amorphous $Fe_{90}Zr_{10}$, it is possible to produce a partly nanocrystalline material having an average crystal size of about 2 to 4 nm and a unique structure. The second looks at the effects of the atmosphere on the nano-structure during the annealing of amorphous $Fe_{87}Zr_7Cu_1B_5$. In this case, elemental reactivity could be used to trigger a specific crystallization path. These examples show that nano-crystallization can open the door to the design of complex and unique nanocrystalline materials.

Keywords: Amorphous precursors; Annealing

1. Introduction

In recent years, nanocrystalline materials have enjoyed a prominent place in the "advanced materials" research field. Many techniques for producing real nanosize structural systems are now well developed, the best known being gas-phase evaporation/condensation [1]. Even if this process was first limited to the production of pure metals or metal-reactant compounds, such as TiO_2 or MnF_2 [2,3], recent modifications (e.g. by using sputtering sources) have opened the door to the possibility of producing complex alloys [4,5]. The starting materials in this process are crystalline compounds which are vaporized and reconstructed in the gas phase, the end products being based on the thermodynamic processes that take place in this phase. Normally, the morphological features of the building blocks are quite uniform in shape, size and composition. Each of these blocks, in its post-deposited state, is sensitive to surface contamination or modification and, in most cases, some compaction methods that will allow the production of dense compacts without losing the nano-characteristics of each individual unit, need to be designed for pratical use. The same densification difficulties exist also for nanocrystalline powders prepared by high-energy mechanical alloying (MA) or mechanical milling, two techniques that are used more and more often to produce nanosize structures. In fact, the production of fully dense compacts from mechanically alloyed powders can be more difficult than with evaporation/condensation produced powders, due to the high amount of internal strain found in the severely deformed crystals [6,7].

The purpose of the present work is to consider another technique, which, in the opinion of the present author, has not received all the attention it deserves: nano-crystallization of amorphous precursors. This neglect is surprising if we consider that, despite the starting materials being less flexible, this method allows the production of different, and, in some cases, unique end-products. In fact, a substantial part of the development in this "nano-field" is based on the production of new soft magnetic materials through the thermal crystallization of amorphous alloys, in particular $Fe_{75.5}Si_{12.5}Cu_1Nb_3B_8$ [8] and $Fe_{87}Zr_7Cu_1B_5$ [9], the former having been commercialized around 1990 by Hi-

tachi under the trade name FINEMET. However, the use of amorphous precursors for developing new nanophase materials can go well beyond new soft magnetic alloys or the temperature–time consideration to control the average crystallite size.

This study presents other factors that could be considered when seeking nanophase materials. We will show that understanding and exploitation of the amorphous nature of an alloy could lead to the development of new nanostructured phases. In particular, we look at the thermodynamics and diffusional parameters of the mechanical crystallization of the $Fe_{90}Zr_{10}$ alloy. Also, in view of its technological importance, we present some interesting structural changes occurring during nanocrystallization of the amorphous $Fe_{87}Zr_7Cu_1B_5$ alloy. For this material we have studied the elemental reactivities that occur during the nanocrystallization. We show that not only the temperature–time factors but also the annealing atmosphere should be considered during the annealing of this alloy. These examples demonstrate that the development of new nanophase materials using amorphous precursors should be further considered in the future and that a wide variety of diverse possibilities exist.

2. Experimental details

$Fe_{90}Zr_{10}$ and $Fe_{87}Zr_7Cu_1B_5$ amorphous ribbons were prepared by normal melt-spinning techniques. The ribbons were thermally annealed in a quartz tube furnace evacuated at about 10^{-5} Torr by a diffusion pump. In some cases O_2 and a mixture of $Ar + 8\%H_2$ were circulated in a continuous flow during the annealing. Some O_3 oxidation was done inside a UV-ozone system from UVOCS. Mechanical milling was performed using a SPEX-8000 as well as a Fritch Pulverisette-5 mill. Steel and tungsten carbide sealed (under argon) vials and balls were used. Details of the milling process have been published elsewhere [10]. The structural nature of the ribbons and powders were verified by X-ray diffraction using a Phillips diffractometer equipped with Mo Kα radiation and by transmission electron microscopy using a Hitachi H-9000 STEM. The width at half maximum of all the X-ray peaks, after proper correction for instrumental broadening and Kα2, was used to obtain the average crystallite size as a function of milling time [11]. Surface compositional analysis of the $Fe_{87}Zr_7Cu_1B_5$ was done using a PHI-5500 XPS from Physical Electronics. Profiling was done using argon ions at 2 kV over a 4×4 mm rastered region. The sputtering rate for SiO_2 under these conditions was about 10 Å min^{-1}. Details of the surface studies will be presented elsewhere [12]. Finally, the room temperature magnetic properties were characterized using a vibrating sample magnetometer from DMS.

3. Results and discussion

3.1. Mechanical nanocrystallization of $Fe_{90}Zr_{10}$

Mechanical milling of an amorphous $Fe_{90}Zr_{10}$ ribbon results in rapid crystallization of the materials [10]. Crystallization can even be started by simply hammering the alloy. Results from mechanical milling are often well explained by metastable thermodynamic considerations [13,14]. Fig. 1 presents a schematic view of the free-energy curves for the amorphous and the bcc structure, based on the work of Krebs et al. [15] and Hellstern and Schultz [7], for an Fe concentration between 60 and 100 at.%. It has been shown that approximate values can be obtained for the concentration limits of metastable structures based on the common tangent rule that can be drawn between free-energy curves [13]. The common tangent between the two functions is also presented in Fig. 1 together with the contact points x_1 and x_2. For this system, under metastable equilibrium, it is possible to obtain a homogeneous amorphous alloy for concentration below about 78 at.% Fe. Also, at very high Fe concentration, a homogeneous bcc structure with a maximum of about 5 at.% Zr in solution can be expected [7]. Between these two values, the material produced will be a mixture of the two structures. Interestingly, it is not possible to use mechanical milling to produce a pure amorphous material at a concentration of about 90 at.% Fe. On the other hand, it is well known that amorphous ribbons with an Fe concentration between 88 and 93 at.% are
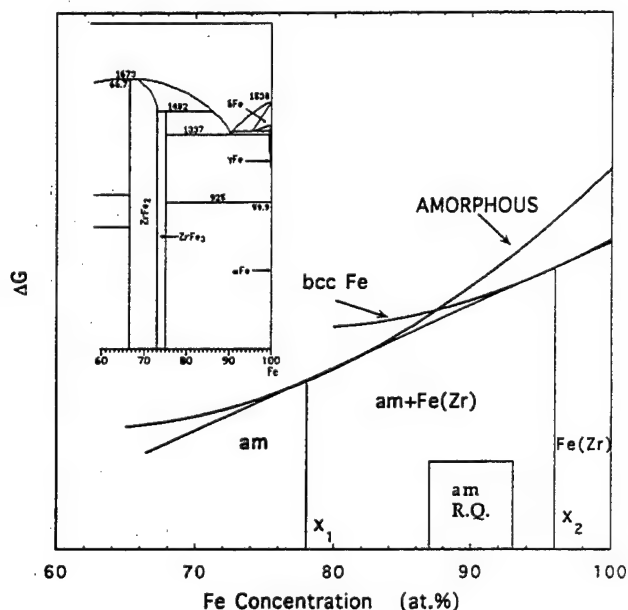
Fig. 1. Schematic representation of the free-energy curves for the Fe-rich side in the Fe–Zr system. Also shown is the common tangent between the amorphous and bcc curves. Finally, the insert presents the stable phase diagram for this concentration region from Ref. [18].

produced using normal melt-spinning processes [16], a result which is explained by the thermodynamic differences between these two processes. Mechanical milling is sometimes described as a metastable equilibrium process. The milling energy is transfered to the stable crystalline structure in the form of strain (dislocation energy), which pushes the energy of the stable system beyond that of the metastable thermodynamic structures such as amorphous phases or super-saturated solutions [7,13]. The cases of melt-spinning and vapor quenching are quite different. These processes are non-equilibrium at first and require kinetic constraints to prevent nucleation and growth of the stable equilibrium compounds. In general, for metallic glasses, it has been found that amorphous alloys can be produced by rapid quenching around deep eutectic compositions. Around these concentration regions simultaneous formation of two crystalline phases occurs, accompanied by some compositional shifts. This requires the development of concentration gradients and significant atomic transport [17]. Amorphous production is then possible because the quenching time is faster that the nucleation time of the crystalline phases due to the large atomic diffusion needed. Referring back to Fig. 1, the insert can be seen to contain the Fe-rich part of the stable phase diagram for the Fe–Zr system [18]. A eutectic composition is present for at Fe concentration around 90 at.%. The normal crystallization of the melt at around this composition results in the formation of α-Fe and $ZrFe_3$ phases. Kinetic conditions are thus present in this concentration range to allow the possibility of the liquid structure to freeze, and, as mentioned earlier, metallic glasses with Fe concentration around 90 at.% to be produced [16]. However, based on the free-energy diagram, this glass is not in metastable equilibrium and whould be thermodynamically unstable in the presence of small perturbations. The formation of crystalline phases is limited only by the kinetics of atomic motions and not by the presence of a nucleation barrier [17]. In their TEM investigation of the crystallization of amorphous $Fe_{90}Zr_{10}$, Zarubova et al. found that pre-crystalline structures or large concentration fluctuations are probably present in this amorphous material and that the crystallization process is mainly controlled, in its early stage, by the diffusion of Fe [19].

Since mechanical milling cannot produce a homogenous amorphous material for this Fe concentration, and considering that milling can yield substantial local displacement, we can expect that, if an amorphous $Fe_{90}Zr_{10}$ ribbon is subjected to a large amount of deformation, it would partly crystallize. Fig. 2 presents a bright-field TEM micrograph for a piece of amorphous ribbon milled for 1 h. It may be observed that, even if parts of the ribbon are still amorphous, some small crystals with an average dimension between 2 to 3.5 nm are present. Fig. 3 presents the increase in the
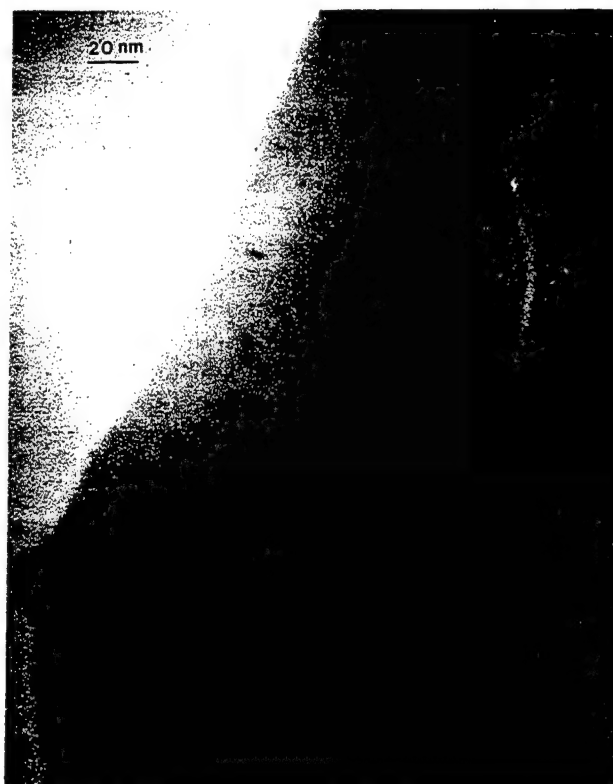
Fig. 2. TEM micrograph showing the composite structure of a piece of $Fe_{90}Zr_{10}$ ribbon after being milled for 1 h.

average crystal size with milling time for this mechanical crystallization (MC) process. The same figure shows the minimum average crystal size obtained by mechanically milling Fe and Zr powders in the same concentration ratio. It is seen that at the beginning of the MC process materials with an average size well below that obtained by MA powder are produced. After 8 h of milling, the average size is still about 4 to 4.5 nm, even if more than 60% of the material is transformed [10]. The X-ray peaks position was found to be constant throughout the milling and similar to that obtained for a MA material [10]. The value of the lattice parameter, based on Vegard's rule, indicates that about 4 at.% Zr is present in solution in the Fe crystallites. This value is not the same as that measured for the α-Fe crystals appearing following thermal crystallization of the ribbon, which was nearly equal to the published value for pure Fe, indicating that a negligible amount of Zr was present in solution. The magnetic and the thermal behavior of the 10 h MC powder were also found to be nearly identical to those of mechanical alloyed powders [10].

As found previously in the FeSiB system [20,21], and more recently for some aluminum-based alloys [22,23], mechanical deformation of the $Fe_{90}Zr_{10}$ is thus responsible for crystallization of the alloy. The end material has an identical structure to powders produced by simply milling the elemental components. In the present case, this deformation-induced crystallization can be

explained by the presence of a driving force for the production of a more "stable" metastable material, the milling energy being used to induce the local diffusion needed for the production of stable nuclei. In the case of the FeSiB alloys, the reason for the observed mechanical crystallization is still unclear. However, it is possible that the same kind of enhanced diffusion (or local rearrangement) in high strain regions, induced by the milling, could also be an important factor. Reports that local strain induces the segregation of boron in these kinds of glasses [24] could be at the origin of such a process. In their recent work, Chen et al. [22] suggest that local displacement along slip bands due to a high value of shear strain can be responsible for changes in the short-range order of the amorphous state leading to the formation of Al nanocrystals.

However, one major factor to be noted is that, at the beginning of this mechanical crystallization, the size of the Fe crystallites, their volume fraction and their composition could not be produced by mechanically alloying the elemental powders. Only a deformation-induced crystallization process of such an amorphous precursor could produce such a fine nanocomposite structure. It may thus be seen that a good understanding of an amorphous state, or of factors that affect it, can lead to the production of new nanocomposite structures through mechanisms such as this deformation-induced crystallization.

Other techniques exist that can produce local changes in the material composition giving rise to the formation

of crystalline nuclei. For example, Stenger et al. [25] have shown that radio-frequency can be used to precipitate α-Fe crystallites in a $Fe_{81}B_{1.5}Si_{3.5}C_2$ amorphous alloy. Another important process is surface reactivity, which has been reported to lead to very local crystallization [26,27]. This effect will be discussed in the next section for the case of the amorphous $Fe_{87}Zr_7Cu_1B_5$ alloy. One could also imagine that, for unstable or easily de-stabilized amorphous states, techniques such as ion implantation, proton irradiation or even laser-induced shock waves could produce similar modifications in the short-range order, leading to local nanocrystallization. With a good thermodynamic understanding of such processes, it would be possible to control the crystallite size as well as their volume fraction.

3.2. Surface reactivity of $Fe_{87}Zr_7Cu_1B_5$

One aspect somewhat overlooked in the case of the amorphous $Fe_{87}Zr_7Cu_1B_5$ was the effect of Zr, its affinity for oxygen and its possible role in the overall magnetic properties of the material. It is known that for the case of pure nanocrystalline iron, made through the evaporation–condensation route, one of the main problems in obtaining good soft properties is the core-shell morphological structure of the individual grains, iron oxide forming readily at the surface of the nanograins. The presence of this iron oxide layer and its coupling effect with the metallic iron core are a major reason for the higher than expected losses of this material [28,29]. In the case of $Fe_{87}Zr_7Cu_1B_5$, nanosize iron crystals are produced by crystallization of the amorphous material. From crystallization studies on FINEMET-type alloys and this material, it is generally admitted that the presence of Cu is necessary to increase the number of nucleation sites and, thus to reduce the final crystallite size [30]. However, Zr could have an significant role to play as an oxygen getter.

Fig. 4 presents the magnetization curve for different $Fe_{87}Zr_7Cu_1B_5$ samples. In the as-prepared state, this material has a low magnetic moment but upon annealing, the moment is greatly increased. From the three annealed samples, the material with the smaller moment was annealed in vacuum (10^{-5} torr) for 1 h at 590 °C. The middle sample was annealed like the previous one but was then exposed to an O_3 atmosphere for 30 h. Finally, the samples having the highest moment correspond to a ribbon annealed in 1 atm $Ar + 8\%H_2$. The increase in moment for this last sample compared to the normal vacuum annealed is about 2.5%. From the X-ray analysis, there seems to be no difference in the average crystallite size of these last three samples (average size about 15 nm). The obvious differences in the total moment indicate that elemental reactivity is a factor to be considered during the thermal crystallization of this alloy.
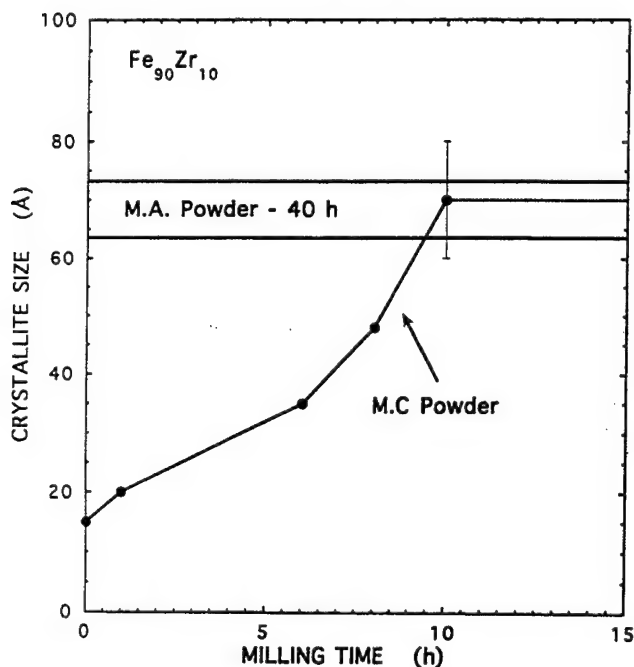
Fig. 3. Increase of the crystal size as a function of milling time during mechanical crystallization of the amorphous $Fe_{90}Zr_{10}$ material. The two double lines represent the average values of the crystallite size found for MA powders.
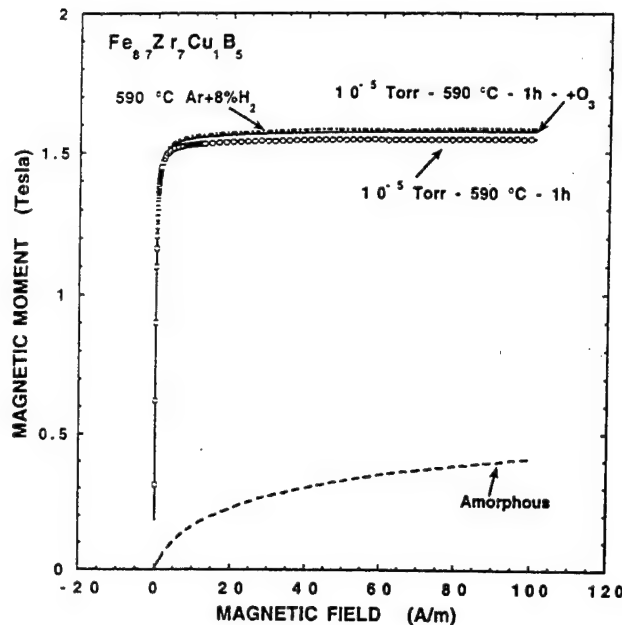
Fig. 4. Magnetic moment of $Fe_{87}Zr_7Cu_1B_5$ ribbons after different annealing treatments.

Fig. 5 presents an XPS depth profile starting at the surface of an amorphous ribbon. The surface is mainly composed of an iron oxide layer. As this layer was sputtered off we found the presence of an enriched Zr layer. Analysis shows that, in this layer, Zr is present mainly as ZrO_2 and as this layer becomes more pronounced, iron is found mainly as a metallic constituent

[12]. Zirconium is then more deeply oxidized than the other alloying elements. For its part Cu was found to be more prominent at the surface than in the bulk. while B was depleted from this oxide surface region.

Fig. 6(a,b) presents the variation in surface composition for a vacuum- and a hydrogen-annealed sample, respectively. The first observation is that, for the vacuum-annealed sample, the oxide layer is much more pronounced, with large amounts of oxygen being found even after more than 80 min of sputtering. As for the amorphous ribbon, the surface is mainly composed of iron oxide, although metallic iron rapidly appears during the depth profiling and all the oxygen found in the sub-layers is observed to be bound to the Zr. On the other hand, in contrast to the amorphous ribbon, boron is more pronounced at the surface. The surface composition is quite different for the sample annealed in a partly H_2 atmosphere. Here boron is more pronounced at the surface than iron. Moreover, contrary to all the previous samples, which showed that Fe was almost completely oxidized at the surface, some observable traces of metallic iron were present, even if the sample remained a long time at room atmosphere before being analyzed. Also, as the iron content increases. both the B and the O content falls. Zr is well depleted from these first layers and, in fact, has been pushed to an extended sub-layer marked also by a drastic increase in the oxygen content. In this oxygen-rich region, Fe remains in a purely metallic state while Zr is mainly in the form of ZrO_2. For both these samples, oxygen's
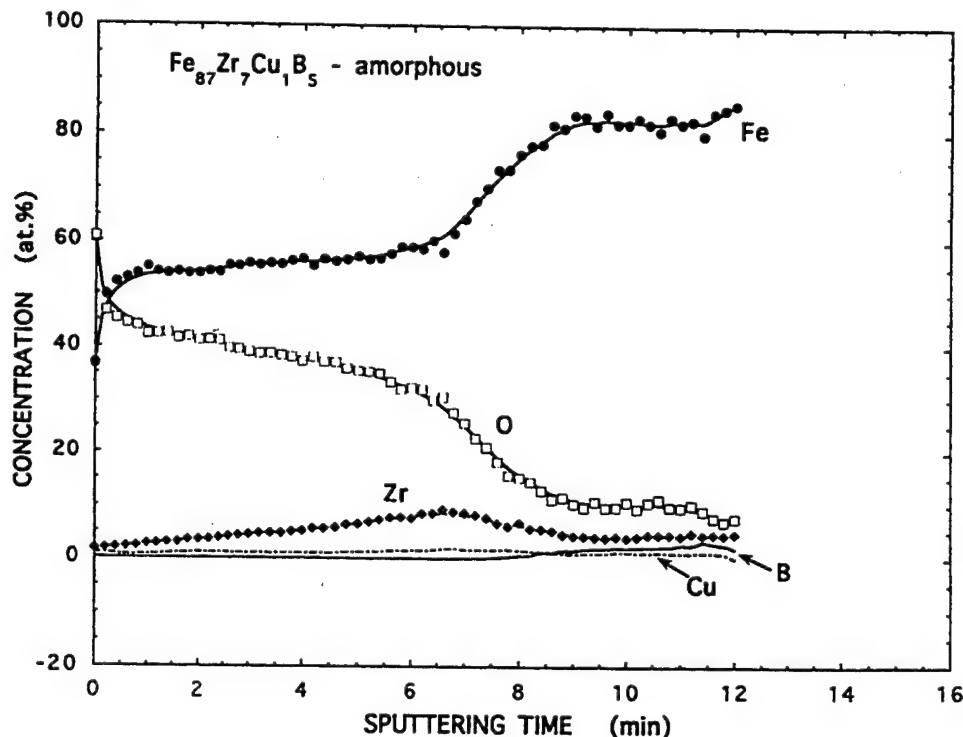
Fig. 5. Compositional depth profile for a $Fe_{87}Zr_7Cu_1B_5$ amorphous ribbon.
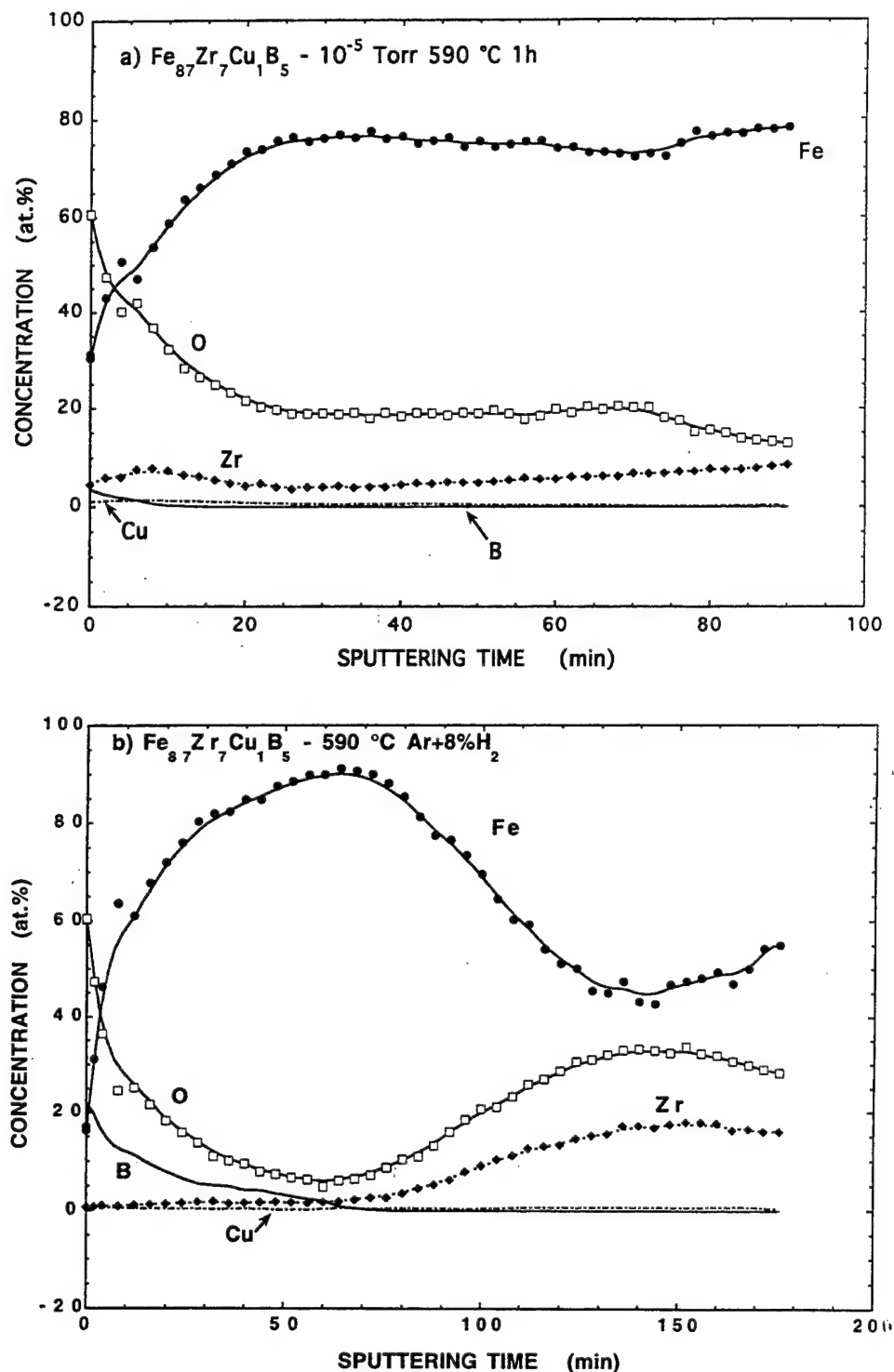
Fig. 6. Compositional depth profile for a $Fe_{87}Zr_7Cu_1B_5$ ribbon after (a) annealing at 10^{-5} torr for 1 h at 590 °C and (b) annealing at atmospheric pressure in flowing $Ar + 8\%H_2$ at 590 °C.

presence in the bulk of the alloy is marked and is more pronounced for the annealing under H_2.

It is not clear at the present time how these chemical changes correlate to the changes in the magnetic moment. Interestingly, Zr seems to perform well as an oxygen getter and no iron oxide is present, except very

close to the surface of the ribbons. Further studies are needed to see what impact such chemical modifications will have on the magnetic losses of this alloy. Morito et al. [27] have found that for $Fe_{78.5}B_{13}Si_{8.5}$ annealing in nitrogen, argon, hydrogen and air significantly improved the iron loss of the amorphous

ribbon, while annealing in $H_2 + H_2O$ deteriorated the properties.

However, the main result that should be considered is that the thermal nanocrystallization process can be modified by the choice of annealing atmosphere. It may be possible to modify some of the magnetic properties of this material by changing the nanoscale ranges of the elemental chemistry (e.g. by varying the amount of Zr oxide). The final bulk nanostructure could then be more precisely tailored by working on the material reactivity in addition to the normal temperature–time parameters. In the engineering of nanostructured materials from an amorphous precursor, this reactivity of some of the alloying elements is an important parameter to be taking into greater consideration, since it could lead to the development of new crystallization paths and hence the production of new structures in the nanoscale range.

4. Conclusion

Amorphous materials offer interesting possibilities for the production of nanostructured or nanocomposite materials. In some cases, such as for $Fe_{87}Zr_7Cu_1B_5$, the use of an amorphous precursor allows the formation of a nanophase composite with unique magnetic properties, without encountering the major problem of material densification. We have shown here that, during the thermal nanocrystallization of this $Fe_{87}Zr_7Cu_1B_5$ alloy, the chemical composition can also be varied through the choice of atmosphere. These modifications of the nanostructure composition could lead to an improvement in the material properties. Similar consideration can also be drawn from the deformation-induced crystallization of the $Fe_{90}Zr_{10}$ alloy. In some cases, deformation processes (such as shock wave) could be used on a deposited amorphous material to generate the right precipitation of nanosize crystals. Since, these changes or modifications are possible at the same time as the crystallization occurs, they can be balanced and controlled more easily than through usual fabrication routes such as evaporation/condensation or mechanical milling. Moreover, since nanocrystallization (thermal, mechanical, environmental, ...) uses some amorphous precursors, the final crystallite size of the material can be smaller than with other techniques such as MA. Also, the possibility of obtaining nanocomposite materials is greater than in evaporation/condensation, which tend to produce uniform building blocks. Finally, since, in some cases, the amorphous precursor is already in a dense compact form, there is no need for post-production densification methods to be designed. In the examples presented here, the main notion to be retained is that new materials with a unique nanostructure can be engineered using an amorphous precursor and that, in some cases, other parameters, apart from an increase in temperature, can be used to nano-crystallize the amorphous structure.

References

[1] For a review of the nanostructured field see the work of H. Gleiter, *Prog. Mater. Sci.*, *33* (1991) 223, and R.W. Siegel, *Annu. Rev. Mater. Sci.*, *21* (1991) 559.
[2] W. Wagner, R.S. Averback, H. Hahn, W. Petry and A. Wiedenmann, *J. Mater. Res.*, *6* (1991) 2193.
[3] S. Bandow, *Jap. J. Appl. Phys.*, *30* 1991 788.
[4] H. Chang, J. Höfler, C. Altstetter and R. Averback, *Mater. Sci. Eng. A*, *153* (1992) 676.
[5] A. Tschöpe and J.Y. Ying, *Nanostruc. Mater.*, *4* (1994) 617.
[6] C. Kuhrt and L. Schultz, *J. Appl. Phys.*, *71* (1992) 1896.
[7] E. Hellstern and L. Schultz, *J. Appl. Phys.*, *63* (1988) 1408.
[8] Y. Yoshizawa, S. Oguma and K. Yamauchi, *J. Appl. Phys.*, *64* (1988) 6044.
[9] K. Suzuki, A. Makino, A. Inoue and T. Masumoto, *J. Appl. Phys.*, *70* (1991) 6232.
[10] M.L. Trudeau, *Appl. Phys. Lett.*, *64* (1994) 3661.
[11] J. Eckert, J.C. Holzer, C.E. Krill III and W.L. Johnson, *J. Appl. Phys.*, *73* (1993) 2794.
[12] M.L. Trudeau, to be published.
[13] Z,H. Yan, T. Klassen, C. Michaelsen, M. Oehring and R. Bormann, *Phys. Rev. B*, *47* (1993) 8520.
[14] M. Oehring, Z.H. Yan, T. Klassen and R. Bormann, *Phys. Stat. Sol. A*, *131* (1992) 671.
[15] H.U. Krebs, D.J. Webb and A.F. Marshall, *Phys. Rev. B*, *35* (1987) 5392.
[16] Z. Altounian, J.O. Strom-Olsen, *J. Appl. Phys.*, *59* (1986) 2364.
[17] W.L. Johnson, *Prog. Mater. Sci.*, *30* (1986) 81.
[18] T.B. Massalski et al., *Binary Alloy Phase Diagrams*, ASM, Materials Park, OH, 2nd edn., 1190.
[19] N. Zarubova, N. Moser and H. Kronmuller, *Mater. Sci. Eng. A*, *151* (1992) 205.
[20] M.L. Trudeau, R. Schulz, D. Dussault and A. Van Neste, *Phys. Rev. Lett.*, *64* (1990) 99.
[21] R. Schulz, M.L. Trudeau, D. Dussault, A. Van Neste and L. Dignard-Bailey, *Mater. Sci. Eng. A*, *179/180* (1994) 516.
[22] H. Chen, Y. He, G.J. Shiflet and S.J. Poon, *Nature*, *367* (1994) 541.
[23] Y. He, G.J. Shiflet and S.J. Poon, *Acta Metall. Mater.*, *43* (1995) 83.
[24] S.V. Pan, Yu V. Milman and A.A. Malyshenko, *Mater. Sci. Eng. A*, *145* (1991) 127.
[25] S. Stenger, M. Sorescu and U. Gonser, *J. Non-Crystal. Solids*, *151* (1992) 66.
[26] U. Köster, B. Punge-Witteler and G. Steinbrink, *Keys Eng. Mater.*, *40/41* (1990) 53.
[27] N. Morito, T. Suzuki, C. Maeda, T. Yamashita and Y. Kitano, *J. Mater. Sci.*, *25* (1990) 5166.
[28] S. Gangopadhyay, G.C. Hadjipanayis, B. Dale, C.M. Sorensen, K.J. Klabunde, V. Papaefthymiou and A. Kostikas, *Phys. Rev. B*, *45* (1992) 9778.
[29] S.U. Jen, C.Y. Lee, Y.D. Yao and K.C. Lee, *J. Magn. Magn. Mater.*, *96* (1991) 82.
[30] K. Hono, K. Hiraga, Q. Wang, A. Inoue and T. Sakurai, *Acta Metall. Mater.*, *40* (1992) 2137.

Nanophase metallic alloys consolidated from powders prepared by mechanical alloying

L. He, E. Ma*

Materials Science and Engineering Program, Department of Mechanical Engineering, Louisiana State University, Baton Rouge, LA 70803, USA

Abstract

Nanocrystalline metals and intermetallic compounds (Fe, Fe_3Al, Ni_3Al) have been prepared by mechanical alloying of elemental powders. This simple and inexpensive route yielded sufficient quantity of powders for consolidation experiments to produce bulk nanophase samples. By employing high pressure, relatively low temperature, and protective Ar atmosphere during hot pressing/forging, mechanically-alloyed nanophase metallic alloy powders have been consolidated to near full density ($\geq 91\%$ of theoretical density) with average grain sizes maintained to below about 20 nm. Contamination of oxygen and carbon in consolidated samples was below about 2 at.% in iron and about 1 at.% in intermetallics. Further improvement of processing steps to achieve full density and reduce contamination is discussed.

Keywords: Metallic alloys; Powders; Mechanical alloying; Consolidation

1. Introduction

As an important new class of nonequilibrium materials, nanocrystalline alloys have drawn wide attention in recent years [1–6]. Aside from their fundamentally new microstructure, nanophase materials are of interest because many properties of materials are known to depend strongly on grain size. In terms of mechanical properties, beneficial effects of nanoscale grain sizes on strength [11–13] as well as ductility (superplasticity) and fracture toughness [4,8] have been reported [7–15]. Also, small grain and particle sizes of nanophase powders are advantageous in sintering: the temperature required for sintering to full density, bulk compacts is significantly reduced [15,16]. To date, a number of techniques have been developed to prepare nanophase powder materials, the most popular being the gas phase condensation method developed by Gleiter et al. [2]. However, this method is not the most efficient for inexpensive mass production of practical quantities of materials. It is thus worthwhile to increase attention to nanophase powders prepared by other, potentially more efficient and cost effective, techniques. Among such techniques, mechanical alloying has been shown to be an attractive alternative [17–19].

Consolidation of powders into bulk, full density compacts while retaining nanoscale grain size is obviously a major challenge for possible practical applications of nanophase materials. The lack of bulk, fully dense samples has been largely responsible for some contradictory reports on the grain size dependence of mechanical properties for nanophase metals and intermetallic compounds [11–14]. Significant progress has been made in recent years in the consolidation of nanophase powders produced by the gas condensation method [15,16]. On the other hand, work on the consolidation of mechanically-alloyed metallic alloy powders is scarce, although successful attempts have been made recently using exotic techniques such as shock-wave consolidation [20,21]. Our goal is to develop effective consolidation procedures to produce bulk, full-dense, nanocrystalline alloys with mechanically alloying as the source of nanophase powders. The work reported in this paper is a step in this direction.

* Corresponding author.

Table 1
Characteristics of as-received powders used in this study

Powder	Particle size (μm)	Nominal purity (wt%)	Chemical analysis	
			C at.%	O at.%
Fe	6–9	99.9	0.1	1.3
Al	<44	99.5	0.01	0.9
Ni	3–7	99.9	0.4	0.3

2. Experimental procedures

Three systems have been selected for this study: Fe, Fe_3Al, and Ni_3Al. The mechanical alloying technique used to produce nanophase alloys was high-energy ball milling of powder mixtures of constituent elements [22]. The original powders (Fe, Al, Ni) were obtained from commercial sources with a nominal purity high than 99.5%. Contents of light contaminants for these as-received powders were determined by chemical analysis. Quantitative oxygen analysis was performed using Leco TC136 inert gas fusion analyzer, and carbon was measured using a Leco EC12 carbon combustion analyzer. The results are tabulated in Table 1 with some other characteristics of the as-received powders used in this work. These chemical analyses were carried out also for ball-milled and consolidated samples (Tables 2 and 3). For mechanical alloying, powders with an overall composition corresponding to the desired intermetallic compound were loaded and mixed in a hardened stainless steel vial with hardened stainless steel balls, and sealed under purified argon. Ball milling was conducted using a SPEX 8000 laboratory shaker mill at room temperature with air cooling. Other information about ball milling conditions has been included in Table 2.

X-ray diffraction patterns were taken with a Siemens 5000 diffractometer in the θ–2θ geometry using Cu Kα radiation for powders after milling and after consolidation. In addition to phase identification, X-ray diffraction line broadening, with strain broadening and instrumental broadening subtracted, was used to determine average grain size by applying the Scherrer formula. Selected consolidated samples were examined in a JEOL JSM-840A scanning electron microscope (SEM) to observe the morphology of the surfaces and distribu-

tion of pores. Energy dispersive X-ray analysis (EDX) attached to the SEM was used to confirm that impurities are below the EDX detection limit in consolidated samples.

Consolidation of nanophase powders was performed by hot pressing and low strain rate hot forging using a high-pressure consolidation unit designed and assembled at LSU. The current unit has been designed for a maximum temperature of about 500 °C, a working pressure of 1.2 GPa for the typical sample size we use (0.25–0.3125 inch in diameter, 0.125 inch in height), and a compact size to allow operation in a glove box continuously purged with purified argon to avoid contamination during hot consolidation. The rationale for these choices is discussed in Section 4.2. The consolidation duration, i.e., the hold time after the sample has reached the desired temperature, was typically 5 h in this work. Tungsten carbide dies shrink-fitted with an H24 tool steel casing were used in these experiments. Zinc stearate was applied to the die walls as lubricant and was also believed to provide a reducing atmosphere during consolidation at elevated temperatures. Before loading into consolidation die, the ball-milled powders were screened with a 200 mesh (75 μm) sieve to remove large agglomerated particles which may contain composition nonuniformity and cause difficulties in densification. Density of the consolidated compact was determined by measurements of sample weight and volume, and, for high density samples, also by using the buoyancy method applying Archimedes Principle. More details about the consolidation procedures will be presented together with results in the next section. Some information about the consolidated samples is given in Table 3.

3. Results

3.1. Mechanical alloying

For pure Fe, mechanical attrition led to significant broadening of X-ray diffraction lines (Fig. 1(a)), indicating the formation of nanoscale grains (Table 2) and strain accumulation. For binary systems, homogenous alloys were obtained with a composition corresponding

Table 2
Characteristics of ball-milled powders

Powder	Ball to powder weight ratio	Milling duration (hr)	Average grain size (nm)	Chemical analysis	
				C at.%	O at.%
Fe	4:1	20	14	0.2	1.6
Fe_3Al + 2Cr	4:1	20	12	0.1	1.1
Ni_3Al	3.5:1	30	11	0.4	2.0

Table 3
Characteristics of consolidated powders

Powder	Temperature (°C)	Pressure (GPa)	Average grain size (nm)	Chemical analysis		Density (% theoretical)
				C at.%	O at.%	
Fe	500	1.2	18	0.2	2.3	93
Fe₃Al + Cr	500	1.2	19	0.1	0.1	91
Ni₃Al	500	1.2	17	0.5	0.9	92

to the overall composition of the original powder blends after ball milling for sufficiently long duration (Table 2). Composition uniformity in the ball-milled samples was confirmed in SEM using backscattered imaging mode and EDX analysis. X-ray diffraction spectra, shown in Fig. 2(a) and Fig. 3(a), indicate that the milled powders are intermetallic compounds Fe_3Al (disordered B2 structure), and Ni_3Al (disordered Ll_2), respectively. These results are consistent with previous findings in these systems [21,22]. From X-ray line broadening, the average grain sizes have been estimated to be on the order of 10 nm (Table 2). Oxygen and carbon content increased from as-received levels due to contamination during ball milling (Tables 1 and 2). Oxygen concentration, in particular, ranged between 1 at.% and 2 at.% after ball milling.

3.2. Consolidation

(a) Fe₃Al

Fe_3Al has been selected for a systematic consolidation study. The first series of experiments utilized single-step hot pressing at different temperatures ranging from room temperature to 500 °C, at a pressure of 1.2 GPa and a holding time of 5 h. Relative density obtained, in percent of theoretical density, is plotted ver-

sus consolidation temperature in Fig. 4 (open circles). It can be seen that relative density increased monotonically with increasing consolidation temperature. The highest density attained, however, was only 80% of theoretical density for these consolidation conditions.

Alternative consolidation procedures were therefore attempted. The first modification we made was to use a two-step consolidation process. In the first step, a preform was compacted at room temperature using a 0.25 inch i.d. WC die at a pressure of 1.2 GPa for 10 h. The resultant green density was around 65% of theoretical density. The preform was then transferred to another WC die with 0.3125 inch i.d. and hot forged at 500 °C for 5 h. This procedure can be regarded as upset hot forging at low strain rate [23]. It avoids the pressure loss due to die wall friction with the powder, creates stress states favorable for pore closure and bonding across collapsed pore interfaces, and allows easier ejection after consolidation. As seen in Fig. 4 (solid circle), 88% of theoretical density was achieved. A similar process involving die-free sinter-forging has been used by Averback et al. for consolidation of ceramic nanophase powders [15,16].

Addition of a small amount of selected impurity elements is known to have significant impact on the mechanical properties of Fe_3Al intermetallic [24,25]. For example, Cr addition has the effect of increasing
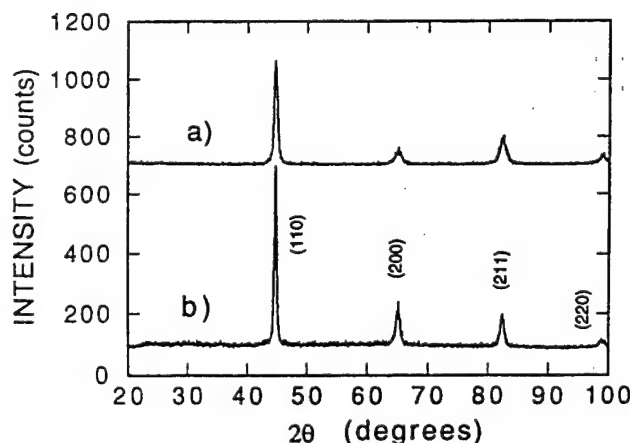
Fig. 1. X-ray diffraction pattern of Fe powder: (a) after ball milling, and (b) after two-step pressing/hot forging consolidation. The ball milling and consolidation conditions are summarized in Tables 2 and 3.
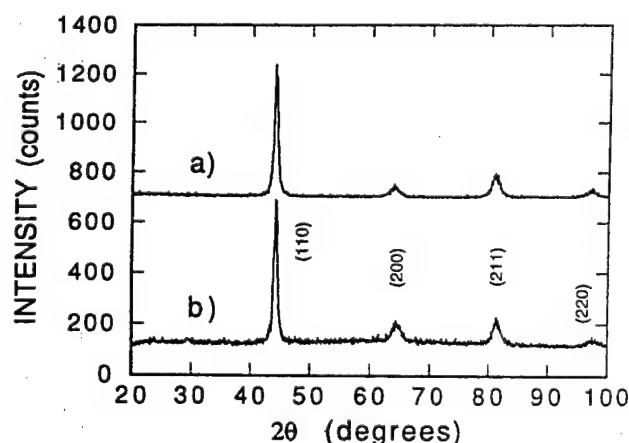
Fig. 2. X-ray diffraction pattern of Fe_3Al + 2Cr powder mixture: (a) alloyed using ball milling, and (b) after two-step pressing/hot forging consolidation. The ball milling and consolidation conditions are summarized in Tables 2 and 3.
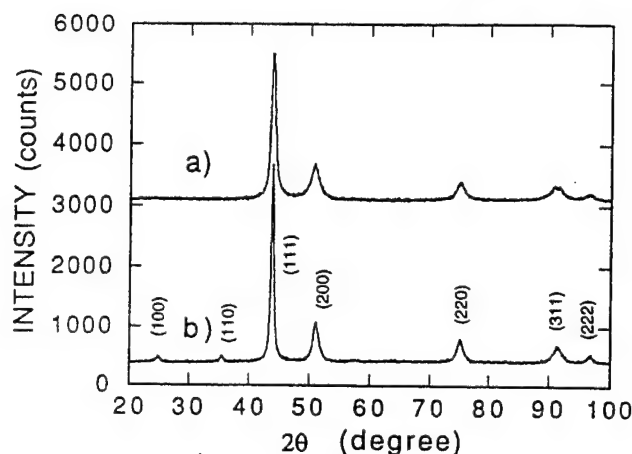
Fig. 3. X-ray diffraction pattern of Ni$_3$Al powder mixture: (a) alloyed using ball milling, and (b) after two-step pressing/hot forging consolidation. The ball milling and consolidation conditions are summarized in Tables 2 and 3.

the ductility of Fe$_3$Al [25]. The enhanced plastic deformation may promote densification during hot pressing. Previous consolidation experiments of this intermetallic have also used Cr-containing Fe$_3$Al [21]. We therefore added 2 at.% Cr into the powder blend during ball milling. The X-ray diffraction pattern for the resultant powder is shown in Fig. 2(a). Consolidation of these powders following the procedure described in the last paragraph yielded 91% of theoretical density.

Fig. 2(b) is the X-ray diffraction pattern after consolidation (triangle in Fig. 4). Comparing it with Fig. 2(a) indicates that the consolidation steps did not result in significant grain growth. The average grain size, estimated from X-ray diffraction line broadening, was
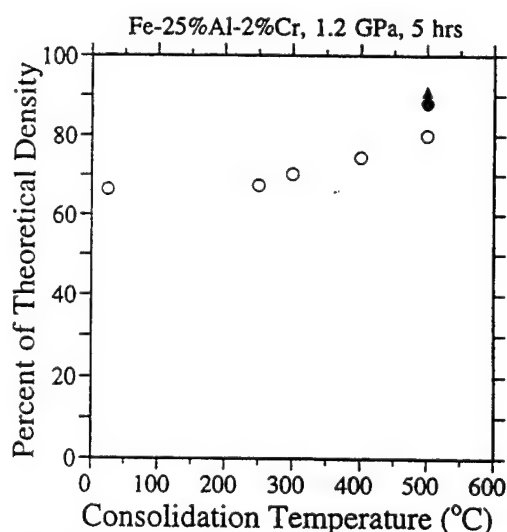
Fig. 4. Relative density of ball-milling alloyed Fe$_3$Al powder after single-step hot pressing at different temperatures (open circles), after two-step pressing/hot forging consolidation (full circle), and containing 2 at.% Cr after two-step consolidation (triangle).

about 19 nm (Table 3). In addition, ordering of the B2 structure is not obvious from the diffraction pattern. According to chemical analysis, while carbon remained at the same level as before consolidation, oxygen content decreased significantly during consolidation. Both were present at only a small fraction of an atomic percent in the consolidated sample.

(b) Fe and Ni$_3$Al

Based on the experience gained through consolidation of Fe$_3$Al, consolidation of nanophase Fe and Ni$_3$Al directly employed the two-step method, with hot forging performed at 500 °C for 5 h. Consolidated Fe and Ni$_3$Al reached 93% and 92% of their respective theoretical densities. X-ray diffraction patterns of these three materials are displayed in Fig. 1(b) and Fig. 3(b), respectively. In all cases, grain growth during consolidation was limited and grain sizes after consolidation remained below 20 nm (Table 3).

Similar to the case of Fe$_3$Al, carbon content in Fe and Ni$_3$Al after consolidation remained at the same level as before consolidation. Oxygen content decreased for consolidated Ni$_3$Al, and increased slightly in Fe. The causes of these observed changes are not clear at present. It can be seen from Table 3 that in all the consolidated samples, carbon concentration was below 0.5 at.% and oxygen concentration was below about 2 at.%. The most oxygen contamination was observed in elemental Fe.

4. Discussion and concluding remarks

4.1. Nanophase intermetallics

In this study, Fe is chosen as an example of elemental nanocrystalline metal. The other two alloys are intermetallic compounds. The choice to study these intermetallics is based on the expectation that nanophase processing may lead to useful properties to these materials. Intermetallic compounds have the drawback of very limited ductility and formability at low temperatures [26–29]. Fine grain size is believed to be beneficial in this regard [30]. It is hoped that by reducing grain size to nanoscale, superplastic deformation processing derived from grain boundary mechanisms (e.g., Coble creep) can be accomplished at low temperatures. After processing into the desired shape, heat treatment at high temperatures can be used to produce grain growth and good creep resistance for high temperature applications. Recent experiments show that nano-sized grains can indeed allow large plastic deformation of otherwise brittle materials [4,7–10,14].

4.2. Consolidation considerations

Most of the consolidation procedures used in this study are similar to those reported for a number of nanophase materials prepared by the gas phase condensation method [15,16]. The best studied systems there have been ceramic oxides, for which near full density compacts have been prepared using sinter-forging at a temperature considerably lower than those used for consolidation of conventional ceramic powders.

A few differences should be noted for mechanically-alloyed nanophase powders. First, mechanically alloyed powders are primarily metallic alloys [17–19]. Consolidation of nanophase metallic alloys is less investigated and the current understanding of their consolidation and deformation behavior is only at a rudimentary stage. Second, these non-oxide metallic powders can become oxidized easily due to their reactive nature and the presence of large surface areas. Powders as-received may already have an oxide layer on particles, and contamination during consolidation at elevated temperatures needs to be carefully protected against. Third, mechanically alloyed powders typically have a wider particle size distribution. These latter two conditions are likely to have observable influence on consolidation [23].

The three major consolidation parameters, temperature, pressure, and contamination control, are briefly discussed in the following.

(a) Consolidation temperature

For conventional materials, pores are removed through sintering at high temperatures for long times, driven by the reduction in surface energy. Nanophase powders will also require elevated temperatures for full densification, but these temperatures are considerably lower compared with those used for conventional coarse-grained counterparts [15,16]. A reduction in sintering temperature can reduce contamination and compositional changes, and stresses and cracking during cooling. A number of factors contribute to this possible processing advantage. For ball-milled powder, particles with varying sizes lead to easier filling of pores of different sizes. Fine grain sizes provide shorter diffusion distances. The high dislocation densities in ball-milled materials are also favorable for sintering. Assisted by some applied stress, densification is possible at relatively low temperatures (see Eq. (1) in (b) below for the effect of grain size on creep).

It should be noted that the diffusional processes that mediate sintering also lead to undesired grain growth. The driving force for grain growth also increases as grain sizes decreases so that the advantage nanophase materials have in sinterability is quickly lost due to concomitant grain growth that destroys the desired nanoscale grain size. Therefore, the consolidation temperature needs to be kept sufficiently low. In the experiments reported in this paper, maximum consolidation temperatures were limited to about 500 °C. As shown above, true nano-size grains (< 20 nm) can be retained under these temperatures (Table 3).

(b) Consolidation pressure

To compensate for the reduced temperature, our strategy is to use hot pressing and forging employing high pressure to enhance the contribution of plastic deformation to densification and bonding, rather than relying primarily on long-range diffusion. Possible stress effects on deformation and densification can be seen from the established formula for creep, in general [31],

$$\frac{\partial \epsilon}{\partial t} = A \frac{\sigma^n}{d^q} \exp\left(- \frac{Q}{RT} \right) f(\rho) \qquad (1)$$

where σ is the applied stress, d the grain size, ϵ the strain, n the stress exponent, A and q constants, Q the activation energy for the process, ρ the density, R the gas constant, and T the temperature. In this expression, n, A, q and Q can have different values for different creep mechanisms (Nabarro-Herring creep, Coble creep, dislocation climb power-law creep, etc. [31]), and $f(\rho)$ accounts for density effects. The enhanced ductility that nano-grained powders may have at low temperatures can contribute to densification by plastic deformation [15,16]. Also, the extensive plastic deformation under high stress ensures disruption of any continuous surface oxides on powder particles which may degrade bonding and properties [23].

(c) Contamination

Oxidation during ball milling and hot consolidation of non-oxide powders can be a serious problem. The incorporated oxygen can have deleterious effects on mechanical properties of the compact [32], and perhaps on consolidation as well. To reduce contamination, mechanical alloying and consolidation have been performed under inert atmosphere. Impurity contents of powders obtained from commercial sources, after mechanical alloying, and after consolidation have been monitored using chemical analysis. The data reported in Section 3 suggest that we have been able to control oxygen content to no more than a couple of atomic percent after ball milling. Oxygen content was not further increased, and in fact appeared to have decreased in some systems, during consolidation. However, effort is needed to acquire as-received powders with lower impurity levels (see Table 1 for impurity analysis of as-received powders), and to modify our ball milling and consolidation equipment and procedures to further reduce contamination during processing.

4.3. Full density processing

We have shown that mechanically alloyed intermetallic alloys can be readily consolidated into near-full density (>90% of theoretical density) samples with grain sizes below about 20 nm and minor oxygen and carbon impurities. The highest density we have obtained so far for intermetallic alloys is in a preliminary experiment for ball-milled tetragonal $MoSi_2$, where 95% of theoretical density has been observed with grain sizes maintained at below 20 nm. Achieving full density, however, remains a challenge and is being pursued in our lab. We note that grain sizes below the level reported in this paper (20 nm) may not be necessary for a large number of potential applications. Grain sizes in the upper nanometer (of the order of 100 nm) scale would still be significantly finer than those in conventional materials. In such cases, full density is possible simply by using a higher consolidation temperature and/or a longer time than have been used in this preliminary study. From the trend of grain growth during consolidation observed in the present work, it appears promising that full density can be attained before the grain sizes increase to beyond the typical range of nanophase materials. This possibility has been demonstrated recently in our laboratory [33].

Acknowledgment

References

[1] H. Gleiter, *Prog. Mater. Sci.*, 33 (1989) 223.

[2] R. Birringer, H. Gleiter, H.P. Klein and P. Marquardt, *Phys. Lett.*, 102A (1984) 365.

[3] R. Birringer and H. Gleiter, in R.W. Cahn (ed.), *Advances in Materials Science and Engineering*, Pergamon Press, New York, 1988, p. 339.

[4] R.W. Siegel, *MRS Bull.*, 15 (1990) 60; R.W. Siegel, S. Ramasamy, H. Hahn, L. Zongquan, L. Ting and R. Gronsky, *J. Mater. Res.*, 3 (1988) 1367.

[5] Council on Materials Science Panel Report, *J. Mater. Res.*, 4 (1989) 704.

[6] F.H. Froes and C. Suryanarayana, *J. Met.*, 40 (1989) 12.

[7] H. Bohn, T. Haubold, R. Barringer and H. Gleiter, *Scripta Metall. Mater.*, 25 (1991) 811.

[8] H. Hahn and R.S. Averback, J. Amer. Cer. Soc. 74, 2918 (1991).

[9] C. Altstetter, presented at NATO Advanced Study Institute. Portugal, June 28–July 10, 1992.

[10] R. Lappalainen and R. Raj, in D. Van Aken, G. Was and A. Ghosh (eds.), *Microcomposites and Nanophase Materials*, TMS. 1991, p. 41.

[11] A.H. Chokshi, A. Rosen, J. Karch and H. Gleiter, *Scripta Metall.*, 23 (1989) 1679.

[12] G.W. Nieman, J.R. Weertman and R.W. Siegel, *Scripta Metall.*, 24 (1990) 145; G.W. Nieman, J.R. Weertman and R.W. Siegel, *J. Mater. Res.*, 6 (1991) 1012; G.E. Fougere, J.R. Weertman, R.W. Siegel and S. Kim, *Scripta Metall. Mater.*, 26 (1992) 1879.

[13] A.M. El-Sherik, U. Erb, G. Palumbo and K.T. Aust. *Scripta Metall. Met.*, 27 (1992) 1185; U. Erb, presented at the *2nd Inter. Conf. Nanostr. Mater.*, Germany, Oct. 1994.

[14] H. Chang, C.J. Alstetter and R.S. Averback, *J. Mater. Res.*, 7 (1992) 2962; H. Chang, J. Höfler, C.J. Alstetter and R.S. Averback, *Mater. Sci. Eng.*, A153 (1992) 676.

[15] H. Hahn, J. Logas and R.S. Averback, *J. Mater. Res.*, 5 (1990) 609.

[16] H.J. Höfler and R.S. Averback, *Mater. Res. Soc. Symp. Proc.*, 286 (1993) 9.

[17] C.C. Koch, in R.W. Cahn, P. Hassen and E.J. Kramer (eds.), *Materials Science and Technology*, Vol. 15, VCH, Weinheim. 1991, p. 193.

[18] A.W. Weeber, and H. Bakker, *Physica B*, 153 (1988) 93.

[19] E. Hellstern, H.J. Fecht, Z. Fu and W.L. Johnson, *J. Appl. Phys.*, 65 (1989) 305; J. Eckert, J.C. Holzer, C.E. Krill, III, and W.L. Johnson, *J. Mater. Res.*, 7 (1992) 1751.

[20] T. Christman and M. Jain, *Scripta Metall. Mater.*, 25 (1991) 767; T. Christman, K. Heady and T. Vreeland, Jr., *Scripta Metall. Mater.*, 25 (1991) 631.

[21] M. Jain and T. Christman, *Acta Metall. Mater.*, 42 (1994) 1901.

[22] E. Ma, J. Pagan, G. Cranford and M. Atzmon, *J. Mater. Res.*, 8 (1993) 1836.

[23] R.M. German, *Powder Metallurgy Science*, Metal Powder Industries Federation, Princeton, NJ, 2nd edn., 1994, p. 321; and in H. Kuhn and A. Lawley (eds.), *Powder Metallurgy Processing*, Academic, New York, 1978, pp. 102 and 142.

[24] C.G. McKamey, P.J. Maziasz and J.W. Jones, *J. Mater. Res.*, 7 (1992) 2089.

[25] C.G. McKamey, J.A. Horton and C.T. Liu, *J. Mater. Res.*, 4 (1989) 1156; *Scripta Metall. Mater.*, 24 (1990) 2119; D.G. Morris and M. Leboeuf, *Acta Metall. Mater.*, 42 (1994) 1817.

[26] H.A. Lipsitt, *Mater. Res. Soc. Symp. Pro.*, 39 (1985) 351.

[27] K. Aoki and O. Izumi, *J. Jpn. Inst. Met.*, 43 (1979) 358.

[28] T. Liu and H. Inouye, *Metall. Trans. A*, 10 (1979) 1515.

[29] P.K. Brindley, in N.S. Stoloff, C.C. Koch, C.T. Liu and O. Izumi (eds.), *High Temperature Ordered Intermetallic Alloys II*, Materials Research Society, Pittsburgh, PA. 1987, p. 419.

[30] A. Inoue, T. Masumoto and H. Tomioka, *J. Mater. Sci.*, 19 (1984). 3097

[31] R.W. Hertzberg, *Deformation and Fracture Mechanics of Engineering Materials*, John Wiley and Sons, New York, 3rd edn., 1989.

[32] R.B. Schwarz, S.R. Srinivasin, J.J. Petrovic and C.J. Maggiore. *Mater. Sci. Eng. A*, 155 (1992) 75.

[33] L. He and E. Ma, *J. Mater. Res.*, in press.

Application opportunities for nanostructured materials and coatings

Maurice Gell

Department of Metallurgy, University of Connecticut, Storrs, CT 06269, USA

Abstract

Nanostructured materials have the potential to change materials science as we know it today significantly, as well as to provide a new generation of materials with a quantum improvement in properties. While many interesting properties have been generated in the laboratory, there is still much work to be done before there are production applications for nanostructured materials and coatings in gas turbine engines and similar demanding strength- and temperature-limited applications. This paper (1) describes the need for improved materials in gas turbine engines, (2) summarizes the improved physical and mechanical properties that have been reported for nanostructured materials, (3) discusses a research and development methodology that has the potential for accelerating technology implementation, and (4) describes high pay-off applications.

Keywords: Nanostructures; Coatings

1. Introduction

The gas turbine engine uses a wide variety of structural materials and coatings (Fig. 1). Over the years, the strong competitive requirement to provide gas turbine materials with higher strength, lighter weight and greater temperature capability has spurred the development and application of new materials and processes, including titanium alloys, nickel and cobalt superalloys, superplastic forging (Gatorizing), directional solidification for columnar- and single-crystal turbine airfoils, oxidation and thermal insulating coatings, etc. Accompanying these pioneering technology implementation efforts are rigorous testing requirements for materials reliability, component fabricability, consistency of properties and cost effectiveness. All these factors must be considered, along with the gas turbine industry's future needs for improved materials, as the technology readiness of nanostructured materials is assessed.

2. Future gas turbine engine requirements

Since the introduction of gas turbine engines into commercial airline service in the 1950s, there has been continual improvement in gas turbine performance as measured by thrust specific fuel consumption (Fig. 2). Fuel efficiencies have been obtained by improvements in engine cycle efficiency, component efficiency and materials strength and temperature capabilities. Since fuel costs can amount to as much as 40% of airline operating costs, there are continuing competitive pressures to improve engine fuel efficiency further. Additional fuel efficiency improvements, of 20% or more, are possible with ultra-high-bypass engines, such as the advanced ducted prop or the propfan, in which the major portion of the air entering the front of the engine "bypasses" the engine core. In addition, NASA is sponsoring design studies and critical materials developed programs for the demanding requirements of the high speed civil transport.

The aircraft industry is expected to undergo significant growth over the next two decades, spurred by increased internationalization of business and enhanced personal wealth around the globe. Gas turbine engine designers have been asked to define how they are going to achieve the aggressive goals established for advanced engines. They have indicated that more than 50% of the performance gains will have to come from improved materials, processing, and coatings. Materials will have to be developed with increased strength per unit weight, higher temperature capability, toughness and ductility, and these new materials must be cost effective. Both on an absolute basis and on a relative basis to other gas turbine engine technologies, the demand for improved materials is as great now as it has been at any time during the history of gas turbine engines.

Nanostructured Materials
Current Materials
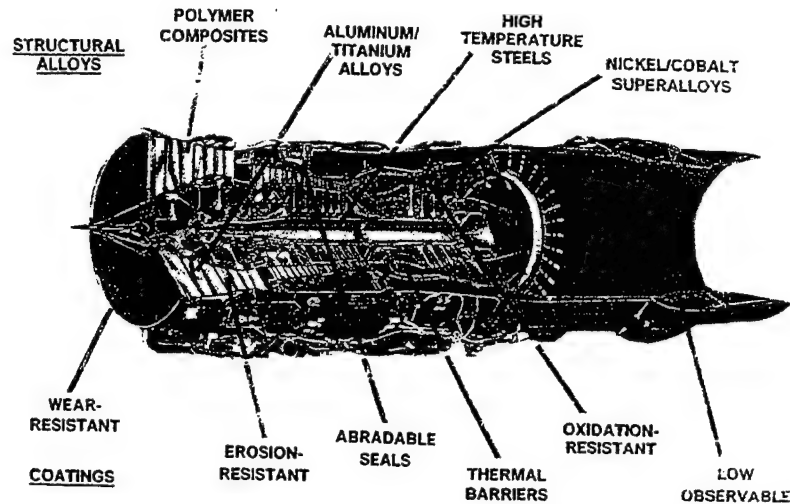
Fig. 1. The cross-section of Pratt & Whitney's F100 military engine showing the wide range of structural materials and coatings employed.

3. The potential for nanostructured materials

Fig. 3 summarizes selected property changes that have been reported in a number of review papers on nanostructured materials [1–6]. Increased strength and hardness combined with engineering levels of ductility and toughness could provide a new generation of structural materials and coatings. Ceramic coatings with reduced thermal conductivity, elastic modulus, and higher thermal expansion coefficient would make attractive thermal barrier coatings. Increased diffusivity and grain boundary plasticity should improve the fabricability of intermetallic and ceramic materials. Based on these properties and potential, which have been discussed more fully elsewhere [7,8], how do we proceed to assess the potential for nanostructured materials applications in gas turbines?

4. Technology assessment and transition

There are strong domestic and international competitive pressures to reduce the time to take a new technology from the laboratory to production application. In the gas turbine industry, new materials and processing techniques have typically taken ten years to be introduced into service, with some technologies requiring as much as 25 years. This lengthy qualification period is associated with the extensive multi-requirement specimen and component testing conducted to ensure materials and processing capability and reproducibility. All this testing provides engines the promised performance, durability and flight safety. With no sacrifice in these important requirements, it is appropriate to explore an aggressive, yet disciplined, new methodology, defined at Pratt & Whitney, to reduce the development time by

Fig. 2. The improvements in commercial gas turbine engine fuel efficiency over time.
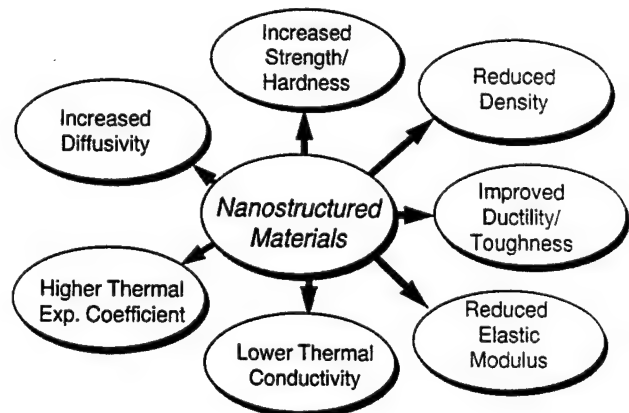
Fig. 3. Summary of selected property changes associated with nanostructured materials.
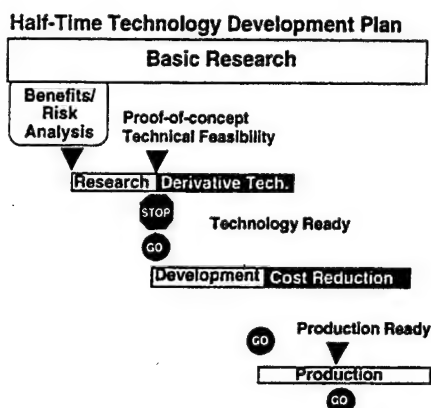
Fig. 4. Methodology for nanostructured materials to reduce technology development and implementation time by one-half.

Fig. 6. The development strategy for nanostructured materials.

more than 50% and to suggest that it be applied to the emerging technology of nanostructured materials.

Fig. 4 shows an outline of this generic half-time methodology. For nanostructured materials, there is a large body of basic research that has produced a wide range of potential property improvements (Fig. 3). This basic research activity should be continued at a high level to promote scientific understanding at the nanoscale, and to generate additional new phenomena and property improvements for a wide range of product applications. However, there is also a strong need for applied research to "harvest the fruit" from these basic studies in order to develop new and improved products.

The applied research phase in Fig. 4 starts with industry looking at its critical competitive needs in light of the initial promising properties for nanostructured materials. A benefits/risk analysis should be conducted to prioritize among the many applied research program options and to ensure that those selected have the potential for an attractive financial return. The next step is to establish "success criteria" for the selected material or process that can be evaluated in the laboratory on specimens or with laboratory scale processing equipment. The success criteria for a new material are a number of quantitative property goals that reflect the complete range of requirements that would have to be satisfied for successful application. For example, the success criteria established for nanostructured steel bearings in gas turbine engines are shown in Fig. 5.

Property	Property goal for Nano M50 (relative to conv. M50)
Rolling contact fatigue life	10.0×
Wear resistance	2.0×
Fracture toughness	1.3×
Strength and hardness	1.1×

Fig. 5. The "success criteria" selected for nanostructured steel bearing materials
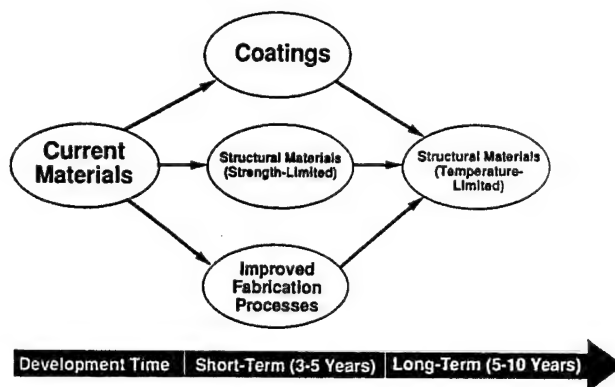
When all of the success criteria have been satisfied, then and only then, do we proceed to the next more expensive development stage, involving large quantities of material, statistically significant multi-heat specimen testing to ensure process and property reproducibility, and component testing in a realistic engine environment. This methodology, if followed, would prevent the wasteful expenditure of hundreds of millions of dollars for the scale-up and development of immature materials technologies, where the basic flaws could have been identified at the applied research stage.

A similar establishment of success criteria are used throughout the framework shown in Fig. 4. This half-time methodology should be conducted as part of an integrated product development teaming environment, in which the success criteria are established and the results periodically reviewed by stakeholders in the entire research, development and implementation cycle, including designers, analysts, researchers, manufacturers, and customers.

5. High pay-off applications

Of all the potential gas turbine engine applications, and as a result of risk/benefit analyses, Fig. 6 suggests that technology focus can be provided by initially conducting applied research on high pay-off applications such as coatings, small, low-temperature structural components, and improved fabrication processes. These are described in turn.

Based on the initial property improvements (Fig. 3), it should be possible to develop a new generation of gas turbine coatings with improved resistance to erosion, wear, oxidation, and hot corrosion, and as thermal insulating coatings. These coatings can be applied using modifications to a number of production deposition processes, including thermal spray, physical vapor deposition, and electrodeposition. Of all coating applications thermal barrier coatings have the highest pay-off because they can provide both enhanced durability and fuel efficiency.
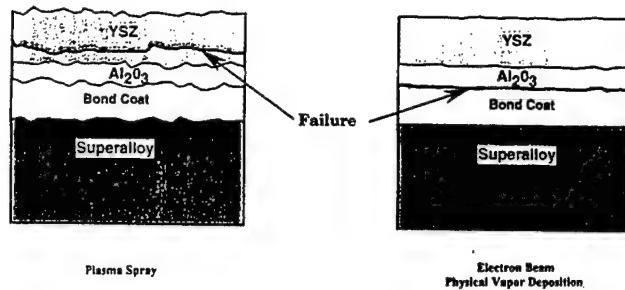
Fig. 7. The layer structure of plasma and physical vapor deposited thermal barrier coatings and the failure (spallation) location.

Thermal barrier coatings consist of a metallic bond coat, usually an MCrAlY or Pt-Aluminide, a thermally grown Al_2O_3 film, and a ceramic layer, usually yttria stabilized zirconia (Fig. 7). These coatings reduce superalloy metal temperatures by as much as 300 °F, and, thereby, provide improved durability to combustors, transition ducts and turbine vanes. In recent years, highly durable thermal barrier coatings applied to turbine blades by electron beam physical vapor deposition processes have been used with reduced turbine blade cooling to provide improved fuel efficiency. Thermal barrier coatings fail by spallation of the coating at or near the ceramic to metal bond line (Fig. 7). The durability of thermal barrier coatings is dependent on the strength of the bond coat to alumina and the alumina to zirconia bonds and the strain tolerance of the zirconia microstructure.

With the gas turbine industry's demand for higher operating temperatures to provide enhanced fuel efficiency and the continued use of superalloy structural materials, thermal barrier coatings with reduced thermal conductivity provide the highest pay-off coating application. Nanostructured ceramics should exhibit enhanced phonon scattering at grain and layer boundaries [9] and provide the basis for a new generation of thermal barrier coatings (Fig. 8). In addition to low thermal conductivity, nanostructured thermal barrier coatings will need high bond strength and strain tolerance, and long-term compositional and microstructural stability.

Fig. 9. Gas turbine engine main shaft bearing.

In addition to higher turbine temperatures, improved engine performance can also be obtained by higher rotor speeds. This requires the development of main shaft bearing materials (Fig. 9) with the success criteria defined in Fig. 5. By fabricating nanostructured M50

Fig. 8. Advances in thermal barrier coatings and the key technical contributors.
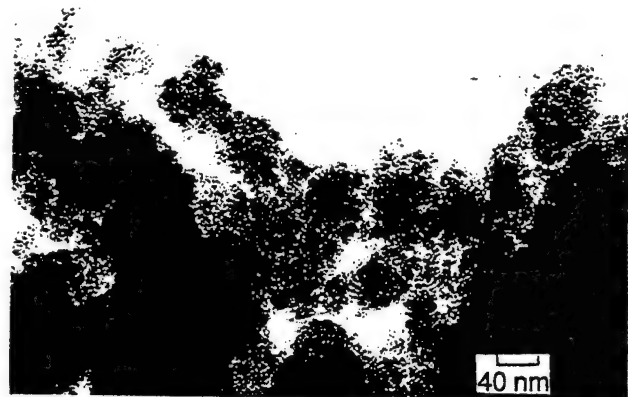
Fig. 10. Nanostructured M50 powder and compaction [11].
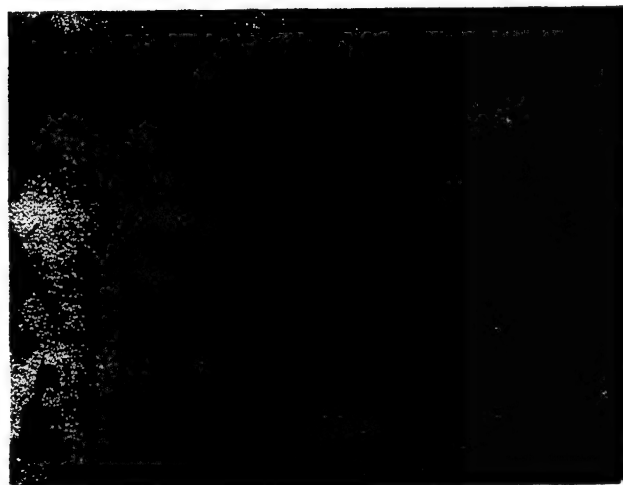
(a)
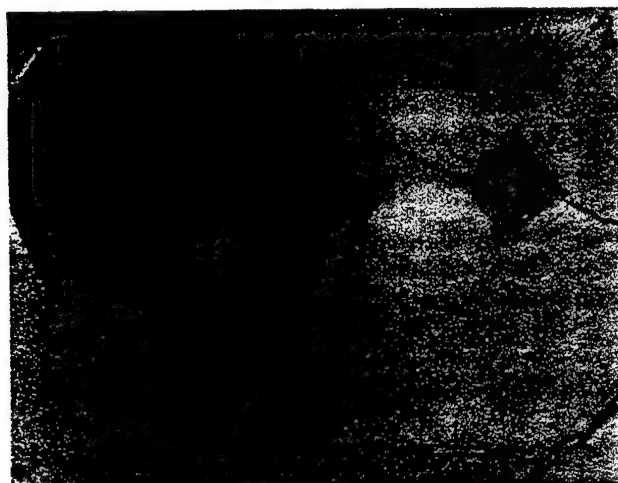
(b)

Fig. 11. Consolidation of ZrO_2 matrix/Al_2O_3 fiber reinforced composite: (a) conventional matrix with processing at 1400 °C and 110 MPa and (b) nanostructured matrix with processing at 1040 °C and 110 MPa [13].

steel, it should be possible to increase the hardness by reducing the grain size and to increase the fracture toughness by refining the carbide size. This is the goal of a recent ONR grant [10,11]. Nanostructured M50 powder has been produced by a chemical synthesis process, consolidated in a vacuum hot press and the compacts are undergoing initial characterization (Fig. 10) [12].

While the nanostructured coatings and bearings just described make use of nanostructured materials properties in the final application, it is also possible to use nanostructure properties to enhance the fabricability of complex materials and components, even if the nanostructure is not retained in the final product. Intermetallic and ceramic matrix composites have traditionally been difficult to fabricate because the high temperatures and pressures necessary for matrix densification pro-

duce fiber damage. Fig. 11 shows for a ceramic composite consolidated at 1400 °C and 110 MPa that there is considerable damage in the alumina fibers, fibre-matrix interaction, and extensive porosity in the conventional zirconia matrix [13]. In contrast, by using a nanostructured zirconia powder matrix, the composite can be consolidated at 360 °C lower temperature with complex matrix densification and no fiber damage or fiber-matrix interaction.

6. Summary

Improved materials and coatings will be required to satisfy the aggressive performance and durability requirements of gas turbine engines to be introduced over the next 20 years. Based on limited laboratory testing, nanostructured materials show the promise for a quantum improvement in a variety of needed properties. In addition to a continuing high level of basic research, there is need for applied research to assess rapidly this new technology and provide for rapid technology transition. A technology development and implementation methodology is described and applied to nanostructured materials that has the potential to reduce technology transition times by more than 50%. High pay-off applications for nanostructured materials in gas turbine engines are defined and initial results are presented for thermal barrier coatings, steel bearings and ceramic composite fabrication.

References

[1] B.H. Kear et al., *Research Opportunities for Materials with Ultrafine Microstructures*, National Materials Advisory Board National Academy Press, 1989.

[2] H. Gleiter, Nanocrystalline solids, *J. Appl. Crystallogr.*, 2- (1991) 79-90.

[3] H. Gleiter, Materials with ultrafine microstructures: retrospectives and perspectives, *Nanostruct. Mater.*, 1 (1992) 1 20.

[4] R.W. Siegel, Nanophase materials: synthesis, structure, and properties. In F.E. Fujita (ed.), *Physics of New Materials* Springer, Heidelberg, 1992.

[5] C. Suryanarayana and F.H. Froes, The structure and mechanical properties of metallic nanocrystals, *Metall. Trans. A*, 23 (1992) 1071-1081.

[6] R.W. Siegel and G.E. Fougere, Mechanical properties of nanophase materials. In G.C. Hadjipanayis and R.W. Siegel (eds.), *Nanophase Materials: Synthesis-Properties-Applications* Kluwer, Dordrecht, 1994.

[7] M. Gell, Applying nanostructured materials to future gas turbine engines, *J. Mater.* (October 1994) 30-34.

[8] M. Gell, The potential for nanostructured materials in gas turbine engines, *NANO '94, Proc. Second Int. Conf. on Nanostructured Materials, Stuttgart, October 1994*, in *Nanostruct Mater.*, 6 (1995) 997-1000.

[9] P.G. Klemens and M. Gell, Thermal conductivity of zirconia and some of its solid solutions, to be published, 1995.

[10] K.E. Gonsalves, C.C. Law, J. Morral and M. Gell, Nanostruc-
tured bearing alloy studies, ONR Grant No. N00014-94-1-0579.

[11] K.E. Gonsalves, C.C. Law and M.G. Chow, Synthesis and
processing of nanostructured M50 type steel, *Nanostruct. Mater.*,
4 (1994) 139–147.

[12] C.C. Law, K.E. Gonsalves and M. Gell, Nanostructured M50
Steel, unpublished resutls.

[13] S. Bose, Applications of nanocrystalline materials as matrices of
composites–processing and performance advantages, *Mater. Sci.
Eng.*, A196 (1995) 105–109.

ELSEVIER

Characterization of humidity-sensing NiO–Ni(OH)$_2$ nanocomposites by impedance spectroscopy

Jin-Ha Hwang[a], T.O. Mason[a], M.F. Buehler[b], J.G. Darab[b], D.W. Matson[b], J.C. Linehan[b]

[a]*Northwestern University, Department of Materials Science and Engineering, Evanston, IL 60208, USA*
[b]*Pacific Northwest Laboratory, Materials and Chemical Sciences Center, Richland, WA 99352, USA*

Abstract

Nanocomposites of NiO and Ni(OH)$_2$ prepared by compaction of powders synthesized by rapid thermal decomposition of precursors in solution (RTDS) were characterized by impedance spectroscopy at room temperature. The marked decrease of resistivity with increasing humidity was attributed to an increase of the water phase and ionic transport therein. Electrical behavior was modeled in terms standard electrocomposite mixing laws.

Keywords: Impedance spectroscopy; Powders; Thermal decomposition

1. Introduction

Since the pioneering work by Gleiter and coworkers [1,2] there has been extensive work on nanophase materials. The interest in nanoscale materials arises because of their potentially enhanced electrical, mechanical, optical, and chemical properties. In particular, nanophase materials have been shown to offer the following advantages over their conventional microphase counterpart: (1) exceptional physical and chemical control, (2) a relatively high fraction of surfaces (interfaces) or grain boundaries, (3) enhanced sinterability due to high driving forces and reduced diffusion distances, and (4) ability to thereby control the ultimate microstructure.

Gas–solid interactions at surfaces, grain boundaries, or interfaces between dissimilar materials are essential for chemical sensing by solid state devices. Thus, nanophase ceramics have the potential for chemical sensing applications due to the large fraction of such interfaces, potentially enhanced chemical surface activity at these interfaces, and a large percent of interconnected porosity in pressed compacts or partially sintered materials. In spite of their potential, little electrical characterization of nanophase ceramics for chemical sensing has been reported.

Humidity control is important for energy conservation in drying operations and for maintenance of indoor relative air quality. A variety of ceramic sensors (e.g., Al$_2$O$_3$, ZrO$_2$) and polymeric sensors (cellulose acetate butyrate) are serving as humidity sensors based upon changes in resistance or capacitance with changes in relative humidity [3,4]. Ceramic thin films and electrocomposites have also been investigated for humidity sensing characteristics [5].

Mechanism(s) of humidity sensing by electroceramics, whether microphase or nanophase, are not completely understood at present. Most work to date has focused on sensing optimization through doping and/or control of processing [6–10]. There is some consensus that proton conduction along hydroxylated surfaces at low levels of humidity plus ion conduction in physisorbed water layers at higher levels of humidity govern the overall conductivity [4]. Surface area, porosity, pore interconnectivity, and pore size distribution are all known to play important roles.

AC impedance spectroscopy (IS) is a powerful tool for investigating the electrical properties of electrochemical systems. IS can be performed without electrode polarization effects. Furthermore, IS has the capability to separate bulk response from electrode-related phenomena. In the event that bulk impedance

arcs are depressed below the real axis in Nyquist plots ($-Z_{imag}$ vs. Z_{real}), IS can provide information concerning the inhomogeneity of the microstructural features governing the bulk response. Furthermore, it can often be established whether a bulk response arises from the solid phase or from interfaces based upon the effective dielectric constant obtained.

The present study focused on the humidity sensitivity of nanocomposites of NiO and Ni(OH)$_2$. Powders were synthesized by rapid thermal decomposition of precursors in solution (RTDS). The humidity sensitivity of electrical resistivity and capacitance were established by in situ impedance spectroscopy measurements vs. relative humidity (RH).

2. Experimental procedure

The rapid thermal decomposition of precursors in solution (RTDS) method was used to synthesize mixed nanophase powders of NiO and Ni(OH)$_2$. The RTDS process applies a high temperature and pressure to a rapidly flowing solution containing dissolved precursors to synthesize ultrafine powders [11,12]. An aqueous solution of 0.1 M Ni(NO$_3$)$_2$ and 0.5 M urea was passed through the heated tube of the RTDS apparatus at temperatures of up to 400 °C, pressures of 40–55 MPa, and flow rates of up to 100 ml min^{-1}. The residence time of the reacting fluid was approximately 2 s. Within the heated tube, nanocrystalline particles nucleated as oxides and hydroxides. The mixture of particles and fluid was then rapidly expanded and quenched using an ice bath. The resulting nanophase particles were subsequently separated by centrifugation. They were washed with deionized water and then dried under flowing nitrogen. The phases present and their relative amounts were determined by X-ray diffraction and thermogravimetric analysis, respectively. The particle size distribution was determined by transmission electron microscopy (TEM).

The resulting nanophase powder was pressed into pellets of 3.2 mm diameter and 1.4 mm thickness at 225 MPa with an overall porosity of 40–45%. The faces were sputter-coated with approximately 20 nm thick silver to make good electrical contacts with the Pt electrodes of the IS apparatus. Samples were held between Pt contacts with very slight spring pressure in a test fixture constructed from alumina. This apparatus was then inserted into the humidity chamber as shown in Fig. 1. Water-saturated vapor was obtained by bubbling compressed air through deionized water at room temperature. Relative humidity (RH) was controlled between 7% and 94% by mixing saturated and dried air streams. A certified NIST-traceable digital hygrometer (Fisher Scientific, Pittsburgh, PA) was employed to verify RH changes. This was especially important at the extremes of RH.

Electrical connections were made from the two Pt electrodes by Pt leads to a Schlumberger impedance gain-phase analyzer (Model SI 1260, Schlumberger Technologies, Farnborough, Hampshire, UK) in two-point configuration. Data were collected from 10 MHz to 1 Hz at 20 points per decade. The spectra obtained were corrected for stray instrumental and cable immitances by a nulling procedure and analyzed for resistance and capacitance equivalent circuit elements vs. RH by a commercial software package [13].

Parallel weight gain experiments were carried out in sealed evacuated chambers using saturated solutions of salt + hydrate mixtures to control RH [14]. Nanophase compacts were weighed dry, then equilibrated in each RH environment for times longer than the equilibration times indicated by the IS measurements, and subsequently reweighed on a calibrated, high resolution laboratory balance.

3. Results and discussion

The particle size distribution of the nanophase starting powder is shown in Fig. 2, based upon TEM analysis. The average particle size was 22.0 ± 9.4 nm. XRD results in Fig. 3 indicate the presence of both NiO and Ni(OH)$_2$. Since Ni(OH)$_2$ decomposes above 200 °C, a TGA study was performed at 240 °C to determine the weight percentages of each phase. These were 53 wt.% and 47 wt.% for NiO and Ni(OH)$_2$, respectively. Ni(OH)$_2$ has been previously reported in nanophase Ni metal produced by the gas condensation method [15]. Typical room temperature impedance

1. Compressed air gas
2. Flowmeter
3. Water bubbler
4. Drierite
5. Hygrometer
6. Specimen chamber
7. Impedance analyzer
8. Oil bubbler
9. Hood
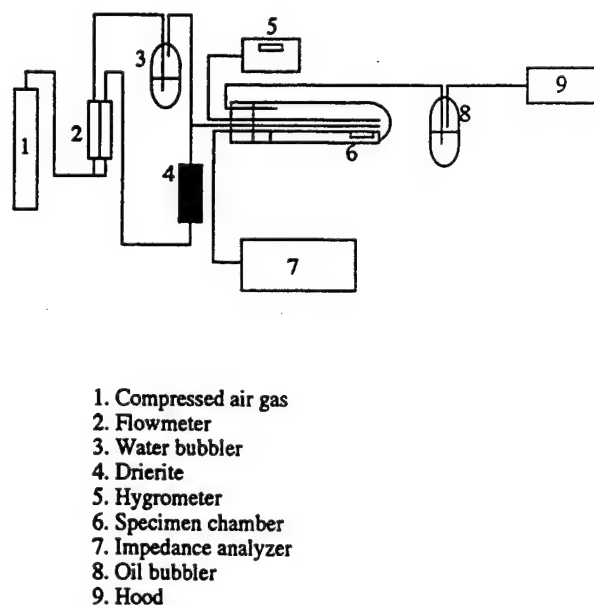
Fig. 1. Schematic of the humidity chamber used for impedance spectroscopy measurements.
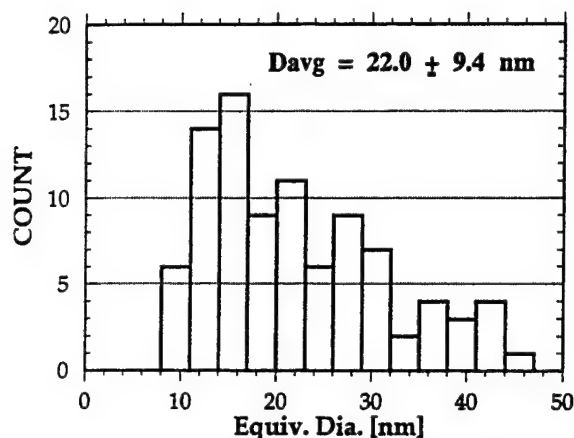
Fig. 2. Particle size distribution of NiO–Ni(OH)$_2$ powders produced by RTDS determined by TEM.

spectra of a NiO–Ni(OH)$_2$ pressed compact ($\sim 56.4\%$ dense) are shown in Fig. 4(a,b). In each spectrum, the frequency increases from right to left. Two arcs are obtained, an incomplete depressed arc (really a super-position of two electrode arcs) at low frequency and a nearly perfect semicircular arc, centered on the real axis, at high frequency. The low frequency arc was confirmed to be an electrode polarization arc on the basis of the capacitance obtained from equivalent cir-cuit fitting ($\sim \mu F$), which was relatively insensitive to RH. The high frequency (bulk) arc shrinks significantly as RH is raised.

The bulk arc was modeled as a resistor and capacitor in parallel. The values of the capacitances and resis-tances obtained are shown in Figs. 5 and 6, respec-tively. Capacitance remains between 2 and 6 pF and is relatively independent of RH. (The 94% RH value was anomalously high, ~ 30 pF, and is not shown. We suspect that this value reflects a condensed surface film at one or both electrodes.) At the same time resistance changes of almost three orders of magnitude with RH, from megohms to kilohms, were observed. There is a
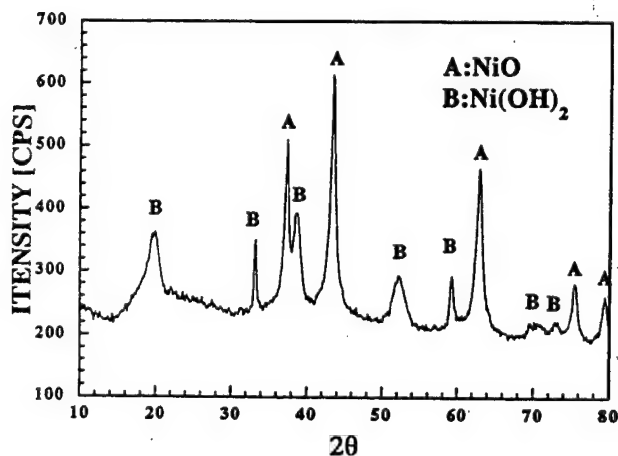
Fig. 3. X-ray diffraction pattern of nanocomposite NiO–Ni(OH)$_2$.
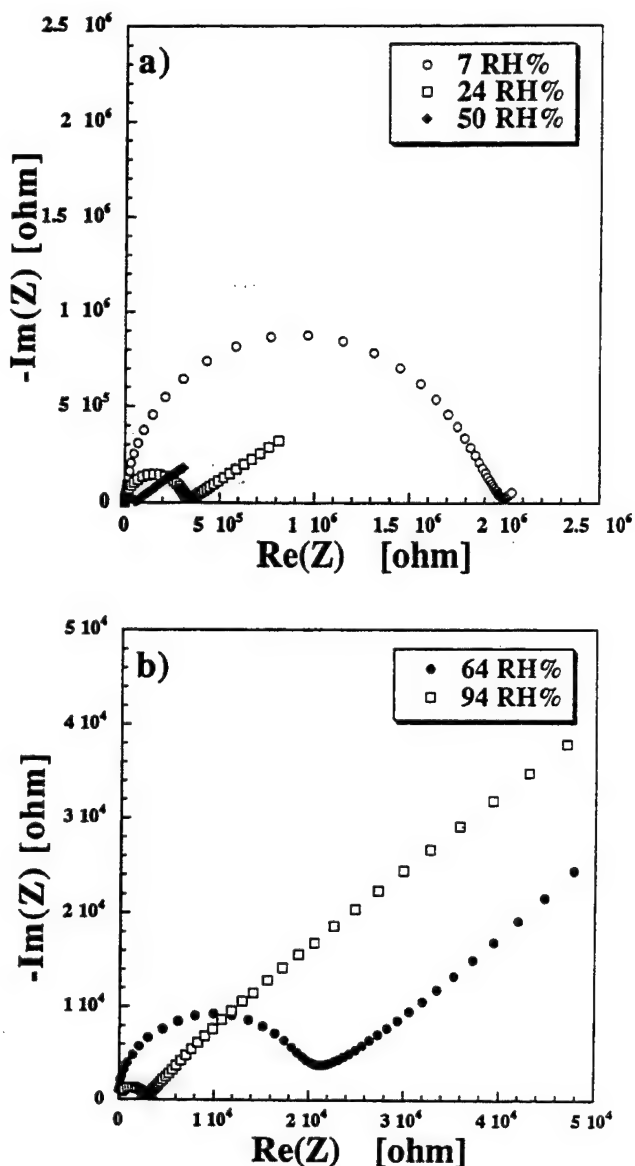
Fig. 4. Impedance spectra at (a) low relative humidity and (b) high relative humidity.

noticeable hysteresis in resistance as RH is cycled from low RH to high RH and back again.

The capacitances obtained suggest that the electrical properties of nanophase NiO–Ni(OH)$_2$ in moist envi-ronments are dominated by the condensed water phase in the pore network. The lines in Fig. 5 represent the predicted behavior if the effective capacitance:

$$C = e_{eff}e_o(A/l) \tag{1}$$

is governed by the solid phases ($e_{eff} \sim 10$ for NiO or Ni(OH)$_2$) or by the water phase ($e_{eff} = 80$ for H$_2$O). The behavior is consistent with a continuous water phase at all values of RH.

To confirm this hypothesis, the weight gain of the NiO–Ni(OH)$_2$ was determined vs. RH and is plotted in Fig. 7. In contrast to microporous α-Fe$_2$O$_3$ ceramics,
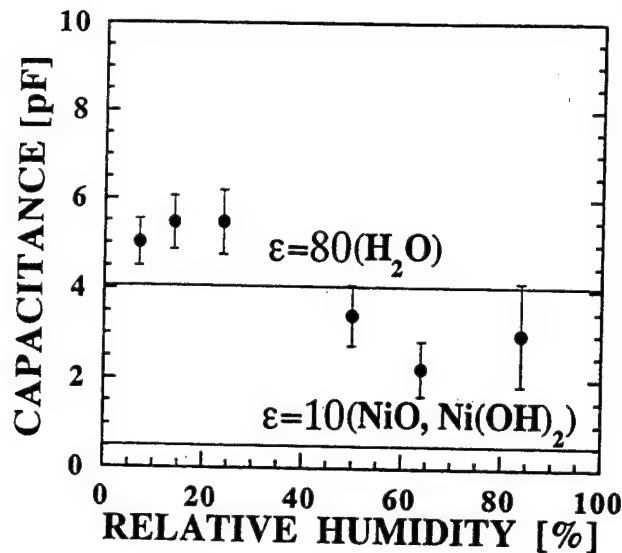
Fig. 5. Capacitances derived by equivalent circuit fitting of the bulk impedance arcs vs. relative humidity. Anticipated capacitances based upon solid and water phases are shown for comparison.

where maximum weight gain at high RH was reported to be 2.7% by weight [16], a value of 10.6 wt.% was obtained at 92% RH. This corresponds to approximately 72% of the pores being filled with water at this RH or water amounting to approximately 31 vol.% of the compact. Even at 7% RH, the water phase amounts to around 4 vol.% of the compact. This finding was confirmed by use of the Kelvin equation:

$$r_c = 2\gamma V_m / \{RT\ln(100/[\mathrm{RH}]\} \qquad (2)$$

where γ is the surface tension of water, V_m is the molar volume of water, T is temperature, R is the gas constant and RH is relative humidity. Condensation of water
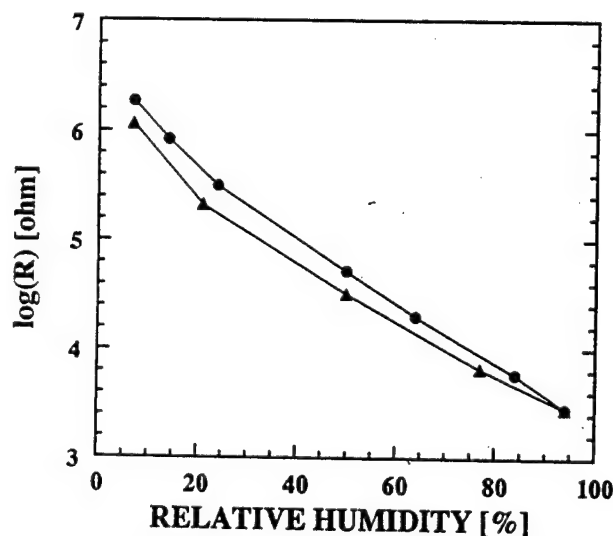
Fig. 6. Resistances derived by equivalent circuit fitting of the bulk impedance arcs vs. relative humidity. (Circles represent data taken during initial increases in RH. Triangles represent data taken during subsequent reduction in RH.)
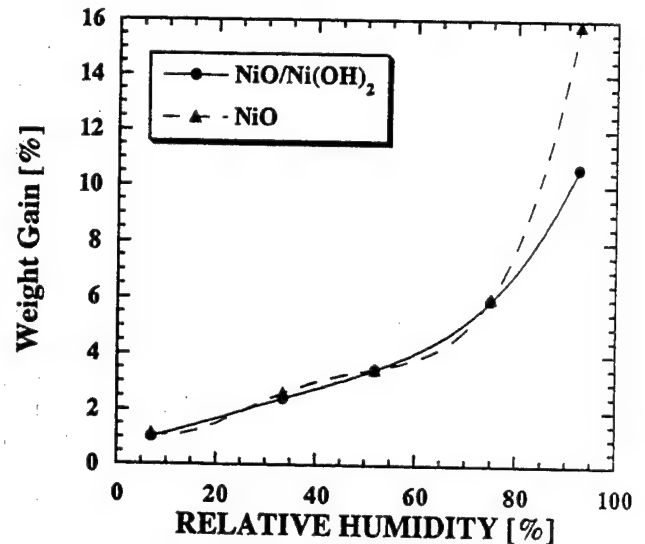
Fig. 7. Weight gain vs. relative humidity before and after decomposition.

takes place in cylindrical pores with critical radius, r_c, or $r_c/2$ if the pores are assumed to be open at both ends. The critical pore radius is calculated to be 0.4 nm at 7% RH and 6.4 nm at 92% RH, not unreasonable values for the nanocomposites under consideration.

The bulk electrical resistivity of nanophase NiO–Ni(OH)$_2$ in a moist environment can be understood in terms of electrocomposite concepts reviewed by McLachlan et al. [17]. The phase connectivity of the present specimens can probably be expressed as 0–3–3, where the numbers represent the NiO (0–D or isolated), the Ni(OH)$_2$ (connected in 3–D) and the condensed water phase (also connected in 3–D). The following development treats electrical conductivity rather than resistivity. The overall conductivity can be approximated as [18]:

$$\sigma \sim \Sigma \sigma_i \beta_i \phi_i \sim \sigma_w \beta_w \phi_w \qquad (3)$$

where σ_i is the phase conductivity, ϕ_i is the volume fraction of that phase, and β_i is a unitless connectivity parameter between 0 and 1. Given the anticipated low conductivity of the NiO phase and the fact that it may not be interconnected ($\beta = 0$), little or no contribution from this phase is anticipated. Similarly, experiments on pure Ni(OH)$_2$ indicated that its conductivity is negligible at room temperature. In contrast, deionized water saturated with the nanophase NiO–Ni(OH)$_2$ powder was found to have a conductivity of 6.8×10^{-3} (ohm-cm)$^{-1}$ at room temperature. The published solubility product of Ni(OH)$_2$ is 5.47×10^{-16} [19]. The solubility product can be combined with the published mobilities of Ni^{2+} and OH$^-$ [20] to calculate the ionic conductivity. The calculated conductivity is 2.4×10^{-6} (ohm-cm)$^{-1}$ which is much less than the conductivity of water saturated with nanocomposite NiO–Ni(OH)$_2$. Furthermore, the pH increased more than 2 units upon

dispersing nanophase $NiO–Ni(OH)_2$. These observations could be the result of increased solubility of RTDS $Ni(OH)_2$ due to its nanocrystalline nature or due to the dissolution of surface impurities from the RTDS nanoparticles which act as sinks for a variety of species. Enhanced $Ni(OH)_2$ and/or impurity solubility and correspondingly higher conductivity support our contention that the condensed water phase dominates the conductivity. Therefore, Eq. (3) reduces to the $\sigma_w \beta_w \phi_w$ product of the water phase (w = water). The β factor is a measure of the connectivity (or inversely of the tortuosity) of the water phase.

Based upon the experimental water contents vs. RH in Fig. 7 (used to calculate ϕ_w) and the measured water phase conductivity of 6.8×10^{-3} (ohm-cm)$^{-1}$, and assuming $\beta = 1$ independent of RH, the predicted resistance vs. RH behavior was calculated and plotted in Fig. 8. Agreement with experiment is poor, especially at low RH. As shown by the Kelvin equation (Eq. (2)), the critical pore size is a function of RH. Therefore, β can be expected to be a function of RH, as the network of water-filled pores changes continuously with RH. If σ_w is assumed to be independent of RH, the β factor can be calculated from the overall conductivity vs. RH (Fig. 6) and the water content vs. RH (Fig. 7). The result is shown in Fig. 9. As RH approaches zero, the factor β approaches zero. The microstructural picture consistent with this result involves isolated small pores with little connectivity at low RH. As larger and larger pores begin to fill with water, the connectivity increases with RH. The connectivity never reaches unity, however, even when 72% of all pores are occupied. This is not unexpected, given the tortuosity of the pore network. Experiments with concentrated suspensions of insulating glass spheres in conductive electrolytes
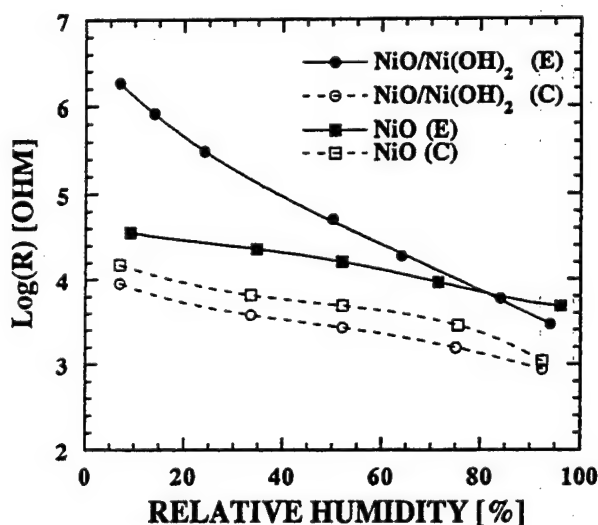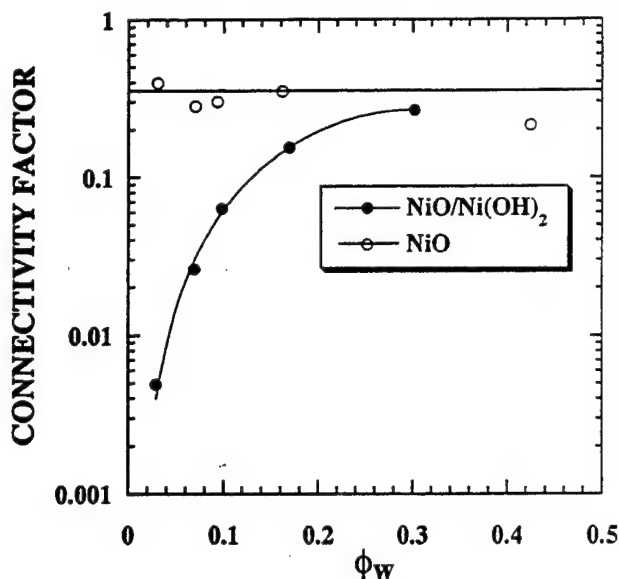
Fig. 9. Calculated connectivity parameter (β) vs. water content (ϕ_w: volume fraction of the adsorbed water phase).

yielded a $(\phi_w)^{1.5}$ relationship for the normalized conductivity, σ/σ_w [21]. This would correspond to $\beta = \phi_w^{0.5}$, or $\beta \sim 0.55$ at $\phi_w(\text{max}) = 0.3$ for the $Ni(OH)_2–NiO$ system at 92% RH. The fact that the experimental value of $\beta = 0.25$ is less than $\phi_w^{0.5}$ may be attributable to particle size and distribution effects, or possibly to uncertainty in the experimental value of σ_w.

The presence and distribution of $Ni(OH)_2$ in nanocomposites appear to be important to humidity sensing. Compacts subjected to pre-treatment at or just above 200 °C to decompose the hydroxide exhibited higher conductivities (lower resistivities) and far less sensitivity to RH at room temperature than the nanocomposites (see Fig. 8). All three variables on the right side of Eq. (3) (σ_w, β_w, ϕ_w) can be changed as a result of hydroxide decomposition. Water saturated with decomposed nanophase powder exhibited a conductivity of 3.3×10^{-3} (ohm-cm)$^{-1}$, or roughly half that of water saturated with nanocomposite $NiO–Ni(OH)_2$. This explains why the resistances cross at the highest RH in Fig. 8. The weight gain vs. RH of pellets made from decomposed powders is plotted in Fig. 7, from which ϕ_w can be readily calculated. Note that the overall porosity increases upon decomposition (see Figs. 7 and 9). The predicted values of conductivity vs. RH from Eq. (3), based upon an assumption of $\beta = 1$, are also shown in Fig. 8, and agree reasonably well with the experimental data. As mentioned above, β is expected to be less than unity, probably of the order of 0.55 at $\phi_w = 0.3$. Assuming that $\sigma_w = 3.3 \times 10^{-3}$ (ohm-cm)$^{-1}$, independent of ϕ_w, the connectivity factor (β) calculated from the measured conductivities appears to also be independent of water content (see Fig. 9). This suggests a fundamental difference in the microstructures

Fig. 8. Comparison of impedance-derived resistance of nanophase $NiO–Ni(OH)_2$ vs. nanophase NiO derived by decomposition of the nanocomposite. E, experimental; C, calculated resistances.

of the as-prepared and decomposed nanophase compacts. The tortuosity of the adsorbed water in the decomposed sample is lower (higher connectivity) and does not appear to vary with water content.

The major drawbacks to nanophase humidity sensors are their slow kinetics and irreversibility. After changes in RH, IS readings stabilized in tens of minutes in the increasing RH direction, but only after hours in the decreasing RH direction. This is due to the difficulty of evaporating water from the fine pore network. Furthermore, capillary forces are extremely large at fine pore sizes, leading to permanent changes in the microstructure with RH cycling, as evidenced by the hysteresis in the resistance measurements (Fig. 6).

4. Conclusion

The humidity-sensing behavior of $NiO–Ni(OH)_2$ nanocomposite is controlled by the ionic conduction through the adsorbed water phase. The decomposition of $Ni(OH)_2$ into NiO affects the pore structure. Before decomposition, the humidity-sensing characteristics depend mainly on the connectivity of pores, while after decomposition the humidity-sensing is controlled solely by the amount of condensed water. Impedance spectroscopy and water gain experiments can be employed to evaluate the microstructural connectivity factor.

Acknowledgments

References

[1] H. Gleiter, in N. Hansen, A. Horsewell, T. Leffers and H. Lilholt (eds.), *Proceedings of the Second Riso International Symposium on Metallurgy and Materials*, Riso National Laboratory, Roskilde, Denmark, 1981, p. 15.
[2] H. Gleiter, *Prog. Mater. Sci., 33* (1989) 223.
[3] B.M. Kulwicki, *J. Am. Ceram. Soc., 74* [4] 1991) 697.
[4] M.J. Madou and S.R. Morrison, *Chemical Sensing with Solid State Devices*, Academic Press, San Diego, CA, 1989, p. 506.
[5] Y. Ushio, M. Miyayama and H. Yanagida, *Sensors Actuators, B17* (1994) 221.
[6] K. Katayama, K. Hasegawa, Y. Takahashi, T. Akiba and H. Yanagida, *Sensors Actuators, A24* (1990) 55.
[7] T. Nitta, Z. Terada and S. Hayakawa, *J. Am. Ceram. Soc., 63* (1980) 295.
[8] T.M. Racheva, I.D. Stambolova and T. Donchev, *J. Mater. Sci., 29* (1994) 281. [9] E. Joanni and J.L. Baptista, *Sensors Actuators, B17* (1993) 69.
[10] K. Tsukamoto, C. Yamagishi, K. Koumoto and H. Yanagida, *J. Mater. Sci., 19* (1984) 2493.
[11] D.W. Matson, J.C. Linehan and R.M. Bean, *Mater. Lett., 14* (1992) 222.
[12] D.W. Matson, J.C. Linehan and M.E. Geusic, *Particulate Sci. Tech., 10* (1992) 143.
[13] B.A. Boukamp, Equivalent Circuit (EQUIVCRT.PAS), University of Twente, Dept. of Chemical Technology, P.O. Box 217, Enschede, The Netherlands.
[14] J.F. Young, *J. Appl. Chem., 17* (1967) 241.
[15] Y. Sakka and T. Uchikoshi, *Powder Metallurgy, 36* (1993) 179.
[16] C. Cantalini and M. Pelino, *J. Am. Ceram. Soc., 75* (1992) 546.
[17] D.S. McLachlan, M. Blaszkiewicz and R.E. Newnham, *J. Am. Ceram. Soc., 73* (1990) 2187.
[18] E.J. Garboczi, *Cem. Concr. Res., 20* (1990) 591.
[19] J.C. Chang, in D.R. Lide et al. (eds.), *CRC Handbook of Chemistry and Physics*, CRC Press Inc., Boca Raton, FL, 1991, pp. 8–43.
[20] P. Vanysek in D.R. Lide et al. (eds.), *CRC Handbook of Chemistry and Physics*, CRC Press Inc., Boca Raton, FL, 1991, pp. 5–111.
[21] R.E. De La Rue and C.W. Tobias, *J. Electrochem. Soc., 106* (1959) 827.

Electrical characterization of nanocrystalline titania—I: (Impedance spectroscopy studies between 300 K and 473 K)

Siddhartha Bhowmik,[a] Kristen P. Constant[a],*, John C. Parker,[b] M. Ali[b]

[a]Department of Materials Science and Engineering, Iowa State University, Ames, IA 50011, USA
[b]Nanophase Technologies, Darien, IL 60561, USA

Abstract

The electrical properties of nanocrystalline titania with gold electrodes were characterized using impedance spectroscopy in the frequency range 10^{-2} to 10^6 Hz and temperature range 300 K to 500 K. An attempt has been made to correlate the microstructural properties of these specimens to the electrical response of the material over the different ranges of temperatures. The results indicate that the conductivity of nanocrystalline titania is dependent on the porosity, grain size, and grain boundaries. The impedance and polarization behavior of the samples, especially at the electrodes, is also affected by the humidity. The electrical behavior of the nanocrystalline material makes it a candidate for use as a low temperature gas sensor.

Keywords: Electrical characterisation; Nanocrystalline titania; Impedance spectroscopy

1. Introduction

Nanocrystalline materials have in recent years been of interest because of the possibility to generate properties that may differ significantly from the microcrystalline material. These differences may arise from the smaller particle size, increased grain boundaries, a larger fraction of atoms residing at these interfaces, and differences in the porosity of the nanocrystalline materials. Differences may also originate due to the high purity of the nanocrystalline material compared with the microcrystalline form. The defect structure of microcrystalline titanium oxide has been studied in detail [1–3] in attempts to describe the conductivity mechanism. These studies included measurements of the d.c. conductivity at high temperatures and the possibility of using titania as an oxygen gas sensor. An attempt was made by Azad et al. [4] to characterize microcrystalline titania using impedance spectroscopy at room temperature.

Impedance spectroscopy (IS) has been used to study the electrical properties of ceramics since Baurle's [5] work with zirconia, where he showed that the effects of electrode, grain interiors and grain boundaries could be resolved in the admittance plane or the impedance plane. IS has since proven to be an effective method in evaluating the microstructural effects on conductivity when combined with other methods of characterization. Characterization of microstructural effects on conductivity is essential in the development of materials for use in electronic components.

In the case of ceramic materials, impedance, Z, usually arises due to capacitive reactance, X_c, and resistance, R. For a capacitor, the capacitive reactance, X_c, is the opposition to current:

$$X_c = 1/\omega C, \tag{1}$$

where $\omega = \nu/2\pi$, ν is the frequency, and C the capacitance.

Z is a complex quantity and can be described [6] in terms of various related functions such as admittance,

$$Y = 1/Z, \tag{2}$$

and complex dielectric permittivity,

$$\epsilon = Y/j\omega C = \epsilon' - j\epsilon'', \tag{3}$$

where $j = \sqrt{(-1)}$. In capacitors [7] having dielectric losses, the loss tangent,

* Corresponding author.

Table 1
The density and cell constant, K_0, of nanocrystalline and microcrystalline TiO_2

Sample	Calcination temperature (°C)	Soak time (h)	Bulk density (g cm^{-3})	True density (pycnometer) (g cm^{-3})	K_0 [a] (cm^{-1})	Structure [c]
Nanocrystalline TiO_2	NA (Green)	NA [b]	~2.2	~4.1	NA	Dominantly rutile: some anatase
Nanocrystalline TiO_2	400°C	4	~2.3	~4.1	0.215	NA
Nanocrystalline TiO_2	500°C	4	~2.3	~4.1	0.185	NA
Nanocrystalline TiO_2	650°C	4	~2.8		0.165	NA
Nanocrystalline TiO_2	800°C	4	~3.6		0.340	NA
Microcrystalline TiO_2	800°C	4	~3.4	~4.1	0.227	Rutile ~80% Anatase ~20%

[a] $K_0 = d/A$, where d = thickness of pellet and A = area of applied electrode.
[b] NA = not available/applicable.
[c] Structures obtained from Ref. [12] indicate the dominance of rutile in all these cases.

$$\tan\delta = \epsilon''/\epsilon', \qquad (4)$$

is used as an estimate of the power dissipation. For capacitors used for charge storage the value of $\tan\delta$ is usually low.

Sensors can be classified [8] according to the basis of the generation of the charge carrier and its transport. Accordingly, the sensing mechanism may be due to bulk effects, i.e. the physical properties of the grain itself, grain boundary effects, as in the case of PTC thermistors, or through surface absorption, as in the case of humidity sensors. In characterizing the electrical properties of microcrystalline titania, the emphasis has been in understanding the bulk or grain interior conductivity. However, in the case of nanocrystalline titania, the effect of grain interior effects is unlikely to be the sole effective mechanism. Porosity and grain boundaries are expected to significantly affect the properties. The purpose of this paper is to discuss the experimental results in terms of porosity, grain size and electrodes and the possible use of nanocrystalline titania as an effective low temperature chemical sensor.

2. Experimental procedure

Nanocrystalline TiO_2 was prepared through inert gas phase condensation [9,10]. In this method atomic clusters of TiO_2 were first formed by the evaporation of Ti in a pure He gas. The Ti vapor was then condensed in a liquid N_2 cold finger and oxidized with the rapid introduction of oxygen into the chamber to form TiO_2.

The loose powders were compacted uniaxially, with pressures ranging from 15,000 to 20,000 psi. The pressure used is an important factor as the pressure is responsible for the breakdown of the particle agglomerates. Test samples were usually ~1 cm in diameter and 0.1 cm in thickness in the green state. The pellets formed were dry pressed with a light coating of stearic acid on the punch to facilitate mold release. To avoid

lamination cracks, care was taken in expelling the pellets.

The green nanocrystalline samples were calcined in air at temperatures between 400°C and 800°C in a tube furnace, with a soak time of 4 h (see Table 1). Calcining at 400°C improved the strength of the samples for handling purposes. Higher temperature calcining of the nanocrystalline TiO_2 enabled examination of the grain growth and porosity on the electrical measurements. Bulk density measurements and 'true density' were measured using pycnometery to monitor changes in porosity. The evolution of the pore structure was examined as a function of temperature and calcination time. Microstructural studies were done in parallel with scanning electron microscopy (SEM) and transmission electron microscopy (TEM) to see the corresponding increase in grain sizes. Since the impedance measurements done to date have been at temperatures much below the calcining temperatures, grain growth was not expected to occur during impedance measurements.

Microcrystalline TiO_2 (Aldrich Chemicals, 99.999%) was pressed between pressures ranging from 14,000 to 20,000 psi and the pellets formed were calcined in air at 800°C for 4 h (soak time). X-ray diffraction (XRD) measurements were done to indicate the phases present at this stage. Electrodes were applied to all the calcined specimens, which were sputter-coated (Polaron SC 502, Sputter Coater) with high purity gold. Sputter-coating ensures the formation of porous electrodes; additionally, all the parameters were kept constant to form electrodes of equal thickness. The application and monitoring of the electrodes are important factors since they play an important role in impedance measurements.

Impedance measurements were performed using a Solarton 1260 Impedance Gain-Phase Analyzer (Schlumberger Technologies, Billerica, MA). The measurements were done in an apparatus designed to take into account the characteristic impedance of the instru-
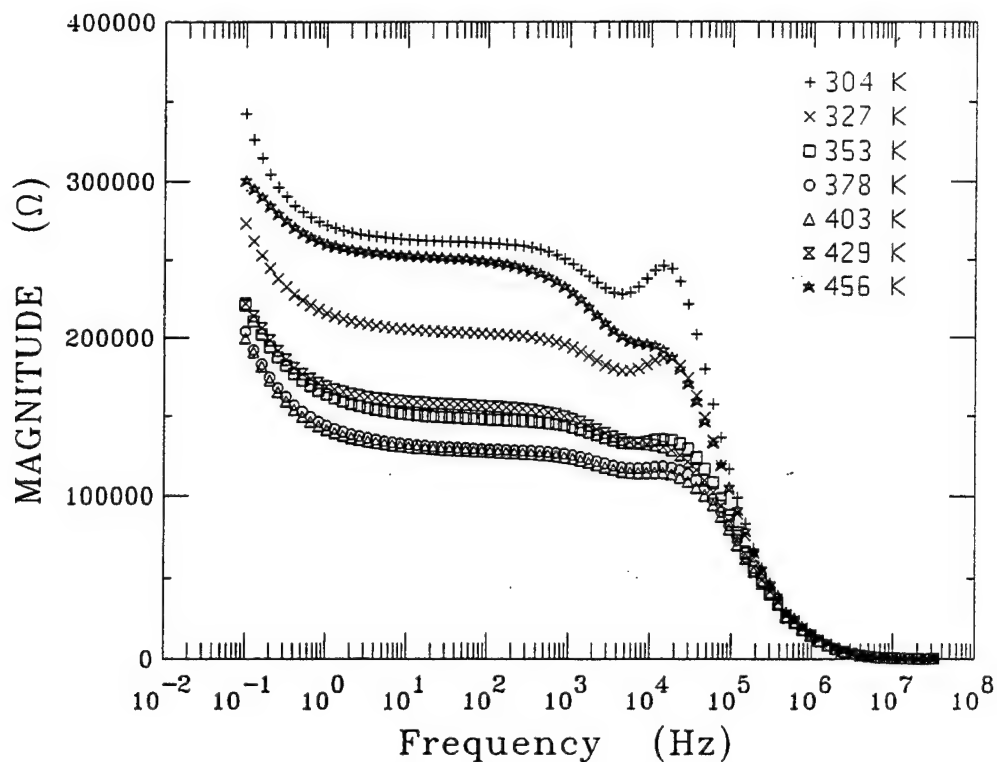
Fig. 1. Impedance vs. frequency for a nanocrystalline TiO_2 sample calcined at 400°C (673 K) at different temperatures.
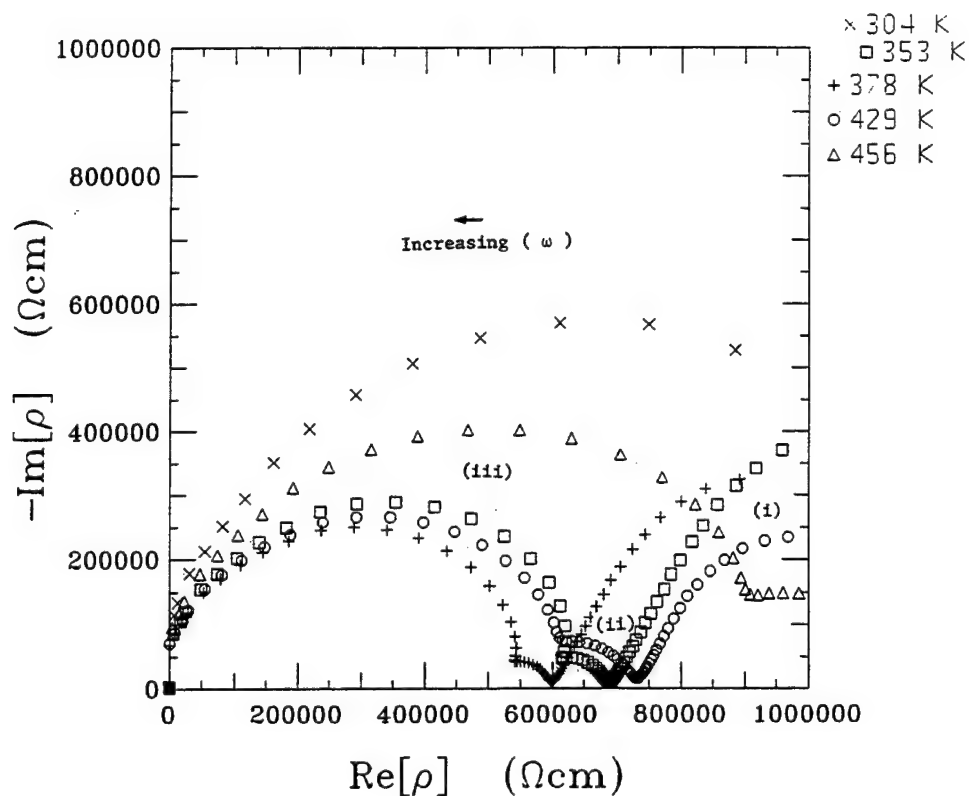
Fig. 2. Cole–Cole plot of nanocrystalline TiO_2 calcined at 400°C (673 K), showing the three major effects of (i) the electrode, (ii) the grain boundaries and (iii) the grain interior.
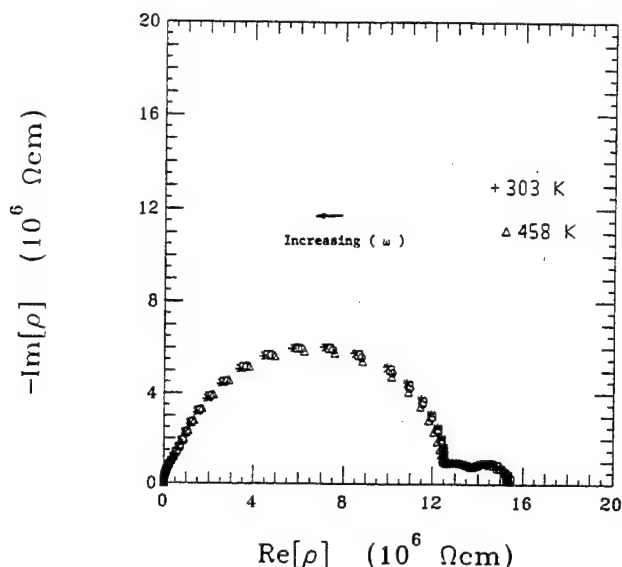
Fig. 3. Cole–Cole plot of nanocrystalline TiO$_2$ calcined at 800°C (1073 K).

type-K thermocouple. A constant amplitude sinusoidal voltage was applied across the sample and the phase shift and amplitude of the current measured at each frequency. The frequency was automatically scanned through the range 10^{-2} Hz to 10 MHz, and data were collected and analyzed [11].

3. Results and discussion

Fig. 1 shows the impedance as a function of frequency for nanocrystalline TiO$_2$ calcined at 400°C (673 K) at some representative temperatures. The impedance, Z, of the sample initially decreases with increasing temperatures but then the trend reverses around 378 K and is seen to increase. The Cole–Cole [12] plot of the impedance data for this sample, Fig. 2, shows that there are three distinct polarizations or arcs. When a system is subjected to an applied potential difference there is a polarization effect at each interface [6]. When the voltage or electric field is reversed, the rate at which the polarized region changes is dependent on the characteristic of that interface. This is slow for chemical reactions at the TiO$_2$/electrode/air, triple phase contacts, leading to polarizations only at low frequencies. This polarization is at higher frequencies for grain boundaries and even greater for grain interiors [5,13]. Thus, from the Cole–Cole plots we can suggest the following effects: (i) the effect of electrodes

ment and also to reduce noise, especially at higher frequencies. Four terminal measurements were used to eliminate contact resistance and lead effects. Rigid cables (or leads) from the sample were of short length and consisted of platinum as the inner conductor and stainless steel as the outer conductor. The sample was then heated within the conductivity apparatus, in air, and the temperature of the sample was monitored using a

Fig. 4. Comparison of impedance of nanocrystalline TiO$_2$ samples calcined at 400°C, 500°C, and 800°C.
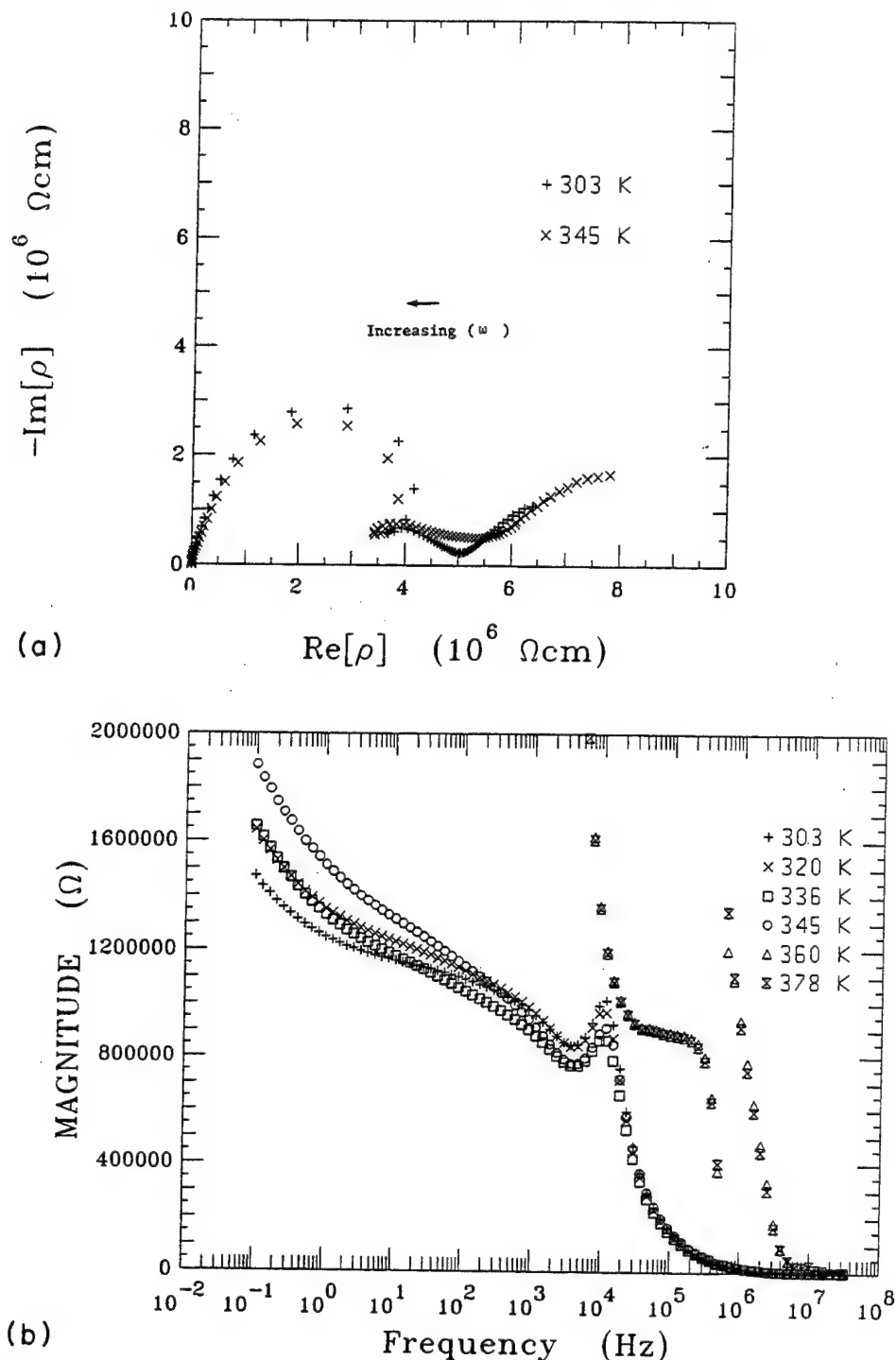
Fig. 5. (a) Cole–Cole plot of a microcrystalline TiO₂ sample calcined at 800°C. (b) Impedance vs. frequency for a microcrystalline TiO₂ sample calcined at 800°C.

(space charge polarizations) at low frequency; (ii) the grain boundary effect at intermediate frequencies; and (iii) the bulk effect at the highest frequency range. Within the bulk effect we actually see the distortion of the semicircle, which is the effect of two arcs with different relaxation times. This may be due to more than one phase (the anatase and the rutile) being present in the material. For samples calcined at 500°C

(773 K) there is no appreciable change in the magnitudes of the impedance or the trends. The Cole–Cole plot also shows a similar pattern for this sample.

Fig. 3 shows the Cole–Cole plots of a nanocrystalline sample calcined at 800°C (1073 K) in the temperature range 303–453 K. As in Fig. 2, there are three distinct semicircles for all ranges of temperature. However, there is less distortion of the grain interior arc.
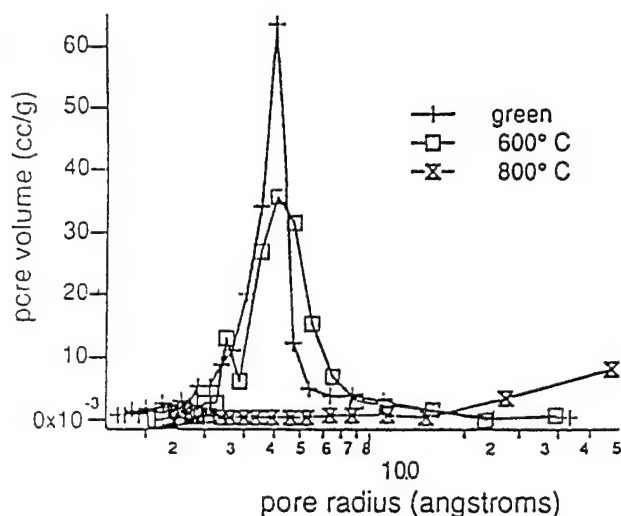
Fig. 6. Pore size distribution in nanocrystalline samples calcined at various temperatures.

Interestingly, there are no changes in the patterns or magnitudes of the arcs through the entire range of temperatures. Obviously such constancy is also reflected in the impedance vs. frequency response . The overall change from the previous behavior of Figs. 1 and 2 is actually noticed at samples calcined above 650°C (923 K). The other important behavior is seen in the flattening of the arcs from the electrode and grain boundary effects or polarizations. The overall difference in the

impedance between samples sintered at 400°C, 500°C, and 800°C is observed in Fig. 4. It is seen that the impedance of the samples calcined at lower temperatures is less than those at higher temperatures by more than an order of magnitude.

Fig. 5(a) shows the Cole–Cole plot of a microcrystalline sample calcined at 800°C. The overall impedance of the microcrystalline titania pellet is significantly higher than that of the nanocrystalline material at any particular temperature. In this case the Cole–Cole plots still suggest three major effects. However, the effect of electrodes and that of grain boundaries are comparatively less than that of the bulk effect. The arc due to the bulk (grain interior) effect seems to be highly skewed in shape, which is indicative of the existence of another phase. Fig. 5(b) shows the impedance vs. frequency response for the same sample at different temperatures.

Table 1 shows the bulk density, 'true density', and the physical properties of some of the representative samples. For the nanocrystalline samples significant densification (bulk density) occurs from 400°C to 800°C. This densification is consistent with the decreasing pore structure of the samples with increasing calcination temperatures (Fig. 6). Bulk and 'true density' measurements of samples in the green state and samples calcined at 400°C also indicate no significant change in the porosity of these materials. TEM studies also indicate no significant grain growth of the nanocrystalline

(a)

(b)

Fig. 7. (a), (b).

(c)

(d)

(e)

Fig. 7. (a) SEM micrograph of a micro-TiO_2 sample calcined at 800°C. (b) TEM micrograph of a nano-TiO_2 sample calcined at 400°C. (c) TEM micrograph of a nano-TiO_2 sample calcined at 500°C. (d) TEM micrograph of a nano-TiO_2 sample calcined at 600°C. (e) TEM micrograph of a nano-TiO_2 sample calcined at 800°C.
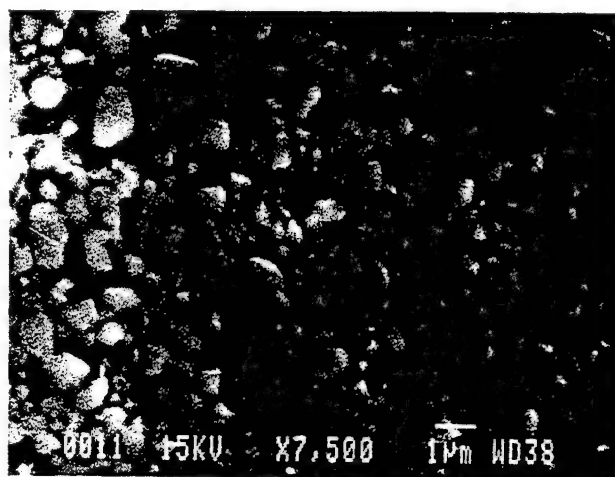
material below 500°C, as was also reported by Hahn et al. [14].

On the basis of these studies, our present hypothesis is that increased porosity and grain boundaries of the nanocrystalline TiO_2 are the most important factors in showing the increased sensitivity of the response. This is also observed by comparing the impedance responses at different temperatures (Figs. 1 and 5(b)). However, we see from the Cole–Cole plots, Figs. 2 and 5(a), that for both the nano and microcrystalline TiO_2 the resistivity is dominated by the grain interior (bulk). It also appears from Figs. 2 and 3 that the increased grain boundaries in nanocrystalline TiO_2 have the net effect of increasing impedance. The effects of densification by
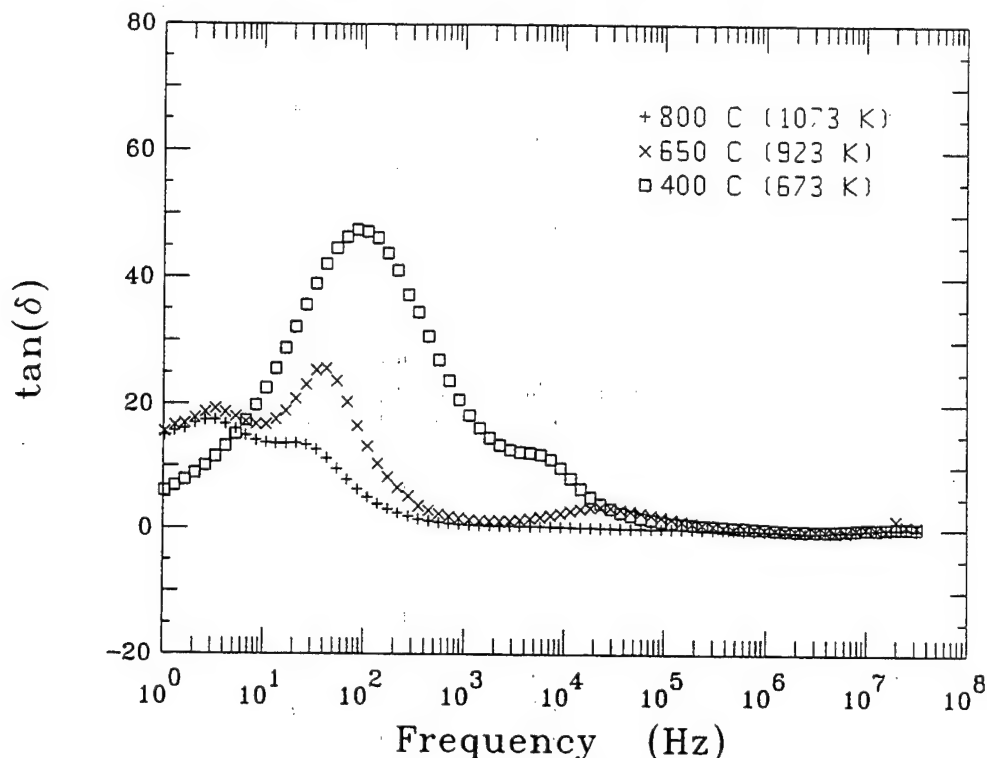
Fig. 8. Dielectric losses as a function of frequencies of nano-TiO$_2$ samples calcined at various temperatures.

sintering may reduce the magnitude of the resistance across the grain boundaries and cause a simultaneous decrease in the surface area associated with interface capacitance, and these elements are obviously in parallel. The conductivity of the grain boundaries is complex and is a function of any other phase present, porosity and grain size. At this point we do not have enough information to entail the detailed behavior of the grain boundaries.

The initial decrease in the overall impedance in Fig. 1 (or the increase in conductivity) and the behavior at the electrode interface is attributed to moisture within the apparatus and sample. Initially, with increasing temperature, the mobility of the (OH)$^-$ ions, which are initially formed by the dissociation of the water molecule into H$^+$ and (OH)$^-$, increases. The introduction of moisture at the surface probably occurs through simple adsorption and might even be due to the 'donor-like' behavior of adsorbed water in semiconductors [15]. Subsequently, with increasing temperature, drying of the sample and its surrounding occurs; with escape of total moisture present, there is a decrease in conductivity or an increase in impedance. Although the mobility of the (OH)$^-$ ions at higher temperatures may increase, there is an overall decrease in the amount of moisture and (OH)$^-$ ions available at higher temperatures. Therefore an increase in impedance occurs at temperatures around 378 K. The samples with high porosity have an enhanced response as they have a larger exposed surface. The samples calcined at higher tempera-

tures (> 650°C) do not have high porosity and have decreased grain boundaries, and subsequently the effect of moisture is not exhibited. Figs. 7(a)–(e) show the SEM and TEM micrographs of microcrystalline TiO$_2$ and nanocrystalline TiO$_2$ samples calcined at different temperatures. From these photo-micrographs it is observed that the grain growth does occur after calcining at 650°C.

The bulk conductivity of microcrystalline TiO$_2$ (rutile) has been proposed as due to the presence of titanium (both Ti^{3+} and Ti^{4+}) interstitials and oxygen vacancies [1]. Considering the simple semiconductor band model, the conductivity is expected to increase with increasing temperature since there is an increase in the number of charge carriers. However, complex defect reactions in this material are not well understood. These defect reactions are also not expected to dominate at lower temperatures in the case of microcrystalline TiO$_2$.

An analysis of XRD spectra confirm the presence of two phases in both nanocrystalline and microcrystalline TiO$_2$. Microcrystalline TiO$_2$ specimens sintered at 800°C reveal the dominant rutile phase (~ 80%) and the rest as anatase. XRD studies of nanocrystalline TiO$_2$ samples show a similar dominant rutile phase and some anatase [16]. The presence of the two phases is consistent with the distorted arcs in Figs. 2 and 5(a), representing the bulk impedance. It has also been reported by Eastman [16] that the conversion of anatase to rutile in nanocrystalline TiO$_2$ is completed after

annealing at 1073 K. This is also consistent with our previous observation for the bulk effect (arc) in Fig. 3, although there still exists some indication of another phase.

On the basis of the above discussions, we can see the presence of a resistive (R_e) and a capacitive element (C_e) at the electrode interface. The resistance may be associated with a chemical reaction at the electrode, TiO_2 and air interface. There is also resistive (R_i) and capacitive (C_i) behavior (in parallel) at the grain boundaries. Finally, we have the bulk or the grain resistance (R_g) and capacitance (C_g), which may be the combination of more than one phase present. The combination of all these elements can be represented as an equivalent circuit, for nanocrystalline TiO_2. The magnitudes of the individual elements associated with each of the effects could be estimated from extrapolation of the data in Fig. 2.

4. Conclusions

Nanocrystalline titania calcined at lower temperatures with a detailed pore structure exhibits enhanced sensitivity to changes in ambient atmosphere, especially in the case of humidity, which is reflected by changes in impedance (or conductivity). It is evident from the above studies that impedance spectroscopy is an effective method to observe the said behavior. It is also evident that further studies are required to determine the effects of different kinds of electrode material, different partial pressures of oxygen, controlled humidity conditions, and different (both lower and higher temperature ranges) before any definite conclusion can be drawn. Our IS studies, have also shown that the loss tangent, $\tan(\delta)$, Eq. (4), for nanocrystalline samples declines with increased sintering temperature (Fig. 8) in the frequency range 1 Hz to 10^6 Hz and, for samples calcined at high temperatures, this loss remains constant in the temperature range studied. This is one of

the important features of low lossy capacitors. Further studies of this aspect should also be considered. An attempt will be made to further discuss these topics in the next paper of this series.

Acknowledgments

References

[1] R.N. Bluementhal, J. Baukus and W.M. Hirthe, *J. Electrochem. Soc.: Solid State Science, 114* (1967) 172.
[2] D.S. Tannhauser, *Experimental Evidence from Conductivity Measurements for Interstitial Titanium in Reduced TiO₂, Solid State Communications, Vol. 1*, Pergamon Press, US, 1963, p. 223.
[3] A.L. Micheli, *Am. Ceram. Soc. Bull., 63 (5)* (1984) 694.
[4] A.M. Azad, L.B. Younkman, S.A. Akbar and M.A. Alim, *J. Am. Ceram. Soc., 77 (2)* (1994) 481.
[5] J.E. Bauerle, *J. Phys. Chem. Solids, 30* (1969) 2657.
[6] J. Ross Macdonald, *Impedance Spectroscopy Emphasizing Solid Materials and Systems*, Wiley, New York, 1987, pp. 3–20.
[7] B. Tareev, *Physics of Dielectric Materials*, Mir, Moscow, 1979. pp. 141–173.
[8] L. Ketron, *Ceram. Soc. Bull., 68 (4)* (1989).
[9] R.W. Siegel, S. Ramaswamy, H. Hahn, L. Zongquan, L. Ting and R. Gronsky, *J. Mater. Res., 3* (1988) 1367.
[10] J.C. Parker and R.W. Siegel, *J. Mater. Res., 5 (6)* (1990) 1246.
[11] H.K. Patel, *Ph.D. Thesis*, Iowa State University, 1993.
[12] K.S. Cole and R.H. Cole, *J. Chem. Phys., 9* (1941) 341.
[13] E.J.L. Schouler, N. Mesbahi and G. Vitter, *Solid State Ionics, 9&10* (1983) 989.
[14] H. Hahn, J. Logas and R.S. Averback, *J. Mater. Res., 5 (3)* (1990) 609.
[15] M.J. Madou and S.R. Morrison, *Chemical Sensing with Solid State Devices*, Academic Press, New York, 1989, pp. 506–513.
[16] J.A. Eastman, *J. Appl. Phys., 75 (2)* (1994).

ELSEVIER

Processing and structural evolution of nanocrystalline Cu–CeO_{2-x} catalysts

Andreas Tschöpe[a,1], Jackie Y. Ying[a,*], Yet-Ming Chiang[b]

[a]Department of Chemical Engineering and [b]Department of Materials Science and Engineering, Massachusetts Institute of Technology, Cambridge, MA 02139, USA

Abstract

Inert gas condensation synthesis and post-treatment of nanocrystalline Cu–CeO_{2-x} were found to provide unique control of the structural evolution of this system. X-ray diffraction and scanning transmission electron microscopy were employed to follow the phase transformation, morphological changes, and chemical dispersion in this material. A strong interaction existed between the components to provide a high dispersion of Cu on CeO_{2-x} that was stable through high temperature treatments. The interstitial and surface dispersion of Cu were related to the system's excellent catalytic performance in CO oxidation.

Keywords: Gas condensation synthesis; Copper; Oxidation

1. Introduction

Metal oxides are widely used as catalysts for oxidation reactions. In general, the catalytic activity of oxides is derived through (i) their provision of adsorbed surface oxygen species for reactions, and/or (ii) easy extraction of their lattice oxygen to form oxygen vacancies in the oxide structure. Cerium oxide has a unique combination of properties which makes it attractive for catalytic oxidation. It exhibits large deviations from stoichiometry under low oxygen partial pressure, enabling high surface reducibility. As a fluorite-structured oxide, it further provides high oxygen ion mobility. We have found that highly non-stoichiometric CeO_{2-x} nanocrystals with high surface area could be synthesized by inert gas condensation [1]. Because of the high melting point of cerium oxide (2600 °C), the nanocrystals derived were thermally stable against grain growth or sintering below 600 °C. This combination of structural characteristics has proven to be extremely useful in our development of nanocrystalline CeO_{2-x} for cata-

lyzing redox and oxidation reactions. The non-stoichiometric CeO_{2-x}-based nanocrystalline catalysts provided excellent activity for SO_2 reduction by CO, CO oxidation, and CH_4 oxidation [2–4]. They offered a lower activation temperature for all three reactions than the ultrafine chemically precipitated stoichiometric CeO_2-based materials. In SO_2 reduction, nanocrystalline CeO_{2-x}-based catalysts further provided negligible hysteresis in the activity profile and unusually high resistance against CO_2 poisoning. We have found that Cu-doped CeO_{2-x} nanocrystals demonstrated the best catalytic activity for selective SO_2 reduction by CO and for CO oxidation. This system also showed enhanced reversible surface reducibility in pulsed reduction–oxidation studies [5].

In this study, we would like to focus on understanding the promoting effect of Cu for the CO oxidation reaction, whereby Cu doping of CeO_{2-x}-based nanocrystals enabled a significant decrease in reaction temperature of about 100 °C. The improved catalytic activity of Cu–CeO_{2-x} might be related to (i) the presence of Cu ions at the surface as preferred adsorption sites for CO, and/or (ii) the interstitial Cu ions that would stabilize Ce^{3+} ions, enhancing the availability of chemisorbed O_2^- species. This paper describes the evolution of the structure and Cu dispersion in nanocrys-

---

[1] Present address: Universität des Saarlandes, Physik, Postfach 15 11 50, FB 10, Bau 43, D-66041 Saarbrücken, Germany.
[*] Corresponding author.

talline $Cu-CeO_{2-x}$ during heat treatments. The changes in morphology and $Cu-CeO_{2-x}$ interaction for this mixed oxide system are linked to the catalytic behavior of the differently treated samples. Establishing such relationships provides insights into the origin of the enhanced catalytic behavior of Cu doping, and helps us in optimizing the catalyst processing conditions for the unique nanocrystalline system synthesized by inert gas condensation and controlled post-oxidation.

2. Experimental details

Nanocrystalline materials were generated in an ultra-high vacuum (UHV) chamber by magnetron sputtering from a mixed metal target of $Cu_{0.15}Ce_{0.85}$ in argon (30 Pa). The metal vapor was thermalized by the inert gas atmosphere and nucleated to form nanometer-sized clusters. The nanoclusters were collected on a liquid-nitrogen-cooled modified ground shield substance [1]. After sputtering for 20 min, the UHV chamber was evacuated and slowly back-filled with oxygen to a final pressure of 1 kPa. This caused partial oxidation of the nanoclusters, indicated by a color change from black to brown. The clusters were scraped off from the substrate, and were either collected as loose powders or compacted under a pressure of 0.5 GPa into porous self-supporting pellets.

Uncompacted powders were used in a packed bed microreactor for catalytic testing. The samples (approximately 100 mg) were supported on a quartz frit in a quartz tube heated by a tube furnace. They were annealed in the microreactor under a gas flow of $1\%CO_2$-He for 12 h at temperatures between 211 °C and 611 °C. After each thermal treatment, the CO oxidation catalytic activity profile of the samples was obtained under steady state reaction conditions. The reactants, 2% CO and 16% O_2, were diluted in He and N_2 and passed over the catalyst at 100 $cm^3 min^{-1}$ for a typical contact time of 0.09 s g cm^{-1} (STP). The composition of the effluent gas was analyzed by a HP-5880A gas chromatograph equipped with a thermal conductivity detector. The catalytic activities of the differently treated samples were compared based on their light-off temperatures at which 50% conversion was achieved.

To follow the structural evolution of the samples, nanostructural pellets were annealed at increasing temperatures in $15\%O_2$-Ar atmosphere for 10 h. X-ray diffraction (XRD) characterizations were performed on the pellets using a Rigaku rotating anode X-ray generator with Cu radiation and Ni filter. Diffraction peak widths were determined by least-square fit of a Cauchy function. The mean crystallite size in each sample was calculated with the Scherrer equation [6], after subtracting out the instrumental line broadening from the Kochendoerfer analysis [7] of the (111) and (222) peaks.

To investigate the sample morphology and Cu dispersion, we employed scanning transmission electron microscopy (STEM) using microscopes equipped with a Link System energy dispersive X-ray fluorescence analyzer for chemical analysis. Uncompacted nanoclusters were annealed at temperatures of interest in $15\%O_2$-Ar atmosphere for 10 h. Gold grids with carbon film were dipped into the annealed powder samples and examined with a Vacuum Generators HB603 STEM (250 kV) or a Vacuum Generators HB5 STEM (100 kV).

3. Results

The effects of annealing pre-treatment of $Cu-CeO_{2-x}$ nanocrystalline catalyst on CO oxidation activity are illustrated in Fig. 1. For samples heated at 211 °C and 311 °C, the light-off temperature was 110 °C. This compared favorably with the pure CeO_{2-x} nanocrystalline sample which required a light-off temperature of 190 °C. The lower light-off temperature of $Cu-CeO_{2-x}$ denotes a promoting effect on catalytic activity from Cu doping. We found that annealing of the nanocrystalline $Cu-CeO_{2-x}$ at 411 °C further reduced the light-off temperatures to 85 °C. Higher annealing temperatures of 511 °C and 611 °C did not correspond to additional changes in catalytic activity.

XRD characterization of the as-prepared $Cu-CeO_{2-x}$ gave only the cubic pattern of the fluorite-structured cerium oxide. Annealing to 500 °C produced similar XRD pattern and peak widths, indicating that only cerium oxide phase with crystals of approximately
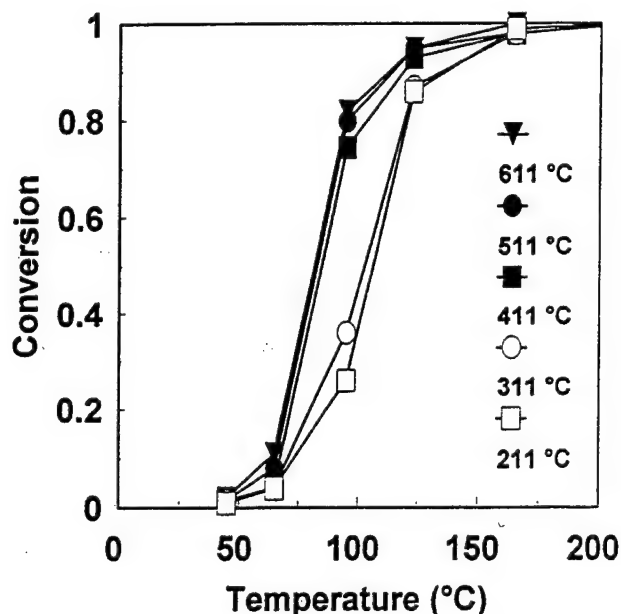
Fig. 1. Catalytic CO oxidation conversion of nanocrystalline $Cu-CeO_{2-x}$ as a function of reaction temperature after sample annealing at the indicated temperatures.
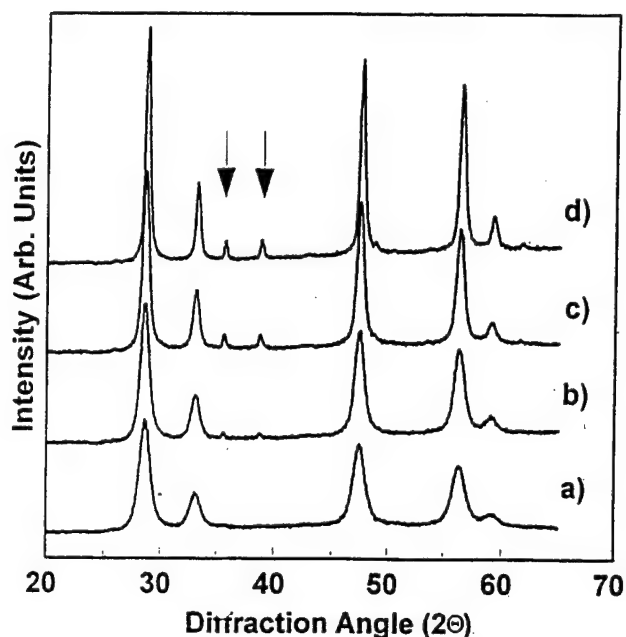
Fig. 2. XRD pattern of nanocrystalline Cu–CeO$_{2-x}$ after annealing in 15%O$_2$–Ar atmosphere at (a) 500 °C, (b) 550 °C, (c) 600 °C, and (d) 650 °C. The diffraction peaks associated with the CuO phase are marked by arrows.

Fig. 4. X-ray fluorescence spectra of Cu–CeO$_{2-x}$: (a) at the center of a grain and (b) at the edge of a grain.

5 nm was present for treatments below or up to 500 °C (Fig. 2). CuO was found as a second phase in samples heated at 550 °C or above. The formation of a separate CuO phase coincided with the commencement of CeO$_{2-x}$ grain growth (see Fig. 3). The XRD phase analysis revealed a significant change in the microstructure of the material at 550 °C, indicating that much of

the Cu was not dispersed in the CeO$_{2-x}$ phase after this annealing temperature.

We note that the light-off temperature was lowered when the Cu–CeO$_{2-x}$ sample was treated to 411 °C. At this temperature range, XRD did not reveal any phase change or grain growth. To investigate the dispersion of Cu in CeO$_{2-x}$ of samples treated around this temperature, STEM studies were performed using the VG HB5 system on powdered Cu–CeO$_{2-x}$ samples heated to 450 °C. The electron beam was focussed to a 10 Å diameter spot at the center of a grain and the fluorescence spectrum taken is shown in Fig. 4(a). The beam was next positioned outside the grain and slowly moved towards its edge. A sudden increase in X-ray counting rate was used as an indication of the position of the edge of the grain, at which point another fluorescence spectrum was obtained (Fig. 4(b)). This set of experiments revealed that the Cu concentration at the edge of the cluster was about two times higher than that at the center of the grain.

VG HB603 STEM and elemental mapping were also employed for investigating the Cu dispersion in the Cu–CeO$_{2-x}$ sample annealed for 10 h at 650 °C. XRD results indicated that heat treatments between 550 °C and 650 °C produced distinct CuO phase in addition to the cerium oxide phase, however, a high catalytic activity was maintained between 411 °C and 611 °C. The STEM image and the elemental maps for Ce and Cu for the same section of the sample are illustrated in Fig. 5(a)–(c). These results confirmed that oxidation at 650 °C gave rise to large Cu-rich clusters. Nevertheless, a substantial portion of Cu remained highly dispersed in the sample even after this high temperature treatment (Fig. 5(c)).

Fig. 3. Volume-weighted mean CeO$_{2-x}$ grain size in the Cu–CeO$_{2-x}$ samples (as calculated from X-ray line-broadening) as a function of annealing temperature.

4. Discussion

The promoting effect of Cu on catalytic CO oxidation was evident from the decrease in light-off temperature from 190 °C for pure CeO_{2-x} to 110 °C for $Cu-CeO_{2-x}$ [4]. However, the as-prepared sample was not the most active state of the $Cu-CeO_{2-x}$ system. The light-off temperature could be further reduced to 85 °C by first annealing $Cu-CeO_{2-x}$ at 411 °C. Sample heat treatment at higher temperatures did not affect the catalytic activity further. However, XRD indicated that copper oxide underwent a phase separation from cerium oxide only after thermal annealing above 550 °C, at which temperature a distinct CuO phase is noted in addition to the cerium oxide peaks present. To elucidate the relationship between catalytic behavior and structural evolution in the $Cu-CeO_{2-x}$ catalysts, we focussed on the issue of Cu dispersion in cerium oxide following the various stages of thermal treatment.

Our preparation of $Cu-CeO_{2-x}$ catalyst is unique in that inert gas condensation was employed to generate this material first as $Cu_{0.15}Ce_{0.85}$ alloy nanoclusters through magnetron sputtering from a mixed metal target. The phase diagram of metallic Cu and Ce [8] shows a series of intermetallic phases indicating chemical affinity and ionic radius mismatch between Cu and Ce. Inert gas condensation does not yield such intermetallic phases readily because of the high quenching rate during thermalization. Therefore, vapor phase synthesis resulted in nanoclusters of a homogeneously dispersed Cu–Ce solid solution. The as-prepared samples were derived from controlled post-oxidation of these Cu–Ce nanoclusters. Unfortunately, the miscibility of the Cu–Ce–O system was not described in any existing phase diagram. We note however that Cu exhibits very low solubility in ZrO_2 [9], which shares the same crystal structure as CeO_2. Taking into account that Ce is an even larger cation than Zr, one might expect that the same low solubility would be true for Cu in CeO_2. However, recent EPR studies indicate that Cu possesses a small solubility in CeO_2 in the form of Cu(II) ion pairs [10]. Cu might also be present in eightfold-coordinated interstitial sites as reported in the case of Cu–ThO_2 [11], or be highly dispersed on surface sites.
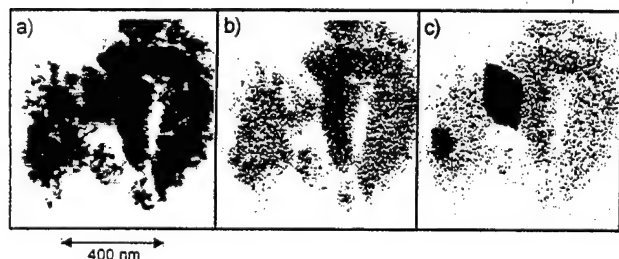
Fig. 5. STEM image (a), Ce elemental map (b), and Cu elemental map (c) of the $Cu-CeO_{2-x}$ samples after annealing at 650 °C.

Considering these thermodynamic constrains, one might anticipate that the $Cu_{0.15}Ce_{0.85}$ nanoclusters underwent the following structural evolution in post-oxidation and thermal treatments: (i) a solid solution of metallic Cu and Ce prior to significant oxidation; (ii) a supersaturated solid solution of Cu in CeO_{2-x} after post-oxidation; (iii) segregation of Cu to the surface of CeO_{2-x} nanocrystals on low-temperature annealing; (iv) formation of a separate copper oxide phase after high-temperature thermal treatment.

The increase in catalytic activity indicated by a lower light-off temperature after annealing at 411 °C might be explained by the segregation of Cu to the surface of possibly supersaturated $Cu-CeO_{2-x}$ grains. At 311 °C or lower temperatures, Cu and CeO_{2-x} might have existed as a solid solution, with the probable interstitial Cu ions in the CeO_{2-x} phase providing the dominant catalytic promoting effects. By treating to 411 °C, surface Cu ions became available from solute segregation in addition to interstitial Cu ions. This is suggested by the STEM results after annealing at 450 °C (see Fig. 5). The Cu concentration at the edge of a CeO_{2-x} nanocrystal was measured to be twice as high as in the center of the grain. The increase in Cu concentration at the surface would provide more active adsorption sites for CO. This might explain the enhanced catalytic activity, which corresponded to a decrease in light-off temperature from 110 °C to 85 °C.

At 550 °C and above, a bulk CuO phase became distinct in addition to the cerium oxide XRD peaks. Substantial grain growth was also noticed by 600 °C. Both of these factors suggested a reduction of Cu dispersion in cerium oxide. However, the low light-off temperature was maintained between 411 °C and 611 °C. This could be explained by (i) a reaction mechanism in which catalytic activity is not dependent on Cu dispersion, or (ii) the sustenance of a high catalytic activity by the presence of residual high dispersed Cu. The second STEM experiment on samples treated at 650 °C illustrated that while the large CuO particles indicated in XRD results were indeed present, substantial Cu remained dispersed within the CeO_{2-x} clusters or on their surfaces. It is unusual to see such high dispersion of a base metal on an oxide support at such high temperatures. It may be attributed to the unique interaction between Cu and CeO_{2-x}, and to the stable support CeO_{2-x} nanocrystals were able to provide. We can also conclude that for this reaction, as long as some Cu remained highly dispersed, the superb catalytic performance will be maintained. This study further indicates that for the Cu-doped CeO_{2-x} system, the Cu dispersion and solubility are the promoting effects that outweigh the non-stoichiometry effect of CeO_{2-x}, since the latter would be negligible after essentially complete oxidation at 600 °C [5,12] yet the excellent catalytic activity remained unchanged at 611 °C.

5. Summary

Nanostructure processing by gas condenstion was employed in the derivation of novel $Cu-CeO_{2-x}$ nanocrystalline catalysts to offer ultrahigh dispersion and unique interactions in multicomponent systems. Starting from a Cu–Ce nanoalloy, structural evolution could be induced in this material through controlled oxidation and gradual thermal treatment to produce (i) a possible supersaturated solid solution of Cu and CeO_{2-x}, (ii) a segregation effect for ultrahigh Cu dispersion on CeO_{2-x} nanocrystals, and (iii) a distinct separate copper oxide phase. The promoting effect of Cu in CO oxidation was noted even at room temperature when only the interstitial Cu ions might have been present in solid solution with CeO_{2-x}, serving towards stabilizing Ce^{3+} ions and enhancing the availability of chemisorbed O_2^- species. Cu segregation was found after thermal treatment at around 411 °C, creating surface sites that facilitated CO adsorption for further improvement in catalytic performance. Even at high temperatures when CuO phase separation was noted, these two mechanisms continued to be active owing to the presence of residual Cu that was highly dispersed on cerium oxide.

This study demonstrates the potential of generating strong synergistic effects with nanocomposite processing for optimizing catalytic performance. In particular, we have shown that it is posssible to achieve ultrahigh Cu dispersion on CeO_{2-x} nanocrystals for outstanding CO oxidation characteristics. The achievement of 100% CO conversion to CO_2 at temperatures below 100 °C is very attractive for automotive emission control under cold-start conditions. The remarkably low reaction temperature requirement is noteworthy since it was accomplished with a supported base metal system, without the usual expensive noble metal additives.

Acknowledgements

References

[1] A. Tschöpe and J.Y. Ying, *Nanostruct. Mater.*, 4 (1994) 617.
[2] A. Tschöpe and J.Y. Ying, in G.C. Hadjipanayis and R.W. Siegel (eds.), *Nanophase Materials: Synthesis–Properties–Applications*, Kluwer, Dordrecht, 1994, p. 781.
[3] A. Tschöpe, J.Y. Ying, W. Liu and M. Flytzani-Stephanopoulos. *Mater. Res. Soc. Symp. Proc.*, 344 p. 133.
[4] A. Tschöpe, W. Liu, M. Flytzani-Stephanopoulos and J.Y. Ying. Redox activity of non-stoichiometric cerium oxide-based nanocrystalline catalysts, *J. Catal.*, in press.
[5] A. Tschöpe, J.Y. Ying, K. Amonlirdviman and M.L. Trudeau. *Mater. Res. Soc. Symp. Proc.*, 351 (1994) 251.
[6] B.D. Cullity, *Elements of X-Ray Analysis* Addison-Wesley. Reading, MA, 1978 p. 284, 2nd edn.
[7] Z. Kochendoerfer, *Kristallogr. Mineral. Petrochem.*, 105 (1944) 393.
[8] P.R. Subramanian and D.E. Laughlin, in T.B. Massalski (ed.). *Binary Alloy Phase Diagrams*, Vol. 2, ASM International Metals Park, OH, 1990, p. 1051, 2nd edn.
[9] E.M. Levin, C.R. Robbins and H.F. McMurdie, in M.K. Reser (ed.), *Phase Diagrams for Ceramists*, *1969 Supplement*, American Ceramic Society, Columbus, OH, 1969.
[10] A. Aboukais, A. Bennani, C.F. Aissi, M. Guelton and J.C. Vedrine, *Chem. Mater.* 4 (1992) 977.
[11] R. Bechara, G. Wrobel, C.G. Aissi, M. Guelton. J.P. Bonnelle and A. Aboukais, *Chem. Mater.*, 2 (1990) 518.
[12] M.L. Trudeau, A. Tschöpe and J.Y. Ying, XPS investigation of surface oxidation and reduction in nanocrystalline $Ce_xLa_{1-x}O_{2-y}$. *Surf. Interface Anal.*, 23 (1995) 219.

Author Index of Volume 204

Ali, M. 258
Andres, R.P. 160
Averback, R.S. 54, 96

Bandow, S. 222
Bhowmik, S. 258
Bi, X.-X. 222
Bossel, C. 107
Bryden, K.J. 140
Buehler, M.F. 252
Buhro, W.E. 193
Bunker, B.C. 169

Castro, D.T. 65
Celino, M. 101
Chiang, Y.-M. 267
Christodoulides, J.A. 30
Cichowlas, A.A. 186
Constant, K.P. 258
Corrias, A. 211
Crawford, P.J. 217

Darab, J.G. 252
D'Agostino, G. 101
Dimitrov, D.V. 25
Dormann, J.L. 165
Dutta, J. 107

Eklund, P.C. 222
Ennas, G. 211
Erb, U. 34, 227

Fang, M. 186
Ferber, M. 1
Filz, T. 43
Fiorani, D. 165
Flagan, R.C. 113
Fougere, G.E. 1

Gell, M. 246
Gibson, J.M. 54
Gleiter, H. 76
Graff, G.L. 169

Hadjipanayis, G.C. 25, 30, 39
Hague, D.C. 83
He, L. 240
Higashi, K. 12
Hilborn, J. 107
Hofmann, H. 107
Holden, J.M. 222
Houriet, R. 107
Huang, B. 217
Huang, J. 205

Hwang, J.-H. 252
Hyeon, T. 186

Ishikawa, K. 12

Jones, R.H. 169

Kirkpatrick, E.M. 19
Krauß, W. 43

Lauer, S. 43
Lavernia, E.J. 217
Lee, W.-T. 222
Lenk, T.J. 59
Liao, S.-C. 152
Linehan, J.C. 252
Liu, J. 169
Lukehart, C.M. 176
Lunden, M.M. 113
Luo, P. 59, 181
Lu, W. 205

Ma, E. 240
Mahoney, W. 160
Majetich, S.A. 19
Maknani, J. 165
Marongiu, G. 211
Maruyama, Y. 222
Mason, T.O. 252
Matson, D.W. 252
Mayo, M.J. 83
Mayo, W.E. 152
McGinn, J.T. 135
McHenry, M.E. 19
Mehta, S.C. 227
Milne, S.B. 176
Montone, A. 165
Mukai, T. 12
Mukherji, T. 135
Murthy, A.S. 25, 30, 39
Musinu, A. 211

Nieh, T.G. 59

Ochoa, R. 222
Olynick, D.L. 54

Pae, K.D. 152
Page, R.A. 201
Pan, Y.-M. 197
Parker, J.C. 258
Paschina, G. 211
Paul, P.P. 197
Perez, R.J. 217

Phillpot, S.R. 76

Rankin, J. 48
Riester, L. 1
Risbud, S.H. 146
Romero, H. 165
Rosato, V. 101

Sanders, P.G. 7
Sastry, S.M.L. 193
Schwab, S.T. 201
Schwab, S.T. 197
Schwartz, A.J. 59
Shan, C.-H. 146
Sharif, A.A. 217
Sheldon, B.W. 48
Shevchenko, N.B. 39
Shull, R.D. 176
Siegel, R.W. 1, 7
Singh, B. 135
Smith, D.A. 227
Spaepen, F. 71
Stock, S.R. 176
Strutt, P.R. 181
Suber, L. 165
Suryanarayanan, R. 193
Suslick, K.S. 186

Testa, A.M. 165
Trentler, T.J. 193
Trudeau, M.L. 233
Tschöpe, A. 267
Turi, T. 34

Valiev, R.Z. 7
Virden, J.W. 169
Vittori, M. 165
Vlachos, D.G. 90

Wang, J. 76
Wang, L.Q. 169
Weertman, J.R. 1, 7
Wichert, T. 43
Witney, A.B. 7
Wittig, J.E. 176
Wolf, D. 76
Wolf, H. 43

Ying, J.Y. 65, 140, 267

Zedda, D. 211
Zhu, H. 96
Zimmer, H.G. 43
Zolla, H.G. 71

MATERIALS SCIENCE & ENGINEERING

A

Subject Index of Volume 204